

# **18<sup>th</sup> Symposium on Application of Plasma Processes**



## **Workshop on Plasmas as a Planetary Atmosphere Mimics**

### **Book of Contributed Papers**

Vrátna, Slovakia  
15-20 January, 2011

Edited by J. Országh, P. Papp, Š. Matejčík

Book of Contributed Papers: 18th Symposium on Application of Plasma Processes and Workshop on Plasmas as a Planetary Atmospheres Mimics, Vrátna, 15.-20.1.2011

Symposium organised by Department of Experimental Physics, Faculty of Mathematics, Physics and Informatics, Comenius University in Bratislava; Society for Plasma Research and Applications, in Vrátna dolina hotel Boboty, 15-20 January 2011

Editors: J. Országh, P. Papp, Š. Matejčík

Publisher: Department of Experimental Physics, Faculty of Mathematics, Physics and Informatics, Comenius University in Bratislava (Slovakia); Society for Plasma Research and Applications in cooperation with Library and Publishing Centre CU, Bratislava, Slovakia

Issued: January 2011, Bratislava, fist issue

Number of pages: 347

Print: 100 pieces

URL: <http://neon.dpp.fmph.uniba.sk/sapp>

ISBN: 978-80-89186-77-8

EAN: 9788089186778



THE WORLD'S  
LEADING  
PTR-MS  
COMPANY PRESENTS

PROTON TRANSFER REACTION - MASS SPECTROMETRY



HIGH-RESOLUTION  
ULTRA-SENSITIVE  
VOC ANALYSIS  
IN REAL-TIME

## PTR-TOFMS SERIES



- Two different high-resolution time of flight variants
- Mass resolution up to 8000  $m/\Delta m$
- Single-digit pptv-level sensitivity ( $< 5$  pptv)
- Full mass range acquisition in a split-second
- Separation of isobaric compounds
- Direct air sampling without preparation
- Soft chemical ionization with  $H_3O^+$ , optionally  $NO^+$  and  $O_2^+$  (SRI: Switchable Reagent Ions)



## PTR-QMS SERIES

- Three different quadrupole variants
- Mass range up to 512 amu
- Detection limit as low as 1 pptv
- Direct air sampling without preparation
- Soft chemical ionization with  $H_3O^+$ , optionally  $NO^+$  and  $O_2^+$  (SRI: Switchable Reagent Ions)

[www.PTRMS.com](http://www.PTRMS.com)

THE SOLUTION FOR REAL-TIME TRACE GAS ANALYSIS

## **International Scientific & Organizing Committee**

|                  |   |                  |
|------------------|---|------------------|
| Miroslav Cernak  | Masaryk University, Brno                | (Czech Republic) |
| Zoltan Donko     | Hungarian Academy of Sciences, Budapest | (Hungary)        |
| Nigel J. Mason   | Open University, Milton Keynes          | (United Kingdom) |
| Tilmann D. Märk  | Leopold-Franzens University, Innsbruck  | (Austria)        |
| Jerzy Mizeraczyk | Polish Academy of Sciences, Gdansk      | (Poland)         |

## **Local Organizing Committee**

|                 |   |            |
|-----------------|---|------------|
| Stefan Matejcik | Chairman, Comenius University, Bratislava | (Slovakia) |
| Peter Papp      | Comenius University, Bratislava           | (Slovakia) |
| Juraj Orszagh   | Comenius University, Bratislava           | (Slovakia) |
| Michal Matejka  | Comenius University, Bratislava           | (Slovakia) |

## **Reading Committee**

|                 |                                 |                  |
|-----------------|---------------------------------|------------------|
| Stefan Matejcik | Comenius University, Bratislava | (Slovakia)       |
| Peter Papp      | Comenius University, Bratislava | (Slovakia)       |
| Juraj Orszagh   | Comenius University, Bratislava | (Slovakia)       |
| Gabriel Horvath | Comenius University, Bratislava | (Slovakia)       |
| Nigel J. Mason  | Open University, Milton Keynes  | (United Kingdom) |
| Frantisek Krcma | Brno University of Technology   | (Czech Republic) |

## **Jan D. Skalny's Prize Awarding Committee**

|                      |   |                  |
|----------------------|---|------------------|
| Stefan Matejcik      | Comenius University, Bratislava         | (Slovakia)       |
| Nigel J. Mason       | Open University, Milton Keynes          | (United Kingdom) |
| Antoni Jowko         | Siedlce University                      | (Poland)         |
| Frantisek Krcma      | Brno University of Technology           | (Czech Republic) |
| Zoltan Donko         | Hungarian Academy of Sciences, Budapest | (Hungary)        |
| Ralf Peter Brinkmann | Ruhr University Bochum                  | (Germany)        |
| Bill Graham          | Queens University Belfast               | (United Kingdom) |

## **Organizers**

Department of Experimental Physics, Comenius University, Bratislava, Slovakia  
Society for Plasma Research and Applications, Bratislava, Slovakia

## Conference Topics

1. Electrical discharges and other plasma sources
2. Elementary processes and plasma chemical reactions
3. Plasma-surface interactions
4. Plasma treatment of polymer and biological material
5. Nanometer-scaled plasma technologies

## Invited Speakers

|                      |   |                  |
|----------------------|---|------------------|
| Pierre Defrance      | Catholic University of Louvain, Louvain-la-Neuve    | (Belgium)        |
| Kurt Becker          | NYU-Poly, Brooklyn NY                               | (USA)            |
| Bill Graham          | Queens University Belfast                           | (United Kingdom) |
| Tilman D. Märk       | Leopold-Franzens University, Innsbruck              | (Austria)        |
| Juergen Roepcke      | INP Greifswald                                      | (Germany)        |
| Mirosław Dors        | Polish Academy of Sciences, Gdansk                  | (Poland)         |
| Hassan Abdoul-Carime | Institut de Physique Nucléaire - Lyon, Villeurbanne | (France)         |
| Ralf Peter Brinkmann | Ruhr University Bochum                              | (Germany)        |
| Radomir Panek        | Academy of Sciences of the Czech Republic, Prague   | (Czech Republic) |
| Ihor Korolov         | Hungarian Academy of Sciences, Budapest             | (Hungary)        |
| Tom Field            | Queens University Belfast                           | (United Kingdom) |
| Juraj Glosik         | Charles University in Prague                        | (Czech Republic) |
| Nathalie Carrasco    | Université de Versailles St Quentin, Guyancourt     | (France)         |

## Workshop on Plasmas as a Planetary Atmosphere Mimics

**Sunday, January 16**

**16:45 – 20:45**

|                   |   |                  |
|-------------------|---|------------------|
| Nigel Mason       | Open University, Milton Keynes                  | (United Kingdom) |
| Nathalie Carrasco | Université de Versailles St Quentin, Guyancourt | (France)         |
| Juraj Orszagh     | Comenius University, Bratislava                 | (Slovakia)       |
| Frantisek Krcma   | Brno University of Technology                   | (Czech Republic) |
| Daniela Ascenzi   | University of Trento, Povo, Trento              | (Italy)          |
| Zoltan Donko      | Hungarian Academy of Sciences, Budapest         | (Hungary)        |

## Foreword

The 18<sup>th</sup> Symposium on Applications of Plasma Processes (SAPP XVIII) is held in Vrátna dolina, the famous valley, in Slovakia from January 15 till January 20, 2011 under the sponsorship of the Society for Plasma Research and Applications and Department of Experimental Physics, Comenius University. For the first time SAPP comes to this part of Slovakia. Vrátna dolina is part of the National Park "Malá Fatra". The SAPP conference is a unique occasion for the plasma scientists to interact with colleagues from abroad in order to establish links that could strengthen the plasma research especially in the Central Europe.

The CD book includes the contributed papers of the invited lectures, progress reports and posters presented at the conference. That is 74 contributions altogether. The invited speakers were chosen by the International Scientific Committee (ISC). The contributed papers have been referred by the reading committee. The ISC has invited 12 outstanding scientists to present their results in the form of invited talks (45 minutes). The local organizing committee has selected 16 contributed papers to be presented in the form of short (25 minutes) talks.

The main topics of the SAPP conferences are:

1. Electrical discharges and other plasma sources
2. Elementary processes and plasma chemical reactions
3. Plasma-surface interactions
4. Plasma treatment of polymer and biological material
5. Nanometer-scaled plasma technologies

The CD also includes 1 invited lecture and 5 short lectures selected by the workshop convenors for oral presentations at the **Workshop on Plasmas as a Planetary Atmosphere Mimics**.

As a new feature of SAPP, the ISC and LOC has announced the creation of a new prize, the "**Jan D. Skalny**" prize for young scientists and students. The prize will be awarded to the best young speaker (up to 35 years old) and to the best poster in each poster session. International committee composed of prominent participants will decide on prize holders.

We hope that everyone will enjoy the conference, leisure activities and their stay in Vrátna dolina.

LOC of the SAPP XVIII

## Contents

|  |                                       |    |
|--|---------------------------------------|----|
| <i>Tilman D. MÄRK</i>  | <i>Innsbruck (AUSTRIA)</i>            |    |
| PTR-MS AND BEYOND: FUNDAMENTALS, DEVELOPMENTS AND APPLICATIONS                                       |                                       | 14 |
| <i>Kurt BECKER</i>   | <i>Brooklyn, NY (USA)</i>             |    |
| ATMOSPHERIC-PRESSURE PLASMAS: SCIENTIFIC CHALLENGES AND TECHNOLOGICAL OPPORTUNITIES                  |                                       | 19 |
| <i>Radomir PANEK</i>   | <i>Prague (CZECH REPUBLIC)</i>        |    |
| STATUS OF FUSION RESEARCH IN TOKAMAKS  |                                       | 24 |
| <i>Nigel J. MASON</i>  | <i>Milton Keynes (UNITED KINGDOM)</i> |    |
| PLASMA DISCHARGES AS A PROBE OF CHEMICAL PROCESSES IN PLANETARY ATMOSPHERES                          |                                       | 25 |
| <i>Nathalie CARRASCO</i>   | <i>Guyancourt (FRANCE)</i>            |    |
| GAS PHASE CHEMISTRY IN A PLASMA SETUP SIMULATING TITAN ATMOSPHERIC REACTIVITY                        |                                       | 34 |
| <i>Juraj ORSZAGH</i>   | <i>Bratislava (SLOVAKIA)</i>          |    |
| CORONA DISCHARGE AS AN ENVIRONMENT FOR SIMULATION OF PLASMA-CHEMICAL PROCESSES IN MARTIAN ATMOSPHERE |                                       | 41 |
| <i>Frantisek KRCMA</i>   | <i>Brno (CZECH REPUBLIC)</i>          |    |
| OPTICAL EMISSION SPECTROSCOPY OF ATMOSPHERIC PRESSURE DISCHARGES IN NITROGEN-METHANE GAS MIXTURES    |                                       | 46 |
| <i>Daniela ASCENZI</i>   | <i>Povo, Trento (ITALY)</i>           |    |
| CHEMISTRY OF MOLECULAR IONS IN PLANETARY ATMOSPHERES AND IN LABORATORY PLASMAS                       |                                       | 51 |
| <i>Zoltan DONKO</i>  | <i>Budapest (HUNGARY)</i>             |    |
| ELECTRON KINETICS IN AIR STUDIED BY MONTE CARLO SIMULATION   |                                       | 53 |
| <i>Pierre DEFRANCE</i>   | <i>Louvain-la-Neuve (BELGIUM)</i>     |    |
| ELECTRON IMPACT FRAGMENTATION OF MOLECULAR IONS  |                                       | 57 |
| <i>Karol WNOROWSKI</i>   | <i>Siedlce (POLAND)</i>               |    |
| ELECTRON IMPACT IONIZATION OF W(CO) <sub>6</sub> : APPEARANCE ENERGIES                               |                                       | 58 |

INFLUENCE OF ENVIRONMENT ON THE MOLECULAR PHOTODISSOCIATION: CLUSTER EXPERIMENTS 64

---

*Ralf Peter BRINKMANN* *Bochum (GERMANY)*

SIMULATION OF CAPACITIVELY COUPLED RF DISCHARGES, INCLUDING NONLINEAR ELECTRON RESONANT HEATING, THE ELECTRICAL ASYMMETRY EFFECT, ELECTROMAGNETIC EFFECTS IN LARGE AREA DISCHARGES 67

---

*Marija RADMILOVIC-RADJENOVIC* *Zemun (SERBIA)*

THE BREAKDOWN VOLTAGE CURVES IN ARGON DC AND RF DISCHARGES FROM LARGE TO SMALL GAP SIZES 70

---

*Hamind GHOMI* *Tehran (IRAN)*

DBD PULSED PLASMA FOR SURFACE STERILIZATION 75

---

*Martin SABO* *Bratislava (SLOVAKIA)*

FORMATION OF NEGATIVE IONS IN CORONA DISCHARGE STUDIED BY ION MOBILITY/MASS SPECTROMETRY TECHNIQUE: APPLICATION ON TRACE GAS DETECTION 79

---

*Zdenka KOZAKOVA* *Brno (CZECH REPUBLIC)*

DIAGNOSTICS OF ELECTRICAL DISCHARGES IN ELECTROLYTES: INFLUENCE OF ELECTRODE AND DIAPHRAGM CONFIGURATION 83

---

*Lucie NEMCOVA* *Brno (CZECH REPUBLIC)*

UNDER WATER DISCHARGE IN BUBBLES IN VERY LOW CONDUCTIVE SOLUTIONS 88

---

*Matej KLAS* *Bratislava (SLOVAKIA)*

THE VALIDITY OF THE PASCHEN'S LAW IN HOMOGENEOUS ELECTRIC FIELD AT MICROMETER SEPARATIONS 93

---

*Julian SCHULZE* *Budaörs (HUNGARY)*

SECONDARY ELECTRONS IN DUAL-FREQUENCY CAPACITIVELY COUPLED RADIO FREQUENCY DISCHARGES 98

---

*Julian SCHULZE* *Budaörs (HUNGARY)*

THE ELECTRICAL ASYMMETRY EFFECT IN MULTI-FREQUENCY CAPACITIVELY COUPLED RADIO FREQUENCY DISCHARGES 101

---

*Aranka DERZSI* *Budapest (HUNGARY)*

COMPARISON OF MODELING APPROACHES FOR THE CATHODE REGION OF DC GLOW DISCHARGES 104

|  |                                 |     |
|--|---------------------------------|-----|
| <i>Marek KUCERA</i>  | <i>Bratislava (SLOVAKIA)</i>    |     |
| DETERMINATION OF ELECTRON ATTACHMENT RATE AT AMBIENT PRESSURE USING THE LAMBERT-BEER LAW                         |                                 | 109 |
| <i>Seyed Hassan TAVASSOLI</i>  | <i>Tehran (IRAN)</i>            |     |
| NUMERICAL SIMULATION OF NANOSECOND LASER-INDUCED PLASMA EMISSION   |                                 | 113 |
| <i>Nail ASFANDIAROV</i>  | <i>Ufa (RUSSIA)</i>             |     |
| ROTATIONALLY EXCITED DIATOMIC $\text{Cl}_2^-$ ANION  |                                 | 118 |
| <i>Ivo SOURAL</i>  | <i>Brno (CZECH REPUBLIC)</i>    |     |
| STUDY OF PRESSURE AND TEMPERATURE INFLUENCE ON THE NITROGEN PLASMA UNDER DISCHARGE AND POST-DISCHARGE CONDITIONS |                                 | 124 |
| <i>Michal HLINA</i>  | <i>Prague (CZECH REPUBLIC)</i>  |     |
| USING OF PLASMA TORCH WITH GERDIEN ARC FOR PLASTIC TREATMENT   |                                 | 129 |
| <i>Matthias DAXNER</i>   | <i>Innsbruck (AUSTRIA)</i>      |     |
| SEQUENTIAL PENNING IONIZATION IN DOPED 4He NANO DROPLETS   |                                 | 133 |
| <i>Jana VYHNALIKOVA</i>  | <i>Brno (CZECH REPUBLIC)</i>    |     |
| DECOMPOSITION OF VOC IN SURFACE DIELECTRIC BARRIER DISCHARGES COMBINED WITH IN SITU PHOTOCATALYZIS               |                                 | 136 |
| <i>Frantisek KRCMA</i>   | <i>Brno (CZECH REPUBLIC)</i>    |     |
| TITRATION OF SELENIUM HYDRIDE INTO THE NITROGEN POST-DISCHARGE   |                                 | 141 |
| <i>Sean HAUGHEY</i>  | <i>Belfast (UNITED KINGDOM)</i> |     |
| DISSOCIATIVE ELECTRON ATTACHMENT TO FLUOROCARBONS  |                                 | 146 |
| <i>Peter PAPP</i>  | <i>Bratislava (SLOVAKIA)</i>    |     |
| ELECTRON IMPACT IONIZATION OF VALINE, LEUCINE AND ISOLEUCINE AMINO ACIDS   |                                 | 148 |
| <i>Karol WNOROWSKI</i>   | <i>Siedlce (POLAND)</i>         |     |
| LOW ENERGY ELECTRON INTERACTIONS WITH TUNGSTEN HEXACARBONYL  |                                 | 153 |
| <i>Wieslawa BARSZCZEWSKA</i>   | <i>Siedlce (POLAND)</i>         |     |
| ELECTRON ATTACHMENT TO SOME FLUORINATED ALCOHOLS   |                                 | 157 |

|  |                                |     |
|--|--------------------------------|-----|
| <i>Tomas KOTRIK</i>  | <i>Prague (CZECH REPUBLIC)</i> |     |
| EXPERIMENTAL STUDY OF COLLISIONAL RADIATIVE RECOMBINATION OF Ar <sup>+</sup> IONS AT LOW TEMPERATURES                |                                | 161 |
| <i>Petr DOHNAL</i>   | <i>Prague (CZECH REPUBLIC)</i> |     |
| STATE SELECTIVE RECOMBINATION OF PARA- AND ORTHO-H <sub>3</sub> <sup>+</sup> AT 140 K                                |                                | 166 |
| <i>Kim DONG HONG</i>   | <i>Jeju (KOREA)</i>            |     |
| DECOMPOSITION OF 1,1,1,2-TETRAFLUOROETHANE (HFC-134A) IN A NONTHERMAL PLASMA-CATALYTIC REACTOR                       |                                | 171 |
| <i>Jan MATUSKA</i>   | <i>Bratislava (SLOVAKIA)</i>   |     |
| VARIOUS METHOD OF THE THEORETICAL CALCULATION OF THE NO <sub>3</sub> <sup>-</sup> ION MOBILITY IN NITROGEN DRIFT GAS |                                | 174 |
| <i>Juraj GLOSIK</i>  | <i>Prague (CZECH REPUBLIC)</i> |     |
| RECOMBINATION IN LOW TEMPERATURE PLASMA  |                                | 179 |
| <i>Lucie POLACHOVA</i>   | <i>Brno (CZECH REPUBLIC)</i>   |     |
| SIMULATION OF TITAN'S ATMOSPHERE PROCESSES USING DC GLIDING ARC DISCHARGE  |                                | 185 |
| <i>Andras TOTH</i>   | <i>Budapest (HUNGARY)</i>      |     |
| SURFACE MODIFICATION OF POLY(ETHYLENE TEREPHTHALATE) BY HELIUM PLASMA IMMERSION ION IMPLANTATION                     |                                | 189 |
| <i>Ihor KOROLOV</i>  | <i>Budapest (HUNGARY)</i>      |     |
| RATE COEFFICIENT MEASUREMENTS OF ASYMMETRIC CHARGE TRANSFER REACTIONS  |                                | 194 |
| <i>Stepan ROUCKA</i>   | <i>Prague (CZECH REPUBLIC)</i> |     |
| STUDY OF ASTROPHYSICALLY RELEVANT HYDROGEN CHEMISTRY: COMBINING AN RF ION TRAP WITH A COLD EFFUSIVE BEAM             |                                | 204 |
| <i>Vera MAZANKOVA</i>  | <i>Brno (CZECH REPUBLIC)</i>   |     |
| INFLUENCE OF MERCURY TITRATION ON KINETIC PROCESSES IN NITROGEN POST-DISCHARGE                                       |                                | 210 |
| <i>Oleksiy CHUMAK</i>  | <i>Prague (CZECH REPUBLIC)</i> |     |
| DISCHARGE FLUCTUATIONS PRESENTATION BY ENTROPY MAPS  |                                | 215 |

*Rodica VLADOIU*

*Constanta (ROMANIA)*

APPLICATIONS OF THE NANOMETER-SCALED CARBON BASED THIN FILMS  
DEPOSITED BY TVA TECHNOLOGY 220

---

*Tom FIELD*

*Belfast (UNITED KINGDOM)*

ELECTRON ATTACHMENT TO RADICALS RELEVANT TO FLUOROCARBON PLASMAS 221

---

*Janina KOPYRA*

*Siedlce (POLAND)*

LOW ENERGY ELECTRON DRIVEN PROCESSES IN HALOSUBSTITUTED ORGANIC  
ACIDS: THE CASE OF TRICHLOROACETIC ACID 223

---

*Takao NAMIHIRA*

*Kumamoto (JAPAN)*

HIGHER YIELD OZONE GENERATION USING NANO-SECONDS PULSED DISCHARGE 227

---

*Mirosław DORS*

*Gdansk (POLAND)*

PLASMA TREATMENT OF DRINKING WATER 233

---

*Milos KONRAD*

*Prague (CZECH REPUBLIC)*

GASIFICATION OF PYROLYTIC OIL FROM WASTE TIRES IN THERMAL PLASMA  
REACTOR 242

---

*Michal PROCHAZKA*

*Brno (CZECH REPUBLIC)*

OPTICAL EMISSION SPECTROSCOPY OF PLASMA DEPOSITION PROCESSES USING  
DIMETHYLPHENYLSILANE PRECURSOR 247

---

*Pavol JUSKO*

*Prague (CZECH REPUBLIC)*

COMBINATION OF AN ELECTRON SPECTROMETER WITH AN ION TRAP: FIRST  
RESULTS FOR  $H^- + h\nu$  AND  $H^- + H$  252

---

*Gabriel HORVATH*

*Bratislava (SLOVAKIA)*

ORGANIC ABUNDANCES IN ATMOSPHERIC PRESSURE  $N_2$ - $CH_4$  DISCHARGES 257

---

*Petr BARTOS*

*Ceske Budejovice (CZECH REPUBLIC)*

INTERACTION OF LOW-TEMPERATURE PLASMA WITH FABRIC: STUDY BY COMPUTER  
SIMULATIONS 262

---

*Vera SAZAVSKA*

*Brno (CZECH REPUBLIC)*

PLASMA TREATMENT OF CORROSION LAYERS FROM BRASS 266

---

*Rodica VLADOIU*

*Constanta (ROMANIA)*

SURFACE ACTIVATION OF THE POLYCARBONATE IN ATMOSPHERIC PRESSURE  
PLASMA GENERATED IN AIR AND HELIUM BY SURFACE DIELECTRIC BARRIER  
DISCHARGE (SDBD) 271

EFFECT OF HELIUM ADDITION IN THE DOUBLE M-EFFECT (MONOCHROMATIZATION EFFECT) 272

---

INVESTIGATION OF THE ELECTRIC FIELD AROUND A CARBON NANOTUBE TIP IN PULSED PLASMA SHEATH 273

---

INTERACTION OF DEUTERATED HYDROCARBON IONS AND Ar<sup>+</sup> WITH CFC SURFACES AT ROOM TEMPERATURE 278

---

HIGH-SPEED AMBIENT AIR PLASMA CLEANING OF FLAT GLASS SURFACES 281

---

BESTOF – A VERSATILE APPARATUS FOR FUSION RELEVANT EXPERIMENTS 285

---

DEVICE FOR APPLICATION OF PEF 289

---

SURFACE PROPERTIES OF ANTIBACTERIALLY PRE-TREATED POLYVINYLCHLORIDE 293

---

HIGH-DENSITY POLYETHYLENE MEMBRANES PRE-TREATED BY DIFFUSE BARRIER DISCHARGE PLASMA 295

---

COATING OF CYCLODEXTRINS ON THE PLASMA ACTIVATED POLYPROPYLENE NON-WOVEN 297

---

THE INFLUENCE OF ATMOSPHERIC PRESSURE PLASMA ON POLYPROPYLENE FILMS 300

---

SURFACE MODIFICATION OF LOW-DENSITY POLYETHYLENE BY POLY(2-ETHYL-2-OXAZOLINE) USING HIGH-PRESSURE PLASMA 303

---

MORPHOLOGICAL AND ELECTRICAL PROPERTIES OF TIN/PLASMA POLYMER NANOCOMPOSITES 307

|  |  |     |
|--|--|-----|
| <i>Mansour KHORAMABADI</i>   | <i>Boroujerd (IRAN)</i>                |     |
| SHEATH STRUCTURE IN A MULTIPLY IONIZED ELECTRONEGATIVE PLASMA  |  | 311 |
| <hr/>  |  |     |
| <i>Marian DANKO</i>  | <i>Bratislava (SLOVAKIA)</i>           |     |
| ELECTRON IMPACT INDUCED FLORESCENCE OF SECOND POSITIVE SYSTEM OF N <sub>2</sub> MOLECULE                                     |  | 316 |
| <hr/>  |  |     |
| <i>Juergen ROEPCKE</i>   | <i>Greifswald (GERMANY)</i>            |     |
| ON PROGRESS USING MID-INFRARED ABSORPTION TECHNIQUES FOR PLASMA DIAGNOSTICS – FROM BASIC RESEARCH TO INDUSTRIAL APPLICATIONS |  | 321 |
| <hr/>  |  |     |
| <i>Martin KORMUNDA</i>   | <i>Usti nad Labem (CZECH REPUBLIC)</i> |     |
| A SINGLE TARGET RF MAGNETRON CO-SPUTTERED IRON DOPED TIN OXIDE FILMS WITH NANO PILLARS                                       |  | 331 |
| <hr/>  |  |     |
| <i>Jan BENEDIKT</i>  | <i>Bochum (GERMANY)</i>                |     |
| DEPOSITION OF SiO <sub>x</sub> FILMS BY MEANS OF ATMOSPHERIC PRESSURE MICROPLASMA JETS                                       |  | 336 |
| <hr/>  |  |     |
| ADDRESS LIST   |  | 341 |

# PTR-MS and beyond: fundamentals, developments and applications

T.D.Märk<sup>1,2</sup>, B.Agarwal<sup>1</sup>, K.Becker<sup>3</sup>, A.Edtbauer<sup>1</sup>, S.Haidacher<sup>1</sup>, G.Hanel<sup>1</sup>, E.Hartungen<sup>1</sup>, S.Jaksch<sup>1</sup>,  
A.Jordan<sup>1</sup>, S.Jürschik<sup>1,2</sup>, C.A.Mayhew<sup>4</sup>, L.Märk<sup>1</sup>, F.Petersson<sup>1,2</sup>, H.Seehauser<sup>1</sup>, R.Schottkowsky<sup>1</sup>,  
P.Sulzer<sup>1</sup>,

<sup>1</sup>Ionicon Analytik GmbH, Eduard Bodem Gasse 3, A-6020 Innsbruck, Austria

<sup>2</sup>Institut für Ionenphysik und Angewandte Physik, Universität Innsbruck, Technikerstr.25, A-6020 Innsbruck, Austria

<sup>3</sup>Polytechnic Institute of New York University, NY 11201, USA

<sup>4</sup>School of Physics and Astronomy, University of Birmingham, Edgbaston, Birmingham, B15 2TT, UK

e-mail: tilmann.maerk@uibk.ac.at

## Abstract

Proton Transfer Reaction- Mass Spectrometry (PTR-MS) is by now a well established technique in trace gas analysis which offers many advantages, such as real-time analysis, no sample preparation, very low detection limits, high selectivity and very short response time. This broad range of advantages has made it an ideal tool in many applications ranging from atmospheric chemistry, food science, biological research, process monitoring and quality control, biotechnological questions, all the way to medical applications. Here we report several recent instrumental developments in PTR-MS, including the following: (i) the improvement of the detection limit that now allows for measuring trace gas compounds in a concentration range from several ppmv down to the ppqv (parts-per-quadrillion) region with a typical response time well below 100 ms; (ii) a mass resolution up to  $m/\Delta m = 8000$  for the latest PTR-TOF-MS instruments, and (iii) the so-called "switchable reagent ions (SRI)" feature, i.e. the possibility to switch between  $\text{H}_3\text{O}^+$ ,  $\text{NO}^+$  and  $\text{O}_2^+$  as reagent ions allowing now to detect compounds with PA values below that of the water molecule, a feature which has very recently been extended to other reagent ions. Finally we will present here the development of the direct aqueous injection (DAI) technique, which allows the direct measurement of trace compounds even in liquid samples. Moreover, in the present work we demonstrate proof-of-principle investigations on all common solid explosives, several chemical warfare agent (CWA) analogues and in addition illicit and controlled prescription drugs. It is shown that not only the sensitivity of PTR-MS instruments is sufficient to detect even the explosives with the lowest vapor pressures (HMX), but it also provides a selectivity that allows for unambiguous identification and therefore avoids false positives or false negatives.

**Keywords:** PTR-MS, SRI, DAI, chemical analysis, illicit substances

## Introduction and Experimental

In a typical PTR-MS instrument (as presented in great detail e.g. in [1] or more recently in [2]) water vapor coming from a distilled water reservoir is converted into hydronium ( $\text{H}_3\text{O}^+$ ) in a highly sophisticated hollow cathode ion source. This source is designed in a way that the purity of the protonated water molecules reaches values of 99% and more, thus making a signal-diminishing mass filter (e.g. quadrupole as used in instruments based on technologies similar to PTR-MS, e.g. SIFT-MS) for purifying the primary ions obsolete. Subsequently the  $\text{H}_3\text{O}^+$  ions are injected into a drift tube together with the sample air. Whenever a substance present in the air possesses a proton affinity (PA) that is larger than the PA of water, proton transfer takes place resulting in neutral  $\text{H}_2\text{O}$  and the protonated substance molecule. Fortunately the PAs of all common air constituents ( $\text{N}_2$ ,  $\text{O}_2$ , Ar,  $\text{CO}_2$ , etc.) are much lower than the PA of water, so the air itself acts as a buffer gas and only the trace compounds will get ionized. Following the drift tube a mass spectrometer analyzes the product ions (see Fig. 1 for a schematic view of a PTR-MS instrument equipped with a quadrupole mass filter). As a result of this setup and its well known parameters, one gets highly accurate concentration readings in real-time (about 100 ms reaction time) without the need of sample preparation down to a typical detection limit in the single digit pptv region.

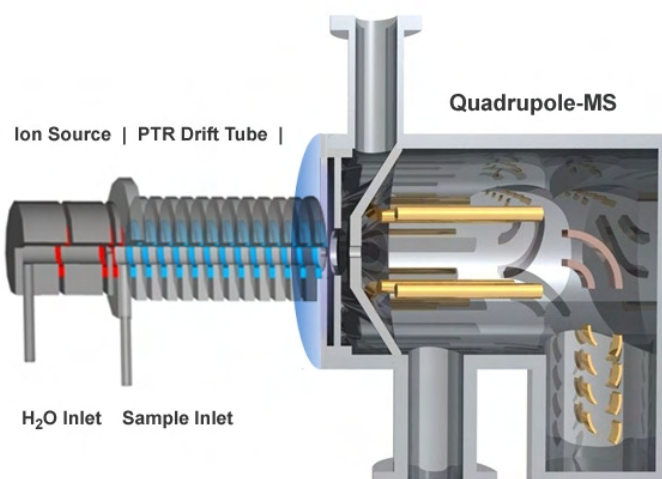


Fig. 1. Schematic view of a quadrupole based PTR-MS instrument.

While utilizing a quadrupole mass filter has its advantages in monitoring the concentration of distinct substances, the mass resolution (unity mass resolving power) makes the identification of unknown substances somehow difficult. The recording of full mass spectra is quite slow (as the mass filter has to scan the whole mass range) and separation of isobaric substances is impossible. Therefore we recently coupled our well established PTR ion source with a high resolution ( $m/\Delta m$  up to 8000) time-of-flight (TOF) mass analyzer. This so-called PTR-TOF 8000 [3] is due to its high mass resolution capable of separating isobars (e.g. ketene and propene) and full spectra are acquired in split-seconds, while still achieving a detection limit of below 10 pptv.

For areas of application where this immense mass resolving power is of less importance, but even more sensitivity is needed, we use a different type of TOF analyzer. In the PTR-TOF 2000 [4] the sensitivity is increased by a factor of five compared to that of the PTR-TOF 8000, at the cost of a somewhat lower mass resolution of about  $m/\Delta m = 2000$ .

Another "limitation" of PTR-MS, was that only  $\text{H}_3\text{O}^+$  could be used as primary ions. This was resolved by us in 2009 [5], by the development of the so-called "switchable reagent ions" (SRI). It is now possible to choose from  $\text{H}_3\text{O}^+$ ,  $\text{NO}^+$  and  $\text{O}_2^+$  as reagent ion with a switching time below 10 s. While all advantages of PTR ionization are preserved with  $\text{H}_3\text{O}^+$ , charge transfer from  $\text{O}_2^+$  extends the number of substances that can be analyzed (e.g. the very important molecules ethylene and acetylene, which possess lower PAs than water).

$\text{NO}^+$  (which is produced in high purity from normal air without the need of a NO cylinder) as a primary ion leads to a different benefit; according to Spanel et al. [6]  $\text{NO}^+$  interactions with aldehydes follow the reaction:  $\text{NO}^+ + \text{XH} \rightarrow \text{X}^+ + \text{NOH}$  whereas ketones follow:  $\text{NO}^+ + \text{XH} \rightarrow \text{XH}^+ + \text{NO}$  (and clustering). This means that we can even detect isomeric compounds on different nominal masses and can identify them unambiguously.

One thing that limits the areas of application for all above-mentioned developments is the fact that PTR-MS requires for proper analysis gas phase samples, i.e. liquids can only be analyzed indirectly via the headspace above the liquids' surface. Especially compounds possessing a high Henry constant therefore need to be present at very high liquid concentrations until they can be detected in the headspace. To overcome this limitation we developed a "direct aqueous injection" (DAI) system, where the liquid can be introduced directly for PTR-MS analysis. Fig. 2 gives a schematic view of this DAI system. In short, the liquid located in a syringe is injected via a computer controlled syringe pump into a purified, dried and heated stream of air, which is subsequently introduced into the drift tube of the PTR-MS instrument. In [7] we present proof-of-principle investigations of this DAI system achieving response times around 20 s and a detection limit of about 100 pptw.

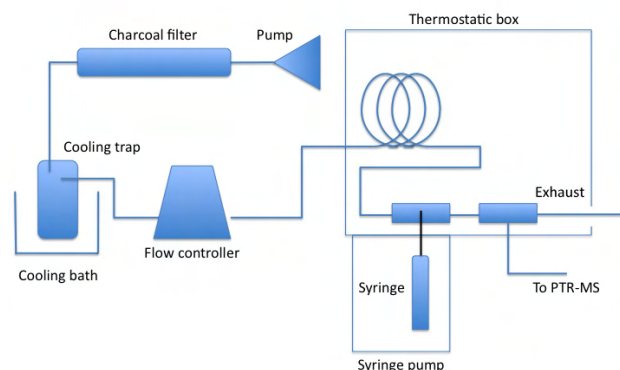


Fig. 2. Schematic view of the novel DAI system.

### Results and discussion

During the development of the above-mentioned SRI functionality we had to apply several changes to the hollow cathode ion source which, besides the possibility to switch between  $\text{H}_3\text{O}^+$ ,  $\text{NO}^+$  and  $\text{O}_2^+$  as primary ions, led to an improved overall performance. In Fig. 3 the results of measurements in hydronium mode for chlorobenzene and trichlorobenzene, including several isotopes at different dilution levels, are presented. The x-axis represents the actual concentration of the compound whereas the y-axis shows the obtained count-rate (in counts per second; cps). It can be immediately seen that the response of the improved PTR-MS instrument is not only linear over many orders of magnitude, but also that the detection limit lies for the first time below the pptv, namely in the ppqv (parts-per-quadrillion), region. A more exact calculation of the detection limit (using three times the standard-deviation of the background noise level of measurements at 0 pptv) give the value of 890 ppqv for trichlorobenzene at an integration time of 180 s.

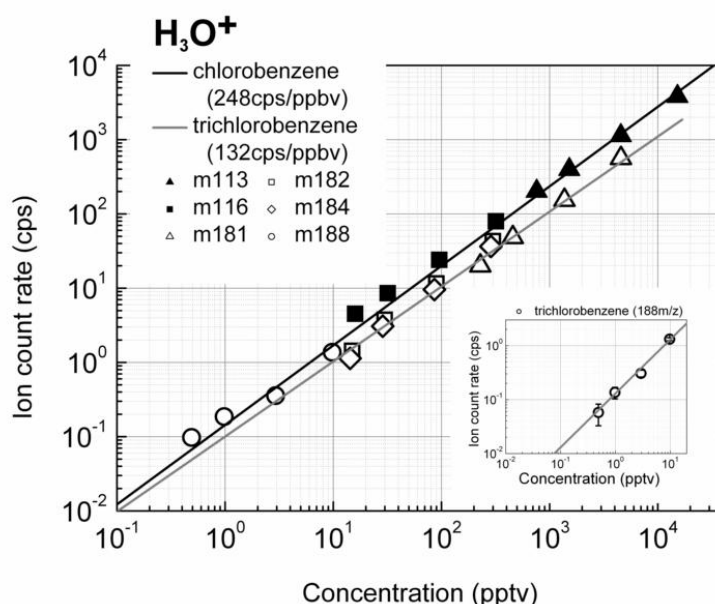


Fig. 3. Linearity range of a quadrupole based PTR-MS instrument equipped with the SRI feature

One very striking example for the importance of high mass resolution, as achieved by the novel PTR-TOF 8000, is the detection of explosives and other illicit substances (CWAs, drugs, etc.). In Fig. 4 the result of a measurement is shown where a small block of the well-known explosive trinitrotoluene (TNT; about 7-8 g) was placed directly in front of the PTR-MS inlet. The inlet line was not modified for this experiment, i.e. the first 2-3 cm were not heated, which results in condensation of the very "sticky" TNT vapor and subsequently to a much slower signal response / signal increase than

it could be obtained with a perfectly heated inlet line without cold spots. However, the quintessence of Fig. 4 is that there is an unidentified but obviously harmless lab-air compound present on the same nominal mass of 228 as TNT. With the mass resolution of about  $8000 \text{ m}/\Delta\text{m}$  this compound can be clearly separated from TNT, thus effectively suppressing the risk of false positives when the PTR-TOF 8000 is used for explosive detection. Furthermore in [4], [8] and [9] we proved that this excellent, nearly unambiguous detectability is not only possible for TNT, but also for all common solid explosives (RDX, PETN, HMX, etc.), chemical warfare agents (mustard gas and numerous CWA analogues) and illicit and prescribed drugs (heroin, cocaine, morphine, ecstasy, etc.) via direct headspace sampling at room temperature.

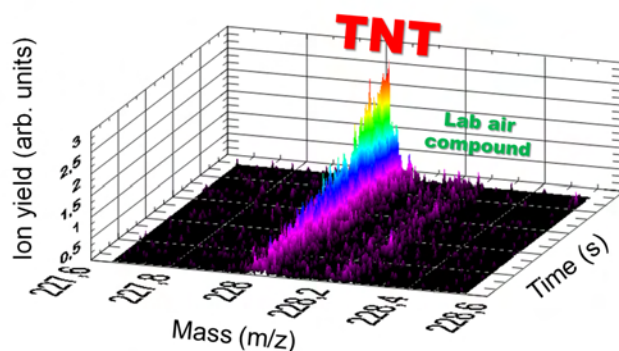


Fig. 4. Separation of the explosive TNT and a harmless lab-air compound with the PTR-TOF 8000.

As explosives detection is a hot-topic (see the recent frequent reports in newspapers from all over the world about terrorist activities) we extended the proof-of-principle measurements of the newly developed DAI system mentioned in the introduction to the detection of TNT in water. TNT, which is extremely toxic, from old bombs and ammunition, as well as wastes from armaments industry that have been dumped into lakes, is known to be a serious threat to the lake's fauna. To simulate the detectability of trace amounts of TNT dissolved in water we put approximately 1 mg of TNT into a vial of 50 ml water and measured without stirring, shaking or heating the TNT, as well as the dinitrotoluene (DNT; is always present in TNT as an impurity) concentration over a period of several months utilizing the DAI system [10]. In Fig. 5 it can be clearly seen that already after one night TNT, as well as the impurity DNT, can be detected in the water. The concentration increases during the next days and weeks and reaches "saturation" after approximately two months.

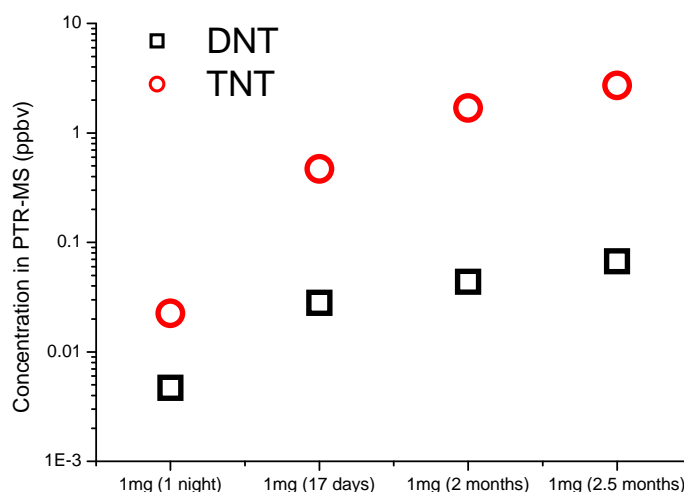


Fig. 5. Analysis of TNT and DNT traces dissolved in water after different time-spans.

## Conclusions

As a consequence of its many analytical advantages, PTR-MS technology represents one of the few devices that can provide a broad-based analytical technique, thereby making it an ideal tool for the many applications mentioned in this abstract. Importantly, we have demonstrated that through a series of new developments, namely switchable reagent ions, improved mass resolution, and direct aqueous injection, we have considerably enhanced the technology's capabilities, not only for the main-stream areas, such as the environment, atmospheric chemistry, food sciences, medical applications etc, but also for completely new fields of application, e.g. the unambiguous detection of illicit substances in gas and liquid phase. PTR-MS has evolved from a niche technique to a universal analytical instrument with unique advantages compared to many established analytical methods.

## References

- [1] W. Lindinger, A. Hansel, A. Jordan; *Int. J. of Mass Spectrom. and Ion Processes*, 173/3 (1998) 191-241.
- [2] R. S. Blake, P. S. Monks, A. M. Ellis; *Chem. Rev.*, 109 (3) (2009), 861-896.
- [3] A. Jordan, S. Haidacher, G. Hanel, E. Hartungen, L. Märk, H. Seehauser, R. Schotchkowsky, P. Sulzer, T.D. Märk, *Int. J. of Mass Spec.*, 286 (2009), 122-128.
- [4] C.A. Mayhew, P. Sulzer, F. Petersson, S. Haidacher, A. Jordan, L. Märk, P. Watts, T.D. Märk, *Int. J. of Mass Spec.*, 289 (2009), 58-63.
- [5] A. Jordan, S. Haidacher, G. Hanel, E. Hartungen, J. Herbig, L. Märk, R. Schotchkowsky, H. Seehauser, P. Sulzer, T. D. Märk, *Int. J. of Mass Spec.*, 286 (2009), 32-38.
- [6] P. Spanel, Y. Ji, D. Smith; *Int.J. of Mass Spectrom. and Ion Processes*, 165/166 (1997) 25-37.
- [7] S. Jürschik, A. Tani, P. Sulzer, S. Haidacher, A. Jordan, R. Schotchkowsky, E. Hartungen, G. Hanel, H. Seehauser, L. Märk, T.D. Märk; *Int. J. of Mass Spec.* 289 (2010), 173-176.
- [8] F. Petersson, P. Sulzer, C.A. Mayhew, P. Watts, A. Jordan, L. Märk and T.D. Märk; *Rapid Commun. Mass Spectrom.* 23 (2009), 3875-3880.
- [9] B. Agarwal, F. Petersson, S. Jürschik, P. Sulzer, A. Jordan, T. Märk, P. Watts, C. Mayhew; *Anal. Bioanal. Chem.* (in press).
- [10] S. Jürschik, P. Sulzer, F. Petersson, C. Mayhew, A. Jordan, B. Agarwal, S. Haidacher, H. Seehauser, K. Becker, T. Märk; *Anal. Bioanal. Chem.* (in press).

# Atmospheric-Pressure Plasmas: Scientific Challenges and Technological Opportunities

J.L. Lopez<sup>1</sup>, W. Zhu<sup>1</sup>, K.H. Becker<sup>2</sup>

<sup>1</sup>Department of Applied Sciences and Technology and Center for Microplasma Science & Technology,  
St Peter's College, 2641 J.F. Kennedy Boulevard, Jersey City, NJ 07306 USA

<sup>2</sup>Department of Applied Physics, Polytechnic Institute of New York University,  
6 MetroTech Center, Brooklyn, NY 11201 USA

e-mail: kbecker@poly.edu or kurt.becker@nyu.edu

## Abstract

High-pressure plasmas represent an environment where collisions and radiative processes are dominated by (i) step-wise processes, i.e. the excitation of states followed by collisions of the excited species with other particles resulting in new energy transfer routes and by (ii) three-body collisions leading e.g., to the formation of excimers. The dominance of collisional and radiative processes beyond binary collisions involving ground-state species allows for many applications of high-pressure plasmas such as high power lasers, opening switches, novel plasma processing applications, electromagnetic absorbers and reflectors, remediation of gaseous pollutants, medical sterilization and biological decontamination, as well as excimer lamps and other non-coherent vacuum-ultraviolet (VUV) light sources [1].

**Keywords:** Atmospheric-pressure plasmas, microplamas

## Introduction

Self-sustained diffuse plasmas tend to be unstable at high pressure due to their susceptibility to filamentation and the transition to an arc (see [2-6]), which limits their practical utility. A promising approach to generate and maintain stable high-pressure plasmas is based on the recognition that plasmas confined to critical dimensions below about 1 mm, so-called “microplasmas”, display a remarkable stability preventing arcing. There are several factors that contribute to the stabilization of microplasmas, not all of them fully understood at this point in time. One stabilizing factor can be explained in terms of “pd scaling”. The voltage required to ignite a discharge, the so-called breakdown voltage, depends on the product of gas pressure “p” and electrode separation “d”. If one increases the pressure for a fixed value of “d”, the required breakdown voltage increases. At atmospheric pressure (and electrode separations of centimeters to tens of centimeters, which are typical for low-pressure plasmas), breakdown voltages are in the kV range. The high breakdown voltage leads to a high current density after the discharge is ignited, particularly in the cathode fall of the discharge. The high current density is the source of discharge instabilities in the cathode fall region, which quickly lead to the formation of an undesirable arc. As a consequence of “pd scaling”, the breakdown voltage can be kept low, if the electrode separation “d” is reduced when the pressure “p” is increased. At atmospheric pressure, d-values below 1 mm are required to keep breakdown voltages sufficiently low to avoid the glow-to-arc transition after plasma ignition. Another factor that at least in part contributes to the stability of high-pressure microplasmas are the high losses of charge carriers to the surrounding walls. The typical operating parameters of microplasmas (pressures up to and exceeding 1 atm (760 Torr) and dimensions below 1 mm) correspond to “pd” values of between 1 and 10 Torr · cm. These “pd” values are similar to those for large-volume, low-pressure plasmas. However, the current and the energy densities in microplasmas are much higher.

The remainder of this contribution deals primarily with microplasmas at atmospheric pressure as perhaps the most important and rapidly advancing category of atmospheric-pressure plasmas, both in terms of scientific challenges as well as technological opportunities.

## Microplasmas at Atmospheric Pressure

Microdischarges generated in spatially confined cavities began to appear in the literature in the mid-1990s. Schoenbach et al. [7] were the first to report the stable atmospheric-pressure operation of a microdischarge in a cylindrical hollow cathode geometry and coined the term “Microhollow Cathode Discharge (MHCD)” for this type of microdischarge. The phrase “hollow cathode” historically refers

to a specific mode of discharge operation, in which the sustaining voltage drops as the current increases, i.e. the discharge has a “negative differential resistance” (hollow cathode or subnormal negative glow mode). Nowadays, MHCDs are often not operated in the hollow cathode mode, but as normal or abnormal glow discharges. Therefore, the inclusion of the phrase ‘hollow cathode’ in the name MHCD might be misleading. As a consequence, other groups have been referring to these discharges simply as “Microdischarges” [8,9] or “Microstructured Electrode Arrays” [10]. In an effort to avoid blurring the distinction between discharge device geometry or structure and its operational characteristics, the phrase “microhollow cathode discharge, MHCD” has largely been replaced by the terms “microplasma”, “microcavity plasma”, or “microdischarge” [11]. Applications of microdischarges often require the use of two-dimensional arrays of individual microdischarges, either operated in parallel or in series, or both. Microdischarges can be operated in parallel without individual ballast resistors, if the discharges are operated in the range where the current-voltage (I-V) curve has a positive slope [7,10,12,13]. In regions where the I-V characteristics has a negative slope (hollow cathode mode or subnormal glow mode) or is flat (normal glow mode), arrays can be generated by using a distributed resistive ballast such as semi-insulating silicon as anode material [14] or multilayer ceramic structures where each microdischarge is individually ballasted [15,16].

Frequently used microplasma sources include the Capillary Plasma Electrode (CPE) discharge, which employs dielectric capillaries that cover one or both electrodes of the device [17-19]. The CPE discharge exhibits a mode of operation, where the capillaries serve as plasma sources and produce jets of high-intensity plasma at high pressure, which emerge from the end of the capillary and form a “plasma electrode”. A variety of microplasma sources were developed for chemical analysis purposes leveraging advances in microfabrication techniques [20]. This allowed the miniaturization of known plasma concepts and their integration into “lab-on-a chip” analytical tools such as plasma atomic spectrometry, plasma mass spectrometry, and plasma gas and liquid chromatography. Miniature inductively and capacitively coupled plasmas are among the most widely used plasma sources used for chemical analysis. Other concepts such as microwave plasmas, microdischarges in hollow cathode geometries and microstructure electrode (MSE) discharges have also been utilized [21]. Several atmospheric-pressure plasma jets at the microscale (micro-APPJs) have been developed by various groups (see e.g. fig. 1 below) and are widely used in applications ranging from thin film deposition to sterilization and biological decontamination to biomedical, medical, and dental applications and the treatment of temperature-sensitive substrates [22].

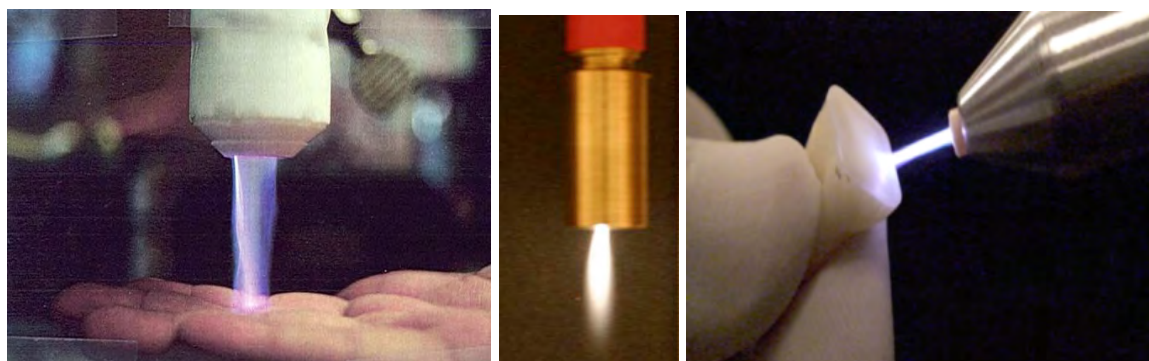


Fig. 1. Three examples of atmospheric-pressure plasma jets.

Variants of the original MHC design have been used [11,20,23-25] such as parallel plates, arbitrarily shaped holes in a solid cathode, slits in the cathode, spirals, micro-tubes with the anode at the orifice, or inserted through the walls, and micro-slots. Common to all these geometries are the dimensions of the cathode hollows which are on the order of hundred microns. A microdischarge, whose characteristic plasma dimensions are near the upper end of the 1 mm size scale, is a variant of the Dielectric Barrier Discharge (DBD) [26], the Cylindrical Dielectric Barrier Discharge [27-30], C-DBD. This source consists of a thin and thin-walled dielectric tube, with two straps of Cu wrapped around it, which serve as the two electrodes. A stable, high-frequency discharge plasma can be generated inside the tube in the space between the electrodes.

## Results and discussion: A Capillary Dielectric Barrier Discharge

Electrical and optical characterization tools are by far the most widely used techniques to characterize (atmospheric-pressure) plasmas. As an example, a Capillary Dielectric Barrier Discharge (Cap-DBD) plasma operated in atmospheric pressure air is briefly discussed here, see fig. 2 below and Ref. [31]. The plasma reactor consists of metal wire electrodes inside quartz capillary tubes powered with a low-frequency AC high voltage power supply. Various reactor geometries (planar, 3-D multilayer, and circular) with wall-to-wall separation ranging from zero up to 500 micron were realized and investigated. For the electrical and spectral measurements, three reactors, each with six tubes, six inches in length, were assembled with gap widths of 500 micron, 225 micron, and 0 micron (i.e. tubes touching). The discharges appeared homogenous across the whole device at separations below 225 micron and turned into filamentary discharges at larger gap spaces. The operating voltage was generally around 3-4 kV (rms). The power consumption by the Cap-DBD was calculated using voltage/charge Lissajous figures with observed powers of a few watts to a maximum of about 14 W for the reactor with no gap spacing. Further studies of optical emission spectroscopy (OES) were employed to evaluate the reactive species generated in the microplasma source. The observed emission spectrum was predominantly within the second positive system of  $N_2$  and the first negative system of  $N_2^+$ .

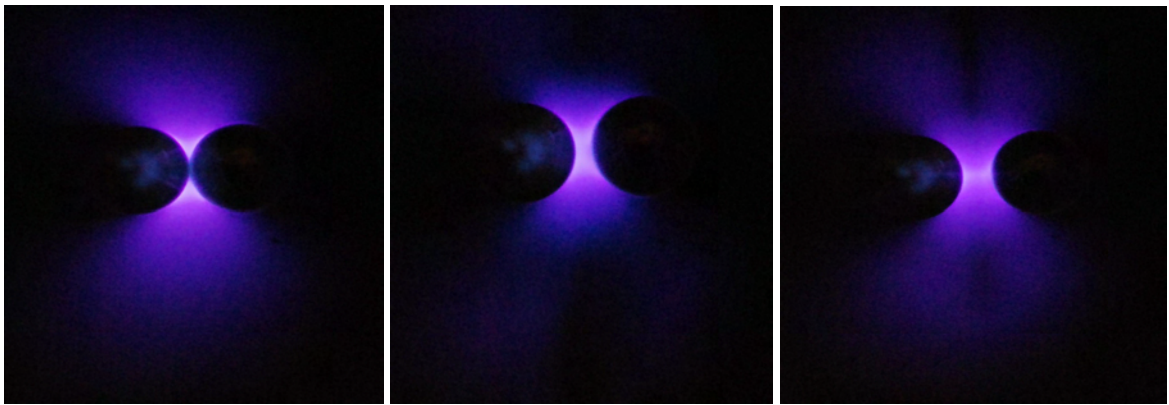


Fig. 2. Cap-DBD with no gap (left), 225 micron gap (center), and 500 micron gap (right.)

Recorded waveforms for applied voltage and discharge current show a pattern similar to what is observed in most atmospheric pressure DBDs. The current flow and power dissipation occurs in a large

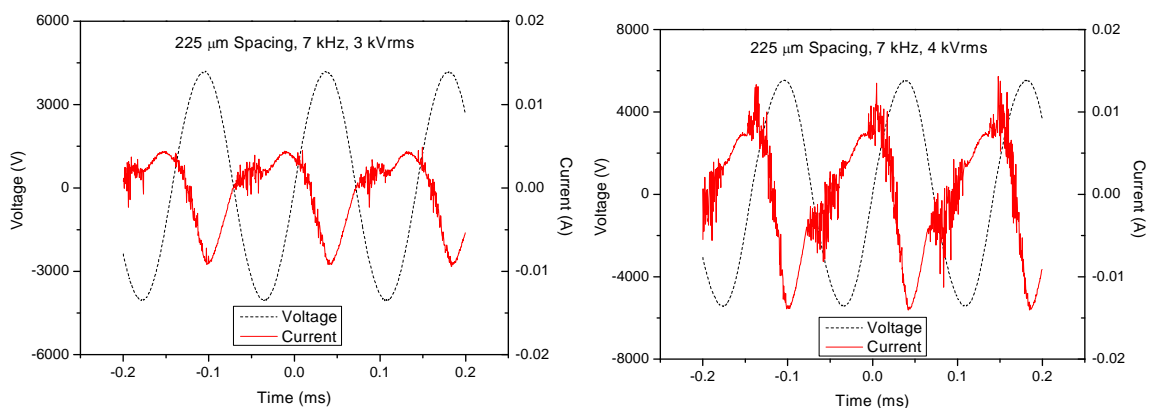


Fig. 3. Current-voltage waveforms for the 225 micron gap reactor at different applied voltages.

number of short-lived microdischarges. When the sinusoidal voltage is applied to the reactor, there are periods of discharge activity when the voltage is high enough for breakdown to occur, as well as

periods of inactivity when the applied voltage is below the level necessary for breakdown. As can be seen in the current waveform in fig. 3, at an applied voltage of 3 kV rms (left), plasma generation occurs at a very early stage in the voltage cycle; this is evident in the few current peaks superimposed on the capacitive current. The breakdown of the gas and the appearance of a plasma glow do not occur uniformly along the length of the tubes, but occur only in certain regions at lower voltages. However, at an applied voltage of 4 kV rms (right), the plasma fills the entire volume. There are alternating periods of discharge activity and discharge pauses. Filamentary streamers form in the air gap at both the positive and negative rising edges of the applied AC voltage, extinguishing at the peaks. The dielectric distributes the charge over the entire surface and causes the plasma to appear more homogeneous. However, with increasing gap width, the microdischarges become more visible. For the reactor with 0  $\mu\text{m}$  spacing, the microfilaments overlap, creating a visually homogeneous appearance. With a gap of 500  $\mu\text{m}$ , the individual filaments can be distinguished.

The observed peaks in the emission spectra [31] (fig. 4) are identified as belonging to the second positive system of  $\text{N}_2$  as well as two weak bands of the first negative system of  $\text{N}_2^+$ . Optical emission spectroscopy is often used to evaluate the bulk electron energy in DBDs. In atmospheric-pressure air, non-equilibrium weakly ionized plasmas the typical mean electron energies are in the range of a fraction of an electronvolt to a few electronvolts. Therefore, only a small fraction of electrons possess energies sufficiently high to ionize  $\text{N}_2$  and excite the upper state that causes the emission of the first negative system of  $\text{N}_2^+$ , which explains the comparatively weak  $\text{N}_2^+$  emissions [31].

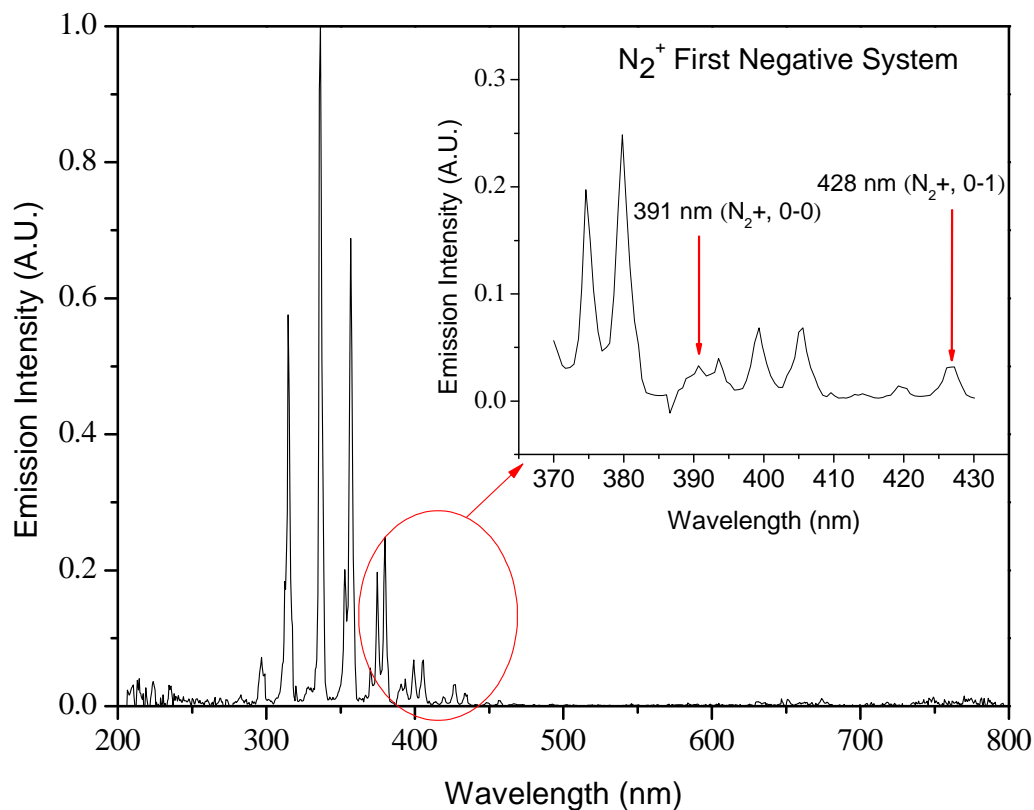


Fig. 4. Optical emission spectrum for the 225 micron reactor.

### Applications

The rapid growth of applications of atmospheric-pressure plasmas, in particular of microdischarges and microplasmas, both in terms of the diversity of applications and in the breadth and depth in a given area of application, renders it impossible to provide a detailed account of all microplasma applications in a single contribution. Two very good sources for information on applications

atmospheric-pressure (micro)plasmas are the 2005 J Phys D Cluster Issue on Microplasmas (volume 38, 2005) and Ref. [1].

It is noteworthy to mention the use of atmospheric-pressure (micro)plasmas in biological, biomedical, and medical (incl. dental) applications as a rapidly emerging field where plasmas are explored as a novel tool for decontamination, sterilization, inactivation applications, surface modification and functionalization, and even wound treatment. The potential for new and revolutionary applications seems to be the main driving force, while efforts to develop a broad base of basic understanding of how plasmas interact with living systems is somewhat lagging behind.

### Acknowledgments

We gratefully acknowledge the contributions of Dr. Jenny Mahoney and Dr. Valencia Johnson in obtaining the results for the Cap-DBD plasma reactors reported here.

### References

- [1] see e.g. "Non-Equilibrium Air Plasmas at Atmospheric Pressure", eds. K.H. Becker, U. Kogelschatz, K.H. Schoenbach, and R. Barker, IOP Publ., Bristol, UK (2004), chapter 9 "Applications of Atmospheric-Pressure Air Plasmas"
- [2] A. von Engel, *Ionized Gases* (Clarendon Press, Oxford, 1955)
- [3] Y. Raizer, "Gas Discharge Physics", (Springer Verlag: Heidelberg, 1991)
- [4] M.A. Lieberman and A.J. Lichtenberg, "Principles of Plasma Discharges and Materials Processing", (John Wiley: New York 1994)
- [5] R. Hippler, H. Kersten, M. Schmidt, and K.H. Schoenbach, "Low Temperature Plasmas", (Wiley-VCH: Weinheim, 2008)
- [6] E.E. Kunhardt, *IEEE Trans. Plasma Sci.* **28**, 1 (2000)
- [7] K.H. Schoenbach, R. Verhappen, T. Tessnow, P.F. Peterkin, and W. Byszewski, *Appl. Phys. Lett.* **68**, 13 (1996)
- [8] J.W. Frame, D.J. Wheeler, T.A. DeTemple, and J.G. Eden, *Appl. Phys. Lett.* **71**, 1165 (1997)
- [9] R.M. Sankaran and K.P. Giapis, *Appl. Phys. Lett.* **79**, 593 (2001)
- [10] C. Penache, A. Braeuning-Demian, L. Spielberger, and H. Schmidt-Boecking, *Proc. Hakone VII*, Greifswald, Germany (2000), **2**, p. 501
- [11] K. Becker, K.H. Schoenbach, and J.G. Eden, *J. Phys. D* **39**, R55 (2006)
- [12] J.W. Frame and J.G. Eden, *Electr. Lett.*, **34**, 1529 (1998)
- [13] J.G. Eden, S.-J. Park, N.P. Ostrom, S.T. McCain, C.J. Wagner, B.A. Vojak, J. Chen, C. Liu, P. von Allmen, F. Zenhausern, D.J. Sadler, J. Jensen, D.L. Wilcox, and J.J. Ewing, *J. Phys. D* **36**, 2869 (2003)
- [14] W. Shi, R.H. Stark, and K.H. Schoenbach, *IEEE Trans. Plasma Science* **27**, 16 (1999)
- [15] P. von Allmen, D.J. Sadler, C. Jensen, N.P. Ostrom, S.T. McCain, B.A. Vojak, and J.G. Eden, *Appl. Phys. Lett.* **82**, 4447 (2003)
- [16] P. von Allmen, S.T. McCain, N.P. Ostrom, B.A. Vojak, J.G. Eden, F. Zenhausern, C. Jensen, and M. Oliver, *Appl. Phys. Lett.* **82**, 2562 (2003)
- [17] E.E. Kunhardt and K. Becker (1999) US Patent 5872426, and subsequent patents 6005349, 6147452, 6879103, and 6900592
- [18] A. Koutsospyros, S.-M. Yin, C. Christodoulatos, and K. Becker, *Int. J. Mass Spectrom.* **233**, 305 (2004)
- [19] A. Koutsospyros, S.M. Yin, C. Christodoulatos, and K. Becker, *IEEE Trans. Plasma Sci.* **33**, 42 (2005)
- [20] R. Foest, M. Schmidt, and K. Becker, *Int. J. Mass Spectrom.* **248**, 87 (2005)
- [21] V. Karanassios, *Spectrochimica Acta B* **59**, 909 (2004)
- [22] J. Schäfer, R. Foest, A. Quade, A. Ohl, and K.D. Weltmann, *Plasma Proc. Polym.* **6**, S519 (2009)
- [23] G. Schaefer and K.H. Schoenbach, "Basic Mechanisms Contributing to the Hollow Cathode Effect" in *Physics and Applications of Pseudosparks*, editors: M. Gundersen and G. Schaefer, Plenum Press, New York (1990), p.55.
- [24] R.M. Sankaran and K.P. Giapis, *J. Appl. Phys.* **92**, 2406 (2002)
- [25] Z.Q. Yu, K. Hoshimiya, J.D. Williams, S.F. Polvinen, and G.J. Collins, *Appl. Phys. Lett.* **83**, 854 (2003)
- [26] see e.g. B. Eliasson, M. Hirth, U. Kogelschatz, *J. Phys. D* **20**, 1421 (1987)
- [27] M. Laroussi, in: *Proc. of the IEEE International Conf. on Plasma Science (ICOPS)*, Monterey, CA (1999), p. 203; J. Yan, A. el-Dakrouri, M. Laroussi, and M. Gupta, *J. Vac. Sci. Technol.* **B20**, 2574 (2002)
- [28] N. Masoud, K. Martus, and K. Becker, *Int. J. Mass Spectrom.* **233**, 395 (2004)
- [29] N. Masoud, K. Martus, M. Figus, and K. Becker, *Contr. Plasma Phys.* **45**, 32 (2005)
- [30] N. Masoud, K. Martus and K. Becker, *J. Phys. D* **38**, 1674 (2005)
- [31] J. Mahoney, W. Zhu, V. Johnson, K.H. Becker, and J. Lopez, *Europ. Phys. J. D*, in press (December 2010 Topical Issue on Microplasmas)

## Status of fusion research in tokamaks

Radomir Panek

Institute of Plasma Physics AS CR, v.v.i., Association EURATOM/IPP.CR, Za Slovankou 3, 182 00 Prague 8, Czech Republic

During the last fifty years an enormous scientific and technological progress has been made in the field of thermonuclear research, namely in so called magnetic confinement represented by tokamaks and stelerators.

The world largest device is he European JET tokamak in Culham, UK. Research on JET is complemented by a several specialized smaller devices operated in individual EU member states and also outside Europe.

The JET operation started in 1983 and JET has successfully produced the world record in fusion power in deuterium/tritium plasmas (up to 16 MW) in the 90's. "Break-even" conditions, where the fusion output power equals the external input power required to heat the plasma, were almost reached ( $Q = 0.6$ ). In addition, JET has demonstrated safe operation of fusion devices with tritium fuel and remote handling of activated in-vessel components.

The next step in fusion research represents an ITER tokamak, which is designed to generate 500 MW fusion power corresponding to  $Q = 10$  (ratio of output to input power). ITER is a large scale, international experiment that should demonstrate the scientific and technological feasibility of using fusion as an energy source on earth. ITER will allow the study of plasmas in conditions similar to those expected in an electricity-generating fusion power plant. It will also test a number of key systems for fusion including the heating, control, diagnostic and remote maintenance that are expected to be needed for a real fusion power station. The current partners in the ITER project are the European Union, Japan, the Russian Federation, China, Korea, India, and the USA. The ITER construction has started in 2006 in Cadarache, in the South of France, and the first plasma operation is scheduled for the end of 2019.

The overall strategy to bring the fusion energy to commercial usage includes a number of different elements. The first step is the development of ITER, followed by a construction of a demonstration reactor called DEMO, which will demonstrate large-scale electrical power production. The DEMO design will be based on experience from ITER construction and operation. The expectation is that after DEMO, the first commercial fusion power stations can be constructed around 2040-2050.

Development of fusion as a future energy source desires very advanced technology, and will ask the utmost from materials, scientific understanding, and international cooperation. The ITER project represents one of the most complex, challenging and innovative project in the world today.

# Plasma Discharges as a probe of chemical processes in planetary atmospheres

N. J. Mason<sup>1</sup>, M. K. Duffy<sup>1</sup>, G. Horvath<sup>2</sup> and J. Orszagh<sup>2</sup>

<sup>1</sup>Department of Physics and Astronomy, The Open University, Walton Hall, Milton Keynes, Mk7 6AA, UK

<sup>2</sup>Department of Experimental Physics, Comenius University, Mlynská dolina, Bratislava 842 45, Slovakia

e-mail: n.j.mason@open.ac.uk

## Abstract

Plasma discharges have been used for more than 60 years to simulate the physical and chemical conditions in planetary atmospheres including the terrestrial ionosphere. However in recent years there has been an increase in such studies engendered by observational data from Titan, Saturn's largest moon, revealing a complex ionosphere and results from Mars revealing a more complex chemistry than its simple CO<sub>2</sub> atmosphere first suggested. Furthermore the development of astrobiology as a mature and rigorous scientific discipline, and with it studies of both the origin of life on Earth and potential for life on exoplanets, has led to the need for studies of chemistry in a wide range of planetary atmospheres. Plasma discharges have been used to explore the prebiotic chemistry of Earth since the classic Urey-Miller experiments of the 1960s and are now being updated to explore prebiotic chemistry in exoplanetary atmospheres and to test various scenarios of early Earth. In this presentation I will review this growing application of plasma science, discuss its strengths and weaknesses as a planetary atmosphere model and discuss how it may be developed in the future.

**Keywords:** Plasma chemistry; Planetary atmospheres, Titan, Mars and Exoplanets

## Introduction

Gas discharges have been used as a laboratory mimic of planetary atmospheres for more than 60 years (1). Initial experiments explored the production of cations in the Earth's ionosphere using air discharges to determine ion yields and ionization rates. These experiments were soon followed by studies of anion formation in oxygen and air discharges once the D region of the terrestrial ionosphere was observed (2). The effect on such ion yields by the presence of trace gases including water and CO<sub>2</sub> were then explored as more sensitive in-situ measurements (first by balloon) were made. Such experiments showed that, quantitatively at least, such laboratory measurements provided a methodology for understanding the main collisional and chemical processes in the ionosphere (3) and that spectroscopic emissions of the plasma were consistent with auroral and airglow observations (4). Furthermore by coupling such laboratory measurements with plasma models insight into the physical and chemical processes occurring in the ionosphere were possible including the role of electron attachment (for anion formation) (5) and dissociative recombination (6).

Consequently when the first planetary missions visited Mars and sent back data on the Martian atmosphere experiments were extended to studies of CO<sub>2</sub> plasmas with the detection of electron induced optical emissions of the Cameron bands, clearly seen in the Martian airglow(7). Subsequent planetary missions to Venus and Jupiter likewise led to corresponding discharge experiments such that use of plasmas to explore physical and chemical processes in planetary atmospheres has become an established methodology within the planetary science community and forms a bilateral exchange between plasma and astrophysics/planetary science community. Perhaps the best example of such an interchange has been in the study of Titan, Saturn's largest moon whose surface is obscured by the presence of a large 'haze'. This haze is now known to be due to the presence of a deep layer of aerosol particles in the upper atmosphere (8). The first clues to the chemical composition of this haze came from discharge experiments in a mixture of CH<sub>4</sub> and N<sub>2</sub> (the main chemical constituents of Titan's atmosphere) which revealed the formation of a dusty material red/orange in colour (incidentally the colour of Titan's atmosphere as observed from Earth) whose chemical composition of carbon hydrogen and nitrogen is broadly classified as 'tholins'(9).

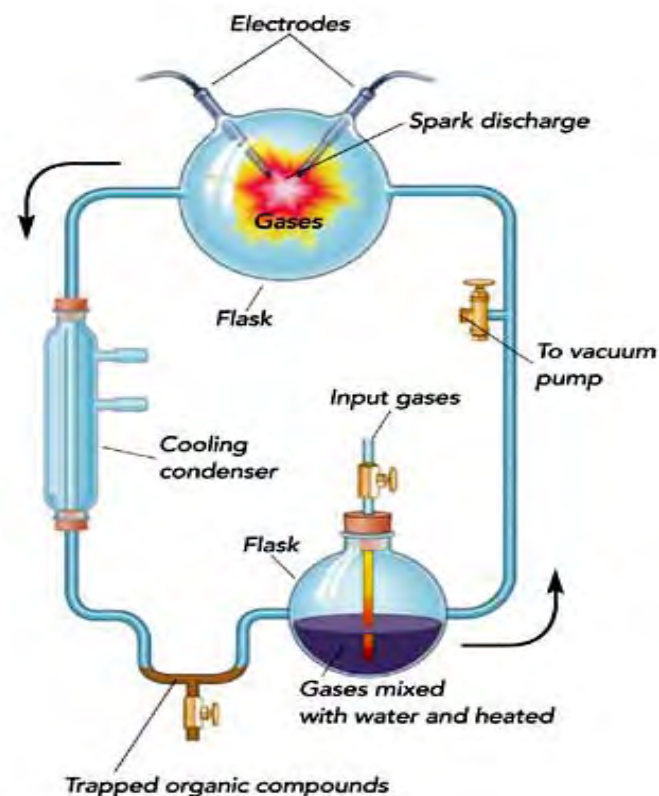


Fig. 1. Schematic of the basic apparatus used by Urey and Miller in their classic experiment that sought to demonstrate that prebiotic molecules could have been formed in the early Earth's atmosphere by atmospheric lightening (10).

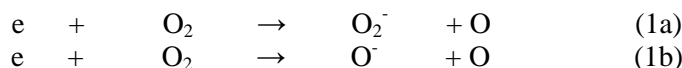
Titan is often discussed as an example of the early Earth's atmosphere and therefore by observing Titan's chemistry we might learn about the most chemistry prevalent on Earth. The use of plasmas to explore how prebiotic material was formed on early Earth was first explored using plasma by Urey and Miller in their classic experiment (10) (Figure1). Using a spark discharge at atmospheric pressure in a gas mixture of hydrogen, methane, ammonia and water (a mixture chosen to represent what was then felt to be the composition of the early Earth's atmosphere) Urey and Miller were able to show that a multitude of amino acids were formed by the discharges. From such experiments it was proposed that lightning in the early Earth's atmosphere could be a source for the prebiotic molecules necessary for the origins of life. Furthermore it was then suggested that similar conditions might exist on other planets such that life itself might be more common throughout the Universe. Thus Urey and Miller founded the subject that today is the flourishing field of 'astrobiology'.

In this article I will briefly review the current status of plasma experiments that are designed to mimic planetary atmospheres before discussing both their strength and weaknesses as such a mimic. I will then describe how such research may develop and the need for collaborations between different research communities.

### **Modeling the terrestrial ionosphere - What can we learn from plasmas ?**

A planetary ionosphere is perhaps one of the most well known examples of a naturally occurring plasma. The terrestrial ionosphere is formed by the interaction of the solar radiation with the Earth's upper atmosphere, the energy of the solar UV is such that it can ionize the two most common molecules  $N_2$  and  $O_2$  (as well as their nascent N and O atoms) creating an avalanche of secondary electrons which may electronically excite these species leading to spectral emissions (the aurora) from the visible to the UV with the red emissions arising predominantly from O atoms and blue/green from the N atoms, whilst excited  $N_2$  molecules are responsible for UV via the Lyman Birge Hopfeld lines. Atmospheric pressure plasmas created using a spark or glow discharge may recreate the terrestrial

ionosphere within the laboratory. By changing the physical parameters of the plasma it is possible to simulate different parts of the ionosphere for example by changing the polarity of the plasma it is possible to favour the formation of cations (positive polarity) or anions (negative polarity). The creation of a region of the ionosphere in which anions are the dominant species (the D region between 60-90 km altitude) came as a surprise and it was only through laboratory studies (e.g. using corona discharges) that the postulated anion formation mechanisms were confirmed, namely electron attachment/charge transfer to molecular oxygen forming  $O_2^-$  (process 1a) and dissociative electron attachment forming  $O^-$  (process 1b)



However measurements of the D-region of the ionosphere revealed other anions such as  $NO^-$  the creation of which could only be explained if such anions participate in chemical reactions e.g.  $O^- + N_2 \rightarrow NO^- + N$ . The study of laboratory plasmas provides a methodology for exploring such ion chemistry, comparing laboratory measurements with observational data and results derived from plasma models. Furthermore by testing the predictions of the model with measurements the values of the rate constants and collision cross sections used in the models may be tested (11).

### Exploring Titan's ionosphere

One of the most surprising observations from the Cassini-Huygens mission to Saturn and its satellites was the discovery that Titan had an ionosphere rich in anions (figure 2) (12). The composition of these anions was the source of considerable discussion since neither of the major components of Titan's atmosphere  $N_2$  and  $CH_4$  are known to be electronegative. The first clues came from a series of experiments that measured anions formed in a negative corona plasma discharge of  $N_2$  and  $CH_4$ . Using a negative corona plasma discharge Horvath et al (13) showed that a series of anions were formed (Figure 3). The  $CN^-$  anion was found to be the most dominant negative ion in the discharge and is believed to be the precursor of heavier negative ions such as  $C_3N^-$  and  $C_5N^-$ . The most likely pathway for the formation of such molecular anions was H-loss dissociative electron attachment to  $HCN$ ,  $H_3CN$  and  $H_5CN$  formed in the discharge.

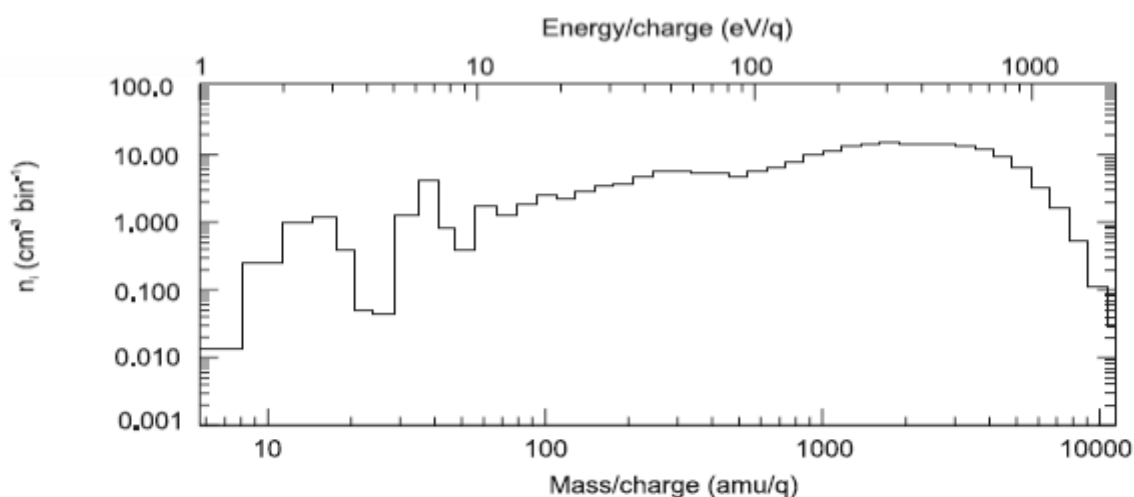


Fig. 2. The anion spectrum recorded by the Cassini-Huygens mission at an altitude of 953 km (Coates et al (2007)) (12).

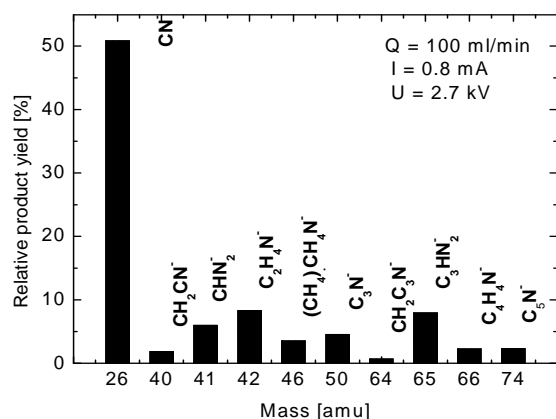
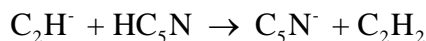
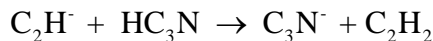
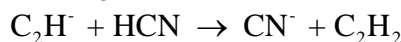


Fig. 3. Relative abundances of the most dominant anions formed in negative corona discharge of N<sub>2</sub>(88%)/Ar(8)/CH<sub>4</sub>(4%) mixture at a reactor pressure of 460 mbar and ambient temperature, 20 °C (13).

Species containing the cyano (CN, C<sub>3</sub>N) or the ethynyl (C<sub>2</sub>H, C<sub>4</sub>H, C<sub>6</sub>H, C<sub>8</sub>H) group have a very high electron affinity ( $\geq 3\text{eV}$ ). The detection of CN<sup>-</sup>, CH<sub>2</sub>CN<sup>-</sup>, C<sub>3</sub>N<sup>-</sup>, CH<sub>2</sub>CN<sup>-</sup> and C<sub>5</sub>N<sup>-</sup> anions therefore provides good evidence of the presence of HCN, CH<sub>3</sub>CN, HC<sub>3</sub>N, CH<sub>3</sub>CN and HC<sub>5</sub>N neutrals that have already been detected by the Cassini flyby (Figure 4). However it was the absence of any hydrocarbon chain ions in the experiment that presented further clues as to the rich chemistry that occurs in Titan ionosphere. The absence of C<sub>2n</sub>H<sup>-</sup> in the spectra could be explained by relatively fast proton transfer reactions, leading to an increase in the yield of N-bearing ions and fast recombination of reactive C<sub>2n</sub>H<sup>-</sup> anions in the drift region of corona discharge:



Thus the C<sub>2</sub>H<sub>2</sub> neutral leads to the formation of CN<sup>-</sup>, C<sub>3</sub>N<sup>-</sup> and C<sub>5</sub>N<sup>-</sup> anions

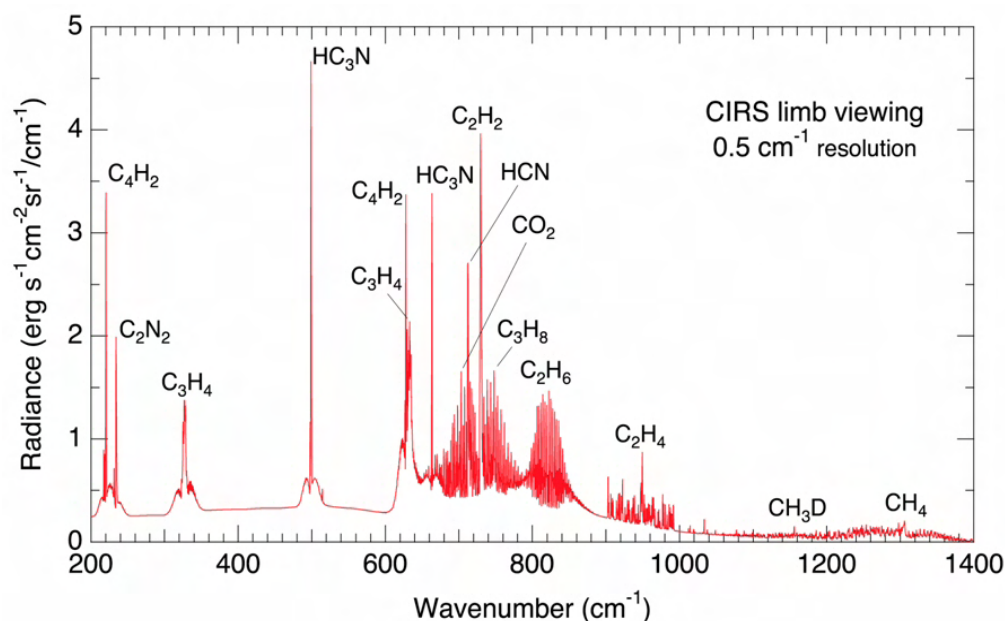


Fig. 4. The chemical composition of Titan's atmosphere as measured by Cassini mission.

The observation of heavier anions (figure 3) suggested that anions may also provide clues as to the formation of the famous ‘Titan haze’. Titan’s surface is obscured by an orange haze which is formed from a dusty aerosol. Again laboratory plasmas provided the first clue as to the chemical composition of Titan’s aerosol with the observation of an orange-red dusty deposit found on the plasma reactor walls. This material has been analysed by various analytical methods and found to be a  $C_xH_yN_z$  composite which are now characterized as ‘tholins’. To date since there are no direct in-situ measurements of Titan’s aerosol these laboratory experiments are the only method for exploring Titan’s aerosol chemistry which may in fact determine much of Titan’s organic chemistry.

### Exploring Mars Chemistry.

Whilst plasmas are obviously excellent media for exploring ion chemistry they also provide a method for exploring neutral chemistry. This may be demonstrated in the use of plasma discharges to explore Martian atmospheric chemistry. The Martian atmosphere is composed predominantly of  $CO_2$  thus it was initially felt that there would be little chemistry other than simple photodissociation to form CO. Initial observations from e.g. Pioneer and Voyager missions confirmed this with the observations of Cameron bands from CO (7). However it was soon apparent that more complex chemistry was present with the observation of ozone (Figure 5). Ozone can only be made by a three body process in which O atoms and oxygen molecules interact in the presence of another molecule (necessary to stabilize the nascent ozone in the Martian atmosphere  $CO_2$ ).



However this in turn requires the creation of molecular oxygen which in the Martian atmosphere can only be formed by recombination of O atoms produced by dissociation of  $CO_2$ . Given the low atmospheric pressure and solar irradiation the creation of ozone seemed unlikely. However experiments using plasmas once again provide a solution to this apparent conundrum. A corona discharge operated in pure  $CO_2$  at typical Martian pressures revealed that ozone is readily formed with concentrations of 100 or 1000s of parts per million (14). Furthermore if trace amounts of water are added to the discharge than ozone concentrations are rapidly reduced through the  $HO_x$  catalytic reaction (as in the Earth’s stratosphere). These results readily explain the observations of the SPICAM instrument on the Mars Express orbiter which showed an anti-correlation between those regions in the Martian atmosphere where ozone is observed and the presence of water vapour (15). Indeed by the conduct of such experiments it is possible to determine whether any significant ozone layer could ever have been present on Mars – it appears not, thus the Martian surface would always have been exposed to sterilizing solar UV radiation making its surface highly unlikely to sustain DNA based life.

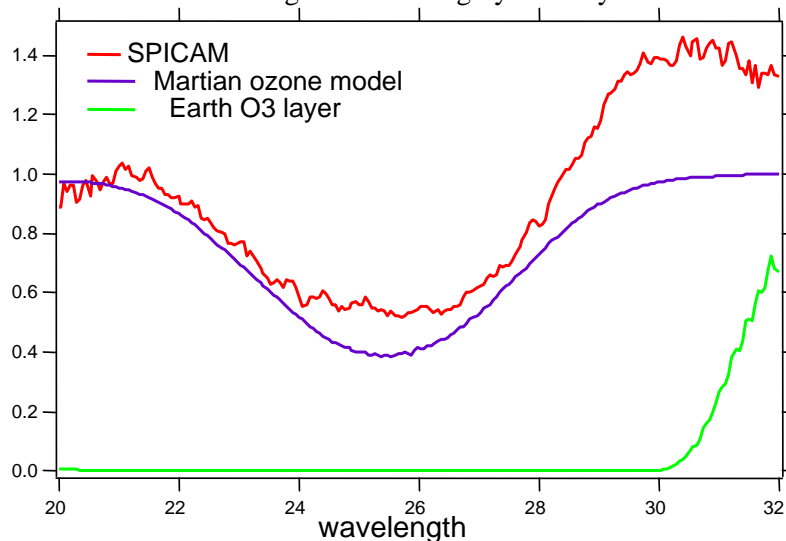


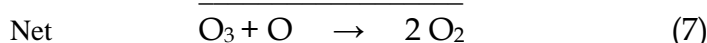
Fig. 5. Martian ozone as measured by SPICAM compared to terrestrial ozone layer, Martian ozone concentrations being 1/200 of that on Earth (15).

## Plasma research and planetary habitability

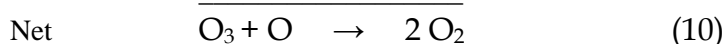
The Martian ozone experiments described above also provided an interesting insight into how life may have developed on Earth. Ozone concentrations are expected to have grown as photosynthesis established itself as the major life process, initially in the seas, leading to an increase in molecular oxygen in the terrestrial atmosphere but such a growth in molecular oxygen need not correspond to an immediate increase in ozone since the large amount of water vapour in the early terrestrial atmosphere would have hampered the formation of ozone in the same way as it precludes formation of ozone layer on Mars. Thus although oxygen concentrations may have risen in the Earth's atmosphere it would not have automatically led to the creation of the ozone layer and the terrestrial stratosphere in turn preventing the Earth's surface from becoming immediately habitable. It is therefore important to determine what concentrations of molecular oxygen *vis a vis* levels of water vapour are necessary for an atmospheric ozone layer to be formed. Ozone is created when solar ultraviolet radiation ( $< \sim 240$  nm) dissociates oxygen molecules to form atomic oxygen (O). Atomic oxygen quickly combines with further oxygen molecules to form ozone:



where M is once again a third body. This is balanced by ozone destruction by OH produced by photodissociation of H<sub>2</sub>O a methodology described by the reaction



These reactions may be reproduced in a simple plasma discharge with different amounts of water vapour being added to the discharge and net concentrations of ozone monitored. In a pure oxygen discharge M is another O<sub>2</sub> molecule but in order to mimic the Earth's atmosphere M is most commonly N<sub>2</sub> (Figure 6). Adding nitrogen also leads to the formation of nitric oxide (NO) which is itself a catalyst for ozone destruction in same way as OH (16).



Such plasma experiments are therefore able to provide insights into the creation of the Earth's early ozone layer suggesting that it formed only several hundred thousand years *after the rapid growth* of the oxygen, in turn providing a limit to the time when life could have emerged from the seas and establish itself on land shielded from the solar UV. The time periods estimated from such experiments can be compared with the geological record (Figure 7) and are in broad agreement.

With the discovery of exoplanets such laboratory experiments may be extended to investigate how oxygen and ozone layers may form on other planets with different atmospheric compositions, for example those with a hydrocarbon content (e.g. methane) and thus whether 'life as we know it' can have developed on such worlds. Questions that could be at least in part answered by conduct of such laboratory plasma experiments include:

- Can photosynthetic life provide a universal biosignature for life in *any* planetary atmosphere?
- How long does it take for photosynthetic oxygen to alter a planetary atmosphere?
- How much (by mass) of photosynthetic life is necessary for it to change a planetary atmosphere?
- How are ozone concentrations related to oxygen concentrations? and is formation of a stratosphere an automatic consequence of ozone formation?

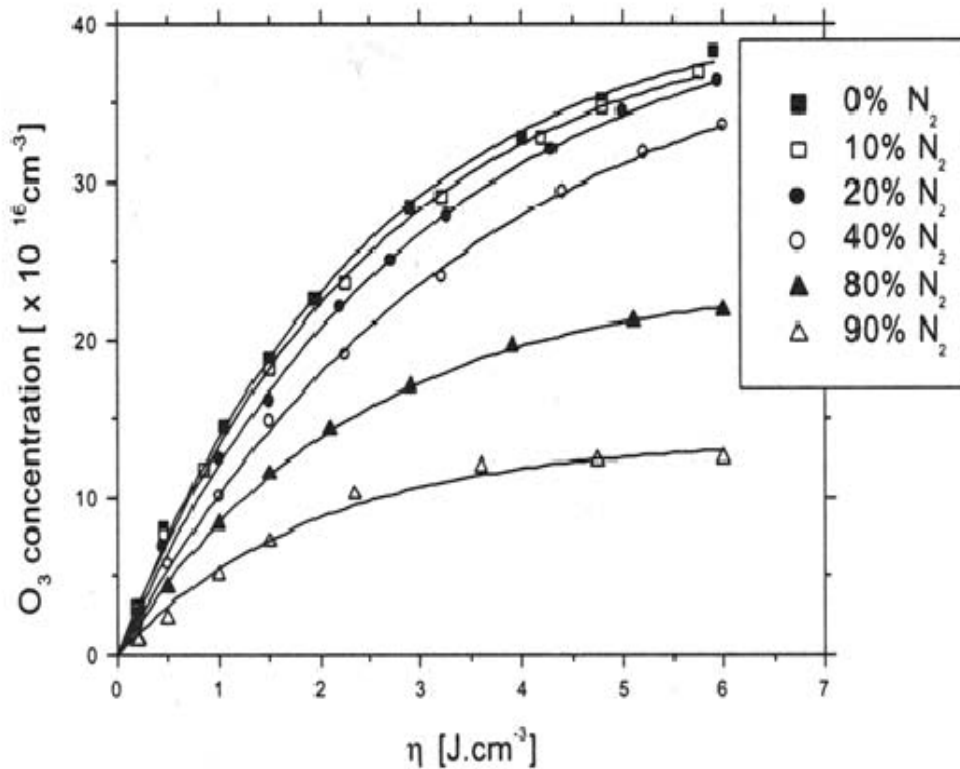


Fig. 6. Ozone concentrations measured as a ratio of nitrogen content in a corona discharge plotted as a function of energy input Mason et al (2002) (17).

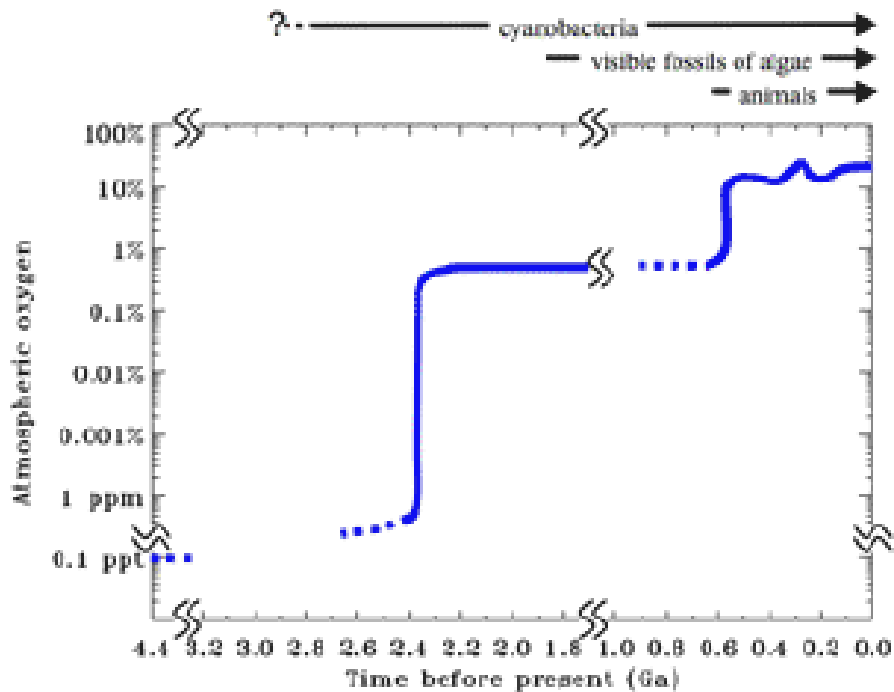


Fig. 7. The rise of oxygen in the Earth's atmosphere. Whilst some oxygen was formed by simple photolysis of water the more rapid increase observed 2.4Ga years ago is ascribed to an onset of photosynthesis.

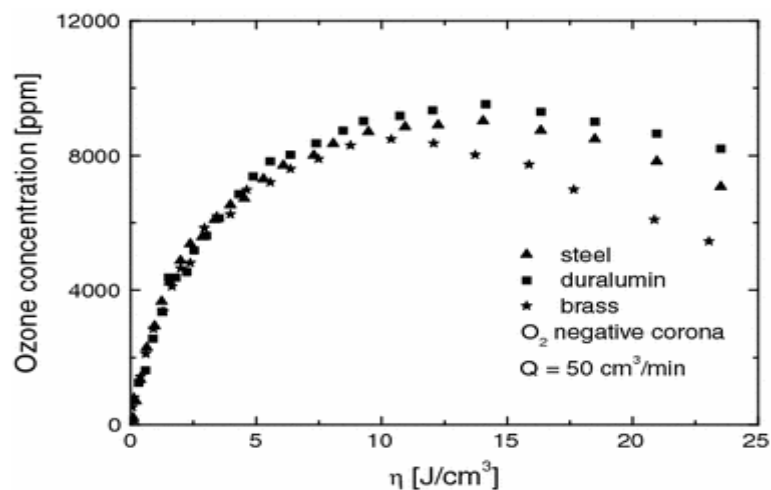


Fig. 8. The effect of electrode material on ozone concentrations in a corona discharge (17).

### Limitation of plasmas as atmospheric mimics

Although plasma discharges have been shown to be a valuable mimic of planetary atmospheres and may provide valuable interpretation of observational data and are an excellent method for testing of planetary atmosphere models it is also necessary to recognise that there are inherent limitations. First much of the physico-chemical processes within an atmosphere are induced by photodissociation not the electron induced dissociation processes dominant in plasmas. Photo-dissociation processes access different electronic states than electrons (which can access so called forbidden states) and so dissociation cross sections and branching ratios in any plasma are different. Secondly in any plasma the chemical and physical processing is dependent upon the *polarity* of the discharge creating different ion yields, indeed the type of discharge (corona, gliding arc, dielectric barrier) all have different characteristics and different chemical yields, this is hard to determine which is the more appropriate atmospheric mimic. Thirdly and perhaps most important, such plasma experiments are performed in plasma reactors and any reactor has walls upon which heterogeneous chemistry may occur -- which is obviously not the case in any planetary atmosphere. Figure 8 shows an example of how different surfaces may lead to different product concentrations (17).

In addition few plasmas are operated at the same temperature as the planetary atmosphere, with Martian and Titan atmospheres being much colder than ambient temperatures within which plasmas are traditionally run, indeed if the reactor is cooled then some of the reactants may freeze out onto reactor walls reducing the apparent product yield and increasing the role of heterogeneous chemistry. However recently plasma experiments to produce Titan tholins have not only been conducted at lower temperatures but by 'levitating' the particulates the effects of heterogeneous chemistry reduced (18) and these experiments are opening a new genre of plasma experiments which may provide the best mimic of a planetary atmosphere.

### Conclusions

In this paper the use of plasma discharges as a tool for studying the physical and chemical processes prevalent in planetary atmospheres has been reviewed. Such plasmas may provide information of the relative ion yields in planetary ionospheres and in the case of Titan have provided clues as to the nature of the anions observed by the Cassini instrument. Such discharges may also provide valuable information on the chemistry prevalent in such atmospheres for example being used to explore ozone formation in the Martian and early Earth atmospheres. Although there are limitations to the use of plasmas for such studies, in particular the effects of heterogeneous chemistry inherent in any plasma reactor, these disadvantages are outweighed by the insights and advances made by the conduct of such studies. Indeed with technological advances making the observation of atmospheres of exoplanets increasingly viable and the simultaneous development of the field of astrobiology and laboratory investigations of the role of planetary atmospheres in prebiotic chemistry such plasma experiments may be expected to grow in the future requiring ever closer links between the plasma science community and the astronomical, geological and planetary science communities.

## References

- (1) R. Roussel-Dupré, J.J. Colman, E. Symbalisty, D. Sentman and V.P. Pasko *Space Sci Rev* **137** 51–82 (2008)
- (2) M Nicolet and A C Aiken *J Geophys Research* **65** 1469-83 (1960)
- (3) F C Fehsenfeld, A L Schmeltekopf, H I Schiff and E E Ferguson *Planetary and Space Science* **15** 373-9 (1967)
- (4) J A Steadman and BA Thrush *J Atmos Chemistry* **18** 301-17 (1994)
- (5) A V Phelps *Canadian Journal of Chemistry* **47** 1783-93 (1969)
- (6) D Smith and P Sapeel *Mass Spectrometry Review* **14** 255-78 (1995)
- (7) A I Stewart, CA Barth, C W Hord and A L Lane *Icarus* 469-74 (1973)
- (8) H Lammer and W Stumptner *Planetary and Space Science* **47** 1341-46 (1999)
- (9) P Pernot, N Carrasco, R Thissen, I Schmitz-Afonso *Analytical Chemistry* **82** 1371-80 (2010)
- (10) S L Miller and H C Urey *Science* **130** 3370 (1959) and *J Molec Evolution* **9** 59-72 (1976)
- (11) J D Skalny, J Orszagh, N J Mason, J A Rees, Y Aranda-Gonzalvo and T D. Whitmore *International Journal of Mass Spectrometry* **272** 12–21 (2008)
- (12) A J Coates, F J Crary, G R Lewis, D T Young, J H Waite and E C Sittler *Geophys Res Letters* **34** L22103 (2007)
- (13) G Horvath, J D Skalny, N J Mason, M Klas, M Zahoran, R Vladioiu and M Manole *Plasma Sources Sci. Technol.* **18** 034016 (2009)
- (14) J D Skalny, S Matejcik, J Orszagh, R Valdiou and N J Mason *Ozone Science and Technology* **29** 399 – 404 (2007) *Plasma Processes and Polymers* **4** 694-700 (2007)
- (15) K E Fast, T Kostiuik, F Lefevre, T Hewagama, T A Livengo, J D Delgado, J Annen and G Sonnabend *Icarus* **203** 20-27 (2004)
- (16) N J Mason, J D Skalny and S Hadj-Ziane *Czech Journal of Physics* **52** 85-94 (2002)
- (17) J D Skalny, J Orszagh, R Vladioiu and N J Mason *Plasma Chemistry and Plasma Process* **30** 43-53 (2010)
- (18) E Quirico et al *Icarus* **198** 218-31 (2008)

# Gas phase chemistry in a plasma setup simulating Titan atmospheric reactivity

N. Carrasco<sup>1</sup>, T. Gautier<sup>1</sup>, A. Buch<sup>2</sup>, C. Szopa<sup>1</sup>, G. Cernogora<sup>1</sup>

<sup>1</sup> LATMOS, Université de Versailles Saint Quentin, 11 Bd D'Alembert 78280 Guyancourt France

Tel : +33 1 80 28 52 72 - E-mail : nathalie.carrasco@latmos.ipsl.fr

<sup>2</sup> LGPM, Ecole Centrale Paris Grande voie des vignes 92295 Chatenay Malabry, France

## Abstract

The gaseous chemistry occurring in Titan's atmosphere is simulated with a CCP RF discharge in N<sub>2</sub> CH<sub>4</sub> mixture. This experiment produces solid particles, which are assumed to be similar to Titan's aerosols. Here are presented results on the conversion of N<sub>2</sub> and CH<sub>4</sub> in more complex gaseous molecules. In situ Mass Spectrometry measurements show the production of hydrogen cyanide (HCN) and acetonitrile (CH<sub>3</sub>CN) in the gas phase. Gases produced in the plasma are also condensed in a trap cooled by liquid nitrogen downstream the plasma. It is shown that the amount of trapped gas increases with the percentage of CH<sub>4</sub> injected in the plasma. Gas trapped are analysed by Gas Chromatography coupled to Mass Spectrometry. This analysis reveals hydrocarbons and a large amount of nitrile species (both until C<sub>5</sub>) in the gas phase. The observed species are in agreement with the recent Cassini-Huygens results as well as with other laboratory setups capable of dissociating nitrogen and methane. This work emphasizes the probable importance of nitrogen-bearing compounds in the chemistry taking place in Titan's atmosphere.

Furthermore, a quantification of mono-nitriles with saturated alkyl chains has been performed relatively to hydrogen cyanide showing a power-law dependence on their concentration. This dependence is also consistent with the Cassini-INMS data and Titan's photochemical models.

## Introduction

The dense atmosphere of Titan, Saturn's largest satellite, is mainly made up of nitrogen and methane. Organic chemical reactions take place in this atmosphere, induced by solar radiation and electrically charged heavy particles coming from Saturn magnetosphere (Sittler Jr et al. 2009). This induced organic chemistry is one among the most complex known in the solar system, and it leads to the formation of solid organic aerosols responsible for Titan's brownish color.

These aerosols present a major interest for planetary science. Knowing how they are formed and what their properties are is a clue to understand better radiative transfer in the atmospheres. The formation process of organic complex molecules presents de facto a large interest for exobiology.

In order to understand Titan's atmospheric chemistry, our approach is to study the chemistry in Titan's atmosphere by experimental simulation on the PAMPRE plasma setup. The principle is to reproduce a gas mixture close to Titan's atmosphere, or at least to a part of its atmosphere, and then deposit energy in order to induce chemistry.

Plasma techniques allow to dissociate molecular nitrogen and provide an energy distribution of the electrons comparable with the energy spectrum of solar photons. Several experiments have been developed using a plasma discharge, either DC (Bernard et al. 2003; Somogyi et al. 2005), or RF (Imanaka et al. 2004; Szopa et al. 2006), as the energy source. The PAMPRE experimental setup uses an RF Capacitively Coupled Plasma (RF CCP) discharge to dissociate N<sub>2</sub>. Previous studies have been done on the plasma physics of the setup and the properties and chemical composition of tholins (Carrasco et al. 2009; Hadamcik et al. 2009; Alcouffe et al. 2010; Pernot et al. 2010).

Here we present the first study of the gas products in PAMPRE and the quantification of the gas to solid conversion yield. It will help to understand the chemistry in the gas phase, highlighting key organic species responsible for the further aerosols formation. This study also allows estimating the pertinence of PAMPRE setup for studying the gas phase reactivity and not only as an aerosols producing device.

## Experimental set-up

RF CCP reactors are well-known for initiating the creation of solid particles (Bouchoule 1999), called tholins, in a reactive gas mixture. These aerosols are electrically charged and can thus grow in levitation in the plasma. They remain in suspension in the plasma, e.g. with no interaction with the reactor wall, until the electrostatic force, responsible of the levitation is no longer stronger than other forces, (particle weight, neutral and ion drag forces), at which point the solid aerosols are ejected out of the plasma.

The experimental device is described in details in Szopa et al. 2006. The plasma is produced by a RF CCP discharge. Gases are injected continuously through the polarized electrode. Gas mixtures are adjusted with gas flow control from pure  $N_2$  and premixed  $N_2+10\% CH_4$ . Influence of pressure and amount of  $CH_4$  on the plasma are given in Alcouffe et al. 2009. Here are presented results on neutral gas chemistry induced by the RF CCP discharge. All results presented here are obtained for a pressure of 1 mbar and 30W of absorbed RF power.

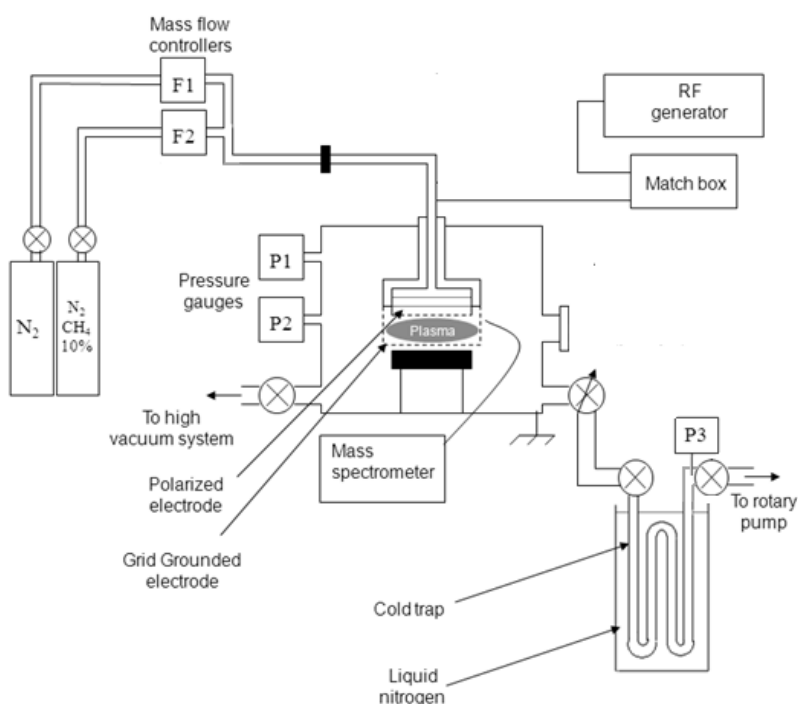


Fig. 1. Schematic of the PAMPRE experimental setup

The most abundant stable neutrals produced in the gaseous phase are directly analysed *in situ* by a Pfeiffer QME 200 quadrupole mass spectrometer. Sampling is done using a stainless steel capillary.

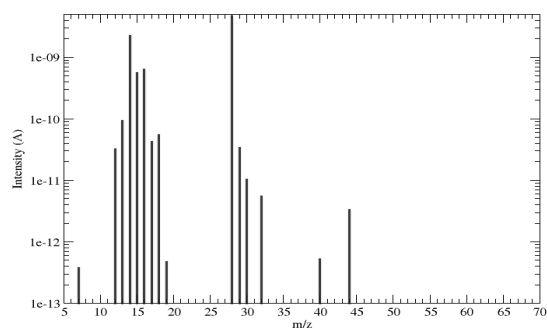
Products are also condensed in a cold trap cooled by liquid nitrogen, downstream between the plasma reactor and the vacuum pump. They are accumulated during 3 hours. Then the trap is heated to the room temperature and connected to a Thermo GC-MS with a MXT-QPlot column (Restek).

## Results and Discussion

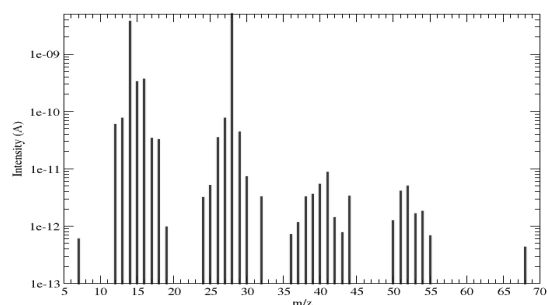
### In situ measurements

The mass spectrometry measurements are done after the transient regime, when the steady state is achieved.

Figure 2 shows typical mass spectra. Figure 2a presents a spectrum of the initial gas mixture  $N_2+10\% CH_4$ , before turning on the RF discharge. Fragments of  $CH_4$  are produced by the ionisation chamber of the mass spectrometer. Figure 2b presents the spectrum of the same gas mixture when discharge is running.



(a) Before plasma discharge



(b) While RF discharge

Fig. 1. In situ mass spectra in a N<sub>2</sub>+10% CH<sub>4</sub>.

We observe that the consumption of methane, detected by the decrease of both the peaks at  $m/z=15$  and  $16$ , is unsurprisingly correlated with an increase of the mass peak  $m/z=2$ , which corresponds mainly to a molecular hydrogen detection. The more methane is consumed, the more hydrogen-rich is the gas phase at stationary state. This is fully consistent with the time-dependent measurement carried out by Majumdar et al. 2005 with a 2:1 CH<sub>4</sub>-N<sub>2</sub> gas mixture.

For initial methane percentages equal to 2, 4 and 10%, we clearly observe HCN at 27 u as the major gas product. Yet surprisingly, with the 1% methane experiment, an important result is the total absence of HCN in the gaseous mixture. This discredits the hypothesis of a polymerization through a poly-HCN pathway, which was commonly admitted. This was already suspected in Vuitton et al.2010, a study on the chemical analysis of the corresponding tholins by ESI-orbitrap : the tholins were confirmed as very different and much more complex than poly-HCN.

### Ex situ measurements

When the trap is warmed up, the gas pressure inside, showing the presence of gases accumulated during the experiment and condensed in the trap. For the different experiments carried out, this pressure depends on the initial methane concentration injected in the reactor during the experiment. This indicates that the total amount of condensable gaseous products changes with the amount of methane introduced in the reactor. The evolution of the total gas pressure measured in the cold trap after warming up to the room temperature as a function of the CH<sub>4</sub> concentration is given in Figure 3. The evolution of the carbon gas to solid conversion yield obtained from a previous study (Sciamma-O'Brien et al. 2010) is also plotted in this figure. This yield is defined as the ratio between the mass of solid carbon incorporated in the tholins and the mass of reactive gaseous carbon coming from the CH<sub>4</sub> consumption in PAMPRE. It reflects the efficiency of the reactive gas mixture to produce solid aerosols, relatively to the carbon element transfer from reactants (CH<sub>4</sub>) to products.

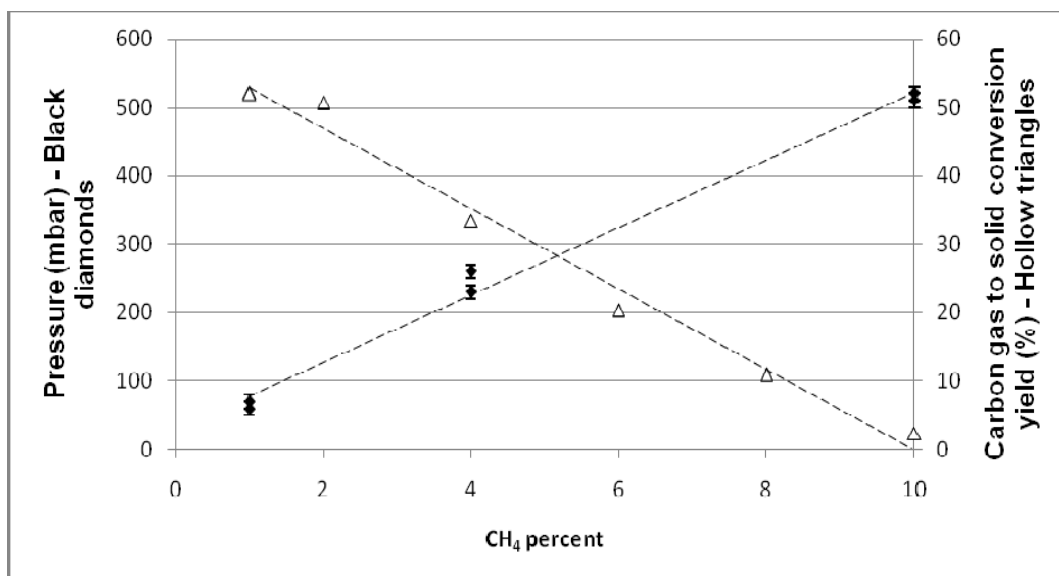


Fig. 2. Pressure in the cold trap after heating up to room temperature compared to carbon gas to solid conversion yield.

Gases trapped are injected in the GC-MS. Fig.3 shows an example of a typical chromatogram obtained.

Main identified peaks correspond to hydrogen cyanide (HCN) and acetonitrile ( $\text{CH}_3\text{-CN}$ ), in agreement with the in situ MS measurements. From the analysis of all the chromatograms obtained, whatever the percentage of methane is, more than 30 species have been detected among which a large amount of nitriles, many hydrocarbons, and a few aromatics, mainly heteroaromatic compounds. The list of compounds detected in the cold trap with GC-MS and presented in table 1 is consistent with the currently known list of Titan's atmospheric compounds (Vuitton et al. 2007; Waite et al. 2007; Lavvas et al. 2008; Cui et al. 2009). In addition, we have been able to detect some heavy nitriles not detected on Titan, such as butanenitrile ( $\text{CH}_3\text{-(CH}_2\text{)}_2\text{-CN}$ ) and pentanenitrile ( $\text{CH}_3\text{-(CH}_2\text{)}_3\text{-CN}$ ). The non detection of these molecules on Titan could be explained by the fact that these molecules are expected to be at very low concentrations, far below the current limit of detection of the instruments onboard Cassini/Huygens.

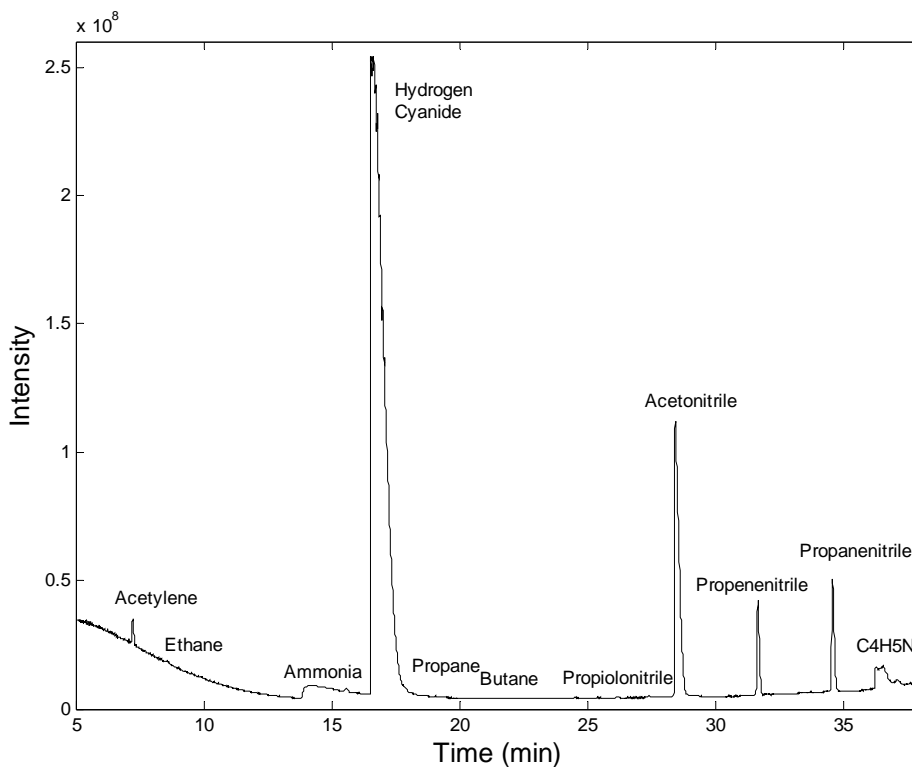


Fig. 3. GCMS spectrum of the condensed gas produced in a  $N_2+4\% CH_4$ .

In order to look for possible growth mechanisms, the area of chromatographic peaks corresponding to nitrile composed were measured. After applying a cross section correction to the areas of the chosen nitrile peaks, the percentage of the nitriles (HCN area normalized) as a function of the number of carbon atoms in the molecules can be plotted.

The first trend observed on Figure 5 is the decrease of nitrile concentrations when the number of carbon inside the molecules increases. The shape of this decrease can be strongly modeled with a power mathematical law.

There are no significant differences between the datasets, whatever the percentage of methane in the experiment. As a consequence a mean power law can be extracted from the experimental data. The experimental data and the associated power-law empirical model are totally consistent with Titan's observational data from INMS (Vuitton et al. 2007) but also with the results from numerical models (Lavvas et al. 2008), showing the capability of the PAMPRE plasma setup to interestingly reproduce the gas-phase chemistry occurring in Titan's atmosphere.

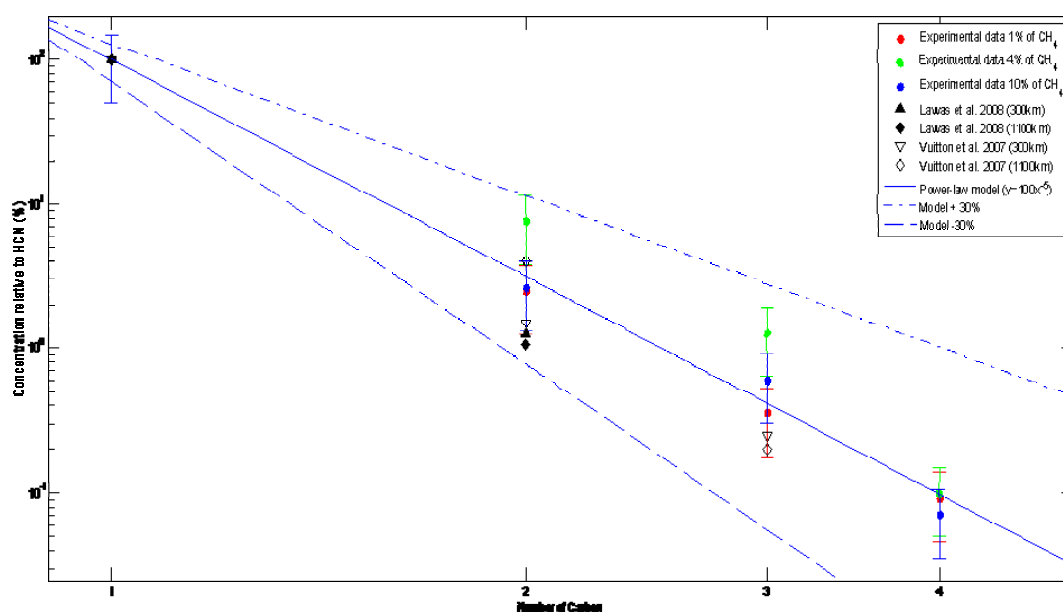


Fig. 4. Relative concentration of the nitriles as a function of the number of carbon in the molecules. The red, green and blue dots represent the experimental data from this work, for experiments with 1%, 4% and 10% of methane in the reactor, respectively. The blue line is the empirical power law model ( $y=ax^b$ ) associated to these experimental data. The empty black diamonds and triangles are data from INMS and CIRS (Vuitton et al. 2007 and reference herein), at 1100 and 300km from Titan's ground, respectively. The full diamonds and triangles are data from computer modeling (Lavvas et al. 2008) at 1100 and 300 km from Titan's ground, respectively.

## Conclusion

Here are presented the first study of the gas phase products in the PAMPRE experiment. A large amount of nitriles has been found. The main product detected is hydrogen cyanide which has also been detected in large amounts in Titan's atmosphere (Teanyby et al. 2007; Vinatier et al. 2010). We have also detected heavier nitriles such as ethanenitrile, propanenitrile and propenenitrile. These heavier nitriles, also detected in Titan's atmosphere, are assumed to be the major compounds in our reactive medium. The results are consistent with Titan's atmospheric composition, tending to demonstrate that lab experiments can be used complementarily to observational data in order to predict both the presence and possible concentrations of compounds which are not yet detected.

On a larger scale, we have detected more than thirty compounds, which, for some of them, had never been detected in experimental simulations before but were expected since they had been observed in Titan atmosphere. Heteroaromatic compounds have also been detected, supporting the hypothesis of PANH pathways for the growth of Titan's tholins.

The results presented here show the possible of nitrogenous compounds in Titan's atmospheric chemistry. With this study we bring more clues to the previously proposed chemical route for aerosol formation in Titan's atmosphere which would predominantly use nitrogen-bearing compounds instead of PAHs (Vuitton et al. 2007; Pernot et al. 2010).

## Acknowledgments

We acknowledge the CNRS (PID OPV, PNP), and the PRES UniverSud and the French National Research Agency (ANR-09-JCJC-0038) for their financial support.

## References

- Alcouffe, G., M. Cavarroc, et al. (2010), "Capacitively coupled plasma used to simulate Titan's atmospheric chemistry." *Plasma Sources Science and Technology*(1): 015008.
- Bernard, J.-M., P. Coll, et al. (2003), "Experimental simulation of Titan's atmosphere: Detection of ammonia and ethylene oxide." *Planetary and Space Science* **51**: 1003-1011.

- Bouchoule, A. (1999), *Dusty Plasmas: Physics, Chemistry, and Technological Impact in Plasma Processing*, Ed. Wiley, Ed., 418p.
- Carrasco, N., I. Schmitz-Afonso, et al. (2009), "Characterization of Titan's Tholins: Solubility, Morphology and Molecular Structure Revisited." *Journal of Physical Chemistry A* **113**: 11195-11203.
- Cui, J., R. V. Yelle, et al. (2009), "Analysis of Titan's neutral upper atmosphere from Cassini Ion Neutral Mass Spectrometer measurements." *Icarus* **200**: 581-615.
- Hadamcik, E., J.-B. Renard, et al. (2009), "Laboratory light-scattering measurements with Titan's aerosols analogues produced by a dusty plasma." *Planetary and Space Science* **57**(13): 1631-1641.
- Imanaka, H., B. N. Khare, et al. (2004), "Laboratory experiments of Titan tholin formed in cold plasma at various pressures: implications for nitrogen-containing polycyclic aromatic compounds in Titan haze." *Icarus* **168**: 344-366.
- Lavvas, P. P., A. Coustenis, et al. (2008), "Coupling photochemistry with haze formation in Titan's atmosphere, Part II: Results and validation with Cassini/Huygens data." *Planetary and Space Science* **56**(1): 67-99.
- Majumdar, A., J.F. Behnke, et al. (2005), "Chemical reaction studies in CH<sub>4</sub>/Ar and CH<sub>4</sub>/N<sub>2</sub> gas mixtures of a dielectric barrier discharge", *J. Phys. Chem.*, **109**: 9371-9377.
- Pernot, P., N. Carrasco, et al. (2010), "Tholinomics-Chemical Analysis of Nitrogen Rich Polymers." *Analytical Chemistry*.
- Sciamma-O'Brien, E., N. Carrasco, et al. (2010), "Titan's atmosphere: an optimal gas mixture for aerosol production." *Icarus*.
- Sittler Jr, E. C., A. Ali, et al. (2009), "Heavy ion formation in Titan's ionosphere: Magnetospheric introduction of free oxygen and a source of Titan's aerosols?" *Planetary and Space Science* **57**(13): 1547-1557.
- Somogyi, A., C.-H. Oh, et al. (2005), "Organic Environments on Saturn's Moon, Titan: Simulating Chemical Reactions and Analyzing Products by FT-ICR and Ion-Trap Mass Spectrometry." *Journal of the American Society for Mass Spectrometry* **16**(6): 850-859.
- Szopa, C., G. Cernogora, et al. (2006), "PAMPRE: A dusty plasma experiment for Titan's tholins production and study." *Planetary and Space Science* **54**: 394-404.
- Teanby, N. A., P. G. J. Irwin, et al. (2010), "Mappint Titan's HCN in the far infra-red: implications for photochemistry." *Faraday Discussion* **147**(3).
- Teanby, N. A., P. G. J. Irwin, et al. (2007), "Vertical profiles of HCN, HC<sub>3</sub>N, and C<sub>2</sub>H<sub>2</sub> in Titan's atmosphere derived from Cassini/CIRS data." *Icarus* **186**(2): 364-384.
- Vinatier, S., B. Bézard, et al. (2010), "Analysis of Cassini/CIRS limb spectra of Titan acquired during the nominal mission: I. Hydrocarbons, nitriles and CO<sub>2</sub> vertical mixing ratio profiles." *Icarus* **205**(2): 559-570.
- Vuitton, V., R. V. Yelle, et al. (2007), "Ion Chemistry and N-containing molecules in Titan's upper atmosphere." *Icarus* **191**: 722-742.
- Vuitton, V., J.Y. Bonnet, et al. (2010) "Very high resolution mass spectrometry of HCN polymers and tholins", *Faraday Discuss.*, **147**: 495-508
- Waite, J. H., D. T. Young, et al. (2007), "The Process of Tholin Formation in Titan's Upper Atmosphere." *Science* **316**: 870-875.

# Corona discharge as an environment for simulation of plasma-chemical processes in Martian atmosphere

J. Országh<sup>1,2</sup>, N.J. Mason<sup>2</sup> and Š. Matejčík<sup>1</sup>

<sup>1</sup>Department of Experimental Physics, Comenius University, Mlynská dolina, Bratislava 842 45, Slovakia

<sup>2</sup>Dept. of Physics and Astronomy, Open University, Walton Hall, Milton Keynes, United Kingdom

e-mail: orszagh@fmph.uniba.sk

## Abstract

The conditions on the Martian surface are the most capable of sustaining life as we know it. That is why this planet is one of the most interesting objects in our solar system. The atmosphere of Mars is composed mainly of carbon dioxide, nitrogen and other minor constituents. Ozone as it can prevent UV radiation from reaching the planet surface is one of the most important atmospheric compounds for life existence. The ways of ozone generation in the conditions of Martian atmosphere are studied by simulation of elementary processes by DC corona discharge.

**Keywords:** corona discharge, Mars, ozone, carbon dioxide

## Introduction

In our solar system Mars seems to be the planet most capable of sustaining life. This has led to a series of space missions to the planet culminating in the NASA Phoenix mission. One of the aims of the mission is to search for water in the Martian soil. However in exploring the possibility for life having established itself on the Martian it is necessary to consider the conditions on the Martian surface at the time when life may have developed. Biological molecules on Earth are susceptible to radiation, the effects of which may lead to damage leading either to direct destruction or, in the case of DNA, mutagenesis in which the self replicating molecule is able to replicate itself after damage but with genetic modifications that can lead to cell death or mutation. On the Earth biomolecules are protected by the presence of terrestrial ozone layer, which filters the damaging solar UV radiation and prevents it from reaching the surface. Hence the creation of terrestrial ozone layer is believed to have been crucial to life emerging on the terrestrial surface. Accordingly in investigating whether the Martian surface was ever capable of sustaining life it is necessary to investigate whether its atmosphere was ever capable of sustaining ozone concentration sufficient to screen its surface from UV radiation. Small concentrations of ozone are found in the present atmosphere of Mars even though today it is composed of almost pure CO<sub>2</sub>. When first detected the presence of ozone was itself a surprise and the mechanisms of its formation questioned. Electrical discharges provide a suitable laboratory analogue of planetary atmospheres with electrical energy mimicking the energy input into the planetary atmospheres by solar radiation [1]. Therefore using a corona discharge we have sought to investigate the chemical processes that lead to formation of ozone and oxygen in the Martian atmosphere. The negative corona discharge is suitable for investigating elementary processes induced by slow electrons as well as the drift region of the discharge contains such electrons and these are colliding with neutral molecules. The output of such research can be useful not only for the Martian atmosphere problems but in the field of industrial ozone production or global warming (as carbon dioxide concentration in the Earth atmosphere is considered to be the main reason) research as well.

## Experiment

The experimental setup in our research is similar despite of using several different analytic techniques. The discharge reactor is usually composed of cylindrical (wire-to-cylinder) system of electrodes. The outer electrode with dimensions (diameter 1.6 cm and length 6.5 cm) is made of stainless steel as well as the inner electrode which diameter was 0.125 mm. The scheme of the apparatus is shown in the figure 1. The reactor is placed in the chamber of either UV-VIS or IR spectrometer. Such experimental setup allows us to analyse the products of the DC corona discharge directly between the electrodes of the reactor. There are two main types of the experiment. In the flowing regime the gas or mixture of more gases is flowing through the reactor at constant rate. In stationary regime the mixture is let into the reactor before the experiment and the reactor input and

output are closed by valves. Then the discharge is switched on and the measurement can start. In the flowing regime we are investigating the effect of gas flow rate and voltage on the discharge current and concentration of discharge products. In the stationary regime we are mainly interested in the time evolution of the discharge current and products concentration. From these measured values various interesting parameters of the discharge such as power of average mobility of charged particles can be calculated.

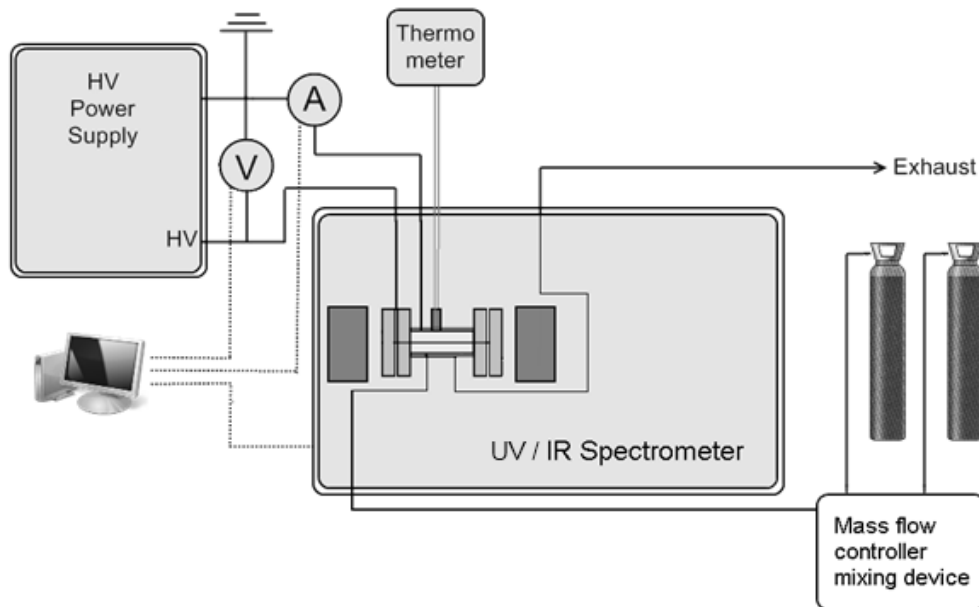


Fig. 1. General scheme of experimental apparatus.

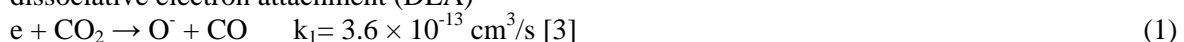
To reach a complex overview of the scientific problem these experiments are accompanied by several other experimental setups. First the ions produced by the corona discharge are investigated by quadrupole mass spectrometer. For this experiment we use DC corona discharge in point-to-plane configuration. For more details see [2]. As the processes active on the inner surfaces of the reactor seem to significantly influence the chemistry in the discharge we are starting a new series of experiments aimed at these problems. Various surface analysis methods such as IR spectrometry or EDS are going to be used.

### Generated ozone influencing the electrical properties of the discharge

In the figure 2 the current-voltage (CV) characteristics of the positive and negative corona discharges fed by carbon dioxide at different levels of gas flow rate is shown. It is evident that the gas flow rate is not affecting the CV characteristics of the positive corona. On the contrary in negative corona the characteristics is getting steeper with increasing gas flow rate.

Before we discuss the observed differences in the macroscopic properties of positive and negative corona discharges in carbon dioxide, it is necessary to recall the different mechanisms for the generation of secondary electrons in these two types of discharges. In discharges with positive polarity the secondary electrons are generated by photoionisation in both the ionising and the drift regions, while secondary electrons in a negative corona discharge are released from the inner electrode by the impact of positive ions. Therefore while the maximum concentration of free electrons in a positive corona discharge is at the inner electrode, the concentration of electrons increases across the ionising region of the negative corona discharge reaching a maximum at the boundary between the ionising region and the drift region.

Secondary electrons formed beyond the ionising region of the positive corona discharge by photoionization are either recombined with positive ions drifting from ionizing region towards the outer electrode or are attached to CO<sub>2</sub> molecules at the boundary between ionizing and drift region by dissociative electron attachment (DEA)



This process is maximised at electron energies close to 4.2 eV i.e. at relatively high mean electron energy. However the rate constant is low. Hence outside the ionising region electron attachment is negligible. If the ozone is formed at voltages slightly above the onset voltage, (100-200) V, some secondary electrons can be removed from the discharge by dissociative attachment to ozone. There are two DEA channels for ozone, one yielding  $O^-$  the other  $O_2^-$  both of them having a maximum production cross section for electrons with energies around 1 eV. The maximum rate constant for process



is  $k_2 = 2 \times 10^{-9} \text{ cm}^3/\text{s}$  and will be dominant in the drift region where the reduced electric field  $E/N$  is low [4].

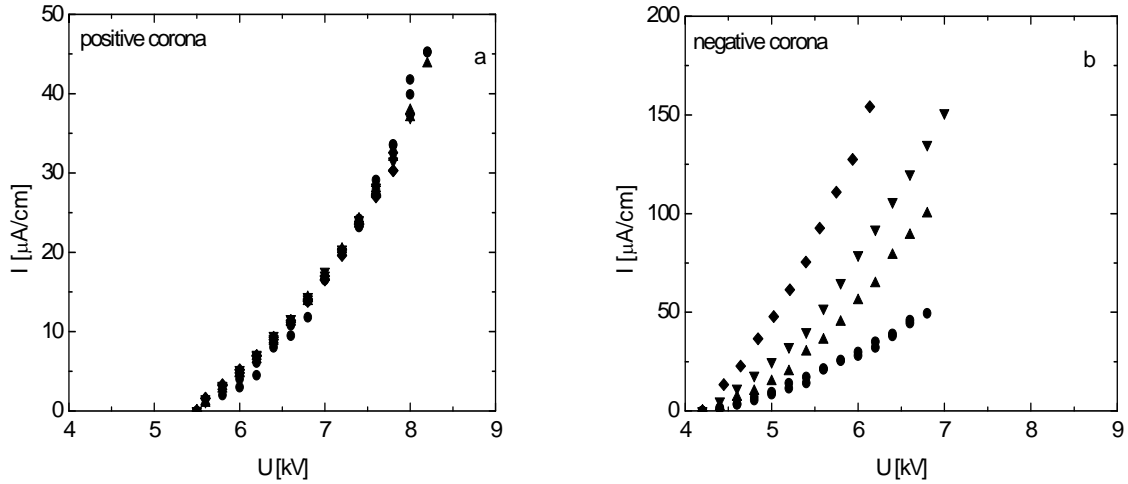


Fig. 2. The current voltage characteristics in flowing carbon dioxide (a positive, b negative, • 10  $\text{cm}^3/\text{s}$ , ▲ 50  $\text{cm}^3/\text{s}$ , ▼ 100  $\text{cm}^3/\text{s}$ , ◆ 200  $\text{cm}^3/\text{s}$ )

Hence some of the secondary electrons, which otherwise could contribute to sustaining a discharge may be converted to less mobile negative ions. The higher the gas flow rate is the lower is the energy put by the discharge into the unit volume of the gas and the lower is ozone concentration. Then the lower is the ozone concentration the lower is the amount of electrons converted into anions and the overall measured discharge current is higher.

In the figure 3 the dependence of the average mobility of charged particles in the positive corona discharge tube on voltage can be seen.

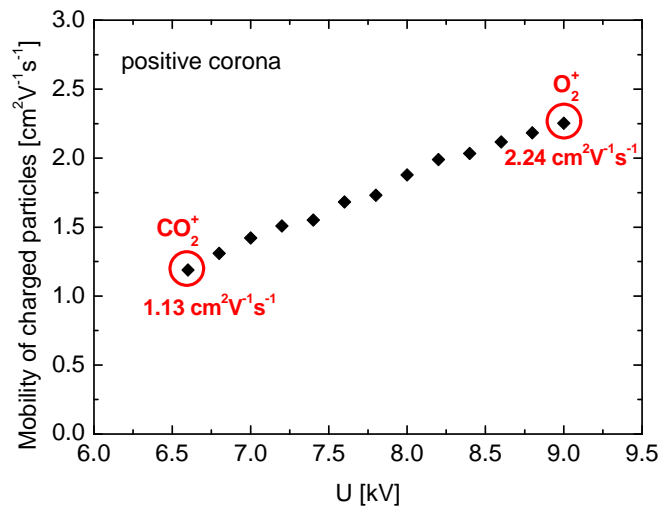


Fig. 3. The dependence of mobility of charged particles on the voltage in positive corona fed by

carbon dioxide.

The mobility of the positive ions in the discharge gap was found to be similar to the mobility of  $\text{CO}_2^+$  ions  $1.13 \text{ cm}^2 \cdot \text{V}^{-1} \cdot \text{s}^{-1}$  [5] only at the voltage just above the onset. Higher mobility values were observed with increasing voltage and the highest value corresponds to the mobility of  $\text{O}_2^+$ . There are two probable explanations for such an effect:

- 1) The  $\text{CO}_2^+$  ions are converted to  $\text{O}_2^+$  ions which have a higher mobility.
- 2) Extra  $\text{CO}^+$  ions with higher mobility are formed via dissociative ionisation of  $\text{CO}_2$ .

However since  $\text{CO}^+$  ions are unstable and are easily converted to  $\text{CO}_2^+$  ions by the very fast ion-molecule reaction



$$k_3 = 1.2 \times 10^{-9} \text{ cm}^3/\text{s} \text{ [6]}$$

this last process can be discounted in any atmospheric discharge.

$\text{CO}_2^+$  ions can also be transformed into  $\text{O}_2^+$  ions through the charge exchange process



$$k_4 = 2.6 \times 10^{-10} \text{ cm}^3/\text{s} \text{ [6]}$$

the rate of this reaction is limited the concentration of oxygen atoms produced by electron impact dissociation of carbon dioxide



$$k_5 = f(E/N) \text{ [6]}$$

once again this reaction is confined to the small volume of the glow region.

Therefore the observed increase in the mobility of positive ions (Fig. 3.) can be attributed to the active role of process (4).

The concentration of oxygen atoms increases with increasing voltage hence reaction (4) becomes increasingly significant at higher voltages and the ratio of  $[\text{O}_2^+]/[\text{CO}_2^+]$  increases. Since the mobility of  $\text{O}_2^+$  ions ( $2.24 \text{ cm}^2/\text{V} \cdot \text{s}$  at  $E/N = 30 \text{ Td}$  [7]) is higher than the mobility of  $\text{CO}_2^+$  ions the average mobility of a mixture  $\text{CO}_2^+$  and  $\text{O}_2^+$  increases as more  $\text{O}_2^+$  are formed. From our lowest mobility we estimate that almost all of the positive ions in the discharge could be  $\text{CO}_2^+$ . In contrast at the highest voltage the average mobility calculated from the CV data equates to the mobility of positive molecular oxygen ions from which we can deduce that at high voltage practically all the  $\text{CO}_2^+$  ions produced are converted into  $\text{O}_2^+$  ions.

Of course the simulation of Martian atmosphere requires taking the effect of other gases into account. The Martian atmosphere contains a few percents of nitrogen, argon, oxygen and water vapour as well. In our research we are also interested in their effects on the production of ozone or carbon monoxide. The humidity effects were analysed e.g. in [8], oxygen effects in [9] and the first results on argon admixture were published recently in [10]. It seems that especially in case of nitrogen and water the role of surface processes is very important. That is why it is needed to study them very carefully in the next step of our Martian atmosphere research.

## Conclusions

The DC corona discharge corona discharge has been used to study the processes that could lead to ozone and other compounds formation in the conditions of the Martian atmosphere. The production of cations  $\text{CO}_2^+$  and  $\text{O}_2^+$  has been explained as well as the effect of generated ozone to the electrical properties of the discharge. In the near future it is necessary to study the surface processes in detail to understand the effects of some admixtures.

This work has been supported by projects Nr. APVV-0365-07, VEGA 1/0558/09 and VEGA 1/0379/11.

## References

- [1] T.H. Dinh Dissertation thesis, Old Dominion University, USA, 2002.
- [2] J.D. Skalny, J. Orszagh, S. Matejcik, N.J. Mason, J.A. Rees, Y. Aranda-Gonzalvo, T.D. Whitmore, International Journal of Mass Spectrometry 277 (2008) 210–214.
- [3] O. Eichwald, M. Yousfi, A. Hennad, D. Benabdessadok, J. Appl. Phys. 82, 4781 (1997).
- [4] J. M. Van Doren, T. M. Miller, S. Williams, A. A. Viggiano, Phys. Rev. Lett. 91, 223201-1 (2003).

- [5] M. Saporoshenko, *Phys Rev. A*, 8, (1973) 1044-1047.
- [6] H. Hokazono, M. Obara, K. Midorikawa, H. Tashiro, *J. Appl. Phys.*, 69 (1991) 6850-6868.
- [7] B. Elliason, *Electrical Discharge in Oxygen Part 1: Basic Data, Rate Coefficients and Cross Sections* Brown Boveri Research Report KLR 83/40 C, Baden-Dättwil, Switzerland, 1985.
- [8] J.D. Skalný, J. Országh, Š. Matejčík, N.J. Mason. *Phys. Scr.* T131 (2008) 014012.
- [9] J. Országh, J.D. Skalný, Š. Matejčík, N.J. Mason. *Phys. Scr.* T131 (2008) 014014.
- [10] J. Országh, M. Duffy, Z. Lichvanová, C. Sima, Š. Matejčík, N.J. Mason, P. Papp, R. Vladioiu, *Book of Contributed Papers HAKONE XII*, Trenčianske Teplice, Slovakia, 2010.

# Optical Emission Spectroscopy of Atmospheric Pressure Discharges in Nitrogen-Methane Gas Mixtures

F. Krčma<sup>1</sup>, K. Klohnová<sup>1</sup>, L. Poláchová<sup>1</sup>, G. Horváth<sup>2</sup>

<sup>1</sup>Faculty of Chemistry, Brno University of Technology, Purkyňova 464/118, 612 00 Brno, Czech Republic

<sup>2</sup>Faculty of Mathematics, Physics and Informatics, Comenius University, Mlynská dolina F2, 842 48 Bratislava, Slovakia

e-mail: krcma@fch.vutbr.cz

## Abstract

The optical emission spectra of abnormal glow and DBD discharges were studied at atmospheric pressure and ambient temperature. The used nitrogen-methane mixtures (0.5–2.5 % of methane) are corresponding to the composition of Saturn's moon Titan atmosphere. Both gases had purity better than 99.999 % and the whole system was evacuated before measurement to suppress oxygen traces. Optical emission spectra were taken in the dependence of applied power and gas mixture composition. Nitrogen, C<sub>2</sub> and CN radical spectra as well as atomic lines of hydrogen and carbon were identified in the case of abnormal glow discharge. Only nitrogen second positive spectra were recorded in the case of DBD due to lower transparency of the system as well as due to lower applied power. The rotational and vibrational temperatures were obtained in both discharge configurations for different species.

**Keywords:** Optical emission spectroscopy, atmospheric pressure discharge, Titan like atmosphere, nitrogen-methane gas mixture.

## Introduction

The Cassini space mission to Saturn and the release of its Huygens probe onto its largest moon, Titan, has led to a wealth of data on the atmospheric and surface composition of Titan, presenting us with a set of unexpected results including the observation of hydrocarbon lakes – the first liquid ‘seas’ on a solar system body outside the Earth; and the observation of anions in the upper atmosphere (ionosphere) [1]. In order to understand the physical and chemical processes leading to such observed phenomena, additional laboratory simulations are required.

The dense atmosphere of Titan is mostly composed of N<sub>2</sub> with a few percent of CH<sub>4</sub>. The presence of clouds and strong convective motions are a particular feature of Titan's lower atmosphere. Moreover, charged particles, originating from the Saturnian magnetosphere, can accumulate on droplets within the clouds of the troposphere. Due to these processes, the charge accumulation is observed in Titan troposphere, and it can induce strong electric field sufficiently high for the discharge generation (corona, lightning). This can evoke a spread number of chemical reactions in the Titan troposphere [2] leading to the production of higher hydrocarbons, nitriles or even aminoacids [3].

Most of recent experimental works have been performed predominantly in DBD, glow, microwave, RF, and corona discharges [4-7] which are considered to be a good environment for the study of electron-molecule and ion-molecule reactions. To understand the molecular kinetics during the discharge, the energy distribution as well as knowledge of plasma composition is necessary. The optical emission spectroscopy is one of the simplest ways how to obtain such information.

In this paper, we report our results of a new investigation of the atmospheric pressure DBD and glow discharges fed by a N<sub>2</sub>-CH<sub>4</sub> gas mixture with CH<sub>4</sub> contents in the range of 0.5–2.5 %.

## Experimental

The experimental set up consists of the vertically oriented cylindrical stainless steel reactor (i.d. 70 mm, length of 25 cm). The electrode system was mounted at the reactor central position. In the case of the glow discharge study (see Fig. 1a), the discharge electrode system had the standard configuration of a classical gliding arc, a pair of stainless steel holders positioned in parallel to the iron electrodes. However in this case the plasma was not gliding due to the low flow rate and therefore stable abnormal glow plasma occurred between the electrodes at their shortest distance of 2 mm. Plasma channel with diameter of 1 mm was formed. The spectra were collected through the fused silica

window situated 10 cm from the discharge perpendicularly to the gas flow through the reactor for the protection of thin layers deposition, and it was centred to the discharge position in parallel to the electrodes plane. With decreasing current (40–15 mA), the voltage was slightly increasing from 350 V to 400 V. Electrical parameters have been measured by a Tektronix TDS 1012 oscilloscope using high voltage probe (1:1000) and non inductance resistor. The discharge was powered by a specially constructed DC HV source.

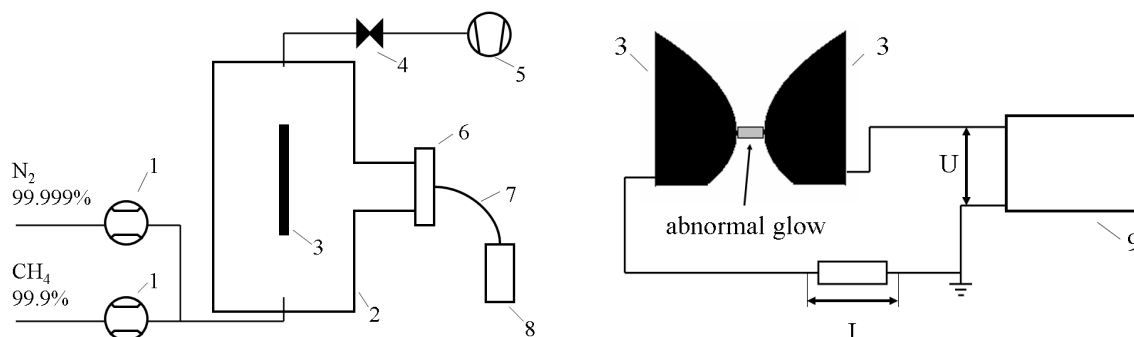


Fig. 1a. Simplified scheme of the experimental device for glow discharge study (left) and electrode system (right): 1 – mass flow controller; 2 – discharge reactor; 3 – stainless steel electrode; 4 – vacuum valve; 5 – rotary oil pump; 6 – fused silica window; 7 – optical quartz fiber; 8 – spectrometer; 9 – HV power supply.

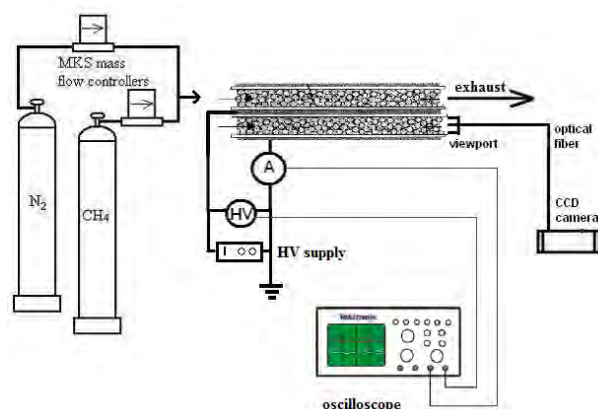


Fig. 1b. Simplified scheme of packed bed DBD apparatus.

A schematic diagram of DBD reactor is shown in Fig. 1b. The packed bed DBD discharge chamber consisted of a HV rod electrode (length of 100 mm, diameter of 10 mm), and grounded cylindrical electrode, was sealed and equipped by a sapphire view port for optical measurements. The electrodes of the DBD discharge reactor had a standard coaxial geometry, but the electrode gap was filled with glass spheres. The discharge was operated at voltages of 17, and 22 kV, respectively, peak-to-peak and frequency of 13.1 kHz using a power supply system consisted of an oscillator, a Behringer amplifier and a specially constructed transformer. The RMS value of discharge power was set up at 5, and 8 W, respectively. The voltage was monitored by the same technique as above, the current was measured by a classical Rogowski current probe. The axial position of the fused silica window down stream of the discharge was used for the DBD spectroscopic observations for various CH<sub>4</sub> molar ratio. The Jobin Yvon TRIAX 550 spectrometer with CCD detector was used to monitor the optical emission from the N<sub>2</sub>/CH<sub>4</sub> plasma. The spectral response of this spectrometer was obtained using the Oriel radiation standard lamp. The 3600 gr/mm grating was used for the rotationally resolved CN violet 0-0 band acquisition; all other spectra were measured with 1200 gr/mm grating. The measurements were carried out in flowing regime for a total flow rate of 200 Sccm. The flow rates for both CH<sub>4</sub> and N<sub>2</sub> channels were regulated using MKS mass flow controllers. The present experiments were performed for different N<sub>2</sub>:CH<sub>4</sub> ratios in the range 0.5–2.5 % CH<sub>4</sub> in N<sub>2</sub> at atmospheric pressure. All experiments were carried out at ambient temperature. The discharge was typically operated from 60 to 120 minutes, and the reactor wall temperature (measured by thermocouples) did not exceed 320 K. the whole device was prevacuated by rotary oil pump to keep the system as oxygen free.

## Results and discussion – glow discharge

The spectra were recorded integrally over the whole plasma volume because our contemporary arrangement did not allow their spatial resolution. The spectra were composed of the following molecular spectral systems: the second positive system of neutral  $N_2$  ( $C^3\Pi_u \rightarrow B^3\Pi_g$ ), the first negative system of  $N_2^+$  ion ( $B^2\Sigma_u^+ \rightarrow X^2\Sigma_g^+$ ), the CN violet ( $B^2\Sigma^+ \rightarrow X^2\Sigma^+ a$ ), and red systems ( $A^2\Sigma^+ \rightarrow X^2\Sigma^+$ ) and the  $C_2$  Swan bands. Besides these the strong atomic  $H^\alpha$  line, weaker  $H^\beta$  line and week lines of C (247 nm - measured in the second order) and  $N^+$  (399.5 nm) were been detected.

Since many emission bands of  $N_2$  and CN overlap, we selected non overlapped rotational bands for the further detailed analysis and plasma parameters calculation. The CN violet 0-0 band was measured with high resolution, and it was used for the rotational temperature calculation by classical pyrometric line procedure using rotational lines  $J = 3, 4, 7-16$  and rotational constant given by Prasad [8]. The LifBase software [9] was used for the rotational lines assignment. The same procedure was applied also for the neutral nitrogen in  $N_2$  ( $C^3\Pi_u$ ) state rotational temperature calculation. In this case, the spectrum of 0-0 nitrogen second positive band (rotational lines with  $J = 40-50$ ) was used. The line assignment was done by SpecAir software [10].

The rotational temperatures calculated from the particles are shown in Fig. 2 for the glow discharge conditions. The  $N_2$  rotational temperature is more or less discharge current independent, but it slightly increases with the increase of methane concentration in the gas mixture. On the other hand, the CN rotational temperature decreases with increasing current in the range from 3200 to 1200 K. These temperature changes reflect mechanisms creating both radiative states. Upper states of both used transitions are populated mainly by direct electron impact but also some other processes must be taken into account from the discharge channel boundaries. Thus  $N_2$  ( $C^3\Pi_u$ ) state rotational distribution is influenced also by pooling reactions of lower metastables and CN by resonant energy transfer from nitrogen ground state metastables. Moreover, CN is created in the discharge by three body recombination of atoms that terminates dominantly at level CN ( $B^2\Sigma^+$ ,  $v=7$ ), and further rotational population redistribution is expected. The detailed kinetic analysis will be done in the near future. The maximal CN rotational temperature was obtained in the nitrogen with 1.5 % of methane, no clear temperature dependence on methane concentration was determined. The experimental uncertainty is of about 300 K in both cases.

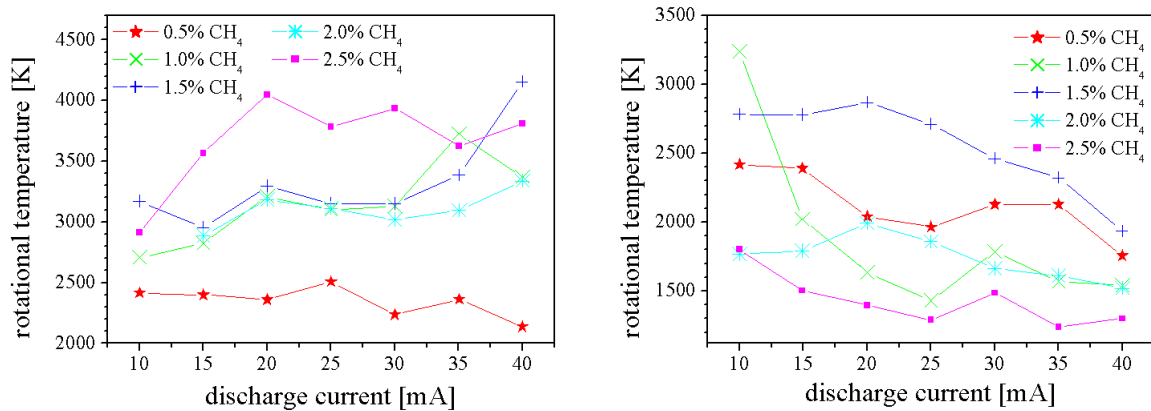


Fig. 2. Rotational temperatures calculated from nitrogen second positive (left) and CN violet (right) 0-0 bands.

Vibrational temperatures were calculated from nitrogen, CN, and  $C_2$  spectra. The used bands as well as references to the used molecular constants are given in Table 1. The non overlapped sequences have been used, only. The use of the most intensive bands was impossible due to the strong overlap of spectral systems. It can be noted that only bands with signal/noise ratio better than 5 were used for these calculations, the other were omitted. The average uncertainty of calculated values was between 10 and 15 %. The electron temperature was not calculated because intensity of  $H^\beta$  line was too low, and it was significantly overlapped by  $C_2$  Swan bands, too.

Tab. 1. Bands used for the vibrational temperature calculations

| Spectral system                     | Used band heads         | Molecular constants from |
|-------------------------------------|-------------------------|--------------------------|
| N <sub>2</sub> 1 <sup>st</sup> neg. | 0-2; 1-3; 2-4; 3-5      | [11]                     |
| N <sub>2</sub> 2 <sup>nd</sup> pos. | 1-0; 2-1; 3-2           | [11]                     |
| CN violet                           | 0-1; 1-2; 2-3; 3-4; 4-5 | [8]                      |
| C <sub>2</sub> Swan                 | 0-1; 1-2; 2-3; 3-4      | [12]                     |

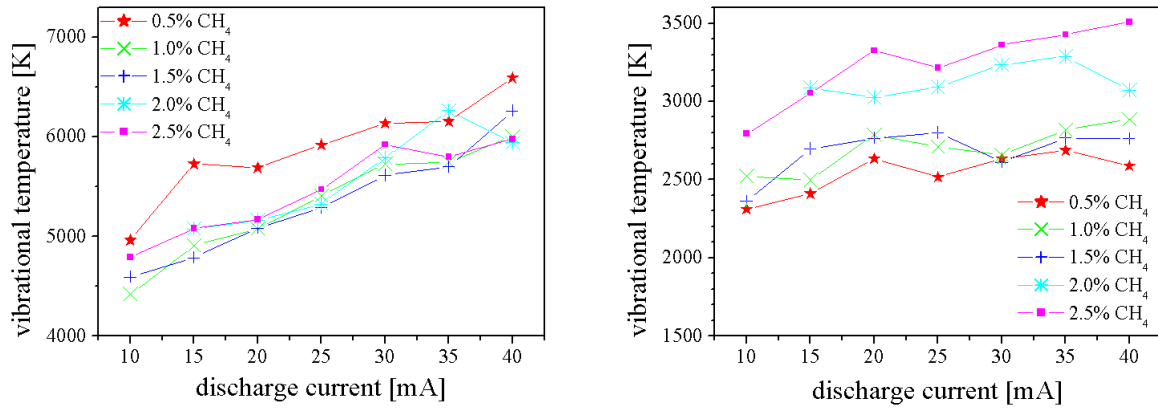


Fig. 3. Vibrational temperatures calculated from the CN violet  $\Delta v = +1$  sequence (left) and C<sub>2</sub> Swan system  $\Delta v = +1$  sequence (right).

The plasma power showed a significant effect on the CN vibrational temperature that was in the interval from 4200 to 6500 K, and it was directly proportional to the current (see Fig. 3). It can be also seen that vibrational temperature was nearly independent on the methane concentration, temperature was a little higher at the lowest used concentration, only. Nearly the same temperatures were observed also for the N<sub>2</sub><sup>+</sup> ion, but temperature was decreased with the increasing CH<sub>4</sub> content (details see in [13]). The vibrational temperature of neutral nitrogen C state was about 500 K lower than for the states mentioned above (3500–5500 K), and it was increased both with methane content and applied energy (details see in [14]). The vibrational temperature of carbon diatomic molecule was significantly lower, and it was increased both with carbon content and applied power as it can be seen in Fig. 3. This difference is connected to the fact that C<sub>2</sub> radiative states are created in two steps – initially, the C<sub>2</sub> molecule is created (probably preferentially in lower vibrational states), and after that, it is excited by electrons.

### Results and discussion – dielectric barrier discharge

In the case of DBD, the light emission was more than 2 orders lower in comparison to the glow discharge, mainly due to the DBD configuration (shielding effect of glass balls). Due to this fact as well as due to the deposition of nitrocarbon films changing the discharge parameters, collection of the spectra allowing plasma parameters calculation was limited. Thus, only the spectra of nitrogen second positive system had the intensity sufficiently high for the calculations. Vibrational temperature was calculated using nitrogen second positive bands of +2 sequence (bands 0-2, 1-3, 2-4, and 3-5), and it is shown in Fig. 4 for two different applied powers as a function of methane concentration.

Vibrational temperature is significantly higher at lower applied power, and it decreases at the highest methane concentration. As the spectra were collected with low resolution (300 gr/mm grating was used), rotational temperature was calculated from nitrogen second positive 0-2 band shape using SpecAir software [10]. The obtained value of (480±60) K was more or less independent both on the applied power and methane concentration. We made also one long time acquisition (10 minutes) at the highest methane concentration and maximal applied power that allowed us the calculation of rotational temperature using CN spectrum using LIFbase software [9]. The obtained result of (500±100) K was much closer to the rotational temperature given above.

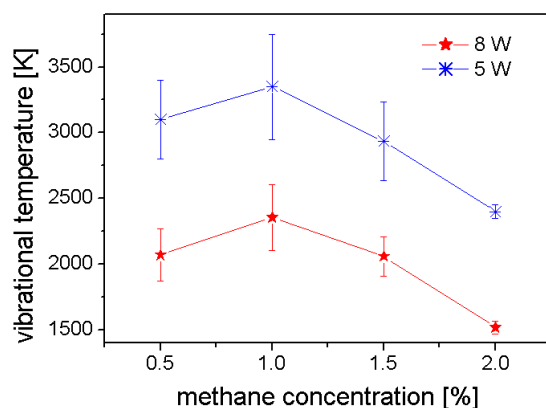


Fig. 4. Vibrational temperatures calculated from the  $N_2$  second positive  $\Delta v = +2$  sequence.

## Conclusions

The optical emission spectra of abnormal glow and DBD discharges were studied at atmospheric pressure and ambient temperature in the gas mixtures corresponding to the composition of Titan troposphere. In the glow discharge, rotational temperatures of about 3000–4000 K were calculated from nitrogen second positive bands, and they increased with applied discharge power; temperatures of 1200–3000 K were obtained from CN radical, and they decreased with applied power. The vibrational temperature calculated from CN violet and nitrogen first negative systems were in the interval 3500–5500 K, and it was increased both with methane content and applied energy. Similar result was obtained also for the temperature calculated from nitrogen second positive system, only the absolute values were about 500 K lower. Temperatures obtained from  $C_2$  spectra were significantly lower, and they increased both with carbon content and applied power. Rotational temperature of 500 K was determined for the DBD configuration. Vibrational temperatures calculated from nitrogen second positive system were of about 2000 K at maximal applied power and about 3000 K at power of 5 W. Both temperatures decreased with the increase of methane concentration in the gas mixture. Based on the presented data, and by comparison of the *ex-situ* diagnostics (FTIR, GC-MS), the kinetic model will be developed in the future.

## Acknowledgements

This work has been supported by the following projects: Research plan of Czech Ministry of Education No. MSM0021630501, APVV 0365-07, Slovak Grant Agency project SK-CN-0029-07, Slovak Research and Development Agency VEGA 1/0051/08, ESF COST Actions CM0601, CM0805 and EIPAM.

## References

- [1] V. Vuitton, P. Lavvas, R.V. Yelle, M. Galand, A. Wellbrock, G.R. Lewis, A.J. Coates, J.-E. Wahlund, *Planet. Space Sci.* 57 (2009) 1558.
- [2] V. Vuitton, R. V. Yelle, P. Lavvas, *Philosoph. Trans. Royal Soc. A*, (2009) doi:10.1098/rsta.2008.0233.
- [3] S. Vinatier *et al*, *Icarus* 188 (2007) 120.
- [4] C.D. Pintassilgo, J. Loureiro, G. Cernogora, M. Touzeau, *Plasma Sourc. Sci. Technol.* 8 (1999) 463.
- [5] Y. Sekine, H. Imanaka, T. Matsui, B.N. Khare, E.L.O. Bakes, C.P. McKay, S. Sugita, *Icarus* 194 (2008) 186.
- [6] S.I. Ramirez, R.N. Gonzalez, P. Coll, F. Raulin, *Adv. Space Res.* 36 (2005) 274.
- [7] K. Plankensteiner *et al*, *Icarus* 187 (2007) 616.
- [8] C.W. Prasad, R.F. Bernath, C. Frum, R. Engelman, *J. Mol. Spectrosc.* 151 (1992) 459.
- [9] J. Luque and D.R. Crosley, "LIFBASE: Database and spectral simulation (version 1.5)", SRI International Report MP 99-009 (1999)
- [10] C.O. Laux, "Radiation and Nonequilibrium Collisional-Radiative Models," von Karman Institute Lecture Series 2002-07, Physico-Chemical Modeling of High Enthalpy and Plasma Flows, eds. D. Fletcher, J.-M. Charbonnier, G.S.R. Sarma, and T. Magin, Rhode-Saint-Genève, Belgium, 2002.
- [11] F.R. Gilmore, R.R. Laher, P.J. Espy, *J. Phys. Chem. Ref. Data* 21 (1992) 1005.
- [12] R.B. King, *Astrophys J* 108 (1948) 429.
- [13] G. Horváth, F. Krčma, L. Poláčková, K. Klohnová, N J Mason, M. Záhoran and Š. Matejčík, *Eur. Phys. J. Appl. Phys.*, DOI: 10.1051/epjap/2010100191 (2010).
- [14] F. Krčma, K. Klohnová, L. Poláčková, G. Horváth, *Publ. Astronomic. Observat. Belgrade* 89 (2010) 371.

# Chemistry of molecular ions in planetary atmospheres and in laboratory plasmas

D. Ascenzi, J. Aysina, P. Tosi

Department of Physics, University of Trento, Via Sommarive 14, I-38122 Povo, Trento, ITALY

e-mail: ascenzi@science.unitn.it

## Abstract

An overview of the most recent research from the Molecular Physics Laboratory at the University of Trento will be presented. The activity is focussed on the reactivity of complex molecular ions of special relevance in the fields of planetary ionospheres and laboratory plasma systems.

**Keywords:** ion-molecule reactions, non-thermal plasma, Titan, polyaromatic hydrocarbons

## Introduction

Studies on the chemistry of planetary atmospheres and the interstellar medium have been historically focussed mainly on small molecules (see Ref. [1] as an example from our laboratory). Due to advances in infrared/ microwave astronomy and the settlement of space missions to outer planets, in more recent years the attention has shifted towards larger molecules, mostly of organic nature. A great research effort is focussed on the modelling of the hydrocarbon atmosphere of Titan, the second largest moon in the Solar system. Heavy ions with masses over 100 a.m.u. have been detected in significant amounts into Titan's ionosphere below 1200 km [2]. Possible chemical structures include PAHs, nitrile aromatic polymers [3], fullerenes and polyphenyls [4] and such heavy particles have been proposed to act as seeds for aerosols formations. In spite of several laboratory investigations, new experimental and theoretical data are still required to provide a quantitative comparison between the *in situ* observations of the Cassini orbiter and the proposed models [5]. Several mechanisms have been suggested for the growth of large organic molecules under extraterrestrial conditions and in the higher atmosphere of Titan, and the idea is put forward that complex molecules build up by association of pre-formed building blocks.

The growth of molecular systems initiated by charged particles is also of relevance to model the chemistry occurring in cold plasmas [6]. Atmospheric pressure non-thermal plasmas [7] present several attractive technological applications ranging from remediation of toxic gases [8] to deposition of nanostructured materials, hydrocarbon reforming [9] and enhanced ion sources for mass spectrometric applications.

## Results and discussion

To shed light on the growth mechanisms of aromatic hydrocarbons initiated by charged particles, we are investigating association processes affording covalently bound species, in particular C-C coupling reactions involving phenyl  $C_6H_5^+$  [10], ethyl  $C_2H_5^+$  [11], naphthyl  $C_{10}H_7^+$  [12] and biphenyl  $C_{12}H_8^+$  cations with neutral arenes (benzene, work is in progress with pyridine).

Ion-molecule reactivity is investigated using tandem mass spectrometric techniques, which allow mass selection and manipulation of both reactant and product ions. The molecular ion under study is generated by dissociative ionization of an adequate precursor, either in an electron impact ion source or in an atmospheric pressure chemical ionization APCI source. The latter source allows the generation of molecular ions with a lower degree of internal excitation than the former. We can estimate absolute values of reactive cross sections as a function of the collision energy and branching ratios (from which rate constant values can be inferred).

When carried out on large molecules, such studies pose several experimental and computational problems related to the increased number of degrees of freedom, and a complementary experimental and theoretical approach is the key to obtain reliable information on reaction mechanisms. We use DFT methods to calculate energy and structures of the most relevant points on the reactive potential hypersurface. All the studied systems are characterized by similar potential energy landscapes: the molecular ion reacts with the aromatic neutral via an exothermic and barrierless formation of a long long-lived, covalently bound, association product with a facile equilibration of the ring H atoms via

1,2 H shifts (hydrogen ring walks). Such product has the structure of protonated biphenyl (for  $C_6H_5^+$  plus  $C_6H_6$ ), protonated ethylbenzene (for  $C_2H_5^+$  plus  $C_6H_6$ ), protonated phenylnaphthalene (for  $C_{10}H_7^+$  plus  $C_6H_6$ ) and protonated terphenyl (for  $C_{12}H_8^+$  plus  $C_6H_6$ ). The highest yields of condensation products are obtained in the absence of internal excitation of the reacting cations and at the smallest collision energies accessible with our experimental set-up, as a consequence of the increased lifetime of the intermediate complex which increases the probability for a stabilization into a long lived species. Internal excitation favors the subsequent evolution of the adduct by loss of small fragments (e.g. H,  $H_2$ ,  $CH_4$ ,  $C_2H_2$ ,  $CH_3$  according to the nature of the ionic reagent).

Absolute values of the cross sections  $\sigma$  show that phenyl cations have the highest reactivity for association with benzene molecules ( $\sigma = 1.9 \pm 0.5 \text{ \AA}^2$  at 0.23 eV) followed by naphthylum ( $\sigma = 0.3 \pm 0.1 \text{ \AA}^2$  at 0.25 eV) and biphenylum, the latter having a reactivity  $\sim 100$  times smaller than naphthylum.

## Conclusions

The growth of aromatic and ring molecules initiated by molecular ions is investigated both experimentally and theoretically. With regard to chemical processes in the atmosphere of Titan, present results imply that termolecular association of hydrocarbon cations with molecules is likely to occur. In particular association reactions lead to an ion-molecule complex having several energy mode where energy can be redistributed. The increased number of degrees of freedom in the complex results in elongated complex lifetimes that may be long enough for stabilization to occur via a second collision with a bath  $N_2$  molecule. Results from present studies should help to improve the matching between the ion yields detected by the Cassini mass spectrometers and those calculated by the atmospheric chemical models.

## References

- [1] P. Tosi, O. Dmitriev, D. Bassi, O. Wick, D. Gerlich, *J. Chem. Phys.* 100 (1994) 4300.
- [2] J.-E. Wahlund, M. Galand, I. Müller-Wodarg, J. Cui, R.V. Yelle, F.J. Crary, K. Mandt, B. A. Magee, J.H. Waite Jr., D.T. Young, A.J. Coates, P. Garnier, K. Agren, M. Andre, A.I. Eriksson, T.E. Cravens, V. Vuitton, D.A. Gurnett, W.S. Kurth, *Plan. Space Sci.* 57 (2009) 1857.
- [3] F.J. Crary, B.A. Magee, K. Mandt, J.H. Waite Jr., J. Westlake, D.T. Young, *Plan. Space Sci.* 57 (2009) 1847.
- [4] M.L. Delitsky, C.P. McKay, *Icarus* 207 (2010) 477.
- [5] I.P. Robertson, T.E. Cravens, J.H. Waite Jr., R.V. Yelle, V. Vuitton, A.J. Coates, J.E. Wahlund, K. Agren, K. Mandt, B.A. Magee, M.S. Richard, E. Fatting, *Plan. Space Sci.* 57 (2009) 1834.
- [6] P. Tosi, D. Ascenzi, P. Franceschi, G. Guella, *Plasma Sources Sci. Technol.* 18 (2009) 034005.
- [7] A. Fridman, A. Chirokov, A. Gutsol, *J. Phys. D- Applied Phys.* 38 (2005) R1.
- [8] J. Van Durme, J. Dewulf, C. Leys, H. Van Langenhove, *Appl. Cat. B-Environ.* 78 (2008) 324.
- [9] M.J. Gallagher, R. Geiger, A. Plevich, A. Rabinovich, A. Gutsol, A. Fridman, *Fuel*, 89 (2010) 1187.
- [10] D. Ascenzi, N. Cont, G. Guella, P. Franceschi, P. Tosi, *J. Phys. Chem. A*, 111 (2007) 12513.
- [11] J. Zabka, M. Polasek, D. Ascenzi, P. Tosi, J. Roithová, D. Schröder, *J. Phys. Chem. A*, 113 (2009) 11153.
- [12] D. Ascenzi, J. Aysina, P. Tosi, A. Maranzana, G. Tonachini, *J. Chem. Phys.* 133 (2010) 184308.

# Electron kinetics in air studied by Monte Carlo simulation

Z. Donkó<sup>1</sup> and F. J. Gordillo-Vázquez<sup>2</sup>

<sup>1</sup>Research Institute for Solid State Physics and Optics, Hungarian Academy of Sciences  
H-1121 Budapest, Konkoly Thege Miklós str. 29-33. Hungary

<sup>2</sup>Instituto de Astrofísica de Andalucía (IAA – CSIC), P. O. 3004, 18080 Granada, Spain

e-mail: donko@mail.kfki.hu

## Abstract

The electron kinetics in air is described by a Monte Carlo simulation, which provides a fully kinetic description of the particle transport. An extensive set of collision processes is considered and the transport parameters of the electrons, as well as their distribution functions are determined for a wide range of the reduced electric field strength.

**Keywords:** Electron kinetics, Monte Carlo simulation, air plasma.

## Introduction

An accurate determination of the distribution function of the electrons and the related transport coefficients requires a mathematical description at the kinetic level [1,2]. One possible approach is to solve the Boltzmann equation, while the second is to use a particle-based approach, like the Monte Carlo (MC) method. Both approaches provide fully kinetic descriptions of the motion of charged particles and, thus, are applicable even under conditions where hydrodynamic equilibrium is not fulfilled.

Here we investigate the characteristics of electron swarms developing in air, under pulsed Townsend discharge conditions by a Monte Carlo simulation. The simulations provide the electron distribution function, collision frequencies associated with different elementary processes, as well as the transport parameters (drift velocity, mean energy, longitudinal and transverse diffusion coefficients, ionization and attachment coefficients). The derivation of these latter quantities from the phase space coordinates of the electrons and their collision events is described in [3]. In our MC code,  $N_0$  electrons are released at time  $t = 0$ , and their motion (as well as the motion of the additional ones created in ionization processes) is traced until a pre-defined time limit  $t_{\max}$ . Tracing of the electrons is also stopped in case they are lost in attachment processes. The time allowed for the development of electron avalanches,  $t_{\max}$ , is chosen long enough to ensure that stationary conditions are reached.  $N_0$  is varied for the different sets of conditions so that the total number of simulated collisions is in the  $10^{10}$ - $10^{11}$  range.

The MC simulations make use of the null-collision technique [4], which significantly improves computational efficiency. We assume isotropic angular scattering in all collision processes. In ionizations the scattered and ejected electrons share equally the remaining kinetic energy. We use the cold gas approximation (the target molecules are assumed to be in rest in collision processes), which limits its applicability at very low  $E/N$  values. Electron-electron collisions are not considered. The MC code has been successfully benchmarked using the RAMP cross sections for which precise values of the transport coefficients are known from previous studies [5,6].

The dry air background composition considered in this work is: N<sub>2</sub> (78.084 % vol), O<sub>2</sub> (20.946 % vol), Ar (0.934 % vol) plus 36 ppm of CO<sub>2</sub>. In the simulations we consider 59 elastic and inelastic electron-impact collision processes (22 additional processes can also be taken into account when H<sub>2</sub>O is also present in air). All the collisions are assumed to take place between electrons and ground-state atoms / molecules. The cross section set used here is the same as in our earlier work [7]. With a few exceptions, the cross sections for N<sub>2</sub>, O<sub>2</sub> and Ar are taken from A. V. Phelps' cross section compilation [8]. The elastic momentum transfer cross sections of N<sub>2</sub> and O<sub>2</sub> are taken from [9], while the high threshold N<sub>2</sub> dissociative excitations are from Christophorou [10]. Most of the cross sections used for CO<sub>2</sub> are taken from Hayashi's compilation [11] except the cross sections for elastic momentum transfer, electron-impact ionization and dissociative attachment, which originate from recent sources of data [12,13]. The cross sections of H<sub>2</sub>O are adopted from the updated set by Yousfi [14]. Plots of

the cross sections and a listing of the elementary processes can be found in [7].

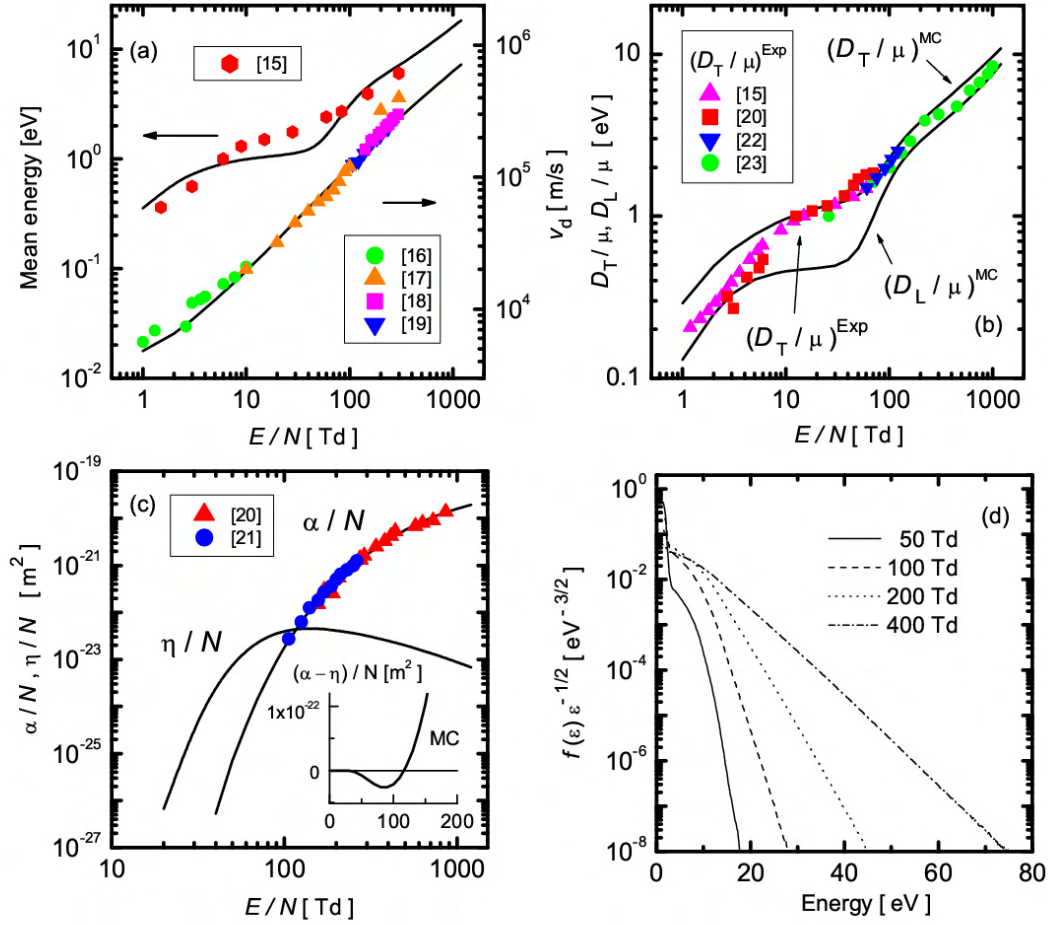


Fig. 1. (a)-(c) Electron transport coefficients as obtained from Monte Carlo simulations (solid lines). The symbols indicate experimental data, references are given in the legends of the individual panels. The inset in (c) shows the net ionization coefficient  $\alpha - \eta$  (the difference between the ionization ( $\alpha$ ) and attachment ( $\eta$ ) coefficients). (d) Electron distribution functions as a function of  $E/N$ .

## Results and discussion

The results for the transport coefficients of electrons and for the electron distribution function in dry air are plotted in Figure 1; the general agreement between the results of the simulations and the available experimental data is quite reasonable, except perhaps in the case of the mean energy at medium values of  $E/N$ . The different experimental data are taken from Crompton *et al.* [15] (mean energy and  $D_T/\mu$ ); Rees [16], Davies [17], Ryzko [18] and Frommhold [19] (drift velocity); Raja Rao and Govinda Raju [20] ( $\alpha/N$  and  $D_T/\mu$ ) and Moruzzi [21] ( $\alpha/N$ ); Rees and Jory [22] and Lakshminarasimha and Lucas [23] ( $D_T/\mu$ ). It is important to note that in [15], [20], and [22] the authors report their measured data as  $D/\mu$ , while from their experimental technique it is quite obvious that they have measured  $D_T/\mu$ . The transition from the attaching to ionizing behavior is clearly seen in Figure 1(c).

Figure 2 shows the velocity distribution functions (VDF) of the electrons for different values of the reduced electric field. As the electric field points into the  $-x$  direction, the “general” velocity distribution function,  $f(\mathbf{v}, \mathbf{r}, t)$ , reduces to  $f(v_x, v_r)$ . Here  $v_r$  is the velocity component perpendicular to the field direction. The VDF is very nearly isotropic at low  $E/N$ . With increasing  $E/N$ , accompanied by an increasing drift velocity (see Figure 1(a)), an anisotropy into the  $x$  direction develops. This

anisotropy is, nevertheless, quite moderate even at the highest reduced electric field value (400 Td) studied, that is why a two-term solution of the Boltzmann equation [7] was found to be satisfactory for the conditions studied here.

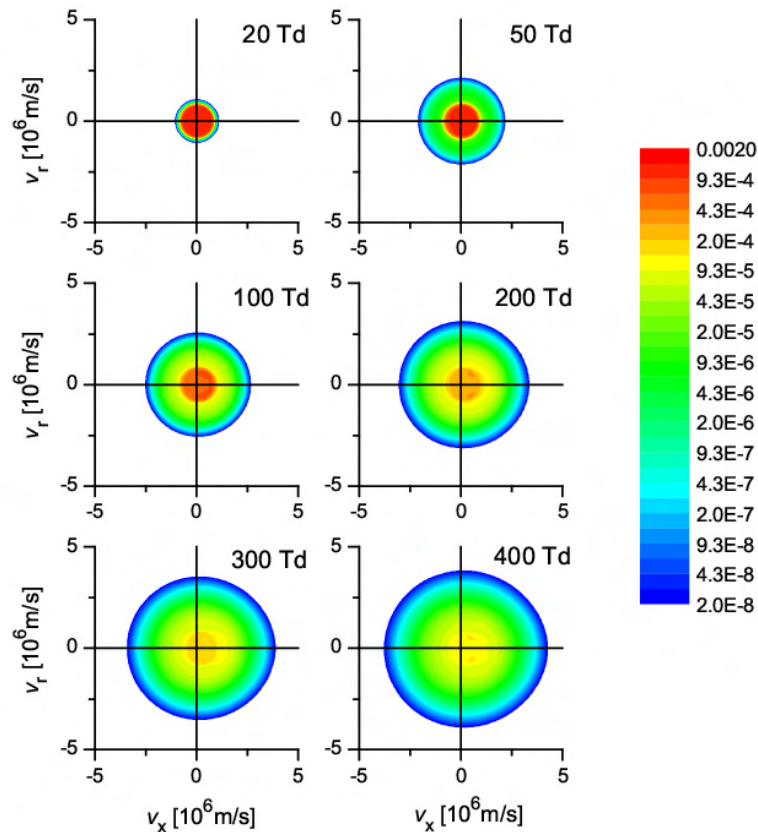


Fig. 2. Velocity distribution functions (VDF-s) of electrons in dry air at the reduced electric field strength values indicated.

This work has been supported by the Hungarian Scientific Research Fund, Grant OTKA-K-77653.

## References

- [1] L. D. Tsendin Phys. Usp. **53** (2010) 133.
- [2] Z. Donkó, "Particle simulation methods for studies of low-pressure plasma sources" Plasma Sources Sci. Technol. (2011) in press.
- [3] B. M. Penetrante, J. N. Bardsley and L. C. Pitchford, J. Phys. D: Appl. Phys. **18** (1985) 1087.
- [4] H. R. Skullerud, Br. J. Appl. Phys. (J. Phys. D: Appl. Phys.) **1** (1968) 1567.
- [5] A. M. Nolan, M. J. Brennan, K. F. Ness and A. B. Wedding, J. Phys. D: Appl. Phys. **30** (1997) 2865.
- [6] Z. M. Raspopovic, S. Sakadzic, S. A. Bzenic and Z. Lj. Petrovic, IEEE Trans. Plasma Sci. **27** (1999) 1241.
- [7] F. J. Gordillo-Vázquez and Z. Donkó, Plasma Sources Sci. Technol. **18** (2009) 034021.
- [8] A. V. Phelps, ftp://jila.colorado.edu/collision\_data/
- [9] M. Elford, S. Buckman and M. Brunger M, *Interactions of Photons and Electrons with Molecules (Landolt-Börnstein vol 17C)* (2003) ed Y Itikawa (Berlin: Springer) chapter 6.3; W. L. Morgan, J.-P. Boeuf and L. C. Pitchford, *The Siglo Data base, CPAT and Kinema Software*, <http://www.siglo-Kinema.com>
- [10] L. G. Christophorou, *Electron-Molecule Interactions and Their Applications vol 1* (1984) (New York: Academic) p 376
- [11] M. Hayashi, *Nonequilibrium Processes in Partially Ionized Gases (NATO ASI Series vol B220)* ed. M Capitelli and J N Bardsley (1990) (New York: Plenum) p 333
- [12] Y. Itikawa, J. Phys. Chem. Ref. Data **31** (2002) 749.
- [13] I. Shimamura, *JILA Report #21092* (1989); I. Shimamura, Sci. Pap. Inst. Phys. Chem. Res. **82** (1989) 1.

- [14] M. Yousfi and M. D. Benabdessadok, *J. Appl. Phys.* **80** (1996) 6619.
- [15] R. W. Crompton, L. G. H. Huxley and D. J. Sutton, *Proc. R. Soc. London. Ser. A* **218** (1953) 507.
- [16] J. A. Rees, *Aust. J. Phys.* **26** (1973) 427.
- [17] D. K. Davies, *Theoretical Notes, Note 346* (1983) Westinghouse R&D Center, Pittsburgh, Pa, USA.
- [18] H. Ryzko, *Proc. Phys. Soc. London* **85** (1965) 1283.
- [19] L. Frommhold, *Fortschr. Phys.* **12** (1964) 597.
- [20] C. Raja Rao and G. R. Govinda Raju, *J. Phys. D: Appl. Phys* **4** (1971) 769.
- [21] J. L. Moruzzi and D. A. Price, *J. Phys. D: Appl. Phys* **7** (1974) 1434.
- [22] J. A. Rees and R. L. Jory, *Aust. J. Phys.* **17** (1964) 307.
- [23] C. S. Lakshminarasimha and J. Lucas, *J. Phys. D: Appl. Phys* **10** (1977) 313.

# Electron Impact Fragmentation of Molecular Ions

P. Defrance

Catholic University of Louvain, Institute of Condensed Matter and Nanosciences, Chemin du Cyclotron, 2, B-1348  
Louvain-la-Neuve Belgium, Tél: 32 (0) 10 473348

e-mail: pierre.defrance@uclouvain.be

A comprehensive modeling of molecular ions transport in tokamak divertors requires a complete set of cross-sections for all collision processes affecting their fragmentation and chemistry. Among these molecular ions, the hydrocarbon and deuterocarbon families ( $C_mH_n^+$  and  $C_mD_n^+$ ,  $m=1-3$ ) evidently play a particular role. For this reason, experimental electron-impact collisions with the deuterocarbon family members are systematically investigated in our laboratory.

Following reactions are considered:  $C_mD_n^+ + e^- \rightarrow F^+$  where singly-charged ionic fragments  $F^+$  (atomic and molecular fragments), are detected, from the lightest to the heaviest possible ones: from  $H^+$  ( $D^+$ ) to  $C_mD_{n-1}^+$ . The doubly-charged species  $C^{2+}$  and  $C_mD_n^{2+}$  are also be subject to investigation. The collected data are analyzed in detail in order to determine separately the contributions of dissociative excitation and ionization, as well as the associated energy thresholds and kinetic energy release distributions (KERD). A standard procedure is applied to put these data in a form which is suitable for plasma modeling applications. These electron impact experiments on various molecular ions are currently performed in our laboratory by means of a crossed electron-ion beam set-up. Each possible singly-charged ionic fragment is detected separately and cross-sections for its production are determined from their respective thresholds up to 2.5 keV.

Results will be discussed at the Conference, for the light hydrocarbon and deuterocarbon species ( $CH_n^+$ ,  $n=1-4$  and  $C_2D_n^+$ ,  $n=1-4$ ) as well as for other molecular ions of interest for fusion plasma ( $H_2^+$  and  $H_3^+$  and their isotopologues).

J. Lecointre, D.S. Belic, J.J. Jureta, R.K. Janev and P. Defrance, European Physical Journal D: At. Mol. Collisions 50 (2008) e2008-00241-9 265-278

J. Lecointre, M.O. Abdellahi El Ghazaly, J.J. Jureta, D.S. Belic, X. Urbain and P. Defrance, J. Phys. B: At. Mol. Opt. Phys. 42 (2009) 075201.

# Electron impact ionization of $W(CO)_6$ : appearance energies

K. Wnorowski<sup>1</sup>, M. Stano<sup>2</sup>, A. Jówko<sup>1</sup>, Š. Matejčík<sup>2</sup>

<sup>1</sup> Department of Chemistry, Siedlce University, 3 Maja 54, 08-110 Siedlce, Poland

<sup>2</sup> Department of Experimental Physics, Comenius University, Mlynská dolina F2, 84248 Bratislava, Slovak Republic

e-mail: karolw@uph.edu.pl

## Abstract

Using crossed electron-molecular beams technique, we have studied Electron Impact Ionization (EII) to  $W(CO)_6$  molecule. In the mass spectrum we have observed 19 fragments of singly charged positive ions ( $W^+$ ,  $CW^+$ ,  $(CO)_xW^+$  ( $x = 1\div 6$ ),  $COWC^+$ ) and doubly charge positive ions ( $W^{++}$ ,  $CW^{++}$ ,  $(CO)_xW^{++}$  ( $x = 1\div 6$ ) and  $(CO)_yWC^{++}$  ( $y = 1, 2$ )). We have estimated the appearance energies (AEs) of the ions formed via electron impact ionization of  $W(CO)_6$ . The Bond Dissociation Energies (BDEs) of the different bonds in the singly and doubly charged ions were estimated.

**Keywords:** electron impact ionization, appearance energy, mass spectrometry, metal carbonyl, tungsten hexacarbonyl

## Introduction

Metal carbonyls are coordination complexes of transition metals with carbon monoxide ligands. These complexes may be homoleptic, i.e., containing only CO ligands. Carbon monoxide is an important building block for the synthesis of many compounds. Metal carbonyls undergo reactions with alkyl, acyl, halide, hydride, carbene, and other substituents, and they belong to the most important precursors in the synthesis of organo-transition-metal complexes.

Tungsten hexacarbonyl is one of such substances. It is a good source of the tungsten and carbonyl group. The decomposition  $W(CO)_6$  proceeds via CO group cleavage, which can be replaced by other organic or inorganic ligands [1, 2]. The pyrolysis of  $W(CO)_6$  in the gas phase leads to unsaturated  $W(CO)_x$  species [3] which are very effective abstractors of halogen atoms from halogenated compounds [4]. The information about the bond dissociation energy (BDEs) of the metal carbonyl compounds derived in fragmentation studies are useful in the organometallic chemistry of important industrial processes, for example metal refining, metal vapor deposition or gas-phase catalysis.

Tungsten hexacarbonyl is most important precursor in many applications especially in the organometallic synthesis, plasma technologies and nanotechnologies (EBID, IBID)[5 - 8]. In these two last techniques the precursor molecules containing target elements (W) are introduced near the substrate and they are adsorbed on it. In results of energetical particle impact (electron or ion-beam) they are decomposed. The tungsten atoms are deposited on the substrate, while the volatile materials are pumped out. Important role in the process of fragmentation of the organometallic substances play the secondary electrons generated in the substrate by the impact of the high energy electrons or ions. The low energy secondary electrons may undergo very efficient reactions (dissociative ionization or dissociative electron attachment) which result in cleavage of the molecules. For this reason the knowledge of the kinetics and the reaction dynamics of interaction of low energy electrons with hexacarbonyl is of great importance for the EBID and IBID techniques.

## Experiment

The experiments were performed using the crossed electron - molecular beam apparatus (Fig. 1) at the Department of Experimental Physics, Comenius University in Bratislava. The electron beam (FWHM 100 meV) was formed by a Trochoidal Electron Monochromator (TEM) and accelerated on desired energy, perpendicularly crossed by a molecular beam formed by effusive molecular beam source (MBS). Negative and positive ions produced in the reaction chamber were extracted by a weak electric field from the interaction region and focused into the entrance of quadrupole mass spectrometer (QMS). The mass selected ions were detected as a function of electron energy in single ion counting mode using a secondary electron multiplier, ion counting electronic and a PC acquisition system [9]. Calibration of the electron energy scale was carried out using the ionization energy of  $Ar^+/Ar$  ( $15.759\pm 0.001$  eV [10]). The measurements were carried out at the room temperature.

The  $W(CO)_6$  with a stated purity of 99% was purchased from Sigma–Aldrich and used without further purification.

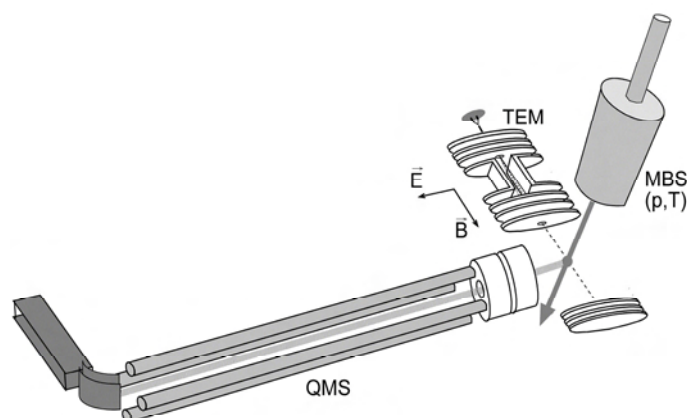
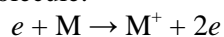


Fig. 1. The schematic view of experimental setup (TEM - trochoidal electron monochromator, MBS - molecular beams source, QMS – quadrupole mass spectrometer).

### Results and Discussion

We have studied the electron impact ionization and dissociative ionization reactions to  $W(CO)_6$  molecule:



which result in very rich fragmentation. The positive ion mass spectrum taken at incident electron energy of 100 eV is presented in the Figure 2.

In the mass spectrum we observe 20 positive ions, from which 19 contain tungsten atom and one tungsten free ion with  $m/z$  28 attributed to  $CO^+$ . The ions in the mass spectrum with mass to charge ratios  $m/z$  352, 324, 296, 268, 240, 224, 212, 196, 184 correspond to singly charged ions and ions with  $m/z$  176, 162, 148, 134, 126, 120, 112, 106, 98, 92 are doubly charged ions. The identification of the singly and doubly charged ions was made on the basis of the isotopic patterns of tungsten. It is very interesting that the intensities of doubly charged ions are almost comparable to that of singly charged positive ions. The list of observed positive ions and corresponding molecular formula are listed in the Table 1.

In the present work we have measured the appearance energies (AEs) of the tungsten ions in the mass spectrum. The AEs of parent and fragment ions were determined by a fitting procedure described in [11]. In this procedure we fit the expected cross section dependence at the threshold (generalized Wannier law [12]) to the measured ion yield curve. The fitting procedure includes a convolution of the cross section energy dependence and the electron energy distribution function. The examples of the ion yield curves and fits are presented in the Figure 3 and the obtained values of appearance energies are listed in the Table 2.

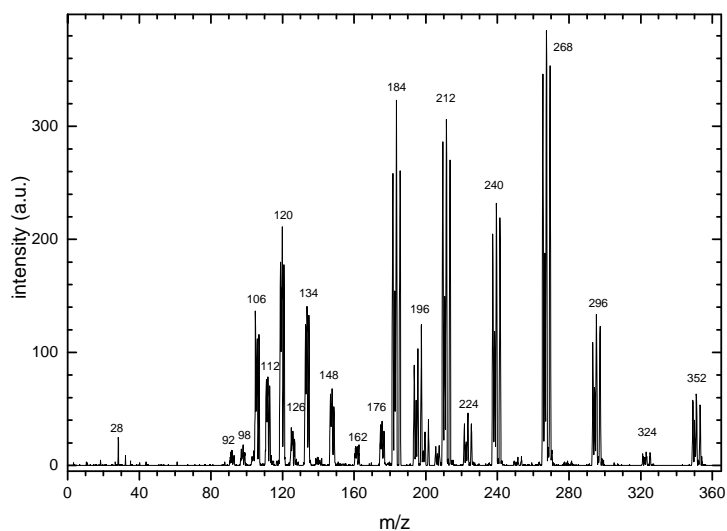


Fig. 2. The mass spectrum of  $W(CO)_6$  consist of singly charged and doubly charged ions.

Tab. 1. List of detected positive ions from  $W(CO)_6$ .

| m/z | Ion         | m/z | Ion             | m/z | Ion            |
|-----|-------------|-----|-----------------|-----|----------------|
| 352 | $(CO)_6W^+$ | 196 | $CW^+$          | 120 | $(CO)_2W^{++}$ |
| 324 | $(CO)_5W^+$ | 184 | $W^+$           | 112 | $COWC^{++}$    |
| 296 | $(CO)_4W^+$ | 176 | $(CO)_6W^{++}$  | 106 | $COW^{++}$     |
| 268 | $(CO)_3W^+$ | 162 | $(CO)_5W^{++}$  | 98  | $CW^{++}$      |
| 240 | $(CO)_2W^+$ | 148 | $(CO)_4W^{++}$  | 92  | $W^{++}$       |
| 224 | $(CO)WC^+$  | 134 | $(CO)_3W^{++}$  |     |                |
| 212 | $COW^+$     | 126 | $(CO)_2WC^{++}$ |     |                |

The values of the AEs determined in this work are in a good agreement with previous studies by Michels [13] or Winters [14] which used EII method, however they measured the AEs only for singly charge positive ions. The formation of a doubly charge ions  $W(CO)_x^{++}$  was reported by Qi and co-workers, who used a combination of VUV photoionization with the time-of-flight mass spectrometry (TOFMS) [15]. They obtained AEs for nine singly charged ions and six doubly charged ions. In this work we have measured AEs for additional doubly charged ions  $W^{++}$ ,  $CW^{++}$ ,  $COW^{++}$ ,  $(CO)WC^{++}$  and  $(CO)_2WC^{++}$ .

The bond dissociation energies (BDEs) of some ions are calculated on the basis of the AEs values listed in Table 2 by the following equation (I) ( $n=6-1$ ):

$$D[(CO)_{n-1}W^+-CO] = AE[(CO)_{n-1}W^+] - AE[(CO)_nW^+] \quad (I)$$

Analogous equations were used to calculate the BDEs of doubly charged ions. The obtained values are listed in the Table 3 and are in good agreement with data obtain by Michels [13] and Winters [14]. The BDEs obtained by Qi [15] are different for several ions especially in the case of doubly charged ions.

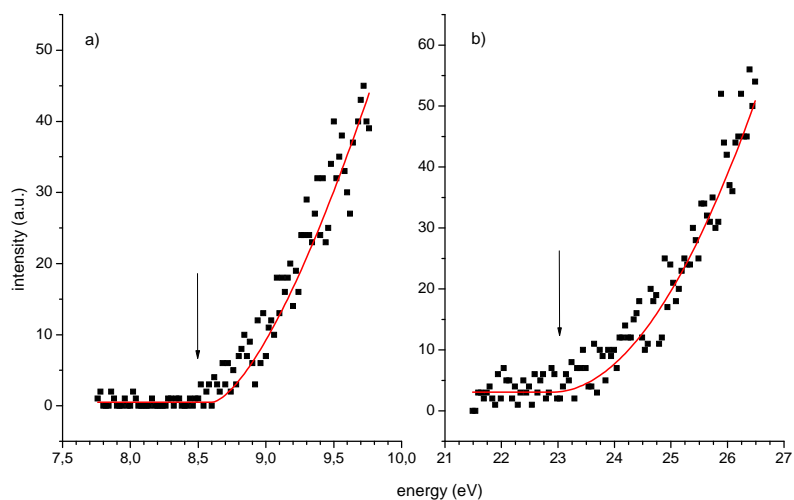


Fig. 3. Ion yield curves of the positive ions: a) –  $W(CO)_6^+$ ; b) –  $W(CO)_6^{++}$ . The fit curves are shown as solid lines. The AEs indicated by arrows are the thresholds derived by averaging several AE values from individual data sets.

Tab. 2. Appearance energies (AEs) for positive ions formed in the electron impact ionization of  $W(CO)_6$  molecule. The AEs given in the table are derived by averaging several AE values from individual data sets.

| Ion         | m/z | AE [eV]   |           | Ion             | m/z | AE [eV]            |           |
|-------------|-----|---|-----------|-----------------|-----|--------------------|-----------|
|             |     | Literature  | This work |                 |     | Literature         | This work |
| $(CO)_6W^+$ | 352 | 8,60 <sup>a</sup><br>8,56 <sup>b</sup><br>8,18 <sup>c</sup>   | 8,47      | $(CO)_6W^{++}$  | 176 | 22,96 <sup>c</sup> | 22,90     |
| $(CO)_5W^+$ | 324 | 10,30 <sup>a</sup><br>9,8 <sup>b</sup><br>9,98 <sup>c</sup>   | 10,31     | $(CO)_5W^{++}$  | 162 | 25,30 <sup>c</sup> | 24,60     |
| $(CO)_4W^+$ | 296 | 12,22 <sup>a</sup><br>12,7 <sup>b</sup><br>12,11 <sup>c</sup> | 12,01     | $(CO)_4W^{++}$  | 148 | 26,95 <sup>c</sup> | 26,90     |
| $(CO)_3W^+$ | 268 | 14,06 <sup>a</sup><br>14,9 <sup>b</sup><br>13,42 <sup>c</sup> | 13,91     | $(CO)_3W^{++}$  | 134 | 29,17 <sup>c</sup> | 29,60     |
| $(CO)_2W^+$ | 240 | 16,29 <sup>a</sup><br>17,6 <sup>b</sup><br>14,45 <sup>c</sup> | 16,43     | $(CO)_2W^{++}$  | 120 | 32,63 <sup>c</sup> | 32,30     |
| $(CO)CW^+$  | 224 | 25,9 <sup>b</sup><br>25,30 <sup>c</sup>                       | 23,48     | $(CO)CW^{++}$   | 112 | <i>no data</i>     | 40,40     |
| $(CO)W^+$   | 212 | 18,36 <sup>a</sup><br>20,2 <sup>b</sup><br>18,48 <sup>c</sup> | 18,35     | $(CO)W^{++}$    | 106 | <i>no data</i>     | 35,90     |
| $WC^+$      | 196 | 28,8 <sup>b</sup><br>29,17 <sup>c</sup>                       | 27,25     | $WC^{++}$       | 98  | <i>no data</i>     | 45,90     |
| $W^+$       | 184 | 21,01 <sup>a</sup><br>22,9 <sup>b</sup><br>21,94 <sup>c</sup> | 20,87     | $W^{++}$        | 92  | <i>no data</i>     | 41,40     |
|             |     |   |           | $(CO)_2CW^{++}$ | 126 | <i>no data</i>     | 37,50     |

a) Reference [13]; b) Reference [14]; c) Reference [15]

The BDE of ( $W^+ - C$ ) and ( $W^{++} - C$ ) fragments were calculated using equation (II):

$$D[W^+ - C] = AE[W^+] + D(C-O) - AE[WC^+] \quad (II)$$

where  $D[C - O]$  is 11,156 eV from Reference [16]. Analogous calculation for ( $W^{++} - C$ ) fragment was performed. The results are listed in Table 3.

Tab. 3. Bond dissociation energies of ions formed from  $W(CO)_6$ .

| Species          | BDE [eV]  |  | Species             | BDE [eV]  |                |
|------------------|-----------|--|---------------------|-----------|----------------|
|                  | This work | Literature   |                     | This work | Literature     |
| $(CO)_5W^+ - CO$ | 1,84      | 1,7 <sup>a</sup><br>1,2 <sup>b</sup><br>1,8 <sup>c</sup> | $(CO)_5W^{++} - CO$ | 1,70      | 2,34           |
| $(CO)_4W^+ - CO$ | 1,70      | 1,9 <sup>a</sup><br>2,9 <sup>b</sup><br>2,1 <sup>c</sup> | $(CO)_4W^{++} - CO$ | 2,30      | 1,65           |
| $(CO)_3W^+ - CO$ | 1,90      | 1,8 <sup>a</sup><br>2,2 <sup>b</sup><br>1,3 <sup>c</sup> | $(CO)_3W^{++} - CO$ | 2,70      | 2,22           |
| $(CO)_2W^+ - CO$ | 2,52      | 2,2 <sup>a</sup><br>2,7 <sup>b</sup><br>1,0 <sup>c</sup> | $(CO)_2W^{++} - CO$ | 2,70      | 3,46           |
| $(CO)W^+ - CO$   | 1,92      | 2,0 <sup>a</sup><br>2,6 <sup>b</sup><br>4,0 <sup>c</sup> | $COW^{++} - CO$     | 3,60      | 4,38           |
| $W^+ - CO$       | 2,52      | 3,46 <sup>c</sup>  | $W^{++} - CO$       | 5,50      | <i>no data</i> |
| $W^+ - C$        | 4,78      | 3,93 <sup>c</sup>  | $W^{++} - C$        | 6,66      | <i>no data</i> |
| $CW^+ - CO$      | 3,77      | 2,9 <sup>b</sup><br>3,87 <sup>c</sup>                    | $CW^{++} - CO$      | 5,50      | <i>no data</i> |
|                  |           |  | $(CO)CW^{++} - CO$  | 2,90      | <i>no data</i> |

a) Reference [13]; b) Reference [14]; c) Reference [15]

The close inspection of the Table 3 shows that for singly charged ions the present values of BDEs are in good agreement with earlier EII data. The agreement with the photoionization experiments is not always satisfactory. We believe that this can be partially related to the method of the AEs estimation in the photoionization experiment. In present experiment we use an fitting procedure, which delivers more accurate values of the AEs. In the photoionization experiment the estimation of the AEs is carried out on less defined way and the values are subjected to subjective errors.

The average BDEs  $D_0[W - CO]$  of  $W(CO)_6$  and  $D_0[W^+ - CO]$  of  $W(CO)_6^+$  were calculated by the equation (III) and (IV) respectively.

$$D_0[W - CO] = (AE[W^+] - IE[W]) / 6 \quad (III)$$

$$D[W^+ - CO] = (AE[W^+] - IE[W(CO)_6]) / 6 \quad (IV)$$

The obtained values  $D[W - CO] = 2,15$  eV ( $IE[W] = 7,98$  eV from Reference [16]) and  $D[W^+ - CO] = 2,11$  eV are very close to the values published by Michels [13].

## Conclusions

Electron impact ionization of tungsten hexacarbonyl in the gas phase results in formation of singly and doubly charged ions and a strong fragmentation, mainly through CO cleavage. We have measured EII mass spectrum of  $W(CO)_6$  at 100 eV electron impact energy and the ion yield curves of 19 ions. From these ion yield curves we have derived the appearance energies of the fragment ions. On the basis of the AEs values we have calculated the BDEs of different bonds in the positive ions formed from  $W(CO)_6$ . The values of AEs of singly and doubly charged positive ions were in reasonable agreement with earlier EII experiment.

## Acknowledgments

This work was supported by the Slovak Research and Development Agency, project Nr. APVV-0365-07, Slovak grant VEGA-1/0558/09 and by the COST Action CM0601 „Electron Controlled Chemical Lithography” (ECCL).

## References

- 
- [1] K. E. Lewis, D. M. Golden, G. P. Smith, *J. Am. Chem. Soc.*, 106, 14 (1984) 3905–3912
  - [2] B. Altintas, C. Bozkurt, *Appl. Organometal. Chem.*, 19 (2005) 1220–1224
  - [3] M. Wrighton, *Chem. Rev.*, 74, 4 (1974) 401–430
  - [4] G. R. Allen, N. D. Renner, D. K. Russell, *Chem. Commun.* (1998) 703–704
  - [5] P. C. Hoyle, J. R. A. Cleaver, H. Ahmed, *Appl. Phys. Lett.*, **64** (1994) 1448
  - [6] I. J. Luxmoore, I. M. Ross, A. G. Cullis, P. W. Fry, J. Orr, P. D. Buckle, J. H. Jefferson, *Thin Solid Films*, 515 (2007) 6791–6797
  - [7] K. Furuya, *Sci. Technol. Adv. Mater.*, 9 (2008) 014110
  - [8] M. Song, K. Furuya, *Sci. Technol. Adv. Mater.*, 9 (2008) 023002
  - [9] S. Matejcik, V. Foltin, M. Stano, J.D. Skalny, *Int. J. Mass Spect.*, 223–224 (2003) 9–19
  - [10] NIST Chemistry WebBook, NIST Standard Reference Database Number 69 – March, 2003 Release, <http://webbook.nist.gov>
  - [11] M. Stano, S. Matejcik, J. D. Skalny, T. D. Märk, *J. Phys. B*, 36 (2003) 261
  - [12] G. H. Wannier, *Phys. Rev.*, 90 (1953) 817
  - [13] G. D. Michels, G. D. Flesch, H. J. Svec, *Inorg. Chem.*, 19 (1980) 479
  - [14] R. E. Winters, R. W. Kiser, *Inorg. Chem.*, 4 (1965) 157
  - [15] F. Qi, S. Yang, L. Sheng, H. Gao, Y. Zhang, S. Yu, *J. Chem. Phys.*, 107, 24 (1997) 10391–10398
  - [16] *CRC Handbook of Chemistry and Physics*, 86th ed., edited by D. R. Lide, CRC Press, Boca Raton, FL, 2005–2006

# Influence of environment on the molecular photodissociation: cluster experiments

J. Fedor, V. Poterya, J. Kočíšek, A. Pysanenko, O. Votava, M. Fárník

J. Heyrovský Institute of Physical Chemistry of the Czech Academy of Sciences, Dolejškova 3, 18225 Prague, Czech Republic

e-mail: juraj.fedor@jh-inst.cas.cz

## Abstract

We investigate the photodissociation dynamics of hydrogen halides with an emphasis on the influence of its environment on the photodissociation process. Experimentally, we deposit molecule on a surface of free clusters using a pick-up technique. The main observable is the kinetic energy of photofragments. Distinct features corresponding to the fragment caging and direct exit were observed in the spectra following pick-up of hydrogen halides on argon clusters. Dramatically different spectra were recorded for the hydrogen halides on water clusters – the spectra were interpreted in terms of the acidic dissociation on the cluster. The resulting fragments originate from the spontaneous dissociation of the hydronium radical which is formed by the recombination to the charge transfer to solvent (CTS) state following the absorption of light.

**Keywords:** clusters, UV photodissociation, acidic dissociation, recombination

## Introduction

Photodissociation and phototization of neutrals is one of the elementary processes leading to radical and charge particle generation in plasmas. In order for this process to be effective, the photon energy must be in ultraviolet region. Although in most plasmas photo-processes are not very significant due to low concentrations of such high-energy photons in most discharge systems, sometimes photon-induced processes play a very essential role – mostly by rapidly supplying seed electrons for subsequent ionization by electron impact [1]. In such cases, the mechanism of photodissociation (or ionization) will depend not only on the dissociating molecule but also on its proximate environment, especially in dusty plasmas.

Experiments with clusters are ideally suited to investigate the influence of the environment on a molecular level. On one hand they sufficiently mimic the macroscopic environment, on the other hand, they enable measurement of some quantities that are inaccessible in bulk, e.g., the kinetic energy of photofragments.

In this paper we focus on hydrogen halides HX (X = Br, Cl, I) and their UV photodissociation at two wavelengths 243 nm (5.1 eV) and 193 nm (6.4 eV). Interaction of such light with the isolated molecules has been widely investigated (e.g. Ref [2]). Previously, in our laboratory, we have extended such studies to molecules on the surface or in the interior of rare gas and water clusters, with a special attention to hydrogen chloride (HCl) and hydrogen bromide (HBr) [2, 3]. Photodissociation of hydrogen halides on heterogeneous surfaces plays an important role stratospheric chemistry of ozone depletion. Here the emphasis is given on the photodissociation of hydrogen iodide HI. Its atmospheric relevance is somewhat smaller due to its lower abundance, however for the complete understanding of the underlying photochemistry processes, it is important to have data on all hydrogen halides in combination with different type of cluster environment.

## Experimental set-up

The cluster beam apparatus is shown schematically in figure 1. Clusters (in this work pure argon or water clusters) are produced by adiabatic expansion in the cluster source. The typical stagnation pressures are 5 bar for either argon gas or heated water vapor, the nozzle diameter and temperature are 50  $\mu\text{m}$  at 249 K for argon and 75  $\mu\text{m}$  and 438 K for water. The resulting cluster sizes under these experimental conditions are  $10^2$ - $10^3$  constituents. The cluster beam is skimmed and in order to deposit the dopant molecules on the clusters the beam passes through a pick-up cell filled with the dopant gas. Its molecules deposited on the host clusters then enter the interaction chamber, where they are photodissociated and photoionized with the laser light. The ionic products are then extracted to the

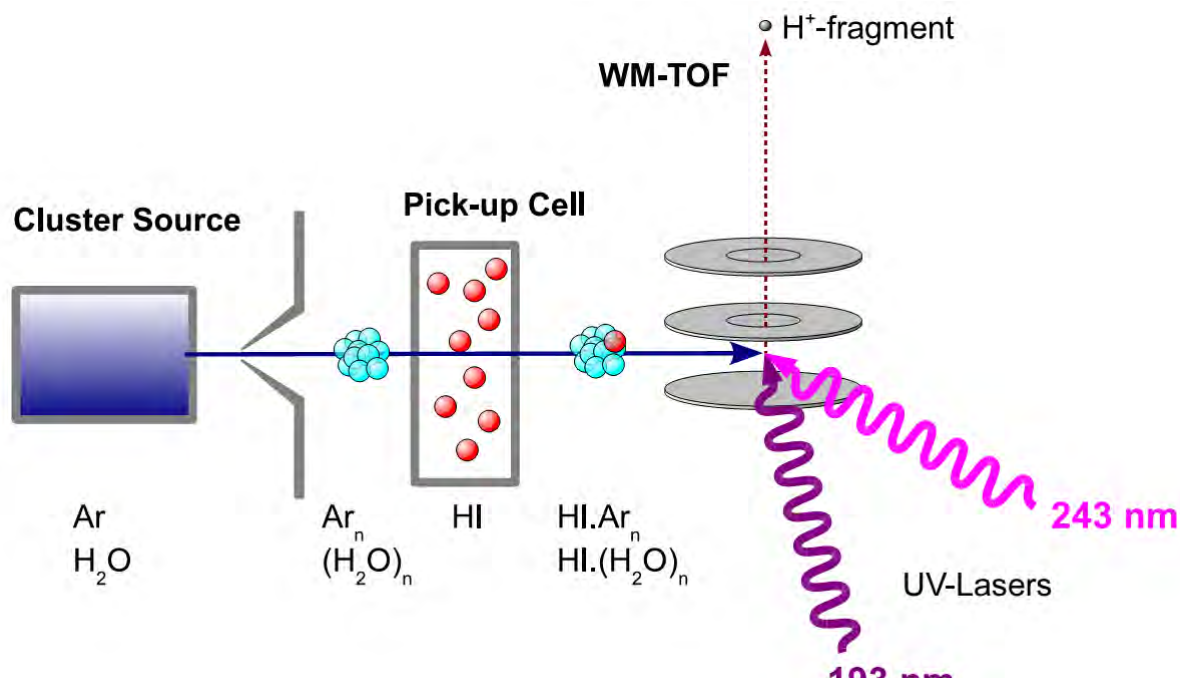


Fig. 1. Schematic picture of the experimental setup.

Wiley-McLaren time-of-flight spectrometer (TOF). The spectrometer is operated in a low-field mode, thus the shape of the TOF signal reflects the kinetic energy distribution of the photofragments. This distribution is derived from the shape of the TOF peak via Monte Carlo simulations.

We investigate the photodissociation at two different wavelengths, 193 nm and 243 nm. The 193 nm radiation is produced by an ArF/F<sub>2</sub> excimer laser, the pulse length is 20 ns and the typical laser energy was 66 mJ/pulse at laser output. The 243 nm laser beam is generated by mixing the fundamental of the Nd:YAG laser (1064 nm) with a frequency-doubled output of a dye laser operated at 630.13 nm. The laser pulses have length of 5 ns, typically 2.5 mJ/pulse at the laser output and are repeated with a frequency of 10 Hz. The 243 nm radiation was chosen because it corresponds to the ionization of hydrogen atom in the 2+1 REMPI (resonance-enhanced multiphoton ionization) scheme. Thus, after the photodissociation, hydrogen atom fragments are primarily ionized and their kinetic energy is recorded via the TOF method.

## Results and discussion

In this work we primarily concentrate on the hydrogen iodide HI. Figure 2a shows comparison of the TOF peaks for the photodissociation of HI deposited on argon and water clusters, figure 2b of the corresponding kinetic energy distributions. In the case of HI deposited on argon clusters, the fast hydrogen fragments – visible as the side peaks in the TOF spectrum – are clearly present. They correspond to kinetic energies from the photodissociation of molecular HI to two different asymptotic states  $H + I(^2P_{3/2})$  and  $H + I^*(^2P_{1/2})$ , the hydrogen atoms exiting from the cluster are unperturbed by the environment. On the other hand, the central peak in the TOF spectrum (corresponding to very low kinetic energies) is a signature of the well-known cage effect: the hydrogen atom undergoes multiple collisions with argon atoms in cluster and loses almost all its kinetic energy.

The TOF spectrum of HI deposited on water clusters looks very different. It is dominated by a broad central peak, which transforms to a peak at low kinetic energies in figure 2b. However, this peak is much broader than in case of HI on the surface of argon clusters, so the cage effect is unlikely to be a cause for such kinetic energy distribution. Also, the fast hydrogen fragments are completely missing from the spectrum. We interpret these results as an occurrence of the acidic dissociation on the water cluster prior to the interaction with the laser light. Upon pick-up of HI on  $(H_2O)_n$  an ionic structure is formed  $IH_3O^+(H_2O)_{n-1}$ . After absorption of the photon, this structure recombines into CTTS (charge transfer to solvent) state  $IH_3O(H_2O)_n$ . The formed hydrodium radical  $H_3O$  is metastable and undergoes spontaneous dissociation to yield H atom fragments with kinetic energies as on figure 2b. There is multiple experimental evidence for occurrence of such acidic dissociation on water clusters:

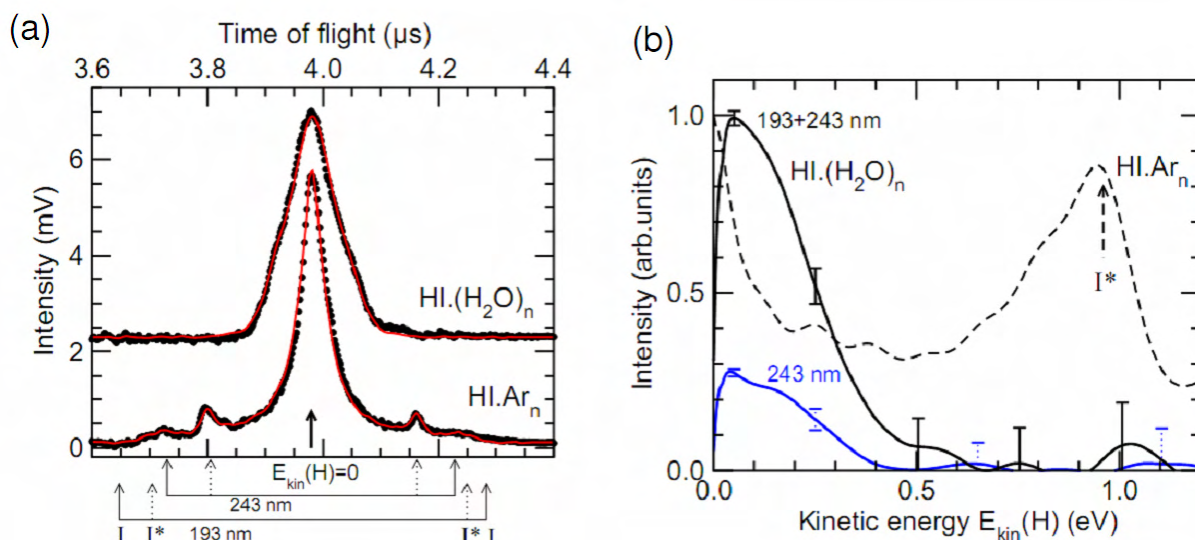


Fig. 2. (a)  $\text{H}^+$  TOF peaks from the photodissociation of hydrogen iodide deposited on argon and water clusters (b) corresponding kinetic energy distributions.

- Very similar kinetic energies were detected for all hydrogen halides HI, HBr and HCl. The intact molecules on the other hand provide fragments with very different kinetic energies, their similarity on the water clusters confirms origin of H atom fragments from the hydronium radical  $\text{H}_3\text{O}^+$ .
- Intensity ratios in experiments with isotopically substituted species  $[\text{HI}(\text{D}_2\text{O})_n, \text{DI}(\text{H}_2\text{O})_n]$  are in excellent agreement with the H-atom ratio in the mixed species  $\text{H}_3\text{O}^+$ ,  $\text{HD}_2\text{O}^+$  and  $\text{H}_2\text{DO}^+$  [5].
- The intensity ratio between 243 nm and 193 nm is in very good agreement with theoretical calculations of the singlet absorption cross sections for the small  $\text{HI}(\text{H}_2\text{O})_n$  clusters which also show formation of the ion pair and absorption to the CTTS state [5].

### Acknowledgements

This work has been supported by the grants Nr. KJB400400902 and 203/09/0422 of the Grant Agency of the Czech Republic, Marie Curie IEF No. 235414 and Marie Curie ITN No. 238671.

### References

- [1] A. Friedman, *Plasma Chemistry*, Cambridge University Press, New York, 2008
- [2] R.J. LeRoy, G.T. Kraemer, S. Manzhoos, *J. Chem. Phys.* 117 (2002) 9353
- [3] V. Poterya, M. Fárník, P. Slavíček, U. Buck and V. V. Kresin, *J. Chem. Phys.* 126 (2007) 071101
- [4] M. Ončák, P. Slavíček, V. Poterya, M. Fárník and U. Buck, *J. Phys. Chem. A* 112 (2008) 5344
- [5] V. Poterya, J. Fedor, A. Pysanenko, O. Tkáč, J. Lengyel, M. Ončák, P. Slavíček, M. Fárník, *Phys. Chem. Chem. Phys.*, 2011, DOI: 10.1039/C0CP01518K

# Simulation of capacitively coupled RF discharges, including nonlinear electron resonance heating, the electrical asymmetry effect, electromagnetic effects in large area discharges

R.P. Brinkmann, T. Mussenbrock, D. Ziegler

Institute for Theoretical Electrical Engineering, Ruhr-University Bochum, 44780 Bochum, Germany

e-mail: ralf-peter.brinkmann@tet.rub.de

## Abstract

A review is given of the state of the art of the simulation of capacitively coupled RF discharges (CCPs). The discussed methods range from simple algebraic formulas over global models to fluid and kinetic models with full temporal and spatial resolution. It is emphasized that all these approaches are required to foster the understanding of the discharges and improve their performance. As example, a selected number of important or newly discovered phenomena are discussed; among them nonlinear electron resonance heating (NERH), the electrical asymmetry effect, and the electromagnetic effects in large area discharges.

**Keywords:** Capacitively coupled discharges, plasma series resonance, nonlinear electron resonant heating, electrical asymmetry effect, electromagnetic effects in large area discharges.

## Introduction

Capacitively coupled discharges (CCPs) were introduced to plasma technology about 30 years ago. Since that time, they serve as one of the pillars of plasma science and plasma technology. In the form of the standard GEC reference cell [1], they are employed and investigated in probably hundreds of research laboratories worldwide, as reactive ion etchers [2] they are indispensable in the fabrication of microprocessors and other semiconductor devices, and as large area PECVD equipment [3] they assist the quest of the photovoltaic industry to lower the cost per watt. CCPs are thus a standard technology; they guarantee a stable and reproducible performance and are economic in terms of investment, operation, and maintenance. Yet, not all their secrets are known, and research is still being conducted. This paper will focus on the current state of the art in the modeling and simulation of the discharges, and highlight some recent advances.

## The puzzle of non-Ohmic heating

Capacitive discharges are easily described. By a combination of gas inlet and pump, a low pressure atmosphere is generated. RF power is applied to two parallel capacitor plates. In the space in between, the RF field produces a plasma which organizes as bulk and sheaths:

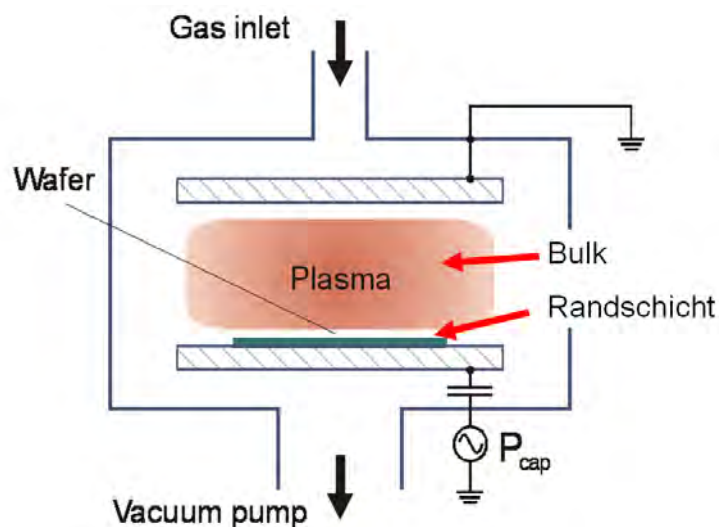


Fig. 1. Schematic of an RF-CCP.

Seemingly, also the operation principle of the discharges is clear. The two sheaths act as capacitors, the bulk as an Ohmic conductor. A lumped element equivalent circuit can represent this view:

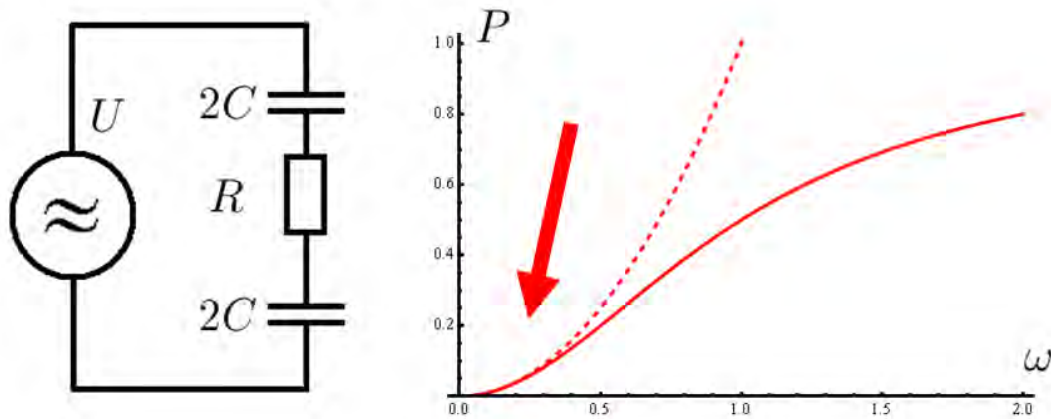


Fig 2. Simple (naïve) lumped element equivalent circuit of an RF-CCP (left) and its frequency-power-characteristics, indicating the capacitive character of the operation.

A quick calculation shows that the resistance of this circuit is dominated by the sheath capacitors. The circuit thus operates in the capacitive mode; and the power dissipated into the plasma should behave as  $P = UI \cos(\phi) \approx \omega^2 C^2 R |U|^2 \sim \omega^2 p$ , i.e., scale linearly with the pressure. However, a classical investigation of Popov and Godyak [4] demonstrated that this is actually only true for higher pressure: At low pressure, the dissipated power is instead nearly independent of  $p$ :

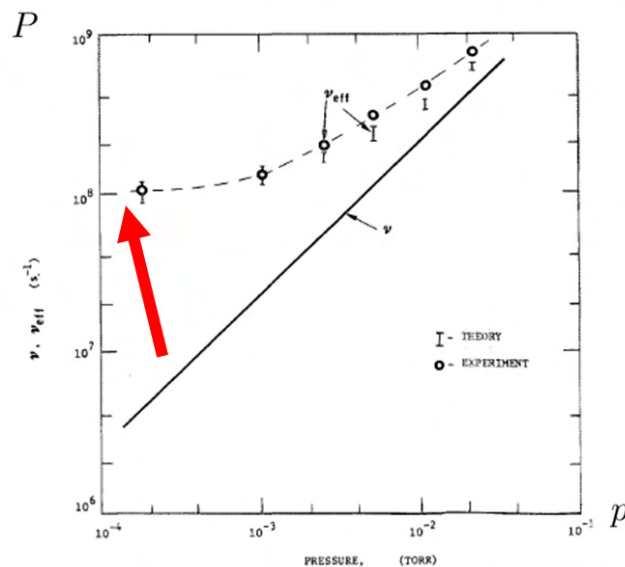


Fig. 3. Evidence of the non-Ohmic nature of the heating at low gas pressure (from [4]).

This new dissipation mechanism was named “anomalous”, “non-Ohmic”, or “stochastic heating”, and the true nature of it has puzzled the plasma community for decades. Recently, however, evidence was accumulated that the observed effect result from the action of two rather unrelated phenomena, namely i) the acceleration of electrons in the inhomogeneous and time-varying fields of the sheath (which corresponds to the classical stochastic-heating picture) [5], and ii) the excitation of the plasma series resonance by the nonlinearities of the sheaths (“nonlinear electron resonance heating” [6,7,8]). Of course, then the question arises how the two mechanisms are related.

### Tools used for the investigation

To reveal the mechanisms of plasma heating (or other mechanisms), experimental and theoretical approaches must be combined. The talk will focus on theoretical models, but will of course also pay attention to recent experimental data. The discussed theoretical methods range from simple algebraic formulas over global models to fluid, kinetic, and hybrid models with temporal and spatial resolution. It is emphasized that all these approaches are required to foster the understanding of the discharges and improve their performance.

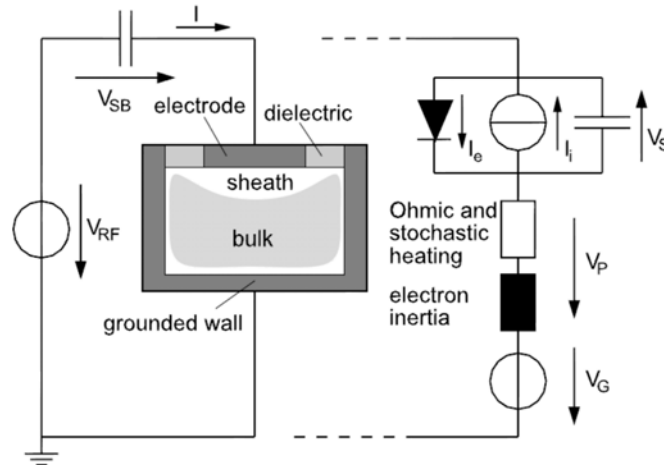


Fig. 4. Representation of a capacitive discharge by a lumped element equivalent circuit [7].

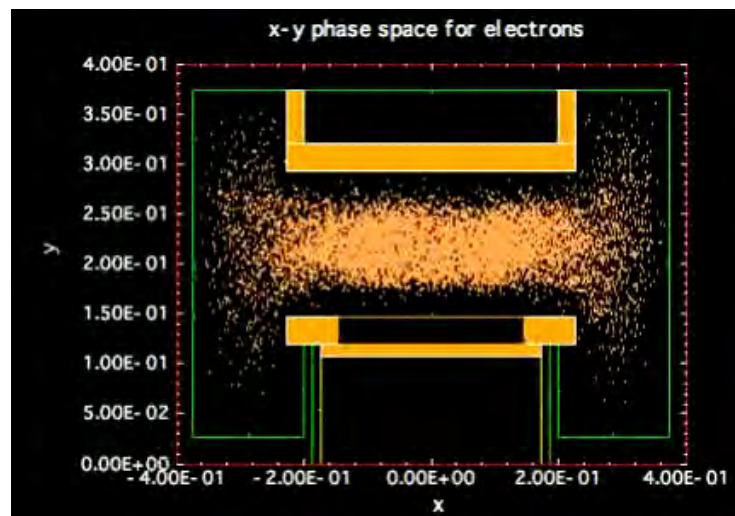


Fig. 5. Snapshot of a PIC simulation, using the open source code XOOPIC [8].

### References

- [1] M.L. Brake, et al., *Physics of Plasmas* **6**, pp 2307-2313 (1999)
- [2] M.A. Lieberman and A.J. Lichtenberg, *Principles of plasma discharges and materials processing*, Wiley, Hoboken, 2005, pp. 571-616
- [3] Jérôme Perrin et al., *Plasma Phys. Control. Fusion* **42**, B353 (2000)
- [4] O. A. Popov and V. A. Godyak, *J. Appl. Phys.* **57**, 53 (1985)
- [5] T. Mussenbrock, R.P. Brinkmann, *Appl. Phys. Lett.* **88**, 151503 (2006)
- [6] D. Ziegler, T. Mussenbrock, and R.P. Brinkmann, *Plasma Sources Sci. Technol.* **17**, 045011 (2008)
- [7] T. Mussenbrock et al., *Phys. Rev. Lett.* **101**, 085004 (2008)
- [8] J.P. Verboncoeur, A.B. Langdon, and N.T. Gladd, *Comp. Phys. Comm.*, **87**, pp. 199-211, (1995).

# The breakdown voltage curves in argon DC and RF discharges from large to small gap sizes

M. Radmilović-Radjenović<sup>1</sup>, M. Savić<sup>1</sup>, M. Šuvakov<sup>1</sup>, B. Radjenović<sup>1</sup>, S. Matejčik<sup>2</sup> and M. Klas<sup>2</sup>

<sup>1</sup>Institute of Physics, Pregrevica 118, 11080 Zemun, Serbia

<sup>2</sup>Department for Experimental Physics, Comenius University, Mlynská dolina F2, 84248 Bratislava, Slovakia

e-mail: marija@ipb.ac.rs

## Abstract

This paper contains results of the experimental and simulation studies of the breakdown phenomena in DC and RF argon discharges, for large and for micro gap sizes. For RF discharges, breakdown voltage has been determined by using a Monte Carlo code that follows transport of electrons. For DC discharges calculations were performed by using a Particle-in-cell/Monte Carlo collisions (PIC/MCC) code with the secondary emission model adjusted to include the energy dependence of the secondary electron yield at large separations as well as the enhancement of the secondary emission coefficient in microgaps. For microdischarges, the results of measurements are compared with the PIC/MCC simulation results and a satisfactory agreement has been found. The simulated breakdown voltages, presented here, indicate that if a proper secondary emission model is implemented in the simulation it may lead to a better agreement with the experimental results.

**Keywords:** discharges, microdischarges, secondary electron yield, breakdown

## Introduction

The understanding and control of electrical breakdown across the interelectrode gap is important for a deeper understanding of fundamental plasma behavior [1,2] as well as for industrial applications [3,4]. The breakdown phenomena represents one of the oldest problems in the researches of low-pressure gas discharges [5,6]. Low pressure gas breakdown in systems with dimensions of the order of a centimeter has been widely studied and is reasonably well understood. According to the Townsend's theory, the Paschen curve represents the voltage needed to achieve a balance between the number of electrons lost by diffusion and drift in the inter-electrode gap and the number of secondary electrons generated at the cathode [7] or in the gas phase for RF breakdown.

When applied to the breakdown at small gaps that correspond to the atmospheric pressure, Townsend mechanism, however, shows certain limitations [8,9]. One possible mechanism responsible for these inconsistencies represents the increase of the secondary electron yield due to the quantum tunneling of electrons from the metal to the gas phase, while the other is field induced emission. The high electric fields generated in micro gaps combined with the lowering of the potential barrier seen by the electrons in the cathode as ion approaches lead to ion-enhanced field emission.

Recently, computer modelling and simulations have emerged as an effective tool for studies the gas discharges that complements laboratory experiments and analytic models [10-12]. Furthermore, the difficulty in achieving well-defined experimental conditions and the limited diagnostic techniques, especially for small scale discharges, favor the investigation of nano scale systems with simulation tools [13]. In this paper we were especially interested in the breakdown phenomena for various gap sizes modeled by means of computer simulations.

In the second part of the lecture we shall focus on the basic representation of the RF breakdown. Several semi analytic models have been developed [14] providing the basic phenomenology for different breakdown regimes. Here we start with the electron induced breakdown dominant at higher RF frequencies when ions cannot reach the electrodes.

## Breakdown mechanism

In general, breakdown may take place if two criteria are satisfied: there must be suitably placed initiatory electrons and a mechanism of ionization must occur to produce amplification of ions or electrons which offset the loss by diffusion. The Townsend mechanism by which successive

ionizations of gas molecules induce the gas breakdown, explains the process satisfactorily at large separations. However, avalanches can not be built up in the same way at micrometer separations so the gas breakdown is initiated by the secondary emission process rather than processes in the gas.

### DC discharges

The DC discharges operate under conditions when secondary electron production at the cathode surface is the key mechanism in discharge maintenance [1,2,10]. Electrons emitted from the cathode due to the ion impact will be driven to the anode by the electric field, creating electron-ion pairs on their way through collisions with the neutrals. The ions generated in this way will travel in opposite direction striking the cathode and thereby causing new electrons to be emitted. If the degree of ionization achieved via this process is high enough a plasma can be formed. For the plasma to be self-sustainable, the generation of electron-ion pairs must be sufficient to make up for the loss of charged particles lost by collision process and diffusion to the walls. At low pressures the ionization process becomes ineffective because the probability for electron-neutral collisions is too small, whereas at high pressures elastic collisions prevent electrons from gaining the energies enough for performing ionization and ion-neutral collisions are responsible for increasing of the ion loss to the walls. Therefore, for a fixed gap an optimum pressure for plasma breakdown exists.

However, as far as the DC breakdown in argon is concerned, in the literature there was an unsatisfactory agreement between the experimental and calculated data. Phelps and Petrovic have developed a revised model of breakdown including different sources of secondary electron emission, nonhydrodynamic processes close to absorbing and reflecting metal boundaries, space charge effects on Townsend discharges and also both linear and nonlinear dependence of secondary electron yields on basic discharge parameters [10]. In particular, these authors have criticized the use of a constant secondary electron yield (of 8% for argon taken from beam surface experiments) in modeling of the dc breakdown and collisional plasmas.

Electrons released at the cathode travel the whole distance to the anode and produce more ionization than electrons created en route. For this reason, the onset of breakdown is determined by  $\gamma$ -effects at the cathode. The secondary electron emission from a surface under the action of an ion is described by the coefficient quantifying the number of secondary electrons produced at the cathode per ion usually known as the electron yield per ion and denoted by  $\gamma_i$ . Although, this coefficient depends on the cathode material and the gas it was often assumed that  $\gamma_i$  is constant [more in ref. [15]]. In order to correct this deficiency first, we implement energy dependence of the coefficient  $\gamma_i$  by using the expression that was suggested by Phelps and Petrovic [10]:

$$\gamma_i(\varepsilon_i) = \frac{0.006 \cdot \varepsilon_i}{1 + (\varepsilon_i / 10)} + 1.05 \cdot 10^{-4} \frac{(\varepsilon_i - 80)^{1.2}}{1 + (\varepsilon_i / 8000)^{1.5}}, \quad (1)$$

where  $\varepsilon_i$  represents the incident energy of the ion.

### RF discharges

Dependence of the breakdown field on the rf wavelength near the oscillation amplitude limit is shown in Figure 1. At very low frequencies, both electrons and ions are able to respond to the ac fields quickly and the oscillation amplitude for both species is well beyond the oscillation limit, so both species reach the chamber walls representing a major loss for the system. Thus, plasma is sustained by secondary electrons produced by ion bombardment of the cathode.

With increasing the frequency, the ion response to the ac field becomes more deliberate, although the electrons follow the ac fields without any difficulty. Consequently, the ion current to the cathode decreases so that the ion bombardment and secondary electron production are depleted and the breakdown field increases.

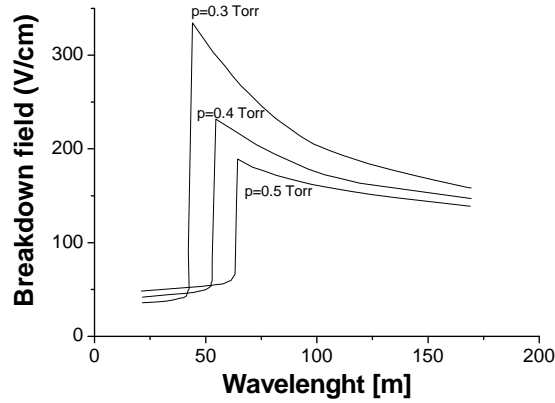


Fig. 1. Dependence of the measured breakdown field strength on the rf wavelength near the oscillation amplitude limit for three different values of the gas pressure [15,16].

Further increases of the frequency leads to a sharp reduction in the ion bombardment of the cathode along and consequently in secondary electron production. This situation takes place typically for rf discharges at frequencies around a few megahertz. At these frequencies, the ions cannot respond to the rf fields, but the electron response is almost instantaneous and the electron loss quite severe. Due to the high deficit of secondary electrons, the discharge is difficult to maintain and the breakdown field strength rises steeply. As the frequency is raised further, the maximum deflection of electrons becomes smaller compare to the oscillation amplitude limit and consequently the loss of electrons and the breakdown field strength drops abruptly.

### Microdischarges

Current models of secondary electron emissions in low fields require ions to be neutralized as a first step in the emission process. Therefore, single-charged ions are capable of extracting a maximum of one electron. The mechanism, however, is completely different in the presence of high electric fields [13]. When the electric field near the cathode is sufficiently large, electron tunneling from the metal to the gas phase needs to be taken into account. Furthermore, as an ion approaches the cathode, it lowers the potential barrier seen by the electrons in the metal resulting in an ion-enhanced electron field emission [17]. An explicit expression for the electron yield per ion ( $\gamma$ ) that incorporates this ion-enhanced field emission is given by [17]:

$$\gamma = K e^{-B/E}, \quad (3)$$

where  $K$  and  $B$  are material and gas dependent constants and  $E$  is the electric field near the cathode. When the electric field in the cathode region becomes larger than the threshold value given by  $B$ , the electron yield per ion increases rapidly. Since field emission is mainly governed by the electric field  $E$  rather than the reduced electric field  $E/N$ , deviations from the Paschen curve are expected when the secondary emission process is governed by ion-enhanced field emissions rather than ion impact. Since field emission is mainly governed by the electric field  $E$  rather than the reduced electric field  $E/N$ , deviations from the Paschen curve are expected when the secondary emission process is governed by ion-enhanced field emissions rather than ion impact.

### Results for RF discharges

Figure 2 shows the pressure dependence of the breakdown voltage in rf argon discharges at 13.56 MHz and the interelectrode gap of 2.3 cm. The simulation [18]

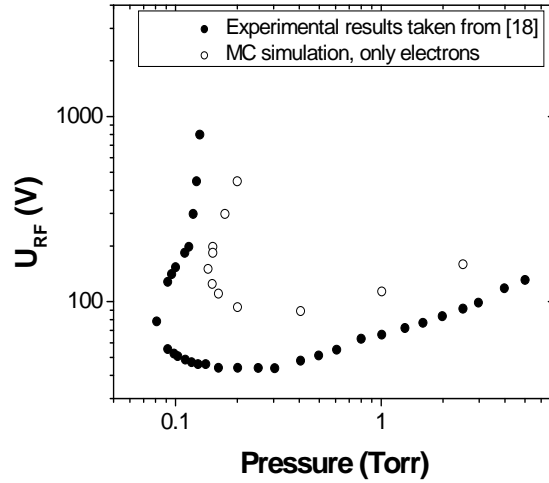


Fig. 2. Comparison between the experimental data taken from ref. [18] (solid symbols) and the Monte Carlo simulation results (open symbols) obtained taking into account only electrons [18].

results obtained by Monte Carlo code considering only electrons motion (open symbols) are compared with the results of measurements by Lisovsky et al. [18] illustrating the role of electrons in the breakdown mechanism. The changes of the electron concentration during the rf breakdown can be observed from Figure 3. Calculations were done for three characteristic points at the Paschen curve (shown in Figure 2): a) voltage of 70 V (slightly below the Paschen curve), b) voltage of 93.4 V (at the breakdown voltage curve) and c) voltage of 170 V (inside the Paschen curve). With increasing voltage, electrons are moving towards electrodes, while their concentration in the central region decreases.

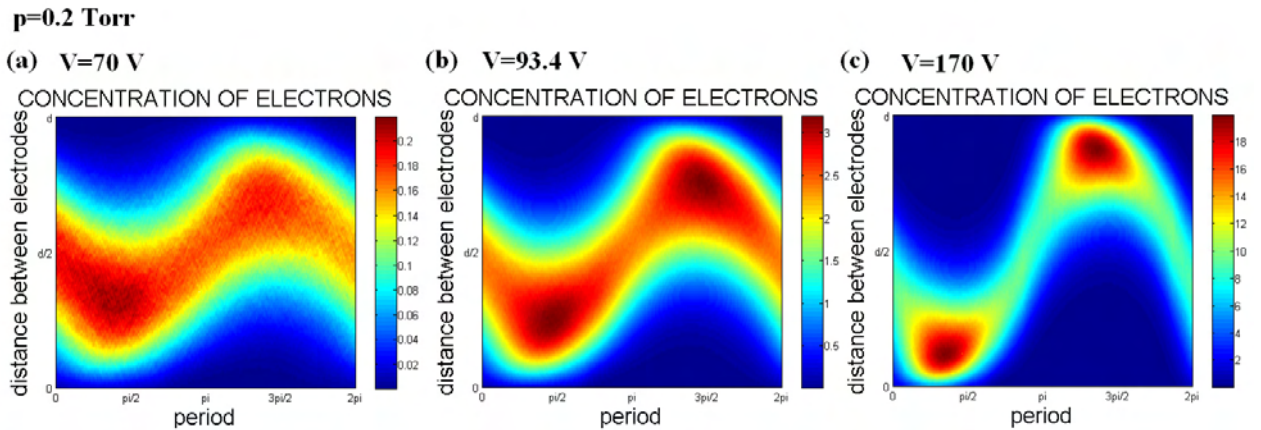


Fig. 3. Spatial distribution of electrons between the electrodes separated by 2.3cm in argon rf discharge at 13.56 MHz, the pressure of 0.2 Torr and the voltage of: a) 70 V, b) 93.4 V and c) 170 V. The point under b) corresponds to the breakdown at the given pd.

### Results for Microdischarges

Results of the experimental (open symbols) and simulation studies (solid symbols) of the breakdown voltage curves in the DC argon discharges for gap sizes of 20 and 100  $\mu\text{m}$  are given in Figure 4. Although there are similar trends for both gap spacing, the breakdown voltage curve for 20  $\mu\text{m}$  is systematically lower as compared to that for 100  $\mu\text{m}$ . Theoretical prediction obtained by employing expression from ref. [19] (crosses) better agree with the results for 20  $\mu\text{m}$  which is expected since the expression has been derived for the gap sizes of the order of a few micrometers

[20].

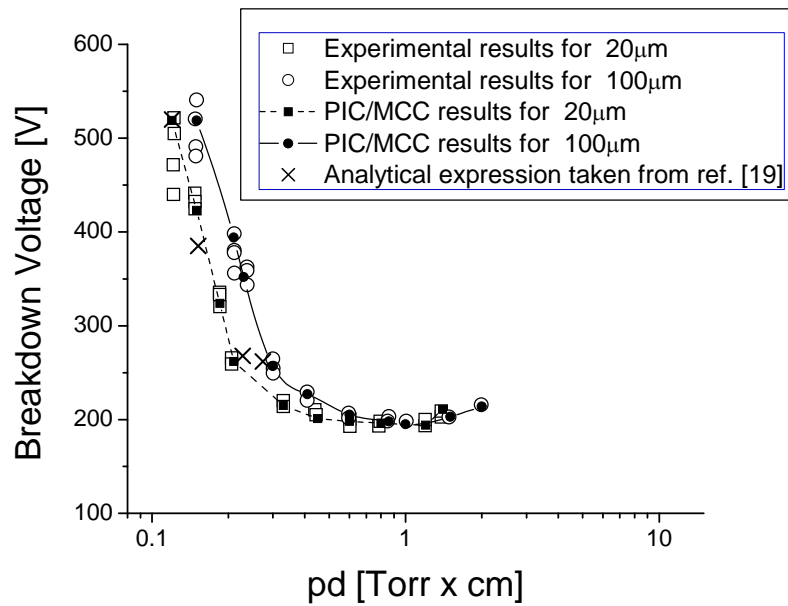


Fig. 4. The breakdown voltage versus the pd product for argon DC discharges at the gap sizes of 20 and 100 micrometers. Experimental results are shown by open symbols while the solid symbols correspond to the PIC/MCC simulation results.

This work has been supported has also been carried out under MNSTR 141025 project.

## References

- [1] J.M. Meek and J.D. Craggs, *Electrical breakdown of gases*, John Wiley&Sons, Norwich, 1953, pp. 1-129
- [2] Y.P. Raizer, *Gas Discharge Physics*, Springer-Verlag, Berlin, 1991, pp. 128-161.
- [3] J. R. Ligenza, *J. Appl. Phys.* 36, (1965) 22703.
- [4] A. C. Eckbreth and J. W. Davis, *Appl. Phys. Lett.* 21, (1972) 25.
- [5] S. C. Brown and A. D. MacDonald, *Phys. Rev.*, 76 (1949) 1629.
- [6] T. Kihara, *Rev. Mod. Phys.*, 24 (1952) 45.
- [7] Yu.D. Korolev and G.A. Mesyats, *Physics of pulsed breakdown in gases*, URO-PRESS, 1998.
- [8] W.S. Boyle and L.H. Germer, *J. Appl. Phys.*, 26 (1955) 571.
- [9] J.M. Torres and R.S. Dhariwal, *Microsystem Technologies*, 6 (1999) 6.
- [10] A.V. Phelps and Z.Lj. Petrovic, *Plasma Sources Sci. Technol.*, 8 (1999) R21.
- [11] J. P. Verboncoeur, M. V. Alves, V. Vahedi and C. K. Birdsall, *J. Comp. Phys.*, 104 (1993) 321.
- [12] S. Hamaguchi, *IBM J. Res. Develop. B*, 43 (1999) 199.
- [13] M. Radmilovic-Radjenovic, J.K Lee, F. Iza and G.Y. Park, *J. Phys. D : Appl. Phys.*, 38 (2005) 950.
- [14] Lisovsky et al., *J. Phys. D: Appl. Phys.*, 31 (1998) 3349.
- [15] M. Radmilovic-Radjenovic and J.K. Lee, *Physics of Plasmas*, 12 (2005) 063051.
- [16] A. Ganguli and R. D. Tarey, *Current Science*, 83 (2002) 279.
- [17] W.S. Boyle and P. Kisliuk, *Phys. Review*, 97 (1955) 255.
- [18] M. Savic, M. Radmilović-Radjenović, M. Švakov, S. Marjanović, D Marić and Z Lj Petrović submitted to IEEE Trans plasma Sci 2010 and unpublished
- [19] M. Radmilovic-Radjenovic and B. Radjenovic, *Europhysic Letters*, 83 (2008) 25001.
- [20] M. Klas, S. Matejckik, M. Radmilovic-Radjenovic and B. Radjenovic, submitted.

# DBD pulsed plasma for surface sterilization

H. Ghomi, K. Ramezani and N. Navab Safa

Laser and Plasma Research Institute, Shahid Beheshti university Evin, 1983963113, Tehran, Iran.

## Abstract

Bacteria inactivation is studied by applying Dielectric Barrier Discharge (DBD) in the presence of a grounded mesh electrode attached to the dielectric. The grounded mesh electrode decreases applied voltage and induces uniform plasma over a sample. A population of  $10^8$  CFU/ml Escherichia Coli is irradiated by DBD and sterilization effective factors are studied. The experiment is done at 5-9 kV applied voltage and complete inactivation less than 8 seconds in dry air is obtained. Atomic Force Microscopy (AFM) is employed to investigate the possible factors in bacterial inactivation.

**Keywords:** Non-thermal plasma. Dielectric barrier discharge. Sterilization. Mesh electrode.

## Introduction

Non thermal plasma treatment of packaging material is a current technology for sterilization at moderate temperatures and alternative for traditional packaging sterilization in food and medical fields. It has the potential to substitute or complete conventional sterilization methods such as heat, chemical solutions and radiations (e.g. UV), which are often time consuming, damaging materials or have toxic residues [1,2].

The main inactivation factors for cells exposed by DBD plasma are chemically reactive species, UV radiation, charged particle and local heat depending on the used process gas [2-5]. The above factors occur in combinations in the gas plasma and can enforce the sterilizing effects synergistically. The amount of each single factor is dependent on the characteristics of the plasma species and the applied electrical power.

In the present study, we present DBD plasma with a grounded mesh electrode for surface sterilization. It is shown that, using the mesh electrode decreases applied voltage and induces uniform non-thermal plasma. We investigate the effects of DBD considering applied voltage and exposure time for complete sterilization in atmospheric pressure and room temperature.

## Materials and methods

### a) Experimental setup

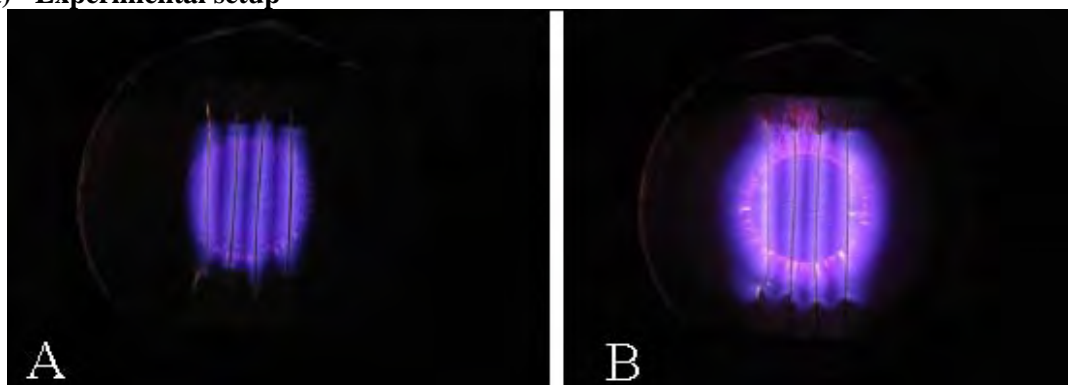


Fig. .1. An image of dielectric barrier discharge in air in presence of a grounded mesh attached to the dielectric at 7 kHz A. Voltage= 5 kV, B. Voltage 9 kV.

Figure 1-a and 1-b shows the plasma around the mesh at 5 and 9 kV, respectively. It is easy to see that, by increasing the voltage the plasma volume becomes larger. The produced plasma covers the grounded mesh. During the experiment, a Petri dish including an electrically non-conducting flat gel type agar surface on which E.coli were cultured is placed under the grounded mesh. The gap distance

between the grounded mesh and the treatment surface is maintained about 1 mm. Please note that, in the absence of the grounded mesh attached to the dielectric, we don't have plasma until 11.6 kV.

**b) Sample preparation:**

Standard E.Coli strain ATCC 105935 is used as the experimental sample. The cell suspension is centrifuged and the supernatant is removed. The pellet is resuspended in sterile phosphate-buffered saline-A (PBSA) to obtain an E.coli concentration of approximately  $10^8$  colony-forming units (CFU)/ml as determined by 0.5 McFarland standard and spectrometer assays. The sample is mixed thoroughly and 200 $\mu$ l each dilution is poured in to sterile Petri dishes containing caso agar media for DBD experiment. After exposure, treated and untreated (control) Petri dishes were incubated. The treated area is determined after incubation of  $37^\circ C$  for 14 hours.

**Result and discussion**

In this work we developed an atmospheric pressure plasma device to inactivate the microorganisms. Figure 2 shows a Petri dish which has covered by a layer of E.Coli bacteria with  $10^8$  CFU/ml concentrations. It is treated by DBD plasma discharge in the presence of the mesh with 9 KV applied voltage in two different part of Petri dish. Experiment is done in two seconds and two times separately. It can be seen that there is no bacterial growth in the exposed areas and complete sterilization is obtained after 2 seconds. This is the shortest time which is reported for surface sterilization by DBD. Please note that, the powered electrode is circular, but the treated (decontaminated) area is not circular.

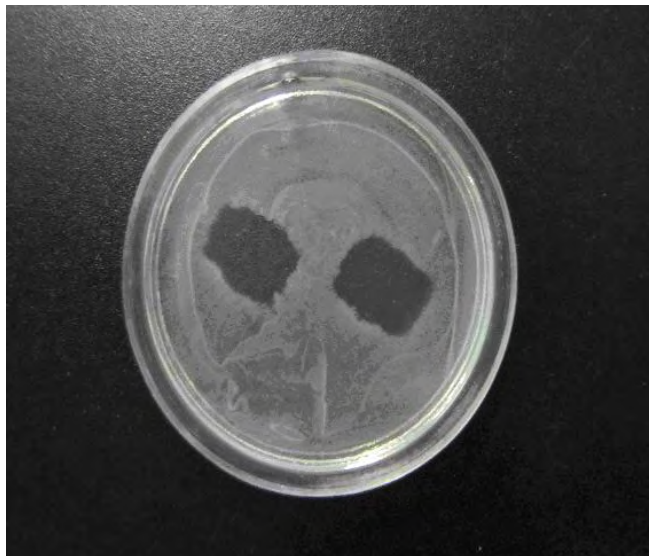


Fig. 2. An image of a Petri dish treated by DBD plasma for 2s; E coli bacteria concentration  $10^8$ CFU/ml, voltage 9kV and frequency 7 kHz.

Figures (3-A) and (3-B) show deflection and topographical AFM images of untreated and plasma treated bacteria. They illustrate morphological change of bacteria cell wall under the plasma influence. It can be easily seen that the cell membrane of bacteria after plasma treatment has severely damaged and rupture in the cell wall of bacteria is apparent. Moreover some pieces of damaged bacteria can be observed in the 3-B images that imply the drastic effect of the DBD plasma on bacteria. As explained before, some factors in plasma like electrostatic force and charged particles impact can result in cell wall rupture. In fact, physical damage to the cell membrane of bacteria can cause the leakage of their cytoplasm and ultimately cell death.

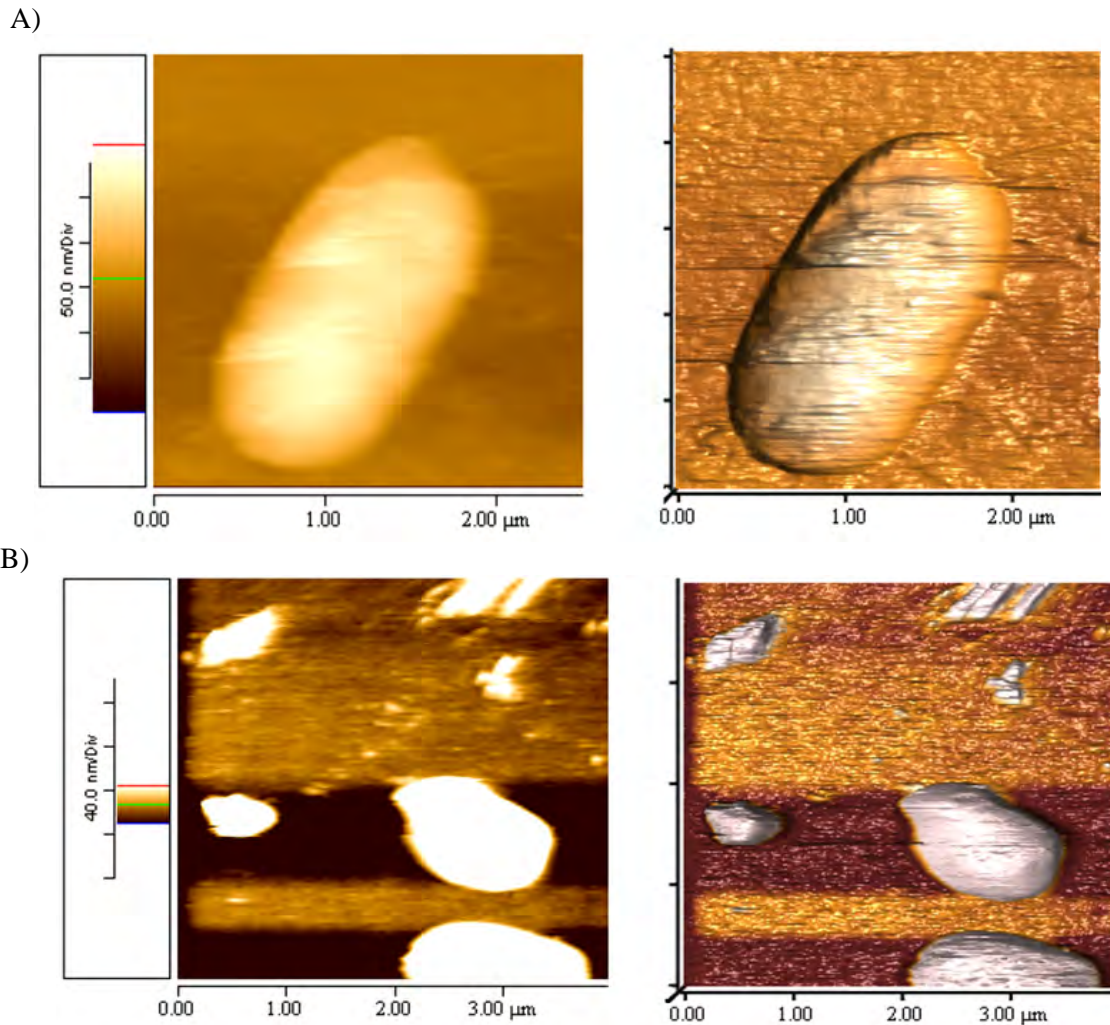


Fig. 3. AFM images of E. Coli bacteria; left column: deflection images; right column: topographic images ;A) untreated bacteria; B) plasma treated bacteria.

In this experiment, total electrical power is 4.2 W at 5 kV and 17.2 W at 9 kV. This is the total electrical power which is consumed from DC power supply. But this is not the exact electrical power which was applied to plasma and also to the sample's surface which is difficult to measure it. However it is clear that by increasing the voltage, the plasma becomes larger and brighter. On the other hand, four main inactivation factors in DBD are: 1) chemically reactive species, 2) UV radiation, 3) charged particles and 4) local heat. By increasing the applied voltage the plasma volume around the mesh increases and results in improving all above four factors. Please note that, the local heat on human body is negligible (photograph was reported by Fridman [6] and we also observed the same effect even at 9 kV and higher). However the other three factors are still important and the further study will be needed to determine the exact role of each factor during the decontamination.

### Conclusions

In this work the decontamination of E. Coli by atmospheric pressure plasma was investigated. The results show that the survival reduction percentage of E.coli by the atmospheric pressure plasma reached to 100% at 9 kV applied voltage in 2 seconds. The sterilization factors are a combination of chemically active species, UV radiation and charged particle collisions. In fact, DBD plasma seems to be a fast and reliable method for surface sterilization.

### References:

- [1] H. Conrads, M. Schmidt. *Plasma sources Sci Technol*, 9, (2000) 441-454.

- [2] M. Moisan, J. Barbeau, M. Crevier, J. Pelletier, N. Philip and B. Saoudi. *Pure Appl Chem* 74, (2002) 349-358.
- [3] A. A. Bol'shakov, B. Cruden, R. Mogul, M. Rao, S. Sharma, B. Khare and M. Meyyappan. *AIAA J* , 42, (2004) 823-832.
- [4] X. Lei, Z. Rui, L. Peng, D. Li-Li and Z. Ru-Juan. *Chinese phys*, 13, (2004) 913-917.
- [5] M. Laroussi. *overview and state-of-the-art. Plasma Process Polym*, 2, (2005) 391-400.
- [6] H. Ayan, G. Fridman, A. Gutsol, V. Vasilets, A. Fridman, G. Friedman. (2009) 18<sup>th</sup> international symposium on plasma chemistry, Bochum Germany.

# Formation of negative ions in corona discharge studied by Ion Mobility/Mass Spectrometry technique: application on trace gas detection

M. Sabo and Š. Matejčík

Department of Experimental Physics, Comenius University, Mlynská dolina, Bratislava 842 45, Slovakia

e-mail: Martin.Sabo@gmail.com

## Abstract

The negative ion chemistry in high purity  $O_2$  and  $O_2/N_2$  mixtures has been investigated by the means of ion mobility/mass spectrometry (IMS/MS) technique. We have demonstrated the ability of the corona discharge (CD) to generate selectively  $O_2^-$ , which important for the detection of the explosives by IMS technique. Additionally, we have proven the ability of CD-IMS instrument to detect TNT at ppt level with and without dopant gases.

## Introduction

The mass spectra of the negative ions generated in negative corona discharge (CD) in air using atmospheric pressure ionization mass spectrometry (APIMS) technique [1-6] show significant differences. This is due to sensitivity of CD and APIMS on many parameters like gas purity, gas flow, the period between ion formation and them detection, by the discharge power and so on.

The ion mobility spectrometry is separation technique based on separation of the ions, which drift in a buffer gas in weak homogenous electric field. The principles of this technique are well described in the book [7]. The CD ion source was proposed for IMS as a non-radioactive alternative to widely used  $^{63}Ni$  as a ionization source [8]. However, the formations of very stable negative ions and radicals and neutral fragments with high electron affinities in negative mode complicated the implementation of CD in negative IMS, especially for explosives detection [9]. Several solutions how to solve this problem have been proposed [6,10,11]. The additional gas flow [6,10] and electronics [11] were required in those methods.

We have developed CD source, which is able selectively generate  $O_2^-(H_2O)_n$  ( $n=0,1$ ) negative ions. We have applied this ion source to the analysis of high purity oxygen by CD-IMS/MS technique in dependence of nitrogen concentration from 0.5 ppm to 80% (zero air) and applied the CD-IMS to detect nitro- compounds and TNT at ppt level.

## Experiment

The IMS/MS (figure 1.) instrument used in our experiment was described elsewhere [12]. The IMS instrument operates in single flow mode with gas outlet behind the CD thus the CD operates in reverse flow regime [6]. The IMS operated in temperature range 295K - 373K.

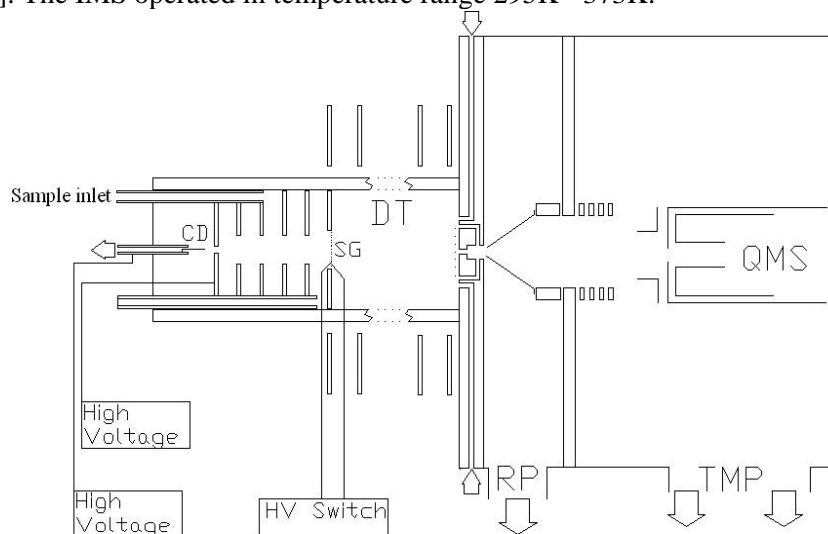


Fig. 1. Schematic view of IMS/MS instrument

The used gases in our experiment were: O<sub>2</sub> of 5.0 and 6.0 quality (with and without additional purification), N<sub>2</sub>of 5.0 quality, synthetic air (LindeGas). The chemicals used in this experiment were chloroform and 2,4,6-trinitrotoluene (Sigma Aldrich). The syringe (Hamilton) with 2,4,6-TNT was heated to 353K in order to increase the vapor density of the TNT. The chemicals were introduced to sample gas stream (synthetic air-100ml/min) by the syringe pump (KentScientific).

## Results and discussion

The IMS spectrum of pure oxygen is depicted in Figure 2a. The dominant peak with reduced mobility  $2.52 \text{ cm}^2\text{V}^{-1}\text{s}^{-1}$  was in our previous study [12] assigned to stable ion  $\text{N}_2\text{O}_2^-$ . The presence of this ion in mobility spectrum is result of the main impurity in high purity O<sub>2</sub> (about 0.5 ppm N<sub>2</sub>). The N<sub>2</sub> is responsible for formation of N<sub>2</sub>O in CD gap [13], which efficiently reacts with O<sup>-</sup> and O<sub>3</sub><sup>-</sup> yielding  $\text{N}_2\text{O}_2^-$ . Due to implementation of reverse flow of gas in the CD we are able to detect O<sub>2</sub><sup>-</sup> and O<sub>2</sub><sup>-</sup>(H<sub>2</sub>O)<sub>n</sub> in the mobility spectrum. The presence of these ions peak in the mobility spectrum is due to efficient removal of neutrals (e.g., N<sub>2</sub>O) from CD gap in reverse flow regime [6]. These ions drift in the thermodynamic equilibrium [7] and their reduced mobility was calculated to value of  $2.44 \text{ cm}^2\text{V}^{-1}\text{s}^{-1}$ . The relative intensity of this peak in IMS spectrum depends on many parameters like rate of the gas flow, CD geometry and CD power. While the decreasing of the nitrogen concentration down to ppm level leads to the presence of O<sub>3</sub><sup>-</sup> in mobility spectrum [14] the increase of the nitrogen concentration leads to efficient thermalisation of electrons in CD and more effective O<sub>2</sub><sup>-</sup> formation. We have reached up to 70% of O<sub>2</sub><sup>-</sup> yield (Figure 2b) in zero air in IMS in our CD. The generation of O<sub>2</sub><sup>-</sup> from CD is very important for explosive detection, which was one of the main reasons for developing of IMS technique [9]. Unlike the radioactive <sup>63</sup>Ni, which is the most common ion source for explosive detection, the CD do not require special permission and the problems related to the special waste disposal also fall off.

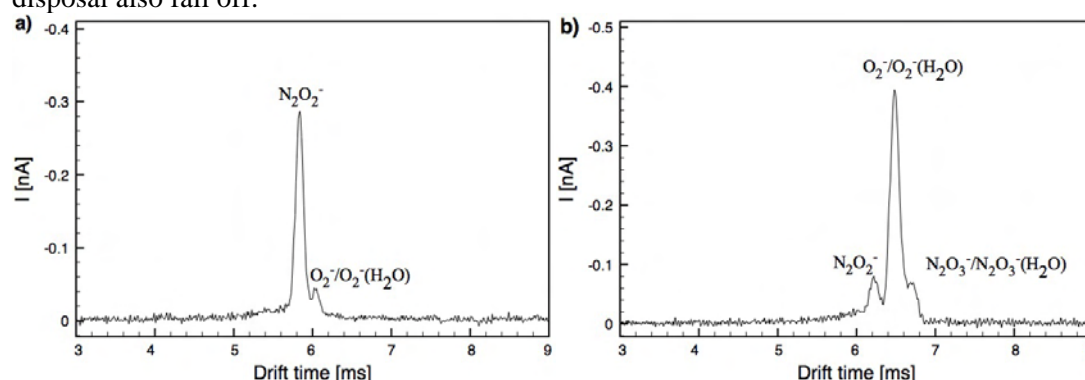


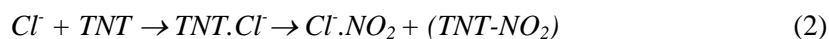
Fig. 2. a) IMS spectrum of 5.0 oxygen dominant peak  $\text{N}_2\text{O}_2^-$  with reduced mobility  $2.52 \text{ cm}^2\text{V}^{-1}\text{s}^{-1}$  and  $\text{O}_2^-/\text{O}_2^-(\text{H}_2\text{O})$  with reduced mobility  $2.44 \text{ cm}^2\text{V}^{-1}\text{s}^{-1}$  b) IMS spectrum in zero air dominant peak  $\text{O}_2^-/\text{O}_2^-(\text{H}_2\text{O})$  with reduced mobility  $2.27 \text{ cm}^2\text{V}^{-1}\text{s}^{-1}$ ,  $\text{N}_2\text{O}_2^-$  and  $\text{N}_2\text{O}_3^-/\text{N}_2\text{O}_3^-(\text{H}_2\text{O})$  with reduced mobility  $2.37 \text{ cm}^2\text{V}^{-1}\text{s}^{-1}$  and  $2.2 \text{ cm}^2\text{V}^{-1}\text{s}^{-1}$ .

The detection of the nitro compounds in IMS was studied. The nitro-compounds were introduced to the IMS in the reaction region. We will present specifically the results for one of the studied compounds TNT. The most stable negative ions formed from TNT at atmospheric pressure is deprotonated anion ( $\text{TNT-H}^-$ ) [9]. In order to maintain the stability [15] and increase the sensitivity [9] of IMS the chlorinated hydrocarbon reagent chemicals are introduced to IMS as dopant gases [16]. These dopant gases are responsible for formation of Cl<sup>-</sup> in reaction region of IMS. The mechanism of formation of deprotonated anions ( $\text{TNT-H}^-$ ) has been described by following equation [9]:



where M is O<sub>2</sub><sup>-</sup> or Cl<sup>-</sup>.

The IMS spectrum of TNT (concentration 10ppt) was measured at temperature 373 K in synthetic air with and without addition of chloroform (see Figure 3). The reduced mobility of ( $\text{TNT-H}^-$ ) was calculated to be  $1.57 \text{ cm}^2\text{V}^{-1}\text{s}^{-1}$  what is in good agreement with values reported in literature [9]. In the MS and IMS spectra strong Cl<sup>-</sup>.NO<sub>2</sub> signal is detected. (figures 3a and 4a). This ion is most probably formed via abstraction of NO<sub>2</sub> group from TNT:



Addition of TNT into IMS without presence of dopant gas (chloroform) results in more complex mass spectrum (figure 4b). There are present several ions, which are most probably associated with the solvents present in the sample. These ions are responsible for the broadening of the dominant peak in the mobility spectrum (figure 3b.) and are directly responsible for lower sensitivity of IMS without addition of chloroform as it is evident from figure 3.

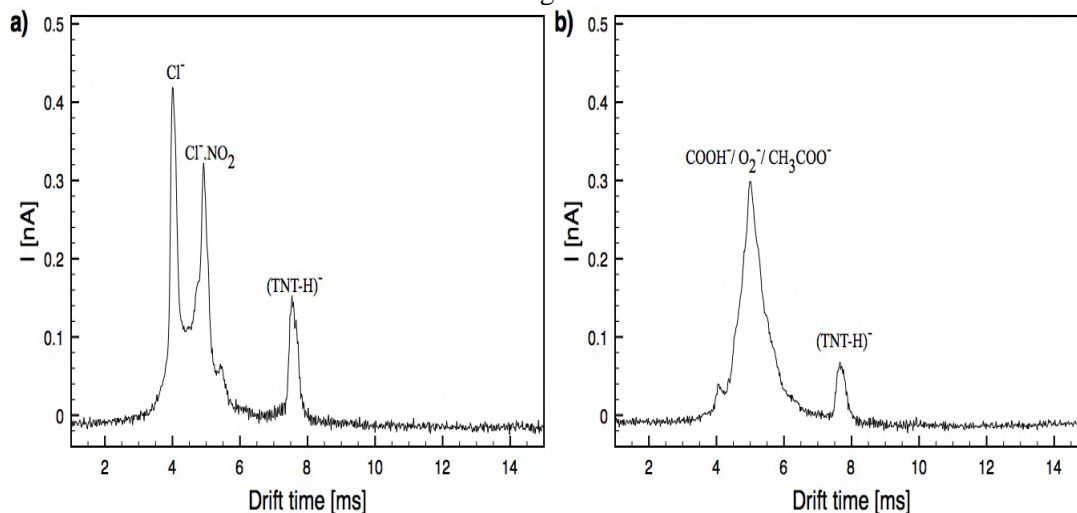


Fig. 3. The IMS spectrum after injection of 10ppt TNT with addition of chloroform (a) and without chloroform (b).

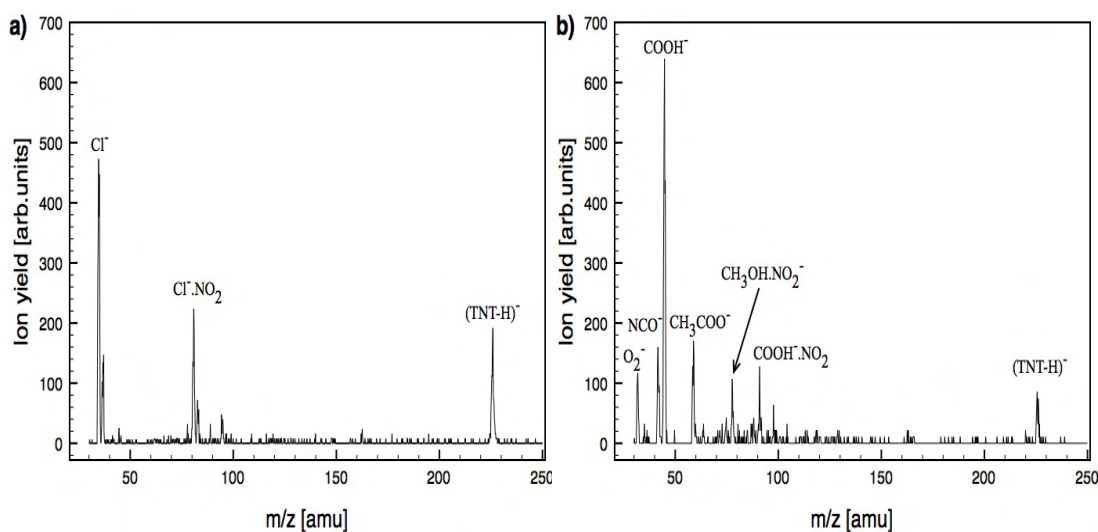


Fig. 4. The mass spectrum after injection of 10ppt TNT with addition of chloroform (a) and without chloroform (b)

The main advantage of the IMS with CD ion source is the fact that the CD by several orders of magnitude stronger primary ions intensity in comparison to the commonly used radioactive  $^{63}\text{Ni}$  [8] ions sources. The intensity of the ions source has a direct impact on the sensitivity of the IMS method. In present study we were able to detected TNT at 10ppt level with and without dopant gas (chloroform), however, we have observed the positive effect of the dopant gas on the sensitivity and selectivity of the method. We believe that the limit of detection for TNT by CD-IMS technique is below this level.

## Conclusion

In this study the negative CD in  $\text{O}_2$  and  $\text{O}_2/\text{N}_2$  mixtures was implemented to IMS as ionization source. The ability of CD to generate selectively  $\text{O}_2^-$  has been presented. The ability of CD-IMS to

detect trace gases (TNT) at 10ppt level has been demonstrated. This study confirmed the positive role of dopant gases on the sensitivity of CD-IMS.

### Acknowledgement

This work was supported by the Slovak research and development agency projects LPP-06-0146, APVV-0365-07 and the VEGA grants No. 1/0051/08, 1/0558/09, 1/0379/11.

### References

- [1] M.M. Shahin, *Appl. Opt., Supplement on Electrophotography.*, 106 (1969) 3.
- [2] P.S. Gardiner, J.D. Craggs, *J. Phys. D: Appl. Phys.*, 10 (1977) 1003.
- [3] J.D. Skalny, T. Mikoviny, Š. Matejčík, N.J. Mason, *Int. J. Mass Spectrom.*, 233 (2004) 317.
- [4] K. Nagato, Y. Matsui, T. Miyata, T. Yamauchi. *Int. J. Mass Spectrom.*, 248 (2006) 142.
- [5] B. Gravendeel, F.J. Hoog, *J. Phys. B: At. Mol. Phys.*, 20 (1987) 6337.
- [6] S.K. Ross, A.J. Bell, *Int. J. Mass Spectrom.*, 218 (2002) L1-L6.
- [7] G.A. Eiceman, Z. Karpas, *Ion Mobility Spectrometry 2nd edition*. CRC press, 2005.
- [8] M. Tabrizchi, T. Khayamian, N. Taj, *Rev. Sci. Instrum.*, 71 (2000) 465.
- [9] R.G. Ewing, D.A. Atkinson, G.A. Eiceman, G.J. Ewing, *Talanta*, 54 (2001) 515.
- [10] M. Tabrizchi, A. Abedi, *Int. J. Mass Spectrom.*, 218 (2002) 75.
- [11] C.A. Hill, C.L.P. Thomas, *Analyst*, 128 (2003) 55.
- [12] M. Sabo, J. Páleník, M. Kučera, H. Han, H. Wang, Y. Chu, Š. Matejčík, *Int. J. Mass Spectrom.*, 293 (2010) 23.
- [13] F. Pontiga, A. Fernández-Rueda, H. Moreno, A. Castellanos, *18th ESCAMPIG Conference*, (2008)
- [14] M. Sabo, Š. Matejčík, J. Páleník, *ISIMS Conference*, Albuquerque, New Mexico (2010).
- [15] J. Puton, M. Nousiainen, M. Sillanpää, *Talanta*, 76 (2008) 978.
- [16] K.A. Daum, D.A. Atkinson, R.G. Ewing, *Talanta*, 55 (2001) 491.

# Diagnosics of Electrical Discharges in Electrolytes: Influence of Electrode and Diaphragm Configuration

Z. Kozáková, L. Hlavatá, F. Krčma

Institute of Physical and Applied Chemistry, Brno University of Technology, Purkyňova 464/118, Brno 612 00, Czech Republic

e-mail: kozakova@fch.vutbr.cz

## Abstract

This paper deals with electrical discharge ignition in water solutions of selected electrolytes (NaCl, NaBr, and Na<sub>3</sub>PO<sub>4</sub>), and it describes particular processes before and after discharge breakdown by DC non-pulsed voltage up to 2 kV. Diaphragm configuration, with possibility to change the electrode distance (from 2 to 8 cm) and with different pin-hole diameters (0.3–0.6 mm), was used in experiments in order to estimate an influence of configuration parameters on the breakdown moment. The diaphragm was made of PET with its thickness of 0.25 mm. It was proved that the breakdown appeared at higher applied voltage when the electrode distance was enhanced. The influence of pin-hole diameter was less obvious in the studied range, but a slight enhancement of breakdown voltage was observed with the increasing pin-hole diameter.

**Keywords:** discharges in water, diaphragm configuration, electrical characteristics, discharge breakdown, bubble formation.

## Introduction

Electrical discharges in liquids have been in a serious focus of researchers for mainly last three decades. Especially formation of various reactive species such as hydroxyl and hydrogen radicals, some ions, and molecules with high oxidation potential (hydrogen peroxide) has been investigated in order to utilize this process in water treatment, removal of organic compounds from water, and sterilization processes [1–4].

Diaphragm discharge configuration consists of two electrode spaces divided by the dielectric barrier with a central pin-hole. Ratio of the pin-hole diameter to the diaphragm thickness is approximately 1:1. Mechanisms of discharge breakdown in liquids are still under an intensive research and their study requires specific approach in all possible configurations (different kind of high voltage, various electrode configuration, etc.). Generally, two types of theories are considered to be the most suitable for discharge breakdown description – thermal (bubble) theory, and electron theory [5]. The thermal theory is based on the process when liquid is heated and subsequently, evaporated due to the current flow (Joule's heating). If applied power is sufficient, discharge ignition appears in bubbles of evaporated liquid. Further propagation of ionized particles in the form of plasma channels (streamers) takes place in liquid, too, as a result of ionization of liquid molecules. On the other hand, electron theory describes discharge ignition analogically to the Townsend's theory of electron avalanches in gases.

Discharge ignition in the diaphragm configuration probably combines both theories. Initially, it starts in the pin-hole when sufficient power is applied. Then, the breakdown moment is probably related to the bubbles formation [6]. By the application of constant DC voltage, water solution is significantly heated due to high current density, and bubbles of water vapor are created in the pin-hole region. It is assumed that the discharge breakdown starts in these bubbles because of high potential gradient between the outer and inner bubble region [6], in correspondence to the thermal theory. On the other hand, further propagation of plasma channels to the bulk solution probably corresponds to the electron theory. Moreover, application of DC voltage initiates creation of two kinds of plasma streamers on both sides of the diaphragm [7, 8]. Longer streamers appear on the side with the cathode because pin-hole in the diaphragm behaves as a positive spot, and the streamers propagate to the positive electrode similarly to the positive corona discharge. On the other side where the anode is placed, shorter streamers in a spherical shape propagate toward pin-hole like in the case of negative corona discharge.

The presented contribution describes diaphragm discharge creation by the means of electrical characteristics, and discusses the influence of electrode and diaphragm configuration on the

breakdown moment. The main studied parameters were: distance of electrodes from the diaphragm, and pin-hole initial diameter.

### Experimental set-up

The batch reactor was divided into two electrode spaces by the dielectric barrier, and non-pulsed DC voltage up to 2 kV was used for the discharge creation. The discharge appeared in a pin-hole in the dielectric diaphragm (PET, thickness of 0.25 mm). Planar electrodes made of stainless steel were installed on each side of the diaphragm. The distance between each electrode and the dielectric barrier was shifted in order to determine its influence on the discharge ignition. Water solution containing selected electrolyte (NaCl, NaBr or Na<sub>3</sub>PO<sub>4</sub>) to provide initial conductivity in the range of 300–600  $\mu\text{S}\cdot\text{cm}^{-1}$  was used as a liquid medium. Total volume of the used solution was 4 liters (2 liters in each electrode space).

Diaphragm configuration in the reactor consisted of the inert PET foil with the thickness of 0.25 mm which was installed within the insulated barrier between two electrode parts. One central pin-hole was made in this diaphragm. Its initial diameter varied from 0.30 to 0.60 mm, with the step of 0.05 mm. It was already proved in [9] that the pin-hole diameter was enhanced during the discharge because of strong erosion environment. On the other hand, experiments focused on electrical measurements took only short time and thus the pin-hole diameter remained more or less the same during the whole measurement.

Oscilloscope Tektronix TDS 1012B operating up to 100 MHz with high voltage probe Tektronix P6015A was used to obtain time resolved characteristics of discharge voltage and current with focus on the breakdown moment. Simplified scheme of oscilloscope integration into the electrical circuit is demonstrated in Figure 1. Mean values of breakdown parameters (voltage, current, power, and resistance) were estimated and subsequently, static V-A characteristics were evaluated for each experiment. Obtained results were compared with respect to the electrode configuration (distance from the dielectric diaphragm or pin-hole diameter).

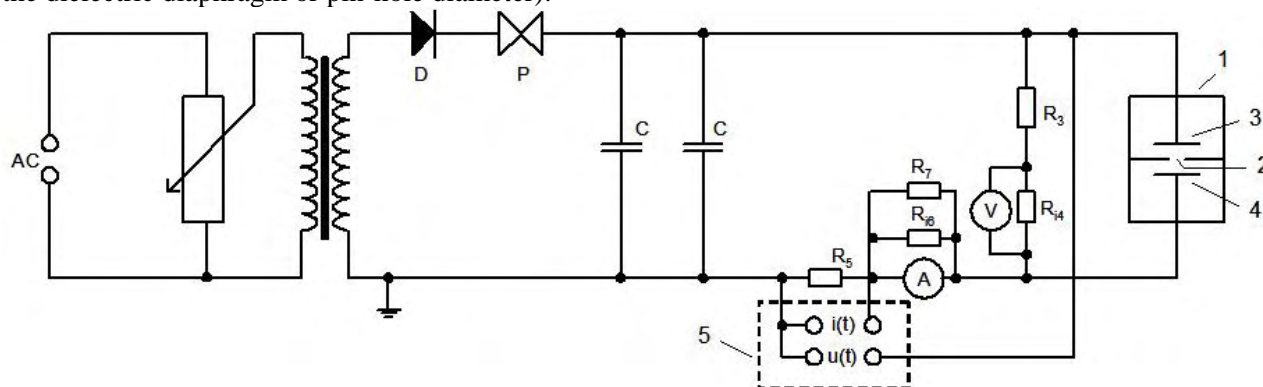


Fig. 1. Simplified scheme of electrical circuit containing discharge reactor and oscilloscope: 1 – discharge reactor, 2 – diaphragm with pin-hole, 3 – anode, 4 – cathode, 5 – oscilloscope Tektronix TDS 1012B, P – safety-fuse (0.5 A), C – microwave capacitor (0.85  $\mu\text{F}$ ), R – resistances: R<sub>3</sub> (100 M $\Omega$ ), R<sub>4</sub> (3.114 k $\Omega$ ), R<sub>5</sub> (5.13  $\Omega$ ), R<sub>6</sub> (105.5  $\Omega$ ), R<sub>7</sub> (0.13  $\Omega$ ).

### Results and discussion

V-A characteristics (i.e. current-voltage curves) of DC diaphragm discharge were constructed from mean values of time resolved characteristics recorded over 50 ms. Figure 2 demonstrates a typical current-voltage curve obtained in Na<sub>3</sub>PO<sub>4</sub> solution with initial conductivity of 500  $\mu\text{S}\cdot\text{cm}^{-1}$ . This curve could be divided into three parts. Increasing the applied DC voltage, measured current slowly increased as well. During this starting part, only electrolysis took place in the system, and the electrolyte solution was heated by the passing current (Joule effect). Going above the voltage of hundreds volts, the first significant breakpoint appeared in the curve – current markedly jumped up. According to the time resolved characteristics (Figure 3, b), we have assumed that this moment was related to the substantial creation of bubbles formed by the evaporating solution. Further enhancement of voltage provided only a small current increase until the second remarkable breakpoint was observed. From this moment, current was rapidly arising with only a small voltage enhancement. This

second breakpoint was assumed to be the discharge breakdown moment which was also confirmed by light emission recorded by the optical emission spectroscopy.

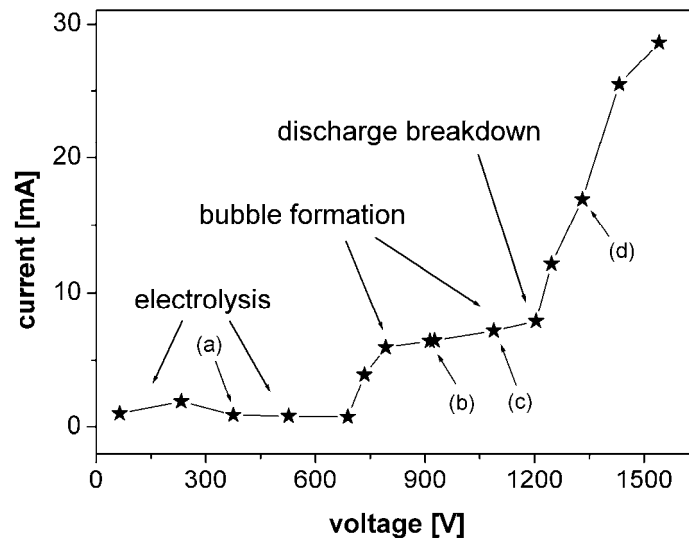


Fig. 2. Typical V-A characteristics of DC diaphragm discharge in  $\text{Na}_3\text{PO}_4$  solution (initial conductivity of  $500 \mu\text{S}\cdot\text{cm}^{-1}$ ). Points (a)–(d) correspond to Figure 3.

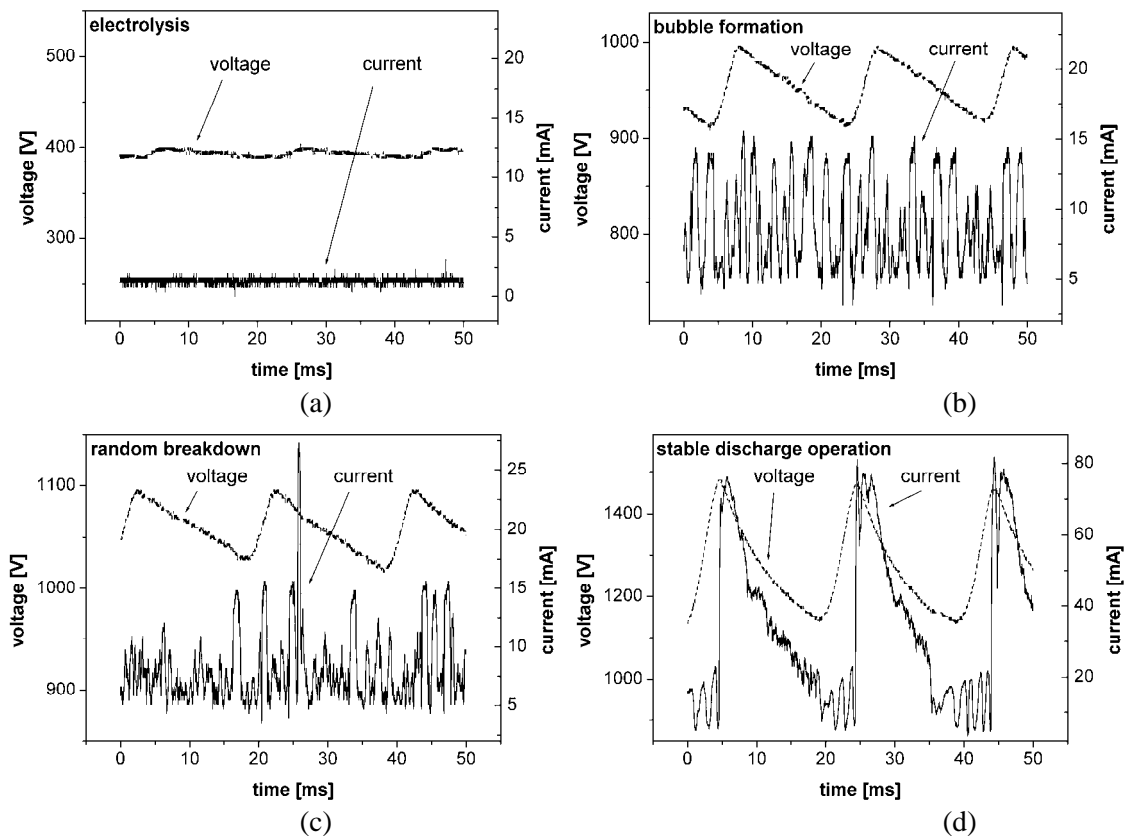


Fig. 3. Time resolved characteristics of voltage and current during electrolysis (a), bubble formation (b), random discharge breakdown (c), and stable discharge operation (d) in  $\text{Na}_3\text{PO}_4$  solution (initial conductivity of  $500 \mu\text{S}\cdot\text{cm}^{-1}$ ).

Figure 3 demonstrates evaluations of voltage and current during three main parts before and during diaphragm discharge ignition: electrolysis, bubble formation, and stable discharge operation. During electrolysis at lower applied voltage up to 700 V, no significant peaks appeared in regular voltage and

current oscillations (Figure 3, a). Voltage oscillations were related to the HV source construction, and they had no significant influence on the observed phenomena. At higher applied voltage (700–1200 V), remarkable higher oscillations of both current and voltage were recorded (Figure 3, b). This phenomenon was related to the bubble formation due to the intensive solution heating by passing current. No light emission was observed during this period. Further enhancement of applied voltage provided irregular sharp current peaks that appeared in the record (Figure 3, c). This phenomenon was related to random breakdown of vapor bubble, and short peaks of emitted light were recorded, too. When breakdown voltage was overstepped (beyond 1200 V), the discharge was ignited in the pin-hole, and regular peaks of current were recorded as well as an intensive light emission (Figure 3, d).

An influence of electrode and diaphragm configuration on breakdown moment and particular discharge periods was studied for two parameters: distance of electrodes and pin-hole initial diameter.

Shifting the electrode distance with respect to the diaphragm had a substantial effect on the discharge ignition while its influence on the bubble formation (and electrolysis, too) was only negligible. Figure 4 demonstrates obtained results when anode distance from the diaphragm was changed from 3 to 8 cm, and cathode distance remained fixed at 2 cm. Presented current-voltage curves show that discharge breakdown voltage was enhanced by the increasing anode distance. Particular values of determined breakdown voltage are listed in Table 1 (left part) for three anode distances (3, 5, and 8 cm). Breakdown voltage increased from 1180 V (anode distance of 3 cm) to 1500 V for 8 cm anode distance. These results were obtained in NaBr solution (initial conductivity of  $350 \mu\text{S}\cdot\text{cm}^{-1}$ ). Similar effect was observed when the cathode was moved, too.

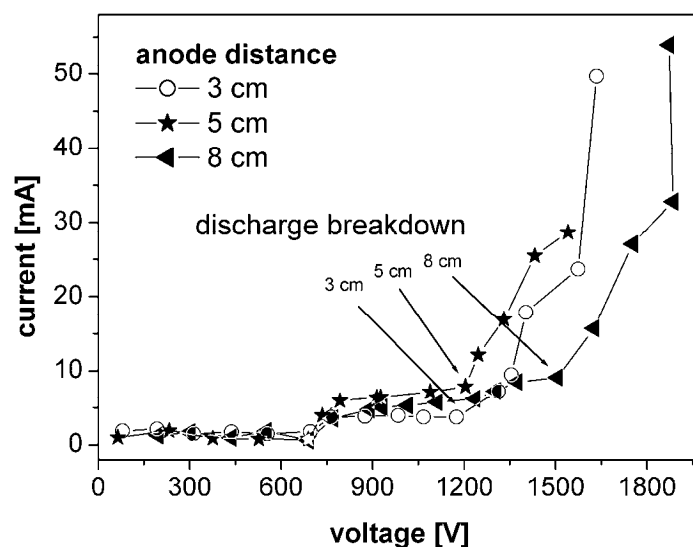


Fig. 4. Comparison of V-A characteristics of DC diaphragm discharge in NaBr solution (initial conductivity of  $350 \mu\text{S}\cdot\text{cm}^{-1}$ ) for different anode distances from the diaphragm (fixed cathode distance of 2 cm).

Tab. 1. Breakdown voltage of DC diaphragm discharge as a function of anode distance (left part) and pin-hole diameter (right part).

| Anode distance [cm]                                       | Breakdown voltage [V] | Pin-hole diameter [mm]                                    | Breakdown voltage [V] |
|---|-----------------------|---|-----------------------|
| 3   | 1180                  | 0.30  | 1470                  |
| 5   | 1200                  | 0.45  | 1500                  |
| 8   | 1500                  | 0.60  | 1570                  |
| NaBr electrolyte ( $350 \mu\text{S}\cdot\text{cm}^{-1}$ ) |                       | NaCl electrolyte ( $550 \mu\text{S}\cdot\text{cm}^{-1}$ ) |                       |

Figure 5 presents current-voltage curves obtained for two marginal pin-hole diameters (0.30, and 0.60 mm) in NaCl electrolyte (initial conductivity of  $550 \mu\text{S}\cdot\text{cm}^{-1}$ ). There was no remarkable difference in determined breakdown moments for studied pin-hole diameters, especially in the range of 0.30, and 0.50 mm. A slight increase of breakdown voltage was observed when the pin-hole was

enhanced to 0.60 mm. Particular values of determined breakdown voltage are listed in Table 1 (right part) for selected three pin-hole diameters (0.30, 0.45, and 0.60 mm). Breakdown voltage slightly increased from 1470 V (pin-hole diameter of 0.30 mm) to 1570 V for 0.60 mm pin-hole diameter.

Based on obtained results, our next study will be focused on more extended pin-hole diameters up to 1.00 mm, and especially, on different pin-hole structure concerning both diaphragm thickness, and pin-hole diameter.

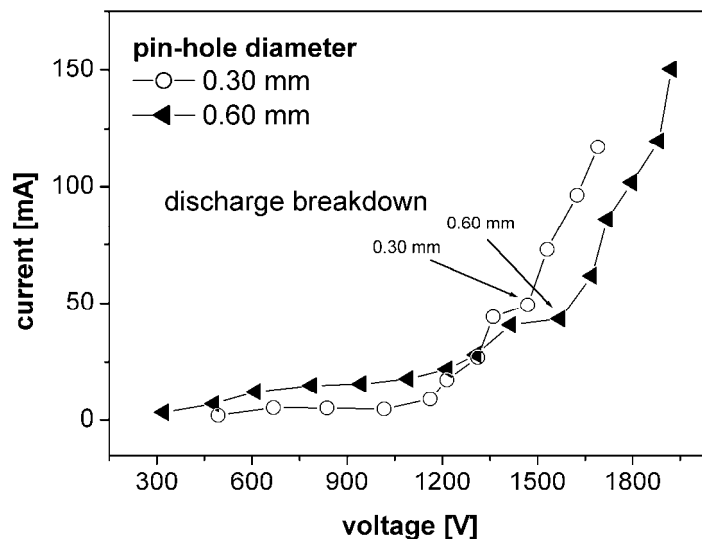


Fig. 5. Comparison of V-A characteristics of DC diaphragm discharge in NaCl solution (initial conductivity of  $550 \mu\text{S}\cdot\text{cm}^{-1}$ ) for various pin-hole diameters in the PET diaphragm.

## Conclusions

Breakdown moment as well as processes of electrolysis, and bubble formation were identified from obtained static (V-A), and time resolved characteristics of DC diaphragm discharge generated in NaCl, NaBr, and  $\text{Na}_3\text{PO}_4$  solutions. Current-voltage evaluation was remarkably influenced by electrode configuration. Increasing the electrode distance from the diaphragm, the process of bubble formation was not effected while discharge breakdown started at significantly higher applied voltage. Influence of pin-hole diameter on the breakdown moment was only negligible, and breakdown voltage was slightly increased by the enhancing pin-hole diameter.

## Acknowledgement

The work was supported by the Czech Science Foundation, project No. 202/07/P371.

## References

- [1] B. Sun, M. Sato, J.S. Clements, *Environ. Sci. Technol.* 34 (2000), 509.
- [2] P. Šunka, V. Babický, M. Člupek, M. Fuciman, P. Lukeš, M. Šimek, J. Beneš, B.R. Locke, Z. Majcherová, *Acta Physica Slovaca* 54 (2004), 135.
- [3] E. Njatawidjaja, A.T. Sugiarto, T. Ohsima, M. Sato, *J. Electrostatics* 63 (2005) 353.
- [4] M. Moisan et al., *Plasma sterilization. methods and mechanisms* 74 (2002) 349.
- [5] M.A. Malik, A. Ghaffar, S.A. Malik, *Plasma Sources Sci. Technol.* 10 (2001) 82.
- [6] R.P. Joshi, J. Qian, K.H. Schienbach, *J. Appl. Phys.* 92 (2002) 6245.
- [7] Z. Stará, F. Krčma, J. Procházková, *Acta Technica CSAV* 53 (2008) 277.
- [8] L. Hlavatá, F. Krčma, Z. Kozáková, *J. Phys.: Conf. Ser.* (2010) accepted.
- [9] J. Procházková, Z. Stará, F. Krčma, *Czech. J. Phys.* 56 (2006) B1314.

# Under Water Discharge in Bubbles in Very Low Conductive Solutions

P. Vanraes<sup>1</sup>, A. Nikiforov<sup>1,3</sup>, Ch. Leys<sup>1</sup>, L. Němcová<sup>1,2</sup>, F. Krčma<sup>2</sup>

<sup>1</sup>Department of Applied Physics, Ghent University, Jozef Plateaustraat 22, Gent 9000, Belgium

<sup>2</sup>Institute of Physical and Applied Chemistry, Brno University of Technology,  
Purkyňova 118, Brno 612 00, Czech Republic

<sup>3</sup>Institute of Solution Chemistry RAS, Laboratory of Non-Linear Plasma Processes,  
Academicheskaya, Ivanovo 153045, Russia

e-mail: xcnemcova@fch.vutbr.cz

## Abstract

This contribution presents experimental results obtained with underwater electric discharge created in rising gas bubbles. This discharge configuration is relatively new, and combines both gas and liquid phase discharges. The properties and mechanism of bubble discharge generation were investigated using a single pulsed high voltage. The electric discharge was generated in a pin-to-plate electrode configuration submerged in deionized water with conductivity of 2.0–5.0  $\mu\text{S/m}$ . The gas bubbles were formed by injecting the gas through a glass filter disc at the bottom of the water tank. Air and helium were used as inlet gas. A spark gap pulse generator triggered the single negative high voltage pulses with rise times below 10 ns and peak voltages of 15–20 kV. The bubble position at the moment of high voltage application was accidental. The measured spectra were qualitatively reproducible, but significant quantitative differences were observed. We observed two types of discharge inside the bubble: delayed and direct spark discharge. The emission spectra of these two discharge kinds were qualitatively very similar.

**Keywords:** Underwater discharge, bubble discharge, pulsed voltage, spectral characterization, electrical characterization.

## Introduction

In the past few years, the scientific community has a high interest in underwater electric discharges, especially because of their possible versatile applications in practical life. A number of papers show their efficiency in different areas of human functioning – biology (extermination of microorganisms) [1], ecology, medicine (destruction of kidney stones by shock waves) [2], electrochemistry and also chemistry (degradation of dangerous toxic compounds in water) [3]. Application of electric discharges for water treatment is called AOP's technology (advanced oxidation processes). These methods seem to be promising answers for future problems concerning waste water. However, they are still more expensive than conventional waste water treatment technologies [4].

Electric discharge in liquid phase is generated by application of high electric energy into liquid medium. The electric energy is accumulated between two submerged electrodes, and consecutively electric discharge occurs. The energy which is supplied into the liquid phase causes the formation of a plasma channel in between the electrodes where highly reactive particles are generated. For water treatment, the most important of these particles are hydroxyl radicals and hydrogen peroxide because they efficiently oxidize harmful compounds in water due to their short lifetime [5–7]. Moreover, the generated strong electric field, shock waves, UV radiation and ozone (in case when oxygen is presented) induces the synergetic effect.

Three kinds of electrode configuration are common for the discharge breakdown in liquid phase. The first configuration consists of two parallel plane electrodes (Figure 1a), the second one is pin-to-plate configuration (Figure 1b) and the third configuration is available for the so called diaphragm discharge (Figure 1c); in the latter, a dielectric plate with a small hole is placed in between two electrodes. The high voltage applied to the electrodes can be DC, AC, HF or pulsed voltage. This contribution is focused on the pin-to-plate electrode configuration. The intensity of the electric field is accumulated on the top of the pin electrode.

In spite of increased research in this area of plasma physics, there is only very limited knowledge about the initiating mechanism and development of plasma discharges in pure water. One proposed theory says that plasma is created in water by means of bubble generation due to heating of the water.

Beside this, an alternative approach is to introduce gas or vapor bubbles in between the electrodes submerged in water in order to generate plasma inside the bubbles. The mechanism of this discharge, so-called bubble discharge, is poorly understood as well. We would like to fill this gap in understanding by researching pulsed plasma discharge in free rising bubbles in water.

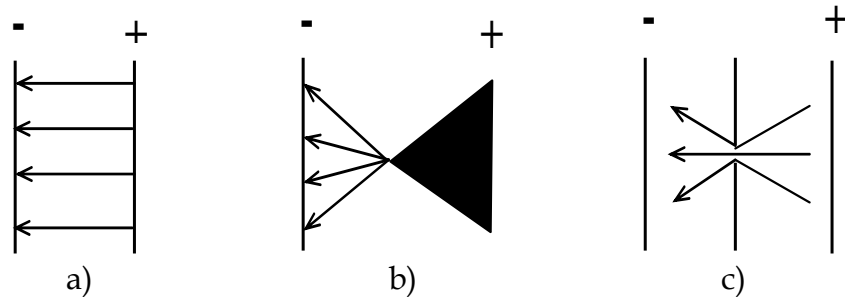


Fig. 1. Possible electrode configurations for the underwater discharge creation: a) two plane electrodes, b) pin-to-plate, c) dielectric diaphragm with a small hole in between the two electrodes. The arrows correspond to the electric intensity vector.

### Experimental technique

The principal scheme of the set-up for the underwater discharge generation in gas bubbles is presented in Fig. 2. The discharge reactor consists of a discharge chamber (solution volume is 3.6 l). The distance between the pin electrode and the plate electrode is 6 mm. Both electrodes are made of stainless steel. The plate electrode (with a diameter of 3 cm) is grounded. The pulsed negative high voltage has been supplied on the pin electrode, which is 4 mm in length and has the shape of a right circular cone with an aperture of  $10^\circ$ . The helium and air are injected into the water at the bottom of the water tank underneath the electrodes through a glass filter disc in order to produce multiple bubbles. The filter disc was made by ROBU (standard filter with a diameter of 40 mm, a thickness of 4.5 mm and porosity class 3). The gas flow of 1.4 slm has been regulated by a mass flow control system (MSK 4000). The multiple bubbles are estimated to be approximately 2 mm in diameter. The pulsed high voltage with rise times below 10 ns has been applied to the pin in parallel with a resistor of 1 M $\Omega$ . The optical emission spectra were measured with an Ocean Optics HR2000 spectrometer.

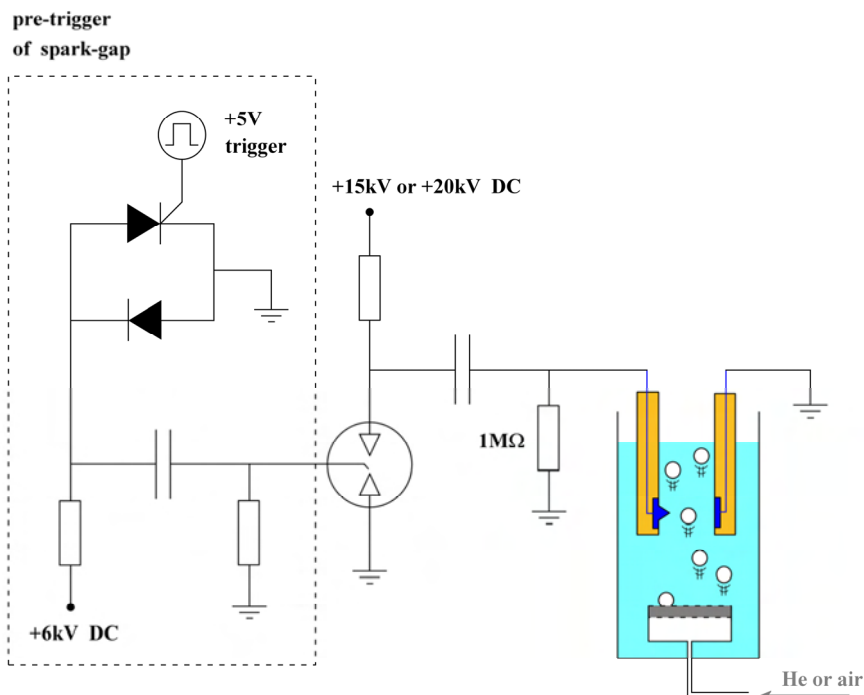


Fig. 2. Scheme of experimental set-up.

## Results and discussion

The electric discharge was generated after applying pulsed high voltage to the system while gas was bubbling. It was found that two kinds of discharges in bubbles are generated: delayed and direct spark discharge. The main difference between these discharges is demonstrated in Figs. 3, and 4. The delay between the start of the high voltage pulse and the start of the discharge inside the bubble varied in wide range from very small delays of less than one hundred nanoseconds to more than ten microseconds. The electric characterization of discharge generated without bubbles is shown in Fig. 5.

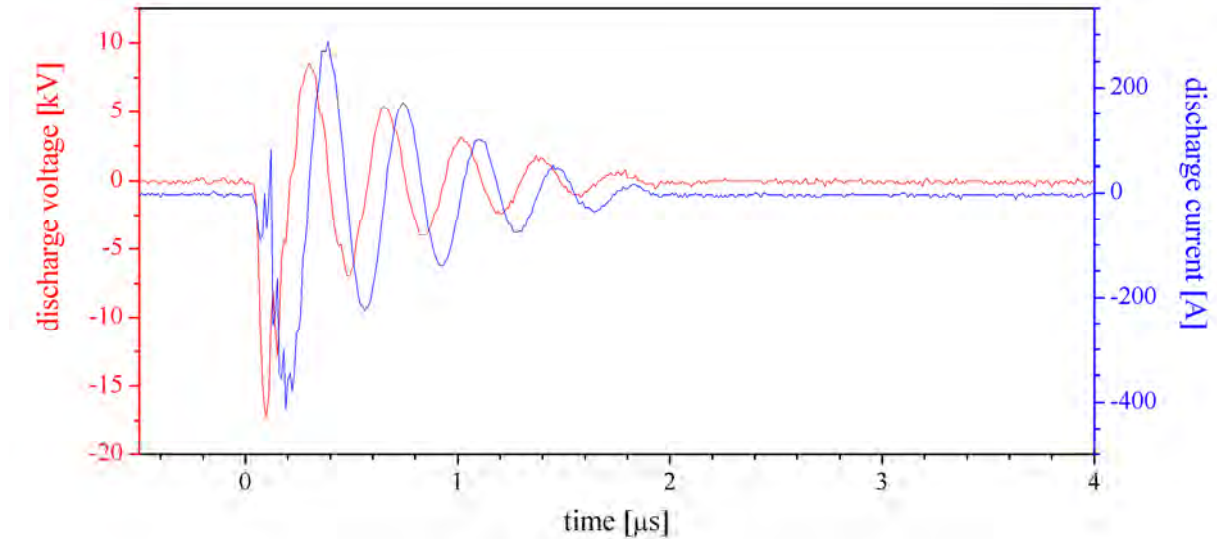


Fig. 3. The current and voltage waveforms of direct spark discharge in air bubbles (applied voltage of 20 kV).

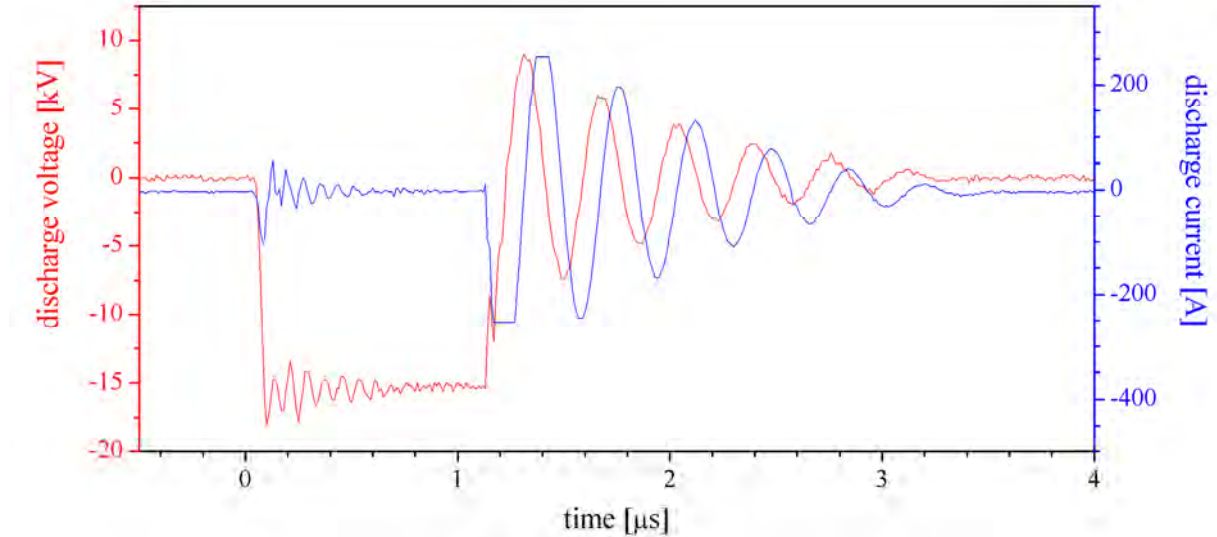


Fig. 4. The current and voltage waveforms of delayed spark discharge in air bubbles (applied voltage of 20 kV).

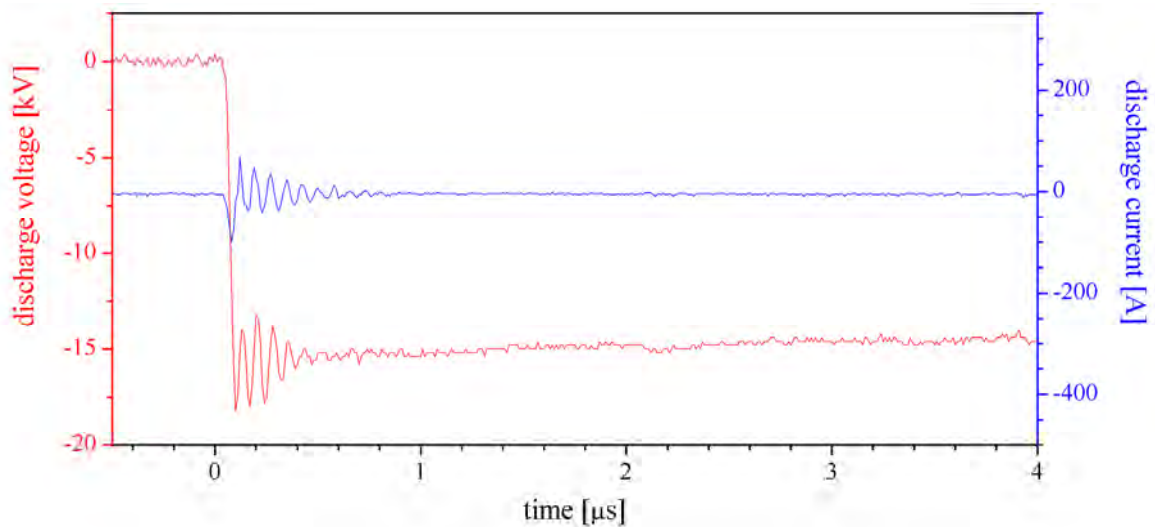


Fig. 5. The current and voltage waveforms of discharge without bubbles (applied voltage of 20 kV).

Examples of optical emission spectra recorded for discharge inside an air bubble at 15 kV are shown in Figs. 6–7 for both discharge kinds at two applied voltages. The most obvious lines are from hydrogen, oxygen, and lines corresponding to the bubbling gas (i.e. helium or nitrogen in case of helium or air bubbles, respectively). The OH radical bands that are usually observed in underwater discharges [8] were not observed. On the other hand, some small peaks of nickel and chromium were recorded because of erosion of the stainless steel electrodes. Spectra of both discharges are qualitatively similar, but the line intensities significantly differ. These differences are probably due to the difference of bubble position at the moment of the discharge, as they are also observed for two different direct spark discharges with the same experimental settings. Changing the value of the applied voltage had a similar effect: the same spectral lines have been observed, but their intensities were not reproducible.

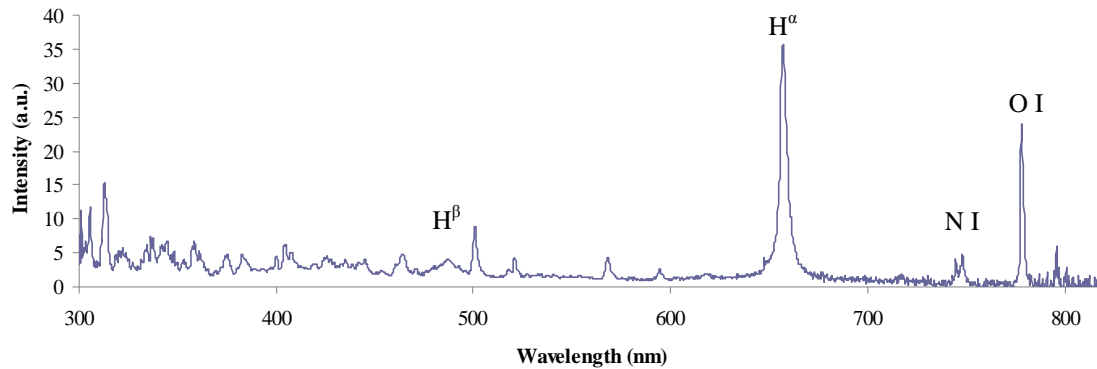


Fig. 6. The spectrum of delayed spark discharge in air bubbles (applied voltage of 15 kV).

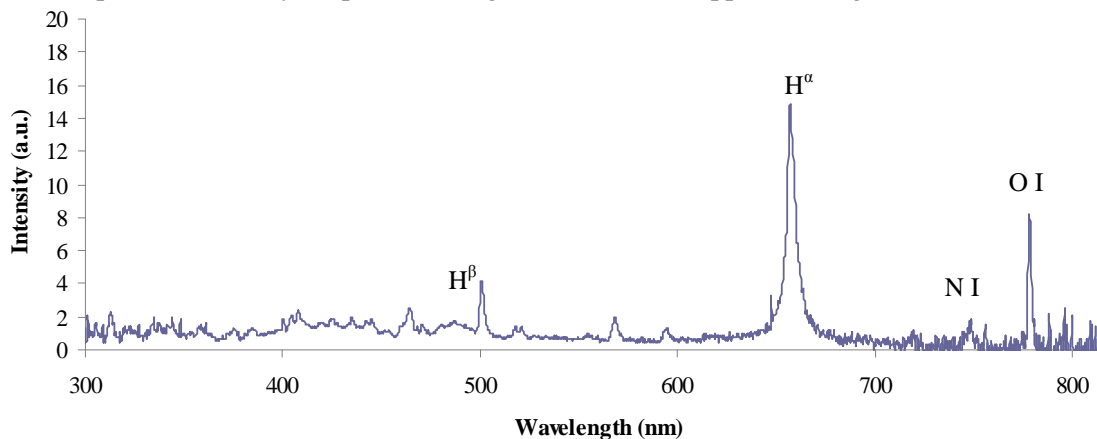


Fig. 7. The spectrum of direct spark discharge in air bubbles (applied voltage of 15 kV).

## Conclusions

Two different types of bubble discharge were observed: direct and delayed spark discharge inside the bubble. This is expected to be due to the variable position of the bubble during the high voltage application. The delay between direct and delayed discharge is expected to be dependent on this position. Further experiments using also a fast camera will be used for this hypothesis confirmation. The hydrogen and oxygen lines are dominant in the spectra. The lines of the most common species present in the bubbling gas (neutral nitrogen atomic lines in case of air, neutral helium lines in case of helium) were recorded, too. Besides them, some weak lines of elements originating from the electrodes were recognized, but no OH bands were found. Spectra of bubble discharge are qualitatively reproducible for the same experimental settings, and they do not change qualitatively when the applied voltage increases. The differences in the spectra of bubble discharge for the same peak voltage and the same bubbling gas for direct spark discharge inside the bubble are expected to be due to the variable position of the bubble during discharge.

## Acknowledgement

This work was done as part of 'Plasma Generation' (WPKI) in the framework of the Interuniversity attraction poles program, Belgian state - Belgian Science Policy, and it was partially supported by Czech Ministry of Education, Youth and Sports, research plan No. 0021630501.

## References

- [1] A.M. Anpilov, et al., *Lett. Appl. Microbiol.* 35 (2002) 90.
- [2] Ch. Chaussy, W. Brendel, and E. Schmiedt., *Lancet* 2, (1980) 1265.
- [3] A. Brablec., P. Slavíček., P. Stáhel., T. Čimžmár, and D. Trunec., *Czech. J. Phys.* 52 (2002) 491.
- [4] K. Sato, K. Yasuoka, and S. Ishii., *Electric. Eng. Japan* 170 (2010) 1.
- [5] T. Miichi., N. Hayashi., S. Ihara., S. Satoh, and Ch. Yababe., *Rep. Fac. Sci. Eng., Saga Univ.* 31 (2002) 1.
- [6] A. Yamatake., H. Katayama, K. Yasuoka, and S. Ishii., *Int. J. Plasma Environ. Sci. Technol.* 1 (2007) 1.
- [7] S. Ihara., T. Miichi., S. Satoh., Ch. Yamabe, and E. Sakai., *J. Appl. Phys.* 38 (1999) 4601.
- [8] J. Procházková, Z. Stará, and F. Krčma, *Czech. J. Phys.* 56 (2006) B1314.

# The validity of the Paschen's law in homogeneous electric field at micrometer separations

M.Klas, M. Matejka, Š. Matejčík

Department of Experimental Physics, Comenius University, Mlynská dolina, Bratislava 842 45, Slovakia

e-mail: matej.klas@gmail.com

## Abstract

In this work we have investigated the validity of the Paschen's law in homogeneous high electric field in different gases. The discharge system consists of two parallel-planar electrodes with electrode spacing from 20 to 200  $\mu\text{m}$  in the pressure range between 8 mbar – 960 mbar. The DC breakdown was measured in  $\text{O}_2$ ,  $\text{H}_2$ , He, Ar, synthetic, dry and ambient air up to 800 V breakdown voltage. The analysis of the experimental data has been carried out in terms of classical and a new, generalized form of semiempirical Paschen's law.

**Keywords:** microdischarges, Paschen's law, deviations, field emission, ion-enhanced field emission

## Introduction

In the recent years a lot of effort has been devoted to find reliable non-equilibrium plasma sources at high pressures [1-3]. One of the most common methods to generate discharge in atmospheric pressure according to Paschen's law is scale down the electrode gaps to the micrometer range [4]. Important relationship between the breakdown voltage and the product of pressure  $p$  and electrode separation  $d$  derived Paschen at the end of 19<sup>th</sup> century [5]. Paschen's law was confirmed for DC discharges at low pressures and distances in the range of several cm in different operating gases. However, already in 50s of the 20<sup>th</sup> century and in the past decades, a number of experimental studies have suggested that Paschen's law does not accurately describe the breakdown voltages at micrometer gaps [6-7]. These studies with microdischarges have shown that field emission and the ion-enhanced field emission affect the left branch of the Paschen curve. When sufficient high electric field is achieved, at electrodes separations below 5  $\mu\text{m}$ , in most cases, the breakdown voltage linearly falls to zero [8]. This behavior strongly depends on the electrode surface condition, gas and applied geometry of discharge system. In spite of many works devoted to measure breakdown voltages at micro separation in inhomogeneous fields there exist only few studies in the literature for separation smaller than 300  $\mu\text{m}$  in homogeneous electric fields [9]. To understand better process leading to breakdown in homogeneous electric fields, a new system was built to measure the DC breakdown from 20 to 500  $\mu\text{m}$  separations between plan-parallel copper electrodes. Our studies deliver new data about DC breakdown under these experimental conditions and on the validity of the Paschen's law in different gases. Moreover, we have determined the effective secondary emission for different gases as a function of electrode separation and present method to evaluate the parameters (ionization coefficient  $A$ ,  $B$ , secondary emission) from Paschen curves.

## Experiment

The schematic view of the apparatus is shown in the Figure 1. The discharge system is located in the high vacuum chamber. The vacuum is generated by the turbo-molecular pump (Pfeiffer Vacuum TMU 071P) and the background pressure of  $2 \times 10^{-5}$  mbar has been achieved. The low pressures were measured by the ionisation gauge (Pfeiffer Vacuum, PKR 261) and the high pressures were measured by the capacitance gauge (Pfeiffer Vacuum, PCR 260 and MKS 626A 100 Torr Barratron). The gas used in the experiment was (Linde, 5.0 purity). The discharge system for generation of the microdischarges consists of two planar oxygen free copper electrodes with diameter of 5 mm. To reduce edge-field effects, the edges on the cylindrical electrodes were rounded of. Both electrodes were equipped with dielectric cap (immune to vacuum, dielectric breakdown strength =13.8 kV/mm) to prevent the ignition of the discharge at longer path at low pressures. Surface roughness is one of the most important parameter. To achieve the minimal influence of roughness the electrodes surface were mechanically polished using diamond paste down to a grain size of 0.5  $\mu\text{m}$  and chemically cleaned in ultrasonic bath. One of the electrodes was fixed to a precision mount with 4 micrometric screws to set optimal parallelism. The other electrode was movable continuously with micrometer scale linear

feed-through. One of the electrodes was earthed, to the second electrode we have applied DC voltage (ISEG HPP 20 407). The 0  $\mu\text{m}$  separation of the electrodes was established by checking the electrical contact between the electrodes and then the movable electrode was pulled away by the means of the micrometer screw. The gap between the electrodes was set to the required distance. Maximum current was set to 1.6 mA.

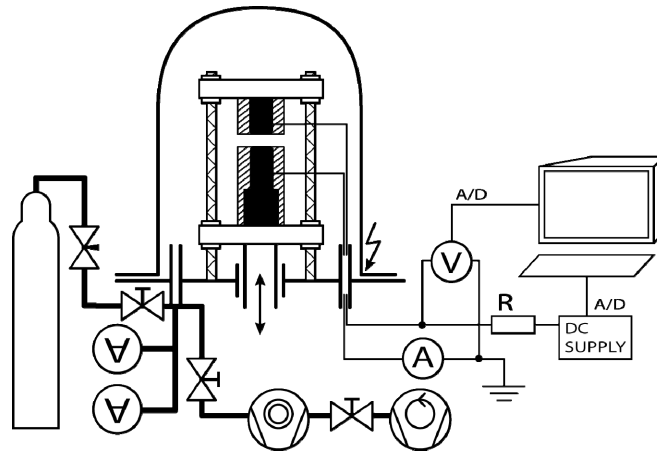


Fig. 1: Experimental setup of apparatus

We have applied very slowly increasing potential to one of the electrodes (ramp speed 0.05 V/s). The DC breakdown voltage was determined from the time dependence of the potential difference across the discharge tube, which has been measured using a digital oscilloscope. The potential across the discharge tube was increasing until the point of breakdown was reached. The breakdown voltage was determined from the maximum potential achieved across the discharge gap. Using this method we were able to measure the breakdown voltage with high reproducibility.

### Results and discussion

The DC breakdown voltage was measured for several discharge gaps from 20 to 500  $\mu\text{m}$  as a function of  $p.d$  (Paschen curves). The pressure was varied in the range from 8 mbar up to 1000 mbar. The Paschen curves have been measured for pure Hydrogen, Argon, Oxygen (5.0) synthetic Air (78%  $\text{N}_2$  and 22%  $\text{O}_2$  both gases of 5.0 purity), dry ambient air and ambient air. In the Figures 2-4 Paschen curves for measured gases at different discharge gaps are shown.

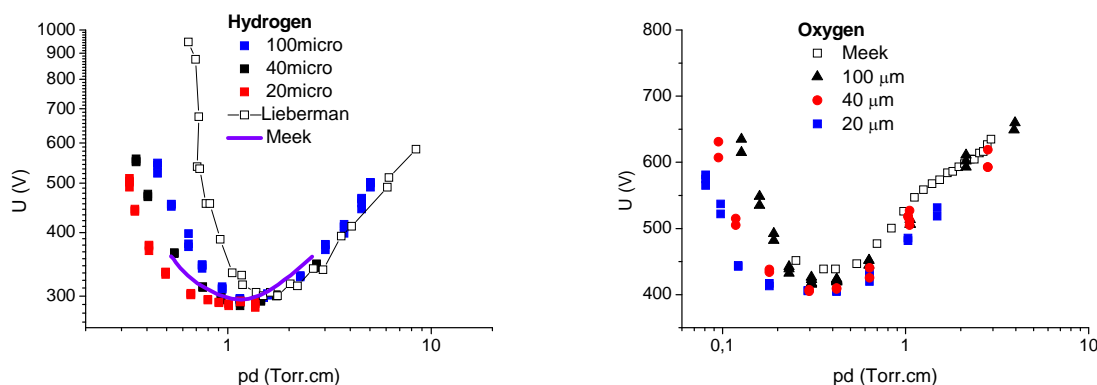


Fig. 2. Experimental Paschen curves for a) Hydrogen compared with Lieberman [10] and Meek [11] and b) Oxygen compared with [11]

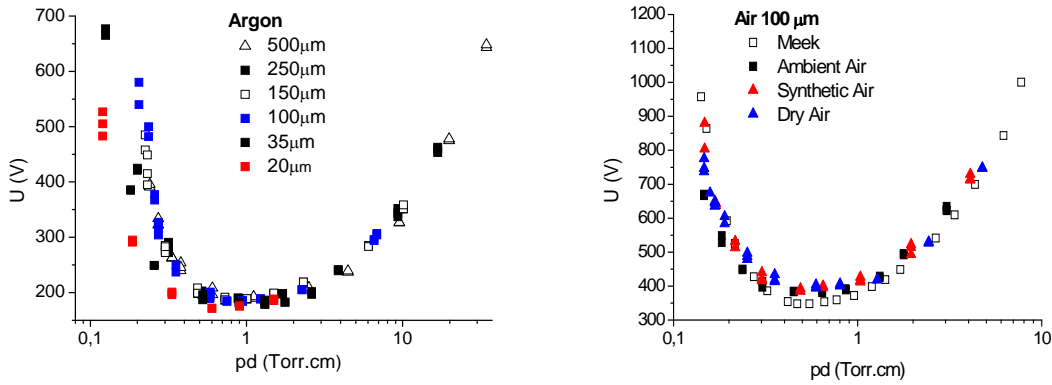


Fig. 3. Experimental Paschen curves for a) Argon and b) different Air at one electrode separation

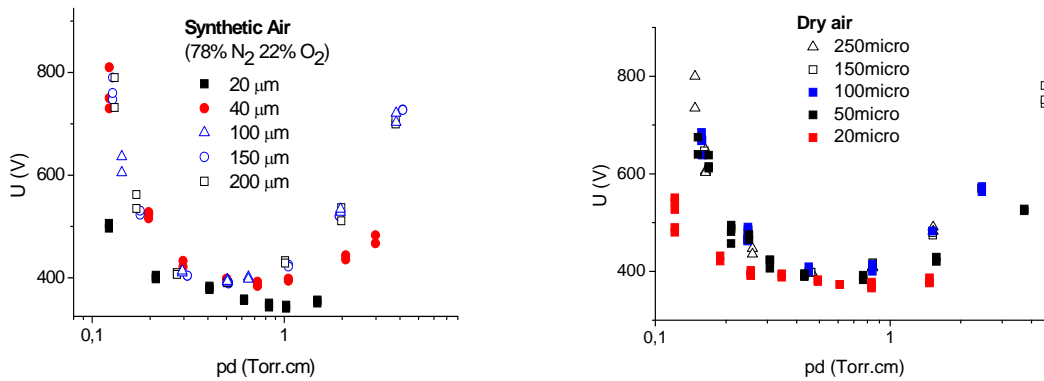


Fig. 4: Experimental Paschen curves for a) Synthetic Air and b) Dry Air at different electrode separation

The left site of the Paschen curve except Air is identical for all discharge gaps, however, the left site depends strongly on the electrode separation. With decreasing electrode separation the DC breakdown voltage is decreasing. We attribute this behaviour to field emission of the electrons from the cathode and to the low pressure. Under these conditions the electrons from cathode are able efficiently ionise the gas and develop discharge. In the Fig. 2a is Paschen curve for hydrogen compared with available data for copper electrodes at higher electrode distances. We suggest that differences between our data and Meek are due to experimental conditions (purity of gas, quality of electrodes, ...) and we suppose that differences between [10] and [11] (also present data) could be due to field emission and ion induced emission higher influence in Hydrogen of. This assumption will be verified with experiment at higher electrode distances. Similar behaviour in Paschen curve is also observed in Argon. Paschen curve for Oxygen is shown in the Fig. 2b. On the right site of the Paschen curve in  $O_2$  is characteristic bump which was also observed earlier by Meek [11]. This structure in the Paschen curve we tentatively associate with non dissociative electron attachment (three body) which is more efficient at high pressures and low reduced electric fields and is responsible for more efficient removal of the electrons under these conditions and thus for higher breakdown voltages. With increasing reduced electric field the capture of the electrons is less efficient and the breakdown voltage may decrease. [12]

The comparison of the Paschen curves for synthetic air, dry air and ambient air at one electrode separation is presented in the Figure 3b. The Paschen curve for ambient air shows some difference to the previous two on the left site of the curve. This difference is resulting from the humidity of the ambient air (approximately 50% at 20 °C). By comparing Paschen curves of synthetic air and dry air at electrode separations more than 100  $\mu\text{m}$  (Fig. 4) we can clearly see that they are very similar in the shape and values. This indicates that at these electrode separations the Paschen's law is valid and the breakdown voltage depends only on the  $p.d$ . However, at small electrode separations under 40  $\mu\text{m}$  are differences in air also at the right side of the Paschen curve. Usually the differences appear only on the left site of the Paschen curve and are related to the field emission and to ion assisted field emission of

the electrons. In order to describe the mentioned differences in Paschen curves at micrometer separations mathematically, we have proposed the generalized form of the Paschen's law and tested it on the case of Paschen curves for hydrogen.

Assuming the second Townsend coefficient  $\gamma$  to be a constant, the well-known Paschen's law [5] is not valid for breakdown mechanism in microdischarges. However, while  $\gamma$  is no more of constant value in microdischarge regime we can look for appropriate functional behavior of  $\gamma$  and apply it into the Paschen's law for breakdown voltage. While the secondary emission coefficient  $\gamma$  depends on the reduced electric field  $\gamma \sim f(E/p)$ , in general, we may assume the dependence of second Townsend coefficient  $\gamma$  on  $p.d$ . Using this assumption we can rewrite the Paschen's law into more general form:

$$U(A, B, a_1, \dots, a_n, pd) = \frac{B^k(pd)}{\left[ \ln \frac{A}{\ln(1/\gamma(a_1, \dots, a_n, pd) + 1)} + \ln(pd) \right]^k}, \quad (1)$$

where  $k$  is semiempirical factor equal to 1 resp. 2 for molecular gases resp. atomic gases [13,14],  $A$  and  $B$  are the coefficients associated with ionization coefficient  $\alpha$  and  $a_1, \dots, a_n$  is a set of parameters representing functional dependence of coefficient  $\gamma$  on  $pd$ . Without any physical constraints, we assumed the following dependence of the second Townsend coefficient on  $pd$ :

$$\gamma(pd) = a_1 + a_2 \cdot pd + a_3 \frac{\ln(pd)}{pd}, \quad (2)$$

where  $a_1$ ,  $a_2$  and  $a_3$  are arbitrary parameters. The parametric function for the second Townsend coefficient can be fitted using non linear least square fitting method to obtain the parameter values. We have tested the proposed functional dependence on the case of hydrogen for electrode separation equal or less than 100  $\mu\text{m}$  since for hydrogen the coefficients  $A$  and  $B$  are of constant values in the whole range of applied reduced electric field ( $A = 5.55 \text{ cm}^{-1}\text{Torr}^{-1}$ ,  $B = 140.05 \text{ Vcm}^{-1}\text{Torr}^{-1}$  [12]). The values of the second Townsend coefficient were obtained from experimental data using (1). The results are listed in Table 1.

Tab 1. Fitted parameter values for the parametric behavior of  $\gamma$  for hydrogen at 3 different electrode separations

| $d$ ( $\mu\text{m}$ ) | $a_1$               | $a_2$                | $a_3$                |
|-----------------------|---------------------|----------------------|----------------------|
| 20                    | $0.0373 \pm 0.0029$ | $-0.0031 \pm 0.0028$ | $-0.0586 \pm 0.0007$ |
| 40                    | $0.0349 \pm 0.0012$ | $-0.0023 \pm 0.0008$ | $-0.0558 \pm 0.0005$ |
| 100                   | $0.0352 \pm 0.0006$ | $-0.0043 \pm 0.0003$ | $-0.0470 \pm 0.0006$ |

Using the parametric function (2) for  $\gamma$  with fitted values listed in Table 1 we can plot generalized Paschen curves using the equation (1). The results depicted in Fig. 5 show a good agreement between the experimental Paschen curve and the new, proposed one. The generalized Paschen's law (1) is valid for hydrogen breakdown voltage dependence on  $pd$  at micrometer separations assuming the suggested functional behavior of the second Townsend coefficient (2). Nevertheless, the new form of Paschen's law should be verified for breakdown in other gases, which will be done in the future.

Principally, having the measured Paschen curves, one can fit experimental data directly by using (1) to obtain  $\gamma(p.d)$  which can be further transformed to  $\gamma(E/p)$  (by applying  $E/p = U/pd$ ). However, fitting process in this case can be a tricky thing while, mathematically speaking, breakdown voltage  $U$  is a singular function of  $pd$  and, moreover, dependent on a number of parameters.

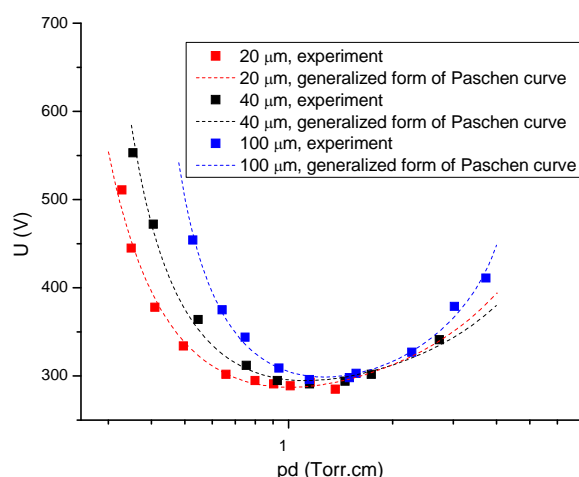


Fig. 5. Experimental Paschen curves for hydrogen at 3 different electrode separations compared to a new, generalized form of Paschen's law assuming the parametric dependence of  $\gamma$  on  $pd$ .

### Conclusions

We have measured DC breakdown curves for Argon, Hydrogen and Oxygen, ambient, dry and synthetic air at micrometer separation of Copper electrodes. The experiment confirmed the validity of the Paschen law for electrode separations greater than 100  $\mu\text{m}$ . For smaller electrode separation departures from Paschen law were observed in the left site of the Paschen curve mainly due to field emission and ion enhanced field emission from the cathode. In the case of air for electrode separations below 100  $\mu\text{m}$  departure from the Paschen law occurs also on the right site of the Paschen curve. A new generalized form of Paschen's law have been suggested and tested to describe the departures from Paschen's law for electrode separations below 100  $\mu\text{m}$ .

### Acknowledgements

This work have been supported by the Slovak Research and Development Agency, project Nr. APVV – 0365-07, VEGA projects Nr.: 1/0379/11, 1/0559/09 and Comenius University Project Nr. UK 456/2010 FMFI

### References

- [1] K. Becker, K.H. Schoenbach and J G Eden, *J. Phys. D: Appl. Phys.* 39 (2008) R55
- [2] K. Becker, U. Kogelschatz, *Non-equilibrium air plasmas at atmospheric pressure* CRC Press, 2004
- [3] F. Iza G. Kim J Lee S M Lee J K Walsh J L Zhang Y T and M G Kong, *Microplasmas: Sources, Particle Kinetics, and Biomedical Applications* Plasma Process. Polym. 5 (2008) 322
- [4] Z. Petrovic, *J. Phys. D: Appl. Phys.* 41 (2008) 194002
- [5] F. Paschen, *Annalen der Physik*, 273 (1889) (5)
- [6] W. S. Boyle and P. Kisliuk, *Phys. Review*, 97(2) (1955) 255
- [7] W. S Boyle and L.H. Germer, *J. Appl. Phys.*, 26, (1955) 571
- [8] D. Go, *J. Appl. Phys.*, (2010) 107, 103303
- [9] R. S. Dhariwal, *Sci. Meas. Technology*, (2000) Vol 147, 5
- [10] Lieberman, *Principles of Plasma Discharges and Materials Processing*, 2005
- [11] Meek, *Electrical Breakdown of Gases*, 1953
- [12] D. J. Rose, *Phys. Rev.*, 104, (1956) 273–277
- [13] M. Sato, *Interpretation of argon breakdown in dc and microwave fields* Bull. Yamagata Univ.(Eng., Vol. 25, No. 2, (1999) 119-125
- [14] A. L. Ward, *J. Appl. Phys.*, 33 (1962) 2789

# Secondary electrons in dual-frequency capacitively coupled radio frequency discharges

J. Schulze<sup>1,2</sup>, Z. Donkó<sup>1</sup>, E. Schüngerl<sup>2</sup>, U. Czarnetzki<sup>2</sup>

<sup>1</sup> Research Institute for Solid State Physics and Optics of the Hungarian Academy for Sciences, Hungary

<sup>2</sup> Institute for Plasma and Atomic Physics, Ruhr-University Bochum, Germany

e-mail: fjschulze@hotmail.com

## Abstract

Two fundamentally different types of dual-frequency (df) capacitive radio frequency discharges can be used for plasma processing applications to realize separate control of the ion mean energy,  $\langle E_i \rangle$ , and flux,  $\Gamma_i$ , at the substrate surface: (i) Classical discharges operated at substantially different frequencies, where the low and high frequency voltage amplitudes,  $\phi_{lf}$  and  $\phi_{hf}$ , are used to control  $\langle E_i \rangle$  and  $\Gamma_i$ , respectively. (ii) Electrically asymmetric (EA) discharges operated at a fundamental frequency and its second harmonic with fixed, but adjustable phase shift between the driving frequencies,  $\theta$ , which is used to control  $\langle E_i \rangle$ . Here, we systematically study the effect of secondary electrons on the ionization dynamics and the quality of this separate control in both discharge types by Particle in Cell simulations complemented with Monte Carlo description of collisions (PIC/MCC) in argon at different neutral gas pressures. We focus on the effect of the control parameter for  $\langle E_i \rangle$  on  $\Gamma_i$  for different secondary yields,  $\gamma$ . We find a dramatic effect of tuning  $\phi_{lf}$  in classical df discharges and almost no effect of tuning  $\theta$  in EA discharges. This is caused by a heating mode transition from  $\alpha$ - to  $\gamma$ -mode, which is induced by changing  $\phi_{lf}$  in classical DF discharges and not induced by changing  $\theta$  in EA discharges. Thus, the quality of the separate control of ion energy and flux is generally better in EA compared to classical DF discharges.

**Keywords:** Electrical Asymmetry Effect, capacitive RF discharge, secondary electrons, ion energy, ion flux.

## Introduction

Two different types of df capacitive radio frequency discharges can be used for plasma processing applications to separately control  $\langle E_i \rangle$  and  $\Gamma_i$  at the substrate surface: In classical df discharges one electrode is driven by the sum of two sinusoidal voltage waveforms with substantially different frequencies:

$$\tilde{\phi}(t) = \phi_{lf} \cos(\omega_{lf} t) + \phi_{hf} \cos(\omega_{hf} t) \quad \omega_{hf} \gg \omega_{lf} \quad \phi_{lf} \gg \phi_{hf} \quad (1)$$

Here,  $t$  is time and, typically,  $\omega_{hf} = 2\pi \cdot 27$  MHz and  $\omega_{lf} = \omega_{hf}/14$ . In such discharges  $\phi_{lf}$  is used as the control parameter for  $\langle E_i \rangle$  and should not affect  $\Gamma_i$ , while  $\phi_{hf}$  is used to control  $\Gamma_i$  without affecting  $\langle E_i \rangle$  [1]. Recent investigations, however, have shown that this concept is limited by the frequency coupling [2,3]. The effect of secondary electrons has not been investigated systematically yet.

Recently, a novel type of electrically asymmetric df discharges driven at two consecutive harmonics with fixed, but adjustable phase shift between the driving harmonics,  $\theta$ , was proposed:

$$\tilde{\phi}(t) = \phi_{lf} \cos(\omega_{lf} t + \theta) + \phi_{hf} \cos(2\omega_{lf} t) \quad (2)$$

Typically,  $\omega_{lf} = 2\pi \cdot 13.56$  MHz in these EA discharges. The concept to control  $\langle E_i \rangle$  separately from  $\Gamma_i$  is fundamentally different compared to classical df discharges: Via the Electrical Asymmetry Effect (EAE) [4-7] a variable DC self bias is generated as an almost linear function of  $\theta$ , which is used as the control parameter for  $\langle E_i \rangle$  at fixed voltage amplitudes. In this way any frequency coupling is avoided. Here, we systematically study the effect of secondary electrons on the ionization dynamics and the quality of this separate control in both discharge types by PIC/MCC simulations in argon at different neutral gas pressures. We focus on the effect of the control parameter for  $\langle E_i \rangle$  on  $\Gamma_i$  for different values of  $\gamma$ .

## Results

Fig. 1 shows  $\langle E_i \rangle$  and  $\Gamma_i$  at the grounded electrode in an argon discharge at 20 Pa as a function of

the control parameter for  $\langle E_i \rangle$ , i.e.  $\phi_{lf}$  and  $\theta$  in classical and electrically asymmetric df discharges, respectively, for different values of  $\gamma$  in both discharge types. The classical discharge is operated at 1.937 MHz+ 27.12 MHz

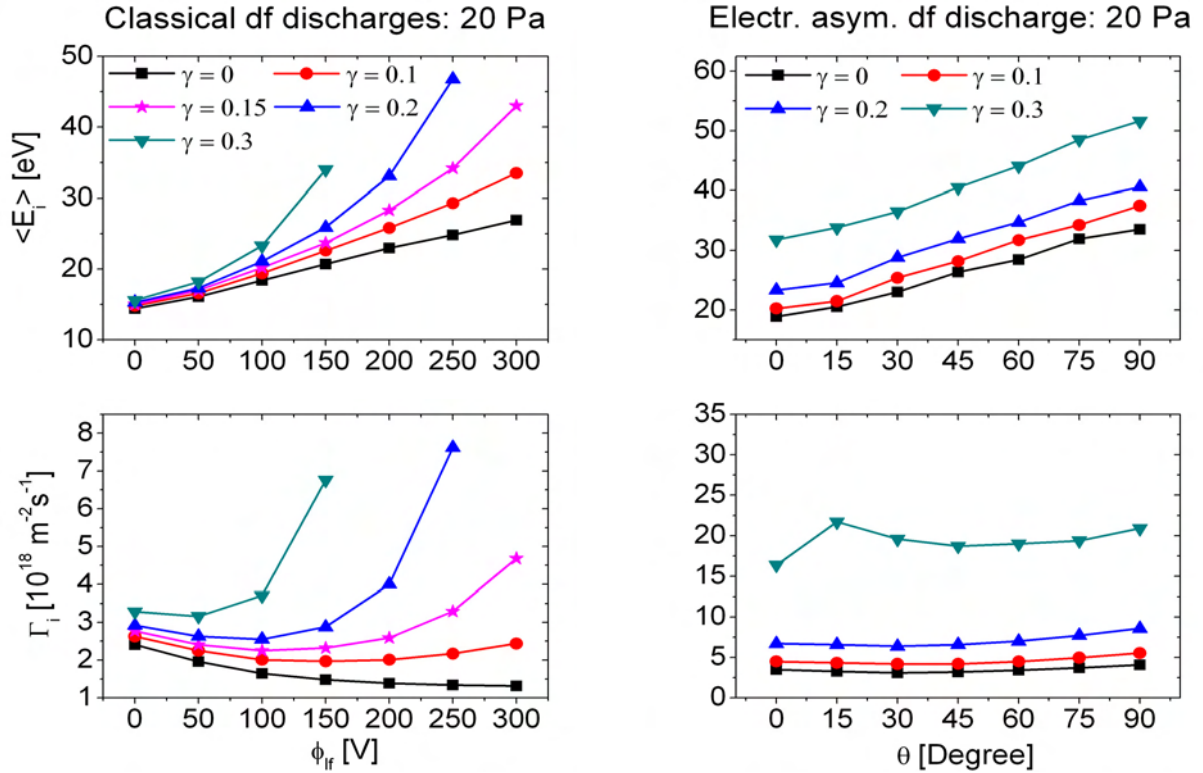


Fig. 1. Mean ion energy and ion flux at the grounded electrode as a function of the control parameter for the mean ion energy in an argon discharge operated at 20 Pa for different values of  $\gamma$  (PIC simulation results). The electrode gap is 2.5 cm. Left column: Classical df discharge ( $\omega_{hf} = 2\pi \cdot 27.12$  MHz,  $\omega_{lf} = \omega_{hf}/14$ ,  $\phi_{lf} = 100$  V). Right column: Electrically asymmetric df discharge ( $\omega_{hf} = 2\pi \cdot 27.12$  MHz,  $\omega_{lf} = \omega_{hf}/2$ ,  $\phi_{lf} = \phi_{hf} = 150$  V).

and  $\phi_{hf}$  is kept constant at 100 V, while the EA discharge is driven by 13.56 MHz + 27.12 MHz and both harmonics' amplitudes are kept constant at 150 V.

In classical df discharges the control parameter for  $\langle E_i \rangle$  is found to strongly affect  $\Gamma_i$  under most discharge conditions [8]. For  $\gamma = 0$ ,  $\Gamma_i$  decreases as a function of  $\phi_{lf}$  due to the frequency coupling. For  $\gamma > 0.1$ ,  $\Gamma_i$  is found to increase dramatically due to a mode transition from  $\alpha$ - to  $\gamma$ -mode induced by the control parameter for the mean ion energy. These simulation results confirm experiments of *Booth et al.* [9]. Only within a rather narrow process window the effects of the frequency coupling and secondary electrons compensate and  $\Gamma_i$  is approximately constant as a function of  $\phi_{lf}$ . However, generally separate control of ion energy and flux is not possible in classical df discharges.

In electrically asymmetric discharges the quality of this separate control is much better. Even for high values of  $\gamma$  the control parameter for the mean ion energy,  $\theta$ , does not significantly affect the ion flux under most discharge conditions due to the fundamentally different concept to control  $\langle E_i \rangle$ . As the voltage amplitudes are kept constant, no heating mode transition is induced by the control parameter for  $\langle E_i \rangle$ .

In conclusion, electrically asymmetric allow a better separate control of ion energy and flux than classical df discharges under most discharge condition, particularly if secondary electrons play an important role.

Funding by the Alexander von Humboldt foundation, the Ruhr-University Research Department Plasma, and the Hungarian Scientific Research Fund through grant OTKA-K-77653.

## References

- [1] P. C. Boyle, A. R. Ellingboe, M. M. Turner, *Plasma Sourc. Sci. Technol.* (2004) 13 493

- [2] T. Gans et al., *Appl. Phys. Lett.* (2006) 89 261502.
- [3] J. Schulze, Z. Donkó, D. Luggenhölscher, U. Czarnetzki, *Plasma Sourc. Sci. Technol* (2009) 18 034011
- [4] B. G. Heil, J. Schulze, T. Mussenbrock, R. P. Brinkmann, U. Czarnetzki, *Trans. on Plasma Sci.* (2008) 36 1404
- [5] B. G. Heil, U. Czarnetzki, R. P. Brinkmann, T. Mussenbrock, *J. Phys. D* (2008) 41 165202
- [6] Z. Donkó, J. Schulze, B. G. Heil, U. Czarnetzki, *J. Phys. D* (2009) 42 025205
- [7] J. Schulze, E. Schüngel, U. Czarnetzki, *J. Phys. D FTC* (2009) 42 092005
- [8] Z. Donkó, J. Schulze, P. Hartmann, I. Korolov, U. Czarnetzki, E. Schüngel, *Appl. Phys. Lett.* (2010) 97 082501
- [9] J. P. Booth, G. Curley, D. Marić, P. Chabert, *Plasma Sourc. Sci. Technol.* (2010) 19 015005

# The Electrical Asymmetry Effect in multi-frequency capacitively coupled radio frequency discharges

J. Schulze<sup>1,2</sup>, Z. Donkó<sup>1</sup>, E. Schüngel<sup>2</sup>, U. Czarnetzki<sup>2</sup>

<sup>1</sup> Research Institute for Solid State Physics and Optics of the Hungarian Academy for Sciences, Hungary

<sup>2</sup> Institute for Plasma and Atomic Physics, Ruhr-University Bochum, Germany

e-mail: fjschulze@hotmail.com

## Abstract

The Electrical Asymmetry Effect (EAE) in geometrically symmetric capacitive radio frequency discharges operated at multiple consecutive harmonics is investigated by a Particle in Cell simulation incorporating Monte Carlo collisions (PIC/MCC) and an analytical model. Compared to electrically asymmetric dual-frequency discharges operated at two consecutive harmonics with adjustable phase shift between the driving frequencies, we find that (i) a stronger DC self bias can be generated electrically and that (ii) the mean ion energies at the electrodes can be controlled separately from the ion flux over a broader range by tuning the phase shifts between the individual voltage harmonics. A recipe to optimize the applied voltage waveform to generate the strongest self bias and to obtain maximum control of the ion energy via the EAE is presented.

**Keywords:** Electrical Asymmetry Effect, capacitive RF discharge, ion energy, ion flux, DC self bias.

## Introduction

Dual-frequency (df) capacitively coupled radio frequency (CCRF) discharges are frequently used for various applications of plasma processing to realize separate control of the mean ion energy,  $\langle E_i \rangle$ , and the ion flux,  $\Gamma_i$ , at the electrode surfaces. The concept to realize this separate control in classical df discharges operated at substantially different frequencies is strongly limited due to the frequency coupling [1-3] and the effect of secondary electrons [2-4]. Therefore, recently a novel type of df discharge operated at two consecutive harmonics with fixed, but adjustable phase shift,  $\theta_1$ , was proposed [5-9]. In these discharges the EAE allows to generate a DC self bias,  $\eta$ , as an almost linear function of  $\theta_1$ , which can be used to control  $\langle E_i \rangle$  without affecting  $\Gamma_i$  [7,8]. Here, we extend the investigations of the EAE from dual- to multi-frequency discharges driven by a series of  $k$  consecutive voltage harmonics to enhance the range of electrical ion energy control (separately from the ion flux) [9]. The following voltage waveform is applied to one electrode:

$$\tilde{\phi}^{(k)}(t) = \sum_{n=1}^k \tilde{\phi}_n^{(k)} \cos(2\pi nft + \theta_n) \quad (1)$$

Here,  $\tilde{\phi}_n^{(k)}$  is the amplitude of the  $n$ -th of  $k$  driving harmonics,  $f = 13.56$  MHz is the fundamental driving frequency,  $t$  is time, and  $\theta_n$  is the adjustable phase shift of the  $n$ -th harmonic. We study  $\eta$ ,  $\langle E_i \rangle$ , and  $\Gamma_i$  as a function of  $\theta_n$  for different  $k$  and neutral gas pressures in argon by a PIC simulation and compare the results for  $\eta$  with an extended version of the analytical EAE model [6]. Based on the voltage balance in the frame of a global model of CCRF discharges this extended model yields the following expression for  $\eta$  [9]:

$$\eta = -\frac{\tilde{\phi}_{m1}^{(k)} + \varepsilon \tilde{\phi}_{m2}^{(k)}}{1 + \varepsilon} + \frac{\phi_{sp}^{(f)} + \varepsilon \phi_{sg}^{(f)}}{1 + \varepsilon} + \frac{1 - \varepsilon}{1 + \varepsilon} \phi_b \quad (2)$$

Here  $\tilde{\phi}_{m1}^{(k)}$ ,  $\tilde{\phi}_{m2}^{(k)}$  is the maximum and minimum of the applied voltage waveform,  $\phi_{sp}^{(f)}$ ,  $\phi_{sg}^{(f)}$  is the floating potential at the powered and grounded electrode,  $\phi_b$  is the bulk voltage, and  $\varepsilon$  is the symmetry parameter defined as the absolute value of the ratio of the maximum sheath voltages at both electrodes. Compared to df discharges we find, that a significantly stronger variable DC self bias can be generated and  $\langle E_i \rangle$  can be tuned separately from  $\Gamma_i$  over a broader range in electrically asymmetric multi-frequency discharges.

## Results

Fig. 1 (left) shows the driving voltage waveform normalized by the sum of the harmonics' amplitudes time resolved within one period of the fundamental frequency for different  $k$  ( $\theta_n = 0^\circ$  for all  $n$ ). The harmonics' amplitudes are chosen according to the following criterion to yield the strongest  $\eta$ :

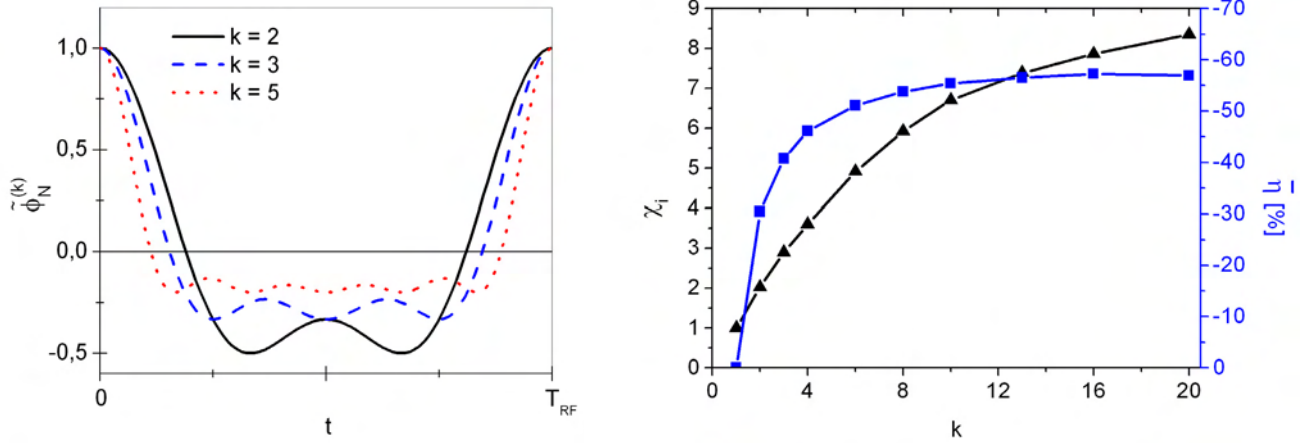


Fig. 1. Left: Normalized driving voltage waveform [equation (1)] with optimized harmonics' amplitudes [equation (3)] for different  $k$ . Right: Ion energy control factor,  $\chi_i$ , and normalized DC self bias ( $\theta_n = 0^\circ$  for all  $n$ ) as a function of  $k$

$$\sum_{n=1}^k \tilde{\phi}_n^{(k)} = 300V$$

(PIC simulation results) in an argon discharge at 10 Pa, optimized harmonics' amplitudes and

$$\tilde{\phi}_n^{(k)} = \phi_0 \frac{k-n+1}{k} \quad (3)$$

Here,  $\phi_0$  is a constant voltage, that determines the plasma density and the ion flux. By adding additional consecutive harmonics the difference between the absolute values of the global extrema of the driving voltage waveform is increased and, thus [equation (2)], a stronger DC self bias is generated. This waveform is similar to the one used by by *Patterson et al.* in hybrid discharges [10]. The right plot of figure 1 shows  $\eta$  normalized by the sum of the harmonics' amplitudes as a function of  $k$  ( $\theta_n = 0^\circ$  for all  $n$ ) resulting from simulations of an argon discharge operated at 10 Pa and optimized harmonics' amplitudes. The sum of the harmonics' amplitudes is kept constant at 300 V. The electrical bias generation is strongly enhanced from about 30 % of the total applied voltage amplitude at  $k=2$  to almost 60 % for  $k > 10$  by adding further consecutive harmonics. These simulation results are reproduced well by the extended EAE model using the floating potentials, bulk voltage, and symmetry parameter from the simulation. By adjusting only the even phase shifts  $\theta_n$  the bias can be tuned from its minimum,  $\eta_{\min}$  (shown in figure 1), to its maximum,  $\eta_{\max} = -\eta_{\min}$ . The factor,  $\chi_i$ , by which  $\langle E_i \rangle$  can be changed via the EAE is strongly increased from about 2 at  $k=2$  to almost 9 at  $k=20$  by adding further consecutive harmonics (right plot of figure 1), while the ion flux remains approximately constant as a function of the phase shifts  $\theta_n$ . This enhancement of the range of ion energy control (separately from the ion flux) by customizing the driving voltage waveform to optimize the EAE is expected to be most relevant for various applications and has already been used successfully to optimize Plasma Enhanced Chemical Vapor Deposition of nc-Si:H for the production of solar cells [11].

## Conclusions

Based on PIC simulation and model results we have demonstrated, that adding further consecutive harmonics with optimized individual amplitudes to the driving voltage waveform strongly enhances the electrical generation of a variable DC self bias and the range of ion energy control (separately from the ion flux) via the EAE in multi- compared to dual-frequency capacitively coupled radio frequency discharges.

Funding by the Alexander von Humboldt foundation, the Ruhr-University Research Department Plasma, and the Hungarian Scientific Research Fund through grant OTKA-K-77653.

## References

- [1] T. Gans et al., *Appl. Phys. Lett.* (2006) 89 261502.
- [2] J. Schulze, Z. Donkó, D. Luggenhölscher, U. Czarnetzki, *Plasma Sourc. Sci. Technol* (2009) 18 034011
- [3] Z. Donkó, J. Schulze, P. Hartmann, I. Korolov, U. Czarnetzki, E. Schüngel, *Appl. Phys. Lett.* (2010) 97 082501
- [4] J. P. Booth, G. Curley, D. Marić, P. Chabert, *Plasma Sourc. Sci. Technol.* (2010) 19 015005
- [5] B. G. Heil, J. Schulze, T. Mussenbrock, R. P. Brinkmann, U. Czarnetzki, *Trans. on Plasma Sci.* (2008) 36 1404
- [6] B. G. Heil, U. Czarnetzki, R. P. Brinkmann, T. Mussenbrock, *J. Phys. D* (2008) 41 165202
- [7] Z. Donkó, J. Schulze, B. G. Heil, U. Czarnetzki, *J. Phys. D* (2009) 42 025205
- [8] J. Schulze, E. Schüngel, U. Czarnetzki, *J. Phys. D FTC* (2009) 42 092005
- [9] J. Schulze, E. Schüngel, Z. Donkó, U. Czarnetzki, *Plasma Sourc. Sci. Technol.* (2010) accepted for publication
- [10] M. M. Patterson, H. Y. Chu, A. E. Wendt, *Plasma Sourc. Sci. Technol.* (2007) 16 257
- [11] E. V. Johnson, T. Verbeke, J. C. Vanel, J. P. Booth, *J. Phys. D FTC* (2010) 43 412001

# Comparison of modeling approaches for the cathode region of DC glow discharges

A. Derzsi<sup>1</sup>, I. Korolov<sup>1</sup>, Z. Donkó<sup>1</sup>, P. Hartmann<sup>1</sup>, J. Karácsony<sup>2</sup>, G. Bánó<sup>3</sup>

<sup>1</sup>Research Institute for Solid State Physics and Optics of the Hungarian Academy of Sciences, H-1525 Budapest, POB 49, Hungary

<sup>2</sup>Babeş-Bolyai University, 400084 Cluj-Napoca, M. Kogalniceanu 1, Romania

<sup>3</sup>Department of Biophysics, P. J. Šafarik Univ. Košice, 04001 Jesenna 5, Košice,

e-mail: derzsi@mail.kfki.hu

## Abstract

Widely used modeling approaches for the description of the cathode region of cold cathode low-pressure DC glow discharges are investigated. Simulation results provided by models known in the literature as fluid models and hybrid models are critically compared to each other for a reference set of discharge conditions. Further check of the simulation results is realized by comparison with experimental data on electron density obtained by Langmuir probe measurements in abnormal Ar glow discharges. We find that the electron densities calculated from the fluid models are far below the experimental values even if the electron energy equation is considered in the calculations. This weakness of fluid models points out the importance of an accurate calculation of the ionization source term, which can only be accomplished by a kinetic approach. In hybrid models Monte Carlo (MC) simulation is used for this purpose, and this approach gives electron densities consistent with our experimental data.

**Keywords:** low-pressure glow discharge, discharge modeling, hybrid model

## Introduction

The accurate mathematical description of low-temperature discharge plasmas has been motivated both by the advance of applications of discharges and by the wish of understanding the rich physics of these systems. The key element of these models is the description of the motion and of the collision processes of the charged particles: electrons and ions. In fluid models both of these types of particles are treated as continuum and are described by a truncated set of moment equations of the Boltzmann equation (BE). The ‘simple’ fluid models consider the first two moments (expressing particle and momentum conservation) by including a pair of continuity equations and a pair of momentum balance equations, for electrons and ions, as well as the Poisson equation. The non-local transport of electrons [1,2] can to some extent be incorporated in ‘extended’ fluid models by including an additional equation for the electron mean energy (the third moment of the BE) in the calculations. As an alternative, particle-based simulations can also be used, which are able to capture the highly non-local character of the electrons’ motion in the cathode region. Such methods, can be, however, computationally very demanding.

The advantages of fluid models (efficiency) and of particle treatment (accuracy) can be jointly utilized in hybrid models [3], in which slow plasma species are treated within the frame of a fluid model, while fast species are treated as particles [4-7]. Although one needs to be aware of their limitations [8], hybrid models have been quite successful in describing a wide range of discharge physics phenomena and in providing deep insight into the operation of different sources [9-16].

One expects that modeling calculations reproduce to certain extent the electrical characteristics of the discharges and the density of the charged species. The verification of the models has been neglected in the majority of works present in the literature: in many cases no comparison with experimental data and/or with the results obtained by different modeling approaches was carried out. Most of the papers in the literature present calculations for different sets of discharge conditions and different electrode configurations, thus it is impossible to deduce the effects of different assumptions incorporated into the models: choice of boundary conditions of the fluid equations, assumptions concerning the transport coefficients, expressions for the ionization source function, and the choice of the secondary emission coefficient. This could be achieved by considering “standard” sets of discharge conditions (pressure, voltage, electrode separation) and a simple discharge geometry.

A study of the performance of various modeling approaches and the effect of different assumptions is shown in the present work. Simulation codes based on different types of models are developed and calculations for common sets of input data are carried out addressing the following questions: (1) to what extent is the accuracy of the fluid models improved by incorporating the balance equation for electron energy, (2) what is the effect of the form of ionization source function on the calculated discharge characteristics, (3) how well fluid modeling calculations approximate the experimental results?

## Results and discussion

We present here one-dimensional fluid modeling calculations for the cathode region of an argon glow discharge both incorporating and disregarding electron energy balance calculation. We also test the effect of the choice of the ionization source term in fluid models. Calculations are also executed with a hybrid approach. The simulation results and experimental data obtained from Langmuir probe measurements of electron density are compared.

In the case of fluid models the calculation of the ionization source function is based on the electron flux or the electron density [17]. In simple fluid models the ‘flux-based source’ calculation uses Townsend’s first ionization coefficient  $\alpha$ , as a function of the local reduced electric field:  $S(x) = \alpha[E(x)/n]|\Phi_e(x)|$ , where  $\Phi_e$  is the electron flux and  $n$  is the gas density. In the extended fluid model  $\alpha$  as a function of the electron mean energy  $\bar{\epsilon}$  is used and the source function is calculated as  $S(x) = \alpha[\bar{\epsilon}(x)]|\Phi_e(x)|$ . The approach based on the electron density,  $n_e$ , uses a rate coefficient  $k_i$ , which depends on the electron mean energy:  $S(x) = k_i[\bar{\epsilon}(x)]n_e(x)N$ . This expression is called here a ‘rate coefficient-based source’ calculation. In hybrid models the source function is directly calculated from the Monte Carlo simulation of the fast electrons, for the actual field distribution in the cathode region.

Regarding the transport coefficients, for positive ions a mobility coefficient  $\mu_i$  depending on the reduced electric field  $E/N$ , is used both in fluid and hybrid models. The diffusion coefficient of positive ions is taken as  $D_i/\mu_i = ekT_i$ , where  $k$  is the Boltzmann constant and  $kT_i$  is the characteristic energy of ions (assumed to be equal to the gas temperature  $T_g$ ). For electrons, in simple fluid models and in hybrid models constant values are used for  $\mu_e$  and  $D_e$ . The mobility coefficient has an experimental value, and constant characteristic energy values between  $kT_e = 0.1$  eV and 1 eV are used to obtain the diffusion coefficient  $D_e$ , via the relation  $D_e/\mu_e = ekT_e$ . The transport coefficients of the electrons and electron energy—used in the extended fluid model—have been obtained as a function of mean energy, via MC swarm simulations.

Figure 1 shows some of the discharge characteristics obtained using the different modeling approaches, for a set of reference conditions:  $p = 40$  Pa (argon),  $V = 441$  V,  $T_g = 300$  K,  $L = 3$  cm,  $\gamma = 0.033$ . The results of the simple fluid and hybrid models are shown for bulk electron temperature values  $kT_e = 0.1$  eV and 1 eV, as well as for 0.28 eV value determined by Langmuir probe measurements for this set of discharge conditions [18].

Figure 1(a) compares the electric field distributions resulting from the different models. The extended fluid model and the hybrid model predict a reversal of the electric field in the negative glow region. The simple fluid model cannot account for the field reversal, as it does not capture the non-local character of electron transport to any extent. The hybrid model results in a significantly shorter cathode sheath length (and consequently, an approximately factor of two stronger electric field at the cathode), compared with the fluid models, due to the enhanced ionization rate.

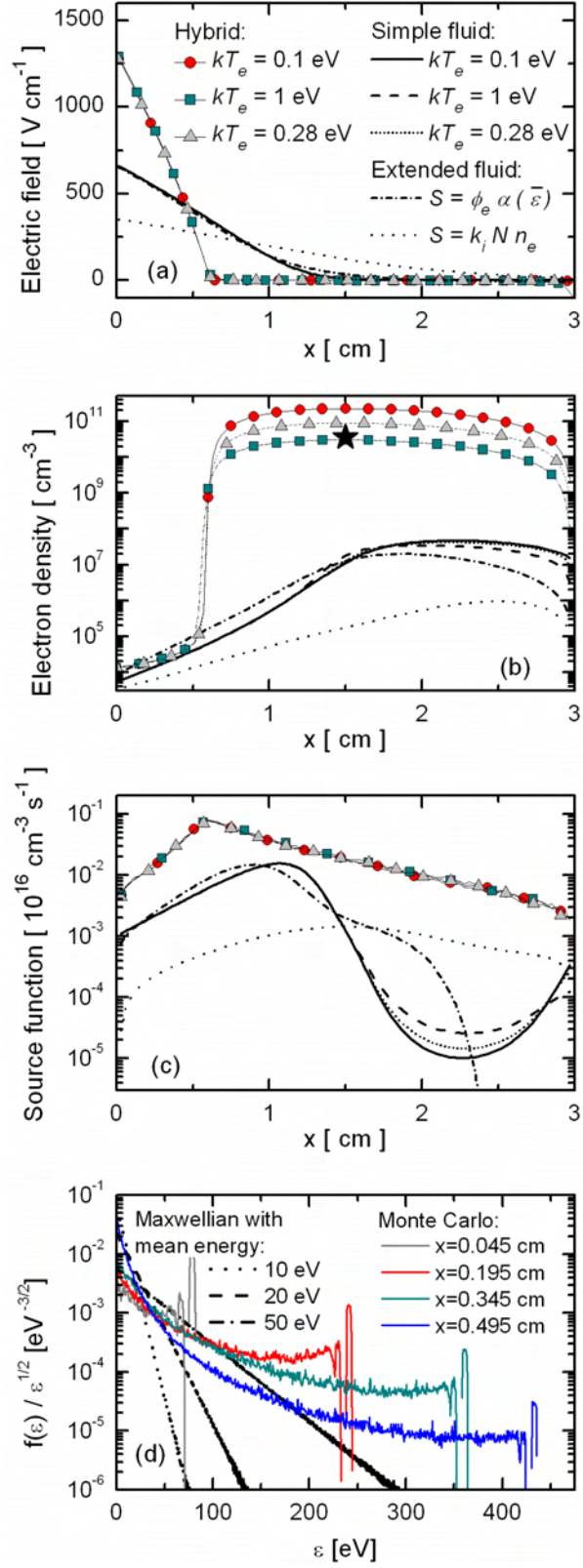


Fig. 1. Results obtained by the different modeling approaches for  $p = 40$  Pa,  $V = 441$  V,  $T_g = 300$  K,  $L = 3$  cm,  $\gamma = 0.033$ . (a) Electric field distributions, (b) electron density distributions and (c) ionization source functions. The symbol in (b) shows the density determined by Langmuir probe measurement [18]. The legend shown in (a) applies to panels (b) and (c), as well. (d) The distribution function of electrons at several places in the cathode sheath and Maxwellian distribution functions with specified mean energy values.

The calculated electron density distributions are plotted in figure 1(b). The peak of the electron density obtained from the different fluid models scatters approximately between  $10^6 \text{ cm}^{-3}$  and  $5 \times 10^7 \text{ cm}^{-3}$ . The hybrid models, in contrast to these values, predict densities in the range  $3 \times 10^{10} - 2 \times 10^{11} \text{ cm}^{-3}$ , depending on the bulk electron temperature assumed. Using the experimentally determined,  $kT_e = 0.28 \text{ eV}$ , the hybrid model gives an electron density value consistent with the experiment.

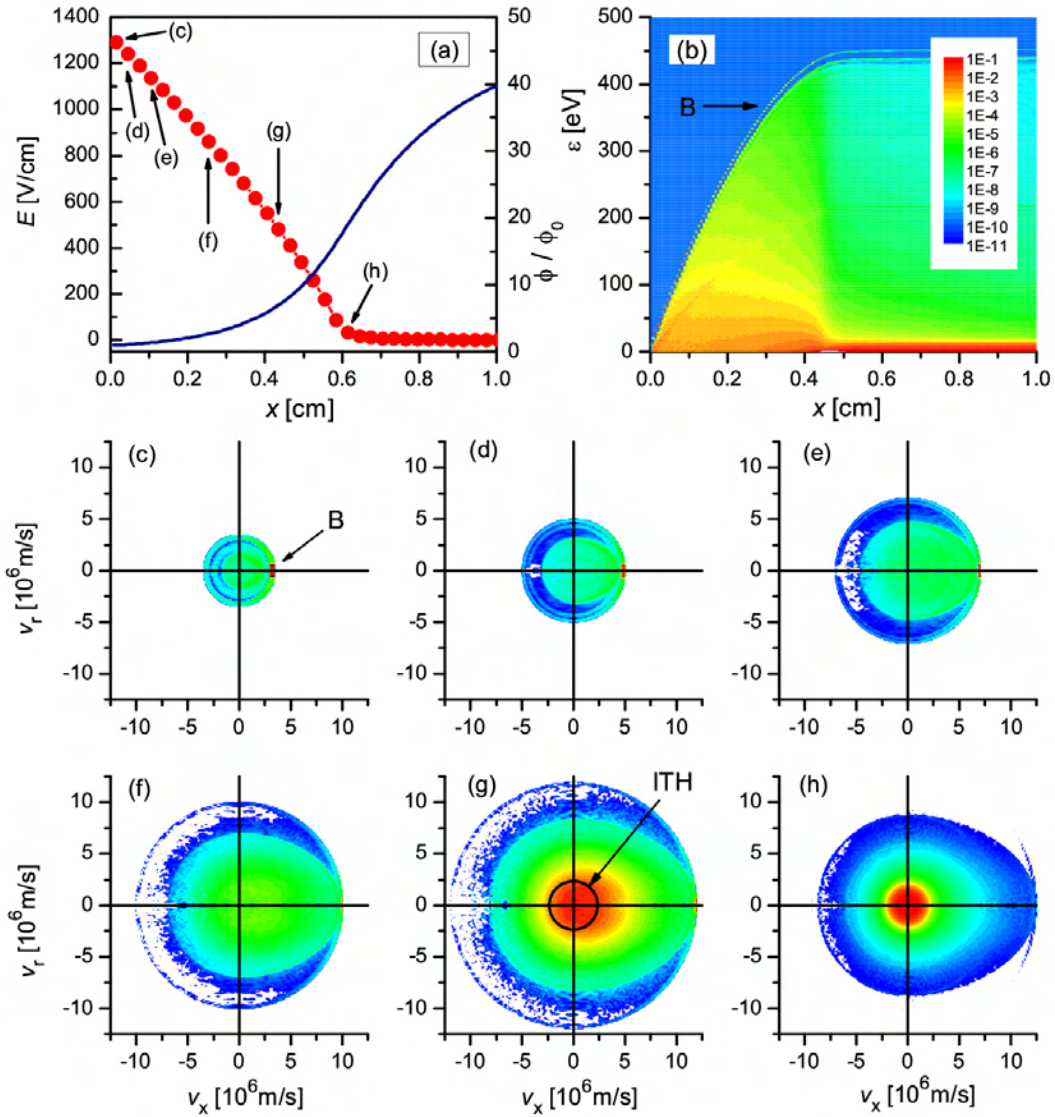


Fig. 2. Characteristics of the cathode fall region of a DC discharge in argon for  $p = 40 \text{ Pa}$ ,  $V = 441 \text{ V}$ . (a) Electric field distribution (circles, left scale) and the flux of electrons normalized to the flux at the cathode (line, right scale). (b) Color map representation of the spatial variation of the electron distribution function. (c)–(h) VDF-s of electrons at different spatial positions, between the cathode and the sheath–glow boundary, defined in panel (a); the color scale of the VDF-s is logarithmic and spans four orders of magnitude. “B” in (b) and (c) indicates a beam of electrons propagating away from the cathode. The circle labeled as “ITH” in (g) shows the velocity corresponding to the ionization threshold.

The ionization source functions are compared in figure 1(c). The different fluid models predict quite different magnitudes and shapes for  $S(x)$ . It is only the hybrid model, which traces the fast electrons by MC simulation that produces an exponential fall-off of the ionization source term past the sheath–glow boundary. As the ionization and excitation cross sections have similar forms and both processes are primarily driven by fast electrons, it is reasonable to assume that the spatial distribution of the excitation rate exhibits the same behavior as the ionization rate. The light intensity in the negative glow is known to decrease exponentially, see, e.g. [19,20], such behavior is predicted by the hybrid model only.

In Figure 2 results for the electron transport through the cathode sheath are presented for the same reference conditions as in Figure 1, including the spatial evolution of the electron velocity distribution function (VDF).

## Conclusions

This work intended to critically compare different modeling approaches applicable for the description of the cathode region of low-pressure DC glow discharges. The electron densities obtained from the different models have scattered over several orders of magnitude, the best agreement with experimental data has been found using the hybrid model. The different fluid approaches, assuming different forms for the ionization source term, underestimated the electron density in the negative glow by three or more orders of magnitude. More accurate results can be obtained from hybrid models than from fluid models, especially if the temperature of bulk electrons can be determined experimentally. The hybrid approach has also been found superior over fluid models in predicting the electrical characteristics of the discharges and the spatial distribution of processes driven by highly energetic electrons. The improvements of the accuracy of fluid models by incorporating the electron energy balance equation (compared to those which neglect it) have proven to be marginal. Thus predictions of fluid models of the cathode region of glow discharges have to be treated with reservations.

## Acknowledgment

This work has been supported by the Hungarian Scientific Research Fund (OTKA-K77653), and by the GLADNET FP6 MRTN-CT-035459 project.

## References

- [1] Tsendin L D 1995 Plasma Sources Sci. Technol. 4 200; 2009 Plasma Sources Sci. Technol. 18 014020
- [2] Kudryavtsev A A, Morin A V and Tsendin L D 2008 Tech. Phys. 53 1029
- [3] Surendra M, Graves D B, Jellum G M 1990 Phys. Rev. A 41 1112
- [4] Boeuf J-P and Pitchford L C 1991 IEEE Trans. Plasma Sci. 19 286
- [5] Bogaerts A, Gijbels R, Goedheer W J 1996 Anal. Chem. 68 2296
- [6] Donkó Z 2001 Phys. Rev. E 64 026401
- [7] Brok W J M, Wagenaars E, van Dijk J, van der Mullen J J A 2007 IEEE Transactions on Plasma Science 35 1325
- [8] Donkó Z, Hartmann P and Kutasi 2006 Plasma Sources Sci. Technol. 15 178
- [9] Revel I, Pitchford L C and Boeuf J-P 2000 J. Appl. Phys. 88 2234
- [10] Donkó Z 2000 J. Appl. Phys. 88 2226
- [11] Bogaerts A and Gijbels R 1997 Spectrochim. Acta B52 765
- [12] Marić D, Hartmann P, Malović G, Donkó Z and Petrović Z Lj 2003 J. Phys. D: Appl. Phys. 36 2639
- [13] Kutasi K and Donkó Z 2000 J. Phys. D: Appl. Phys. 33 1081
- [14] Callegari Th, Ganter R and Boeuf J-P 2000 J. Appl. Phys. 88 3905
- [15] Bogaerts A and Gijbels R 1998 Spectrochim. Acta B53 437
- [16] Boeuf J-P and Garrigues L 1998 J. Appl. Phys. 84 3541
- [17] Hagelaar G J M and Pitchford L 2005 Plasma Sources Sci. Technol. 14 722
- [18] Derzsi A, Hartmann P, Korolov I, Karácsony J, Bánó G and Donkó Z 2009 J. Phys. D: Appl. Phys. 42 225204
- [19] Rózsa K, Gallagher A and Donkó Z 1995 Phys. Rev. E 52 913
- [20] Marić D, Kutasi K, Malović G, Donkó and Petrović Z Lj 2002 Eur. Phys. J. D 21 73

# Determination of electron attachment rate at ambient pressure using the Lambert-Beer law

M. Kučera<sup>1</sup>, M. Stano<sup>1</sup>, Š. Matejčík<sup>1</sup>

<sup>1</sup>Department of Experimental Physics, Comenius University, Mlynská dolina, Bratislava 842 45, Slovakia

e-mail: [kucera@fmph.uniba.sk](mailto:kucera@fmph.uniba.sk)

## Abstract

Electron attachment rate constant to oxygen in a nitrogen buffer gas was determined from electron transmission through a drift tube using the Lambert-Beer law. The effect of electron beam intensity is studied and an apparent increase of the electron decay at elevated electron beam intensities was observed. The effect was attributed to a space charge barrier formed by negative ions produced by the electron attachment process. The measurements were performed at ambient pressure at two values of  $E/n$  1.0 Td and 2.0 Td and concentration of oxygen from 0.1% to 2%.

**Keywords:** electron attachment rate, Lambert-Beer law, space charge effects.

## Introduction

Electron attachment to molecules in a high pressure gaseous environment is an object of study due to its importance to atmospheric chemistry as well as to detection of trace compounds in air using the ion mobility spectrometry. Several methods have been used for determination of electron attachment rate in gases at ambient pressure [1, 2, 3]. One approach is to determine the attachment rate from electron transmission through a drift tube acting as a cuvette using the Lambert-Beer law. However, both electrons and negative ions possess an electric charge and repel each other due to the coulomb force. Attachment of fast moving electrons and formation of slow negative ions results in significant increase of the space charge which may affect the transmission of electrons through the drift tube. The measurement of electron attachment rate must therefore be carried out with a low intensity electron beam so that the electric field formed by the space charge is kept negligible. On the other hand, low intensity electron beam limits the sensitivity and accuracy of the measurement.

In the present work electron attachment rate to O<sub>2</sub> in a nitrogen buffer gas at ambient pressure was determined from electron transmission through a drift tube using the Lambert-Beer law. The effect of electron beam intensity is studied and the results are compared with the previous work by Chanin and Phelps[1].

## Experiment

The work was performed using a home made ion mobility spectrometer. Detailed description of the instrument is given in [4]. Free electrons are produced by a discharge in a point-to-plane geometry. Negative potential is applied to the point electrode. Electrons exit the discharge area through an aperture in the plane electrode. Diameter of the aperture varied from 0.5 to 5 mm in order to control the electron beam intensity.

Electrons are periodically released into drift tube in pulses of 10 μs duration controlled by a shutter grid. The electron current is measured on a collector situated at the end of drift tube, it is amplified and recorded by an oscilloscope. In order to distinguish current of electrons from the current of negative ions formed by electron attachment inside the drift tube, the background voltage is subtracted from the peak voltage. This way of reading the electron current also avoids possible errors due to DC offset of the amplifier. The shutter opening time is long enough to allow reliable reading of the electron current on the collector.

The electron source was fed by pure nitrogen. The drift tube was fed by nitrogen with 0.1% to 2.0% of oxygen. Purity of both nitrogen and oxygen gases were 99.999%. The gas mixture was prepared using MKS mass flow controllers. The length of drift tube was 11.1 cm.

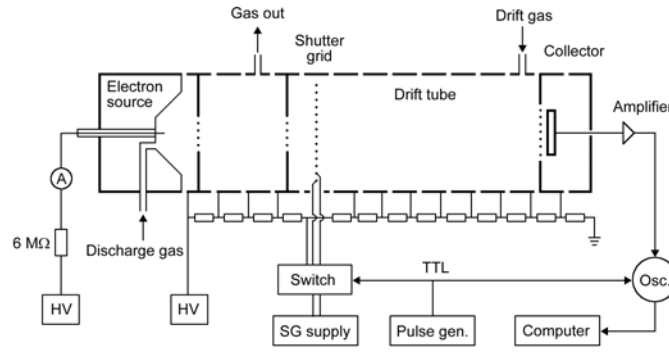


Fig. 1. The experimental setup

Attachment of low energy electrons to oxygen at high pressure is a three body process [1]. The reaction can be expressed as



where  $X$  is the third particle. The speed of reaction can be expressed as

$$\frac{d[M^-]}{dt} = -\frac{d[e]}{dt} = k[M][e][X] \quad (2)$$

where  $[M^-]$ ,  $[e]$ ,  $[M]$  is a number density of negative ions, electrons and electron attaching molecules, respectively.  $[X]$  is a number density of the gas molecules and  $k$  is the electron attachment rate.

The amount of electrons in the drift tube is decreasing with increasing distance from the shutter grid  $d$  according to

$$[e]_d = [e]_0 \exp\left(-\frac{k[M][X]d}{w_e}\right) \quad (3)$$

where  $w_e$  is the drift velocity of electrons.

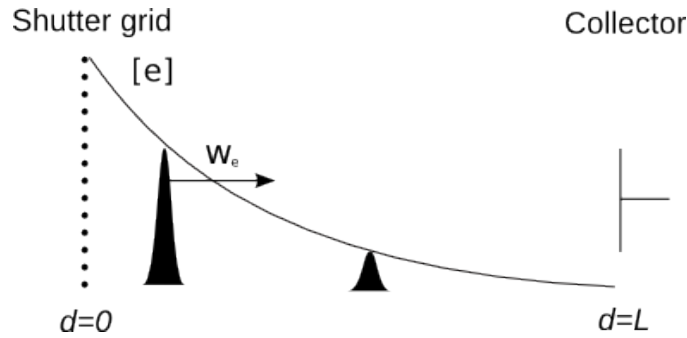


Fig. 2: Profile of the electron concentration in the drift tube.

If  $I_0$  is the electron current on the collector when no electron attaching gas is present and  $I_{[M]}$  stands for electron current when concentration of electron attaching gas inside the drift tube is  $[M]$  the rate constant can be expressed as

$$k = -\frac{w_e}{d[M][X]} \ln \frac{I_{[M]}}{I_0} \quad (4)$$

The relation between the electron current and electron number density is given by

$$I = S q_e [e] w_e \quad (5)$$

where  $S$  is the electron beam cross section and  $q_e$  the elementary charge.

### Results and discussion

The measurements of electron attachment rate to oxygen seeded in nitrogen buffer gas were carried out at different electron beam intensities. The intensity of the electron beam was regulated using apertures with different diameters in the plane electrode of the electron source. The aperture diameter varied from 0.5 to 5 mm. Figure 3 shows the electron current on collector as a function of the aperture diameter. The measurements were taken at 1 and 2 Td with drift tube filled with pure nitrogen. The electron current varied from 29 nA to 262 nA at 1Td and 82 nA to 806 nA at 2 Td.

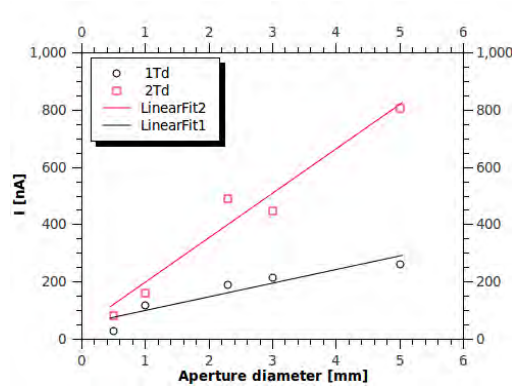


Fig. 3. Electron current on the collector at different aperture diameter and drift tube filled with pure nitrogen.

Figures 3 and 4 show the electron current as a function of oxygen concentration in the drift tube at  $E/n$  equal 1 Td and 2 Td respectively. According to equation (4) the logarithm of the electron current on collector decreases linearly with concentration of electron attaching gas. The slope of the curve is proportional to the electron attachment rate. The figures show that the slope of the curve decreases with decreasing intensity of the electron beam regulated by the aperture diameter. Rate constants are obtained using a linear fit to logarithm of electron current versus oxygen concentration dependence.

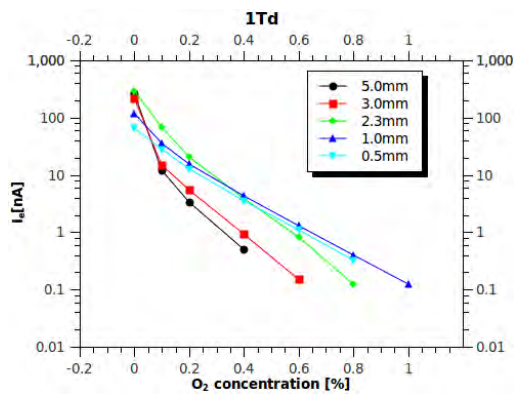


Fig.4. Transmitted electron current at 1 Td.

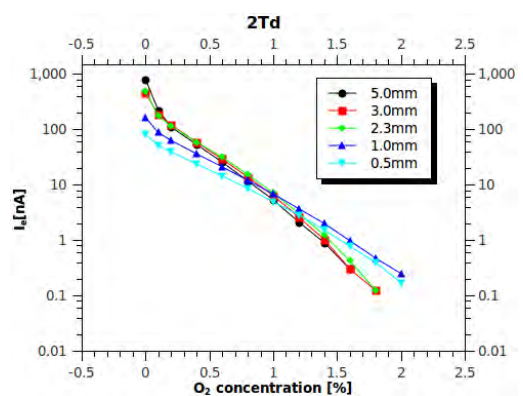


Fig.5. Transmitted electron current at 2 Td .

The electron attachment rate constants to oxygen obtained at different apertures regulating the electron beam intensity are shown on the figure 6. The  $k$  apparently decreases with decreasing electron beam intensity. The rate constants obtained with 0.5 mm aperture are  $4.32 \times 10^{-32} \text{ cm}^6 \text{ s}^{-1}$  for 1 Td and  $2.71 \times 10^{-32} \text{ cm}^6 \text{ s}^{-1}$  at 2 Td. The values nearly match the results reported by Chanin and Phelps [1].

The electron attachment rate does not intrinsically depend on electron beam intensity or electron number density. However, increase of electron beam intensity leads to increase of number density of slowly moving negative ions. The effect is especially important in the area before the shutter grid where a continuous electron current is passing through an electron attaching gas. Negative ions at sufficient concentration form a space charge acting as a potential barrier and limit the current of electrons transmitted through the drift tube. The electron current measured on the collector is decreased not only by electrons lost due to electron attachment but also due to negative space charge formed by the produced ions. This results in apparently higher value of the electron attachment rate. Figure 5 also shows that the slope of electron current logarithm versus oxygen concentration increases at higher oxygen concentration. The effect is observed at all electron beam intensities used and indicates an increase of the electron attachment rate at elevated concentration of oxygen. In their work [4] Chanin and Phelps reported that electron attachment to oxygen in a three body process depends on nature of the third particle. The electron attachment rate in a pure oxygen is about two orders of magnitude higher than to oxygen seeded in a nitrogen buffer gas. The increase of attachment rate at elevated oxygen concentration is probably due to increased role of oxygen acting as a third particle.

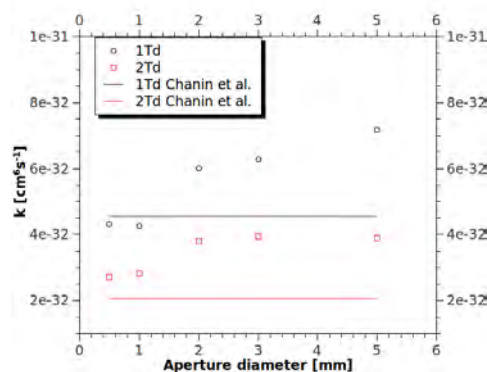


Fig. 6. Electron attachment rate constant at different aperture diameters obtained using the equation (4). Lines represent values by Chanin et al [1].

## Conclusions

Electron attachment rate can be determined by evaluating the electron transmission through a drift tube using the Lambert-Beer law. The experiment must be carried out with a low intensity electron beam to keep the space charge formed by slowly moving negative ions produced in the attachment process negligible. Otherwise the space charge acts for electrons as a potential barrier and the electron current is decreased not only by electrons involved in the attachment process but also due to the potential barrier formed by the negative ions. Transmitted electron current appears to decrease exponentially with increasing concentration of the electron attaching gas also at high intensity of the electron beam. This may result in incorrect determination of the electron attachment rate exceeding the correct value.

## Acknowledgement

This work was supported by the slovak grants VEGA 1/0051/08, 1/0379/11 and by the Slovak Research and Development Agency, project Nr. APVV-0365-07.

## References

- [1] L.M.Chanin, A.V.Phelps and M. A. Biondi, *Phys. Rev* **128** (1962) 219
- [2] M. Tabrizchi and A. Abedi, *J. Phys. Chem. A*, **108** (2004) 6319-6324
- [3] C.A. Mayhew, A.D.J. Critchley, D.C. Howse, V. Mikhailov, M.A. Parkes, *Eur. Phys. J. D* **35** (2005) 307-312
- [4] M. Stano, E. Safonov, M. Kučera, Š. Matejčík, *Chem. Listy* **102** (2008) 1414-1417

# Numerical simulation of nanosecond laser-induced plasma emission

F. Rezaei, S. H. Tavassoli,

Laser and Plasma Research Institute, Shahid Beheshti University G. C., 1983963113, Tehran, Iran

e-mail: f\_rezaei@sbu.ac.ir , h-tavassoli@sbu.ac.ir

## Abstract

Laser-induced plasma emission of aluminum target at 1 atm argon gas is numerically investigated. Three kinds of plasma emission, including Bremsstrahlung, recombination and spectral emission is considered. Bremsstrahlung and recombination emissions which are due to free-free and free-bound electron transitions have a continuous wavelength. A plasma spectrum is obtained by adding eleventh neutral and ionic spectral lines of aluminum to the continuous emission due to the Bremsstrahlung and recombination mechanisms. Temporal behavior of plasma emission up to 500 ns after the plasma formation is studied. Effect of laser pulse energy on the plasma emission is obtained. Although at early times the continuous radiation dominates the spectral radiations, the aluminum spectral emission is the dominant radiation in later times.

**Keywords:** Laser-induced breakdown spectroscopy, Bremsstrahlung emission, Recombination emission.

## Introduction

Line profiles emitted from a plasma are very useful quantities for describing the properties of emitter and environment around the plasma. Laser-induced breakdown spectroscopy (LIBS) is an analytical technique for elemental analysis of different kind of materials. In this technique a plasma is produced by focusing a high power laser beam on a target surface. The plasma emission is a combination of background emission, atomic and ionic spectral lines as well as a continuous radiation due to the Bremsstrahlung and recombination mechanisms. Electron transitions between two bound levels leads to spectral emissions and electron transitions between free-free and free-bound levels led to Bremsstrahlung and recombination radiation, respectively. In a LIBS experiment, some qualitative and quantitative information about the sample surface elements, electron density, plasma temperature and etc is obtained by spectroscopic analysis of plasma emission. Investigating the plasma emission has a critical role in specifying the optimized time and position of the spectral emission that would be of practical use in LIBS.

In the present paper, temporal behavior of plasma emission containing spectral, Bremsstrahlung and recombination radiation at the initial stages, up to 500 ns after the plasma formation is numerically investigated. The plasma is created on an aluminum target at 1 atm argon gas by laser pulses of 0.5, 0.7, 0.9, 1.1 GW. Here, the contribution of background emission that is caused by the system noise is neglected. This paper is an expansion of the work done in Ref [1]. Input parameters including electron density, plasma temperature and density of neutral and ionized atoms are taken from Ref. [1]. Temporal evolution of eleventh strongest aluminum lines is obtained in order to obtain the spectrum of plasma emissions from an aluminum target at different delay times.

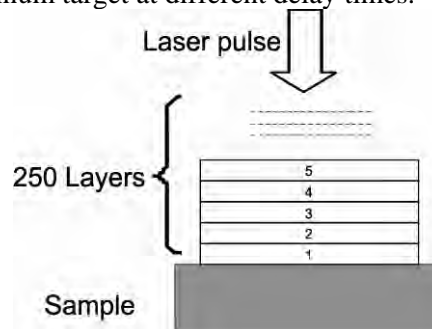


Fig 1. One dimensional expansion of the plasma

## Theoretical Background

Because of dealing with the early times after plasma formation, a one-dimensional (1D) plasma expansion is considered. Figure (1) shows a schematic of the plasma plume and its expansion. The plasma is supposed to be homogeneous and optically thin and self absorption of outer layers is neglected. The plasma volume is divided to 250 layers. Each layer is composed of uniform density and temperature. All input data including electron density, plasma temperature and density of neutral and ionized atoms at each layer are taken from Ref [1]. Some atomic data are taken from NIST<sup>1</sup> and Ref. [2]. Table 1 show the aluminum lines and their atomic parameters.

As it mentioned above, laser induced plasmas emit three kinds of emissions; spectral, Bremsstrahlung and recombination emission which are due to the bound-bound, free-free and free-bound electron transitions, respectively. Spectral emission (energy radiated per unit time, per unit volume and per unit frequency) is calculated by [3]:

$$E_{spec} = N^* A_{ul} \hbar \omega L(\omega) \quad (1)$$

where  $\hbar$  is the Planck's constant and  $A_{ul}$  is the probability transition between the upper level  $k$  and the lower level  $i$ .  $N^*$  is the number density of atoms in the upper level and  $L(\omega)$  is the spectral line profile:

$$L(\omega) = \frac{\left(\frac{\gamma_{ul}}{4\pi}\right)}{(\nu - \nu_0)^2 + \left(\frac{\gamma_{ul}}{4\pi}\right)^2} \quad (2)$$

$$N^* = N_{tot}(1-f) \frac{g e^{\frac{-E_u}{k_B T}}}{U} \quad (3)$$

where  $\nu_0$  is the frequencies of aluminum lines,  $N_{tot}$  is the total density of neutrals and ions,  $g$  is degeneracy of the upper level,  $T$  is plasma temperature,  $E_u$  is energy of upper level,  $k_B$  is the Boltzmann constant,  $U$  is the partition function for the species (dimensionless) and  $f$  is the ionization fraction (total ion density divided by total concentration).  $\gamma_{ul}$  is decay rate and is

Tab 1. Spectral data of ten neutral and one ionized lines of aluminum from NIST and Ref. [2]

| Wavelength (nanometer) | Einstein coefficient $A$ ( $s^{-1}$ ) | Energy of upper level (joule) | Degeneracy $g$ | Stark parameter       |
|------------------------|---------------------------------------|-------------------------------|----------------|-----------------------|
| 226.9096               | $7.9 \times 10^7$                     | $0.8790 \times 10^{-18}$      | 6              | $2.52 \times 10^{-1}$ |
| 236.7052               | $7.2 \times 10^7$                     | $0.8405 \times 10^{-18}$      | 4              | $8.32 \times 10^{-2}$ |
| 237.3124               | $8.6 \times 10^7$                     | $0.0841 \times 10^{-17}$      | 6              | $8.32 \times 10^{-2}$ |
| 257.5094               | $2.8 \times 10^7$                     | $0.7748 \times 10^{-18}$      | 6              | $4.48 \times 10^{-2}$ |
| 281.6185               | $3.83 \times 10^8$                    | $0.1897 \times 10^{-17}$      | 1              | $4.29 \times 10^{-3}$ |
| 308.2153               | $6.3 \times 10^7$                     | $0.0645 \times 10^{-17}$      | 4              | $2.81 \times 10^{-2}$ |
| 309.2710               | $7.4 \times 10^7$                     | $0.0645 \times 10^{-17}$      | 6              | $2.81 \times 10^{-2}$ |
| 309.2839               | $1.2 \times 10^7$                     | $0.6455 \times 10^{-18}$      | 9              | $2.81 \times 10^{-2}$ |
| 394.4006               | $4.93 \times 10^7$                    | $0.0504 \times 10^{-17}$      | 2              | $1.52 \times 10^{-2}$ |
| 396.1520               | $9.8 \times 10^7$                     | $0.0504 \times 10^{-17}$      | 2              | $1.52 \times 10^{-2}$ |
| 466.3056               | $5.3 \times 10^7$                     | $0.2128 \times 10^{-17}$      | 3              | 1.39                  |

<sup>1</sup>. National Institute of Standard and Technology.

obtained by:

$$\gamma_{ul} = 2\pi\Delta\nu_{stark} \quad (4)$$

where  $\Delta\nu_{stark}$  is spectral line broadenings. Since at the start of laser irradiation, there are many electrons and ions in the plasma, Stark effect is the main mechanism of line broadening. In the present model other mechanisms of broadening such as Doppler, natural, resonance and van der waals broadening is neglected.

The second part of plasma emission comes from Bremsstrahlung mechanism. Bremsstrahlung is electromagnetic radiation in plasma that is the consequence of deceleration of electrons when they deflected by other charged particle, like an ion. Energy of Bremsstrahlung emission per unit volume, per unit time and per unit frequency is obtained by [4]:

$$p(\nu) = p_{tot} \frac{h}{k_B T} e^{-\frac{h\nu}{k_B T}} \quad (5)$$

where  $p_{tot}$  is the total power radiated due to the electrons moving in the field of plasma ions:

$$p_{tot} = \frac{\sum_i n_i z_i^2 n_e e^6}{24\pi^2 \epsilon_0^3 c^3 m_e \hbar} \sqrt{\frac{k_B T}{m_e}} \quad (6)$$

where  $c$  is the speed of light,  $m_e$  is the electron mass,  $n_i$  and  $n_e$  are ion (Al II, Al III, Ar II) and electron number density respectively,  $z_i$  is atomic number and  $\epsilon_0$  is permeability of vacuum.

Recombination emission is the third part of plasma emission. The power emitted per volume, per frequency is calculated by [3]:

$$E_{recom} = p_{tot} \frac{h}{k_B T} e^{-\frac{h\nu}{k_B T}} e^{-\frac{\chi_i}{T}} \frac{\chi_i}{T} \frac{\xi}{n^3} \quad (7)$$

where  $\xi$ ,  $n$  and  $\chi_i$  are number of holes in the lowest unfilled shell of an ion, quantum number of that shell and ionization potential of the recombined ion respectively.

At each point, and each delay time, three different kinds of emissions are calculated. Then, the spectrum of plasma emission is obtained by summation on three emissions at different wavelength.

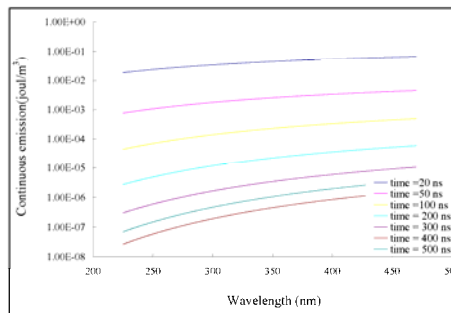


Fig 2. Continuous spectrum at delay times of 20, 50, 100, 200, 300, 400, 500 ns at pulse intensity of 0.5GW.

## Results and discussions

Figures 2 shows continuous spectrum due to the Bremsstrahlung and recombination radiation at different delay times; 20, 50, 100, 200, 300, 400, 500 ns for laser pulse intensity of 0.5GW. As it seen, continuous emission increases with wavelength and decreases very fast with increasing delay time.

Figures 3 show total spectrum of aluminum at different delay times and at pulse intensity of 0.5GW.

As it seen, at early times (20 and 50ns), the plasma emission is dominated by strong continuous light (Bremsstrahlung and recombination). When the time evolves, the continuous emission decreases very faster than the spectral lines. So at longer times spectral emission becomes more intense than the continuous emission. In LIBS method, spectral lines contain some information about the atomic concentration and should be decoupled from the continuous spectrum. According to the different decay rates of continuous and spectral emission, time resolves spectroscopy in which the plasma emission is detected after an appropriate delay time, is a key technique for decoupling between the continues and spectral emission. In a usual LIBS experiment optimum delay time in which line to continues intensity ratio has a maximum value is determined by several experiments. Results in Fig. 3 show that an optimum delay time can be determined by the simulation which ultimately leads to the time and money saving. For example at delay time 200 ns, the intensity ratios of 394.4 and 396.1 nm lines have maximum values and therefore, the optimum time for detecting spectral lines in these wavelengths is 200 ns. It is clear that each line has its specific life time and specific optimum delay time.

As it seen in Fig. 3, total emission becomes weaker and line widths decrease with delay time. This means that plasma becomes cooler and electron density decreases with time.

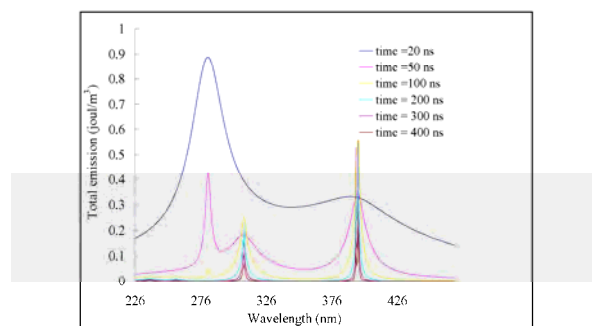


Fig. 3. Temporal evolution of the total emission at 20, 50, 100, 200 , 300, 400, 500 ns at intensity of 0.5GW.

At early times the spectral lines of ionized atoms are stronger than the neutral lines. However, at longer times the spectral lines of ionized atoms decreases very fast and the neutral lines dominate to the ionized lines. This is because at early times the plasma is hot and density of ionized atoms is high. When the time evolves, plasma be cooled and density of ionized atoms and accordingly spectral emission of ionized atoms decreases.

Figure 4 show the influence of laser energy on spectral line emissions. It is clear from this figure that increasing the laser energy leads to an increase in the plasma radiations. because of increasing the ionization process.

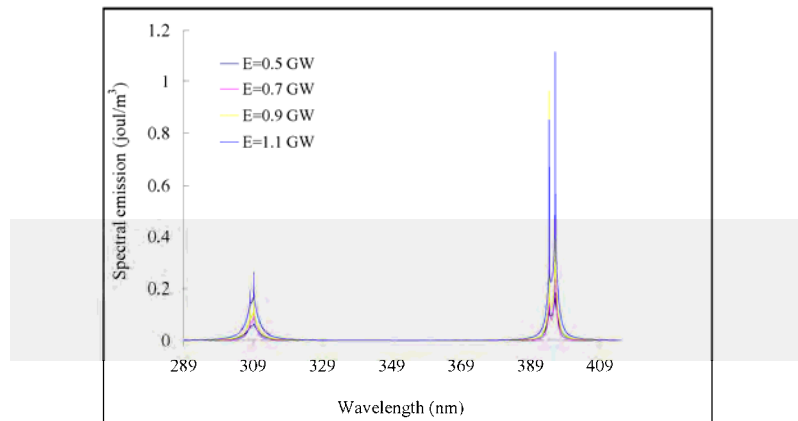


Fig 4: Effect of laser pulse energy on spectral emission at 500 ns delay time.

### Conclusions

In this paper the spectrum line profile of aluminum in 1atm argon gas is numerically investigated. Three kinds of plasma emission including Bremsstrahlung, recombination and spectral emission are considered. The evolution of the spectral and continuous emissions in wavelength at different delay times is calculated. The effect of laser energy on plasma radiations is investigated. Results show that increasing the laser energy cause to intensify the spectral emission. Also the different contributions of plasma radiations is distinguished in order to find the appropriate delay time for the best time resolved spectroscopy. By this method optimum delay time in which line to continues intensity ratio has a maximum value can be calculated.

### References

- [1] M. Aghaei, S. Mehrabian, S.H Tavassoli, *Simulation of nanosecond pulsed laser ablation of copper samples: A focus on laser induced plasma radiation*, Applied physics, 2008
- [2] H. Greim, *Plasma spectroscopy*, McGraw Hill press, 1964,
- [3] Miziolek, Anderzej, *Laser-Induced breakdown spectroscopy (LIBS) Fundamentals and Applications*, Cambridge University Press, 2006.
- [4] C. W. Allen, *Astrophysical Quantities*, Athlone, University of London, London, 1973.
- [5] F. Bredice, F.O. Borges, H. Sobral, M. Villagran-Muniz, H.O. Di Rocco, G. Cristoforetti, S. Legnaioli, V. Palleschi, L. Pardin, A. Salvetti, E. Tognoni, *Evaluation of self-absorption of manganese emission lines in Laser Induced Breakdown Spectroscopy measurements*, Elsevier, Argentina, Brazil, Mexico, Italy, 2006

# Rotationally Excited Diatomic $\text{Cl}_2^-$ Anion

N. L. Asfandiarov, S. A. Pshenichnyuk, A. S. Vorob'ev, and E. P. Nafikova  
Institute of the Physics of Molecules and Crystals, Russian Academy of Sciences, Ufa, 450075 Russia

e-mail: nail\_asf@mail.ru

## Abstract

The dissociative capture of slow electrons by tetrachlorethylene ( $\text{C}_2\text{Cl}_4$ ) has been investigated by resonant electron capture negative ion mass spectrometry. Metastable ions with fractional mass numbers 7.5, 17.5, and 19 corresponding to the  $\text{C}_2\text{Cl}_4^- \rightarrow \text{Cl}^- + \text{C}_2\text{Cl}_3$  and  $\text{Cl}_2^- \rightarrow \text{Cl}^- + \text{Cl}$  decays occurring at the microsecond timescale have been detected. It has been revealed that  $\text{Cl}_2^-$  anions, which are fragment ions, can dissociate at the microsecond timescale, which is very surprising for a system with one internal degree of freedom. This process is assumingly attributed to the rotational excitation of  $\text{Cl}_2^-$  anions. Thus, the experimental estimate of the time of rovibronic relaxation in the  $\text{Cl}_2^-$  anion has been obtained.

**Keywords:** Dissociative electron attachment lifetime

## Introduction

Chlorosubstituted ethylenes, which are widely used in chemical industry, are among the main pollutants of the environment. They are found in soil and groundwater. For these reasons, the investigations of their destruction rates are of current interest and supported by such organizations as the National Center for Environmental Research (United States) [1]. The first investigations of temporary states of ethylene anions were performed by Sanche and Schulz, who have developed electron transmission spectroscopy. They obtained [2] an electron transmission spectrum containing a 1.74 eV peak attributed to the capture of an additional electron on the lowest unoccupied molecular orbital (LUMO) of the  $\pi^*$  type belonging to the irreducible representation  $b_{2g}$  of the  $D_{2h}$  point group. The history of the investigations of ethylene and its fluorine and chlorine derivatives by electron transmission spectroscopy (ETS) and dissociative electron attachment spectroscopy (DEAS) can be found in [3–10]. An increase in the number of chlorine atoms is accompanied by a decrease both in the vertical attachment energy (VAE) of the electron on the LUMO of the  $\pi^*$  type and in the width of the peaks. On the contrary, the successive introduction of fluorine atoms increases the energy VAE and leads to the broadening of the bands of the electron transmission spectrum.

The energy VAE is minimal for the tetrachlorethylene molecule, where it is lower than 0.3 eV, but remains positive [4]. This means that the  $\text{C}_2\text{Cl}_4$  molecule in the equilibrium geometry has negative electron affinity. Thus, the existing data on electron transmission spectroscopy indicate that the vertical electron affinity is negative for all of the chlorine and fluorine derivatives of ethylene. Individual representatives of the series of the molecules under consideration were investigated by various variants of DEAS [5–9]. The chlorine derivatives are characterized by intense decay channels of negative molecular ions with the formation of  $\text{Cl}^-$ ,  $\text{Cl}_2^-$ , and  $(\text{M}-\text{Cl})^-$  ions, and long\_lived negative molecular ions with an autodetachment lifetime of  $14 \pm 3 \mu\text{s}$  are observed only for tetrachlorethylene [6]. This is direct evidence that adiabatic electron affinity of the tetrachlorethylene molecule is positive [6]. The situation where the signs of the vertical and adiabatic electron affinities of the molecule are different is quite unusual and requires special analysis, although the observation of long\_lived  $\text{C}_2\text{Cl}_4^-$  ions was explained earlier [8, 10]. Figure 1 illustrates this effect. At the equilibrium distances between the nuclei of the molecule, the electron is captured on the  $\pi^*$ \_type LUMO of the  $b_{2g}$  symmetry at an energy of 0.23 eV, according to the HF/6-311G(d) calculation, corrected by Eqs. (1) and (2) similar to [11]:

$$VAE^{\text{calc.}}(\pi^*) = -2.36111 + 0.91332 \cdot VOE(\pi^*), \quad (1)$$

$$VAE^{\text{calc.}}(\sigma^*) = -2.65453 + 1.1065 \cdot VOE(\sigma^*), \quad (2)$$

here,  $VAE^{calc.}$  are the calculated vertical attachment energies and  $VOE$  are the calculated energies of virtual molecular orbitals. The excitation of out-of-plane vibrations of the  $b_{2g}$  symmetry reduces the potential energy of the ion in the  $\pi^*$  state and dynamically reduces the point group of the negative molecular ion from  $D_{2h}$  to  $C_{2h}$ . Note that the calculated adiabatic electron affinity of the  ${}^2B_{2g}$   $\pi^*$  state is 0.61 eV, which coincides with the measured adiabatic electron affinity  $EA=0.640\pm 0.030$  eV within the measurement error [12].

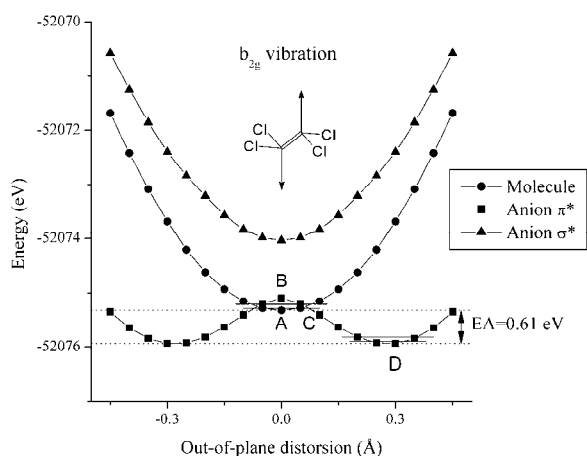


Fig. 1. Potential energy of the molecule and anion in the  $\pi^*$  and  $\sigma^*$  states undergoing out-of-plane vibrations of the  $b_{2g}$  symmetry type.

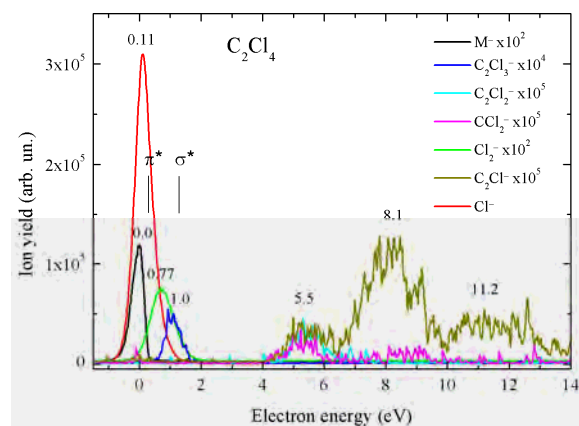


Fig. 2. Effective yields of anions in the dissociative electron capture by tetrachlorethylene. The dashes mark the positions of the peaks in the electron transmission spectrum.

In the cited works, fragment ions were observed for nonzero energy electrons. According to our experience, this is a standard phenomenon in the mass spectra of the negative ions of polyhalogen substituted molecules, see, e.g., [13, 14]. However, the formation of such ions occurs through rearrangement processes [15] whose duration is much longer than the typical vibration period of nuclei in an ion. As is known, the chlorine molecule capturing electrons in the gas phase does not form molecular ions [16–18]. The formation of  $Cl^-/Cl_2^-$  ions is an exothermal process [18],



The cross section of dissociative electron capture by  $Cl_2$  molecules was theoretically investigated in detail in [19, 20]. In particular, the effect of the vibrational [20] and rotational excitations [19] of the target molecules on the cross section of dissociative electron capture was analyzed.

## Experimental Procedure

The design of the mass spectrometer and the procedure of obtaining mass spectra and effective yield curves of negative ions were described in [13, 14]. An electron beam of a certain energy (the FWHM of the energy distribution is estimated as 0.4 eV) passes through a collision cell containing a gas of the substance under investigation. The current of negative ions passed through the mass spectrometer is detected as a function of the energy of electrons varying in the range of 0–14 eV. The electron beam current at the collector is 1  $\mu A$ . The resonance identification accuracy is 0.1 eV. The accelerating voltage is  $-4$  kV, the time of the extraction of ions with  $m/e = 146$  a.m.u. from the ionization chamber is about 10  $\mu s$ , the time of flight of these ions from the time of the formation under the capture of the electron to the

detection time is estimated as 26  $\mu\text{s}$ , and the residual pressure in the ionization chamber is about  $10^{-4}$  Pa, which excludes the effect of double collisions.

## Results and Discussion

Figure 2 shows the effective yields of ions as functions of the incident electron energy. The resonance states of negative ions observed in the spectrum are located in two energy ranges of 0–1 eV and above 4.5 eV in good agreement with the previous data [6–10]. The first two resonance states corresponding to the  $\text{C}_2\text{Cl}_4^-$ ,  $\text{C}_2\text{Cl}_2^-$ ,  $\text{Cl}_2^-$  and  $\text{Cl}^-$  ions are attributed to the states of negative molecular ions with the capture of the electron on unoccupied  $\pi^*$  and orbitals observed in the electron transmission spectra. It is reasonable to assume that the peak of molecular ions for thermal electrons with a mean autodetachment lifetime of about 50  $\mu\text{s}$  (see Fig. 2), as well as fragment  $\text{Cl}^-$  ions with the maximum effective yield at an energy of 0.11 eV, is formed when an additional electron is captured on the LUMO. Experiments with high resolution in the electron energy [9, 10] make it possible to resolve two peaks in the cross section for the formation of  $\text{Cl}^-$  ions. The first peak is close to zero electron energy and the second peak is manifested as an unresolved arm at an energy of 0.3–0.4 eV. In view of the lower resolution in our experiment, these peaks merge into one peak with the maximum at 0.11 eV. We do not interpret high-energy spectroscopic states of ions, because they are apparently due to the capture of an additional electron through the core excited resonance mechanism. We consider only the region of low electron energies up to 2 eV, where the formation of ions occurs through the shape resonance mechanism with the capture of the electron on two LUMOs of the  $\pi^*$  and  $\sigma^*$ . In this energy range, the  $\text{C}_2\text{Cl}_4^-$ ,  $\text{C}_2\text{Cl}_3^-$ ,  $\text{Cl}_2^-$ , and  $\text{Cl}^-$  ions are observed (see Fig. 2).

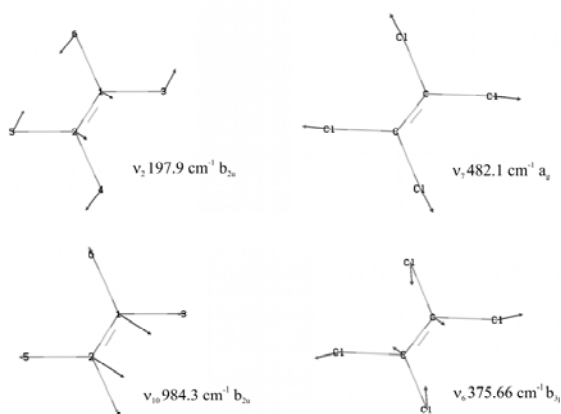


Fig. 3. Normal vibrations of the  $\text{Cl}_2\text{C}=\text{CCl}_2^-$  that are necessary for its dissociation with the formation of the  $\text{Cl}_2^-$  ion and dichloroacetylene molecule.

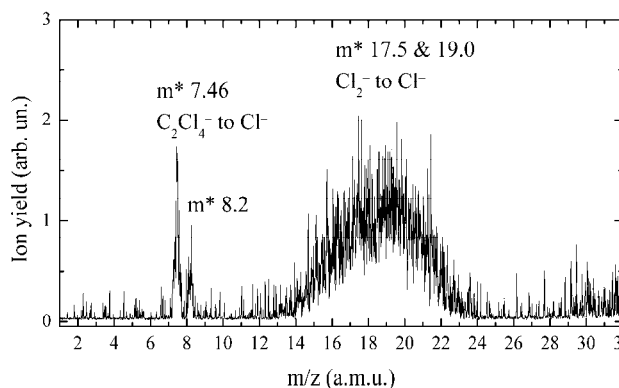


Fig. 4. Metastable ions observed in the mass spectrum of the negative ions of  $\text{C}_2\text{Cl}_4$ .

The channel of the formation of fragment  $\text{Cl}^-$  ions is evidently the most energy favorable channel, but does not completely suppress the yield of negative molecular ions. According to the estimates made in [9], the overwhelming majority of  $\text{Cl}^-$  ions are formed at a timescale of  $\sim 10^{-9}$  s, which is much longer than the characteristic period of vibrations of the C–Cl bond. This relation is due to the fact that no normal vibrations of the  $\text{C}_2$  ion can be responsible for the direct dissociation with the formation of the chlorine ion and neutral  $\text{C}_2\text{Cl}_3$  fragment. An analog is the classical case of the dissociation of the  $\text{CO}_2$  molecule considered in [21]. Neither symmetric nor antisymmetric valence vibrations of the C–O bonds in the  $\text{CO}_2$  molecule lead to the dissociation of the molecule into the O atom and CO molecule. Only the combination of these vibrations having much different frequencies can lead to the considered dissociation channel. In the classical approximation, it is possible to analyze the motion of the figurative point of the system in the phase space of the vibrations under consideration through the Lissajous figures and to calculate the probability of its falling to a valley leading to isolated O and CO fragments, see Fig. 163 in [21]. The

dissociation of  $\text{Cl}_2^-$  with the formation of the  $\text{Cl}^-$  ion is more complicated, should involve at least three normal vibrations (see Fig. 3) and, therefore, is much delayed in time. Indeed, in the experiment, we observed so-called metastable ions with noninteger mass numbers given by the expression [15]  $m^* = m^2/M$ , where  $m$  and  $M$  are the masses of the daughter and parent ions, respectively (see Fig. 4). The metastable ions with  $m^* = 7.4$  and  $8.15$  a.m.u. correspond to the detachment of the  $^{35}\text{Cl}^-$  and  $^{37}\text{Cl}^-$  isotopes from the molecular ions with  $m/z = 166$  and  $168$ , respectively. Note that the mass width of these peaks is small, although it certainly exceeds the typical width of “normal” ions formed before the extraction of ions from the ionization chamber (see Fig. 4). This indicates that the kinetic energy of the fragment scattering in the  $\text{C}_2\text{Cl}_4^- \rightarrow \text{C}_2\text{Cl}_3^* + \text{Cl}^-$  reaction is sufficiently low.

The most surprising experimental observation is apparently the detection of an anomalously wide peak of metastable ions whose detected mass ranges from 15 to 23 a.m.u. with the maxima near  $m/z = 17.5$  and 19 (see Fig. 4). This peak is undoubtedly a manifestation of the dissociation of ions with the formation of chlorine ions having a high translational energy. This phenomenon is unusual at least because the ion has only one internal degree of freedom and, consequently, either should dissociate “immediately” if its vibrational energy exceeds the bond rupture energy or is stable, because the “reservoir” of the vibrational energy, which is typical of complex molecules, is absent in the absence of collisions with another particle. Therefore, the delay of dissociation by a time of about several microseconds is caused by the features of the formation of ions themselves. The maximum of the effective yield of ions is at an energy of 0.75–0.8 eV, the maximum of the effective yield of the metastable ions with  $m^* \sim 19$  a.m.u. at 0.6 eV. The effective yield curve of the daughter  $\text{Cl}^-$  ions is extended from 0 to  $\sim 1$  eV, covering the effective yield curves of the and metastable ions. It was found earlier that the overwhelming majority of  $\text{Cl}^-$  ions are formed quite rapidly at the nanosecond timescale [9]. For this reason, it is impossible to separate the fraction of  $\text{Cl}^-$  ions formed at the microsecond timescale. According to the quantum-chemistry calculations performed in the HF/6-311G(d) theory level, the formation of ions  $\text{Cl}_2^-$  with the formation of the neutral fragment  $\text{Cl}-\text{C}\equiv\text{C}-\text{Cl}$  (the detachment of the chlorine atoms at substitution positions 1 and 2) has a threshold of -0.07 eV, i.e., is possible at zero energy of incident electrons. According to the calculations, the detachment of the chlorine molecular ion from one of the carbon atoms of the molecular ion  $\text{Cl}_2\text{C}=\text{CCl}_2^-$  has a threshold of 2.18 eV. The detachment of  $\text{Cl}_2^-$  from the molecular  $\text{C}_2\text{Cl}_4^-$  ion should evidently involve a set of normal vibrations, at least, the vibrational modes  $\nu_5$ ,  $\nu_7$ , and  $\nu_9$  (see Fig. 3). The reasons for such a conclusion are similar to those presented in [21] when analyzing the dissociation of the  $\text{CO}_2$  molecule. The vibration  $\nu_2$  approaches chlorine atoms and the combination of the symmetric and antisymmetric vibrations  $\nu_7$  and  $\nu_{10}$ , respectively, removes the ion from the neutral dichloroacetylene molecule. We emphasize that only one antisymmetric vibration  $\nu_{10}$  cannot induce the desired dissociation, because the approach of the opposite chlorine atoms (with respect to detached chlorine ions) with the carbon atoms at sufficiently high excitations prevents dissociation. Only the combination of the vibrations  $\nu_{10}$  and  $\nu_7$  can lead the system to a valley asymptotically corresponding to the  $\text{ClC}\equiv\text{CCl} + \text{Cl}_2^-$  dissociation [21].

However, even the small addition of the antisymmetric vibrations  $\nu_6$  should lead to the rotation of the detached ion as a whole<sup>1</sup>. Note also that the ion has one vibrational mode and two degenerate rotational degrees of freedom between which the excess of the internal energy of the ions is shared. However, the energy is not equidistributed over the degrees of freedom in this case. The rotation effect should shift the Morse curve upwards and rightwards with an increase in the rotational quantum number  $J$  (see Fig. 5, which is similar to Fig. 165 in [22]). According to the calculation in the HF/6-311G(d), the vibrational quantum in the ground state of the ion is 0.03 eV. The ion formed in the rotationally excited state  $J_k$  is metastable and can transit to the state  $J_i$  transferring a fraction of the rotational energy to the vibration of the Cl–Cl bond. The state  $J_i$  is unstable with respect to dissociation, see Fig. 5. Thus, even the diatomic negative ions formed under certain conditions can exhibit properties typical of multiatomic systems, in particular, can dissociate at the microsecond timescale with the formation of so called metastable ions.

---

<sup>1</sup> This is evident for a person who at least once attempts to throw a cigarette stub into a refuse bin: the stub usually flies with rotation.

An alternative explanation of the dissociation of the ions at the microsecond timescale is the tunneling of the chlorine atom through the centrifugal barrier appearing in the rotating ions. The choice between two explanations requires accurate calculations of the probabilities of the rovibronic transitions in the ion and the tunneling of the chlorine atom.

## Conclusion

It has been shown experimentally that the dissociation of at least some of the ions formed after the dissociation of  $\text{Cl}_2^-$  molecular ions occurs at the microsecond timescale. This delay is assumingly attributed to the rotational excitation of ions. If this interpretation is valid, the experimental estimate of the time of rovibronic relaxation in the ion has been obtained.

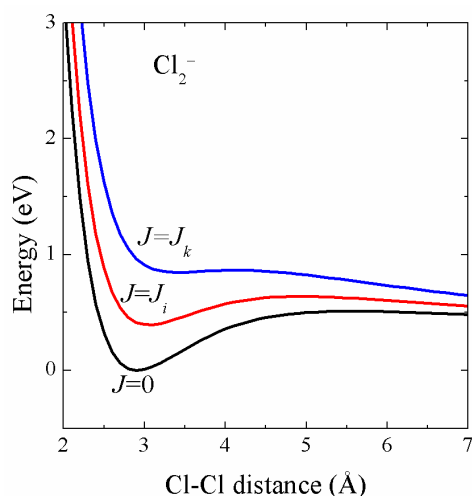


Fig. 5. Illustration of the effect of the rotational excitation on the potential energy curves of the  $\text{Cl}_2^-$  ion.

## References

- [1] <http://cfpub.epa.gov/ncer/abstracts/index.cfm/fuseaction/display.abstractDetail/abstract/5813/report/F>.
- [2] L. Sanche and G. J. Schulz, *J. Chem. Phys.* 58 (1973) 479.
- [3] P.D. Burrow and K.D. Jordan, *Chem. Phys. Lett.* 36 (1975) 594.
- [4] P.D. Burrow, A. Modelli, N.S. Chiu, K.D. Jordan, *Chem. Phys. Lett.* 82 (1981) 270.
- [5] K.A.G. MacNeil and J.C.J. Thynne, *Trans. Faraday Soc.* 64 (1968) 2112.
- [6] J. P. Johnson, L. G. Christophorou, and J. G. Carter, *J. Chem. Phys.* 67(1977) 2196.
- [7] H. Drexel, W. Sailer, V. Grill, et al., *J. Chem. Phys.* 118 (2003) 7394.
- [8] J. K. Olthoff, J. A. Tossel, and J. H. Moore, *J. Chem. Phys.* 105 (1985) 5627.
- [9] Yu. V. Vasil'ev, V. G. Voinov, D. F. Barofsky, and M. L. Deinzer, *Int. J. Mass Spectrom.* 277 (2008) 142.
- [10] E. Illenberger, H. Baumgartel, and S. Suzer, *J. Electron Spectr. Rel. Phen.* 33, 123 (1984).
- [11] S. W. Staley and J. T. Strnad, *J. Phys. Chem.* 98 (1994) 116.
- [12] E.C. M. Chen, J. R. Wiley, C. F. Batten, and W. E. Wentworth, *J. Phys. Chem.* 98 (1994) 88.
- [13] S. A. Pshenichnyuk, I. A. Pshenichnyuk, E. P. Nafikova, and N. L. Asfandiarov, *Rapid Commun. Mass Spectrom.* 20 (2006) 1097.
- [14] S. A. Pshenichnyuk, N. L. Asfandiarov, W. Barszczewska, et al., *Nat. Inst. Fusion Sci., Res. Report of NIFS-DATA Series, NIFS\_DATA*, 92 (2005) 1.
- [15] J. H. Beynon, *Mass Spectrometry and Its Applications to Organic Chemistry*, Elsevier, Amsterdam, 1960, pp. 258-267.
- [16] L. G. Christophorou and J. K. Olthoff, *J. Phys. Chem. Ref. Data* 28 (1999) 131.
- [17] W. C. Tam and S. F. Wong, *J. Chem. Phys.* 68 (1978) 5626.
- [18] P. Tegeder and E. Illenberger, *J. Phys.: Conf. Ser.* 86 (2007) 012007.1.
- [19] P. Koloren and J. Horacek, *Phys. Rev. A* 74 (2006) 062703; I. Fabrikant, T. Leininger, and F. X. Gadña, *J. Phys. B* 33 (2000) 4575.
- [20] M.W. Ruf, S. Barsotti, M. Braun, et al., *J. Phys. B* 37 (2004) 41.

- [21] G. Herzberg, *Molecular Spectra and Molecular Structure* Toronto, New York, London, 1966; Mir, Moscow, 1969, pp. 445-451.
- [22] G. Herzberg, *Molecular Spectra and Molecular Structure, I. Diatomic Molecules*, New York, 1939; Mir, Moscow, 1949, pp. 305-312.

# Study of Pressure and Temperature Influence on the Nitrogen Plasma under Discharge and Post-Discharge Conditions

I. Soural, F. Krčma, V. Mazánková

Faculty of Chemistry, Brno University of Technology, Purkyňova 118, Brno 612 00, Czech Republic

e-mail: xcsoural@fch.vutbr.cz

## Abstract

In presented work, the decaying plasma in Pyrex tube was studied by the optical emission spectroscopy. DC discharge in flowing regime was used. The emission of three nitrogen spectral systems (1<sup>st</sup> and 2<sup>nd</sup> positive and 1<sup>st</sup> negative) was studied in time evolution for pressures of 500–5000 Pa and two wall temperatures: ambient and liquid nitrogen. Results showed that all three nitrogen systems had their intensity maxima in the afterglow part. These maxima decreased with the increase of pressure for all systems, and moved to the later decay time. Based on the band intensities, the relative vibrational populations of corresponding states were calculated. While populations of N<sub>2</sub>(B), and N<sub>2</sub><sup>+</sup>(B) states were higher at the ambient wall temperature, the populations of N<sub>2</sub>(C) state were higher at the decreased wall temperature. Besides the nitrogen bands, some weak bands, mainly originating at NO(A,  $\nu = 0$ ) level, were observed. Their intensities increased with the increase of pressure, and they showed the same temperature dependence as the nitrogen 2<sup>nd</sup> positive system.

## Introduction

The discharges and post-discharges in nitrogen are subjects of many studies during last more than 50 years. Processes in the active discharge and mainly in the post-discharge are dependent on many conditions, such as temperature, pressure, power, presence of various traces and admixtures and wall processes [1–3]. The detail knowledge about these processes is needed not only for the basic understanding, but it forms a great input for a spread number of applications as nitriding [4], surface treatment of various materials, and sterilization [5]. The post-discharge conditions, where nearly no ion bombardment is observed and also neutral gas temperature is close to the ambient one, are very promising mainly for the treatment of temperature sensitive materials as polymers [6].

The first period of any nitrogen post-discharge is characterized by a strong decrease of the light emission. It takes a few milliseconds, and electron ion recombination is the main process during this period. After that, the energy in the system is conserved by dissociated molecules and various metastables. In case of nitrogen, a specific effect can be observed. The intensity of emitted light significantly increases for period of about 20 ms with maximum at about 10 ms depending on the experimental conditions. This effect is known as a pink afterglow by its characteristic color or nitrogen short live afterglow by its time duration. The strong emission of the nitrogen molecular ion bands (the nitrogen first negative spectral system) is characteristic for this post-discharge period [7]. If the pink afterglow is not created or after that, the yellow-orange color is characteristic for the nitrogen afterglow and it is known as Lewis-Rayleigh afterglow [8].

The electron concentration strongly increases during the nitrogen pink afterglow due to various collisionally induced ionization processes [9] and thus the electron concentration should reach relatively high value (in order of percents with respect to their concentration in the active discharge). But there is no external source of energy and thus these electrons are relatively cool (about 0.8 eV [10]). They are not able ionize the neutral species directly, and also their ability for heavy particles excitation is limited. The pink afterglow creation mechanisms are not fully understood up to now, but many studies confirmed that energy transfer reactions among various metastables (mainly highly vibrationally excited ground state and electronically excited A, a, a') are the ionization precursors [11].

The effect of the nitrogen pink afterglow can be studied in pure nitrogen or in its mixtures with noble gases with high purity. Various traces (especially carbon and oxygen) quench it [12] so very high purity of incoming nitrogen is necessary to use. The experimental [13] as well as theoretical [14] studies of nitrogen post-discharge are carried out mainly at low pressures up to a few hundreds Pascals, however, some experimental data are available at atmospheric pressure [15], too. The presented paper significantly extends the contemporary knowledge of nitrogen post-discharge at pressures of a few kPa, and the effect of wall temperature is included, too.

## Experiment

The experiments were carried out in the flowing regime using device schematically showed in Fig. 1. A Pyrex discharge tube (i.d. of 12 mm) with molybdenum electrodes in the side arms was continuously pumped by a rotary oil pump separated by a liquid nitrogen trap. Nitrogen (purity of 99.999 %) was further cleaned by an Oxiclear trap, where trace oxygen, CO<sub>2</sub> and water were removed. Gas flow was regulated by a Bronkhorst mass flow controller. Nitrogen flow was varied from 122 to 1200 sccm to keep constant gas velocity of 4 m/s in the whole studied pressure range. The discharge power of 290 W was kept in the whole pressure range of 500–5000 Pa.

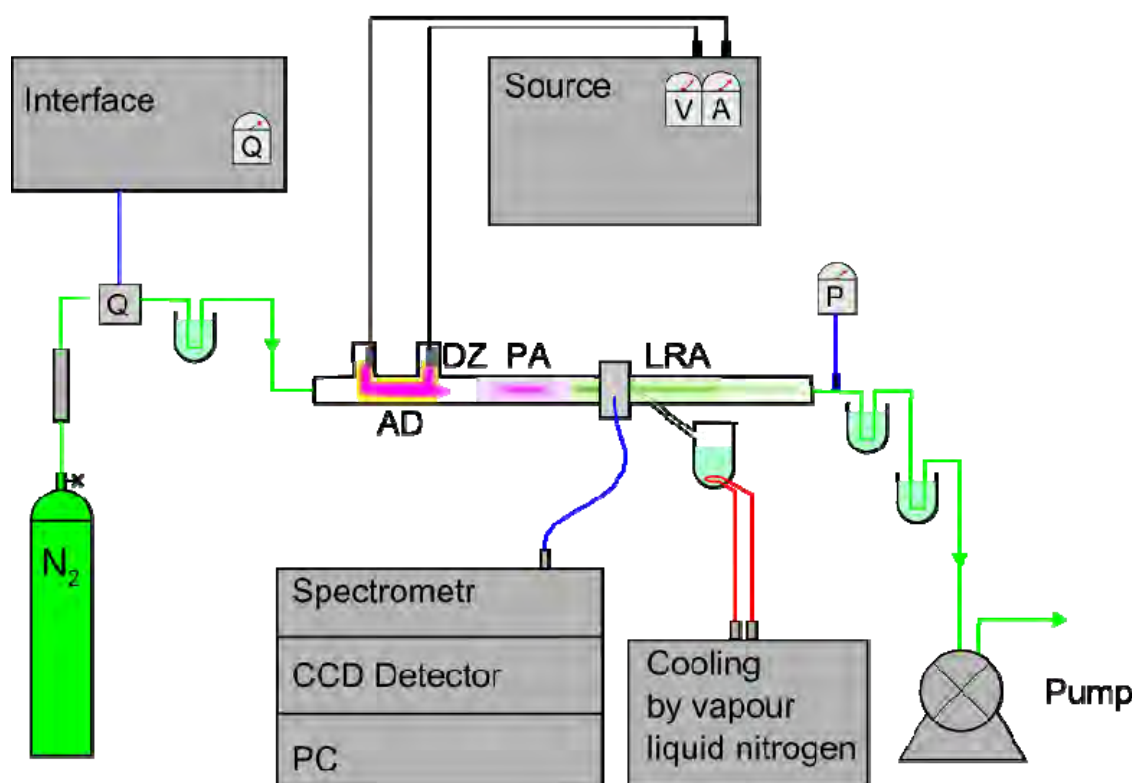


Fig. 1. Schematic drawing of the experimental setup (AD – active discharge, DZ – dark zone, PA – pink afterglow, LRA – Lewis-Rayleigh afterglow [4]).

A movable cooling device containing an optical fiber holder was installed on the Pyrex tube at its post-discharge part. Due to this fact, the post-discharge observations at decreased wall temperatures started at the decay time of 15 ms. The cooling was done by liquid nitrogen vapor which flow was regulated by liquid nitrogen evaporation. Distances along the tube were converted to post-discharge times using the state equation of the ideal gas. The numeric simulation of nitrogen first positive 2-0 band showed that temperature inside the plasma was around 150 K at the cooling [16].

Optical emission spectra were measured in interval from -2 to 50 cm with respect to the end of the active discharge in case of laboratory temperature, and from 11 to 50 cm at decreased wall temperature. These distances correspond to post discharge times -5–137 ms, and 15–150 ms, respectively. The spectra were measured by Jobin Yvon TRIAX 550 spectrometer with a CCD detector. The 300 gr/mm grating was used for the spectra acquisition in the range of 320–780 nm.

The relative populations of nitrogen N<sub>2</sub>(B,  $\nu = 2-20$ ), N<sub>2</sub>(C,  $\nu = 0-4$ ), and N<sub>2</sub><sup>+</sup>(B,  $\nu = 0-6$ ) states were calculated from the band head intensities of the nitrogen first, and second positive, and first negative systems using constants given by *Gilmore* [17]. The intensities were corrected for the spectral response of measuring spectrometer that was obtained using the standard Oriel lamp.

## Results and discussion

The relative populations at selected vibrational levels are shown in Figs. 2–4. The pink afterglow effect, i.e. the increase of population during the post discharge, can be seen at all observed molecular states at the ambient wall temperature, and it has nearly the same shape for all three states. The decay time of the maximal pink afterglow population is nearly constant of about 8 ms at pressures below 2000 Pa. The non-linear shift to the later decay times can be observed with the pressure increase from 2000 to 5000 Pa. The maximal pink afterglow populations is reached at pressures of 1000–1500 Pa; the populations at PA maximum is about one order lower in case of neutral nitrogen states, and about one and half order lower in molecular ion at lower pressure (500 Pa). This decrease can be explained by lower density as well as by lower collision frequency between metastables that are responsible for the PA creation. The population decrease at higher pressures and its shift to the later decay times is probably a result of non radiative quenching processes, both of radiative state, and metastables. Due to this fact, the higher populations of all states can be seen at later Lewis-Rayleigh afterglow. This can be seen up to the end of our experiments at 140 ms in case of neutral nitrogen states, and up to about 80 ms for molecular ion. The molecular ion populations are very low at later LRA, and they are decreasing with the increase of gas pressure.

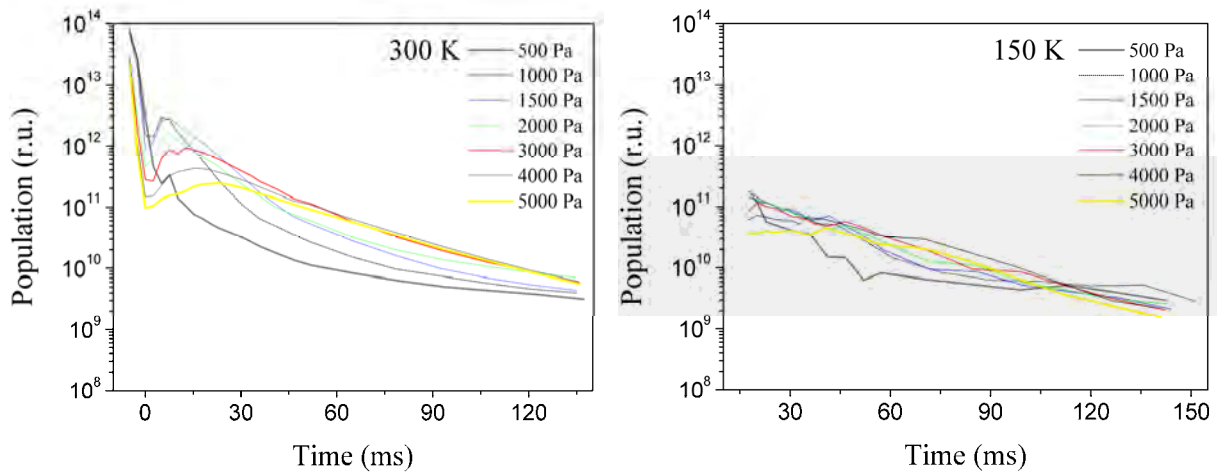


Fig. 2. Time dependence of population  $N_2(B, v = 2)$  at two temperatures and various gas pressures.

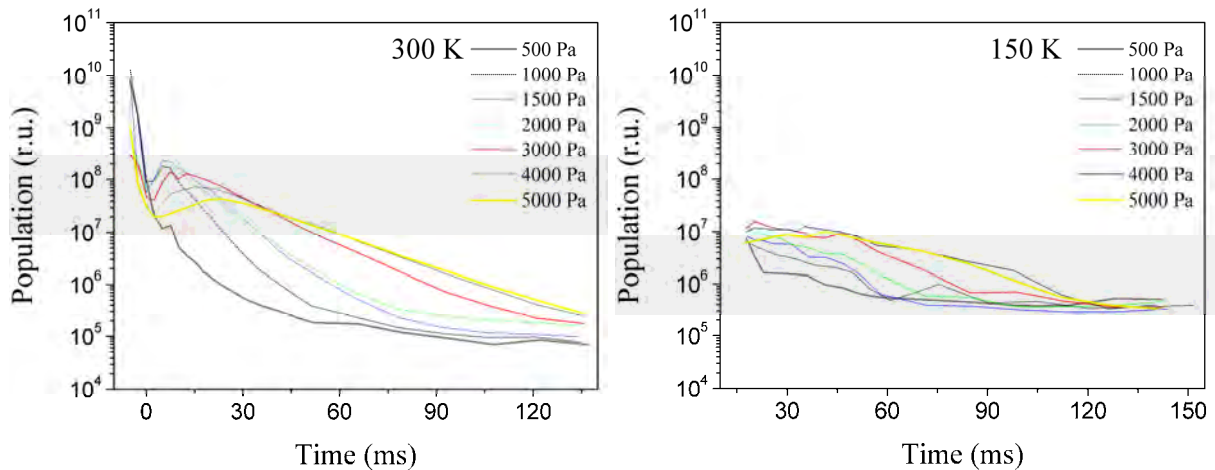


Fig. 3. Time dependence of population  $N_2(C, v = 0)$  at two temperatures and various gas pressures.

The results at the decreased wall temperature are significantly different. As it was pointed in the experiment description, we were not able to collect the spectra during the first 15 ms of the post-discharge. Due to this fact, we were able to recognize something like PA maximum at the highest pressure, only. The pressure dependencies of vibrational populations of neutral nitrogen states are very similar as at the ambient wall temperature up to about 110 ms. The decrease of populations with the pressure increase can be seen at the decay times later than 110 ms. In the case of molecular ion, the pressure dependence character changes at the decay time of about 50 ms, i.e. also earlier with respect

to the situation at the ambient wall temperature. These results are probably connected to the increase of plasma density at the decreased temperature that is followed by the increase of collision frequency, and consequent increase of quenching efficiency. The other process, see below, support this result, too.

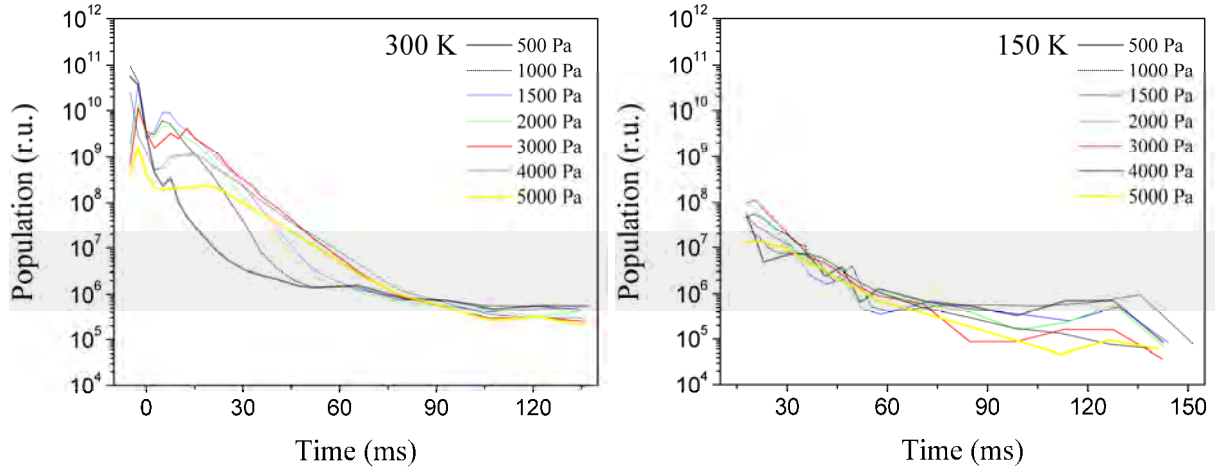


Fig. 4. Time dependence of population  $N_2^+(B, v = 0)$  at two temperatures and various gas pressures.

Although we used nitrogen of high purity that was further cleaned to suppress the impurities, as we pointed in the experimental section, the weak bands of  $NO^\beta$  system (originating at level 0) were recorded. The intensity of 0–9 band of this spectral system is depicted at Fig. 5 at the same conditions as for the nitrogen populations. It can be seen that intensity of  $NO^\beta$  shows something like PA at the ambient wall temperature at all pressures, and this dependence is very similar to the dependence of the neutral nitrogen populations. After PA, i.e. at decay times later than 30 ms up to the end of the post-discharge, the  $NO^\beta$  intensities are increasing with the increase of pressure, but they are more or less independent on the decay time. On the other hand, the  $NO^\beta$  intensity decreases with the increase of pressure at decreased wall temperature, and the intensity is time independent since about 60 ms.

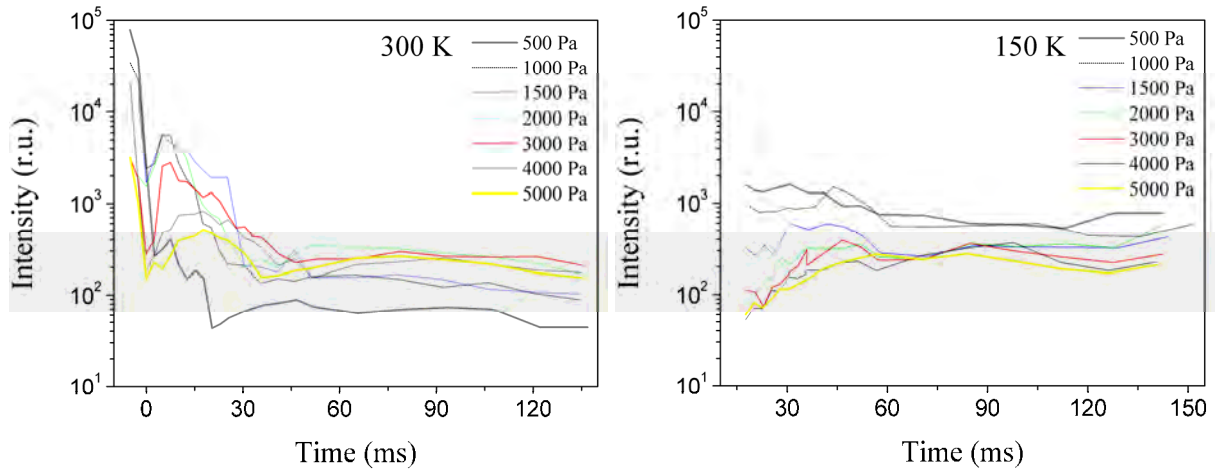


Fig. 5. Time dependence of  $NO^\beta$  0–9 band head at two temperatures and various gas pressures.

The explanation of these results can be based on the  $NO$  species kinetics during the post-discharge. The  $NO^\beta$  spectral system is excited by three body recombination of nitrogen and oxygen atoms in the ground state. The  $NO$  molecules in their ground state can be effectively redissociated by collisions with neutral nitrogen metastables and thus the atomic oxygen concentration during the whole post-discharge is nearly constant. The concentration of atomic nitrogen decreases very slowly [7] and thus no significant decrease of  $NO^\beta$  intensity can be observed at later decay times. The pressure dependence of  $NO^\beta$  intensities, that have the opposite character at the studied temperatures, is probably connected to some resonances in energy transfer reactions or in heterogeneous reactions of

oxygen atoms. The NO redissociation leads to the decrease of nitrogen metastables that is reflected in the decrease of radiative states populations. The detailed analysis of these results should be done using the numeric kinetic model.

### Conclusions

This work was focused on the study of nitrogen post-discharge as a function of pressure, and wall temperature. The results showed that nitrogen pink afterglow shifts its maximum to the later decay times with the increase of pressure over 2000 Pa; no change was observed at lower pressures. The pink afterglow maximal populations are observed at pressures of 1000–1500 Pa. The pink afterglow effect was not observed at decreased wall temperature except the highest pressure due to the construction of our experimental device. The dependencies of nitrogen states populations as well as NO<sup>β</sup> bands observation were explained by the elementary kinetic processes. The full understanding of the experimental results will be done using the post-discharge kinetic model in the future.

### Acknowledgment

This work was supported by the Czech Science Foundation 202/08/1106 and 104/09/H080.

### References

- [1] M.E. Pillow, A.J. Rogers: *Proc. Phys. Soc.* 81 (1963) 1034.
- [2] J. Hubeňák, F. Krčma, *J. Phys. D: Appl. Phys.* 33 (2000) 3121.
- [3] V. Kanický, V. Otruba, A. Hrdlička, P. Krásenský, F. Krčma, *J. Atom. Anal. Spectrom.* 22 (2007) 754.
- [4] S. Bockel, T. Belmonte, H. Michel, D. Ablitzer, *Surf. Coat. Technol.* 97 (1997) 618.
- [5] C. D. Pintassilgo, J. Loureiro, V. Guerra, *J. Phys. D: Appl. Phys.* 38 (2005) 417.
- [6] T. Belmonte, C. Pintassilgo, T. Czerwiec, G. Henrion, V. Hody, J. M. Thiebaut, J. Loureiro, *Surf. Coat. Technol.* 200 (2005) 26.
- [7] J. Loureiro, P.A. Sá, V. Guerra, *J. Phys. D: Appl. Phys.* 39 (2006) 122.
- [8] K.D. Bayes, G.B. Kistiakowsky, *J. Chem. Phys.* 32 (1960) 992.
- [9] F. Paniccia, C. Gorse, M. Cacciatore, M. Capitelli, *J. Appl. Phys.* 61 (1987) 3123.
- [10] C.D. Pintassilgo, G. Alcouffe, G. Cernogora, J. Loureiro *Proc. ICPIG XXVIII*, Praha 2007.
- [11] L.G. Piper, *J. Chem. Phys.*, 88 (1988) 231.
- [12] F. Krčma, V. Mazánková, I. Soral, *Publ. Astronom. Observatory Belgrade* 82 (2007) 133.
- [13] V. Mazankova, K. Krčma, I. Bockova, I. Soral, V. Guerra, *Proc. SPIG XXV*, 1722, Novi Sad 2010.
- [14] V. Guerra, P. A. Sa, J. Loureiro, *Eur. Phys. J. – Appl. Phys.* 28 (2004) 125.
- [15] F. Clement, B. Rouffet, J-P. Sarrette, S. Cousty, A. Ricard, M. Yousfi, E. Panousin, B. Held, *Proc. ISPC IXX*, 645, Bochum, 2009.
- [16] F. Krčma, V. Mazánková, I. Soral, M. Šimek, *Proc. ICPIG XXVIII*, 1722, Praha 2007.
- [17] F.R. Gilmore, R.R. Laher, P.J. Espy, *J. Phys. Chem. Ref. Data* 21 (1992) 1005.

# Using of Plasma Torch with Gerdien Arc for Plastic Treatment

M. Hlina, T. Kavka, M. Korad, M. Hrabovsky, V. Kopecky  
Institute of Plasma Physics, ASCR, Za Slovankou 3, Prague 8 183 00, Czech Republic

e-mail: hlina@ipp.cas.cz

## Abstract

Gasification of plastics was carried out in the reactor equipped with hybrid gas-water stabilized DC plasma torch. The plasma torch features relatively low mass flow rate of plasma and very high energy that leads to the low dilution of produced gases that is in good accordance with results which revealed high concentrations of hydrogen and carbon monoxide.

**Keywords:** Plasma, gasification, plastics, DC plasma torch.

## Introduction

Great effort is made to develop high efficiency technologies for the utilizing of plastic waste due to declining landfill capacity as well as increasing cost of petroleum products. There are many methods for plastic waste treatment – from simple incineration with heat production to catalytic depolymerization. The plasma gasification of plastics might one of the possible ways especially in cases of excess of electricity.

Produced gas (syngas – synthetic gas) is composed mostly of CO and H<sub>2</sub> - the higher content of these two components, the better. Principle problem of common gasification technologies, based on an autothermal process utilizing reaction between a heated carbon source with oxygen, air or steam, consists in limited possibility of control of gas quality and production of tar, which is formed from complex molecules of hydrocarbons created during the process. The necessity of production of clean syngas with controlled composition has led to technologies based on allothermal processes with external energy supply for materials gasification. Plasma is a medium with the highest energy content and thus substantial lower plasma flow rates are needed to supply sufficient energy for gasification compared with other media used for this purpose. This results in minimum contamination and dilution of produced syngas by plasma gas and easy control of syngas composition.

Thermal plasma offers possibility of decomposition of organic materials by pure pyrolysis without addition of oxygen, or with stoichiometric amount of oxygen added for complete gasification of carbon present in treated material. Oxygen needed for complete gasification of materials can be supplied either by addition of O<sub>2</sub>, air, steam or CO<sub>2</sub>. Utilization of air is the cheapest option but it results in dilution of produced syngas by nitrogen. Gasification with CO<sub>2</sub> can be used for transformation of CO<sub>2</sub> to CO. Energy needed for dissociation of CO<sub>2</sub> is deposited in calorific value of produced syngas. The process thus can act as energy storage – electrical energy is transferred to plasma energy and then stored in produced syngas. This can be used for storage of energy produced by new renewable sources of electrical energy that are often characterized by large fluctuations of energy production. Moreover, the process offers utilization and transformation of CO<sub>2</sub> produced by industrial technologies.

Plasma gasification of plastics has been studied in the recent years in several papers [1, 2]. The experiments performed up to now were made with relatively small scale systems. This paper presents experimental results obtained in medium scale thermal plasma gasification reactor equipped by the gas/water DC plasma torch [3] with arc power ~ 130 kW. Gasification of wood was made using O<sub>2</sub> and CO<sub>2</sub> as oxidizing media.

## Plasma Gasification setup

The simplified scheme of experimental system is shown in Fig. 1. The water cooled walls of the reactor are separated from the inner reactor volume by 400 mm thick sandwich ceramic walls for reduction of power loss. Temperature of inner surface of ceramic insulation was measured in several positions in the reactor and also in connecting ducts. The total power loss to the walls was determined from calorimetric measurements on cooling circuits. Material is supplied into the reactor by screw feeder with controlled feed rate.

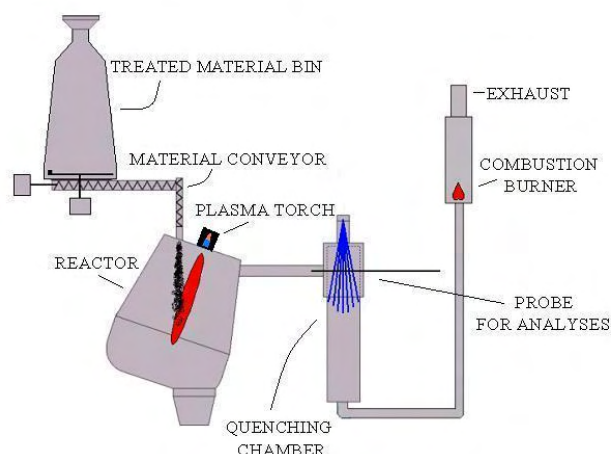


Fig. 1. Simplified scheme of system

Gases for control of the process are supplied into the reactor volume in several positions. O<sub>2</sub> and CO<sub>2</sub> are supplied for complete gasification of materials with surplus of carbon, Ar is used as a sampling gas for determination of syngas flow rate from measured gas composition, and nitrogen is used to flow hydrogen out of the reactor to reduce the danger of explosion before opening. The plasma input point is in central position at the top of the reactor. Material particles fall into plasma jet at a location about 300 mm downstream of plasma input. The output of gas is positioned close to the plasma input and thus outgoing gas passes high temperature region with high level of UV radiation. Gaseous reaction products flow into the quenching chamber where their temperature is reduced to 300 °C in water spray with automatically controlled flow rate. The gas then flows into the combustion chamber at the outlet of the system.

Plasma torch with hybrid gas/water stabilization of arc [3] is attached at the top of the reactor (Fig.2).

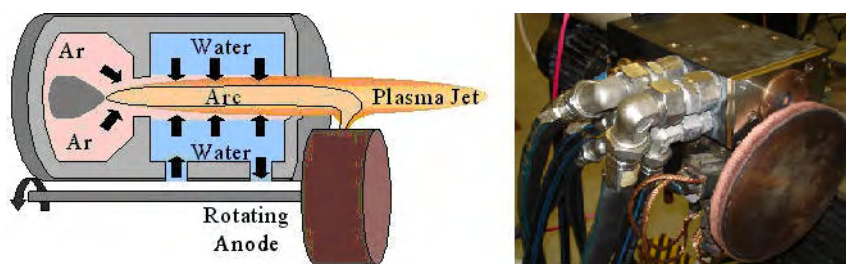


Fig. 2. Schematics and real view of the gas/water DC plasma torch

The torch generates an oxygen-hydrogen-argon plasma jet with extremely high plasma energy (~150 MJ/kg) and temperature (bulk plasma temperature ~ 15 500 K). Plasma gas is a mixture of steam (0.3 g/s) with small amount of argon (6 slm). Arc power was set up to 100 kW (250 A, torch efficiency ~ 60 %). Due to the principle of arc stabilization by a water vortex the flow rate of plasma gas is very low, plasma enthalpy and plasma temperature is very high. This is the main difference with gas plasma torches using steam as plasma gas with temperatures below 8 000 K. The utilization of high energy, high temperature plasma is advantageous for the adjustment of a high reaction temperature and easy control of syngas composition.

The measuring system included monitoring of plasma torch operation parameters, temperatures in several positions inside the reactor and calorimetric measurements on cooling water loops. The

temperature of the inner wall of the reactor was measured in six positions by thermocouples. The flow rate of reaction gas was measured using a Pitot tube flow meter and it was also determined from the measured gas composition from argon concentration. The gas temperature was measured at the input and output of the quenching chamber by thermocouples. The composition of gases is measured on line in the duct connecting reactor with quenching. The sampling tube was cooled by the water spray at the input of the quenching chamber. The main gas analysis was made by a quadrupole mass spectrometer Pfeiffer Vacuum Omnistar GSD. As the gas contains some amount of steam, the freezing unit was connected into the gas sample circuit.

## Results and discussion

There were polyethylene (PE) pellets with diameter of 3 mm and crushed plastic waste (CPW, irregular particle size differs from 1 mm to 6 mm with 1mm thickness) used for the gasification. The crushed plastic waste was composed of PE (89 %), polypropylene (PP - 10 %) and polyethylene terephthalate (PET – 1%). For all materials gasification by reaction with CO<sub>2</sub> or with mixture of CO<sub>2</sub> and O<sub>2</sub> was studied. The gasification of PE pellets was performed at two different feed rates and the gasification of CPW could be interpreted just for a single feed rate. Table 1 presents basic experimental parameters, composition of syngas measured by mass spectrometer, calculated flow rate of syngas (for that the known amount of argon was added into the reactor) and carbon yield. The carbon yield shows ratio of amount of carbon in syngas to total amount of input carbon. The concentration values in the Table 1 are calculated as average in stable region for each set of parameters when also stable conditions in the reactor were achieved. The reactor and syngas temperatures ranged between 1 200 °C and 1 400 °C.

Tab. 1. Basic experimental parameters, composition of syngas and derived values

|                              |          | TREATED MATERIAL |      |      |      |      |
|------------------------------|----------|------------------|------|------|------|------|
|                              |          | PE               | PE   | PE   | CPW  | CPW  |
| <b>INPUT PARAMETERS</b>      |          |                  |      |      |      |      |
| Flowrate of treated material | kg/h     | 5.3              | 10.6 | 10.6 | 11.2 | 11.2 |
| CO <sub>2</sub> (added)      | slm      | 210              | 210  | 210  | 300  | 300  |
| O <sub>2</sub> (added)       | slm      | 80               | 80   | 80   | 0    | 0    |
| Ar (added)                   | slm      | 0                | 87   | 0    | 0    | 87   |
| Power available              | kW       | 48.4             | 52.1 | 59.3 | 37.1 | 39.2 |
| <b>GAS COMPOSITION</b>       |          |                  |      |      |      |      |
| CO                           | vol. %   | 39.2             | 37.8 | 45.4 | 45.0 | 45.7 |
| CO <sub>2</sub>              | vol. %   | 21.0             | 16.2 | 12.6 | 6.8  | 2.9  |
| H <sub>2</sub>               | vol. %   | 37.1             | 28.2 | 39.8 | 46.5 | 39.3 |
| CH <sub>4</sub>              | vol. %   | 0.1              | 0.0  | 0.1  | 0.1  | 0.0  |
| O <sub>2</sub>               | vol. %   | 1.4              | 1.6  | 1.2  | 1.1  | 1.2  |
| Ar                           | vol. %   | 1.3              | 16.2 | 0.9  | 0.7  | 10.8 |
| <b>DERIVED VALUES</b>        |          |                  |      |      |      |      |
| Flowrate (from Ar derived)   | slm      | 458              | 575  | 654  | 903  | 858  |
| Total outlet                 | g/min    | 449              | 649  | 578  | 690  | 750  |
| Total inlet                  | g/min    | 644              | 888  | 732  | 805  | 960  |
| Mass comparison              | (OUT/IN) | 0.70             | 0.73 | 0.79 | 0.86 | 0.78 |
| Carbon yield                 | (OUT/IN) | 0.79             | 0.63 | 0.77 | 0.78 | 0.70 |

High H<sub>2</sub> and CO concentrations were obtained in all runs while the concentrations of CO<sub>2</sub> and CH<sub>4</sub> stayed quite low. The sum of H<sub>2</sub> and CO ranged from 76 to 94 % when Ar supplied just because of the calibration of the flow rate of syngas (Ar (added) – Table 1.) is not taken into account. Higher CO<sub>2</sub> concentrations in runs with PE in general are probably caused by slightly higher amount of oxidizing media (CO<sub>2</sub> and O<sub>2</sub>) than it would agree with stoichiometric amount. O<sub>2</sub> content was close to 0 during the whole measurement. It is in good accordance with theory. Also CH<sub>4</sub> concentrations are almost

negligible that is caused by high reaction temperatures; CH<sub>4</sub> is formed under 600 °C at atmospheric pressure. The amount of carbon transferred into gas phase revealed gasification approximately at the level of 75 % that means 25 % of treated material forms especially carbon soot and water. This is quite high value due to our previous experiments [4,5] and it is probably caused by much bigger particle size of PE and CPW which strongly influenced chemical kinetics [6].

### **Conclusions**

The plasma gasification of plastics was studied in reactor equipped by hybrid gas/water plasma torch. High enthalpy, high temperature and low flow rate plasma jet was generated in the hybrid torch. Synthesis gas with high caloric value, high content of hydrogen and carbon monoxide and low concentration of other species was produced. The main advantage of the use of the plasma torch with water-stabilized arc is in the composition and low flow rate of plasma. The content of other gases commonly present in gas-stabilized systems is very low. Lower values of carbon yield are related to less intensive energy transfer to the material due to less intensive mixing of particles with plasma flow and due to lower ratio of particle surface to its mass

### **Acknowledgement**

The authors gratefully acknowledge the support by the Grant Agency of the Czech Republic under the project No. P 205/11/2070.

### **References**

- [1] H. Sekiguchi, T. Orimo, Gasification of polyethylene using steam plasma generated by microwave discharge, *Thin Solid Films* 457, 44–47, 2004
- [2] R. Kezelis, V. Mecius, V. Valinciute, V. Valincius, Waste and biomass treatment employing plasma technology, *J. of High Temp. Mat. Process.* 8, 2, 273-282, 2004
- [3] M. Hrabovský, V. Kopecký, V. Sember, T. Kavka, O. Chumak, M. Konrád, Properties of Hybrid Water/Gas DC Arc Plasma Torch, *IEEE Trans. on Plasma Science* 34, Issue 4, Part 3, 1566- 1575, 2006
- [4] M. Hrabovsky, M. Hlina, M. Konrad, Thermal Plasma Gasification of Biomass for Fuel Gas Production, *High Temperature Material Processes*, 13, 299-313, 2009
- [5] M. Hrabovsky, M. Konrad, V. Kopecky, Pyrolysis of wood in arc plasma for syngas production, *High Temperature Material Processes*, 10, 557-570, 2006
- [6] S. Dresvin, J. Amouroux, S. Zverev, Heat transfer of particles in thermal plasma, *Proc. 17th Int.Sym.on Plasma Chemistry*, Toronto, Canada, August 7-12 (2005) 813-814, 2005

# Sequential penning ionization in doped $^4\text{He}$ nano droplets

M. Daxner<sup>1</sup>, H. Schöbel<sup>1</sup>, P. Bartl<sup>1</sup>, C. Leidlmair<sup>1</sup>, S.Zöttl<sup>1</sup>, S. Denifl<sup>1</sup>, T. D. Märk<sup>1</sup>,  
P. Scheier<sup>1</sup>, Daniel Spangberg<sup>2</sup>, Andreas Mauracher<sup>2</sup> and D. K. Bohme<sup>3</sup>

<sup>1</sup>Institute of Ion Physics and Applied Physics, University of Innsbruck, Innsbruck, Austria

<sup>2</sup>Department of Materials Chemistry, Uppsala University, SE-751 21 Uppsala, Sweden

<sup>3</sup>Department of Chemistry, York University, Toronto, Canada

e-mail: c7441077@uibk.ac.at

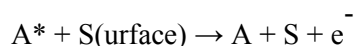
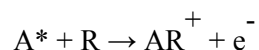
## Abstract

We report the observation of doubly charged ions caused by collision of excited  $^4\text{He}$  atoms with ions. Doping superfluid  $^4\text{He}$ -Cluster and exposing them to electrons enhances the formation of doubly charged iodine atoms at the threshold for the production of two metastable He-atoms. These observations point toward a novel ionization process where doubly-charged ions are produced by sequential Penning ionization. We observed also changes in the cluster distribution of Argon within He-Clusters, due to coulomb explosion, at the threshold for the production of two or three metastable He-atoms [1].

**Keywords:** Penning - Ionization, excited Helium, Methyl iodine,

## Introduction

In 1927 Frans Michel Penning suggested an ionization process due to the inelastic scattering between a target atom or molecule R and metastable atoms  $A^*$  (in our case  $\text{He}^*$ ), when he was studying discharge phenomena in rare gases [2].



Now known as Penning Ionization, this process results in the production of a radical cation plus an electron and can trigger the ionization of activated gases in high temperature chemistry and plasma physics. Nanodroplets are a perfect environment to investigate chemical reactions under controlled conditions. Atoms or molecules that collide with a droplet are picked up and transferred in most cases to its center [3]. Due to fast evaporation of He atoms, a stable temperature of 0.37K is obtained inside the droplet and the dopants are effectively cooled [4]. When these droplets are exposed to electrons at energies below the ionization energy of He (24.6eV), ionization with metastable He ( $2^3\text{S}$  with 19.8eV excitation energy) becomes the dominant ionization process [5]. Electrons with more than twice the the excitation energy of He can excite more than one helium atom [6].

## Experimental setup

A cluster source generates the helium cluster beam by supersonic expansion. The beam is doped with an analyte within the pick-up chamber. In the next step the beam is ionized by electron ionization and the mass spectrum is recorded with an orthogonal time-of-flight mass spectrometer with high mass resolution (5000 FMHW).

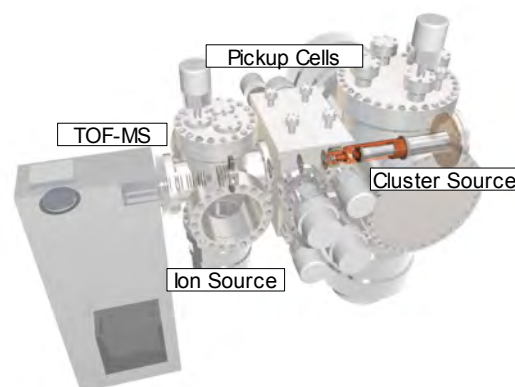


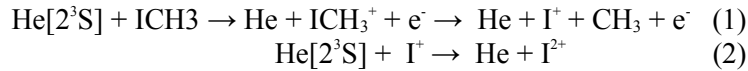
Fig.1. Experimental Setup of CLUSTOF

## Results and discussion

Stable and efficient pick-up conditions are achieved

at a constant pressure of 1mPa (for CH<sub>3</sub>I) and 5mPa (for Hg) and both materials have vapor pressures sufficiently high at room temperature, therefore not requiring additional heating. Electrons of variable energies from 0eV to 150eV are emitted by an tungsten filament. The energy resolution was about 1eV and the achieved accuracy of the ionization energies lies in the range of 0.3eV.

In the first step an electron with more than 39.6eV will excite 2 He to the metastable 2<sup>3</sup>S state. The first metastable He dissociatively ionizes the embedded methyl iodide and produce atomic and molecular cations (reaction 1). The final reaction (2) is exothermic too, since the second ionization energy of iodine is 19.13eV.



Measurements with He-droplets doped with mercury show similar results. We observed both isotopes doubly charged and with helium attached. Energy transfer from metastable He atoms to molecular or cluster ions may also lead to the formation of multiply charged ions by Penning ionization, albeit this

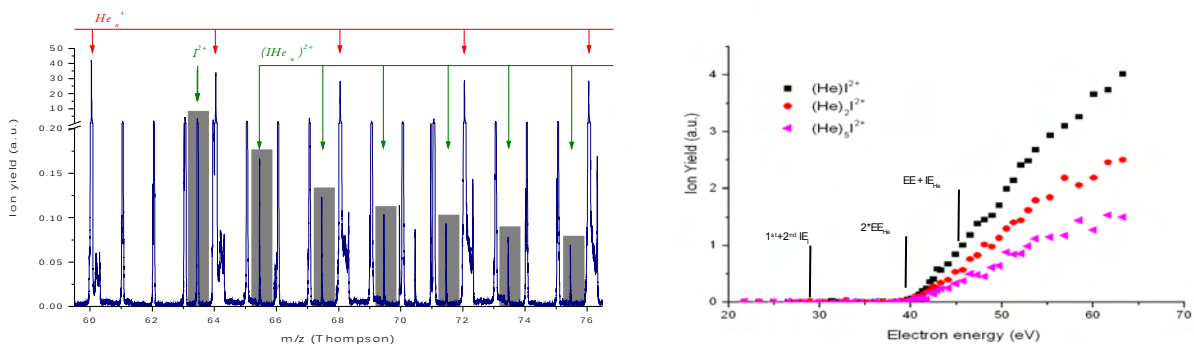


Fig 2. Left: High resolution mass spectrum with methyl iodide as the dopant. The spectrum was recorded at an electron energy of 70eV. The green arrows mark the doubly charged iodine peaks with attached helium.

Right: For electron energies higher than twice the excitation energy of He a new series of the adduct ions (IHe<sub>n</sub>)<sup>2+</sup> appears.

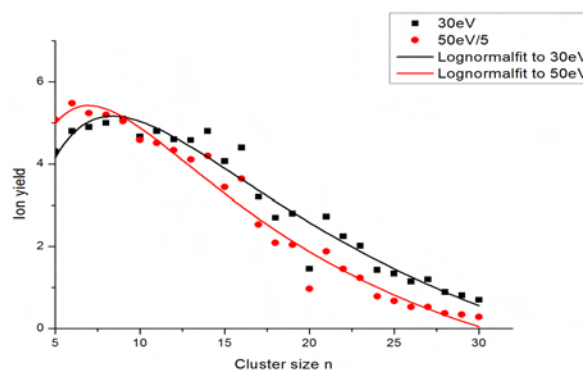


Fig 3. The cluster size distribution of Ar clusters formed within He droplets is shifted at electron energies above 40eV to the left, due to coulomb explosion.

transfer will often be accompanied by Coulomb explosion. As we have demonstrated with the Penning ionization of Ar-cluster ions, where this process leads to smaller cluster sizes due to asymmetric Coulomb explosion [7] (Fig.3).

The calculated polarizabilities of He and metastable He (2<sup>3</sup>S) reached values of 0.204Å<sup>3</sup> and 42.160Å<sup>3</sup>,

respectively. The high value of the polarizability of the excited He atom, more than 200 times that of the He ground state atom, causes a large attractive charge-induced dipole interaction and explains the substantial long-range attraction between metastable He ( $2^3S$ ) and an ion.

### Conclusions

Our experimental results clearly demonstrate evidence that Penning ionization can occur sequentially and lead to multiple ionization. The excitation energy of the metastable atom with its enhanced size and polarizability is effectively transported to an ion by long-range attraction and the excitation energy of the neutral is harvested then by the ion (produced already in an initial Penning ionization step). The process is both fundamental and universal and should also occur in different environments with different excited metastable species. In liquids both transport of the excited species to the ion as well as transport of the excitation energy via excitons may be possible. In solids only the latter process is operational.

### Acknowledgement

This work was supported by by the Fonds zur Förderung der wissenschaftlichen Forschung FWF, Wien (P 19073) and the University of Innsbruck via the “*Doktoratsstipendium aus der Nachwuchsförderung der Universität Innsbruck*”. SD gratefully acknowledges an APART grant from the Austrian Academy of Sciences. AM gratefully acknowledges a FWF Erwin-Schrödingerabroad fellowship (J 2973-N20). As holder of a Canada Research Chair in Physical Chemistry, DKB also thanks the support of the Canada Research Chair Program.

### References

- [1] H. Schöbel, ... Phys. Rev. Lett. (2010) in print
- [2] F. M. Penning, Naturwissenschaften, 15, 818 (1927).
- [3] F. Stienkemeier, J. Higgins, W. E. Ernst, and G. Scoles, Phys. Rev. Lett., 74, 3592 (1995).
- [4] S. Grebenev, J. P. Toennies, and A. F. Vilesov, Science, 279, 2083 (1998).
- [5] S. Deni, M. Stano, A. Stamatovic, P. Scheier, and T. D. Märk, J. Chem. Phys, 124, 054320 (2006)
- [6] F. Zappa, S. Deni, I. Mähr, A. Bacher, O. Echt, T. D. Märk, and P. Scheier, J. Am. Chem. Soc., 130, 5573 (2008).
- [7] H. Schöbel et al., to be published.

# Decomposition of VOC in Surface Dielectric Barrier Discharges Combined with in situ Photocatalysis

J. Vyhnalíková, F. Krčma, R. Balašítková, P. Dzik

Institute of Physical and Applied Chemistry, Faculty of Chemistry, Brno University of Technology, Purkyňova 118, Brno 612 00, Czech Republic

e-mail: xcvyhnalikova@fch.vutbr.cz

## Abstract

The problem of VOCs is one of the urgent tasks in contemporary research. Besides the classical techniques, the plasma assisted combustion methods are widely developed. The contemporary experiment was focused on the VOC decomposition in planar surface dielectric barrier discharges using alumina ceramics. The photocatalytic TiO<sub>2</sub> was prepared by various techniques based on ink-jet printing on inner side of discharge ceramic plates. The exhaust gas analysis was carried out by simple gas analyzer Testo 350-XL that was used for the detection of simple low molecular weight discharge products as CO, NO<sub>2</sub>, NO, H<sub>2</sub>, etc. The analyzes of discharge exhaust gas showed the high concentration of CO in decomposition of xylene. For measurements, the different layers of TiO<sub>2</sub> photocatalyzer were used. The higher concentrations of all low weight discharge products was observed then smoother layer was used and a strong frequency dependence of its efficiency was observed if cyclohexane was used.

**Keywords:** VOC decomposition, surface discharge, photocatalysis, TiO<sub>2</sub>

## Introduction

VOCs (volatile organic compounds) are organic chemical compounds that have vapor pressures under normal conditions high enough to significantly evaporate and enter the atmosphere. They are sometimes accidentally released from the industrial processes into the environment where they can damage soil and groundwater. Vapors of VOCs escaping into the air contribute significantly to the air pollution (e.g. they cause photochemical smog, and also contribute to the global warming). In recent years, their influence on the quality of indoor environment has started to be a serious task, too. Common artificial sources of VOCs include paint thinners, wood preservatives or cleaning solvents. Regarding the medical risks, it is known that many VOCs are toxic, several of them are known as human carcinogens [1].

VOC's vapors escaping into the air contribute significantly to the air pollution. Decomposition of VOC using atmospheric-pressure nonthermal plasma (NTP) technology has been a subject of extensive studies since the early 1990s. The first step evaluation of technical feasibility seemed to be successful at least in terms of destruction and removal efficiency (DRE) [2, 3].

Conventional techniques for the abatement of VOCs, such as thermal and catalytic oxidation, are able to completely decompose the VOCs, but they suffer from the low energy efficiency given by the high operating temperature. Moreover, some other hazardous compounds can be synthesized during the relaxation of thermal decomposition, mainly if halogenated compounds are presented. The biological degradability of VOCs is also very problematic due to low concentration of VOCs in the gas phase. This degradation way is also impossible for many VOCs based on aromatic ring that could not be biologically destroyed. Technologies based on non-thermal plasmas could offer an alternative, and they are capable to remove various pollutants in the gas phase [3]. The plasma decomposition process of VOC is rather complex, and the hydrocarbons are attacked in several ways. In the plasma reactor, the hydrocarbons are partly transformed into oxygenated compounds and into CO and CO<sub>2</sub>. Unfortunately, undesirable toxic by-products can be formed.

Various non-thermal atmospheric plasma sources have been studied with respect to VOC destruction [1, 4, 5]. This study presents the first results obtained using recently developed surface discharge operating at the atmospheric pressure, that is nowadays widely used mainly in the surface treatment processes [6]. The progress in our research is an application of TiO<sub>2</sub> photocatalyst directly in the discharge reactor and thus the TiO<sub>2</sub> activation is done by discharge UV radiation as well as by various active species created by this discharge. Moreover, the photocatalyst can be directly heated by the discharge up to temperatures of about 200 °C, both by radiation and impact of hot particles, and

thus the photocatalytic efficiency can be further increased. Two different kinds of photocatalytic TiO<sub>2</sub> layers were tested in our study.

### Experimental setup

The schematic drawing of the experimental device is shown in Fig. 1. The discharge reactor consisted of a surface discharge electrode 10x10 cm<sup>2</sup> connected to the HF power supply with frequency variable up to 10 kHz. The upper side of the discharge reactor was made of Al<sub>2</sub>O<sub>3</sub> plate covered or non-covered TiO<sub>2</sub> photocatalyst. The reactor gap was 2 mm. The reactor side walls were made of Teflon with one fused silica window oriented in parallel to the gas flow through the reactor. The gas inlet into the reactor was realized by the system of equidistant holes (distance of 5 mm, i.d. 1 mm); the outlet was possible through the open reactor wall on the opposite side. This system guaranteed nearly homogeneous flow of the reacting gas mixture through the discharge.

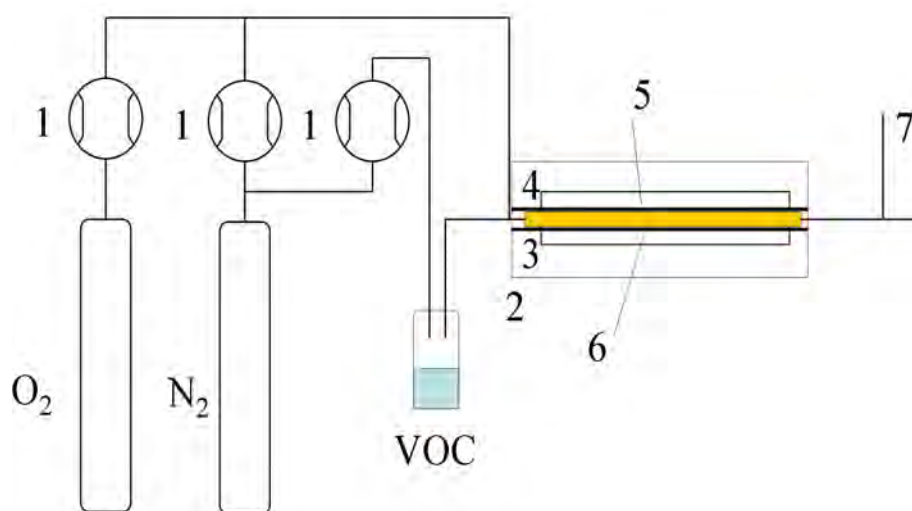


Fig. 1. Scheme of the experimental set up.

1 – mass flow controllers; 2 – Teflon discharge reactor; 3 – surface discharge electrode; 4 – Al<sub>2</sub>O<sub>3</sub> plate; 5 – Quartz window; 6 – discharge; 7 – sampling point for the chemical analyzes.

Synthetic dry air was used as a carrier gas, and it was enriched by the VOC (xylene, cyklohexane) just in front of the reactor. VOC concentration in the reactor was constant at about 1 %. The N<sub>2</sub> of technical purity (99.99 %) was used as a carrier gas for VOC. The total gas flow was 4.5 l/s, gas mixture composition was controlled by Omega mass flow controllers. The velocity of gas flow through the reactor was 0.4 m/s, and residence time in discharge was 0.2 s.

The exhaust gas analyzes were carried out by the simple gas analyzer Testo 350 XL. It allowed the detection of low molecular weight discharge products as CO, NO<sub>2</sub>, NO, H<sub>2</sub>, only. Measurements were carried out by changing the discharge frequency.

Two different photocatalytic layers were prepared using sol-gel processes:

- TiO<sub>2</sub> photocatalyst layer – E05

Layer was prepared according to the procedure by Klusoň [7]. It was Sol-gel process using reverse micelles (Triton TX102 in toluene). The TiO<sub>2</sub> precursor was titane isobutoxid, and his hydrolyzsis took place inside reverse micelles. The sol was printed by ink jet printer, and after drying, it was baked at 450 °C.

- TiO<sub>2</sub> photocatalyst layer – D11

This layer was also prepared using the Sol-gel process. The sol was based on ethanol, titanium isopropoxid, acetylacetone, and polyethylene glycole. The layer was prepared according to the procedure by Heller [8] that was further modified [9].

The layers had different structure. While E05 layer was the globular smooth structure, as it can be seen in Fig. 2, the D11 layer was with some clusters at surface. Both layers had in general the island structure that increased their active surface.

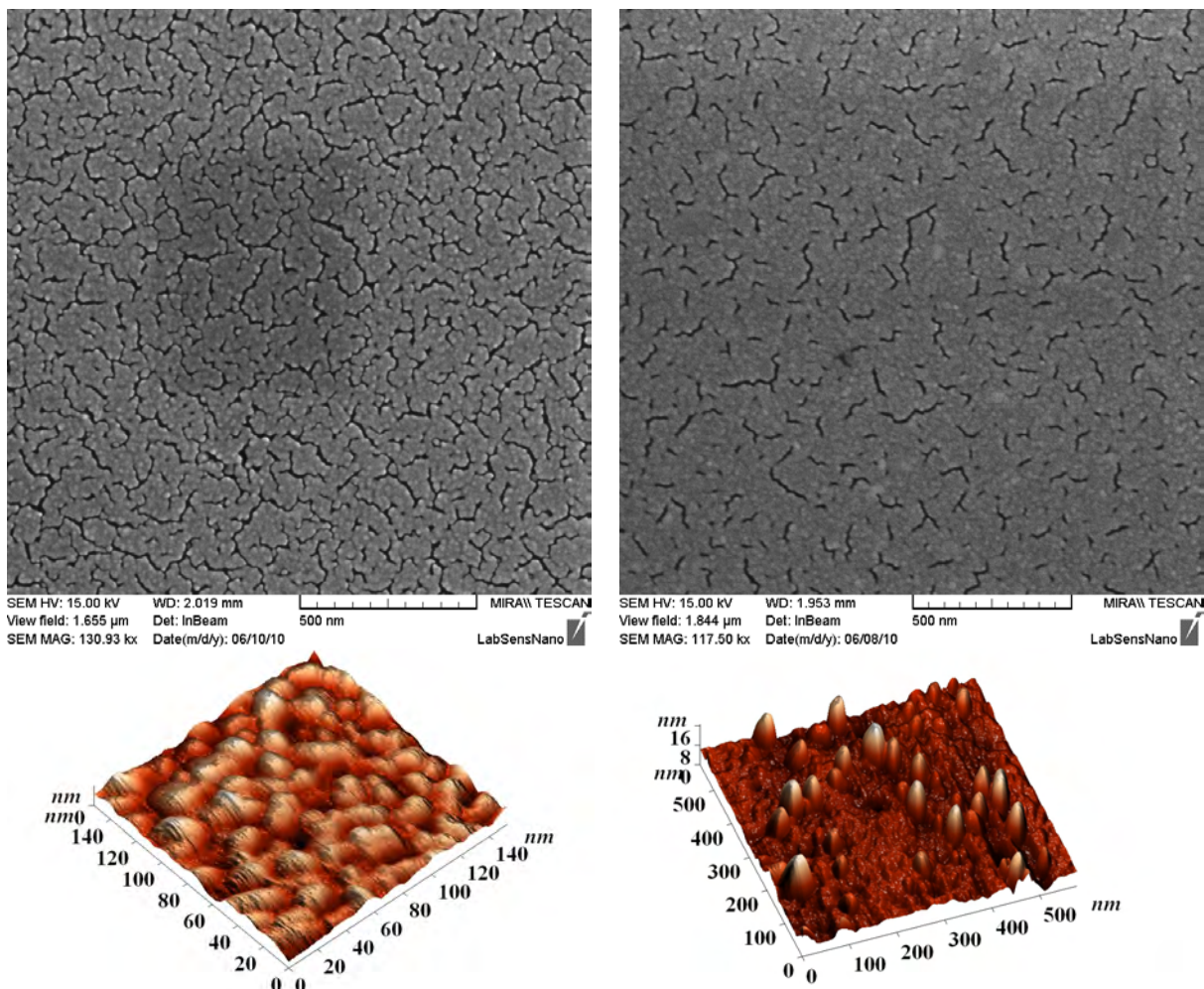


Fig. 2. Surface structures of E05 (left) and D11 (right) photocatalytic layers.

### Results and discussion

The experimental results obtained during the cyclohexane decomposition are shown in Figs. 3–5. It can be seen that the measured concentrations of all determined species are slightly dependent on the applied frequency in case that no catalyst was applied. If E05 photocatalytic layer is applied, the evolution of the dependencies is nearly unchanged. However, all the determined concentrations are significantly higher; about two times for CO and NO<sub>2</sub>, and about 30 % in case of molecular hydrogen.

Completely different situation can be seen if D11 photocatalytic layer is applied. The maximal efficiency of the CO and H<sub>2</sub> molecules is observed at operating frequency of about 3 kHz, but nearly no difference is observed for low as well as for high frequencies. In case of NO<sub>2</sub>, that is typically negative by-product of atmospheric discharges, the increase of concentration is observed at all frequencies. Concentration of NO molecules was just at the detection limit (1 ppm) at all conditions and thus they are not presented here.

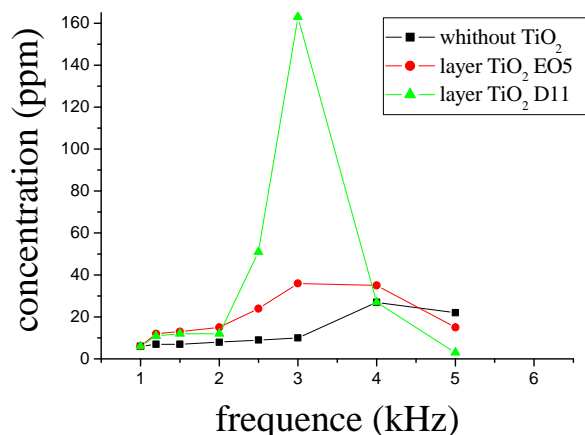


Fig. 3. Concentration of CO generated by surface discharge in synthetic air with cyklohexane.

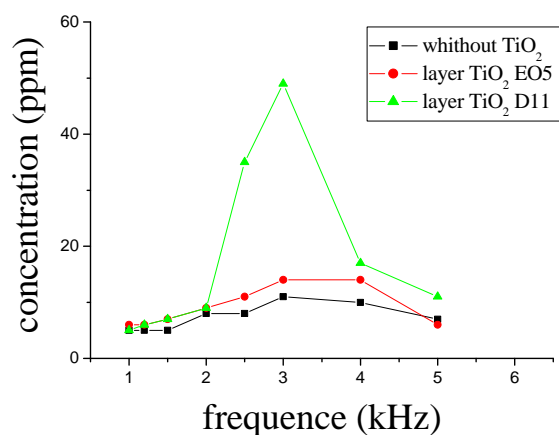


Fig. 4. Concentration of H<sub>2</sub> generated by surface discharge in synthetic air with cyklohexane.

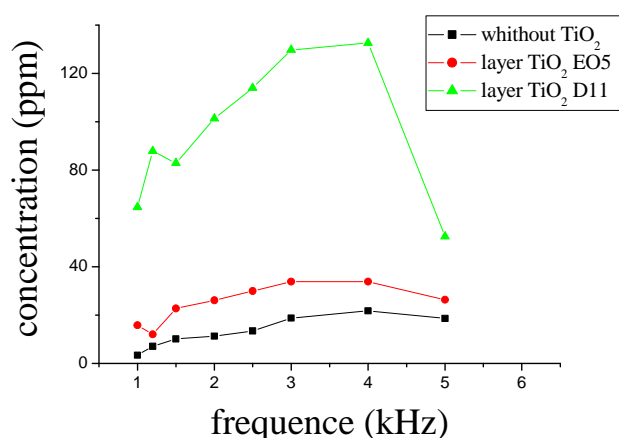


Fig. 5. Concentration of NO<sub>2</sub> generated by surface discharge in synthetic air with cyklohexane.

Significantly different results were obtained for the xylene as it can be seen from Figs. 6–9. In this case, the strong dependence on the applied discharge frequency was observed for CO and NO<sub>2</sub> generation if no photocatalyst was used. Application of both photocatalysts decreased concentrations of both these species significantly (by the factor of 3–5), and EO5 layer was more efficient. On the other hand, presence of NO and H<sub>2</sub> was relatively small in the exhaust gas, and their concentrations increased if the photocatalyst was applied.

## Conclusions

This article gives the first results relevant to the surface discharge combined with in situ photocatalysis for the environmental application. The cyclohexane and xylene were used as the model VOC compounds for the decomposition using synthetic air gas mixture at the atmospheric pressure. The experiment showed that using different TiO<sub>2</sub> photocatalyst layers can be efficient for the modification of the discharge exhaust gas composition. Unfortunately, the obtained results have not given the clear data what kind of photocatalytic layer is better for the application. Our contemporary data also do not allow the detail explanation of the obtained results using any kinetic model of the discharge processes because we have no knowledge about higher molecular products. The GC-MS and ex-situ FTIR spectroscopy will be applied for this study.

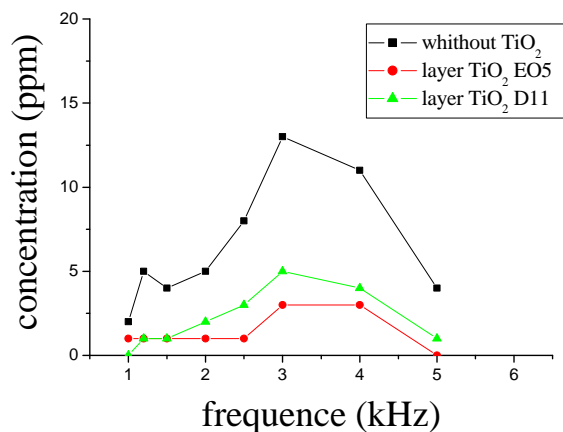


Fig. 6. Concentration of CO generated by surface discharge in synthetic air with xylene.

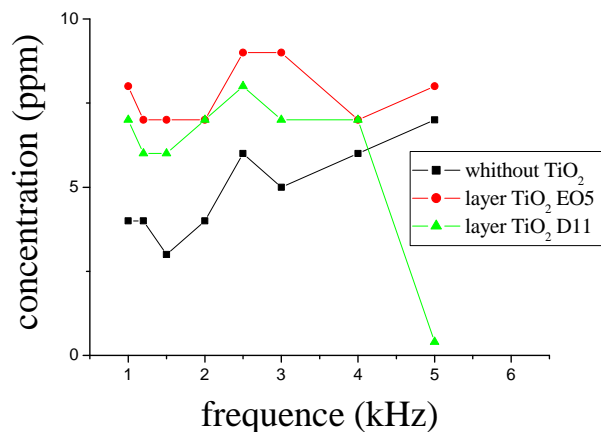


Fig. 7. Concentration of H<sub>2</sub> generated by surface discharge in synthetic air with xylene.

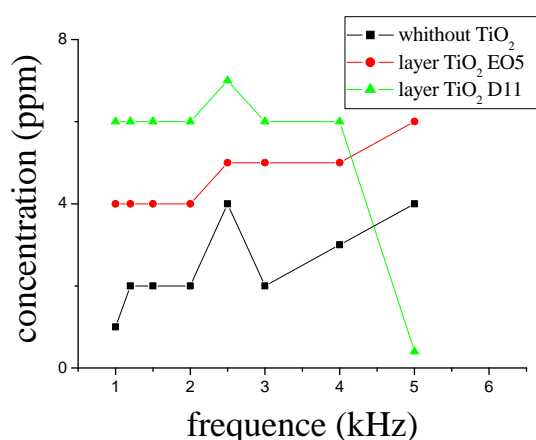


Fig. 8. Concentration of NO generated by surface discharge in synthetic air with xylene.

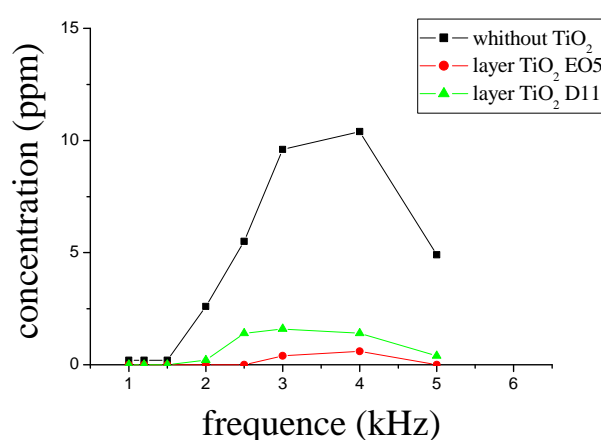


Fig. 9. Concentration of NO<sub>2</sub> generated by surface discharge in synthetic air with xylene.

### Acknowledgement

This work was supported by the Ministry of Education, Youth and Sports, research plan No. 0021630501, and by the Czech Science Foundation, project No. 104/09/P165.

### References

- [1] S. P. Jones, *Atm. Envir.* 33 (1999) 4533.
- [2] H.H. Kim, A. Ogata, S. Futamura, *Appl. Catal. B: Environ.* 79 (2008) 356.
- [3] H.H. Kim, J.H. Kim, A. Ogata, *Int. J. Plasma Environ. Sci. Technol.* 2 (2008) 106.
- [4] H.H. Kim, *Plasma Proces. Polym.* 2 (2004) 91.
- [5] Ö. Mutaf-Yardimci, A. Savaliiev, A. Fridman, L. A. Kennedy, *J. Appl. Phys.* 87 (2000) 1632.
- [6] A. Fridman, Gutsol, Y.I. Cho, *Adv. Heat Transf.* 40 (2007) 1.
- [7] P. Klusoň, H. Lusková, O. Šolcová, L. Matějová, T. Cajthaml, *Mater. Lett.* 61 (2007) 2931.
- [8] A. Heller, *Self-Cleaning Glass and Method of Making Thereof*, WO 97/07069.
- [9] P. Dzik, M. Veselý, J. Chomoucká, *J. Adv. Oxid. Technol.* 13 (2010) 172.

# Titration of Selenium Hydride into the Nitrogen Post-Discharge

F. Krčma<sup>1</sup>, V. Mazánková<sup>1</sup>, M. Procházková<sup>2</sup>, A. Hrdlička<sup>2</sup>

<sup>1</sup>Faculty of Chemistry, Brno University of Technology, Purkyňova 118, Brno 612 00, Czech Republic

<sup>2</sup>Institute of Chemistry, Masaryk University, Kamenice 5/A10, Brno 611 37, Czech Republic

e-mail: krcma@fch.vutbr.cz

## Abstract

This presented work gives new preliminary results about the influence of other species added into the nitrogen post-discharge. DC nitrogen flowing discharge was created at 1000 Pa in the quartz tube, and the discharge current was adjusted at 150 mA. Selenium hydride was generated on line and it was further dried by a molecular sieve. The hydride was introduced into the nitrogen post-discharge at the decay time of 15 ms using Pyrex capillary oriented from down stream side of the main discharge tube. The plasma was studied by optical emission spectroscopy in the range of 320–780 nm at the fixed post-discharge position of 15 ms decay time. The three nitrogen spectral systems (first and second positive, and first negative) were detected in the spectra, only. Based on the spectra, the relative distributions of nitrogen radiative states were calculated. The strong decrease of population at all vibrational levels was observed. The experimental results show that the main influence of the added selenium hydride is through the changes of Quartz wall properties.

**Keywords:** post-discharge, selenium hydride, optical emission spectroscopy.

## Introduction

Nitrogen discharges and post-discharges in various configurations are widely used in different processes and technologies [1–3]. The neutral nitrogen molecule can form many electronic states. All molecular states under 7.4 eV are metastables that conserve the excitation energy for the long time up to seconds. There mutual collisions as well as the recombination of atomic species, and heterogeneous reactions with walls create various radiating states, and consequently the visible light emission can be observed up to one second after switching off the active discharge. Although, various very complex kinetic models were developed during the last years [4], it is very difficult to obtain information about all non-radiative metastables. During the recent years, the Cavity Ring Down Spectroscopy [5], two photon or optical-optical [6] LIF techniques allowed the direct access to the determination of highly excited metastables, mainly to  $N_2(A^3\Sigma_u^+)$ . During the post discharge, it is nearly impossible to obtain an information about highly excited nitrogen ground state molecules.

Some possible energy transfer reactions between nitrogen ground state metastables and other species that result in the light emission were proposed during the last decade. For example, the reaction between  $N_2(X^1\Sigma_g^+, v \geq 22)$  and NO leads to the formation of NO<sup>y</sup> system [7]. CN violet (by the reaction with  $N_2(X^1\Sigma_g^+, v \geq 12)$ ) [8] and red (by reaction with  $N_2(X^1\Sigma_g^+, v \geq 4)$  systems emission [9] are observed. Very recently, we also proposed [10] and confirmed [11] excitation of mercury 254 nm line by energy transfer from  $N_2(X^1\Sigma_g^+, v = 19)$  state, and various zinc lines excitation from different vibrational levels [12]. All these data can significantly help to understand the post-discharge kinetics because they bring information about metastables. Unfortunately, not all species mentioned above can be introduced into the post-discharge in well defined amount. Due to this fact, we are looking for other molecules that should be easily introduced in exact amount, and which should be excited by some resonance energy transfer reactions. The presented paper gives the preliminary results of selenium hydride titration into the nitrogen post-discharge.

## Experimental set-up

The DC flowing post-discharge was used for the experimental study. A general schematic drawing of the experimental setup is given in Figure 1. The active discharge was produced in a Quartz discharge tube at the constant discharge current of 150 mA. The total gas pressure was 1000 Pa. Hollow molybdenum electrodes were placed in the side arms (at interelectrode distance of 12 mm). Nitrogen was of 99.9999% purity, and it was further cleaned by Oxiclear and LN<sub>2</sub> traps. The reactor

system was pumped continuously by a rotary oil pump separated from the discharge tube by another LN<sub>2</sub> trap. The nitrogen flow of 800 Sccm was automatically controlled by a Bronkhorst mass flow controller. The total gas pressure in the discharge tube was measured by a capacitance gauge connected to the end of the discharge tube. The moveable titration capillary tube was made of Pyrex, and it was immersed upstream from the discharge into the Quartz tube at its axis. Its position was fixed at the decay time of 15 ms for the presented experiments, i.e. at the end of the nitrogen pink afterglow [9].

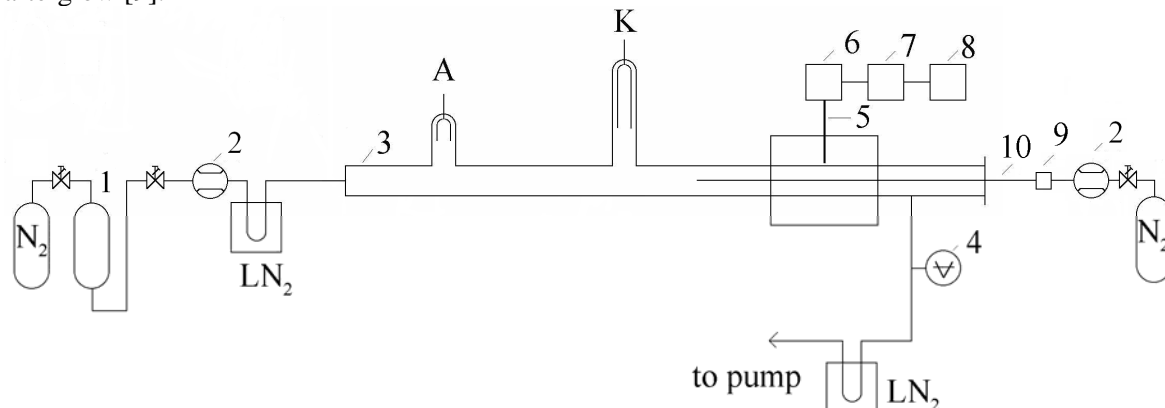


Fig. 1. General scheme of the experimental set up. 1 – catalyzer Oxiclear; 2 – mass flow controller; 3 – Quartz discharge tube; 4 – capacitance gauge; 5 – quartz optical fiber; 6 – monochromator Jobin Yvon Triax 550; 7 – CCD; 8 – PC, 9 – vial with mercury, 10 – movable Pyrex titration capillary tube.

The selenium hydride was generated directly during the experiment using the set up presented in Fig. 2, where also the experimental conditions are shown. Nitrogen of 99.999% purity was used as a carrier gas for the hydride generation. The gas mixture after the hydride generation contained also molecular hydrogen and water vapor. The Anhydron molecular sieve placed in the tube of 30 cm length was used to remove water vapor. A part of the obtained gas mixture was introduced into the titration capillary using the Bronkhorst mass flow controller, the rest of the gas mixture was outgoing through a small valve (it caused some overpressure in the system) into the exhaust.

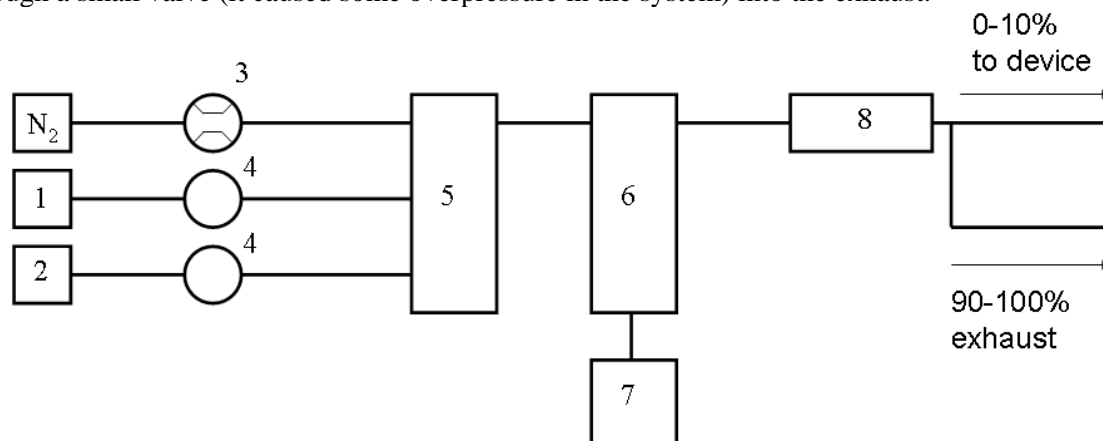


Fig. 2. Scheme of the selenium hydride generator. 1 – 1% NaBH<sub>4</sub> + 0.1% NaOH, flow of 2.5 ml/min; 2 – Se 1-100 mg/l in 50% HCl, flow of 5ml/min; 3 – mass flow controller Omega FMA; 4 – peristaltic pump; 5 – reaction coil; 6 – liquid/gas phase separator; 7 – liquid waste; 8 – column with Anhydron molecular sieve.

Optical emission spectra were collected at the fixed position at the end of the titration capillary, i.e. at the decay time of 15 ms. The spectra were measured by Jobin Yvon TRIAX 550 spectrometer with a CCD detector. The 300 gr/mm grating was used for the spectra acquisition in the range of 320–780 nm. The spectra of the nitrogen first, and second positive, and first negative systems were recorded in all spectra, no other emission was recognized. The relative populations of nitrogen N<sub>2</sub>(B,  $\nu = 2-19$ ), N<sub>2</sub>(C,  $\nu = 0-4$ ), and N<sub>2</sub><sup>+</sup>(B,  $\nu = 0-6$ ) states were calculated from the band head intensities of nitrogen

bands using constants given by *Gilmore* [13]. The intensities were corrected for the spectral response of measuring spectrometer that was obtained using the standard Oriel lamp.

### Results and discussion

Two series of the experimental observations were carried out. First of all, the titration of pure nitrogen into the post discharge was applied. A quenching of all radiative states is demonstrated in Figs. 3–5. This can be explained by the quenching of nitrogen metastables by non-excited nitrogen molecules that are added as the titration flow. Moreover, the titration nitrogen flow has relatively high speed that is about one half at the maximal flow and thus the interaction time between plasma and titration nitrogen increases with the flow increase. The photography of a similar effect is given in our other contribution at this conference [14].

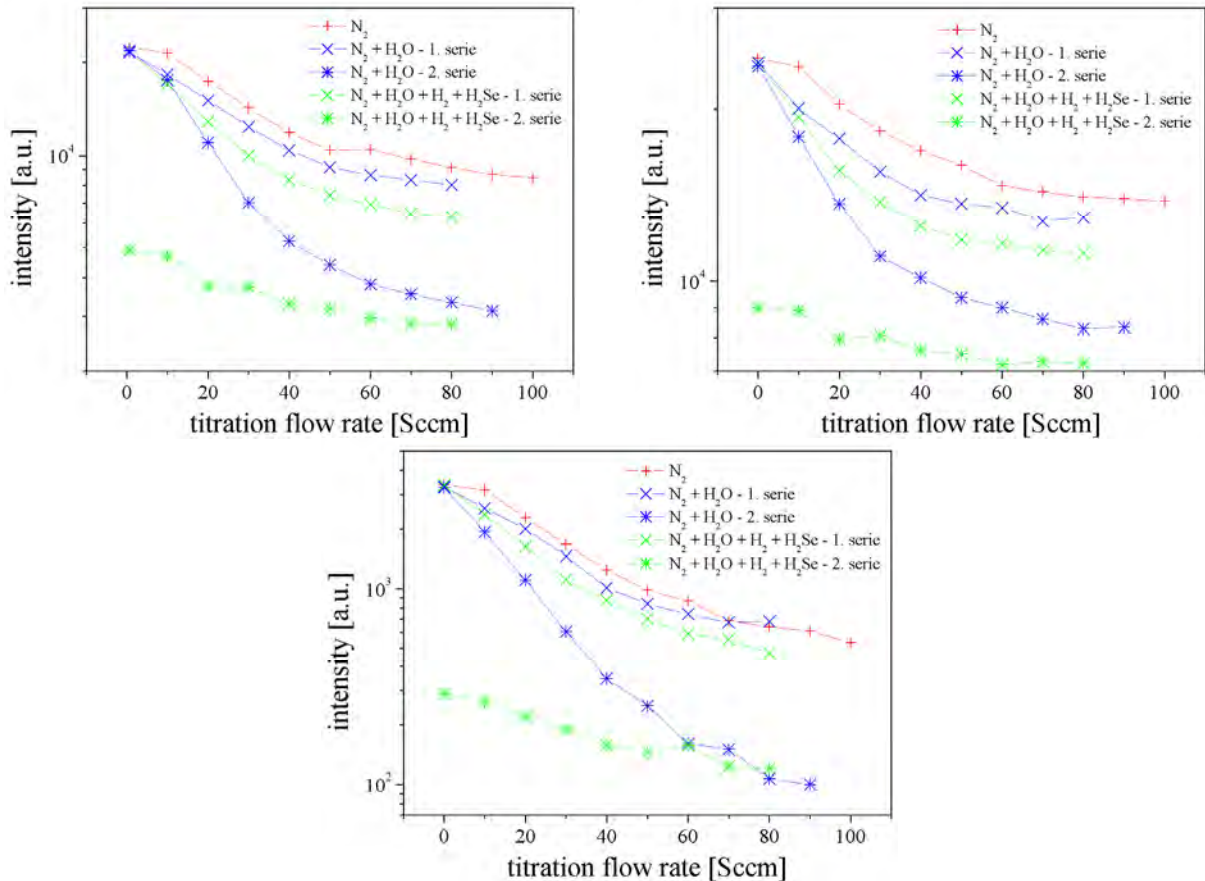


Fig. 3. Dependence of the band head intensities of the selected bands of the nitrogen first positive system: 2-0 – left; 11-7 – right; 17-12 – bottom.

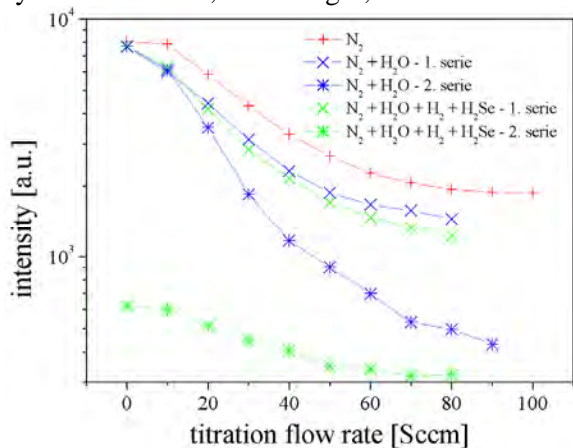


Fig. 4. Dependence of the 0-0 band head intensity of the nitrogen second positive system.

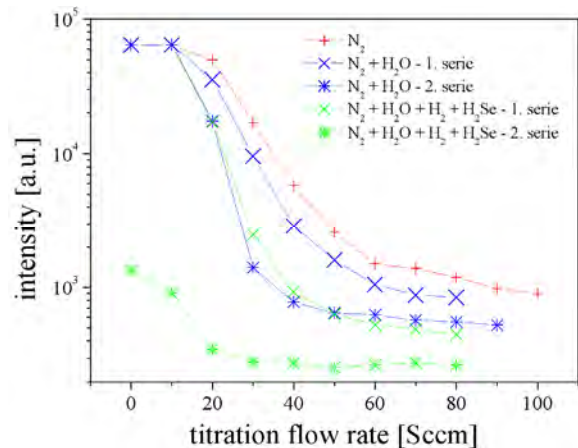


Fig. 5. Dependence of the 0-0 band head intensity of the nitrogen first negative system.

The second experiment was realized using the titration apparatus without selenium hydride generation, i.e. only distilled water was added before the molecular sieve into the titration nitrogen flow. The spectra showed further decrease of all intensities.  $\text{NO}^\beta$  emission was observed with a negligible intensity and thus we can conclude that some oxygen, originating from water vapor, was introduced. By comparison to our detailed studies carried out in nitrogen-oxygen mixtures [15], we can conclude that oxygen presence in the post-discharge was below 50 ppm, i.e. below 0.5 % in the titration flow. This result confirmed a good water vapor removal by the molecular sieve.

Finally, we started to generate the selenium hydride. The further decrease of all intensities was observed in this case. The spectrum of nitrogen molecular ion was the most sensitive to the hydride presence as it can be seen in Fig. 5. The  $\text{NO}^\beta$  emission was nearly the same as in the previous case.

After these experiments, we returned to the pure nitrogen afterglow, but its visual appearance was rather different than before the hydride titration. Due to this fact, we repeated the water as well as the hydride titration. The results obtained during this second series of experiments showed that the post-discharge sensitivity on the titration significantly increased, i.e. all nitrogen spectra were much more quenched by the titration of water or hydride. Finally, the post-discharge changed its shape after this second series of experiments. As the shape of the band intensity dependences presented in Figs. 3–5 is nearly the same in all cases, we can conclude that probably some thin film was deposited on the reactor wall. Thus the heterogeneous processes that play a great role in the post-discharge kinetics in our case were changed. The detail study of these phenomena will be subject of our further studies.

Figs. 3–5 show the band head intensity dependencies for the selected nitrogen spectral bands. The detailed analyzes of the obtained results need more complex information. Due to this fact, we calculated relative vibrational distributions of the upper states of observed nitrogen spectral systems. The results are shown in Figs. 6–8.

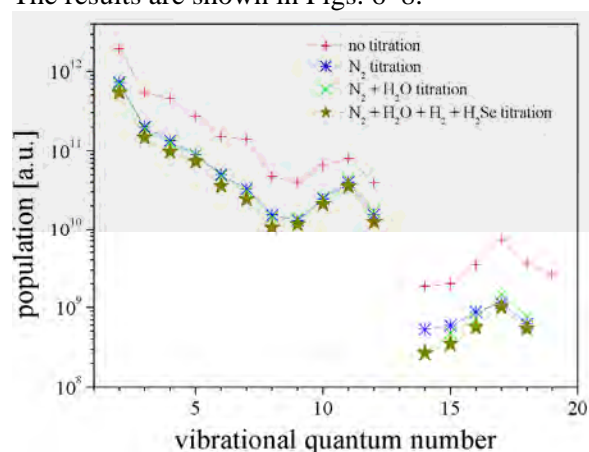


Fig. 6. Vibrational distribution of the  $\text{N}_2(\text{B } ^3\Pi_g)$  state at the titration of various mixtures.

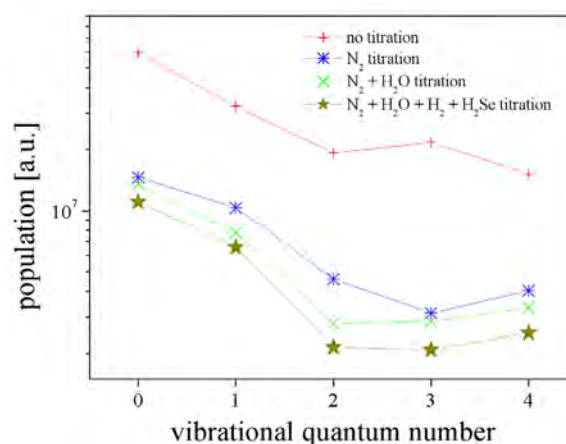


Fig. 7. Vibrational distribution of the  $\text{N}_2(\text{C } ^3\Pi_u)$  state at the titration of various mixtures.

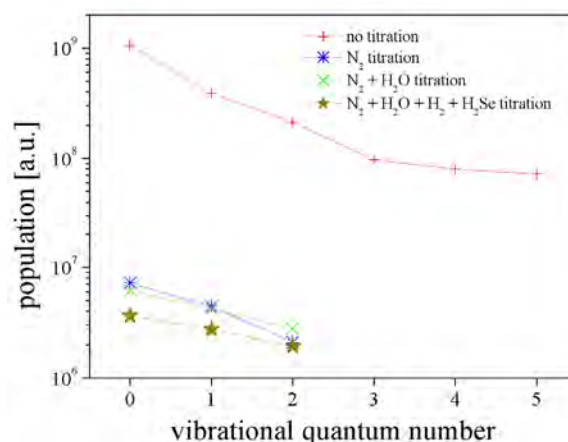


Fig. 8. Vibrational distribution of the  $\text{N}_2^+(\text{B } ^2\Sigma)$  state at the titration of various mixtures.

The vibrational distributions clearly show that the vibrational distribution functions are not significantly changed by any titration mixtures, but the absolute populations are strongly dependent on

the titration gas mixture kind. Generally, the strongest quenching of all populations is observed by the titration of pure nitrogen. Nitrogen containing some low traces of water vapor has nearly the same effect, and quenching by hydride is the highest one. The most quenched is the highest laying state, i.e. nitrogen molecular ion, the lowest quenching is observed for the lowest state, i.e.  $N_2(B^3\Pi_g)$  state. From this result, we can conclude that probably the highly excited metastable states, that are the main precursors for the molecular ion creation under the post-discharge conditions, are quenched much more effectively. There is no great difference of quenching by hydride, so it can be concluded that hydride changes concentrations of all metastables similarly, and we suppose that its role is mainly in the wall processes. The further experiments including introduction of hydride at different post-discharge positions will be carried out to confirm this hypothesis.

## Conclusions

The influence of the on line generated selenium hydride on the flowing post-discharge in pure nitrogen was experimentally studied. Three nitrogen spectral systems (the first and second positive, and first negative), as well as the vibrational distribution of the corresponding nitrogen states, were observed in the dependence on the titration flow of different composition. Although, the main changes were observed at titration of pure nitrogen due to significant quenching of nitrogen metastables by neutral nitrogen in its ground state, addition of selenium hydride increased the quenching. The results showed that selenium hydride changed populations of all states by the nearly same factor and thus we suppose that its role is mainly in the changes of reactor wall conditions. This was also confirmed by the second series of measurements. Further experiments using titration at different post-discharge positions will be carried out to confirm these preliminary results.

## Acknowledgements

This work was supported by the Czech Science Foundation project No. 202/08/1106.

## References

- [1] S. Bockel, T. Belmonte, H. Michel, D. Ablitzer, *Surf. Coat. Technol.*, 97 (1997) 618.
- [2] S. Meikle, H. Nomura, Y. Nakanishi, Y. Hatanaka, *J. Appl. Phys.*, 67 (1990) 483.
- [3] C. D. Pintassilgo, J. Loureiro, V. Guerra, *J. Phys. D: Appl. Phys.*, 38 (2005) 417.
- [4] V. Guerra, P.A. Sa, J. Loureiro, *Eur. Phys. J. – Appl. Phys.*, 28 (2004) 125.
- [5] G.D. Stancu, M. Janda, F. Kaddouri, D.A. Lacoste, C.O. Laux: *J. Phys. Chem. A* 114 (2010) 201.
- [6] P.F Ambrico, M. Šimek, G. Dilecce, S. DeBenedictis, *Plasma Chem. Plasma Proces.* 28 (2008) 299.
- [7] M. Mrázková, P. Vašina, V. Kudrle, A. Tálský, C.D. Pintassilgo, V. Guerra, *J. Phys D: Appl. Phys.* 42 (2009) 75202.
- [8] J. Janča, A. Tálský, F. Krčma, L. Hochard, A. Ricard, *Acta Phys. Univ. Comenianae* 35 (1995) 197.
- [9] J. Hubeňák, F. Krčma, *J. Phys. D: Appl. Phys.* 33 (2000) 3121.
- [10] V. Kanický, V. Otruba, A. Hrdlička, P. Krásenský, F. Krčma, *J. Atom. Anal. Spectrometry*, (2007) 22.
- [11] F. Krčma, I. Bocková, V. Mazánková, I. Soural, A. Hrdlička, V. Kanický, *J. Phys. Conf. Ser.*, 2010 – submitted.
- [12] Z. Stará, F. Krčma, V. Mazánková, V. Kanický, A. Hrdlička, P. Krásenský, *Proc. 17<sup>th</sup> Int. Conf. Gas Discharg. Appl.*, 421, Cardiff 2008.
- [13] F.R. Gilmore, R.R. Laher, P.J. Espy, *J. Phys. Chem. Ref. Data* 21 (1992) 1005.
- [14] V. Mazánková, F. Krčma, I. Bocková, *Proc. SAPP XVIII, Vrátna* 2011 – submitted.
- [15] F. Krčma, V. Mazánková, I. Soural, *Publ. Astronom. Observ. Belgrade*, 82 (2007) 133.

# Dissociative Electron Attachment to Fluorocarbons

S. A. Haughey<sup>1</sup>, T. A. Field<sup>1</sup>, K. Graupner<sup>1</sup>, M. Duffy<sup>1</sup>, L. Graham<sup>1</sup>, A. Mauracher<sup>2</sup>,  
A. W. Edtbauer<sup>3</sup>, C. Mitterdorfer<sup>3</sup>, P. Scheier<sup>3</sup>, T. Märk<sup>3</sup>

<sup>1</sup>Centre for Plasma Physics, Queen's University Belfast, University Road, Belfast BT7 1NN, N. Ireland, U.K.

<sup>2</sup>Department of Materials Chemistry, Uppsala Universitet, P.O. Box 538, 751 21 Uppsala, Sweden

<sup>3</sup>Institut für Ionenphysik und Angewandte Physik and Center for Molecular Biosciences Innsbruck, Leopold Franzens Universität, 6020 Innsbruck, Austria

e-mail: t . field @ qub . ac . uk

## Abstract

Electron attachment to a number of fluorocarbon molecules has been observed prompted by the wealth of negatively charged ions observed in electron attachment to gas from a fluorocarbon plasma discharge. For large fluorocarbons, X, electron attachment at low energies below 1 eV tends to give metastable parent ions, X<sup>-\*</sup>; at higher energies fragment ions are formed, principally F<sup>-</sup>.

**Keywords:** Fluorocarbon Plasma, Anions, Dissociative Electron Attachment,

## Introduction

A recent experimental investigation of dissociative electron attachment to the molecules formed in a fluorocarbon discharge of He/C<sub>3</sub>F<sub>6</sub> (perfluoropropene) observed the formation of many large anions with electron energies between 0 and 1 eV [1]. This observation prompted the present investigation of electron attachment to large fluorocarbon molecules such as C<sub>9</sub>F<sub>20</sub>. The molecules investigated may be present in fluorocarbon plasmas and their behaviour may also be indicative of the typical behaviour of large fluorocarbon molecules.

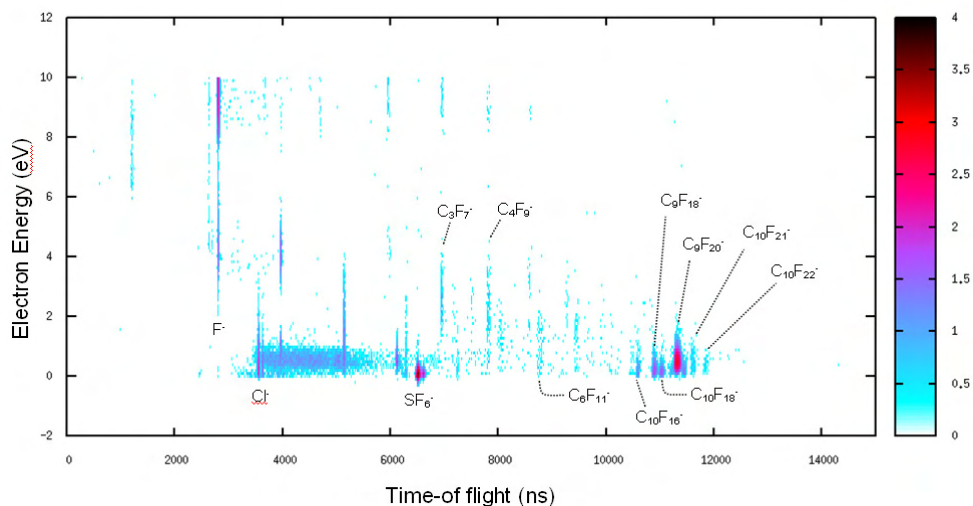
In an electron attachment resonance an electron becomes attached to a molecule for longer than the expected transit time of the electron past the molecule. Electrons with non-zero angular momentum around the molecule become trapped behind a centrifugal potential barrier around the molecule in a shape resonance. Another common resonance is the Feshbach resonance where the incoming electron loses energy to the molecule and becomes attached. The lifetimes of shape resonances are typically of the order of femtoseconds; this is very short, but long enough for the excited negatively charged molecular ion formed in electron attachment to dissociate to give one or more neutral and a single negatively charged fragment. The overall process of electron attachment followed by molecular fragmentation is dissociative electron attachment. Feshbach resonances can have considerably longer lifetimes. The lifetimes of some resonance states can be so long that the negatively charged parent ions can be observed on microsecond or longer timescales in mass spectrometers.

## Experiment, Results, Discussion, Conclusions

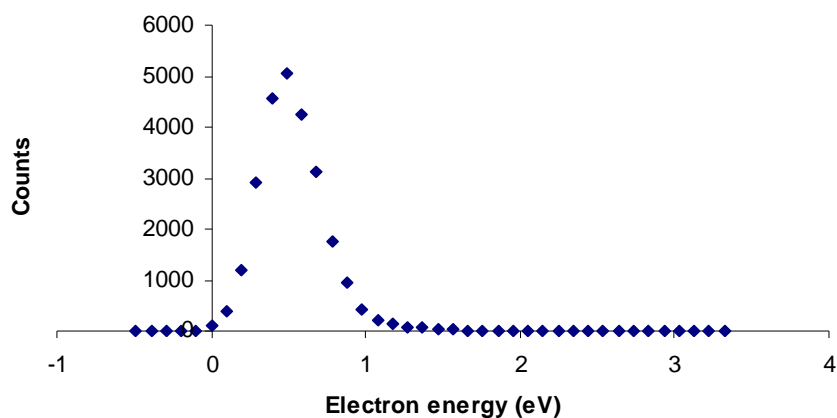
Experiments to study dissociative electron attachment to fluorocarbons including Heptacosane, (C<sub>4</sub>F<sub>9</sub>)<sub>3</sub>N, and Perfluorocarbons (PFCs) of the type C<sub>x</sub>F<sub>y</sub> (where y = 2x + 2), such as perfluorononane (C<sub>9</sub>F<sub>20</sub>), were conducted with ERIC [2], a trochoidal electron monochromator (TEM) time-of-flight (TOF) mass spectrometer. C<sub>9</sub>F<sub>20</sub>, is relevant to SiO<sub>2</sub> etching in the semiconductor industry. Heptacosane is a well known mass spectroscopic standard and its positive ionization spectrum is well characterised.

The experiments in Belfast to investigate C<sub>9</sub>F<sub>20</sub> identified metastable parent anions C<sub>9</sub>F<sub>20</sub><sup>-\*</sup>, which do not dissociate but do autodetach on μs timescales. The lifetime of these anions as well as that of C<sub>6</sub>F<sub>14</sub> were measured using the double focusing two sector field mass spectrometer at the University of Innsbruck.

Perfluorocarbons have been used to replace chlorofluorocarbons (CFCs) as plasma processing gases since the 1980s because they do not deplete the stratospheric ozone layer. They are, however, greenhouse gases with C<sub>6</sub>F<sub>14</sub> having a global warming potential over a century of 9200 times that of CO<sub>2</sub> [3] and as PFCs can have extremely long atmospheric lifetimes [4] it is desirable to monitor the emission of these gases.



An example of a negative mass spectrum (that of  $C_9F_{20}$ ) is shown above. The electron energy is indicated on the ordinate. The lower abscissa shows ion time-of-flight and the identities of the principal ions are shown although it is difficult to assign these fragment ions to dissociation of the parent molecule as there was evidence of heavier impurities in the sample that was analysed. There is a strong signal from the parent anion at close to 0eV electron energy. Integrating the parent ion signal indicates that the resonance is at approximately 0.5eV (see below).



## References

- [1] K. Graupner *et al.*, *New J. Phys.* 12 (2010) 083035 M
- [2] T.A. Field *et al.*, *J. Phys., B*, 38 (2005) 255
- [3] L.G. Christophorou *et al.*, *J. Phys. Chem. Ref. Data*, 27. (1998) 889
- [4] A.R. Ravishankara *et al.*, *Science*, 259 (1993) 194

# Electron Impact Ionisation of Valine, Leucine and Isoleucine Amino Acids.

P. Papp<sup>1</sup>, P. Shchukin<sup>2</sup>, J. Kočišek<sup>1,3</sup>, M. Stano<sup>1</sup>, Š. Matejčík<sup>1</sup>

<sup>1</sup>Department of Experimental Physics, Faculty of Mathematics, Physics and Informatics, Comenius University, Mlynská dolina, 842 48 Bratislava, Slovakia

<sup>2</sup>Institute of Physics of Molecules and Crystals, Ufa Research Center of the Russian Academy of Sciences, 450075 Ufa, Russia

<sup>3</sup>J. Heyrovsky Institute of Physical Chemistry, Academy of Sciences of Czech Republic, Dolejškova 3, 18223 Prague, Czech Republic

e-mail: papp@fmph.uniba.sk

## Abstract

Systematic experimental and theoretical studies of electron impact ionisation to gas phase valine, leucine and isoleucine amino acids are presented. Crossed electron-molecule beams technique equipped with quadrupole mass analyzer was used for measurements. Supporting calculations on *ab initio* level with Density Functional Theory and G3MP2 method were performed to get the energies and structures of neutral parent molecules, neutral and positive ionic fragments. Similar structures of these parent (P) molecules are reflected in some common features of their mass spectra. Creation of positive ionic fragments like (P-COOH)<sup>+</sup>, (P-COOH-NH<sub>3</sub>)<sup>+</sup>, (P-COOH-NH<sub>2</sub>)<sup>+</sup>, (P-R-COOH)<sup>+</sup>, (P-R)<sup>+</sup>, (R)<sup>+</sup>, (COOH)<sup>+</sup> and more are discussed, moreover supplementary data on neutral fragments are reported.

**Keywords:** electron impact ionisation, valine, leucine, isoleucine, *ab initio* calculations.

## Introduction

Processes leading to damages and repair on biological systems were studied with increasing attention in the last decades. One of the possible ways to study these processes is the electron impact ionisation; in this work namely of aliphatic amino acids. Amino acids are the building blocs of the peptides and proteins, therefore having an important role in physico-chemical processes in living organisms. This work brings new results on experimental and theoretical approaches of electron impact ionisation of valine, leucine and isoleucine in gas phase.

Valine, leucine and isoleucine belong to the group of so called aliphatic amino acids. They are characterized by the amino (NH<sub>2</sub>) and carboxylic (COOH) groups and can be described by a common formula NH<sub>2</sub>CH(R)COOH. The side chain R is a isopropyl group in valine amino acid, its chemical formula is then (NH<sub>2</sub>CH(CH(CH<sub>3</sub>)<sub>2</sub>)COOH). Extending the R in valine by one CH<sub>2</sub> gives the formula for leucine and isoleucine amino acids which are structural isomers, the chemical formula is then NH<sub>2</sub>CH(CH<sub>2</sub>CH(CH<sub>3</sub>)<sub>2</sub>)COOH and NH<sub>2</sub>CH(CH(CH<sub>3</sub>)CH<sub>2</sub>CH<sub>3</sub>)COOH respectively.

## Experiment

Using the crossed electron/molecule beams apparatus built on Faculty of Mathematics, Physics and Informatics of Comenius University in Bratislava we performed the experimental part of this work. The apparatus has been described in detail elsewhere [1]; therefore we give only a brief description. The electron beam is formed in a trochoidal electron monochromator. The electron energy resolution of the electron beam in present experiment was set to a value of about 200 meV in order to increase the electron current. The calibration of apparatus for these type of experiments carried out in positive mode is done by electron impact ionisation to Ar gas. As a result we obtain the electron energy scale and the estimation of the electron energy resolution.

The molecular beam was formed in effusive molecular beam source where the gas is flowing through a channel (0.5 mm diameter and 4 mm long) and an external aperture. The amino acids valine, leucine and isoleucine (Fluka, 99% purity) are under normal conditions in solid state. The sample was placed directly into the stainless steel container of the effusive molecular beam source; that was resistively heated to temperatures of about 160 °C in order to achieve sufficient vapour pressure. The positive ions formed in the intersection volume between the electron and the molecular beams are extracted by a weak electric field into the quadrupole mass spectrometer with the mass range 2–2000

amu. Apparatus is working in two modes: (a) energy of electrons is set constant and defined mass/charge ratio ( $m/q$ ) region is scanned using quadrupole mass analyzer, (b) the  $m/q$  ratio is set constant and energy is tuned through defined region. The later mode (b) provides us detailed information on electron energy dependent ion yields for different  $m/q$  and their near threshold regions quantified with appearance energies (AE).

### Theory

Recent theoretical methods of quantum chemistry are used to obtain the fragmentation reaction energies that can be compared with the experimental appearance energies. The inclusion of theoretical modelling to these studies gives us mostly the advantage to identify the fragmented products (the chemical formula and structure of ionic products with given  $m/q$  as well as the same for neutral products) that are unknown from experiment. Density Functional Theory (DFT) with B3LYP functional [2,3] was used for geometry optimizations of ionic and neutral products and for construction of a theoretical scheme of reactions and their reaction energies. Vibrational analysis is necessary to be performed to exclude any transition states of fragmented products.

For better accuracy the appropriate products can be then recalculated using a complex energy computational method G3MP2 [4] that is included in GAUSSIAN program package [5]. Energies in this complex method are calculated on *ab initio* levels with HF, MP2 and QCISD(T). Moreover thermal and empirical correction is involved in this method; thus the resulting reaction energies are in better agreement with the experimental appearance energies.

The introduced combination of experimental and theoretical studies was previously successfully applied on dissociative electron attachment to valine [6], leucine and isoleucine [7]. We continue with these systematic studies on amino acids with the present fragmentations to positive ions by electron impact ionisation.

### Results and discussion

The appearance energies reported in this work for parent molecule and the corresponding fragmented ions were evaluated by fitting an expected dependence of ionisation cross section on electron energy  $S(E)$  at the threshold based on a modified Wannier law to the measured data.

$$S(E) = b \quad E < AE$$

$$S(E) = b + a(E - AE)^d \quad E > AE$$

The fitting procedure involves a convolution of the expected cross section dependence and electron energy distribution function

$$K(E) = \int_0^{\infty} S(U) f(E - U) dU$$

Several works were published about the conformational studies of neutral amino acids; the most recent has been used as an initial guess of structures of valine [8,9], leucine [10] and isoleucine [11] in our calculations. However a lot of corresponding conformers exist with energies close to the ground state of valine, leucine or isoleucine. Therefore we took only the two lowest for each in our calculations, see Fig. 1. They differ by the stabilization via hydrogen bonding on amino and carboxyl group. Conformers labelled I are stabilized via  $\text{NH}_2 \cdots \text{O}=\text{C}$  interaction; while conformers labelled II via  $\text{H}_2\text{N} \cdots \text{O}-\text{H}$ . No conformers stabilized via  $\text{NH}_2 \cdots \text{OH}-\text{C}$  were considered for these studies.

General fragmentation schemes to positive ions for a common group of amino acids, depending on the constitution of their side chain group (R), were proposed in previous work of Junk and Svec [12]. For R being an alkyl, that is the case of valine, leucine and isoleucine presented in this work, the scheme shows possible fragmentation of parent molecule (P) to cationic products like  $(\text{P}-\text{COOH})^+$ ,  $(\text{P}-\text{COOH}-\text{NH}_3)^+$ ,  $(\text{P}-\text{COOH}-\text{NH}_2)^+$ ,  $(\text{P}-\text{R}-\text{COOH})^+$ ,  $(\text{P}-\text{R})^+$ ,  $(\text{R})^+$ ,  $(\text{COOH})^+$ . Multiple bond ruptures can be presented, however many times followed by considerable structural rearrangements of cationic or/and neutral products (ions typically having  $m/q$  values 75, 57, 44 and 30 amu).

Figure 2 brings us the comparison of mass spectra for valine, leucine and isoleucine (from top to bottom). It is apparent that except the main fragmented product  $(\text{P}-\text{COOH})^+$  (common for all three molecules) the other fragmented positive ions mostly with lower masses appear in 4 mass regions: the smallest products with mass up to 30 amu; then products like  $(\text{COOH})^+$  around 40-45 amu; fragments

with masses around 57 amu and finally the (P-R)<sup>+</sup> and 75 amu fragments.

Let us look at some common features or arising differences of the measured data. It was expected that the most intensive signal could be assigned to a positive ionic fragment of parent without COOH, 72 amu from valine and 86 amu from leucine and isoleucine. Moreover the probability of staying of the positive charge on COOH fragment is two orders lower if we look at the yield of ion with 45 amu. Almost for each channel the appearance energies were fitted, these values are listed in table 1 with the suggested fragmented products and corresponding calculated reaction energies.

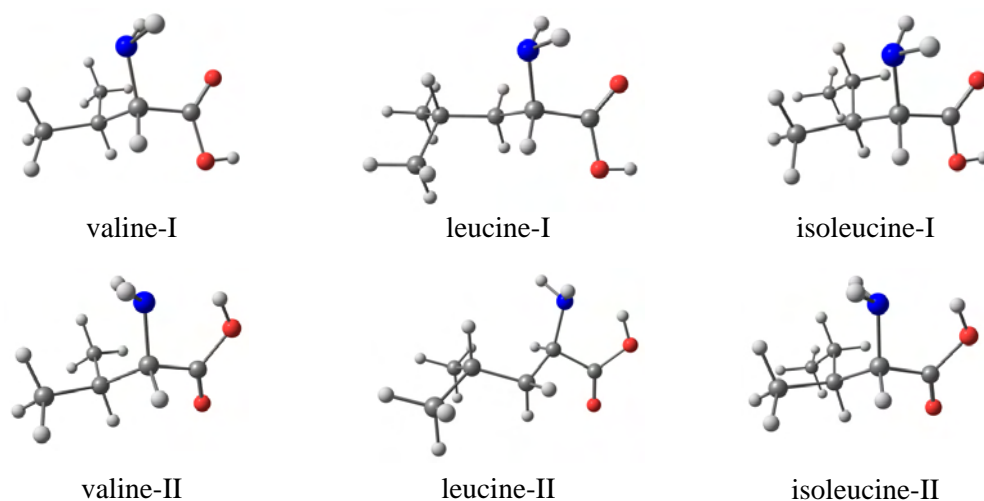


Fig. 1. Structures of the energetically lowest conformers of neutral valine, leucine and isoleucine.

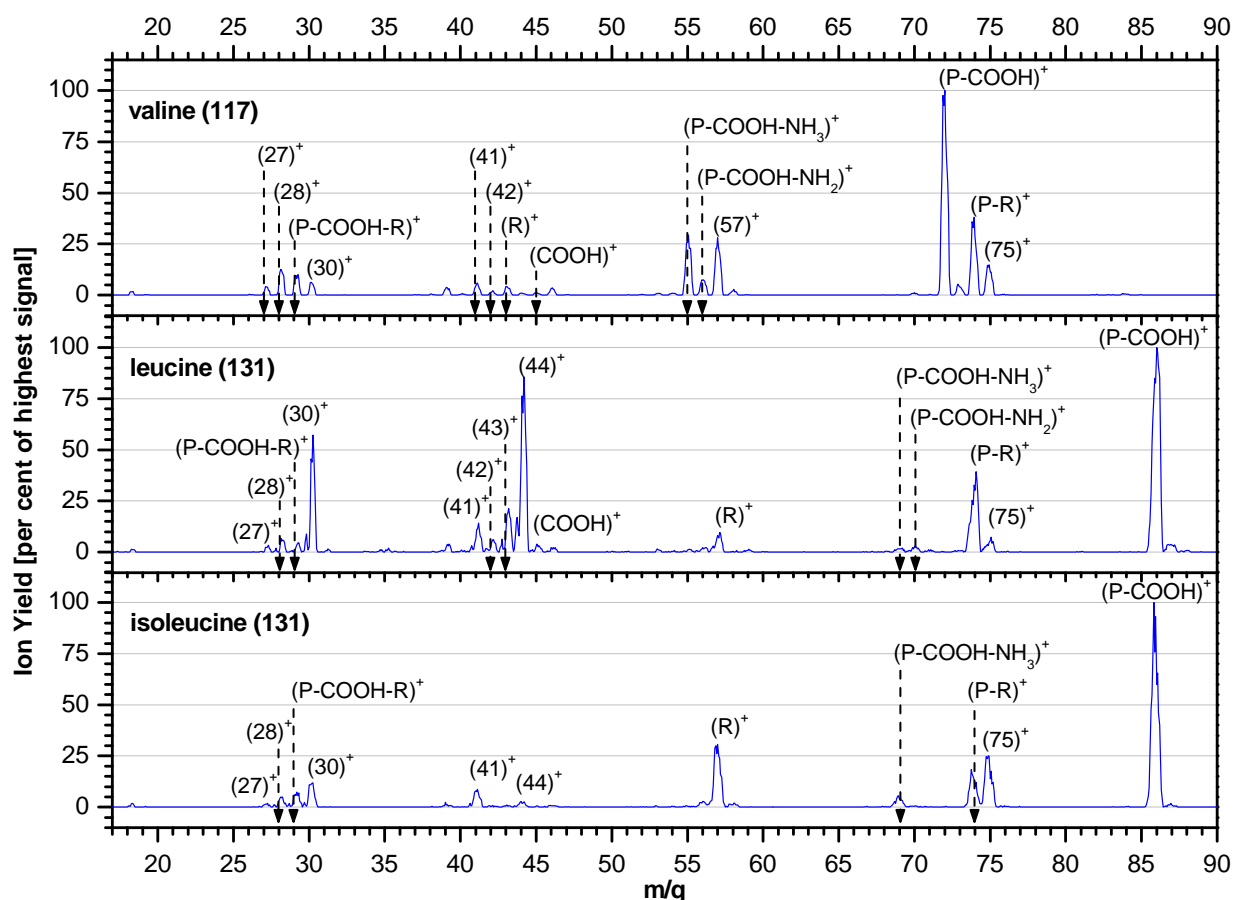


Fig 2 The electron impact ionisation ion yield count as a function of mass charge ratio measured for valine (mass 117 amu), leucine and isoleucine (both 118 amu).

Tab. 1. List of the fitted appearance energies [AE], calculated reaction energies on G3MP2 or *B3LYP*, corresponding ionic and neutral fragment chemical formulas. All values are in eV. DNC and FRAG means that the optimized structure Did Not Converge or is Fragmented.

| VALINE |  | LEUCINE                          |  | ISOLEUCINE                      |  |                                    |
|--------|--|----------------------------------|--|---------------------------------|--|------------------------------------|
| [m/q]  | Fragments  | [AE]<br>G3MP2                    | Fragments  | [AE]<br>G3MP2                   | Fragments  | [AE]<br>G3MP2                      |
| [86]   |  | -                                | $\text{NH}_2\text{CHCH}_2\text{CH}(\text{CH}_3)_2^+$<br>COOH   | [8.84]<br>9.39                  | $\text{NH}_2\text{CHCH}(\text{CH}_3)\text{CH}_2\text{CH}_3^+$<br>COOH  | [8.86]<br>9.33                     |
| [75]   | $\text{NH}_2\text{CHC}(\text{OH})_2^+$<br>$\text{C}_3\text{H}_6$   | [9.99]<br>9.92                   | $\text{NH}_2\text{CHC}(\text{OH})_2^+$<br>$\text{CH}_2\text{C}(\text{CH}_3)_2$   | [9.11]<br>9.36                  | $\text{NH}_2\text{CHC}(\text{OH})_2^+$<br>$\text{CH}_2\text{CHCH}_2\text{CH}_3$  | [9.71]<br>9.51                     |
| [74]   | $\text{NH}_2\text{CHCOOH}^+$<br>$\text{CH}_3\text{CHCH}_3$   | [9.96]<br>10.06                  | $\text{NH}_2\text{CHCOOH}^+$<br>$\text{CH}_2\text{CH}(\text{CH}_3)_2$  | [10.31]<br>10.11                | $\text{NH}_2\text{CHCOOH}^+$<br>$\text{CH}_3\text{CHCH}_2\text{CH}_3$  | [10.29]<br>10.07                   |
| [72]   | $\text{NH}_2\text{CHCH}(\text{CH}_3)_2^+$<br>COOH  | [9.37]<br>9.37                   |  | -                               |  | -                                  |
| [70]   |  | -                                | $\text{CH}_3\text{CH}_2\text{CHCHCH}_3^+$<br>$\text{NH}_3+\text{CO}_2$   | [9.52]<br>9.43                  |  | -                                  |
| [69]   |  | -                                | $\text{CHCHCH}(\text{CH}_3)_2^+$<br>$\text{NH}_3+\text{COOH}$  | [11.22]<br>12.93                | $\text{CH}_3\text{CH}_2\text{C}(\text{CH}_2)_2^+$<br>$\text{NH}_3+\text{COOH}$   | [11.41]<br>11.91                   |
| [57]   | $\text{NHCHCOH}^+$<br>$\text{CH}_3\text{CHCH}_2+\text{H}_2\text{O}$<br>$\text{NH}_2\text{CHCHCH}_3^+$<br>$\text{CH}_4+\text{CO}_2$ | [11.73]<br><b>12.34</b><br>8.15  | $\text{NH}_2\text{CHCHCH}_3^+$<br>$\text{CH}_2\text{CH}_2+\text{HCOOH}$<br>$\text{R}^+$  | [10.22]<br>9.87<br><b>DNC</b>   | $\text{NH}_2\text{CHCHCH}_3^+$<br>$\text{CH}_2\text{CH}_2+\text{HCOOH}$<br>$\text{CH}_3\text{CHCH}_2\text{CH}_3^+$<br>$\text{NH}_2\text{CHCOOH}$   | [10.64]<br>9.85<br>10.30           |
| [56]   | $\text{CH}_2\text{C}(\text{CH}_3)_2^+$<br>$\text{NH}_2+\text{COOH}$<br>$\text{NH}_3+\text{CO}_2$                                   | [11.99]<br>14.15<br>9.47         |  | -                               |  | -                                  |
| [55]   | $\text{CH}_3\text{CCHCH}_3^+$<br>$\text{NH}_3+\text{COOH}$   | [12.26]<br>12.33                 |  | -                               |  | -                                  |
| [45]   | $\text{COOH}^+$<br>$\text{NH}_2\text{CHCH}(\text{CH}_3)_2$   | [11.54]<br>11.90                 | $\text{COOH}^+$<br>$\text{NH}_2\text{CHCH}_2\text{CH}(\text{CH}_3)_2$  | [-]<br>11.84                    |  | -                                  |
| [44]   |  | -                                | $\text{NH}_3\text{CHCH}_2^+$<br>$\text{CH}_2\text{CHCH}_3+\text{COOH}$<br>$\text{C}_3\text{H}_6+\text{COOH}$                                 | [9.94]<br><b>10.41</b><br>11.45 | $\text{NH}_3\text{CHCH}_2^+$<br>$\text{CH}_2\text{CHCH}_3+\text{COOH}$<br>$\text{C}_3\text{H}_6+\text{COOH}$   | [11.09]<br><b>10.34</b><br>11.43   |
| [43]   | $\text{CH}_3\text{CHCH}_3^+$<br>$\text{NH}_2\text{CHCOOH}$   | [11.46]<br>10.52                 | $\text{CH}_3\text{CHCH}_3^+$<br>$\text{NH}_2\text{CH}(\text{CH}_2)\text{COOH}$   | [11.98]<br>11.35                |  | -                                  |
| [42]   | $\text{CH}_3\text{CCH}_3^+$<br>$\text{NH}_2\text{CH}_2\text{COOH}$   | [-]<br>11.73                     | $\text{CH}_3\text{CCH}_3^+$<br>$\text{NH}_2\text{CH}(\text{CH}_3)\text{COOH}$  | [12.08]<br>11.62                |  | -                                  |
| [41]   | $\text{CH}_2\text{CHCH}_2^+$<br>$\text{NH}_2\text{CHCOOH}+\text{H}_2$<br>$\text{NH}_2\text{CH}_2\text{COOH}+\text{H}$              | [12.80]<br>11.95<br>13.02        | $\text{CH}_2\text{CHCH}_2^+$<br>$\text{NH}_2\text{CH}(\text{CH}_2)\text{COOH}+\text{H}_2$<br>$\text{NH}_2\text{CH}_2\text{COOH}+\text{CH}_3$ | [12.31]<br>12.79<br>12.47       | $\text{CH}_2\text{CHCH}_2^+$<br>$\text{NH}_2\text{CH}_2\text{COOH}+\text{CH}_3$  | [12.07]<br>12.44                   |
| [30]   | $\text{NH}_2\text{CH}_2^+$<br>$\text{CH}_3\text{CHCH}_2+\text{COOH}$<br>$\text{C}_3\text{H}_6+\text{COOH}$                         | [11.32]<br><b>10.49</b><br>11.50 | $\text{NH}_2\text{CH}_2^+$<br>$\text{CH}_2\text{C}(\text{CH}_3)_2+\text{COOH}$<br>$\text{CH}_2\text{CH}_2\text{CH}(\text{CH}_3)+\text{COOH}$ | [10.93]<br>10.95<br>11.41       | $\text{NH}_2\text{CH}_2^+$<br>$\text{CH}_2\text{CHCH}_2\text{CH}_3+\text{COOH}$<br>$\text{CH}_3\text{CHCHCH}_3+\text{COOH}$  | [10.24]<br>11.09<br>10.98          |
| [29]   | $\text{NH}_2\text{CH}^+$<br>$\text{CH}_3\text{CHCH}_3+\text{COOH}$   | [12.57]<br><b>FRAG</b>           | $\text{NH}_2\text{CH}^+$<br>$\text{CH}_2\text{CH}(\text{CH}_3)_2+\text{COOH}$  | [12.98]<br><b>FRAG</b>          | $\text{NH}_2\text{CH}^+$<br>$\text{CH}_3\text{CHCH}_2\text{CH}_3+\text{COOH}$  | [12.40]<br><b>FRAG</b>             |
| [28]   | $\text{NHCH}^+$<br>$\text{CH}_3\text{CH}_2\text{CH}_3+\text{COOH}$<br>$\text{CH}_3\text{CHCH}_3+\text{HCOOH}$                      | [12.96]<br>11.87<br>11.81        | $\text{NHCH}^+$<br>$\text{CH}_3\text{CH}(\text{CH}_3)_2+\text{COOH}$<br>$\text{CH}_2\text{CH}(\text{CH}_3)_2+\text{HCOOH}$                   | [13.53]<br>11.79<br>11.86       | $\text{NHCH}^+$<br>$\text{CH}_3\text{CH}_2\text{CH}_2\text{CH}_3+\text{COOH}$<br>$\text{CH}_3\text{CHCH}_2\text{CH}_3+\text{HCOOH}$<br>$\text{CH}_2\text{CH}_2\text{CH}_2\text{CH}_3+\text{HCOOH}$ | [13.39]<br>11.85<br>11.82<br>11.91 |
| [27]   | $\text{NCH}^+$<br>$\text{NHC}^+$<br>$\text{CH}_3\text{CH}_2\text{CH}_3+\text{HCOOH}$   | [-]<br>14.89<br>13.95            | $\text{NCH}^+$<br>$\text{NHC}^+$<br>$\text{CH}_3\text{CH}(\text{CH}_3)_2+\text{HCOOH}$   | [17.30]<br>14.80<br>13.87       | $\text{NCH}^+$<br>$\text{NHC}^+$<br>$\text{CH}_3\text{CH}_2\text{CH}_2\text{CH}_3+\text{HCOOH}$  | [15.40]<br>14.86<br>13.93          |

Another common feature can be seen for masses 74 and 75 amu. These are relatively strong lines with comparable relative intensities and shape for valine and isoleucine. However a difference in relative intensities and strength appears in isoleucine. Mass 75 was assigned to  $\text{NH}_2\text{CHC}(\text{OH})_2^+$  with three

different neutral products for valine, leucine and isoleucine. 74 amu is assigned to the loss of side chain R, good agreement of experiment and theory is evident from the table each for 74 and 75 amu. While the positive charge is mostly on P-R fragment in valine (low signal for  $R^+$ , 43 amu), appearance of  $R^+$  increases in leucine and seems to be more favourable in isoleucine (57 amu) than the  $P-R^+$ . However we were not able to stabilize the  $R^+$  from leucine; another possible product seems to be  $NH_2CHCHCH_3^+$  that energetically fits well for each molecules.

The only reasonable signal for products when dissociating the amino group from parent molecule was measured for valine. Cations like  $P-COOH-NH_2^+$  and  $P-COOH-NH_3^+$  can be seen at 56 and 55 amu respectively, contrary to a weak signal at 69 and 70 amu in leucine or isoleucine (except a small amount of 69 amu ion in isoleucine).

Ions between 41 and 44 amu are really intensive only in leucine molecule. It is interesting that up to 90% of the most intensive peak cation of 44 amu was detected, assigned to  $NH_3CHCH_2^+$ , but almost at zero level in isoleucine or valine. Also the dissociation of  $CH_3CHCH_3^+$  seems to be more affective in leucine contrary to valine (should be the  $R^+$  ion). Chanell 42 amu could be interesting only that one can expect glycine or alanine amino acids as neutral products, however their intensity is really small. Finally for this group mass 41 is assigned to  $CH_2CHCH_2^+$  for each molecule with comparable ion yield. All corresponding neutral products can be found in table 1.

We are coming to the last group of peaks appearing from 30 amu lower. Except the peak at 30 amu in leucine all the other lines have a similar shape for valine, leucine and isoleucine. Although it is not so hard to find cationic products with chemical formulas  $C_xH_yN_z$  that could have the appropriate mass, however the calculated reaction energies do not fit well the experimental appearance energies. For the mass 30 amu we still have a good agreement for  $NH_2CH_2^+$  fragment. However at 29 amu the expected cation according to Junk [12] has to be  $NH_2CH^+$ ; it was fragmented on each level of theory used and no other reaction path was found that could fit this appearance energy. Therefore we were not able to show the production of  $(P-COOH-R)^+$  that could have this mass.

### Acknowledgments

Financing of this work was by the Slovak Grant Agency VEGA-1/0558/09, VEGA-1/0379/11. This work was supported by the Slovak Research and Development Agency, project Nr. APVV-SK-SRB-0011-09, APVV-0365-07.

### References

- [1] M. Stano, S. Matejcik, J. D. Skalny et al., *J. Phys. B*, 2003, 36, pp. 261
- [2] C. T. Lee, W. T. Yang, and R. G. Parr, *Phys. Rev. B*, 1988, 37, pp. 785
- [3] A. D. Becke, *Phys. Rev. A*, 1988, 38, pp. 3098
- [4] A. G. Baboul, L. A. Curtiss, P. C. Redfern et al., *J. Chem. Phys.*, 1999, 110, pp. 7650
- [5] G. W. T. M. J. Frisch, H. B. Schlegel et al., GAUSSIAN 03, Gaussian, Inc., Wallingford, CT, 2004
- [6] P. Papp, J. Urban, S. Matejcik et al., *J. Chem. Phys.*, 2006, 125, pp. 204301
- [7] P. Papp, P. Shchukin, S. Matejcik, *J. Chem. Phys.*, 2010, 132, pp. 014301
- [8] S. Shirazian, S. Gronert, *J. Mol. Struct.: THEOCHEM*, 1997, 397, pp. 107
- [9] S. G. Stepanian, I. D. Reva, E. D. Radchenko et al., *J. Phys. Chem. A*, 1999, 103, pp. 4404
- [10] E. J. Cocinero, A. Lesarri, J.-U. Grabow et al., *ChemPhysChem*, 2007, 8, pp. 599
- [11] A. Lesarri, R. Sanchez, E. J. Cocinero et al., *J. Am. Chem. Soc.*, 2005, 127, 12952
- [12] G. Junk, H. Svec, *J. Am. Chem. Soc.*, 1963, 85, pp. 839

# Low energy electron interactions with tungsten hexacarbonyl

K. Wnorowski<sup>1</sup>, M. Stano<sup>2</sup>, Š. Matejčík<sup>2</sup>

<sup>1</sup> Department of Chemistry, Siedlce University, 3 Maja 54, 08-110 Siedlce, Poland

<sup>2</sup> Department of Experimental Physics, Comenius University, Mlynská dolina F2, 84248 Bratislava, Slovak Republic

e-mail: karolw@uph.edu.pl

## Abstract

We present an experimental crossed electron/molecule beams study of Dissociative Electron Attachment (DEA) to tungsten hexacarbonyl -  $W(CO)_6$ . This study was performed in the electron energy range 0–14 eV and at a room temperature. The relative partial cross sections for fragment negative ions  $W(CO)_5^-$ ,  $W(CO)_4^-$ ,  $W(CO)_3^-$ ,  $W(CO)_2^-$  have been estimated and the threshold energies and resonances for DEA channels have been determined. In addition the electron affinities of  $W(CO)_x$  ( $x = 5, 4, 3, 2$ ) have been estimated.

**Keywords:** electron attachment, mass spectrometry, metal carbonyls, tungsten hexacarbonyl

## Introduction

Transition metal carbonyl complexes are substances with great potential for applications in various field of chemistry and technology. In recent years the application of metal carbonyl complexes have been used in the field of plasma technology or preparation of metallic layers [1] and nanotechnology to prepare metallic structures [2, 3]. The tungsten hexacarbonyl belongs to the most important molecules of this class. Due to its chemical properties it is widely used to prepare tungsten layers and tungsten interconnection in the EBID and IBID techniques [4, 5]. In these techniques high energy electrons or ions are used to form metallic structures from adsorbed organometallic molecules on the surface. It has been recognized that low energy secondary electrons play an important role in the processes of dissociation of the organometallic molecules and formation of the metallic structures on the surfaces.

In present work we have studied the kinetics and reaction mechanics of the DEA reaction to  $W(CO)_6$  molecule. We did not find in the literature any DEA study to  $W(CO)_6$ . The DEA to  $W(CO)_6$  was studied in the electron energy range from 0 to 14 eV. It turned out that DEA process is able efficiently dissociate the molecule by cleavage of one or more CO groups. Especially the cleavage of one CO group appeared to be very efficient and proceed already at thermal electron energies.

## Experiment

We have studied the dissociative electron attachment (DEA) to  $W(CO)_6$  using the crossed electron – molecular beams technique [6] at the Department of Experimental Physics, Comenius University in Bratislava. The electron beam is formed in a Trochoidal Electron Monochromator. The ions formed in the interaction region are extracted by a weak electric field towards the entrance of the quadrupole mass spectrometer. The mass selected negative ions are detected by a secondary electron multiplier and the pulses are processed using a pulse counting technique and computer. This technique allows to observe resonant energies of DEA reactions and to estimate cross sections for the various fragment negative ion formation in the electron energy range from 0 to 14 eV. The measurements were carried out at the room temperature.

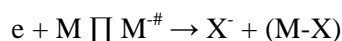
The  $W(CO)_6$  with a stated purity of 99% was purchased from Sigma–Aldrich and used without further purification.

Tab. 1. Appearance energies of the ions and the resonances in DEA to  $W(CO)_6$

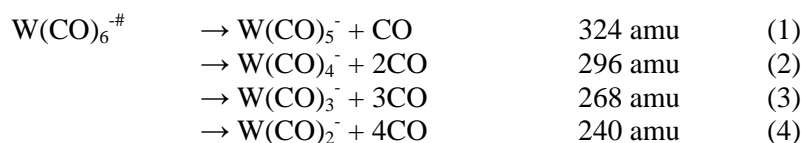
| Ion         | m/z | neutral fragments | Appearance Energy (eV) | Resonances (eV) |     |     |     |     |
|-------------|-----|-------------------|------------------------|-----------------|-----|-----|-----|-----|
| $W(CO)_5^-$ | 324 | CO                | 0                      | 0               | 1.5 |     |     |     |
| $W(CO)_4^-$ | 296 | 2.CO              | $0.9 \pm 0.1$          | -               | 1.8 | 3.2 | -   | 7.5 |
| $W(CO)_3^-$ | 268 | 3.CO              | $2.9 \pm 0.1$          | -               | -   | 3.6 | 4.7 | 7.8 |
| $W(CO)_2^-$ | 240 | 4.CO              | $6.5 \pm 0.1$          | -               | -   | -   | -   | 8.5 |

## Results and discussion

In the present work we have studied DEA to  $W(CO)_6$ . DEA reaction is a resonant process, which proceeds via formation of Transient Negative Ion (TNI) usually in relatively narrow range of electron energy. The TNI may then further dissociate so that fragment negative ions are finally detected:



In this equation M represents the molecule,  $M^\#$  the Transient Negative Ion,  $X^-$  the fragment negative ion and (M-X) the neutral fragment. In the case of tungsten hexacarbonyl, we were not able to detect TNI. The reason is that the life time of this ion is shorter than the time scale of present experiment (tens of  $\mu$ s). We have observed four dissociative channels:



The observed negative ions were formed as a result of cleavage of one or more carbonyl groups from the TNI. The most favourable reaction channel was (1) related to the formation of  $W(CO)_5^-$  (324 amu), by abstraction one of the carbonyl groups. The formation of this ion was most efficient in thermal electron energy range. The second fragment  $W(CO)_4^-$  (296 amu) has a threshold at 0.9 eV, the third  $W(CO)_3^-$  (268 amu) at  $\sim 2.9$  eV and the fourth  $W(CO)_2^-$  (240 amu) at approximately 6.5 eV. The appearance energies of the ions are summarised in the Table 1. The Figure 1 shows the relative cross sections for DEA channels (1) - (4). The cross sections are in arbitrary units; however, the values can be compared, they reflect the efficiencies of particular reaction channels. From the Figure 1 we can see that the efficiencies of the DEA were decreasing with the number of carbonyl groups detached.

The DEA reaction to  $W(CO)_6$  proceed via several resonances. The reaction channel (1) associated with cleavage of one CO group has very high relative cross section already at energies close to 0 eV. In the ion yield curve we can recognise additional structure at  $\sim 1.5$  eV (see Table 1). The high reaction efficiency already at thermal energies implicates exothermicities of this reaction channel, i.e., the W-CO bond is weaker than the electron affinity of the  $W(CO)_5^-$  anion.

The reaction channel (2) associated with cleavage of two CO groups has a threshold at 0.9 eV and three resonances are present in the ion yield curve at 1.8, 3.2 eV and a weak resonance at approximately 7.5 eV. The abstraction of three CO groups is associated with the reaction channel (3). The threshold for this channel is at 2.9 eV and three resonances at 3.6, 4.7 and 7.8 eV are present in the ion yield curve. The ion yield for the  $m/z = 240$  exhibits two resonances the first one at thermal electron energies  $\sim 0$  eV and the second one at 8.5 eV. We believe that the first one is an artefact due to impurities in the sample. The high energy resonance we associate with cleavage of four CO groups, i.e., reaction (4).

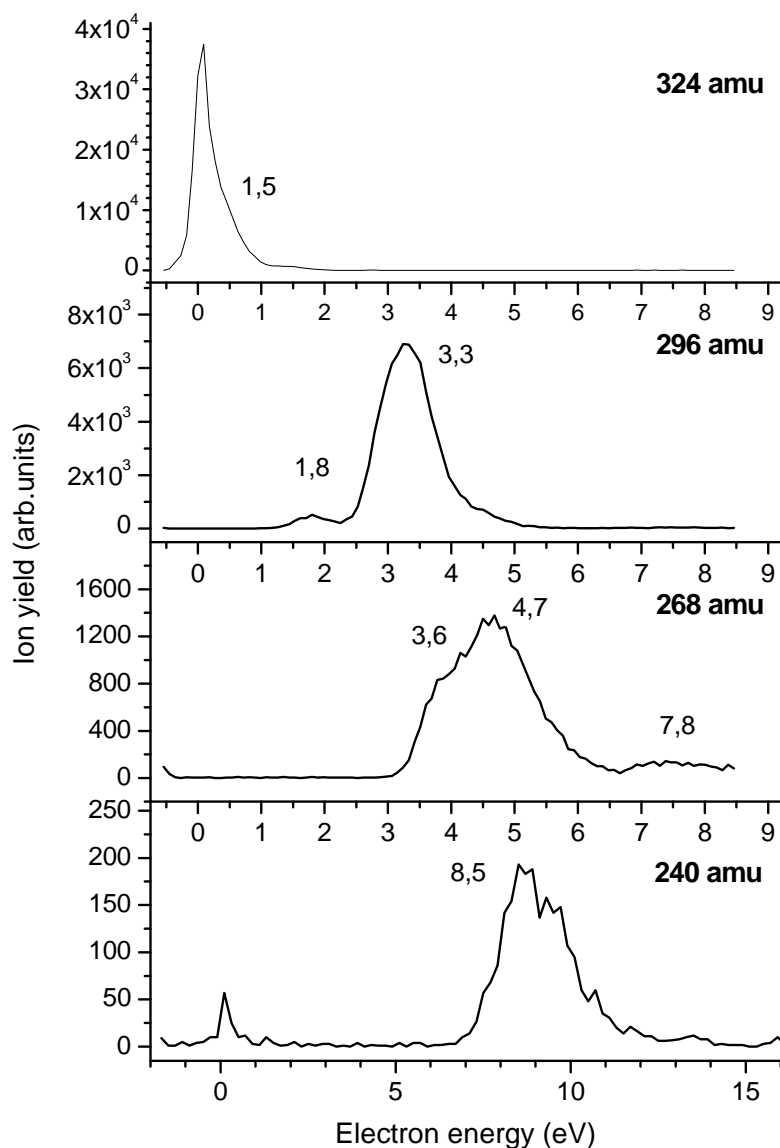


Fig. 1. Ion efficiency curves of negatively charged fragments formed by dissociative electron attachment to tungsten hexacarbonyl.

The appearance energies of the fragment ions could be used for estimation of the electron affinities of the  $W(CO)_x$  ( $x = 2, 3, 4, 5$ ) fragments. According to our EII studies of  $W(CO)_6$ , the average value of W-CO bond is 2.15 eV and 2.11 eV in  $W(CO)_6^+$ . We can expect the in the anion the average BDE is about 2 eV. Using this value we may estimate the electron affinities using following formula:

$$EA(W(CO)_x) = AE(W(CO)_x^-) - (6-x) \cdot BDE(W-CO)$$

Where EA denotes electron affinity of the fragment, AE appearance energy of the ion and BDE is the bond dissociation energy of the W-CO bond. Using this formula the electron affinities of  $W(CO)_x$  fragments are  $EA(W(CO)_5) \leq 2$  eV,  $EA(W(CO)_4) \leq 3.1$  eV,  $EA(W(CO)_3) \leq 3.1$  eV and  $EA(W(CO)_2) \leq 1.5$  eV. These values give only estimates of the electron affinities due to high uncertainties of the BDE in the anions.

## Conclusions

We have measured DEA to tungsten hexacarbonyl in the electron energy range from thermal up to 14 eV. The reaction proceeds via CO cleavage from TNI. One electron may dissociate up to 4 CO groups from one  $W(CO)_6$  molecules. We have obtained relative cross section for DEA reaction, observed several resonances and determined the appearance energies of the fragment negative ions. We have estimated the values of the electron affinities of  $W(CO)_x$  fragments.

## Acknowledgments:

This work was supported by the Slovak Research and Development Agency, project Nr. APVV-0365-07, slovak grant VEGA-1/0558/09 and partially by the COST Action CM0601 „Electron Controlled Chemical Lithography” (ECCL).

## References

- [1] Ken K. Laia, H. Henry Lamb, *Thin Solid Films*, 70, 114 (2000)
- [2] C.W. Hagen, W.F. van Dorp, P.A. Crozier, P. Kruit, *Surface Science*, 602, 3212 (2008)
- [3] K. E. Lewis, D. M. Golden, G. P. Smith, *J. Am. Chem. Soc.*, 106, 14 (1984) 3905–3912
- [4] I. J. Luxmoore, I. M. Ross, A. G. Cullis, P. W. Fry, J. Orr, P. D. Buckle, J. H. Jefferson, *Thin Solid Films*, 515 (2007) 6791–6797
- [5] M. Song, K. Furuya, *Sci. Technol. Adv. Mater.*, 9 (2008) 023002 (10pp)
- [6] S. Matejčík, V. Foltin, M. Stano, J.D. Skalny, *Int. J. Mass Spect.*, 223–224 (2003) 9–19

# Electron attachment to some fluorinated alcohols

W. Barszczewska, J. Wnorowska, J. Kopyra, I. Szamrej

Department of Chemistry, Siedlce University, 08-110 Siedlce, 3 Maja 54, Poland  
e-mail: wbar@uph.edu.pl

## Abstract

The results of thermal electron attachment investigations by three fluoroalcohols:  $\text{CF}_3\text{CH}_2\text{OH}$ ,  $\text{CF}_3\text{CF}_2\text{CH}_2\text{OH}$ ,  $(\text{CF}_3)_2\text{CHOH}$  in the gas phase are reported. The fundamental quantities such as rate coefficients ( $k$ 's) and activation energies ( $E_a$ 's) for the electron capture processes were determined. We have used Pulsed Townsend technique. Measurements were carried out in the temperature range 298K to 413K. The obtained rate coefficients depended on temperature in accordance to Arrhenius equation. From the fit to the experimental data points with function  $\ln(k) = \ln(A) - E_a/k_B T$  the activation energies ( $E_a$ 's) were determined.

**Keywords:** activation energy, electron attachment rate coefficient, fluorinated alcohols, pulse Townsend technique.

## Introduction

The studies of electron attachment processes are very important for understanding the electron-molecule interactions, negative ions formation, basic processes occurring in plasmas [1,2]. Those investigations are important also from the environmental protection point of view, especially if processes of the organofluorine contaminations in the earth atmosphere are considered.

The concentration of the man-made organofluorine compounds has substantially increased during the past few decades. Of particular interest is the fate of perfluoroalkyl substituents, such as the trifluoromethyl groups. Up to now most evidences suggest that such groups resist defluorination, although they can confer significant biological activity. Certainly, some volatile fluorinated compounds can be oxidized in the troposphere yielding nonvolatile compounds, such as trifluoroacetic acid.

In recent years the interest was turned to fluorinated alcohols, which are applied more often and often. For example, they are used as pharmaceuticals, inhalation anesthetics, herbicides, polymers, refrigerants, etchants, lubricants, heat transfer fluids, and so on [3,4]. Recently fluoroalcohols have been suggested as substitutes for CFCs.

Fluoroalcohols have been marketed as replacements for the stratospheric ozone depleting chlorofluorocarbons, however they may be equally hazardous to the environment. In spite of fluoroalcohols have zero ozone depletion potential (ODP), they still must be considered as possible greenhouse gases contributing to global warming stemmed from the strong IR activity of the C-F bonds [5,6]. For those reasons the further information are required on the degradation mechanisms.

This work is a continuation of the systematical studies on the rate coefficients ( $k$ 's) and activation energies ( $E_a$ 's) of thermal electron captures by various molecules using Pulsed Townsend technique. In our previous papers we have presented results concerning some halocarbons [7,8]. We have demonstrated then the linear dependence between  $\log(k)$  and  $E_a$ . We have found also that the activation energy is the main factor determining the rate coefficient for thermal electron capture.

At present we have started the electron capture studies on the new group of compounds — fluorinated alcohols. Below, we present the data on the thermal electron attachment to  $\text{CF}_3\text{CH}_2\text{OH}$ ,  $\text{CF}_3\text{CF}_2\text{CH}_2\text{OH}$  and  $(\text{CF}_3)_2\text{CHOH}$ .

## Results and Discussion

The present data were obtained by using the recently established swarm method, known as the Pulsed Townsend technique. This technique allows us to study electron attachment processes at elevated temperature. The experimental procedure has been described in detail previously [8]. In brief, the electron acceptor was introduced into the chamber in the excess of carbon dioxide as a buffer gas. The electron swarm was produced at the cathode using laser. The electron swarm moved to the

collecting electrode (anode) due to uniform electric field, through the gas mixture containing buffer gas and an electron acceptor. The pressures of the electron attaching gases depended on their efficiency in attaching electrons and were chosen to reach the rate of the process equal to ca.  $10^5 \text{ s}^{-1}$ . The drifting electrons create a pulse change in the potential of the collecting electrode. The pulse signal is amplified, registered on an oscilloscope and saved in a computer memory. The electron attachment rate coefficients were determined from the shape of the output signal of the electron pulse.

We have measured the electron attachment rate coefficients ( $k$ 's) in the temperature 298K for  $\text{CF}_3\text{CH}_2\text{OH}$ ,  $\text{CF}_3\text{CF}_2\text{CH}_2\text{OH}$  and  $(\text{CF}_3)_2\text{CHOH}$  used as attaching gases diluted with carbon dioxide. We have found that the rate coefficients ( $k$ 's) did not depend neither on the  $\text{CO}_2$  concentration nor the electron acceptor concentration. That means that only second order electron attachment processes were involved. All rate coefficients obtained for 298K are presented in Table 1. To our knowledge they have been measured for the first time.

We have also measured rate coefficients in the temperature range 298K-413K. The obtained results are shown in Figs.1-3.

Tab. 1. Thermal electron attachment rate coefficients ( $T = 298 \text{ K}$ ) and activation energies ( $E_a$ 's) calculated from kinetic data,  $T_{\text{range}}$  - the temperature range applied for  $E_a$ 's determinations.

| Molecule                                     | $k_{298} (\text{cm}^3 \text{molec}^{-1} \text{s}^{-1})$ | $E_a$ 's (eV) | $T_{\text{range}} (\text{K})$ |
|--|---|---------------|-------------------------------|
| $\text{CF}_3\text{CH}_2\text{OH}$            | $5.1 \times 10^{-11}$                                   | 0.24          | 298-368                       |
| $\text{CF}_3\text{CF}_2\text{CH}_2\text{OH}$ | $1.1 \times 10^{-10}$                                   | 0.28          | 298-413                       |
| $(\text{CF}_3)_2\text{CHOH}$                 | $3.0 \times 10^{-10}$                                   | 0.20          | 298-368                       |

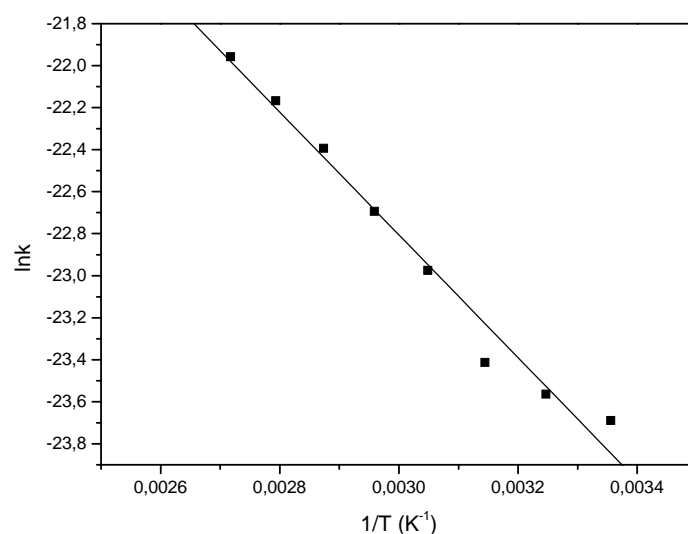


Fig.1. The dependence of  $\ln(k)$  on  $1/T$  for  $\text{CF}_3\text{CH}_2\text{OH}$

As you can see (Figs., 1-3), in all cases we observed the increase of the rate coefficients with temperature what suggest that the investigated processes require some activation energies. Since the dependencies plotted in Figs. 1-3 were linear and well described by Arrhenius equation ( $\ln(k) = \ln(A) - E_a/k_B T$ ) from the slopes of the lines we could have derived the proper activation energies ( $E_a$ 's). The obtained activation energies for all investigated molecules are collected in Table 1. To our knowledge, those values were obtained for the first time too.

Dissociative electron attachment to ethanol and trifluoroethanol has been previously studied in gas phase by using electron-molecule crossed beam technique [9]. The formations of negative ions have been measured in the energy range from 0 to 19 eV. Those studies showed that gaseous ethanol generates the ionic fragments  $\text{O}^-$ ,  $\text{OH}^-$ , located at 5.5eV and 8.2 eV respectively and comparatively small signal at 8.0 eV ascribed to  $\text{CH}_3\text{CH}_2\text{O}^-$  ion. In the case trifluoroethanol the following fragments negative ions:  $\text{CF}_3\text{CH}_2\text{O}^-$ ,  $\text{C}_2\text{F}_2\text{HO}^-$ ,  $\text{C}_2\text{FO}^-$ ,  $\text{CF}_3^-$  and  $\text{F}^-$  were observed.

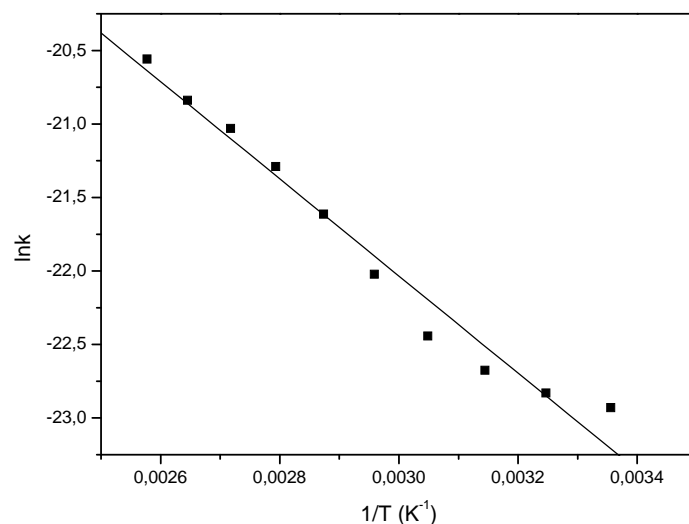


Fig.2. The dependence of  $\ln(k)$  on  $1/T$  for  $\text{CF}_3\text{CF}_2\text{CH}_2\text{OH}$

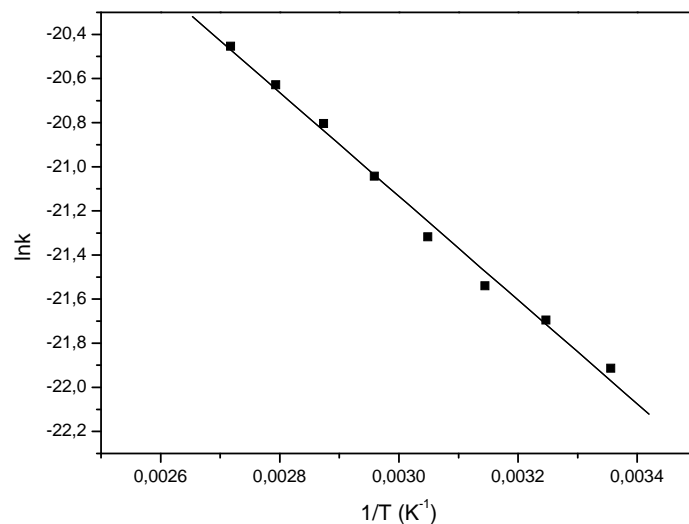


Fig.3. The dependence of  $\ln(k)$  on  $1/T$  for  $(\text{CF}_3)_2\text{CHOH}$

So, trifluoroethanol have been shown a completely different behaviour. The most striking difference was the comparatively intense signal at 1.7 eV exclusively associated with the ion  $\text{CF}_3\text{CH}_2\text{O}^-$  arising from the loss of a neutral H atom.

Additionally, the fluorination considerably increases the cross section for dissociative electron attachment. The ethanol forms exclusively products of simple bond cleavage while the fluorinated alcohol shows a tendency to abstract the stable molecule hydrogenfluoride. A common reaction channel for both alcohols is the loss of hydrogen atom and the formation of the stable alkoxy anion [9].

In our previous paper [7,8] we have shown the linear correlation between the thermal electron attachment rate coefficients ( $k$ 's) and activation energies ( $E_a$ 's) for some halocontaining molecules. In Fig. 4 we present thermal electron capture rate coefficients as a function of the activation energies for three fluoroalcohols investigated just now together with our previous data. As you can see the results fit to each other. That agree also to theoretically obtained values (solid line in Fig.4) of the rate coefficients for  $T = 298\text{K}$  when electron was considered as de Broglie wave [8].

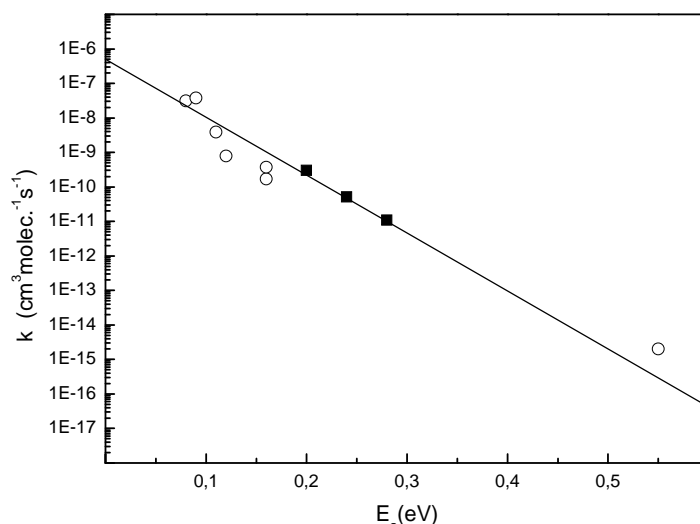


Fig.4. Thermal electron capture rate coefficients as a function of the activation energies (!) present data, (-) our previous data for some halogenated hydrocarbons [7, 8].

On the basis of our findings we confirmed that the activation energy is the main factor influencing the rate coefficient. Additionally the experimental kinetic results are much more reliable if both kinetic parameters i.e. reaction rate coefficients and activation energies are determined in the same experiment.

### Conclusions

1. New set of the reaction rate coefficients and activation energies for electron capture by fluoroalcohols (Table 1) have been completed.
2. The second order processes only were responsible for the electron capture.
3. The dependence of the thermal electron attachment rate coefficients ( $k$ 's) on the activation energies ( $E_a$ 's) has been demonstrated.
4. The simultaneous determination of the reaction rate coefficients and activation energy seems to elevate the reliability of the obtained values. On the other hand it can be treated as quality indicator of the experiment.

### References:

- [1] L.G. Christophorou (Ed.), *Electron-Molecule Interactions and Their Applications*, vol. I-II, Academic, Orlando, 1984.
- [2] E. Illenberger and J. Momigny, *Gaseous Molecular Ions. An Introduction to Elementary Processes Induced by Ionization*, Steinkopff, Darmstadt, Springer, New York, 1992.
- [3] *Organofluorine Chemistry, Principles and Commercial Applications.* / Eds/ Banks R.E., Smart B.E., Tatlow J.C. Plenum Press: New York. 1994.
- [4] G.G. Furin, A.A. Ilyin, U.L. Bakhmutov, A.N. Ilyin, L.M. Ivanova, *Fluorine Notes Journal*, Vol. 1(50), 2007.
- [5] M.D. Hurley, T.J. Wallington, M.P.S. Andersen, D.A. Ellis, J.W. Martin, S.A. Mabury, *J. Phys. Chem. A*, 108, (2004) 1973.
- [6] B. Rajakumar, J.B. Burkholder, R.W. Portmann, A.R. Ravishankara: *Phys. Chem. Chem. Phys.*, 7, (2005) 2498.
- [7] J. Kopyra, J. Wnorowska, M. Forys, I. Szamrej, *Int. J. Mass Spectrom.* 268, (2007) 60.
- [8] J. Kopyra, J. Wnorowska, M. Forys, I. Szamrej, *Int. J. Mass Spectrom.* 291, (2010) 13.
- [9] M. Orzol, I. Martin, J. Kocisek, I. Dabkowska, J. Langer and E. Illenberger, *Phys. Chem. Chem. Phys.*, 9 (2007) 3424.

**Acknowledgments:** This work has been supported by the Polish Ministry of Science and Higher Education.

# Experimental study of Collisional Radiative Recombination of Ar<sup>+</sup> ions at low temperatures

T. Kotrík, P. Dohnal, R. Plašil, Š. Roučka, J. Glosík

Department of Surface and Plasma Physics, Faculty of Mathematics and Physics, Charles University,  
V Holešovičkách 2, Praha 180 00, Czech Republic

e-mail: kotrik.tomas@gmail.com

## Abstract

Presented is the flowing afterglow study of Collisional Radiative Recombination of Ar<sup>+</sup> ions with electrons in He/Ar plasma at temperatures 77 – 200 K and electron densities up to  $n_e \sim 10^{10} \text{ cm}^{-3}$ . The obtained ternary recombination rate coefficient at 77 K is  $K_{\text{CRR}}(77 \text{ K}) = (1.1 \pm 0.4) \times 10^{-17} \text{ cm}^6 \text{ s}^{-1}$ . The measured temperature dependence of  $K_{\text{CRR}}$  is in good agreement with theoretical prediction ( $K_{\text{CRR}} \sim T^{-(4.5 \pm 1.8)}$ ).

**Keywords:** Collisional radiative recombination, flowing afterglow, Ar<sup>+</sup>, low temperature plasma.

## Introduction

Binary recombination of atomic ions with electrons is in general slow process comparing to dissociative recombination (DR) of molecular ions (like O<sub>2</sub><sup>+</sup> etc.). However, the overall recombination process can be enhanced by ternary recombination, where part of the recombination energy is transferred to the third particle. If the third particle is an electron we are talking about Collisional Radiative Recombination (CRR).

The theory of CRR, was originally developed by Bates [1] and Mansbach with Keck [2]. Based on this work Stevefelt [3] derived analytical formula for effective binary rate coefficient of CRR:

$$\alpha_{\text{CRR}} = 3.8 \times 10^{-9} T_e^{-4.5} n_e + 1.55 \times 10^{-10} T_e^{-0.63} + 6 \times 10^{-9} T_e^{-2.18} n_e^{0.37} \text{ cm}^3 \text{ s}^{-1}, \quad (1)$$

where  $T_e$  is electron temperature given in K and  $n_e$  is electron number density given in  $\text{cm}^{-3}$ . The first term represents pure collisional recombination, the second term corresponds to radiative recombination and the third term describes the competition between collisional and radiative recombination. At our experimental conditions ( $n_e \sim 10^9 \text{ cm}^{-3}$ ,  $T_e < 200 \text{ K}$ ) the first term (recombination through collision with electron) is dominant and the other two can be neglected. A simple approximate ternary recombination rate coefficient can be defined:  $K_{\text{CRR}} = \alpha_{\text{CRR}}/n_e = 3.8 \times 10^{-9} T_e^{-4.5} \text{ cm}^6 \text{ s}^{-1}$ , which is strongly dependent on temperature and independent on  $n_e$ . Formula (1) has been affirmed to certain extend also by later quantum mechanical calculations [4,5] and experimental works. Experiments have been carried out mostly at higher electron temperatures (1000 – 4000 K) (see compilation in [4]) and in only few cases also at 300 K [6,7,8,9]. To our knowledge there are up to now no experimental measurements of CRR rate coefficient at temperatures below 300 K. A few studies have been carried out in ultracold plasmas but the presence of strong magnetic field confining the plasma could influence the recombination process [10, 11, 12]. In the paper we present the results of the CRR study of Ar<sup>+</sup> ions in temperature range 77 – 200 K.

## Experiment

Modified version of Flowing Afterglow with Langmuir Probe (FALP) apparatus [13] – Cryo-FALP [14,15,16,17] was used to study slow recombination processes at temperatures down to 77 K. Scheme of the Cryo-FALP is shown in figure 1. Cooling of the flow tube is achieved by filling liquid nitrogen reservoirs attached to the flow tube wall. The upstream section A of the apparatus (see figure 1) is kept at 300 K, section B is cooled to a temperature near 150 K and section C is cooled to 77 K. For experiments at higher temperatures the cooling is stopped and the data are taken during increase of the flow tube temperature. Microwave discharge in helium gas of high purity is ignited in the glass part of the section A. Created plasma consisting mainly of He<sup>+</sup> ions and He<sup>m</sup> metastables is then driven along the flow tube by a fast flow of helium gas. Downstream from the discharge region argon gas is added to the flow tube and in sequence of ion-molecule reactions Ar<sup>+</sup> dominated plasma is formed

[18]. Plasma is precooled in section B via collisions with helium buffer gas to 100 – 150 K. In section C plasma is already thermalized with the temperature equal to the temperature of the flow tube wall (see discussion below). Recombination coefficients are derived from the plasma parameters measurements along the section C using axially movable Langmuir probe (for details see refs. [15,19]).

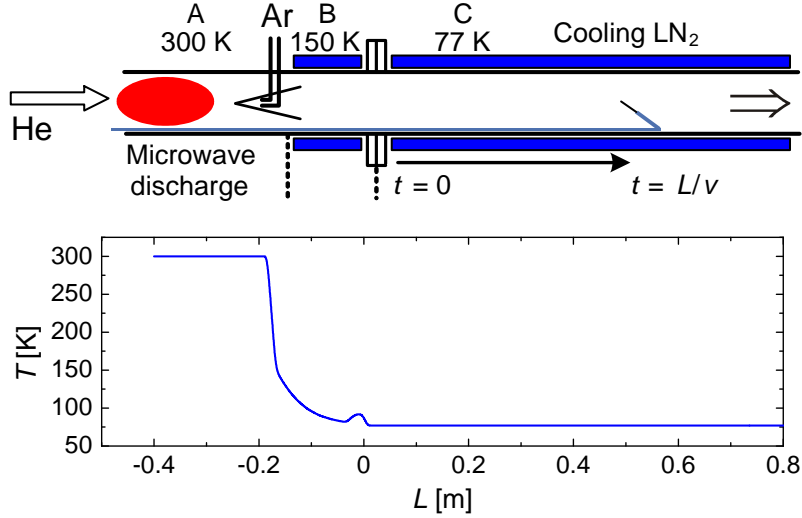


**Fig. 1.** Simplified diagram of the Cryo-FALP apparatus. Sections A, B, C of the apparatus correspond to parts with different wall temperatures (see plot). The plasma decay time is given by a position of the probe along the axis  $t = L/v_{\text{PLASMA}}$ .

The decay of the electron density due to CRR and diffusion in quasineutral plasma ( $[Ar^+] = n_e$ ) can be described by differential equation:

$$\frac{dn_e}{dt} = -K_{\text{CRR}} [Ar^+] n_e^2 - \frac{n_e}{\tau_D} = -K_{\text{CRR}} n_e^3 - \frac{n_e}{\tau_D} \quad (2)$$

where  $\tau_D$  is characteristic diffusion time.  $K_{\text{CRR}}$  and  $\tau_D$  can be obtained from the fit of the experimental electron density decay under the assumption of  $K_{\text{CRR}}$  and  $\tau_D$  being constant. By time integration of equation (2) we obtain the expression:

$$Y = \ln\left(\frac{n(t_b)}{n(t_a)}\right) + (t_b - t_a) \frac{1}{\tau_D} = -K_{\text{CRR}} \int_{t_a}^{t_b} n^2(t) dt = -K_{\text{CRR}} X, \text{ where } X = \int_{t_a}^{t_b} n^2(t) dt. \quad (3)$$

Slope of a plot of  $Y$  vs.  $X$  gives the coefficient  $K_{\text{CRR}}$ . We call this analysis “integral analysis” and the examples are shown in figure 2.

## Results and discussion

The temperature dependence of CRR is very strong ( $T^{-4.5}$ ), thus it is critical to ensure constant plasma temperature over the section C. In lower panel of figure 3 three electron density decay curves measured at fixed helium pressure ( $p$ ) but with different buffer gas velocities ( $v$ ) are plotted. At fixed pressure, the buffer gas velocity is proportional to the helium flow rate. For the smallest velocity the fit of the experimental data using our integral analysis is good over the whole length of section C. For higher velocities the length of part of the section C where the fits are acceptable is shorter. We assume that the ion and electron temperatures in section C are equal to the temperature of the buffer gas. At higher velocities the helium flows a significant distance into section C before cooling down to the wall temperature. In order to understand the buffer gas temperature evolution along the flow tube we have derived numerical solution describing the heat transfer from the walls to the gas using the proper parabolic velocity profile of the flowing gas. The calculated evolution of buffer gas temperature in section C plotted for different gas velocities is shown in upper panel of figure 3. On the lower panel of figure 3 we have marked the positions ( $L_T$ ) at which the calculated gas temperature and wall temperature corresponds to within 15 %. The calculated and observed temperature equilibration is in a good agreement. The following measurements were carried out at conditions where the buffer gas

velocities were low, thus the “thermal equilibration distance” was reasonably short.

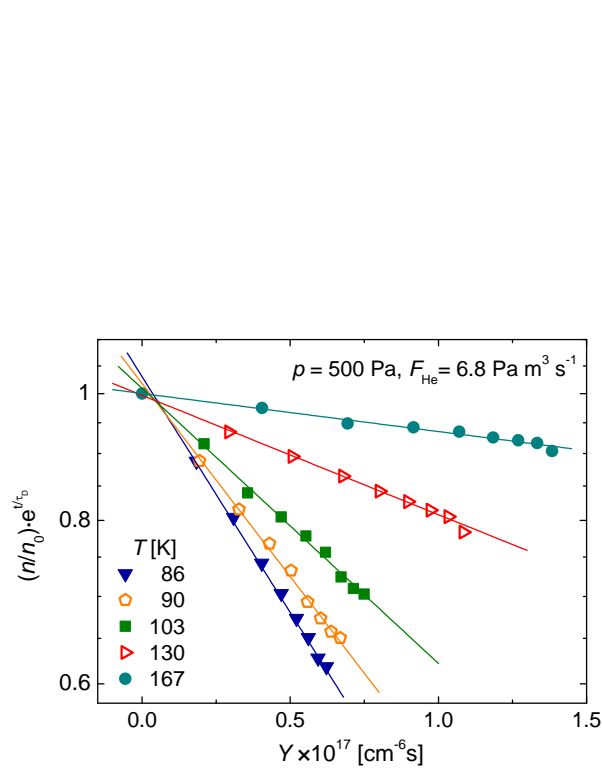


Fig. 2. Plotted examples of “integral analysis” data measured at different gas temperatures. From the slopes of the plots coefficients  $K_{\text{CRR}}$  are obtained. For further details see text.

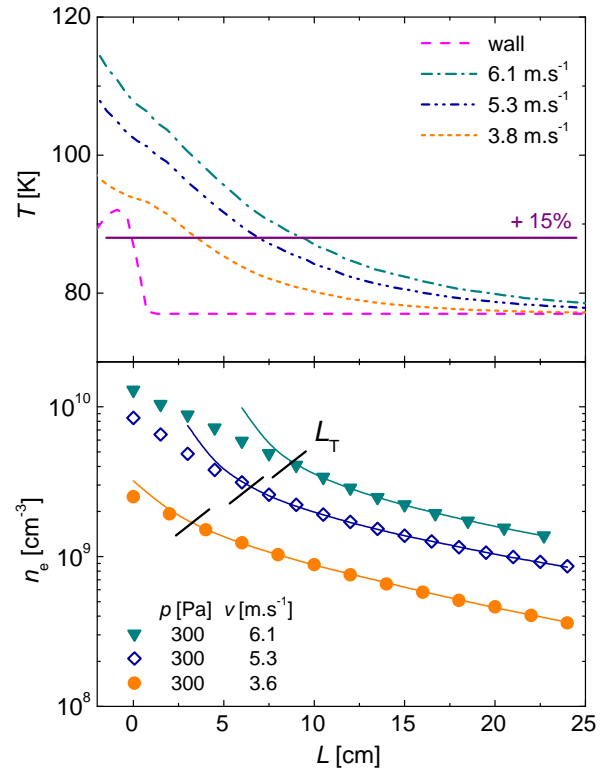


Fig. 3. Upper panel: Evolution of buffer gas temperature in section C calculated for different gas velocities. Lower panel: Electron density decay curves measured at fixed helium pressure and different buffer gas velocities.  $L_T$  denotes the position at which the calculated gas temperature approaches the wall temperature to within 15 %. Solid lines represent the fits of the data.

The examples of measured temperature evolutions of  $K_{\text{CRR}}$  in the temperature range 77 – 200 K and different experimental conditions are plotted in figure 4. The theoretical dependence (1) is plotted by dashed line (collisional term only) and by dotted lines (all terms in equation (1)) for two different electron number densities. We also show the results of two earlier CRR studies carried out at  $T = 300$  K. The preliminary experimental results show an excellent agreement of measured  $K_{\text{CRR}}$  with theory [3] and that the theory is valid also for temperatures down to 77 K. Further studies of CRR in  $\text{Ar}^+$  dominated plasma are in progress.

The actual temperatures were verified by determining diffusion time constant  $\tau_D$  from the measured decay curves. The time constant is defined by relation  $\tau_D = \lambda^2/D_a$ , where  $\lambda$  is a characteristic diffusion length and  $D_a$  is ambipolar diffusion constant for  $\text{Ar}^+$  ions in helium. Exploiting the dependence of  $D_a$  on buffer gas number density  $[\text{He}]$  and temperature  $T$  we obtain  $\tau_D \sim \lambda^2[\text{He}]/\mu_0 T$ , where  $\mu_0$  is reduced zero field mobility (see e.g. [20]). Under the assumption of constant  $\mu_0$  over the studied temperature range 77 – 300 K the plot of  $[\text{He}]/\tau_D$  versus  $T$  will be linear with the slope given by  $\mu_0$ . In upper panel of figure 5 we plotted the experimental values of  $[\text{He}]/\tau_{D\text{Exper}}$  together with the theoretical values of  $[\text{He}]/\tau_{D\text{Theory}}$  (solid line) as a function of temperature. The theoretical line was plotted using value of  $\mu_0$  measured at 300 K in independent experiments [21,22]. Dashed lines refer to theoretical values at  $\pm 10\%$  deviation of  $\mu_0$ . For comparison, we also show data measured with Cryo-FALP apparatus at temperatures 250 K and 300 K. The agreement between experimental and theoretical values is very good, thus proving that the gas temperature and the temperature of the flow tube wall were nearly equal.

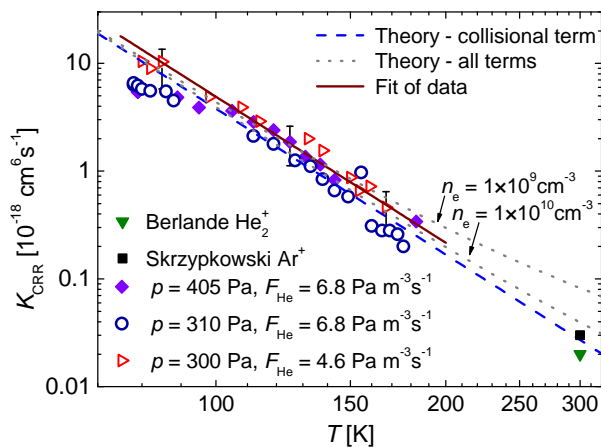


Fig. 4. Measured  $K_{\text{CRR}}$  coefficient as a function of temperature. Dashed line corresponds to theoretical value calculated from collisional term of equation (1). Dot lines indicate theoretical values of  $K_{\text{CRR}}$  for two electron densities calculated using all terms of relation (1). Closed square and triangle are data measured by Skrzypkowski et al. [7] and by Berlande et al. [9]

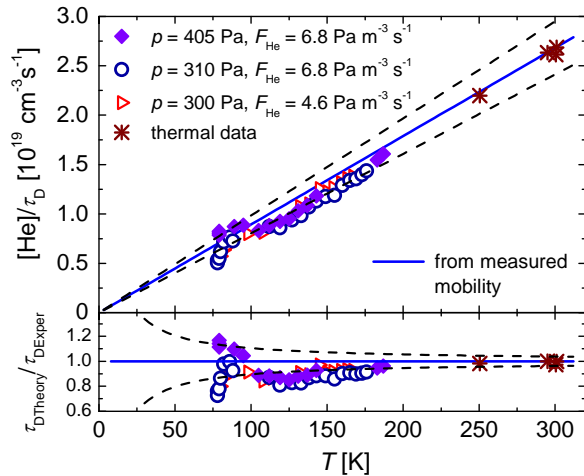


Fig. 5. Upper panel: Experimental data of  $[\text{He}]/\tau_{\text{DExper}}$  plotted as a function of temperature at different experimental conditions. Lower panel: Ratio  $\tau_{\text{DTheory}}/\tau_{\text{DExper}}$  versus temperature. Full lines refer to theoretical values of  $[\text{He}]/\tau_{\text{DTheory}}$  calculated from mobility of  $\text{Ar}^+$  in He [21,22]. Dashed lines refer to theoretical values at  $\pm 10\%$  deviation of  $\mu_0$ .

## Conclusions

Our results of CRR study of  $\text{Ar}^+$  ion are in very good agreement with theory and show that the theoretical formula (1) holds also in region of lower temperatures from 77 K – 180 K, and that due to strong temperature dependence the recombination at low temperature is dominated by the collisional term. According to theory, the formula applies also for other atomic ions, as for the collisional radiative process the crucial are high, nearly hydrogenic Rydberg states.

Numerical solution of heat exchange between the flow tube wall and the buffer gas helped us to understand the temperature evolution of helium gas along the flow tube and allowed us to set the experimental conditions at which the buffer gas temperature approached the temperature of the wall along the whole length of the section C. Measurements of ambipolar diffusion time constants provided a decent proof of the thermal equilibration between the buffer gas and the flow tube wall.

## Acknowledgments

This work is a part of the research plan MSM 0021620834 and grant OC10046 financed by the Ministry of Education of the Czech Republic and was partly supported by GACR (202/07/0495, 202/08/H057, 205/09/1183, 202/09/0642), by GAUK 92410, GAUK 86908, GAUK 54010, GAUK 25709 and by COST Action CM0805 (The Chemical Cosmos).

## References

- [1] D.R. Bates, A.E. Kingston, R.W.P. McWhirter, *Proc. Roy. Soc. A*, 267 (1962) 297.
- [2] P. Mansbach, J. Keck, *Phys. Rev.*, 181 (1969) 275.
- [3] J. Stevefelt, J. Boulmer, J-F. Delpech, *Phys. Rev. A*, 12 (1975) 1246.
- [4] G.J. Pert, *J. Phys. B: At. Mol. Opt. Phys.*, 23 (1990) 619.
- [5] S.X. Hu, *Phys. Rev. Lett.*, 98 (2007) 133201-1.
- [6] M. Tsuji, T. Matsuzaki, T. Tsuji, *Chem. Phys.*, 285 (2002) 335.
- [7] M.P. Skrzypkowski, R. Johnsen, R. E. Rosati, M. F. Golde, *Chem. Phys.*, 296 (2004) 23.
- [8] G.E. Veatch, H.J. Oskam, *Phys. Rev. A*, 1 (1970) 1498.
- [9] J. Berlande, M. Cheret, R. Deloche, A. Gonfalone, C. Manus, *Phys. Rev. A*, 1 (1970) 887
- [10] R.S. Fletcher, X. L. Zhang, S.L. Rolston, *Phys. Rev. Lett.*, 99 (2007) 145001-1.
- [11] S.X. Hu, D. Vranceanu, S. Mazevet, L.A. Collins, *Phys. Rev. Lett.*, 95 (2005) 163402-1.

- [12] M. Amoretti et al., *Phys. Lett. B*, 583 (2004) 59.
- [13] D. Smith, N.G. Adams, A.G. Dean, M.J. Church, *J.Phys. D*, 8 (1975) 141.
- [14] J. Glosík, O. Novotný, A. Pysanenko, P. Zakouril, R. Plasil, P. Kudrna, V. Poterya, *Plasma Sources Sci. Technol.*, 12 (2003) 117.
- [15] I. Korolov, O. Novotný, J. Varju, T. Kotřík, R. Plašil, M. Hejduk, J. Glosík, *Contrib. Plasma Phys.*, 48 (2008) 521-526.
- [16] J. Glosík, R. Plašil, I. Korolov, T. Kotřík, O. Novotný, P. Hlavenka, P. Dohnal, J. Varju, V. Kokoouline, C. H. Greene, *Phys. Rev. A*, 79 (2009) 052707.
- [17] T. Kotřík, P. Dohnal, I. Korolov, R. Plašil, Š. Roučka, J. Glosík, C. H. Greene, V. Kokoouline, *J. Chem. Phys.*, 133 (2010) 034305
- [18] R. Plasil, J. Glosík, V. Poterya, P. Kudrna, J. Ruzs, M. Tichy, A. Pysanenko, *Int. J. Mass Spectrom.*, 218 (2002) 105.
- [19] J.D. Swift, M.J.R. Schwar, *Electrical Probes for Plasma Diagnostics*, Illiffe, London, 1970.
- [20] E.A. Mason, E.W. McDaniel, *Transport Properties of Ions in Gase*, John Wiley and Sons, New York, 1988.
- [21] W. Lindinger, D.L. Albritton, *J. Chem. Phys.*, 62(9) (1975) 3517.
- [22] R. Johnsen, M.A. Biondi, *Phys. Rev. A*, 20 (1979) 221.

# State selective recombination of para- and ortho- $\text{H}_3^+$ at 140 K

P. Dohnal, J. Varju, M. Hejduk, T. Kotrík, P. Rubovič, R. Plašil, J. Glosík

Department of Surface and Plasma Science, Faculty of Mathematics and Physics, Charles University in Prague,  
V Holešovičkách 2, Praha 8, 180 00, Czech Republic

e-mail: pr.dohnal@seznam.cz

## Abstract

The preliminary results of experimental state selective study of  $\text{H}_3^+$  recombination with electrons are presented. By using different ratios of para and ortho  $\text{H}_2$  in normal and para enriched hydrogen we produced different populations of para- $\text{H}_3^+$  in  $\text{H}_3^+$  dominated decaying plasma at 140 K. Absorption spectroscopy (NIR-CRDS) was used to measure the time evolution of densities of two lowest rotational  $\text{H}_3^+$  states in afterglow plasma. By measuring plasma decays at different populations of ortho- and para- $\text{H}_3^+$  we were able to evaluate binary and helium assisted ternary recombination rate coefficient of ortho- $\text{H}_3^+$  and para- $\text{H}_3^+$ :  ${}^o\alpha_{\text{bin}}(140 \text{ K}) = (0.3 \pm 0.9) \times 10^{-7} \text{ cm}^3 \text{ s}^{-1}$ ,  ${}^p\alpha_{\text{bin}}(140 \text{ K}) = (1.3 \pm 0.9) \times 10^{-7} \text{ cm}^3 \text{ s}^{-1}$ ,  ${}^oK_{\text{He}}(140 \text{ K}) = (0.1 \pm 3.3) \times 10^{-25} \text{ cm}^6 \text{ s}^{-1}$  and  ${}^pK_{\text{He}}(140 \text{ K}) = (4.3 \pm 3.3) \times 10^{-25} \text{ cm}^6 \text{ s}^{-1}$ .

**Keywords:** Afterglow plasma,  $\text{H}_3^+$ , NIR-CRDS, recombination.

## Introduction

$\text{H}_3^+$ , the simplest polyatomic ion, is the dominant ion species in many types of hydrogen containing plasmas e.g. in ionospheres of large planets [1] and astrophysically relevant plasmas [2]. The recombination of  $\text{H}_3^+$  has been studied since fifties but the understanding of the detailed properties of this process grew only slowly [3]. For a long period of time there was a big difference between experimental values and theoretical predictions [4,5]. Moreover the recombination rate coefficients obtained using different experimental techniques differed substantially [3,6,7,8,9]. Few years ago the process of binary dissociative recombination of  $\text{H}_3^+$  was successfully described by taking into account the Jahn-Teller coupling [10]. Recombination cross sections and recombination rate coefficients measured in recent storage ring experiments [11,12,13,14] are in good agreement with calculated ones [15,16,17].

Recent experiments have shown that the effective recombination rate coefficient  $\alpha_{\text{eff}}$  determined from plasma decay during the afterglow is composed of two components. The binary dissociative recombination is enhanced by helium assisted ternary process [18,19,20,21,22].

The theory of dissociative recombination predicts that the recombination rate coefficients will be different for different spin states ( ${}^o\alpha_{\text{DR}}$  and  ${}^p\alpha_{\text{DR}}$  for ortho- and para- $\text{H}_3^+$  respectively) for temperatures below 300 K. The results from storage ring experiments are partly in agreement with this prediction [11,13,14]. But in these experiments, the quantum state of the recombining ions is determined prior to their injection in the accelerator. We are not aware of storage ring experiments with *in-situ* determination of the populations of the states of the recombining  $\text{H}_3^+$  ions.

In this article we present the preliminary results of our measurements of recombination rate coefficients  ${}^o\alpha$  and  ${}^p\alpha$  of pure ortho- and pure para- $\text{H}_3^+$  respectively. We made direct (*in situ*) determination of para- $\text{H}_3^+$  and ortho- $\text{H}_3^+$  densities in plasma ignited in He/Ar/ $\text{H}_2$  mixture at 140 K.

In this paper we use following notation: upper left index o, p, n, e to indicate “ortho”, “para”, “normal” and “para enriched” respectively. In this sense  ${}^o\text{H}_3^+$  and  ${}^p\text{H}_3^+$  for ortho- $\text{H}_3^+$  and para- $\text{H}_3^+$  ions means generally all ortho states and all para states. For relative populations of  ${}^o\text{H}_3^+$  and  ${}^p\text{H}_3^+$  states we use symbols  ${}^of = [{}^o\text{H}_3^+]/[\text{H}_3^+]$  and  ${}^pf = [{}^p\text{H}_3^+]/[\text{H}_3^+]$  ( ${}^of + {}^pf = 1$ ). Similarly we use  ${}^o\text{H}_2$ ,  ${}^p\text{H}_2$ ,  ${}^e\text{H}_2$  and  ${}^n\text{H}_2$  for ortho- $\text{H}_2$ , para- $\text{H}_2$ , para enriched  $\text{H}_2$  and normal- $\text{H}_2$  (normal  $\text{H}_2$  means that the populations of  ${}^o\text{H}_2$  and  ${}^p\text{H}_2$  are according to thermodynamic equilibrium – 1/4 of the molecules are in para and 3/4 in ortho states).

We can write following balance equations for processes in low temperature hydrogen afterglow plasma:

$$\frac{d[{}^{\circ}\text{H}_3^+]}{dt} = -{}^{\circ}\alpha_{\text{eff}}[{}^{\circ}\text{H}_3^+]n_e - \frac{[{}^{\circ}\text{H}_3^+]}{\tau_D} + \nu_{\text{po}}[{}^{\text{p}}\text{H}_3^+] - \nu_{\text{op}}[{}^{\circ}\text{H}_3^+], \quad (1)$$

$$\frac{d[{}^{\text{p}}\text{H}_3^+]}{dt} = -{}^{\text{p}}\alpha_{\text{eff}}[{}^{\text{p}}\text{H}_3^+]n_e - \frac{[{}^{\text{p}}\text{H}_3^+]}{\tau_D} - \nu_{\text{po}}[{}^{\text{p}}\text{H}_3^+] + \nu_{\text{op}}[{}^{\circ}\text{H}_3^+], \quad (2)$$

where  ${}^{\circ}\alpha_{\text{eff}}$  and  ${}^{\text{p}}\alpha_{\text{eff}}$  are the rate coefficients of overall recombination of  ${}^{\circ}\text{H}_3^+$  and  ${}^{\text{p}}\text{H}_3^+$  ions,  $\nu_{\text{po}}$  and  $\nu_{\text{op}}$  are the frequencies of  ${}^{\text{p}}\text{H}_3^+$  to  ${}^{\circ}\text{H}_3^+$  transitions and reverse transitions respectively,  $\tau_D$  is the time constant of ambipolar diffusion. Under assumption that the plasma is quasineutral and  ${}^{\circ}\text{H}_3^+$  and  ${}^{\text{p}}\text{H}_3^+$  are dominant ions, by summing equations (1) and (2) we obtain:

$$\frac{dn_e}{dt} = -({}^{\text{p}}\alpha_{\text{eff}} f + {}^{\circ}\alpha_{\text{eff}} f)n_e^2 - \frac{n_e}{\tau_D} = -\alpha_{\text{eff}}n_e^2 - \frac{n_e}{\tau_D}, \quad (3)$$

If the fractions  $f$  and  $f$  are constant during the afterglow then the decay of plasma is described by effective recombination rate coefficient  $\alpha_{\text{eff}} = {}^{\circ}\alpha_{\text{eff}}f + {}^{\text{p}}\alpha_{\text{eff}}f$ . Hence the values of  ${}^{\circ}\alpha_{\text{eff}}$  and  ${}^{\text{p}}\alpha_{\text{eff}}$  can be obtained by measuring at least at two different values of  $f$ . The effective recombination rate coefficient is composed of two parts - the binary dissociative recombination and helium assisted ternary recombination [18,19,20,21]:

$$\alpha_{\text{eff}}(T, [\text{He}]) = \alpha_{\text{bin}}(T) + K_{\text{He}}(T)[\text{He}], \quad (4)$$

where  $\alpha_{\text{bin}}(T)$  is binary coefficient of dissociative recombination and  $K_{\text{He}}(T)$  is ternary recombination rate coefficient. Similar equations can be written for  ${}^{\circ}\alpha_{\text{eff}}$  and  ${}^{\text{p}}\alpha_{\text{eff}}$  with  ${}^{\circ}\alpha_{\text{bin}}$ ,  ${}^{\circ}K_{\text{He}}$  for  ${}^{\circ}\text{H}_3^+$  and  ${}^{\text{p}}\alpha_{\text{bin}}$ ,  ${}^{\text{p}}K_{\text{He}}$  for  ${}^{\text{p}}\text{H}_3^+$  respectively.

## Experiment

In presented experimental set up plasma is formed in pulsed microwave discharge in a fused silica tube cooled by liquid nitrogen vapour. The falling edge of the microwave pulse is short ( $<50 \mu\text{s}$ ) to prevent the microwaves from influencing the decaying plasma during afterglow. The discharge is ignited in the central section of the discharge tube in a mixture of He/Ar/ $\text{H}_2$  (typically used number densities  $10^{17}/10^{14}/10^{14} \text{ cm}^{-3}$ ). A schematic picture of used NIR-CRDS apparatus is shown in figure 1.

To produce para enriched hydrogen ( ${}^{\text{p}}\text{H}_2$ ) from normal  $\text{H}_2$  we used  $\text{Fe}_2\text{O}_3$  as a catalytic converter cooled below 20 K [23,24]. The nuclear magnetic resonance was used to determine the fraction of  ${}^{\text{p}}\text{H}_2$  ( $>87 \pm 5 \%$ ). This ratio was sufficient to produce significantly enriched  ${}^{\text{p}}\text{H}_3^+$ .

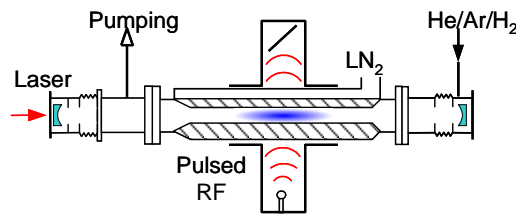


Fig. 1. The CRDS apparatus. Mixture of He, Ar and  $\text{H}_2$  is ionized in a pulsed discharge. The decay of ion density is measured using 1.38 nm laser.

The evolution of ion density was measured by a near infrared cavity ring down absorption spectrometer (NIR-CRDS, for details see e.g. [25,26]). Three rotational states of  $\text{H}_3^+$  were observed using transitions  $0v_2^0(1,1) \leftarrow 3v_2^1(2,1)$  for  ${}^{\text{p}}\text{H}_3^+$ ,  $0v_2^0(1,0) \leftarrow 3v_2^1(2,0)$  and  $0v_2^0(3,3) \leftarrow 3v_2^1(4,3)$  for  ${}^{\circ}\text{H}_3^+$ . Time evolutions of absorption at center of the mentioned lines have been measured during the discharge and afterglow and used to calculate the time evolution of ion densities of  ${}^{\circ}\text{H}_3^+$  and  ${}^{\text{p}}\text{H}_3^+$ . The kinetic temperature of  $\text{H}_3^+$  ions was obtained from Doppler broadening of absorption lines. An example of three Doppler profiles of above mentioned transitions is shown in Figure 2. The lowest rotational energy levels of  $\text{H}_3^+$  ion are plotted in figure 3.

As mentioned before, the densities of helium buffer gas,  $\text{H}_2$  and  $n_e$  are very high. Therefore, prior to its recombination with electrons, a recombining ion undergoes in average  $10^5$  collisions with helium,

approximately ten collisions with electrons [27] and more than ten collisions with H<sub>2</sub>. Therefore we assume that the population within the <sup>p</sup>H<sub>3</sub><sup>+</sup> and <sup>o</sup>H<sub>3</sub><sup>+</sup> manifold is thermalised to measured kinetic temperature during the afterglow. The <sup>p</sup>H<sub>3</sub><sup>+</sup> to <sup>o</sup>H<sub>3</sub><sup>+</sup> ratio is determined mainly by <sup>p</sup>H<sub>2</sub> to <sup>o</sup>H<sub>2</sub> ratio and is not thermal if nonthermal <sup>p</sup>H<sub>2</sub> to <sup>o</sup>H<sub>2</sub> ratio is used.

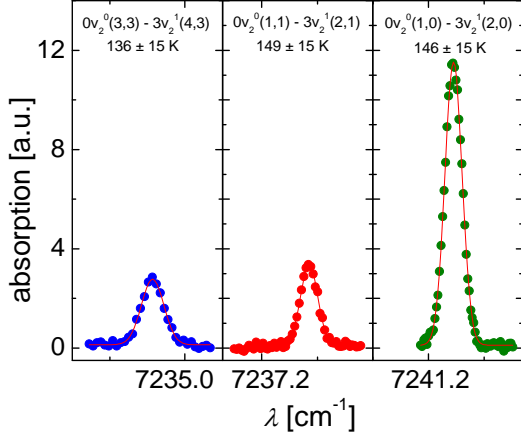


Fig. 2. Examples of measured absorption line profiles of H<sub>3</sub><sup>+</sup> ion at 140 K. Used transitions are noted in the figure.

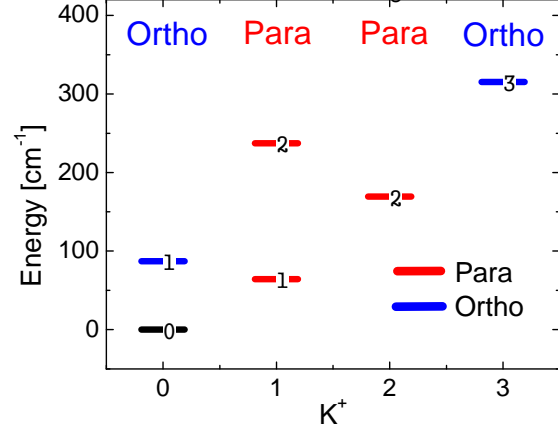


Fig. 3. Distribution of H<sub>3</sub><sup>+</sup> rotational energy levels of the ground vibrational state. Levels are labeled with the corresponding value of the quantum number N<sup>+</sup>. The non populated (0,0) state is black. Compiled from data in [28].

## Results and discussion

At used H<sub>2</sub> densities ( $8 \times 10^{13}$ - $7 \times 10^{14}$  cm<sup>-3</sup>) and normal H<sub>2</sub> as precursor the two lowest rotational states of H<sub>3</sub><sup>+</sup> ion and higher lying state of o-H<sub>3</sub><sup>+</sup> (N<sup>+</sup> = 3, K<sup>+</sup> = 3) ion have populations in accordance with thermal equilibrium at 140 K (see lower plot in figure 4). When using <sup>e</sup>H<sub>2</sub> as a precursor the ratio of number densities of both measured ortho states (o-H<sub>3</sub><sup>+</sup> (N<sup>+</sup> = 1, K<sup>+</sup> = 0) and o-H<sub>3</sub><sup>+</sup> (N<sup>+</sup> = 3, K<sup>+</sup> = 3), see upper plot in figure 4) is almost the same as in thermal equilibrium so we can assume that the equilibrium is maintained in the <sup>o</sup>H<sub>3</sub><sup>+</sup> and <sup>p</sup>H<sub>3</sub><sup>+</sup> manifolds.

The evolutions of <sup>o</sup>H<sub>3</sub><sup>+</sup>(1,0) and <sup>p</sup>H<sub>3</sub><sup>+</sup>(1,1) densities were measured for each set of experimental conditions. Under assumption that the populations within the <sup>o</sup>H<sub>3</sub><sup>+</sup> and <sup>p</sup>H<sub>3</sub><sup>+</sup> manifolds are in thermal equilibrium we obtained density of <sup>o</sup>H<sub>3</sub><sup>+</sup> and <sup>p</sup>H<sub>3</sub><sup>+</sup> respectively. From these density evolutions we obtained  $\alpha_{\text{eff}}$  and  $^p f$ . The effective recombination rate coefficients measured in normal-H<sub>2</sub> and para enriched H<sub>2</sub> as a function of helium density are plotted in upper part of figure 5. The data were fitted using equation (4). When <sup>n</sup>H<sub>2</sub> was used as a precursor ( $^o f = ^p f = 0.5$  – open circles in figure 5) the obtained binary recombination rate coefficient is  $\alpha_{\text{bin}}(140 \text{ K}) = (7.6 \pm 1.9) \times 10^{-8} \text{ cm}^3 \text{ s}^{-1}$  and the ternary recombination rate coefficient is  $K_{\text{He}}(140 \text{ K}) = (2.2 \pm 0.5) \times 10^{-25} \text{ cm}^6 \text{ s}^{-1}$ .

To increase the fraction of <sup>p</sup>H<sub>3</sub><sup>+</sup> in plasma we used <sup>e</sup>H<sub>2</sub> as a precursor. Depending on experimental conditions the  $^p f$  varied in the range 0.68 - 0.76 (full circles in lower part of figure 5). From the values of  $\alpha_{\text{eff}}$  and  $^p f$  measured using <sup>n</sup>H<sub>2</sub> and <sup>p</sup>H<sub>2</sub>, we calculated the values of  $^o \alpha_{\text{eff}}$  and  $^p \alpha_{\text{eff}}$  (stars and triangles in the middle plot of figure 5).

These calculations were done as follows: we used the fit of  $\alpha_{\text{eff}}$  in <sup>n</sup>H<sub>2</sub> as a reference ( $^n \alpha_{\text{eff}}$  in middle plot of figure 6). After the calculation of  $^o \alpha_{\text{eff}}$  and  $^p \alpha_{\text{eff}}$  we fitted those data with linear helium dependence (equation (4)) and obtained corresponding binary a ternary recombination rate coefficients of <sup>o</sup>H<sub>3</sub><sup>+</sup> and <sup>p</sup>H<sub>3</sub><sup>+</sup>:  $^o \alpha_{\text{bin}}(140 \text{ K}) = (2.5 \pm 9.0) \times 10^{-8} \text{ cm}^3 \text{ s}^{-1}$ ,  $^p \alpha_{\text{bin}}(140 \text{ K}) = (1.3 \pm 0.9) \times 10^{-7} \text{ cm}^3 \text{ s}^{-1}$ ,  $^o K_{\text{He}}(140 \text{ K}) = (0.1 \pm 3.3) \times 10^{-25} \text{ cm}^6 \text{ s}^{-1}$  and  $^p K_{\text{He}}(140 \text{ K}) = (4.3 \pm 3.3) \times 10^{-25} \text{ cm}^6 \text{ s}^{-1}$ . The theoretical values of binary dissociative recombination rate coefficients at 140 K are  $^o \alpha_{\text{bin theory}} = 6.6 \times 10^{-8} \text{ cm}^3 \text{ s}^{-1}$  and  $^p \alpha_{\text{bin theory}} = 1.0 \times 10^{-7} \text{ cm}^3 \text{ s}^{-1}$  [17]. Our values are in good agreement with these predictions.

There are shown 1/n plots of electron number density in afterglow using <sup>n</sup>H<sub>2</sub> and <sup>e</sup>H<sub>2</sub> as precursor in figure 6. The straight lines indicate that the early afterglow is recombination dominated. Dashed lines are fits of data.

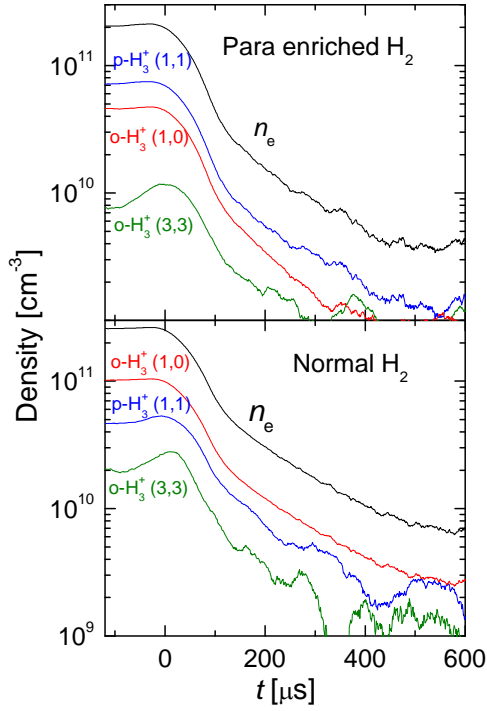


Fig. 4. The decay curves measured for three different  $\text{H}_3^+$  rotational quantum states. The numbers in brackets are quantum numbers  $N^+$  and  $K^+$ . The line labeled  $n_e$  is the sum of ortho- and para- $\text{H}_3^+$  densities (see in text). End of discharge is at  $t = 0$   $\mu\text{s}$ .

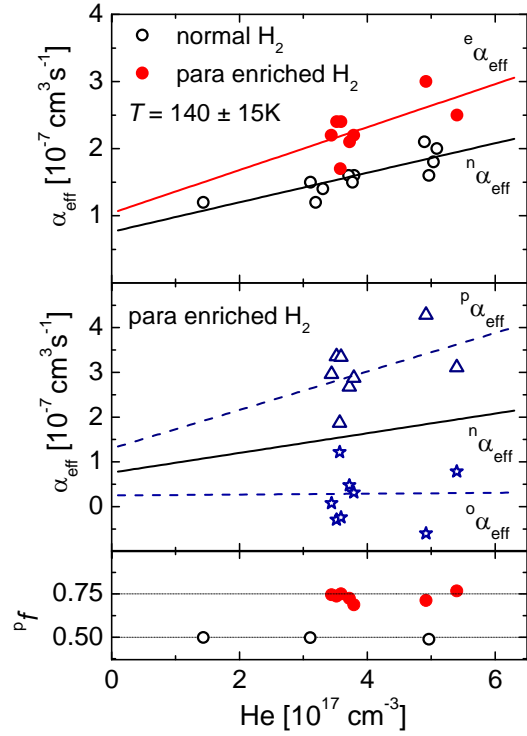


Fig. 5. Upper plot: The dependence of effective recombination rate coefficient on helium number density for normal and para enriched hydrogen. Middle plot: calculated values of  ${}^p\alpha_{\text{eff}}$  and  ${}^o\alpha_{\text{eff}}$ . Lower plot: Measured fraction of  ${}^p\text{H}_3^+$ .

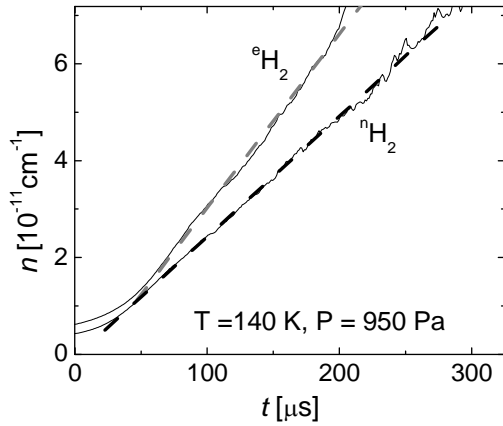


Fig. 6.  $1/n$  plot of electron number density evolution in afterglow using  ${}^n\text{H}_2$  and  ${}^e\text{H}_2$ . The early afterglow is clearly recombination dominated. The slope of the curves gives corresponding  $\alpha_{\text{eff}}$ .

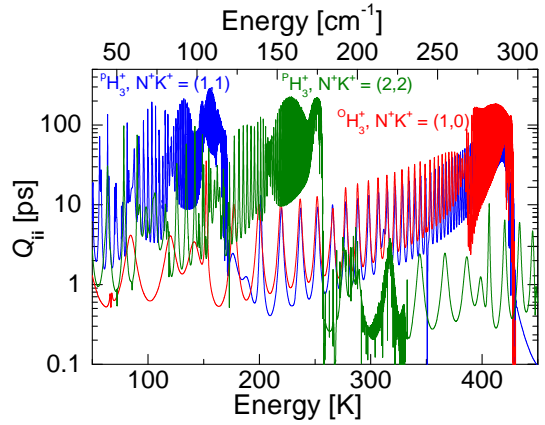


Fig. 7. Diagonal elements of Smith's lifetime matrix for collision of  $\text{H}_3^+$  with electron. Only three lowest rotational states ( $N^+, K^+$ ) = (1,0), (1,1) and (2,2) are shown [19].

The helium assisted ternary recombination rate coefficient is much higher for  ${}^p\text{H}_3^+$  than for  ${}^o\text{H}_3^+$ . This large difference was recently predicted by calculation of lifetimes of neutral  ${}^o\text{H}_3^*$  ( ${}^p\text{H}_3^*$ ) states formed in collision of  ${}^o\text{H}_3^+$  ( ${}^p\text{H}_3^+$ ) with electrons. The lifetimes calculated for three lowest rotational states [19] are plotted in figure 4. At low temperatures (below 300 K) the lifetime of neutral  ${}^p\text{H}_3^*$

(formed from  ${}^{\text{p}}\text{H}_3^+(1,1)$ ) is much longer than the lifetime of  ${}^{\text{o}}\text{H}_3^*$ . This could explain the large difference between  ${}^{\text{o}}K_{\text{He}}$  and  ${}^{\text{p}}K_{\text{He}}$  [18,19].

## Conclusions

We have monitored *in situ* the evolution of the ortho- and para- spin modifications of  $\text{H}_3^+$  ion in afterglow using time resolved CRDS. For a particular ortho- $\text{H}_3^+$  to para- $\text{H}_3^+$  ratio we obtained the effective recombination rate coefficient of  $\text{H}_3^+$  dissociative recombination at 140 K. From these effective recombination rate coefficient, we evaluated the effective recombination rate coefficients of both spin modifications of  $\text{H}_3^+$  ion ( ${}^{\text{o}}\alpha_{\text{eff}}$  and  ${}^{\text{p}}\alpha_{\text{eff}}$ ). From dependence of these recombination rate coefficients on helium density we obtained the binary recombination rate coefficient ( ${}^{\text{p}}\alpha_{\text{BIN}}$  and  ${}^{\text{o}}\alpha_{\text{BIN}}$ ) and ternary recombination rate coefficient ( ${}^{\text{o}}K_{\text{He}}$  and  ${}^{\text{p}}K_{\text{He}}$ ) for both nuclear spin states.

The preliminary results show that the ternary recombination rate coefficients of helium assisted recombination  ${}^{\text{o}}K_{\text{He}}(140\text{ K}) = (0.1 \pm 3.3) \times 10^{-25} \text{ cm}^6\text{s}^{-1}$  and  ${}^{\text{p}}K_{\text{He}}(140\text{ K}) = (4.3 \pm 3.3) \times 10^{-25} \text{ cm}^6\text{s}^{-1}$  are partly in agreement with predictions based on calculation of lifetimes of neutral  $\text{H}_3$  formed in collision of  $\text{H}_3^+$  ion in corresponding rotational state with electrons. The obtained binary dissociative recombination rate coefficients of ortho- $\text{H}_3^+$   ${}^{\text{o}}\alpha_{\text{bin}}(140\text{ K}) = (2.5 \pm 9.0) \times 10^{-8} \text{ cm}^3\text{s}^{-1}$  and para- $\text{H}_3^+$   ${}^{\text{p}}\alpha_{\text{bin}}(140\text{ K}) = (1.3 \pm 0.9) \times 10^{-7} \text{ cm}^3\text{s}^{-1}$  are in good agreement with theoretical predictions.

## Acknowledgements

This work is a part of the research plan MSM 0021620834 and grant OC10046 financed by the Ministry of Education of the Czech Republic and was partly supported by GACR (202/07/0495, 202/08/H057, 205/09/1183, 202/09/0642), by GAUK 92410, GAUK 86908, GAUK 54010, GAUK 25709 and by COST Action CM0805 (The Chemical Cosmos).

## References

- [1] E. Herbst, *Phil. Trans. R. Soc. Lond. A*, 358 (2000) 2523.
- [2] S. Miller et al., *Phil. Trans. R. Soc. Lond. A*, 358 (2000) 2485.
- [3] M. Larsson, A. Orel, *Dissociative Recombination of Molecular Ions*, Cambridge University Press, Cambridge, 2008.
- [4] T. Oka, *Phil. Trans. R. Soc. Lond. A*, 358 (2000) 2363.
- [5] R. Johnsen, *J. Phys.: Conf. Ser.*, 4 (2005) 83.
- [6] D. Smith, P. Španěl, *Int. J. Mass Spectrom.*, 129 (1993) 163.
- [7] T. Amano, *J. Chem. Phys.*, 92 (1990) 6492.
- [8] R. Plašil et al., *Int. J. Mass Spectrom.*, 218 (2002) 105.
- [9] S. Laubé, et al., *J. Phys. B*, 31 (1998) 2111.
- [10] V. Kokoouline, C. H. Greene, B. Esry, *Nature*, 412 (2001) 891.
- [11] H. Kreckel et al., *Phys. Rev. Lett.*, 95 (2005) 263201.
- [12] B. J. McCall et al., *Nature*, 422 (2003) 500.
- [13] A. Petrigani et al., *J. Phys. Conf. Ser.*, 192 (2009) 012022.
- [14] B. A. Tom et al., *J. Chem. Phys.*, 130 (2009) 031101.
- [15] V. Kokoouline, C. H. Greene, *Phys. Rev. A*, 68 (2003) 012703.
- [16] S. dos Santos, V. Kokoouline, C. H. Greene, *J. Chem. Phys.*, 127 (2007) 124309.
- [17] L. Pagani et al., *Astron. Astrophys.*, 494 (2009) 623.
- [18] J. Glosik et al., *J. Phys. B: At. Mol. Opt. Phys.*, 41 (2008) 191001.
- [19] J. Glosik et al., *Phys. Rev. A*, 79 (2009) 52707.
- [20] J. Glosik et al., *Phys. Rev. A*, 80 (2009) 042706.
- [21] J. Glosik et al., *J. Phys. Conf. Ser.*, 192 (2009) 012005.
- [22] T. Kotrik et al., *J. Chem. Phys.*, 133 (2010) 034305.
- [23] S. Tam, M. Fajardo, *Rev. Sci. Instrum.*, 70 (1999) 1926.
- [24] B. A. Tom et al., *Rev. Sci. Instrum.*, 80 (2009) 016108.
- [25] P. Macko et al., *Int. J. Mass Spectrom.*, 233 (2004) 299.
- [26] P. Hlavenka et al., *Int. J. Mass Spectrom.*, 255 (2006) 170.
- [27] V. Kokoouline et al., *Mon. Not. R. Astron. Soc.*, 405 (2010) 1195.
- [28] L. Neale, S. Miller, J. Tennyson, *Astrophys. J.*, 464 (1996) 516.

# Decomposition of 1,1,1,2-Tetrafluoroethane (HFC-134a) in a Nonthermal Plasma-Catalytic Reactor

D. H. Kim, D. I. Jang, E. J. Jwa, S. B. Lee, Y. S. Mok\*

Department of Chemical and Biological Engineering, Jeju National University, 1, Aradong, Jeju City, Jeju Province 690-756, Korea

\*e-mail: smokie@jejunu.ac.kr

## Abstract

A nonthermal plasma reactor packed with dielectric pellets was applied to the decomposition of 1,1,1,2-Tetrafluoroethane (HFC-134a). This work focused on the dependence of HFC-134a decomposition on reactor temperature (~400°C), type of packing material and electrical power (~100 W). With the other conditions kept constant, increasing reactor temperature or electrical power tended to increase HFC-134a decomposition efficiency. Below a certain temperature around 150°C, all three packing materials examined, i.e., alumina, zirconia and glass beads, showed a similar relationship between the reactor temperature and the HFC-134a decomposition efficiency, but above that temperature the plasma reactor packed with alumina beads acting as a catalyst decomposed HFC-134a more effectively than that with glass beads or zirconia beads. At temperatures of 430°C and 360°C (flow rate: 60 L h<sup>-1</sup>; HFC-134a: 2,000 ppm), the decomposition efficiency in the presence of alumina approached 100% at input powers of 60 W and 100 W, respectively.

**Keywords:** 1,1,1,2-tetrafluoroethane, nonthermal plasma, catalyst, temperature effect

## Introduction

Hydrofluorocarbons (HFCs) are chemically very stable, have long atmospheric lifetimes, and strongly absorb infrared. 1,1,1,2-Tetrafluoroethane (HFC-134a) that has been widely used as a high temperature refrigerant is considered as a significant greenhouse gas due to its long lifetime and strong infrared absorption. The 100-year global warming potential (GWP) of HFC-134a is reported to be 1,300 times that of carbon dioxide. Currently, several methods, including thermal incineration, catalytic decomposition, thermal or nonthermal plasma decomposition and adsorption, are actively being developed to reduce the emission of fluorinated compounds [1-6].

In this work, the decomposition of HFC-134a by using a nonthermal plasma-catalytic reactor was investigated with a simulated exhaust gas consisting of HFC-134a, oxygen and nitrogen over a temperature range up to 400°C. A cylindrical dielectric barrier discharge (DBD) reactor in which dielectric pellets were packed was employed for the generation of nonthermal plasma. To make comparison, zirconia and glass beads as well as alumina were used as the packing material. The behavior of HFC-134a decomposition in the plasma-catalytic reactor was characterized with respect to the reactor temperature and the electrical power delivered to the reactor, because catalytic activity and the performance of nonthermal plasma primarily depend on them.

## Experimental

Fig. 1 shows the schematic representation of the experimental apparatus. The DBD reactor referred to as the plasma reactor was composed of a ceramic tube (inner diameter: 24.5 mm; outer diameter: 28 mm), a concentric 6-mm-thick stainless steel screw and a copper foil wrapping around the ceramic tube. In this reactor configuration, the stainless steel screw and the copper foil act as the discharging and ground electrode, respectively. The effective reactor length for creating nonthermal plasma was 150 mm. The plasma reactor was packed with 3 mm alumina beads, 3 mm zirconia beads or glass beads (Daihan Scientific, Korea). The amount of the packing material was 127 cm<sup>3</sup>. An AC high voltage power supply (operating frequency: 400 Hz) was used to power the plasma reactor. The voltage applied to the discharging electrode was varied in the range of 10-16 kV (peak value) to change the electrical power delivered to the plasma reactor. The voltage was measured with a high voltage probe (P6015, Tektronix, USA) and a digital oscilloscope (TDS 3032, Tektronix, USA). The input power was measured by a digital power meter (Model WT200, Yokogawa, Japan).

The simulated exhaust gas was formed by mixing pure HFC-134a (formula weight: 102.03 g mol<sup>-1</sup>), oxygen and nitrogen (balance) whose flow rates were separately regulated by mass flow controllers

(MFC) (MKS Instruments, Inc., USA). The concentration of HFC-134a in the simulated exhaust gas was fixed at 2,000 ppm (parts per million, volumetric) with the oxygen content kept constant at 2% (v/v). The overall flow rate of the simulated exhaust gas was  $60 \text{ L h}^{-1}$ . The temperature effect on the decomposition of HFC-134a was examined in the range up to  $400^\circ\text{C}$ . To change the reactor temperature to a desired value, heat was applied to the plasma reactor by a heating tape, being controlled by a PID controller. The reactor temperature was measured at the midpoint of the plasma reactor wall by using a K-type thermocouple. The simulated exhaust gas processed in the plasma reactor was directed to the Fourier transform infrared (FTIR) spectrometer (Bruker IFS 66/S, Germany) for analysis.

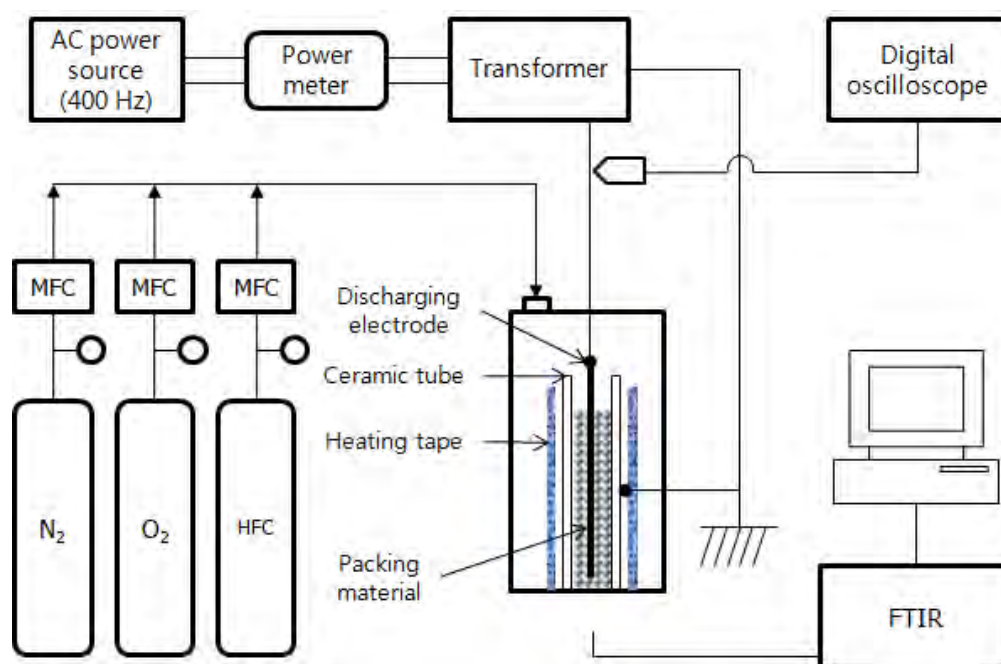


Fig. 1. Schematic diagram of the experimental apparatus for decomposing HFC-134a.

## Results and discussion

The effect of the reactor temperature on the decomposition of HFC-134a is shown in Fig. 2, which was obtained with alumina beads as the packing material. The input power was changed up to 100 W by varying the applied voltage. In Fig. 2, catalyst alone means that HFC-134a decomposition was carried out without applying high voltage. In general, higher reactor temperature resulted in higher decomposition efficiency due to thermal activation of solid catalyst. Compared to the results obtained with catalyst alone, the HFC-134a decomposition was largely enhanced by the nonthermal plasma at all temperatures examined, obviously because various reactive species produced by the nonthermal plasma help decompose HFC-134a. The reaction mechanisms for nonthermal plasma decomposition of HFC-134a were discussed in detail in a previous study [7]. The carbon-containing products identified by the FTIR included CO<sub>2</sub> and CO (data not shown).

The HFC-134a decomposition efficiency in the plasma reactor can strongly depend on the type of packing material in it, especially at high temperatures that the contribution of catalysis is significant. In this work, a comparison between alumina, zirconia and glass beads was made under the same input power condition. It should be noted that zirconia and glass beads have negligible catalytic activity for HFC-134a decomposition. Fig. 3 shows the variations of the HFC-134a decomposition efficiencies as a function of reactor temperature, when the electrical power was 60 W. In all cases, increasing the reactor temperature enhanced the HFC-134a decomposition, indicating that the reactions related to the decomposition of HFC-134a are favorable at higher temperatures. As can be seen in Fig. 3, the difference in the decomposition efficiency between the packing materials was inconsiderable at lower temperatures below about  $150^\circ\text{C}$ . In this temperature region, it is believed that the decomposition of HFC-134a was mainly caused by gas-phase reactions. On the other hand, at temperatures above  $150^\circ\text{C}$ ,

the difference in the decomposition efficiency became pronounced, because the catalytic action significantly contributed to the HFC-134a decomposition. With glass or zirconia as the packing material, HFC-134a decomposition produced CO<sub>2</sub>, CO and carbonyl fluoride (COF<sub>2</sub>). On the other hand, COF<sub>2</sub> was disappeared when alumina was used.

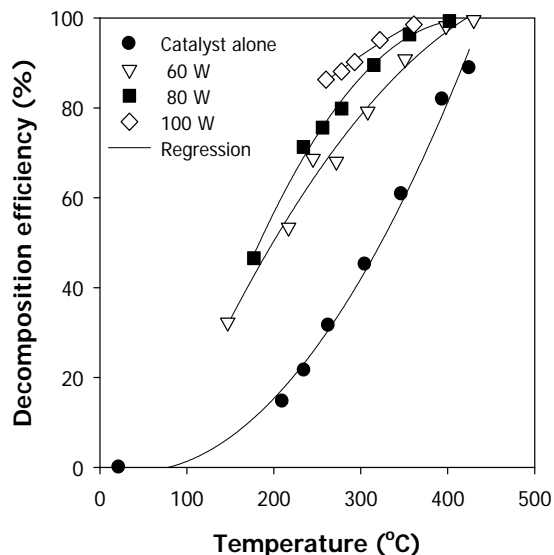


Fig. 1. Effect of the reactor temperature on the decomposition of HFC-134a

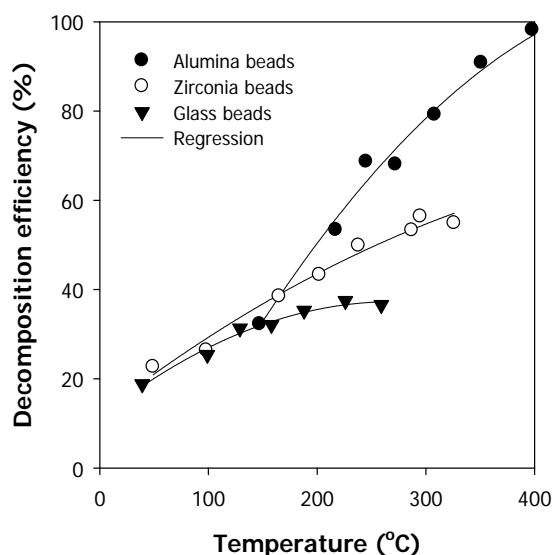


Fig. 2. Comparison between alumina, zirconia and glass beads

## Conclusions

This study has shown that the plasma-catalytic reactor may be an effective method to decompose fluorinated compounds. Operating the nonthermal plasma reactor at elevated temperatures was advantageous, especially with alumina beads as the packing material, because of its catalytic activity. The temperature dependence on the HFC-134a decomposition with zirconia or glass beads was not as remarkable as with alumina beads. The problem of nonthermal plasma process, i.e., low decomposition efficiency for fluorinated carbons, may be resolved by introducing a catalyst and operating the process at elevated temperatures.

## References

- [1] W.-T. Tsai, H.-P. Chen, W.-Y. Hsien, *J. Loss Prev. Process Ind.*, 15 (2002) 65.
- [2] K. Takaki, K. Urashima, J.S. Chang, *Thin Solid Films*, 506-507 (2006) 414.
- [3] T. Fujita, T. Kawano, L. Huang, Y. Kojima, H. Matsuda, K. Ushiroebisu, *J. Mater. Cycles Waste Manag.*, 9 (2007) 15.
- [4] K. Urashima, K.G. Kostov, J.S. Chang, Y. Okayasu, T. Iwaizumi, K. Yoshimura, T. Kato, *IEEE Trans. Ind. Appl.*, 37 (2001) 1456.
- [5] K. Takaki, K. Urashima, J.S. Chang, *IEEE Trans. Plasma Sci.*, 32 (2004) 2175.
- [6] J.L. Delattre, T.L. Friedman, A.M. Stacy, *J. Vac. Sci. Technol. B* 17 (1999) 2664.
- [7] Y. S. Mok, V. Demidyuk, J. C. Whitehead, *J. Phys. Chem. A*, 112 (2008) 6586.

# Various Method of the Theoretical Calculation of the $\text{NO}_3^-$ ion Mobility in Nitrogen Drift Gas

J. Matúška<sup>1</sup>, M. Krajčí<sup>2</sup>, J. Urban<sup>2</sup>, Š. Matejčík<sup>1</sup>

<sup>1</sup>Department of Experimental Physics

<sup>2</sup>Department of Nuclear Physics and Biophysics,

Faculty of Mathematics, Physics and Informatics, Comenius University Bratislava, 842 48, Bratislava, Slovak Republic

e-mail: matuska@fmph.uniba.sk

## Abstract

We have applied the methods of Molecular Dynamics (MD) to calculate the reduced ion mobility of the  $\text{NO}_3^-$  ion in  $\text{N}_2$  gas. We have used two methods for the calculation of the reduced ion mobility. The  $\text{NO}_3^-$  is an important atmospheric negative ion and thus there exist a deep interest in the transport properties of this ion. The calculations have been performed using the MD computational code DL\_POLY 3.09 with the forcefield parametrized in our group.

**Keywords:** IMS, molecular dynamics, mobility

## Introduction

The Ion Mobility Spectrometry (IMS) is an ion separation method based on the fact that different ions have different drift velocities as they drift in a drift gas in a weak homogeneous electric field. IMS has many advantages, e.g., small size, fast response, high sensitivity and that IMS can operate at atmospheric pressure. One of the difficulties in the IMS is connected with the identification of the ions, as there exists only small and very limited number of data linking ion mobilities to the mass of the ion.

One of the possibilities how to link ion mobilities to the mass of the ions is the calculation of ion mobilities using the Molecular Dynamics methods. Molecular dynamics methods are based on the classical Newton mechanics of the studied system. Equations of the motion are solved by numerical integration. The number of particles (atoms, molecules, ions) in the model system are limited only by the performance of the computer. The known trajectories of the ions can be utilized for the calculation of the diffusion coefficient of selected ion. The mobility of the ion in the buffer gas is obtained by using the Einstein equation for diffusion coefficient.

The Ion mobility spectrometer at Department of Experimental Physics, Comenius University is used to analyze the ions produced in the corona discharge at atmospheric pressure. One of the last studied systems was the formation of the ions in the negative corona discharge in the  $\text{O}_2/\text{N}_2$  mixtures in the nitrogen drift gas. In this experiment the  $\text{NO}_3^-$  is the most stable negative ion [1].

## Numerical model

The present numerical model consists of two parts. The first is represented by 5000 studied ions and 5000 molecules of the buffer gas. The second part consisted from the one studied ion and 5000 molecules of the buffer gas. The initial velocities and positions of the molecules have been defined randomly. The edge of the simulated cell had a length of  $5.89 \times 10^{-8}$  m in both cases. We have used cubic periodic boundaries. The size of the simulated cell was chosen to obtain atmospheric pressure at the temperature 300 K with respect to ideal gas law in the numerical model with only one  $\text{NO}_3^-$  ion. The first step of the calculation was represented by the equilibration of the system for 5 ns. We have used the NVT ensemble with the Berendsen thermostat. After that we have used the NVE ensemble to perform the calculation and obtain the mean square displacement and the velocity autocorrelation function. The evolution of the system was lasted for time period 5 ns. The calculations were performed by using the computational code DL POLY 3.09 [2].

We have divided the numerical model into two parts because we had to fulfill two contradictory conditions. The first one was represented by the demand to investigate the diffusion of the ion with very low concentration in drift gas. It corresponds to the model with one particle. The second condition represented the fact that the mean square displacement and the velocity autocorrelation

function are statistical quantities. Their values are meaningful for a large numbers of particle. This condition was fulfilled in the model with 5000 ions. The ion-ion interaction has been set to zero value because the diffusion coefficient in drift gas without the mutual ion-ion interaction is the desired quantity. This results in the fact that the one calculation gives us the 5000 independent trajectories.

Previous calculation has shown, that the general forcefield parametrization (e.g. UFF [3]) does not yield accurate results. Therefore we have decided to create our own forcefield parametrization for  $\text{NO}_3^- - \text{N}_2$  potential based on the quantum chemical calculations. We have performed B3LYP density functional method with 6-311+G(3d) basis set. We have calculated the energy dependence on the distance from 42 different directions equally spread. We have acquired these directions from tessellation of the sphere. One point of the shell was calculated by the minimization of the contributions to the energy caused by the rotational freedom of the  $\text{N}_2$  molecule. The values of the one shell were averaged by equation:

$$E(r) = \frac{\sum_i E_i e^{\left(\frac{E_0 - E_i}{kT}\right)}}{\sum_i e^{\left(\frac{E_0 - E_i}{kT}\right)}} \quad (1)$$

where  $E_0$  is the minimal energy of the shell,  $E_i$  is the energy from the  $i$ -th direction,  $T$  is the thermodynamic temperature 300K and  $k$  is the Boltzmann constant.

The calculated dependence of the interaction energy on the distance of the molecules has served as input data for the fit of the parameters. To describe the interaction we have chosen Morse potential in form (2)[4].

$$E(r) = E_0 \left\{ \left[ 1 - e^{-k(r-r_0)} \right]^2 - 1 \right\} \quad (2)$$

where  $E_0$  is the energy of the minimum,  $r_0$  is the equilibrium distance and  $k$  is parameter describing the ‘‘slope’’ of the potential. This potential has been the most accurate representation of the calculated data. The fitted parameters are in Table 1

Tab. 1. Fitted parameters of the Morse potential

|                           | Value                  | Std error              |
|---------------------------|------------------------|------------------------|
| $E_0$ [eV]                | $5.2936 \cdot 10^{-2}$ | $1.0768 \cdot 10^{-3}$ |
| $r_0$ [ $\text{\AA}$ ]    | 3.87                   | $1.8474 \cdot 10^{-2}$ |
| $k$ [ $\text{\AA}^{-1}$ ] | $8.0476 \cdot 10^{-1}$ | $2.1848 \cdot 10^{-2}$ |

The result of the MD calculation of the above described system has been represented by the time dependence of the mean square displacement and the velocity autocorrelation function of the  $\text{NO}_3^-$ . This two quantities are used to calculate the diffusion coefficient[5].

In Fig. 1 there is shown the dependence of the mean square displacement (MSD) on the time. The dependence consists of the quadratic and linear part. The slope of the linear part defines the diffusion coefficient as:

$$D = \frac{1}{6} S \quad (3)$$

where  $S$  is the slope of the linear part. The slope was obtained by least-square fitting of the linear part of the curve.

The dependence of the velocity autocorrelation function (VACF) on the time is given in the Fig. 2. The diffusion coefficient is defined as:

$$D = \frac{1}{3} \int_{t=0}^{\infty} \langle \vec{v}(0) \cdot \vec{v}(t) \rangle dt \quad (4)$$

Where  $v(0)$  is the initial velocity, the  $v(t)$  is the velocity in time  $t$  and the angle bracket means the

average over the number of particles.

We obtain the mobility of the ion from the diffusion coefficient  $D$  using the Einstein equation:

$$\mu = \frac{Dq}{kT} \quad (5)$$

where  $q$  is charge of the ion,  $k$  Boltzmann constant and  $T$  temperature.

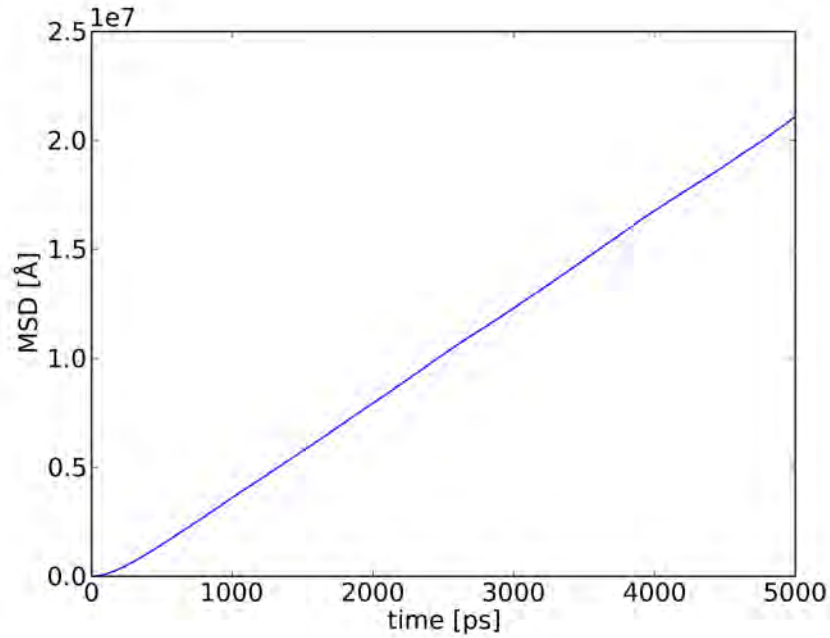


Fig. 1: Mean square displacement (MSD) of the  $\text{NO}_3^-$  ion in nitrogen drift gas. Result of calculation 1 (Tab. 2).

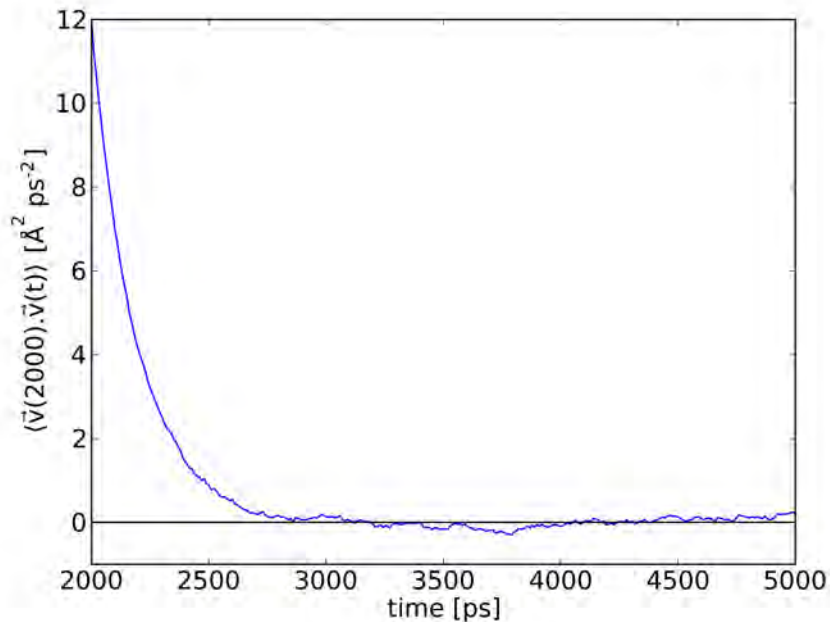


Fig. 2: Velocity autocorrelation function (VAF) of the  $\text{NO}_3^-$  ion in nitrogen drift gas. Result of calculation 1 (Tab. 3).

### Results and discussion

We have calculated the  $\text{NO}_3^-$  ion mobility tree times. Each calculation started with the different initial positions of the molecules. We have observed the influence of the initial condition on the

diffusion coefficient and mobility. The ideal case is that the molecules initial positions do not affect the final values. The differences suggest that the numerical model is not optimal. The possible reasons can be explained by the small number of particles or the fact that the system has not been in equilibrium. The results of our initial condition test are presented in Tab. 2 and Tab. 3. The values in Tab. 2 were obtained from the slope of the MSD and the values in Tab. 3 were obtained from the VACF. The small differences in Tab. 2 indicate that the numerical model is well defined. The differences in Tab. 3 are larger but it is caused by the different calculation method. The numerical integration is sensitive to errors caused by the noise of the statistical movement of the molecules. The noise on the tail of the VACF is larger than the theoretical value of the VACF itself, so the tail influences the final value of the integral more than we have expected.

Tab. 2: The results of initial condition test – mean square displacement. The std error is determined from the deviation of the fitting parameters.

| Calculation | Mobility<br>[cm <sup>2</sup> s V <sup>-1</sup> ] | Std error estimate<br>[cm <sup>2</sup> s V <sup>-1</sup> ] |
|-------------|--|--|
| 1           | 2.815  | 0.001  |
| 2           | 2.805  | 0.001  |
| 3           | 2.812  | 0.001  |

Tab. 3: The results of initial condition test – velocity autocorrelation function(VACF). The std error is estimated from the noise of the VACF

| Calculation | Mobility<br>[cm <sup>2</sup> s V <sup>-1</sup> ] | Std error estimate<br>[cm <sup>2</sup> s V <sup>-1</sup> ] |
|-------------|--|--|
| 1           | 2.868  | 0.004  |
| 2           | 2.776  | 0.002  |
| 3           | 2.983  | 0.004  |

We have used two methods to obtain a diffusion coefficient from the calculated data. First method is presented by the calculation of the diffusion coefficient using (3) from mean square displacement. The example of the obtained data are given in the Fig. 1. We have used the linear part of the curve from 2 ns to 5 ns to obtain the slope and to calculate the diffusion coefficient. According to (5) we need the temperature of the gas to calculate the ion mobility. We have used the average temperature of the system with the 5000 studied ions on interval from 2 ns to 5 ns. The average temperature of the system was 300 K. The values of the ion mobility are showed in Tab. 2. The average mobility calculated from the data in Tab. 2 has the value 2.811 cm<sup>2</sup> s<sup>-1</sup> V<sup>-1</sup>. As the mobility depends on the collisions of the ion with the drift gas it depends also on the density of the drift gas. The density of the drift gas is represented by the pressure. The drift gas pressure was the pressure of the system with one studied atom, because the studied ion was interacting only with the molecules of the drift gas. So the effective collisions of the ions in big system were the same as the real collisions of the ion in the small system. Therefore a correction to the standard conditions (T<sub>0</sub>=273 K, p<sub>0</sub>=101.3 kPa) is made and resulting value is reported as reduced mobility K<sub>0</sub> given by the formula:

$$K_0 = K \frac{T_0}{T} \frac{p}{p_0} \quad (6)$$

The calculated value of the reduced mobility of the NO<sub>3</sub><sup>-</sup> in nitrogen is 2.553 ± 0.005 cm<sup>2</sup> s<sup>-1</sup> V<sup>-1</sup>.

Second method is presented by the calculation of the diffusion coefficient using (4) from velocity autocorrelation function. The VACF was calculated on interval from 2 ns to 5 ns. The example of the obtained data are in the Fig. 2. The integral under the curve was calculated numerically using a trapezoidal rule and the result of the ion mobility is showed in Tab. 3. The average value of mobility is 2.876 ± 0.104 cm<sup>2</sup> s<sup>-1</sup> V<sup>-1</sup>. The average temperature and the average pressure have the same values as previous. Then the reduced mobility is 2.612 ± 0.094 cm<sup>2</sup> s<sup>-1</sup> V<sup>-1</sup>.

## Conclusions

We have investigated two methods to obtain the diffusion coefficient and then the mobility. The more reliable calculation was based on the investigation of the dependence MSD on the time. The reduced mobility of the  $\text{NO}_3^-$  ion in nitrogen gas was  $2.553 \pm 0.005 \text{ cm}^2 \text{ s}^{-1} \text{ V}^{-1}$ .

## Acknowledgement

This work has been supported by the Slovak Grant Agency VEGA, projects Nr. 1/0051/08, 1/0379/11, 1/0558/09 and by the by the Slovak Research and Development Agency, project Nr. APVV – 0367 – 07.

## References

- [1] K. Nagato, Y. Matsui, T. Miyata, T. Yamauchi, *Int. J. Mass Spectrom.* 248 (2006) 142.
- [2] I.T. Todorov and W. Smith: The DL\_Poly 3 User Manual, STFC Daresbury Laboratory, 2008
- [3] A.K. Rappe et al., *J. Am. Chem. Soc.*, 114 (1992) 10024-10035
- [5] P. M. Morse, *Phys. Rev.*, 34 (1929) 57-64
- [6] Herman J. C. Berendsen, *Simulating the Physical World: From Quantum Mechanics to Fluid Dynamics*, Cambridge University Press, 2007, p. 505-522

# Recombination in low temperature plasma

J. Glosík, R. Plašil, T. Kotrík, P. Dohnal, M. Hejduk, P. Jusko, Š. Roučka and P. Rubovič

Charles University, Faculty of Mathematics and Physics, V Holešovičkách 2, 180 00, Prague, Czech Republic

e-mail: juraj.glosik@mff.cuni.cz

## Abstract

In present contribution we will discuss electron-ion recombination in low temperature plasma containing electrons, positive ions and buffer gas. We will concentrate predominantly on recent experimental studies of binary recombination but some ternary recombination processes will be also mentioned. Particular attention will be paid to recent studies of recombination of  $H_3^+$  including recombination of para- and ortho- $H_3^+$ .

**Keywords:** Plasma, recombination, afterglow, recombination rate coefficient,  $H_3^+$

## Introduction

Recombination is a process of mutual neutralization of particles with opposite charge. In recombination free, electron recombines with positive ion only if at least part of its energy is removed and electron is captured to bound state. In case of atomic ion the excess of energy can be carried away by emission of photon or in collision with third particle. If photon is emitted the process is named radiative recombination. The radiative recombination is very inefficient process and in general photon is emitted only in one from many thousand electron–ion collisions. The situation is more complicated in case of molecular ions, where internal degrees of freedom of ion can be used to remove energy of electron and finally recombination can be terminated by dissociation of excited molecule. The efficiency of such process depends on properties of molecular ion and particularly on presence of suitable dissociative states of neutral molecule (direct and indirect process).

Electron-ion recombination is important process in ionized gases and plasmas. In recombination charged particles are removed and new neutral, very often highly excited and highly reactive particles are produced. To understand and to describe chemistry of discharges, laser and technological plasmas, Earth's ionosphere, planetary atmospheres and astrophysically relevant plasmas [1], we need to know rate coefficients of recombination processes, products distributions and their temperature (energy) dependence. In high pressure plasmas dependence of recombination rate coefficients on pressure of neutral gas is also required. In plasma with high electron density dependence of electron density can also play a role in deionization process.

Despite the fact that recombination is studied intensively for over 50 years many questions remain, e.g. up to now there is lack of information on dependence of recombination on internal excitation of recombining ions. Products distributions were measured just for recombination of few ions. Ternary recombination assisted by neutrals was studied many times but predominantly in discharges in rare gas but there is absence of data obtained at low electron temperatures in low temperature plasma. Ternary recombination assisted by electron named collisional radiative recombination (CRR) was described long time ago [2] and further appreciated recently [3] but experimental studies did not go to temperatures below 300 K [4]. Below we will mention some recent experimental studies of CRR going down to 77 K.

The aim of present paper is to discuss some of more recent results of studies of recombination in low temperature plasma. The theory will be discussed here just in connection with recent studies of recombination of  $H_3^+$  ions.

## Experimental methods used in recombination studies

Over long history of studies of recombination many techniques have been used. Detail description of these experimental techniques is given in recent monography on dissociative recombination by M. Larsson and A.E. Orel [5]. Generally experiments can be divided into two groups: beam experiments and plasma experiments. In order to obtain low collisional energy in beam experiments monoenergetic beams of ions and electrons are merged at small angle over precisely known distance. The collisional

energy is than given by difference of velocities of ions and electrons and angle of beam intersection. In last nearly twenty years cross sections of recombination of many ions were measured by using large storage rings (e.g. ASTRID, CRYRING, TSR and TARN). In these experiments ions are formed in separate ion source and then they are injected to ring. Ions circulating in the ring are cooled rotationally and vibrationally by spontaneous emission of radiation (if radiative lifetime is shorter than the storage time). Translational cooling of the stored ions occurs by interaction with mono-energetic beam of electrons (electron cooler working on principle of friction). Recombination cross section of cold ions with electrons from the electron beam is than measured by varying electron velocity and monitoring the neutral products, eventually using two electron beams – electron cooler and electron target [6].

In plasma experiments plasma is formed in a discharge and the recombination rate coefficient is determined by monitoring decrease of electron and/or ion densities during an afterglow. There are two types of afterglow experiments: Stationary afterglow (SA) and Flowing Afterglow (FA). Stationary afterglow was introduced by Biondi and Brawn in 1949 and with small modifications is used up to now. The name Stationary Afterglow expresses the fact that gas is not moving in the experiment, in opposite fast flow of gas is used in Flowing Afterglow (FA). For long time, microwave technique was used for electron density measurements, exceptionally also absorption spectroscopy [7,8,9] or Langmuir probes [10,11,12] were used to monitor evolution of ion or electron densities.

### Stationary Afterglow

As an example Figure 1 shows a diagram of the Advanced Integrated Stationary Afterglow - AISA apparatus used in our previous studies of recombination of  $H_3^+$  and  $D_3^+$  ions with electrons [11,13].

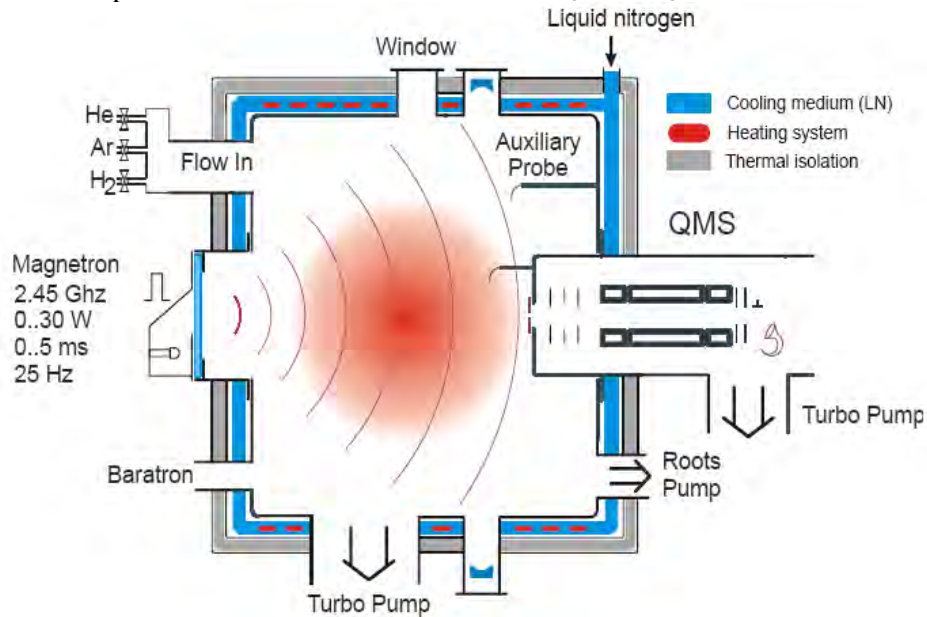


Fig. 1. Advanced Integrated Stationary Afterglow - AISA apparatus. Plasma is ignited by pulse of microwaves entering the discharge chamber via quartz window. The electron density is measured by electrostatic Langmuir probe, ion composition is measured by quadrupole mass spectrometer. The discharge chamber can be cooled down to 77 K. For detailed description see refs. [14]

The AISA was designed to study recombination and to measure recombination rate coefficients down to  $1 \times 10^{-8} \text{ cm}^3 \text{ s}^{-1}$ . To achieve this, diffusion losses have to be minimized by using high pressure of the buffer gas and large characteristic diffusion length. Obtained characteristic diffusion time was  $\sim 20$  ms. Electron density after the short pulse of microwave is of the order of  $5 \times 10^9 - 5 \times 10^{10} \text{ cm}^{-3}$ . If recombination of ion  $A^+$  and ambipolar diffusion are the dominant loss processes than the balance equation has a form:

$$\frac{dn_e}{dt} = -\alpha n_e [A^+] - \frac{n_e}{\tau_D}$$

where  $\alpha$  is recombination rate coefficient and  $\tau$  is characteristic time of ambipolar diffusion. If a recombination is dominant the solution of this equation can be written in the form:

$$\frac{1}{n_e} = \frac{1}{n_{e0}} + \alpha t$$

Assuming that electron density decay is dominated by recombination of particular ions than by monitoring electron density decay (decay curve) recombination rate coefficient can be determined. Fig. 2 shows measured decay curves for  $O_2^+$ ,  $H_3^+$ ,  $He^+$  and  $Ar^+$ . In lower panel corresponding values of  $1/n_e$  are plotted. The corresponding recombination rate coefficients can be obtained from the slope of the  $1/n_e$  plots or more precisely by the fit of the data using analytical solution of balance equation.

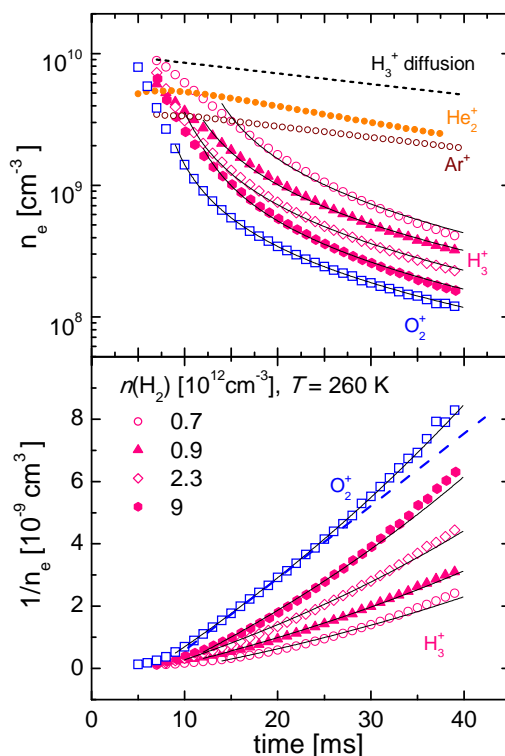


Fig. 2. Electron density evolutions (decay curves) measured with Langmuir probe in plasmas dominated by recombination of  $O_2^+$ ,  $He^+$ ,  $Ar^+$  and  $H_3^+$  (measured at several partial densities of hydrogen) ions. In lower panel values  $1/n_e$  are plotted, the recombination rate coefficient is proportional to slope of the curve in early afterglow.

Recently we have used also laser absorption spectroscopy (CRDS) to measured evolution of density of ions in specific quantum state. This apparatus is used to study dependence of recombination rate coefficient on rotational state of recombining para- and ortho- $H_3^+$  (see accompanying paper by Dohnal et al in present volume [15]). Advantage of CRDS-SA is *in situ* monitoring of quantum state of recombining ions, their densities and kinetic temperatures.

### Flowing Afterglow

The technique is known in experimental chemistry for long time, nevertheless to ion chemistry it was reinvented by Fehsenfeld et al. [16] as a Flowing Afterglow. Ferguson et al. [17] and Smith and Adams [18,19] used it to study recombination in low temperature plasma. Because Langmuir probe is used for electron density measurements it is named Flowing Afterglow with Langmuir Probe – FALP. In FALP plasma is generated continuously by the discharge and fast flow of gas (buffer gas) is used to carry plasma along the flow tube. In this way plasma formation and plasma decay are geometrically

separated. The time of the decay is given by position in the flow tube and the velocity of the plasma. High flow of a buffer gas, usually He, is necessary to minimize diffusion losses.

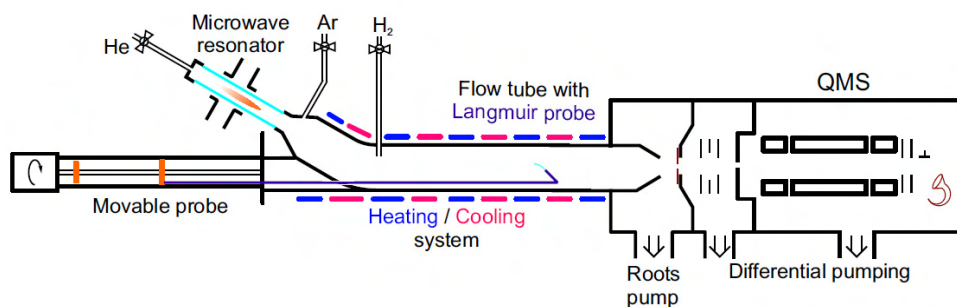


Fig. 3. High pressure Flowing Afterglow with Langmuir Probe – HPFA (modification of FALP) used at Charles University in Prague to study pressure dependence of recombination rate coefficients. For detailed description see refs. [20]

Advantage of FALP is that plasma is formed in geometrically separated discharge in pure helium and reactant gasses necessary for formation of studied ions are added downstream to already cold plasma. If helium is used as a buffer gas first Ar is added to He<sup>+</sup> and He<sup>m</sup> (metastables) dominated afterglow to form cold Ar<sup>+</sup> dominated plasma and only further downstream second reactant is added to form plasma dominated by studied ions. For detailed description of principle, diagnostics and data evaluation see e.g. refs. [21,22]. Many different variants of FALP were developed e.g. FLAPI in Rennes devoted to study recombination of large PAH ions [23] or HPFA (see Fig. 3) in Prague to study pressure dependence of recombination rate coefficients.

### Some recent results, recombination of HCO<sup>+</sup>, DCO<sup>+</sup>, H<sub>3</sub><sup>+</sup>, D<sub>3</sub><sup>+</sup>

We will show some typical experimental results obtained recently using afterglow techniques in study of recombination of HCO<sup>+</sup>, DCO<sup>+</sup>, H<sub>3</sub><sup>+</sup> and D<sub>3</sub><sup>+</sup> ions. These ions were studied many times using several techniques, the compilation of recent results is shown in Fig. 4 for HCO<sup>+</sup>, DCO<sup>+</sup> (for details and references see ref. [24]).

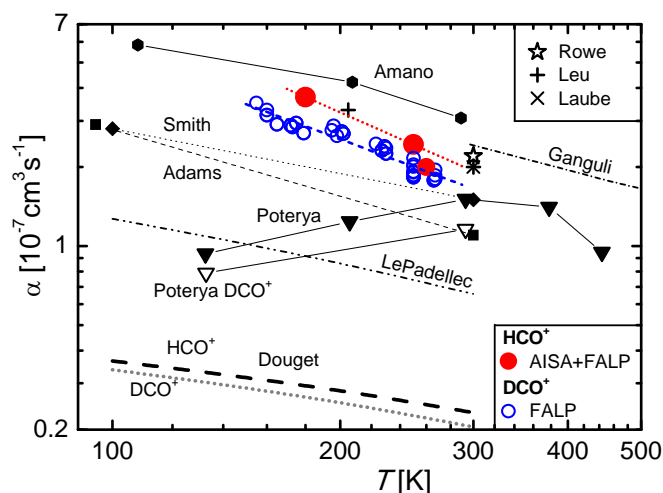


Fig. 4. Recombination of HCO<sup>+</sup> and DCO<sup>+</sup>, the compilation of recent results. Indicated are name of first author (for details and references see ref. [24]). Circles and closed circles indicate data obtained in our experiments with FALP and AISA.

The differences are too large and we can expect some additional process which is influencing the experiments and evaluation of data. First possibility is influence of ternary recombination coupled with high pressure of the buffer gas. In Fig. 5 are plotted recombination rate coefficients measured in several afterglow experiments using different pressures of helium.

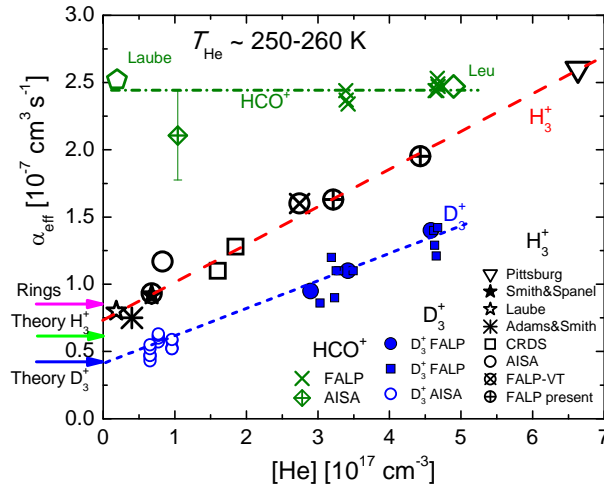


Fig. 5. Dependence of measured recombination rate coefficients on helium (buffer gas) density, the compilation of recent results for  $\text{H}_3^+$ ,  $\text{D}_3^+$  and  $\text{HCO}^+$  ions measured at 250 K. Indicated are name of first author (for details and references see ref. [20,25,26,27,28,29]). Used experimental technique is indicated for some data.

From the plotted data is obvious that there is strong ternary recombination for  $\text{H}_3^+$  and  $\text{D}_3^+$  ions (this process was in details discussed in our previous papers, see references [20,25,26,27,28,29]) and negligible ternary channel in case of  $\text{HCO}^+$  ions, at least not comparable with ternary recombination of  $\text{H}_3^+$  and  $\text{D}_3^+$ .

### Collisional Radiative Recombination, CRR.

Recently we measured recombination rate coefficients of collisional radiative recombination (CRR) of  $\text{Ar}^+$  with electrons at temperatures from 77 K to 180 K in a helium-buffered flowing- afterglow (Cryo-FALP) experiment at electron densities  $n_e$  from  $10^8$  to  $10^{10} \text{ cm}^{-3}$ . The measured  $\text{Ar}^+$  ions ternary rate coefficient  $K_{\text{CRR}}$  at 77 K  $(1.0 \pm 0.4) \times 10^{-17} \text{ cm}^6 \text{ s}^{-1}$  and the observed variation with electron temperature  $T_e$  agree well with the theoretical  $T_e^{-4.5}$  dependence [3,30]. It is first time that ternary rate coefficient of CRR was measured at temperatures below 300 K. In Fig. 6 are plotted effective binary recombination rate coefficients measured recently for several ions as a function of plasma temperature.

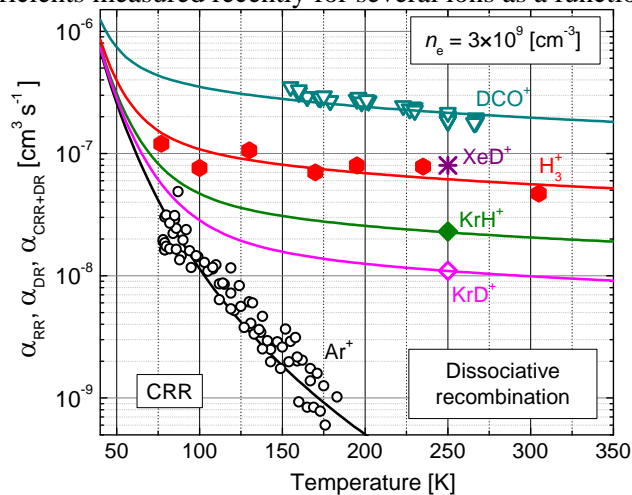


Fig. 6. Effective binary recombination rate coefficients measured recently for several ions as a function of plasma temperature. Curves indicate calculated effective binary recombination rate coefficients assuming existence of two parallel channels –binary and ternary channel. The data for  $\text{Ar}^+$  ions were calculated from measured ternary rate coefficient  $K_{\text{CRR}}$  assuming electron density to be  $5 \times 10^9 \text{ cm}^{-3}$ .

Plotted are data for true binary rate coefficients and for Ar<sup>+</sup> ions data calculated from measured ternary rate coefficient  $K_{\text{CRR}}$  for electron density  $5 \times 10^9 \text{ cm}^{-3}$ . Curves indicate calculated effective binary recombination rate coefficients for different ions assuming existence of two parallel channels – binary (value taken from our experiments) and ternary channel (calculated values based on values measured for Ar<sup>+</sup> ions).

The data plotted in Fig. 6 indicate how CRR can influence recombination in low temperature plasma. Further studies at temperatures below 100 K and at electron densities above  $5 \times 10^9 \text{ cm}^{-3}$  are needed to understand process of recombination in region where binary and ternary channels overlap.

**Acknowledgments.** This work is a part of the research plan MSM 0021620834 and grant OC10046 financed by the Ministry of Education of the Czech Republic and was partly supported by GACR (202/07/0495, 202/08/H057, 205/09/1183, 202/09/0642), by GAUK 92410, GAUK 86908, GAUK 54010, GAUK 25709 and by COST Action CM0805 (The Chemical Cosmos).

---

## References

- [1] E. Herbst, *Phil. Trans. R. Soc. Lond. A*, **358** (2000) 2523.
- [2] D.R. Bates, et al., *Proc. Roy. Soc. A* **267** (1962) 297
- [3] J. Stevefelt, J. Boulmer, J.-F. Delpech, *Phys. Rev. A* **12** (1975) 1246.
- [4] G.J. Pert, *J. Phys. B: At. Mol. Opt. Phys.* **23** (1990) 619
- [5] M. Larsson and A. Orel, *Dissociative Recombination of Molecular Ions*, Cambridge University Press, Cambridge, 2008.
- [6] Kreckel H. et al., *Phys. Rev. A* **82** (2010) 042715.
- [7] T. Amano, *J. Chem. Phys.* **92** (1990) 6492.
- [8] P. Macko et al., *Int. J. Mass Spect.* **233** (2004) 299.
- [9] P. Hlavenka et al., *Int. J. Mass Spect.* **255** (2006) 170.
- [10] D. Smith and P. Španěl, *Int. J. Mass Spectrom.* **129** (1993) 163.
- [11] R. Plašil et al., *Int. J. Mass Spectrom.* **218** (2002) 105.
- [12] S. Laubé, et al., *J. Phys. B* **31** (1998) 2111.
- [13] V. Poterya et al., *Phys. Rev. Lett.* **88** (2002) 4 AR 044802.
- [14] J. Glosík et al., *J. Phys.: Conf. Ser.* **4** (2005) 104.
- [15] P. Dohnal et al., *present volume*, SAPP 2010.
- [16] F. C. Fehnsfeld et al., *J. Chem. Phys.* **44** (1965) 4087.
- [17] E. E. Ferguson, et al., *Phys. Rev.* **138** (1965) A381.
- [18] D. Smith et al., *J. Phys. D* **8** (1975) 141.
- [19] G. Adams et al., *J. Chem. Phys.* **81** (1984) 1778.
- [20] J. Glosík et al., *Molecular Physics* **108** 17 (2010) 2253.
- [21] J. Glosík et al., *Plasma Sources Sci. Technol.* **12** 4 (2003) S117.
- [22] I. Korolov et al., *Contrib. Plasma Phys.* **48** 5-7 (2008) 521.
- [23] O. Novotný et al., *J. Chem. Phys.* **123** (2005) 104303.
- [24] I. Korolov et al., *Int. J. Mass Spectrom.* **280** (2009) 144-148.
- [25] J. Glosík et al., *J. Phys. B: At. Mol. Opt. Phys.* **41** (2008) 191001.
- [26] J. Glosík et al., *Phys. Rev. A* **79** (2009) 52707.
- [27] J. Glosík et al., *Phys. Rev. A* **80** (2009) 042706.
- [28] J. Glosík et al., *J. Phys. Conf. Ser.* **192** (2009) 012005.
- [29] T. Kotřík et al., *J. Chem. Phys.* **133** (2010) 034305.
- [30] D.R. Bates et al., *Proc. Roy. Soc. A* **267** (1962) 297.

# Simulation of Titan's atmosphere processes using DC gliding arc discharge

L. Polachova<sup>1,3</sup>, G. Horvath<sup>2,3</sup>, J. Watson<sup>4</sup>, N.J. Mason<sup>3</sup>, F. Krema<sup>1</sup>, M. Zahoran<sup>2</sup> and S. Matejcik<sup>2</sup>

<sup>1</sup>Faculty of Chemistry, Brno University of Technology, Purkynova 119, 612 00, Brno, Czech Republic

<sup>2</sup>Department of Experimental Physics, Comenius University, Mlynska dolina F-2, 842 48 Bratislava, Slovakia

<sup>3</sup>Department of Physics and Astronomy, Open University, Walton Hall, Milton Keynes MK7 6AA, Unit Kingdom

<sup>4</sup>Planetary and Space Sciences Research Institute, Open University, Milton Keynes MK7 6AA, Unit Kingdom

e-mail: xcpolachova@fch.vutbr.cz

## Abstract

The gaseous products formed in nitrogen/methane discharge were analysed a GC-MS (Gas Chromatograph-Mass Spectrometer). During the experiments the formation of stable products and their dependence on the flow rate and discharge power was investigated. The main products formed in our atmospheric glow discharge were found to be C<sub>2</sub>H<sub>2</sub>, HCN, and CH<sub>3</sub>CN. These same molecules have been detected in Titan's atmosphere and the present experiments may provide some insights into the plasma chemical mechanisms prevalent in Titan's atmosphere.

**Keywords:** reaction from nitrogen to methane, abnormal glow discharge, lock syringe, GC-MS.

## Introduction

Simple organic molecules play an important role in the formation of complex organics in planetary atmospheres. Recently, several lower hydrocarbons and nitriles have been found in the atmosphere of Titan, the largest moon of the Saturn. Its atmosphere composition is principally nitrogen with 2 – 6 % methane and some other gases that could be generated at low power discharges in the methane clouds [1]. It may be that the low power discharges can evoke also high energetic discharge. In this high energetic discharge, various complex compounds could be formed.

Titan's chemical and physical properties are similar to Earth's assumed prehistoric properties. The Titan's temperature range is such that methane exists in three phases, much like as water on Earth. This has led to suggestions that there is a "hydrological" methane cycle on Titan with methane clouds and rain, although the methane raindrops may evaporate before they reach the ground [2]. The atmospheric temperature falls from its surface value of 94 K at a pressure of 1.5 bar to a minimum of 71 K at a height of 42 km and pressure of 0.128 bar at the tropopause [3]. The temperature at this level is no closer than 5 K to the condensation temperature of nitrogen, coming closest at 30 km. It is therefore unlikely that nitrogen clouds can be formed [4]. At low temperatures measured on the surface of Titan (about 93 K) an origin of life is hard to imagine [5]. The physical and chemical properties are: physical state is liquid, intermolecular forces are Van der Waals. The bigger particles in atmosphere are formed by negatively charged-organic aerosol covered with CH<sub>4</sub> [6].

However, the mechanism of such organic chemistry is still unclear. Several researchers use plasmas to simulate Titan's atmosphere and generate solid aerosols (named tholins) that cause haze which covers Titan's surface. In order to understand formation of these aerosols it is necessary to explore the chemistry of such plasmas. The tholin is consisting largely of polymeric sets of compounds with C<sub>x</sub>H<sub>y</sub>H<sub>z</sub> chemical composition [7].

## Experiment

The apparatus used in our experiments is shown schematically in Fig. 1. The flow rates through the reactor for both CH<sub>4</sub> and N<sub>2</sub> were regulated using MKS mass flow controllers. The measurements were carried out in a flow regime in range from 100 and 200 sccm at atmospheric pressure, room temperature and lower temperature by using dry ice around the reactor. The discharge electrode system had the standard configuration of a classical gliding arc, a pair of stainless steel holders positioned in parallel to the iron electrodes but in this case the plasma was not gliding due to the low flow rate and therefore stable abnormal glow plasma occurred between the electrodes at their shortest distance of 2 mm, thus forming plasma channel with diameter of 1 mm. Electrical parameters have been measured by Tektronix oscilloscope using high voltage probe and Rogowsky current probe. The

reactor chamber had a volume of 0.3 L. The discharge was powered by a DC HV source. The discharge was ignited when voltage of 5500 V was applied on the electrodes then voltage drop reached a value at about 400 V. With increasing current between 15 and 40 mA, the voltage was slightly decreasing from 400 to 350 V. The present experiments were performed for different  $N_2:CH_4$  ratios in range from 2 % and 5 %  $CH_4$  in  $N_2$ .

The gaseous samples of the products formed in the discharge for GC-MS analysis were taken out of the gas outlet using lock syringe. The sample in the lock syringe was immediately analysed by Gas Chromatography and Mass spectrometry. GC-MS analysis was carried out using an Agilent Technologies 6890 gas chromatograph coupled to a 5973 mass spectrometer. Separation was performed on a J&W GS-Q PLOT column (30 m length, 0.32 mm internal diameter). Helium at column flow rate of 2 sccm was used as the carrier gas. Injection was at a 5:1 split and injector temperature was 220°C. The GC oven temperature was held for 2 min at 35°C and then programmed at 10°C min<sup>-1</sup> to 220°C, the final temperature was held for 5 min. The MS was operated in electron impact (70eV) mode and scanned between 12-120 amu at approximately 11 scans/sec.

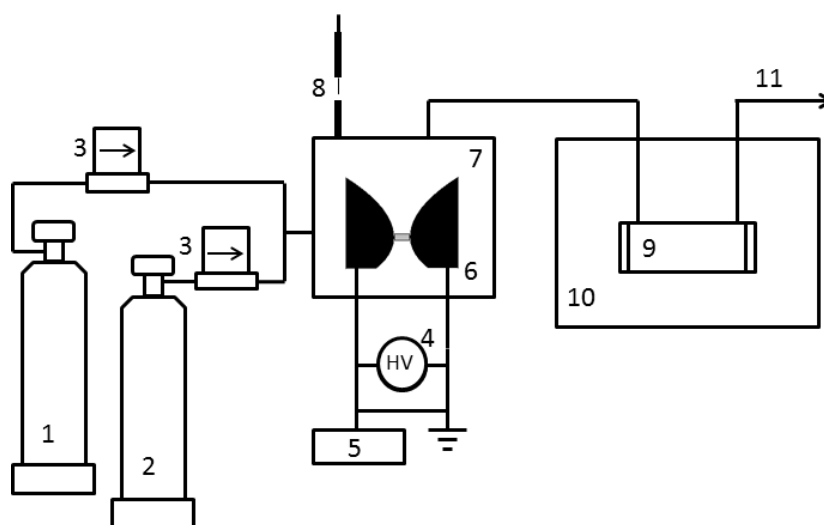


Fig. 1. Experimental set up: 1- storage bottle of nitrogen, 2-storage bottle of methane, 3- MKS mass flow controllers, 4- DC power supply, 5- oscilloscope, 6- electrode system, 7- reactor body 8- lock needle for GC-MS, 9- IR gas cell, 10- FTIR spectrometer, 11- exhaust

### Results and discussion

The results from GC-MS analysis are shown in Fig. 2. The major products were found to be acetylene, hydrogen cyanide, and acetonitrile. Minor products detected were: ethane, ethene, cyanogens, propene, propane, propyne, propadiene, butenyene, butadiene, butadiyne, acetonitrile 2-propenenitrile and 2-propennitril, benzene and toluene. It should be mentioned that only products having concentration higher than 5 ppm have been considered in the analysis. Many of these have either been detected or are predicted to be in Titan's atmosphere.

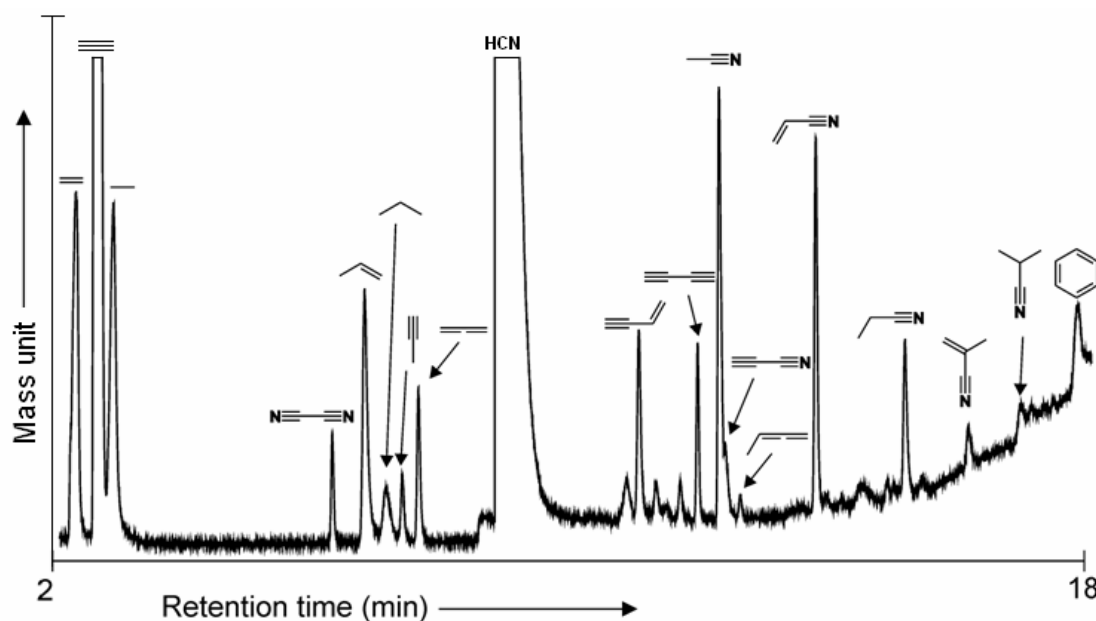


Fig. 2. Sample chromatogram of analysed products formed in a gas mixture  $\text{CH}_4:\text{N}_2 = 2:98$  at flow rate of 200 sccm.

Fig. 3 show the quantitative analysis of some hydrocarbons formed at different experimental conditions. The concentration unit is shown in ppm and the concentration is related to the standard concentration of ethane. As it is shown in Figure 3a, the concentration depends on the initial methane content and flow rate. Fig. 3a shows concentration of major products (ethene, acetylene, ethane, cyanohydrogen) which are related to the concentration standards of ethane. Since experiments have been carried out for different  $\text{CH}_4\text{-N}_2$  mixture ratios, gas flow rates and reactor temperature, the evolution of product concentration at various conditions was different. Concentrations observed at lowered temperatures are shown in Fig. 3b. It is evident from Figures 3 that a decrease in the gas flow rate and reactor temperature causes significant raise in the product concentration. Increasing the initial  $\text{CH}_4$  content from 2 to 5% causes increase in the total product yield. However, it has more significant effect on the hydrocarbon-like products: the yield of N-containing products increased only by 50% max, while this factor reached 120% in case of hydrocarbons. Furthermore, as it was expected, lowering the gas temperature produced higher concentration yield of products. Highest yield for all products was reached for 5% of  $\text{CH}_4$  at the lowest temperature.

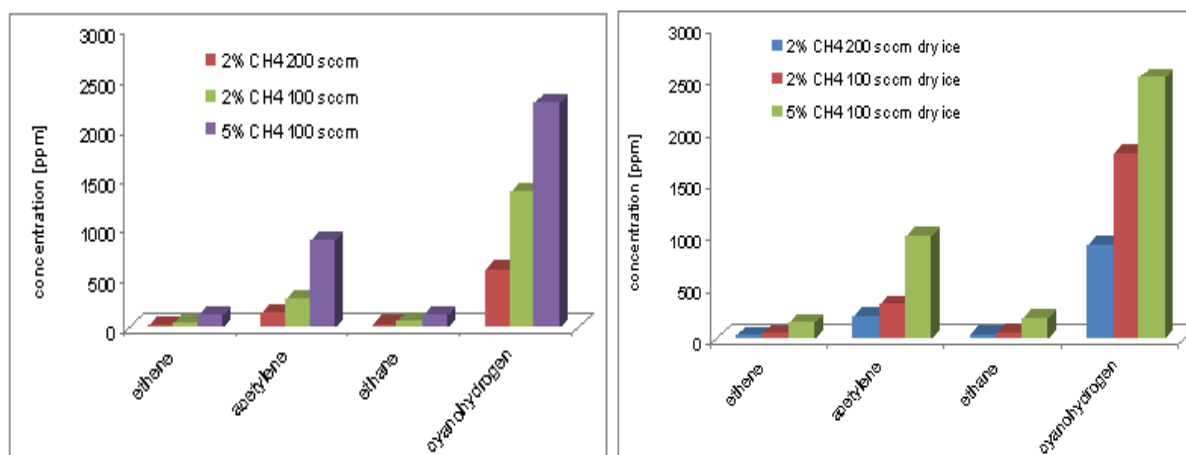


Fig. 3a-3b. Results of quantitative analysis for major products formed in the discharge at different experimental conditions. The concentration unit is given in ppm and it is related to the standards of ethane.

Same quantitative analysis has been performed for the minor discharge products (propene, acetonitrile, propenenitrile, propanenitrile). Figures 4 show concentrations of minor products formed at various flow rates, temperature and initial CH<sub>4</sub> content. In this case The concentration unit is shown in ppm and it is related to the standards of propane. The dependence of product concentrations on the flow rate, CH<sub>4</sub> content and gas temperature has had the same behavior as in case of major products, except of acetonitrile that reached higher yield in 2% CH<sub>4</sub> at lower temperature.

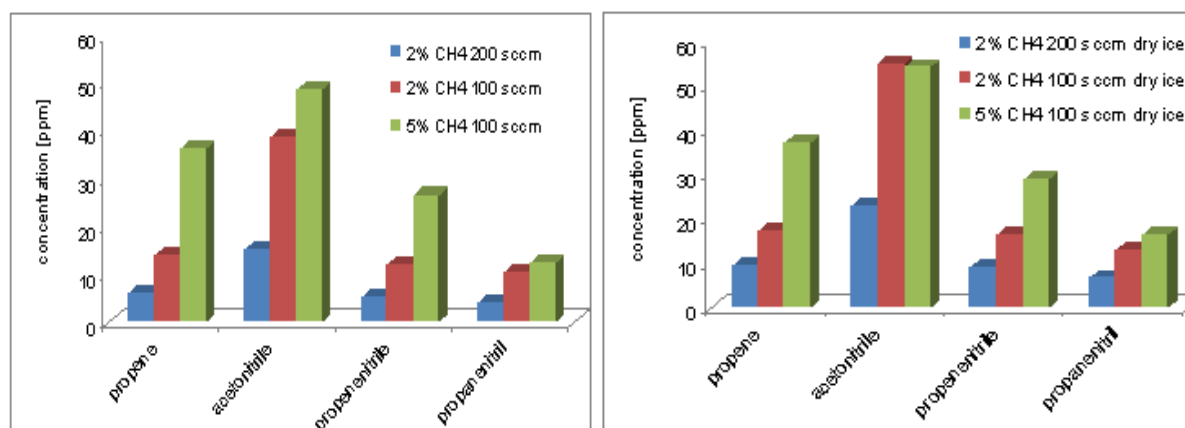


Fig. 4a-4b. Results of quantitative analysis for major products formed in the discharge at different experimental conditions. The concentration unit is given in ppm and it is related to the standards of propane.

## Conclusions

In this paper we present the results of GC-MS study of stable gaseous products formed in atmospheric glow discharge fed by different atmospheric pressure mixtures of N<sub>2</sub>:CH<sub>4</sub> (2 and 5 % CH<sub>4</sub>) operated in a flowing regime at various discharge currents (from 15 up to 40 mA), at room temperature and lower temperature. GC-MS analysis of the gaseous products showed that HCN, C<sub>2</sub>H<sub>2</sub>, CH<sub>3</sub>CN are the major products in our CH<sub>4</sub>/N<sub>2</sub> abnormal glow plasma. The yields of these compounds are such that HCN > C<sub>2</sub>H<sub>2</sub> > CH<sub>3</sub>CN. Minor products detected were: ethane, ethene, cyanogens, propene, propane, propyne, propadiene, butenyene, butadiene, butadiyne, acetonitrile 2-propenenitrile and 2-propennitril, benzene and toluene. The discharge current had a significant effect on the product synthesis. Such experiments can provide information that could aid our understanding of processes in Titan's atmosphere.

**Acknowledgments.** This work has been supported by the Grant UK/140/2010, Slovak Research and Development Agency VEGA 1/0051/08, APVV 0365-07, ESF COST Actions CM0601, CM0805 and EUROPLANET TNA2. Research plan of Czech Ministry of Education No. MSM0021630501.

## References

- [1] K. L. Aplin. "Atmospheric Electrification in the Solar System", *Surveys in Geophysics*, vol. 27, (2006), pp 63-108.
- [2] T. Tokano, G. J Molina-Cuberos, H. Lammer, and W. Stumptner: "Modelling of Thunderclouds and Lightning Generation on Titan", *Planetary and Space Science*, vol. 49, (2001), pp 539–560.
- [3] D-M. Hunten, M.G. Tomasko, F.M. Flaser, R.E. Samuelson, D.F. Strobel, and D.J. Stevenson: *Titan, in Saturn*, ed. T. Gehrels and MS. Matthews, (1984), pp. 671-759.
- [4] R. Navarro-González, S.I. Ramírez: "Corona discharge of Titans troposphere", vol. 19, (1997), pp 1121-1133.
- [5] K. Plankensteiner, H. Reiner, BM. Rode et al.: *Discharge experiments simulating chemical evolution on the surface of Titan*, *ICARUS* 187 (2) 616-619 (2007).
- [6] K. Rinnert: "Lightning on other Planets", *J. Geophys. Res.*, vol. 90, (1985), 6225-6237.
- [7] A. Somogyi, Chu-Ha Oh, M.A. Smith: "Organic Environments on Saturn's Moon, Titan: Simulating Chemical Reaction an Analyzing Products by FT-ICR and Ion-Trap Mass Spectrometry", 2005, pp 1044-0305.

# Surface Modification of Poly(ethylene terephthalate) by Helium Plasma Immersion Ion Implantation

A. Tóth\*, K. Kereszturi, M. Mohai, I. Bertóti, J. Szépvölgyi  
Institute of Materials and Environmental Chemistry, Chemical Research Center,  
Hungarian Academy of Sciences, Pusztaszeri út 59-67, H-1025 Budapest, Hungary

e-mail: totha@chemres.hu

## Abstract

The surface of poly(ethylene terephthalate) (PET) was modified by helium plasma immersion ion implantation (PIII). The induced effects were studied by XPS, nanoindentation, scratch and multipass wear tests and measurements of surface electrical resistance. Surface carbonisation with degradation of the ester group was observed. The reduced modulus decreased and the surface layer became brittle. The hardness correlated directly with the critical load of cracking. Wear resistance increased, since the volume loss decreased to about 6% of the value measured for the untreated PET. The surface electrical resistance decreased upon treatment by several orders of magnitude, but increased with time elapsed after treatment by about an order of magnitude within a month.

**Keywords:** PET, PIII, XPS, wear, electrical resistance

## Introduction

The investigation of the process of plasma immersion ion implantation (PIII) of poly(ethylene terephthalate) (PET) is a topic of current interest [1]. The background is its promising application in areas including packaging and biomaterial devices, in particular in the fields of improvement of gas-barrier properties of beverage-containing PET bottles [2-8], decrease of bacterial adhesion in cardiovascular implants like heart valve sewing rings and artificial blood vessels [9-11], etc.

In this work the surface modification of PET by He PIII was studied. To our knowledge, no previous report has been published on this topic. To limit the number of treatments and samples to be characterised, the approach of design of experiments was applied. A three-level fractional factorial design was used with three factors (voltage  $U$ , fluence  $F$ , and fluence rate  $FR$ ) and nine treatment combinations. Fig. 1 shows the treatment parameters in the factorial space.

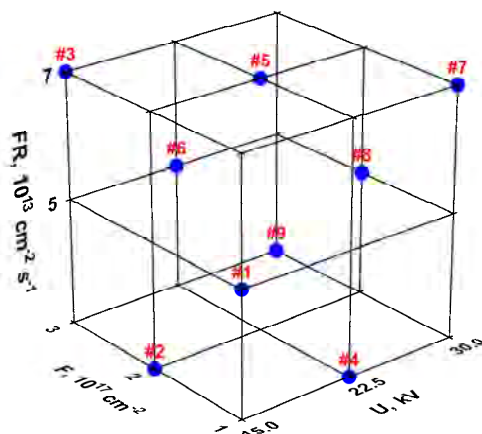


Fig. 1. Parameters of He PIII treatment of PET

Alterations in the surface chemical composition and bonding of the elements were studied by XPS. Nanoindentation, topographic and scratch tests were performed to reveal the modification of surface hardness, reduced modulus, surface topography and wear resistance. Changes in the surface electrical resistance and dependence of the latter on the time elapsed after treatment was also determined.

The experimental details were similar to those described in our previous publication [12].

## Results and discussion

### XPS analysis

Fig. 2 reflects a strong surface degradation of PET upon He PIII treatment, involving the elimination of O-rich fragments, since the O/C atomic ratio of the untreated sample (theory=0.4, found=0.38) decreased strongly for each treated sample to values ranging between 0.14 and 0.25.

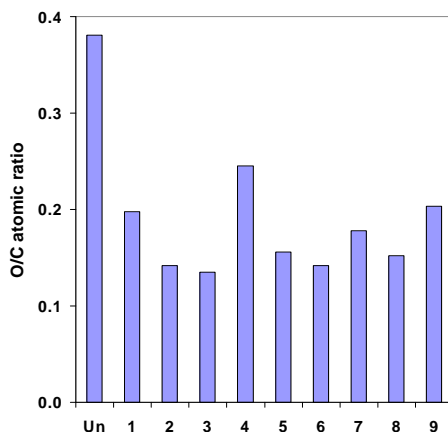


Fig. 2. Alterations in the O/C ratio of PET upon PIII-treatment.

Figs. 3 and 4 show the C 1s and O 1s photoelectron peaks of PET before and after He PIII treatment. These corroborate the degradation upon treatment, since the C 1s components at 286.6 and 289.1 eV (assignable [13] respectively to carbon atoms in C-O and O=C-O groups) decreased substantially. Simultaneously, a new component developed at 288 eV, assignable [13] to C=O and/or O-C-O groups. The components of the O 1s peak at 532 and 533.6 eV (assignable [13] to oxygen atoms respectively doubly and singly bonded to carbon) broadened. The relative intensity of the component at lower binding energy decreased. The XPS results suggest a strong degradation of the ester group. According to SRIM calculations [14], the dominant energy deposition mechanism under the conditions applied is electronic stopping, which (together with its known crosslinking effect) can be responsible for the damage of the ester group. In addition, contribution of UV-radiation of the He plasma is expected, leading to crosslinking via radical recombination and formation of double bonds [15].

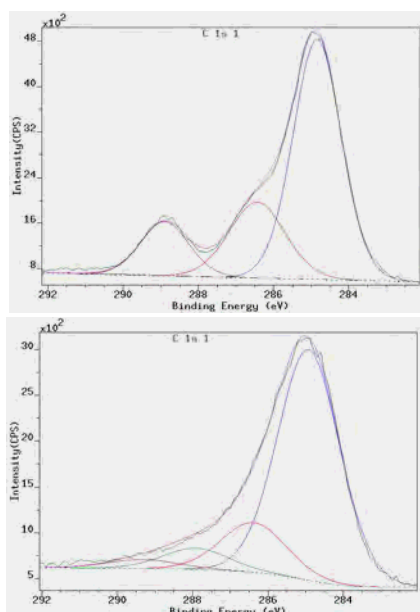


Fig. 3. C 1s peak before (top) and after (bottom) treatment

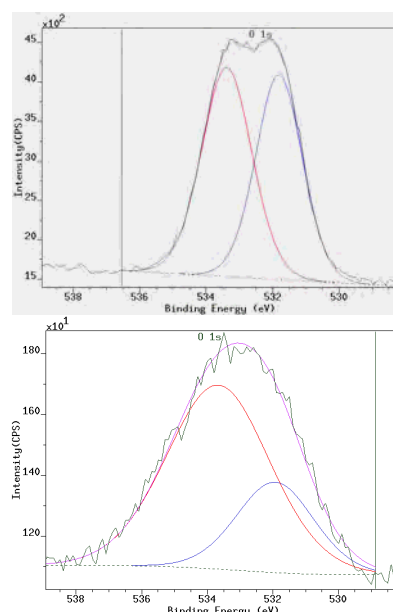


Fig. 4. O 1s peak before (top) and after (bottom) treatment

*Mechanical, scratch and wear tests*

Fig. 5 demonstrates the PIII-induced changes in the hardness ( $H$ ) and reduced modulus ( $E_r$ ) of PET determined by nanoindentation at 100 nm depth. It can be seen that the reduced modulus of each He PIII-treated sample decreased substantially. At the same time, the hardness of the surface layer could increase or decrease upon PIII treatment.  $H$  and  $E_r$  for the PIII-treated samples show a linear correlation.

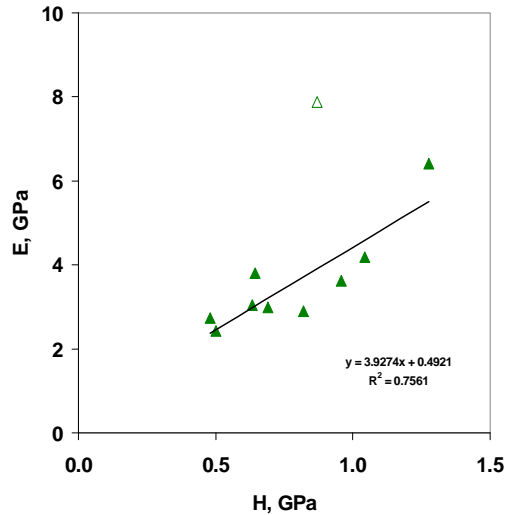


Fig. 5. PIII-induced changes in the mechanical properties (Open symbol: untreated, filled symbol: treated samples).

Fig. 6 shows the scratch tracks for the untreated (0) and for the PIII-treated samples (1-9), obtained with a sharp Rockwell type diamond probe under a load increasing linearly between 100 and 600  $\mu\text{m}$ , at a rate of  $0.04 \text{ mN } \mu\text{m}^{-1}$ . Comparing the tracks obtained for the untreated and PIII-treated samples, it is clearly seen that the permanent plastic deformation appears at scratch distances (proportional to scratch loads) higher for the PIII-treated samples than for the untreated one. Furthermore, the scratch track of the untreated sample is smooth, while the track edges of the PIII-treated samples crack at certain loads, testifying to the formation of brittle surface layers. Based on the visual examination of the micrographs of the scratch tracks, a critical load  $L_c$  can be determined for each track, corresponding to the load of the first appearance of the cracked edge. (See the marks in Fig. 6).

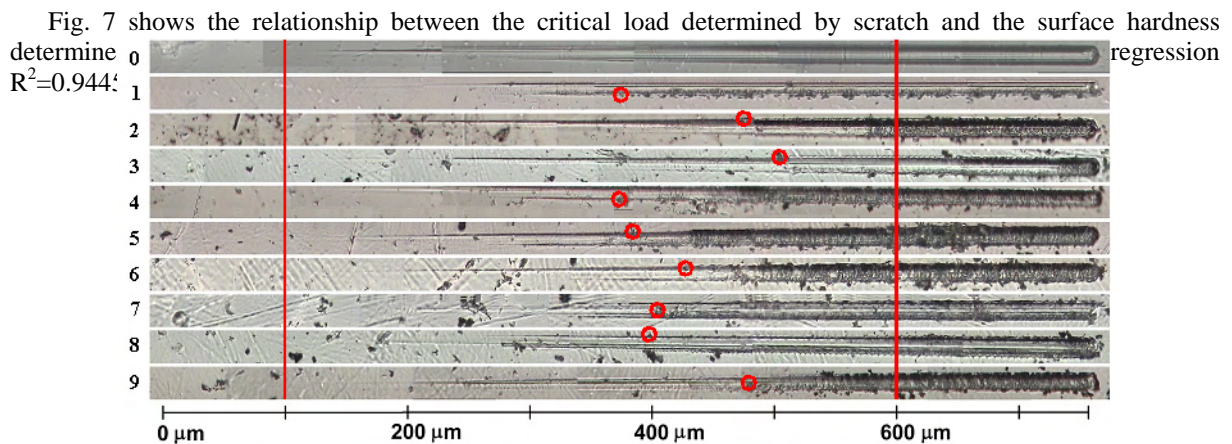


Fig. 6. Scratch tracks for the untreated (0) and He PIII-treated (1-9) PET

The abrasive wear was characterised by the volume loss  $V$  of a standard multipass wear test, in which five sequential scratches were done by a sharp Rockwell-type diamond head over the same track (load=20 mN), with a low-load topography measurement performed between each scratch. The volume loss for the untreated sample

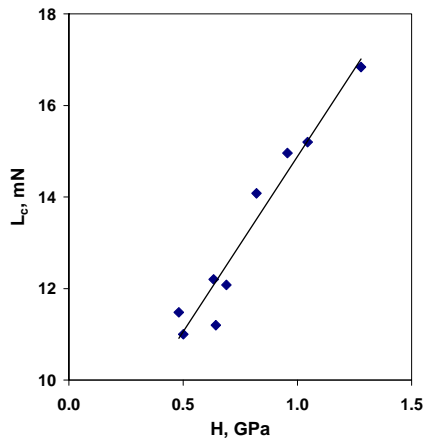


Fig. 7 Critical load vs. hardness

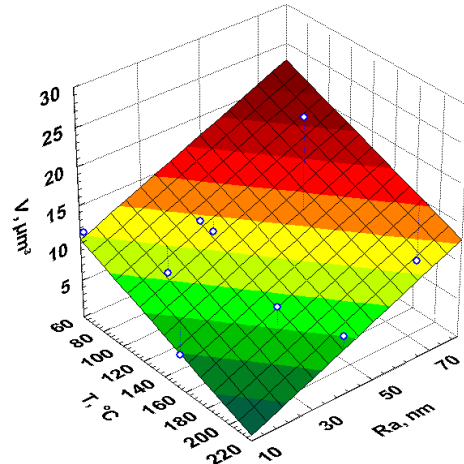


Fig. 8 Volume loss vs. surface temperature and roughness

$V_0$  under these conditions was  $46.0 \mu\text{m}^3$ . Each applied He PIII treatment decreased the volume loss, to values ranging between  $2.4$  and  $25.5 \mu\text{m}^3$ . The ratio of  $V_{\text{min}}/V_0=2.4/46.0=0.057$ , which implies an increase in the wear resistance by a factor of more than 17. The volume loss did not show clear relationship with the main process parameters. As seen in Fig. 8, however, it correlated directly with the average surface roughness  $R_a$  determined by topographic measurements, and inversely with the surface temperature  $T$  developed during treatment.

#### Surface electrical resistance

The surface electrical resistance  $R$  was measured at room temperature, by a specially designed equipment, considering the ASTM D257 standard test method for DC resistance.  $R$  for the untreated PET was higher than the upper limit of the measurement range of the equipment applied, which implies a starting value  $R_0 > 10^{17} \Omega$ .

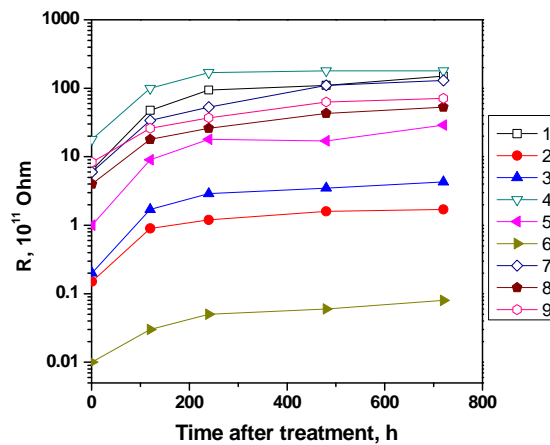


Fig. 9 Electrical resistance vs. time elapsed after He PIII-treatment

As seen in Fig. 9, for the PIII-treated samples  $R$  decreased reaching values ranging between  $1.1 \times 10^9$  and  $1.8 \times 10^{12} \Omega$ . This means a decrease by about 5 to 8 orders of magnitude. Such a decrease can be explained by the surface carbonisation detected above by XPS and the formation of double bonds. With the time elapsed after treatment, however,  $R$  increased in each case, typically by about one order of magnitude within a month, tending to reach saturation.

## Conclusions

- He PIII treatment of PET led to strong decrease in surface O/C atomic ratio due to degradation of the ester group.
- The reduced modulus of the surface layer decreased, while the surface hardness could increase or decrease upon treatment.
- Scratch tests testified to the formation of brittle surface layer. The critical load corresponding to the appearance of cracks correlated directly with surface hardness.
- The volume loss under multipass wear test decreased up to about 6% of the value measured for the untreated sample. The volume loss correlated directly with the surface roughness and inversely with the surface temperature developed upon treatment.
- The surface electrical resistance decreased by 5 to 8 orders of magnitude. Due to the post-treatment type surface relaxation, the electrical resistance increased with elapsed time by about an order of magnitude within a month, approaching saturation.

## Acknowledgement

This work was co-sponsored by the National Scientific Research Fund (OTKA) and the National Office for Research and Technology (NKTH) through project K-67741.

## References

- [1] A. Tóth, K. Kereszturi, M. Mohai, I. Bertóti, *Surf. Coat. Technol.* 204 (2010) 2898; and references therein.
- [2] S. Watanabe, M. Shinohara, H. Kodama, T. Tanaka, M. Yoshida, T. Takagi, *Thin Solid Films* 420-421 (2002) 253.
- [3] N. Sakudo, D. Mizutani, Y. Ohmura, H. Endo, R. Yoneda, N. Ikenaga, H. Takikawa, *Nucl. Instrum. Methods B* 206 (2003) 687.
- [4] M. Ueda, K.G. Kostov, A.F. Beloto, N.F. Leite, K.G. Grigorov, *Surf. Coat. Technol.* 186 (2004) 295.
- [5] N. Sakudo, H. Endo, R. Yoneda, Y. Ohmura, N. Ikenaga, *Surf. Coat. Technol.* 196 (2005) 394.
- [6] S. Okuji, M. Sekiya, M. Nakabayashi, H. Endo, N. Sakudo, K. Nagai, *Nucl. Instrum. Methods B* 242 (2006) 353.
- [7] M. Ikeyama, S. Miyagawa, S. Nakao, J. Choi, T. Miyajima, *Nucl. Instrum. Methods B* 257 (2007) 741.
- [8] M. Ikeyama, S. Miyagawa, Y. Miyagawa, Y. Hayakawa, T. Miyajima, *Surf. Coat. Technol.* 201 (2007) 8112.
- [9] J. Wang, N. Huang, P. Yang, Y.X. Leng, H. Sun, Z.Y. Liu, P.K. Chu, *Biomaterials* 25 (2004) 3163.
- [10] J. Wang, N. Huang, C.J. Pan, S.C.H. Kwok, P. Yang, Y.X. Leng, J.Y. Chen, H. Sun, G.J. Wan, Z.Y. Liu, P.K. Chu, *Surf. Coat. Technol.* 186 (2004) 299.
- [11] N. Huang, P. Yang, Y.X. Leng, J. Wang, H. Sun, J.Y. Chen, G.J. Wan, *Surf. Coat. Technol.* 186 (2004) 218.
- [12] K. Kereszturi, A. Tóth, M. Mohai, I. Bertóti, J. Szépvölgyi, *Appl. Surf. Sci.* 256 (2010) 6385.
- [13] G. Beamson, D. Briggs, *High Resolution XPS of Organic Polymers. The Scienta ESCA300 Database*, Wiley, Chichester, 1992.
- [14] J.F. Ziegler, M.D. Ziegler, J.P. Biersack, *Nucl. Instrum. Methods B* 268 (2010) 1818.
- [15] A. Holländer, J.E. Klemberg-Sapieha, M.R. Wertheimer, *J. Polym. Sci. A: Polym. Chem.* 34 (1996) 1511.

# Rate coefficient measurements of asymmetric charge transfer reactions

I. Korolov<sup>1</sup>, G. Bánó<sup>2</sup>, Z. Donkó<sup>1</sup>, A. Derzsi<sup>1</sup>, P. Hartmann<sup>1</sup>

<sup>1</sup>Research Institute for Solid State Physics and Optics of the Hungarian Academy of Sciences, H-1525 Budapest, POB 49, Hungary

<sup>2</sup>Department of Biophysics, P J Safarik University in Kosice, 04001 Jesenna 5, Kosice, Slovakia

e-mail: ihor.korolov@gmail.com

## Abstract

An experimental apparatus has been designed and developed to measure the rate coefficient of asymmetric charge transfer (ACT) reactions between noble gas ions and ground state metal atoms. The measurements rely on the combination of plasma diagnostics methods and a kinetic model of the afterglow plasma, which allows monitoring of the temporal evolution of the densities of different species. The metal vapor was created inside a discharge cell by cathode sputtering, its density was monitored by atomic absorption spectroscopy. Here we present experiments on the Ar<sup>+</sup>-Fe reaction. The rate coefficient was evaluated from the emission intensity decay of Fe<sup>+\*</sup> lines pumped by the ACT reaction in He-Ar-Fe and Ar-Fe afterglow plasmas. The rate coefficient for the ACT reaction between Ar<sup>+</sup> and Fe atoms has been determined to be  $k = 7.6(\pm 3.0) \times 10^{-9} \text{ cm}^3 \text{ s}^{-1}$  at  $T = 300 \text{ K}$ .

**Keywords:** asymmetric charge transfer, rate coefficient.

## Introduction

Asymmetric charge transfer (ACT) reactions between ground state noble gas ions (A<sup>+</sup>) and metal atoms (M) play an important role in many glow discharge applications, such as various hollow cathode lamps [1,2], analytical plasma sources [3-6], as well as different metal ion lasers (e.g. Ne-Cu<sup>+</sup>, He-Ag<sup>+</sup>, He-Au<sup>+</sup>, He-Cu<sup>+</sup>, He-Zn<sup>+</sup>, etc.) [7-12]. During the ACT reaction, a ground state metal atom is ionized and excited in a single step:



Unlike other ionization processes (like Penning ionization, or electron impact ionization), the ACT is a selective mechanism. The process is efficient for excited metal ion M<sup>+\*</sup> levels having an energy  $0 \leq \Delta E \leq 1 \text{ eV}$  below that of the ground state noble gas ion A<sup>+</sup>, with highest cross sections belonging to an energy difference around  $\Delta E \approx 0.1\text{-}0.3 \text{ eV}$  [13]. Earlier rate coefficient measurements of ACT reactions between noble gas ions and metal atoms were motivated by the development of different metal ion lasers. Most of the experiments were carried out with volatile metals, like Hg, Pb, Cd, Zn, or Tl [14-18]. There are very few rate coefficient and cross-section data available for other elements, that are difficult to evaporate, e.g. Cu, Fe, Ti, Ni, Mo, etc. For the Ne-Cu<sup>+</sup> system, data have been published [19] for thermal energies ( $\sim 2000 \text{ K}$ ). Cross sections for the interaction of Xe<sup>+</sup> ions and various metals have been determined for a wide range of ion energies  $1 \text{ eV} \leq \varepsilon \leq 5000 \text{ eV}$  [20]. To our best knowledge, there are no experimental cross section or rate coefficient data available for ACT reactions between Ar<sup>+</sup> ions and metal atoms at thermal energies, which are of high importance in many glow discharge applications [21,22]. ACT reactions play a very important role in glow discharge mass spectrometry, GDMS [21-23], and glow discharge optical emission spectroscopy, GD-OES [24], which are widely used by industry for analytical studies of metal alloys. The plasma sources of GD instruments are mostly operated in argon buffer gas. Detailed understanding of the operation of these plasma sources requires sophisticated numerical modeling of the discharge plasmas, the accuracy of which depends critically on the correctness of the input parameters. To date, the lack of knowledge of ACT rate coefficients has prevented precise modeling predictions of the relative sensitivity factors (RSF) [25-27] in GD-MS and limited the accuracy of the calculated emission spectra in GD-OES.

Among all the metals, iron plays a distinguished role in GD-MS, as it is usually used as an internal standard (RSF = 1). There are several levels of Fe<sup>+\*</sup> that can be populated by ACT with Ar<sup>+</sup> ions, therefore the reaction is expected to be fast. Evidence for the ACT reaction between these species has been given by other authors, see Refs. [28–32], however, the rate coefficient of the reaction has not been measured yet, to our best knowledge. As to theoretical efforts, the semi-classical calculations of ACT rate coefficients between Ar<sup>+</sup> ions and different metal atoms by Bogaerts et al [33] are to be

mentioned. Their typical calculated rate coefficients are in the range of  $k = 10^{-10}$ - $10^{-8}$  cm<sup>3</sup> s<sup>-1</sup>, for iron a value of  $13.76 \times 10^{-9}$  cm<sup>3</sup> s<sup>-1</sup> has been given.

In this paper we report our experimental investigation on the ACT process between argon ions and iron atoms and the determination of its rate coefficient.

## Experimental

The rate coefficient of the ACT reaction between argon ions and iron atoms is measured in a stationary afterglow experiment. The metal vapor is generated by means of cathode sputtering in a pulsed glow discharge operated either in He-Ar mixture or in pure Ar buffer gas. Our method relies on the measurement of the decay rate of the Ar<sup>+</sup> ion density (monitored by the intensity of Fe-II lines excited by ACT) during the afterglow period, at different metal atom concentrations, allowing the evaluation of the ACT rate coefficient. A detailed description of the experimental setup and the data evaluation method follows.

The main part of the experimental setup, the discharge cell (see Fig. 1), is situated inside the vacuum chamber of the apparatus. It consists of two plane cathodes (PC) and two hollow cathodes (HC), which are used to create the plasma and the metal vapor inside the central cavity of the cell. The two different sets of cathodes (PC-s and HC-s) allow establishing plasmas with densities in a wide range. In presents experiments the cathodes are made of pure (>99.8%) iron. The plane cathode has an active area of 50 mm (length) × 5 mm (width). Dimensions of the rectangular hollow cathode cavity are 50×5×5 mm. The inner diameter and the length of the reaction cell are 15 mm and 70 mm, respectively. The discharges are operated in a pulsed regime, with a typical pulse duration of 1-2 ms for plane cathode and 5-12 ms for hollow cathode. During the measurements the temperature of the cell is monitored using a K-type thermocouple installed inside the anode body.

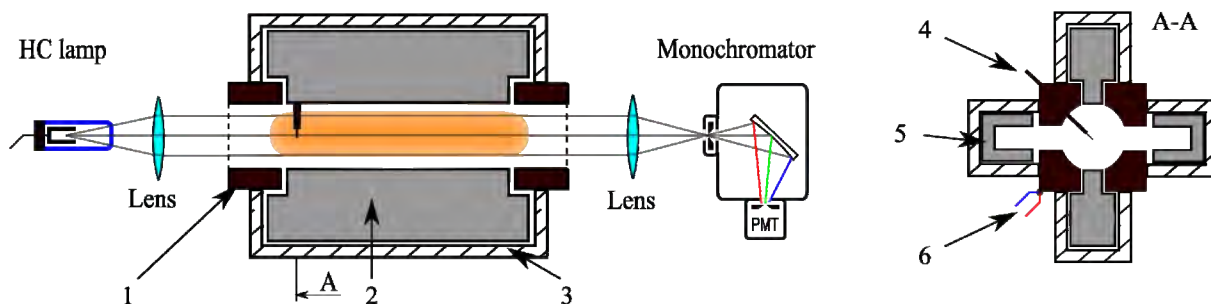


Fig. 1. Schematic view of the reaction cell and the optical setup. The A-A section is perpendicular to the optical axis. 1 - Anode (Ground), 2 - Plane Cathode, 3 - Ceramic insulator, 4 - Langmuir Probe, 5 - Hollow cathode, 6 - thermocouple.

The vacuum system is sketched in Fig. 2. The apparatus is equipped with a Residual Gas Analyzer. The working pressure (1-20 mbar) is monitored by a capacitance pressure gauge. Because of the high purity requirements, prior to the measurements, the discharge chamber and the gas tubing are heated, while pumping, above 480 K to evaporate volatile impurities from the walls. For this purpose, heating wires and tapes are wrapped around the different parts of the apparatus. Independent control of the heating power applied to these parts avoids temperature gradients that can lead to re-condensation of evaporated gas onto the colder parts. Before the experiments the main chamber is evacuated below  $5 \times 10^{-9}$  mbar by a turbomolecular pump. The experiments are performed using 6.0 purity argon and helium gases with a slow gas flow, up to 30 sccm, measured and controlled by flow meters/controllers. To achieve a higher cleanliness level during the experiments, the gases are further purified using liquid nitrogen traps and a VICI P100-2 purifier, before entering the vacuum chamber.

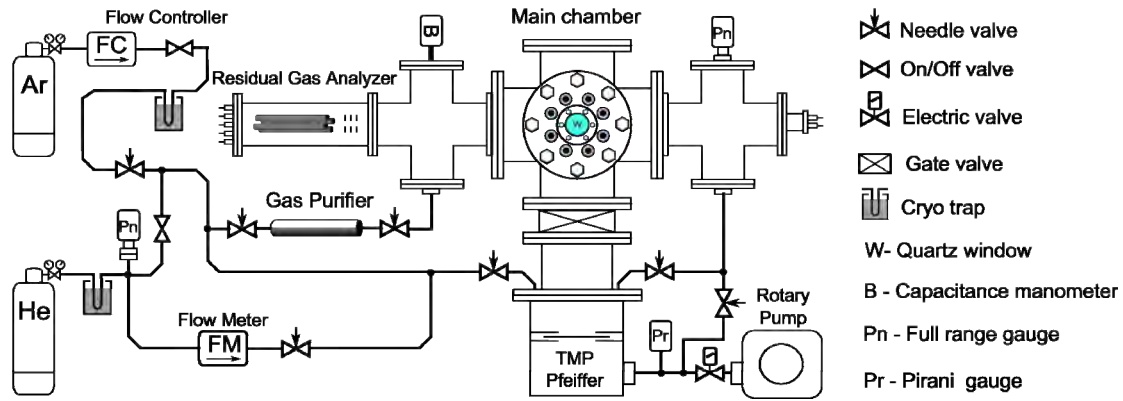


Figure 2. The vacuum system of the apparatus.

### Langmuir Probe measurements

The evaluation of ACT rate coefficients presented in this work does not directly rely on the results of Langmuir probe measurements. However, it is essential to have a good understanding and control of the plasma processes during the afterglow period. The Langmuir probe is utilized as a complementary discharge diagnostic tool (i) to validate the results of the kinetic model, (ii) to test the gas purity in the discharge cell, and (iii) to get information on the electron temperature of the decaying plasma. The Langmuir probe is situated at a fixed position inside the discharge cell (see Fig. 1). It is made of a tungsten wire, having diameter of  $20 \mu\text{m}$  and length of 2.5 mm. The probe support consists of two coaxial glass tubes with the diameter of the outer one being  $\sim 0.6$  mm. To avoid the formation of an electrical contact between the probe and the metal layer deposited onto the outer support surface, the inner glass tube is made 1 mm shorter as compared to the outer one (see also Ref. [34]). During the measurements the probe surface is periodically cleaned by ion bombardment applying a negative bias voltage of  $\sim 80$  V during the discharge pulses. The typical cleaning current to the probe is about 1-3 mA. The switching between the cleaning and the measurement regime is controlled by a computer. As all the measurements are performed using pulsed discharges, the probe characteristic is scanned in the following way: the probe potential is kept constant for a preset number of discharge pulses (to allow averaging of the measured data) and the probe current is measured during and between the discharge pulses as a function of time; the probe potential is subsequently changed by a constant and new data are recorded, until the whole time dependent voltage-current probe characteristic is acquired. An example of such a measured probe characteristic is shown in Fig. 3.

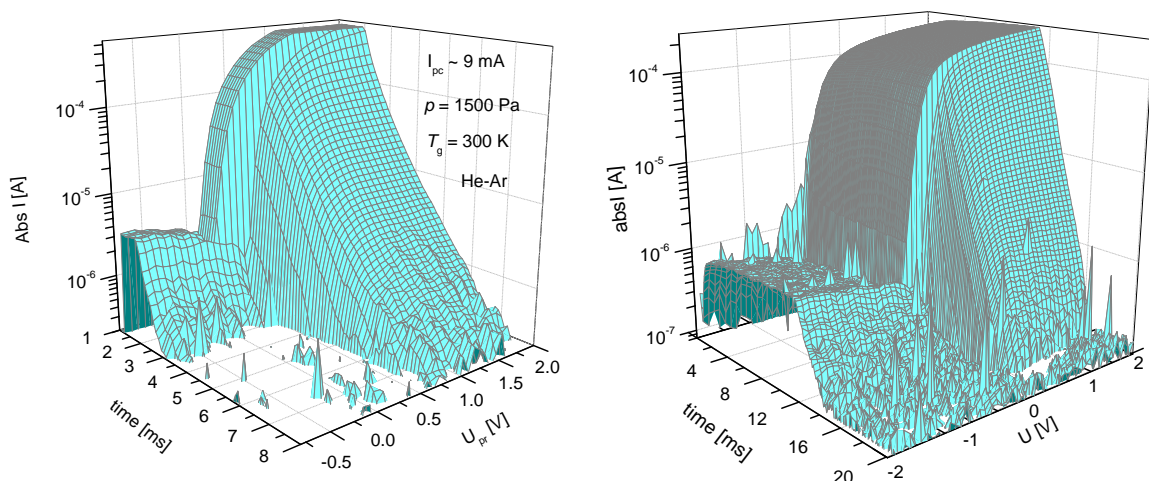


Fig. 3. An example of the time evolution of the probe characteristic during the discharge pulse (of length 1.8 ms) and the subsequent afterglow period in He-2%Ar mixture. Left panel: Plane cathode discharge of length of 1.8 ms. Right panel: Hollow cathode discharge with pulse length of 11 ms, discharge current of 200 mA,  $T_g \sim 300$  K, and  $p \sim 1700$  Pa.

The electron density at a given time is obtained from the electron current part of the probe characteristic in the acceleration region using the "I-squared" method [35], which gives reliable results for our experimental conditions. The electron temperature  $T_e$  and the Electron Energy Distribution Function (EEDF) are determined from the second derivative of the characteristic. Detailed information about Langmuir probe theory and the estimation of different plasma parameters from the probe data is given elsewhere [34-38].

### Fe density measurements

The density of sputtered iron atoms inside the cell is determined using atomic absorption spectroscopy. An iron-neon hollow cathode lamp (type: L233-26NU) is used as a light source and an Acton VM-502 monochromator equipped with a Hamamatsu (H7732P-11) photomultiplier tube (PMT) serves as a detector (see Fig. 1). To achieve the best possible signal to noise ratio, the PMT signal is recorded in a time-resolved photon counting mode by an AMETEK Multi Channel Scaler (MCS) pci-card, which is synchronized to the discharge pulses. During the experiments the emission intensity of the Fe-I (372.0 nm) line passing through the discharge cell is measured with ( $I$ ) and without ( $I_0$ ) iron vapor present inside the cell. The absorbance is calculated as  $A = \lg(I_0/I)$ . We have found that for lamp currents below 8 mA the absorbance does not depend on the lamp current. To avoid self-absorption [39] and to optimize the emission line profile, the current of the lamp is set to 5 mA. The expected temperature of the metal vapor inside the HC lamp is 350+/-50 K [40]. The highest absorbance observed during the measurements was 0.25. For most of the elements the absorbance is proportional to the absorbing metal density [39] up to an absorbance value of 0.3-0.4. Thus, our measurements are performed within a range of validity of the Lambert-Beer law. The iron density  $N$  is calculated using the following equation [41]:

$$N = \frac{\log\left(\frac{I_0}{I}\right) \cdot 2\varepsilon_0 \cdot \Delta\nu_D \sqrt{\pi} m_e c}{\Phi l \log e \cdot \sqrt{\ln 2} \cdot e^2 f} \quad (2)$$

where  $\Delta\nu_D$  is the Doppler width of the absorption line,  $l = 0.05$  m is the effective path length,  $\varepsilon_0$  is the permittivity of vacuum,  $m_e$  and  $c$  are the electron mass and the speed of light, respectively. The oscillator strength  $f = 0.0411$  is taken from Refs. [42] and [43]. The line-profile factor  $\Phi$  expresses the departure of the measured absorbance from the idealized case of an unsplit pure Doppler broadened absorption line and a monochromatic emission line [41]. This factor is calculated from the measured

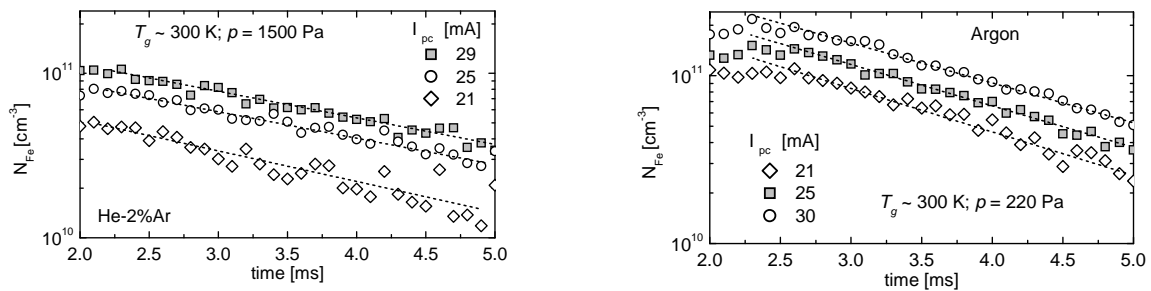


Fig 4. An example of calculated ground-state iron concentration from the measured absorbance of Fe I (372.0 nm) line during the afterglow period of the pulsed discharges as a function of time. Left panel: He-2%Ar mixture. Right panel: pure argon. The pressure and temperature of the buffer gas are indicated.  $I_{pc}$  is the discharge current. The duration and the frequency of the discharge pulses are 1.8 ms and 3 Hz, respectively.

hyperfine structure of the Fe I 372.0 nm resonance line [44] and is found to be  $\approx 1$ . For the present experimental conditions the uncertainty of the measured atomic absorption data due to pressure

broadening and Stark broadening effects is estimated to be below 5%. We expect the total error of the metal density measurements to be approximately 25-30%, which is the major factor limiting the precision of our ACT rate coefficient measurements. Typical time-dependent decays of the measured iron density during the afterglow period of the pulsed discharges (in He-2%Ar mixture, at a pressure of 1500 Pa and in pure Argon at  $p = 220$  Pa) are plotted in Fig. 4 for three different PC discharge currents.

### Plasma formation and rate coefficient measurements

In the present experiments  $\text{Ar}^+$  ions are produced inside the discharge cell by running discharges under two different plasma conditions. In the first case, the discharges are operated in a He-2%Ar buffer gas mixture, while in the second case in pure Ar gas. In the following we describe these two different types of discharges, introduce a kinetic model to follow the time-evolution of the densities of plasma species, discuss the way of the determination of the ACT reaction rate coefficient, and address the effect of impurities.

#### Discharges in He-Ar mixtures

In He-Ar buffer gas mixtures mainly  $\text{He}^+$  ions and  $\text{He}^m$  metastable atoms are formed during the active discharge pulse period. During the afterglow, due to the relatively high buffer gas pressure (1400-1800 Pa), the  $\text{He}^+$  ions are first converted to  $\text{He}_2^+$  ions in three body association processes. Next, an  $\text{Ar}^+$  dominated plasma is formed in a sequence of ion molecule reactions, including ACT reactions of  $\text{He}_2^+$  ions with Ar atoms, and Penning ionization collisions of Ar atoms with  $\text{He}^m$  metastable atoms. Such an afterglow plasma becomes thermal [35,38]  $T_{\text{ion}} \approx T_e \approx T_{\text{gas}} \approx 300$  K (proved also by Langmuir probe and the thermocouple measurements) approximately 0.5 ms after switching the discharge off. The fast thermalization is mostly related to the fact, that  $\text{He}^m$  metastables are converted to Ar ions, which hinder them to produce fast electrons in metastable-metastable collisions. This is the main advantage of using the He-Ar mixture. The metal vapor inside the discharge region is created by cathode sputtering during the PC discharge pulses. The sputtering rate and, as consequence, the iron atom density inside the cell can be adjusted by setting different discharge current values, as is clearly demonstrated in Fig. 4. To gain a better understanding of the details of plasma processes inside the cell and to optimize the experiments, a numerical kinetic model of the afterglow period has been developed. An example of calculated plasma evolution of the PC discharge afterglow is shown in Fig. 5.

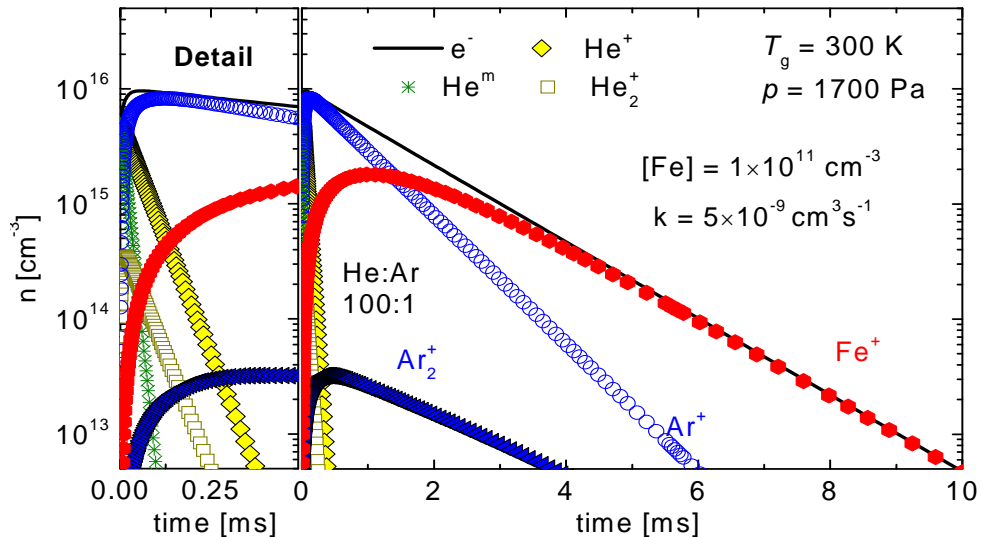


Fig. 5. Time evolution of the densities of different plasma species in the discharge cell calculated with the kinetic model in the He-1%Ar mixture. The iron atom density is taken to be constant and the ACT reaction rate is assumed to be  $k = 5 \times 10^{-9} \text{ cm}^3 \text{ s}^{-1}$ . Note the rapid decay of the density of all helium species. (The evolution of the density of species at early times is made visible in the left panel.)

The data have been obtained by solving a set of coupled partial differential equations describing the densities of plasma species at the actual experimental conditions (temperature, gas pressure, cell geometry etc.). The ion and metastable reactions are taken into account in this model. The diffusion coefficients of the ions were calculated using measured reduced zero-field mobilities in helium and argon [45].

Once the formation of  $\text{Ar}^+$  ions is completed (at about 0.5 ms in Fig. 5), the balance equation for their density,  $[\text{Ar}^+]$ , can be written in the following form:

$$\frac{d[\text{Ar}^+]}{dt} = -k [\text{Ar}^+][\text{Fe}] - \frac{D}{\Lambda^2} [\text{Ar}^+]; \quad (3)$$

where the first term represents the ACT reaction between  $\text{Ar}^+$  ions and Fe atoms with a rate coefficient  $k$ , the second term is the ambipolar diffusion to the wall with a diffusion constant  $D$  and a characteristic diffusion length  $\Lambda$ . Assuming a constant iron number density  $[\text{Fe}]$  – which is a reasonable approximation for short ( $< 1$  ms) time periods – the solution of (3) can be written as:

$$[\text{Ar}^+]_t = [\text{Ar}^+]_0 \exp(-t/\tau), \quad (4)$$

where

$$1/\tau = D/\Lambda^2 + k[\text{Fe}], \quad (5)$$

where  $[\ ]_t$  denotes time dependence. The first term on the right side of equation (5) is a constant. Thus, the plot of  $1/\tau$  versus the iron number density,  $[\text{Fe}]$ , will be a straight line, the slope of which is given by the rate coefficient  $k$ . The absolute value of the iron number density, needed for the evaluation of  $k$ , is provided by the atomic absorption measurements. On the other hand, we do not need the absolute density of argon ions, the characteristic decay time  $\tau$  can be obtained from relative values. In our experiment, the relative number density of argon ions is determined from the intensity ( $I_{\text{CT}}$ ) of Fe-II lines pumped by the ACT reaction between  $\text{Ar}^+$  ions and Fe atoms. The intensity of these lines is directly proportional to  $[\text{Ar}^+]_t[\text{Fe}]_t$ . It follows, that the relative  $\text{Ar}^+$  ion density decay can be obtained from the ratio of  $I_{\text{CT}}=[\text{Fe}]_t$ , or  $I_{\text{CT}}=A$ , where  $A$  is the measured absorbance of Fe atoms. Fitting the time evolution of this ratio by an exponential decay gives us the value of  $\tau$ .

#### Discharges in pure Ar

The rate coefficient of the ACT reaction can also be determined using pure argon gas discharges. In this case one has to be aware of the effect that argon metastable atoms, which are not destroyed

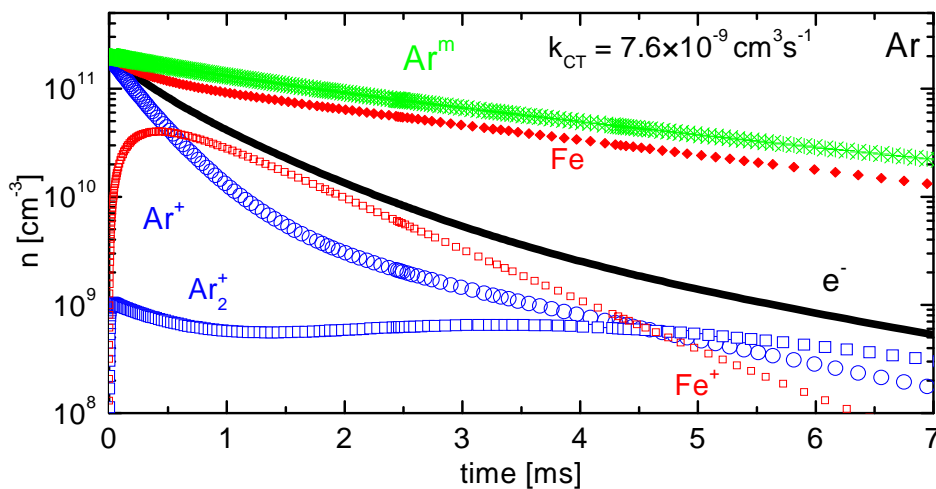


Fig. 6. Ion formation and destruction in the discharge cell calculated with the kinetic model in pure argon at  $p = 220$  Pa and  $T_g = 300$  K.

rapidly during the afterglow, can serve as an additional source of Ar ions and fast electrons via  $\text{Ar}^m + \text{Ar}^m$  collisions. As a consequence, equation (4) becomes invalid, and the plasma is not thermalized rapidly after switching the discharge off. Moreover, at high pressures argon ions can be converted to  $\text{Ar}_2^+$  ions. Our kinetic model indicates that for relatively low pressures (200-300 Pa) the influence of  $\text{Ar}_2^+$  ions,  $\text{Ar}^m$  metastables, and the slowly cooling electron temperature  $T_e(t)$  on the  $\text{Ar}^+$  decay is negligible during the very first few ms period of the afterglow. Thus, in contrast to the He-Ar plasma (where it takes about 0.5 ms to form the  $\text{Ar}^+$  dominated afterglow), the very early afterglow is to be used for the evaluation of  $k$  in pure argon discharges (see Figure 6). Apart from this peculiarity, the data evaluation proceeds in the same way as described for He-Ar discharges.

### *Effect of impurities*

In the afterglow plasmas of interest here the decay of the ion and electron density is caused mainly by ambipolar diffusion and by reactions with impurities followed by fast recombination [55]. This way impurities influence the density of argon ions via an additional loss channel. Under quasi-neutral conditions the level of impurities can be estimated by measuring the decay time of the electron density. This can be accomplished in our case by using Langmuir probe. At experimental conditions, He-2%Ar mixture at  $p = 1500$  Pa and  $T = 300$  K, in the  $\text{Ar}^+$  dominated afterglow plasma of a low current ( $\sim 4$  mA) pulsed PC discharge we typically obtained a purity level below 0.8 ppm (particle per million). As long as the level of impurities is kept so low and constant during the experiments, the reactions of argon ions with impurities add only a small constant to the right hand side of equation (5), which does not effect the value of  $k$  determined by the evaluation procedure described above. To ensure that the measurements are carried out under proper conditions, purity tests relying on the Langmuir probe electron density measurements in an  $\text{Ar}^+$  dominated afterglow plasma are always performed at the beginning and at the end of measurements.

### **Results and discussion**

Iron ions have several excited states with energies right below the energy of ground state  $\text{Ar}^+$  ions (within 1 eV), which are thus suitable for ACT reaction. There are numerous Fe-II transitions (e.g. 249.1, 275.7, 247.8, 275.3 nm, etc.) originating from these levels, which are efficiently excited by the ACT reaction. Assuming that the ACT reaction strongly dominates over other (e.g. electron impact) excitation channels of these transitions, and that the emission lifetimes are much shorter than the characteristic decay of the afterglow plasma, the intensities of all these ACT-excited lines are proportional to the Fe atom and  $\text{Ar}^+$  ion number densities during the afterglow. It follows that all the ACT-excited lines have the same relative decay in the afterglow, as it was indeed confirmed by our measurements at identical PC discharge conditions (pressure, current, etc.).

Examples of the measured 249.1 nm line intensities in He-2%Ar and Ar afterglow plasmas are shown in Fig. 7. The fast decay of the ACT-excited line in the He-2%Ar mixture within  $<0.5$  ms after switching the PC discharge off is (i) due to plasma relaxation (electron and ion temperature), not included in our kinetic model, and (ii) due to the possible pumping of  $\text{Fe}^{+*}$  levels by  $\text{He}^+$ ,  $\text{He}^m$ , and  $\text{He}_2^+$  ions, which quickly disappear (see Fig.5). In the case of the pure Ar plasma, the fast decay is not observed. The hatched rectangles in Fig. 6 represent the time intervals during which the characteristic decay time of  $\text{Ar}^+$  ions is determined.

Both, the intensity measurements of ACT-excited lines,  $I_{\text{CT}}(t)$ , and the detection of the Fe atomic absorbance  $A(t)$  are synchronized with the discharge pulses. Thus, the time evolution of the relative  $\text{Ar}^+$  ion density during the afterglow is readily obtained from the ratio of  $I_{\text{CT}}(t)=A(t)$ . In principle, the  $\text{Ar}^+$  ion density decay obeys the exponential form of (4) only when there is a constant metal density present in the cell. In our sputtered metal source the iron density gradually decreases during the afterglow. However, within a relatively short time interval (typically 0.5-1 ms, see Fig. 7) used for fitting the  $\text{Ar}^+$  ion density decay, the iron number density does not vary more than  $\pm 10-15\%$ . Thus, during this short period of time the metal density is approximated by a constant (average) value and the  $\text{Ar}^+$  ion density decay is fitted by a single exponential function. During the course of measurements the discharge current,  $I_{\text{pc}}$ , is set to different values (ranging from 5 to 30 mA), which results in different metal atom densities. The frequency and the width of the discharge pulses are selected in a way, that the temperature of the discharge cell is kept nearly constant ( $300 \pm 3$  K) for the different discharge current values.

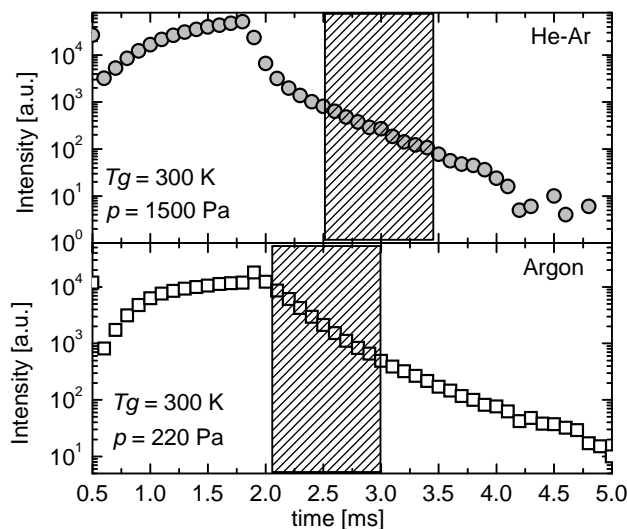


Fig. 7. Measured emission intensity of the 249.1 nm Fe-II charge transfer-excited line in He-2%Ar (upper panel) and Ar (lower panel) afterglow plasmas averaged over 5000 pulses. The PC discharge pulses are 1.8 ms long with a repetition rate of 3 Hz.  $I_{pc} = 25$  mA. The hatched rectangles represent the time intervals during which the characteristic decay time of  $Ar^+$  ions is determined. The falling edge of the current pulses is shorter than  $30\mu s$ .

The measured dependence of the characteristic decay time of  $Ar^+$  ions on the iron atom density is shown in Fig. 8. The experiments were performed using the PC discharges in He-2%Ar mixture and in pure Ar buffer gas at pressures of 1500 Pa and 220 Pa, respectively. The different data sets in this figure represent results taken on different days – confirming a good reproducibility of the measurements. It is evident, that the data points of  $1/\tau$  versus the metal density give a straight line, for both He-2%Ar and Ar buffer gases, with the same slope of  $k = 7.6(+/-3.0)\times 10^{-9} \text{ cm}^3 \text{ s}^{-1}$ ; which is the rate coefficient of the ACT reaction (see equation (5)). The vertical shift of the two fitted lines originates from the different speed of diffusion of  $Ar^+$  ions in He-Ar and Ar buffer gases. The fact, that these lines are parallel (within the limits of accuracy) adds confidence to the measured reaction rate value. As already mentioned earlier, the estimated error of 35-40% in the ACT rate is mainly due to the uncertainties in the iron number density determination inside the cell.

In another experiment to create the iron vapour pressure we used the hollow cathodes instead the plane cathodes. The measurements showed that even for high currents of the HC discharge (0.5-1 A and pulse length 8 ms) in argon (at  $p \sim 200$  Pa) the iron number density inside the cell was less than  $8\times 10^{-9} \text{ cm}^{-3}$ , which is not enough for proper determination of the ACT rate coefficient. The results of the calculation with the kinetic model showed that due to the high rate of asymmetric charge transfer, the sputtered iron atoms created in the HC discharge are mostly converted to  $Fe^+$  ions during the diffusion from the hollow cathodes into the cell, where a  $Fe^+$  dominated plasma is formed. The calculated ratio between the density of iron ions to that of iron atoms was more than  $10^2$ . To confirm this, a glass tube ( $d = 15$  mm) was inserted half-length (35 mm) into the discharge cell and then using the pulsed HC discharge metal was sputtered onto the glass. During the sputtering process, the optical absorbance was also measured (as explained above). The experiment was performed for different currents of the HC discharge. Knowing the total number of pulses and using the data obtained from the spectroscopic measurements, the total mass of the sputtered iron was found to be less than  $1 \mu\text{g}$  per  $10^4$  pulses. In the next step the material from the glass tubes was dissolved in hydrochloric acid. This mixture has high absorbance in UV region, which was measured by a Shimadzu UV-2400PC spectrophotometer. The measured absorbance of the samples was compared with the absorbance of

known samples. The mass values obtained this way showed linear dependence with the HC current and were found to be 40-150  $\mu\text{g}$  per  $10^4$  pulses at currents ranging from 550 to 1000 mA. This mass is more than 100 times higher compared to the above value inferred from absorption measurements during discharge operation, indicating that the vast majority of the deposit originates from iron ions, from the  $\text{Fe}^+$  dominated plasma.

Based on the above results, we conclude that the ACT reaction between  $\text{Ar}^+$  ions and Fe atoms plays an important role in ionization of iron atoms in Ar-Fe discharges. For instance, the rate coefficient calculated by Bogaerts et al. [33] for Penning ionization of Fe atoms by  $\text{Ar}^m$  metastables is  $2.3 \times 10^{-10} \text{ cm}^3 \text{ s}^{-1}$ , which is more than an order of magnitude lower than the measured rate for the ACT reaction. The same authors [33] have also calculated ACT rate coefficients: for the Ar-Fe system they gave a value of the rate coefficient ( $13.76 \times 10^{-9} \text{ cm}^3 \text{ s}^{-1}$ ), which is about a factor of two higher than our measured value. However, when calculating the corresponding RSF-s they have used a four times lower rate coefficient value ( $3.44 \times 10^{-9} \text{ cm}^3 \text{ s}^{-1}$ ) to get a reasonable agreement with the experiments.

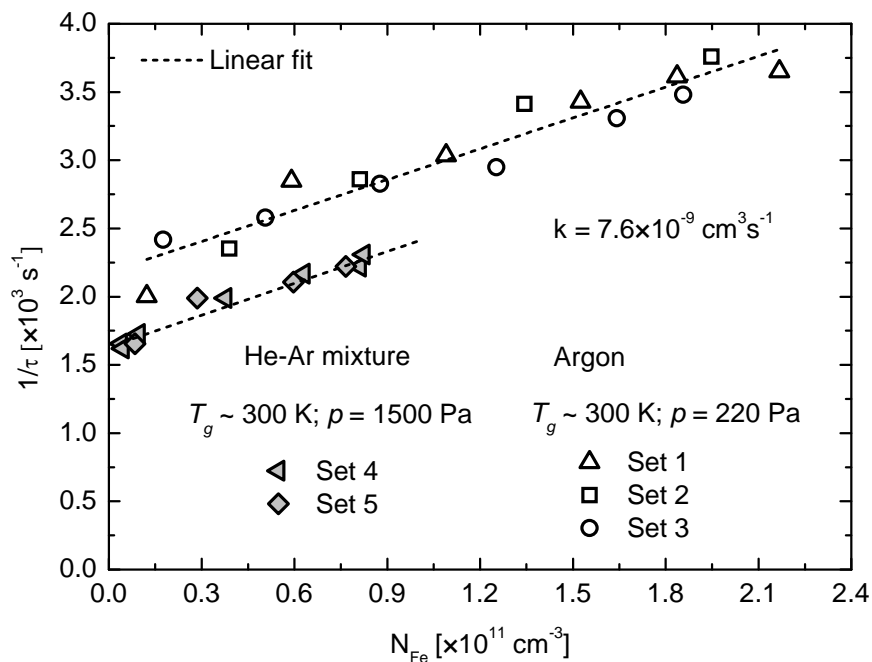


Fig. 8. The dependence of the characteristic decay time of  $\text{Ar}^+$  ion density on iron atom density during the afterglow period.

### Summary

We have developed an experimental apparatus to investigate the asymmetric charge transfer reaction between  $\text{Ar}^+$  ions and Fe atoms. The combination of different plasma diagnostics methods (emission and absorption spectroscopy, as well as Langmuir probe measurements) with a kinetic model of the plasma processes made it possible to determine the rate coefficient of the asymmetric charge transfer process between  $\text{Ar}^+$  ions and Fe atoms. The measurements were carried out in the afterglow of pulsed, plane cathode sputtering discharges in Ar and He-Ar mixtures at pressures of 220 Pa and 1500 Pa, respectively. The value of the ACT rate coefficient was determined to be  $7.6(+/-3.0) \times 10^{-9} \text{ cm}^3 \text{ s}^{-1}$  at  $T = 300 \text{ K}$ . The experimental apparatus and the analysis techniques developed and presented here are planned to be used for further studies of the ACT reactions between other elements.

### Acknowledgements

The authors gratefully acknowledge the support provided by the MRTN-CT-035459 GLADNET project, useful discussions with E. Steers and A. Bogaerts, as well as the contributions of P. Horváth, J. Thoman Forgács, J. Tóth, Gy. Császár and E. Sárközi to the construction of the experimental apparatus.

## References

- [1] K. Danzmann and M. Kock, *J. Phys. B: At. Mol. Phys.*, 14 (1981) 2989
- [2] S. Johansson and U. Litzen, *J. Phys. B: Atom. Molec. Phys.*, 11 (1978) L703
- [3] E. B. M. Steers and R. J. Fielding, *J. Anal. At. Spectrom.*, 2 (1987) 239
- [4] Y. Zhao and G. Horlick, *Spectrochimica Acta Part B: Atomic Spectroscopy*, 61 (2006) 660
- [5] E. B. M. Steers, *J. Anal. At. Spectrom.*, 12 (1997) 1033
- [6] Z. Weiss, *J. Anal. At. Spectrom.*, 21 (2006) 691
- [7] G. Bánó, P. Horvath, T. M. Adamowicz, Rózsa, *Appl. Phys. B*, 89 (2007) 333
- [8] G. Bánó, L. Szalai, K. Kutasi, P. Hartmann, Z. Donkó, K. Rózsa, A. Kiss, T. Adamowicz, *Appl. Phys. B*, 70 (2000) 521
- [9] Z. Donkó, P. Apai, L. Szalai, K. Rózsa, R. C. Tobin, *IEEE Transactions on Plasma Science*, 24 (1996) 33
- [10] F. de Hoog, F. McNeil, F. Collins, K. Persson, *J. Appl. Phys.*, 48 (1977) 3701
- [11] G. J. Collins, *J. Appl. Phys.*, 44 (1973) 4633
- [12] D. C. Gerstenberger, R. Solanki, G. J. Collins, *IEEE J. Quantum Electron.*, 16 (1980) 820
- [13] A. R. Turner-Smith, J. M. Green, C. E. Webb, *J. Phys. B: Atom. Molec. Phys.*, 6 (1973) 114
- [14] R. Johnsen and M. A. Biondi, *J. Chem. Phys.*, 73 (1980) 5045
- [15] A. Belyaev, *J. Phys. B: Atom. Molec. Phys.*, 26 (1993) 3877
- [16] P. Baltayan, J. C. Pebay-Peyroula, N. Sadeghi, *J. Phys. B: Atom. Molec. Phys.*, 18 (1985) 3615
- [17] P. Baltayan, J. C. Pebay-Peyroula, N. Sadeghi, *J. Phys. B: Atom. Molec. Phys.*, 19 (1986) 2695
- [18] K. A. Temelkov, N. K. Vuchkov, R. P. Ekov, N. V. Sabotinov, *J. Phys. D: Appl. Phys.*, 41 (2008) 105203
- [19] K. A. Temelkov, N. K. Vuchkov, N. V. Sabotinov, *Plasma Process. Polym.*, 3 (2006) 147
- [20] J. A. Rutherford and D. A. Vroom, *J. Chem. Phys.*, 74 (1981) 434
- [21] N. H. Bings, A. Bogaerts, J. A. C. Broekaert, *Anal. Chem.*, 80 (2008) 4317
- [22] A. Bogaerts and R. Gijbels, *Spectrochimica Acta Part B*, 53 (1998) 1
- [23] V. Hoffmann, M. Kasik, P. K. Robinson, and C. Venzago, *Anal. Bioanal. Chem.*, 381 (2005) 173
- [24] A. Bogaerts, R. Gijbels, J. Vlcek, *J. Appl. Phys.*, 84 (1998) 121
- [25] W. Vieth and J. C. Huneke, *Acta Part B*, 46 (1991) 137
- [26] C. Venzago and M. Weigert, *J. Anal. Chem.*, 350, (1994) 303
- [27] A. Bogaerts and R. Gijbels, *J. Anal. At. Spectrom.*, 11 (1996) 841
- [28] E. Steers and A. Thorne, *J. Anal. At. Spectrom.*, 8 (1993) 309
- [29] K. Wagatsuma and K. Hirokawa, *Spectrochimica Acta Part B*, 51 (1996) 349
- [30] R. S. Hudson, L. L. Skrumeda, W. Whaling, *J. Quant. Speerosc. Radial. Transfer*, 38 (1987) 4pp
- [31] E. Steers, P. Smid, and Z. Weiss, *Spectrochim. Acta Part B*, 61 (2006) 414
- [32] V. Weinstein, E. B. M. Steers, P. Smid, J. C. Pickering, S. Mushtaq, *J. Anal. At. Spec.*, 25 (2010) 1283
- [33] A. Bogaerts, K. A. Temelkov, N. K. Vuchkov, R. Gijbels, *Spectrochimica Acta Part B*, 62, (2007) 325
- [34] G. Bánó, P. Hartmann, K. Kutasi, P. Horváth, R. Plasil, J. G. P. Hlavenka, and Z. Donkó, *Plasma Sources Sci. Technol.*, 16 (2007) 492
- [35] P. Spanel, *Int. J. Mass Spectrom. Ion Processes*, 149-150 (1995) 299
- [36] J. Swift and M. J. R. Schwar, *Electrical Probes for Plasma Diagnostics* (Ilfie, London, 1970)
- [37] I. Korolov, R. Plasil, T. Kotrik, P. Dohnal, O. Novotny, J. Glosik, *Contrib. Plas. Phys.*, 48 (2008) 461
- [38] R. Plasil, I. Korolov, T. Kotrik, P. Dohnal, G. Bano, Z. Donko, J. Glosik, *Eur. Phys. J. D*, 54 (2009) 391
- [39] L. H. J. Lajunen, *Spectrochemical analysis by atomic absorption and emission* (Royal Society of Chemistry, Cambridge, 1992).
- [40] C. Bruce and P. Hannaford, *Spectrochimica Acta Part B: Atomic Spectroscopy*, 26 (1971) 207
- [41] P. Hannaford and D. C. McDonald, *J. Phys. B: Atom. Molec. Phys.*, 11 (1978) 1177
- [42] T. R. O'Brian, M. E. Wickliffe, J. E. Lawler, W. Whaling, J. W. Brault, *J. Opt. Soc. Am. B*, 8 (1991) 1185
- [43] D. Engelke, A. Bard, M. Kock, *Z. Phys. D*, 27 (1993) 325
- [44] S. Krins, S. Opiel, N. Huet, J. von Zanthier, T. Bastin, *Phys. Rev. A*, 80 (2009) 062508
- [45] W. Lindinger and D. L. Albritton, *J. Chem. Phys.*, 62 (1975) 3517

# Study of Astrophysically Relevant Hydrogen Chemistry: combining an RF Ion Trap with a Cold Effusive Beam

Š. Roučka<sup>1</sup>, P. Jusko<sup>1</sup>, I. Zymak<sup>1</sup>, R. Plašil<sup>1</sup>, D. Gerlich<sup>1,2</sup>, J. Glosík<sup>1</sup>

<sup>1</sup> Charles University, Faculty of Mathematics and Physics, V Holešovičkách 2, 180 00, Prague, Czech Republic

<sup>2</sup> Institut für Physik, Technische Universität, 09107 Chemnitz, Germany

e-mail: stepan@roucka.eu

## Abstract

This contribution presents recent progress made with an ion trapping instrument which is operated in the Department of Surface and Plasma Physics of Charles University. A special feature of the experimental setup is the combination of a low temperature 22-pole trap (22PT) with a cold effusive source for neutrals. This allows us to study the interaction of trapped ions with slow and cold neutrals. Using a discharge tube also radicals can be produced, especially H- or D-atoms. Recent experimental progress includes the extension of the temperature of the neutrals,  $T_{\text{ACC}}$ , down to 4 K and various improvements on the accommodator for getting stable dissociation degrees. Using an MCP detector, the chemistry of both cations and anions can be studied. The instrument is presently used to explore a variety of pure hydrogen reactions at low temperatures. As a typical result, the formation of  $\text{H}_3^+$  via radiative and ternary association of  $\text{H}^+$  and  $\text{H}_2$  at 10 K will be discussed as well as the following formation of small hydrogen clusters. The conclusion and outlook give some hints to planned activities such as determination of state specific rate coefficients, the role of nuclear spin, and deuteration.

## Keywords:

ion traps, interstellar chemistry, H-atom beam, radiative association, ortho and para- $\text{H}_2$ , deuteration

## Introduction

Hydrogen is the most abundant baryonic species in the universe. It plays, both in its atomic and molecular form, a central role in many fields of natural science. Hydrogen plasmas can be found in laboratory discharges, flames, atmospheres, and astrophysical environments. Although pure hydrogen plasmas seem to be rather simple, the interactions of its components ( $\text{H}$ ,  $\text{H}^+$ ,  $\text{H}^-$ ,  $\text{H}_2$ ,  $\text{H}_2^+$ ,  $\text{H}_3^+$ , electrons, and photons) are usually rather complex since many processes compete with each other. In order to model such a system, many relevant parameters are needed. The state of the knowledge, covering the energy range from thermal up to keV, has been reviewed recently [11]. This energy range is suitable for modeling the plasma physics of the solar corona and solar wind or technical applications, e.g. for describing the boundary region of a magnetically confined fusion plasma.

For questions raised in astrochemistry, the interactions of various forms of hydrogen, especially H and D atoms, need to be understood at low temperatures, down to a few K. At such cold conditions, other processes such as small barriers, isotope enrichment, nuclear spin restrictions, or cluster formation play a role [4]. Recent publications emphasize that more experimental information on low temperature hydrogen chemistry is needed for tracing the chemical and physical processes occurring in the cosmic dark age of our universe [10] or in dense interstellar clouds [18].

In addition to hydrogen, there is a small fraction of deuterium which plays a special role in low temperature chemistry. Despite a deuterium abundance of only  $10^{-5}$  (relative to H), many deuterated molecules have been detected in the interstellar medium including doubly and even triply deuterated species. This phenomenon, called 'isotope fractionation' is due to a complex interplay between zero point energies, symmetry selection rules, and barriers. Many details of D-H exchange reactions must be known in order to correlate observed abundances of deuterated molecules with the cosmic D/H isotopic abundance ratio. An important experimentally unexplored class of reactions is isotope enrichment in collisions of ions or neutrals with D-atoms.

The instrument which is used in the detailed studies of hydrogen chemistry has been developed at the Technical University in Chemnitz [12], [2], [6]. It is a "standard" rf trapping instrument which are used today for a variety of applications in reaction dynamics, spectroscopy etc. A tutorial and more

references can be found in [19], [5], [20]. A special feature of our instrument is the integration of a temperature variable source for cold neutrals, especially hydrogen molecules or atoms. A recent series of measurements has concentrated on reactions between cold  $\text{CH}_n^+$  with H and  $\text{H}_2$  [7]. Especially interesting is the dependence of the reaction of  $\text{CH}^+$  with H on the rotational state of the molecular ion [15], [13].

This contribution summarizes the present status of our experimental activities to study various  $\text{H}_m\text{D}_n^+$  ( $m+n \leq 5$ , also  $\text{H}_m\text{D}_n^-$ ) collision systems, especially at the energies required for astrochemistry. Simple systems include the endothermic electron transfer from D to  $\text{H}^+$  or the associative detachment in  $\text{H}^+ + \text{H}$  collisions, more complex and experimentally unexplored is the deuteration of  $\text{H}_3^+$  in collisions with D or the formation of ortho- $\text{H}_3^+$  in collisions of para- $\text{H}_3^+$  with para- $\text{H}_2$ .

## Experimental

The modular design of the apparatus allows us to operate it in many different configurations. Fig. 1. shows the present version of the so-called CEB-22PT apparatus (Cold Effusive Beam – 22-Pole Trap). Primary ions are produced in a storage ion source which is capable of producing pulses of pre-cooled (350 K) molecular ions [8]. After selecting the desired ion mass using the QP mass filter, the ions are injected into the 22-pole trap. There they can be cooled down to 10 K via collisions with a buffer gas. For reactions, the neutral target gas can be just leaked into the trap chamber; injected in a pulsed supersonic beam, or in a cold effusive beam. The gas can be dissociated using a discharge leading to a cold beam of radicals. The optical transparency of the trap on axis allows to perform spectroscopic measurements on the ions. The reaction products are analyzed using a second mass spectrometer. The MCP can detect as well positive as well negative ions.

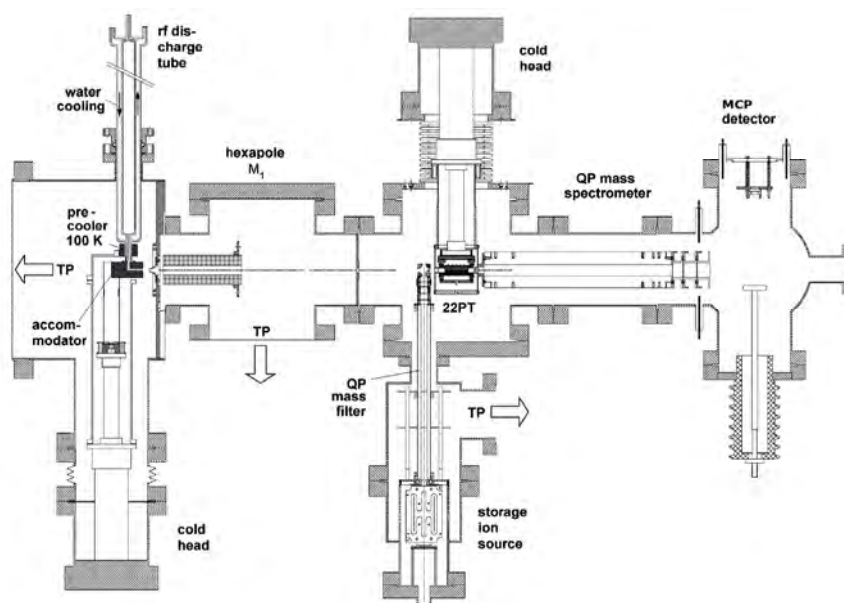


Fig. 1 Ion trapping instrument for studying the interaction of ions stored in the temperature variable 22-pole trap (22PT) with a cold effusive beam of H atoms,  $\text{H}_2$  molecules or deuterated isotopologues [2]. Recent innovations on the cold effusive beam include the integration of a new cold head (Sumitomo RDK-101E, lowest temperature 3.6 K), a Teflon coated accommodator, and a rather weak hexapole magnet for focusing slow H-atoms.

Details of the design of the hydrogen atom source and many tests have been described in the PhD thesis of G. Borodi [1]. A short summary can be found in [2]. As indicated in the left part of Fig. 1, molecular hydrogen is dissociated in a discharge tube (Pyrex glass, inner diameter of 19 mm, length 330 mm, terminated with two capillaries, inner diameter 2 mm, length 5 cm). The exit capillary is cooled to 100 K (precooler), followed by an accommodator which is thermally connected to a cold

head (Sumitomo RDK-101E, lowest temperature 3.6 K). The gas leaves effusively the accommodator and the flow is formed into a beam by a skimmer and several apertures. The dissociation degree is influenced by the surface material and temperature. The literature contains many hints, recipes and tricks for delivering dissociation degrees up to 95% [16], [17]. Very efficient but not so stable is the coating with H<sub>2</sub>O as described in [1]. In the current configuration we use a PTFE coated copper accommodator. Tests with a PTFE tube did not lead to full thermalization of the beam.

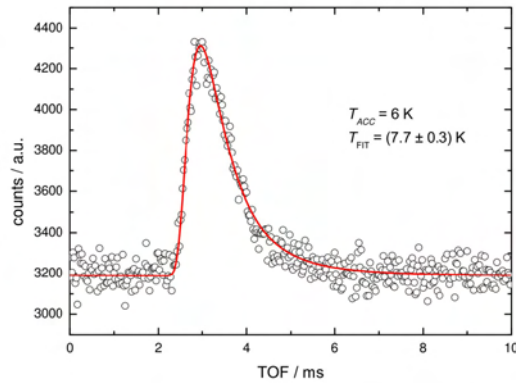


Fig. 2 TOF distribution of H atoms running the accommodator at 6 K. Comparison with the temperature, derived from the fit, reveals that the PTFE film is slightly warmer than the copper tube.

The thermalization of the atomic beam was verified by determining its velocity distribution via time-of-flight (TOF) measurements. For this purpose, a chopper wheel with 2 slits interrupts periodically the beam (time resolution  $\sim 20 \mu\text{s}$ ). The neutrals are detected using an electron impact ionizer at a distance of 58 cm. The data shown in Fig. 2. have been recorded at  $T_{\text{ACC}} = 6 \text{ K}$  for H-atoms. The measured distribution was fitted with a convolution of a Maxwellian with the instrument function calculated from the shape of the atomic beam and the chopper aperture and frequency. Comparison with the fit,  $T_{\text{FIT}} = 7.7 \text{ K}$ , reveals that there is still a slight temperature gradient in the teflon layer. It is also possible that thermalizing collisions with the PTFE surface are not so efficient as the layer of water ice [1].

As explained in detail in [2] the number density of hydrogen atoms at the location of the trap can be determined using an electron bombardment ionizer or, directly in the trap, using chemical probing. In both cases measurements are performed with the discharge switched ON and OFF and using a shutter for blocking or passing the direct beam. A typical result (in relative units) is plotted in Fig. 3.

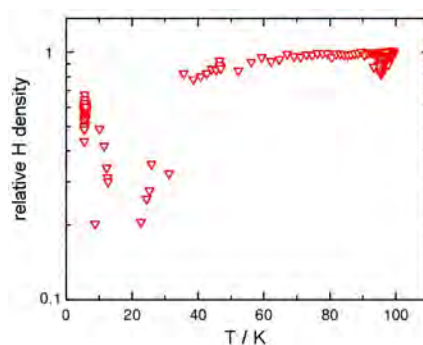


Fig. 3 Relative H-atom density ( $\sim$ dissociation degree) of the H atom source as a function of the accommodator temperature. The accommodator has been coated with a thin PTFE film. Between 10 and 30 K, fast recombination reduces the flux of atoms.

Below 30 K, the H atoms are lost due to efficient recombination on the surface of the accommodator. Going further down in temperature, the situation becomes again better. Most probably

this is due to coating with H atoms or reduced mobility. For a detailed understanding, more tests are needed. The overall flux of H atoms is sensitive to changes in experimental conditions. Therefore the hydrogen atom density is routinely calibrated in situ using  $\text{CO}_2^+$  as probing ion [2]. Results and discussion

The capabilities of the instrument are demonstrated by extending previous measurements of  $\text{H}_3^+$  formation towards lower temperatures. As described in detail in [9], two processes contribute, the stabilization of the collision complex via emission of a photon (radiative association) or via the collision with a third body (ternary association),

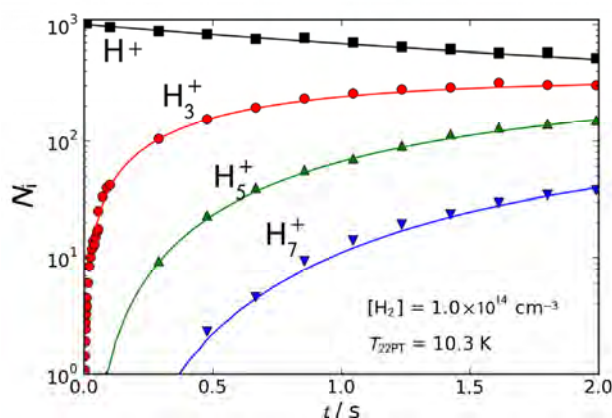


Fig. 4. Reactions of  $\text{H}^+$  ions with  $\text{H}_2$  at  $T_{22\text{PT}} = 10.3$  K. Plotted is the number of primary and product ions per filling,  $N_i$ , as a function of the storage time  $t$ . Solid lines represent a solution of chemical kinetic equations.

Fig. 4 shows a typical set of data measured at  $T_{22\text{PT}} = 10.3$  K and at a hydrogen number density of  $1 \times 10^{14} \text{ cm}^{-3}$ . The number of injected protons (typically 1000 per filling) decays exponentially. They are directly converted into  $\text{H}_3^+$  followed by subsequent collisions leading to larger hydrogen clusters. The formation of clusters has been discussed in detail in [14]. The ternary rate coefficients for cluster formation were obtained from least squares fit of measured data resulting,  $k_3(\text{H}^+) = (4.3 \pm 0.1) \times 10^{-29} \text{ cm}^6 \text{ s}^{-1}$ ,  $k_3(\text{H}_3^+) = (6.4 \pm 0.5) \times 10^{-29} \text{ cm}^6 \text{ s}^{-1}$ ,  $k_3(\text{H}_5^+) = (6 \pm 2) \times 10^{-29} \text{ cm}^6 \text{ s}^{-1}$ . Association of  $\text{H}_7^+$  and fragmentation of all clusters were also included in the model, but their rates could not be reliably determined from the fit. The rate coefficients of  $\text{H}_3^+$  and  $\text{H}_5^+$  formation via ternary association are a factor 0.4 smaller in comparison with [14]; this may be due to differences in the actual temperature or in the number density.

Evaluating such measurements performed at different number densities of  $[\text{H}_2]$ , one obtains the effective rate coefficients  $k^*$ , shown in Fig. 5. The observed behavior is typical for the combination of ternary association, prevailing at higher densities and radiative association which plays only a role at low densities. This dependence can be described by the equation

$$k^* = k_3 [\text{H}_2] + k_r \quad (3)$$

Fitting the data with Eq. (3) leads to a radiative association rate coefficient of  $2 \times 10^{-16} \text{ cm}^3 \text{ s}^{-1}$ . This result is 2 times higher than the value measured previously at 80 K while a simple RRKM based theory predicts a much steeper temperature dependence [9]. In order to clarify this unexpected result, more measurements will be made, including studies with para- $\text{H}_2$ .

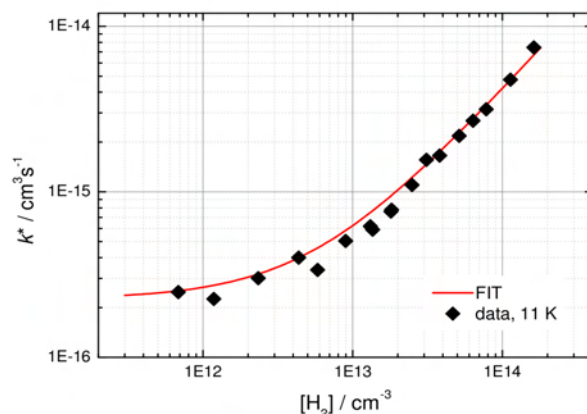


Fig. 5. Dependence of the effective rate coefficient for  $\text{H}^+ + \text{H}_2$  association as a function of the  $\text{H}_2$  number density. The ion trap was operated at 11 K. The measured values have been approximated by the function  $k^* = k_3 [\text{H}_2] + k_r$  (red line) leading to  $k_r = 2 \cdot 10^{-16} \text{ cm}^3 \text{ s}^{-1}$ .

### Conclusions and outlook

The goal of our present activities is to study in detail various elementary steps of the hydrogen chemistry at low temperatures using the combination of a linear rf multipole ion trap with an effusive source of hydrogen molecules and atoms. This contribution describes recent improvements: the H-atom beam velocity and density has been characterized using TOF and chemical probing, respectively. New results are reported for ternary and radiative association of  $\text{H}^+$  with  $\text{H}_2$  at 11 K proofing the high sensitivity of the instrument. A critical test for the apparatus will be the 3.6 meV endothermic electron transfer from D to  $\text{H}^+$  since the threshold behavior is well characterized by theory [3]. Other challenges in hydrogen chemistry are the associative electron detachment reaction  $\text{H}^+ + \text{H} \rightarrow \text{H}_2 + \text{e}^-$  (see separate contribution) and all the other  $\text{H}_m\text{D}_n^+$  collision systems such as  $\text{H}_3^+ + \text{D}$ . Unique in our approach is not only the atomic beam but also the combination trap - effusive molecular beam. The possibility to vary independently  $T_{\text{ACC}}$  and  $T_{22\text{PT}}$  and the use of normal- $\text{H}_2$  and para- $\text{H}_2$  makes it possible to measure state specific rate coefficients, e.g. for  $\text{H}^+ + \text{D}_2$ .

### Acknowledgment

This work is a part of the research plan MSM 0021620834 and grant OC10046 financed by the Ministry of Education of the Czech Republic and was partly supported by GACR (202/07/0495, 202/08/H057, 205/09/1183, 202/09/0642), by GAUK 25709, GAUK 92410, GAUK 86908, GAUK 54010 and by COST Action CM0805 (The Chemical Cosmos). The development of the instrument has been supported by the Deutsche Forschungsgemeinschaft (DFG), especially via the Forschergruppe FOR 388 "Laboratory Astrophysics".

### References

- [1] G. Borodi, *On the combination of a low energy hydrogen atom beam with a cold multipole ion trap. PhD Thesis TU Chemnitz* (2008).
- [2] G. Borodi, A. Luca, D. Gerlich, *Reactions of  $\text{CO}_2^+$  with H,  $\text{H}_2$  and deuterated analogues. Int. J. Mass Spectrom.* **280** (2009) 218.
- [3] B. D. Esry, H. R. Sadeghpour, E. Wells and, I. Ben-Itzhak, *Charge exchange in slow  $\text{H}^+ + \text{D}(1s)$  collisions. J. Phys. B: At. Mol. Opt. Phys.* **33** (2000) 5329.
- [4] D. Gerlich, F. Windisch, P. Hlavenka, R. Plašil, J. Glosik, *Dynamical constraints and nuclear spin caused restrictions in  $\text{H}_m\text{D}_n^+$  collision systems and deuterated variants. Philos. Trans. R. Soc. London, Ser. A* **364** (2006) 3007.
- [5] D. Gerlich, *The production and study of ultra-cold molecular ions. in: Low temperatures and cold molecules, World Scientific Publishing, ed. by Ian W M Smith, ISBN 978-1-84816-209-9* (2008) 295.
- [6] D. Gerlich, G. Borodi, *Buffer gas cooling of polyatomic ions in rf multi-electrode traps. Faraday Discuss.* **142** (2009) 57.
- [7] D. Gerlich, G. Borodi, A. Luca, C. Mogo, M. Smith, *Reactions between cold  $\text{CH}_n^+$  with H and  $\text{H}_2$ . submitted to Zeitschrift für Physikalische Chemie* (2011).
- [8] D. Gerlich, *Inhomogeneous Electrical Radio Frequency Fields: A Versatile Tool for the Study of*

- Processes with Slow Ions. Adv. Chem. Phys.* **LXXXII** (1992) 1.
- [9] D. Gerlich, S. Horning, *Experimental investigations of radiative association processes as related to interstellar chemistry. Chem. Rev.* **92** (1992) 1509.
- [10] S. C. O. Glover, T. Abel, *Uncertainties in H<sub>2</sub> and HD chemistry and cooling and their role in early structure formation. Mon. Not. R. Astron. Soc.* **388** (2008) 1627.
- [11] R. K. Janev, D. Reiter, U. Samm, *Collision Processes in Low-Temperature Hydrogen Plasmas. Berichte des Forschungszentrums Jülich* **4105** (2003) .
- [12] A. Luca, G. Borodi, D. Gerlich, *Interactions of ions with hydrogen atoms. Progress report in XXIV ICPEAC 2005, Rosario, Argentina, July 20-26, 2005, Edited by F.D.Colavecchia, P.D.Fainstein, J.Fiol, M.A.P.Lima, J.E.Miraglia, E.C.Montenegro, and R.D.Rivarola* **XXIV** (2005) 20.
- [13] T. Mehner, *Experimente mit und an kalten Atomstrahlen. Diplom Thesis, Techn. Univ. Chemnitz* (2009) .
- [14] W. Paul, B. Lücke, S. Schlemmer, D. Gerlich, *On the Dynamics of the Reaction of Positive Hydrogen Cluster Ions (H<sub>5</sub><sup>+</sup> to H<sub>23</sub><sup>+</sup>) with Para and Normal Hydrogen at 10 K. Int. J. Mass. Spectrom. Ion Phys.* **150** (1995) 373.
- [15] R. Plasil, T. Mehner, P. Dohnal, T. Kotrik, J. Glosik, D. Gerlich, *Reactions of cold trapped CH<sup>+</sup> ions with slow H atoms.* (2011) .
- [16] J. Slevin, W. Stirling, *Radio frequency atomic hydrogen beam source. Rev. Sci. Instrum.* **52** (1981) 1780.
- [17] D. Szczerba, L. D. van Buuren, J. F. J. van den Brand, H. J. Bulten, M. Ferro-Luzzi, S. Klous, H. Kolster, J. Lang, F. Mul, H. R. Poolman and M. C. Simani, *A polarized hydrogen/deuterium atomic beam source for internal target experiments. Nucl. Instrum. Methods Phys. Res., Sect. A* **455** (2000) 769.
- [18] C. M. Walmsley, D. R. Flower, G. Pineau des Forets, *Complete depletion in prestellar cores. Astron. & Astrophys.* **418** (2004) 1035.
- [19] R. Wester, *Radiofrequency multipole traps: tools for spectroscopy and dynamics of cold molecular ions. J. Phys. B: At. Mol. Opt. Phys.* **42** (2009) 154001-1.
- [20] B. Yuan, Z. Scott, G. Tikhonov, D. Gerlich, M.A. Smith, *Variable-temperature rate coefficients for the electron transfer reaction N<sub>2</sub><sup>+</sup> + H<sub>2</sub>O measured with a coaxial molecular beam radio frequency ring electrode ion trap. J. Phys. Chem. accepted* (2011)

# Influence of Mercury Titration on Kinetic Processes in Nitrogen Post-Discharge

V. Mazánková, F. Krčma, I. Bocková

Faculty of Chemistry, Brno University of Technology, Purkyňova 118, Brno 612 00, Czech Republic

e-mail: mazankova@fch.vutbr.cz

## Abstract

This work extends our recent investigation of mercury excitation under post-discharge conditions and presents results obtained during spectroscopic observations of mercury titration in nitrogen DC flowing post-discharges. DC discharge in quartz tube was created at 1000 Pa and 290 W. The plasma was studied by optical emission spectroscopy in the range of 300–800 nm. Besides three nitrogen spectral systems (first and second positive and first negative), the mercury line at 254 nm was recorded in the second order spectrum at 508 nm under these conditions. Its intensity was dependent on the mercury vapor flowing. No other mercury lines were observed. The upper state of observed mercury spectral line is  $^3P_1$ , and it is probably created by the resonance excitation energy transfer from vibrationally excited nitrogen ground state  $N_2(X^1\Sigma_g^+, \nu = 19)$ .

**Keywords:** post-discharge, mercury, optical emission spectroscopy, resonance energy transfer.

## Introduction

Nitrogen discharges and post-discharges in various configurations are widely used in different processes and technologies [1-3]. Relaxation processes of atomic and various very long live metastable nitrogen molecular states created during an active discharge lead to the common thermal equilibrium. These processes are connected with the emission of visible light that can be observed up to one second after switching off the active discharge. Processes depend on the experimental conditions as a pressure and excitation energy dissipated in the active discharge. Besides collisional processes in volume the heterogeneous reactions at the reactor walls and the light emission plays a significant role in the relaxation. However there is long interest of nitrogen post-discharge kinetics itself, there are still various open problems.

The neutral nitrogen molecule can form many electronic states. All molecular states under 7.4 eV are metastables that conserve the excitation energy for the long time up to seconds. There mutual collisions as well as the recombination of atomic species and heterogeneous reactions with walls create various radiating states and consequently the visible light emission can be observed up to one second after switching off an active discharge. However various very complex kinetic models were developed during the last years [4], there is very difficult to obtain information about all non-radiative metastables. The Cavity Ring Down Spectroscopy [5], two photon or optical-optical [6] LIF techniques allowed direct access to the determination of highly excited metastables during the recent year. But is nearly impossible to obtain any information about highly excited nitrogen ground state molecules, mainly to  $N_2(A^3\Sigma_u^+)$  state, during the post discharge.

The post-discharge kinetics is very sensitive on various impurities, as it was shown for various species [7-10]. Unfortunately, not all species that are added into the pure nitrogen (both into the active discharge and post-discharge) creates directly any radiative states. Therefore they are not be used for the direct determination of the metastables concentration [7-9]. Our recent work [11] pointed a direct excitation of some zinc radiative states by collisions with nitrogen metastables. But it is not applicable to use these reactions for the determination of metastables concentration because there is impossible to add zinc vapors in exactly known amount. Recently, we observed influence of mercury vapor on the nitrogen post-discharge [12] and we proposed some reactions leading to the mercury radiative states creation by collisions with highly excited nitrogen ground state molecules. The last published results [13] demonstrated the possibility of mercury titration into the post-discharge for the determination of  $N_2(X^1\Sigma_g^+, \nu=19)$  metastables. The presented results extend our knowledge in this field.

## Experimental set-up

The DC flowing post-discharge was used for the experimental study. A simplified schematic drawing of the experimental setup is given in figure 1. The active discharge was produced in a Quartz discharge tube at the constant discharge power of 290 W. The total gas pressure was 1000 Pa. Hollow

molybdenum electrodes were placed in the side arms (at interelectrode distance of 12 mm) of the main discharge tube to minimize their sputtering and also to minimize scattering of the light emitted in the electrode regions. Nitrogen was of 99.9999 % purity and it was further cleaned by Oxiclear and LN<sub>2</sub> traps. The reactor system was pumped continuously by rotary oil pump separated from discharge tube by another LN<sub>2</sub> trap. The gas flow of 800 Sccm was automatically controlled by Bronkhorst mass flow controller. The total gas pressure in the discharge tube was measured by a capacitance gauge connected to the end of the discharge tube. The moveable titration capillary tube was made of Pyrex and it was immersed upstream from the discharge into the quartz tube at its axis. The mercury was placed in a bulb at the entrance to the capillary and it was flowed by auxiliary nitrogen flow. The nitrogen of 99.999 % purity with flow (again controlled by Bronkhorst mass flow controller) up to 37.5 Sccm was used for this titration flow. This corresponds to mercury flow up to 1 μg min<sup>-1</sup> Hg at laboratory temperature of 30 °C in a steady state in the post-discharge. The position of the output end of capillary tube was fixed at 25 cm from the active discharge for these experiments. This position corresponds the decay time of 20 ms.

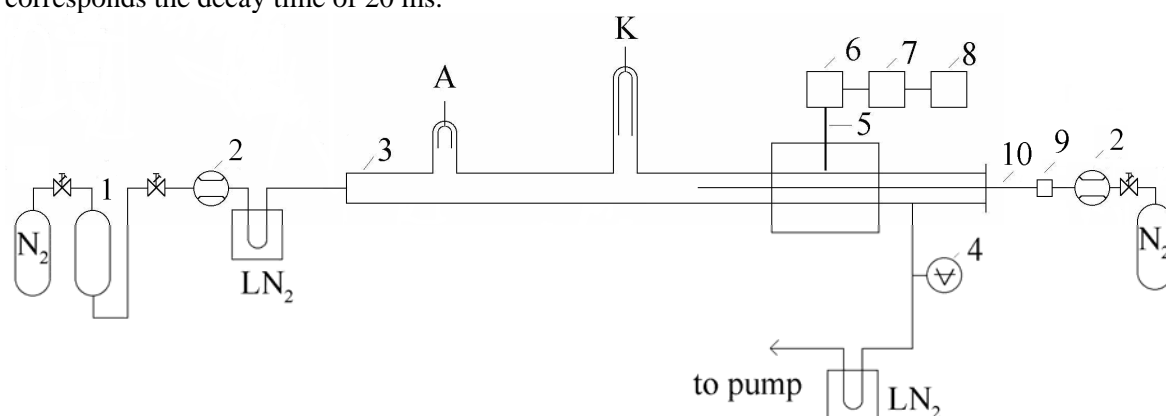


Fig. 1. Scheme of the experimental set up. 1 – catalyzer Oxiclear; 2 – mass flow controller; 3 – Quartz discharge tube; 4 – capacitance gauge; 5 – quartz optical fiber; 6 – monochromator Jobin Yvon Triax 550; 7 – CCD; 8 – PC, 9 – bulb with mercury, 10 – movable Pyrex titration capillary tube.

The optical spectra were measured by Jobin Yvon monochromator TRIAX 550 with CCD detector. The 300 gr/mm grating was used for overview spectra (300 -800 nm), grating with 3 600 gr/mm was used for the mercury line observations. The emitted light was led to the entrance slit of the monochromator by the multimode quartz optical fiber movable along the discharge tube. The 1<sup>st</sup> positive (N<sub>2</sub> (B <sup>3</sup>Π<sub>g</sub>) → (A <sup>3</sup>Σ<sub>u</sub><sup>+</sup>)), 2<sup>nd</sup> positive (N<sub>2</sub> (C <sup>3</sup>Π<sub>u</sub>) → (B <sup>3</sup>Π<sub>g</sub>)) and 1<sup>st</sup> negative (N<sub>2</sub><sup>+</sup> (B <sup>2</sup>Σ<sub>u</sub><sup>+</sup>) → (X <sup>2</sup>Σ<sub>g</sub><sup>+</sup>)) nitrogen spectral systems and mercury line at 254 nm (observed in the spectrum of the second order) were recorded in the spectra. No other atomic or molecular emissions were observed.

## Results and discussion

An example of the recorded post-discharge spectrum with mercury addition is given in figure 2.

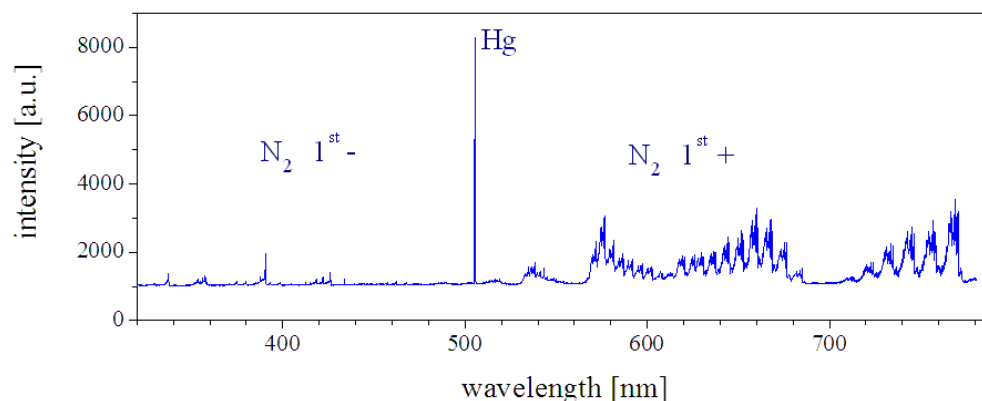
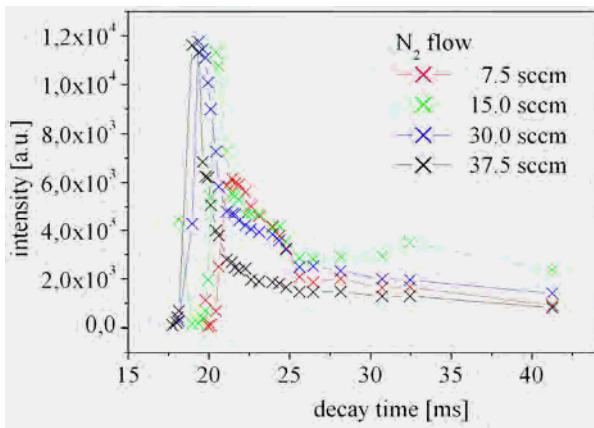


Fig. 2. Example of nitrogen post-discharge spectrum at the decay time of 31 ms with mercury line at 254 nm observed in the second order spectrum. Mercury was introduced at the decay time of 20 ms.

The titration was arranged in a position of 20 ms downstream of the active discharge. This position corresponds to the end of short live afterglow (known also as pink afterglow). However the titration flow rate was up to 5% of the main flow it influenced the post-discharge flow as it is demonstrated in figure 3 because the titration flow speed was about one half of the main flow speed. Thus, the mercury line was identified even a few ms before the titration point and its intensity reached rapidly maximal value due to the effective mixing. The post-discharge emission intensity profiles of representative bands of all three observed nitrogen spectral systems and mercury spectral line are shown in figures 4-7 as a function of the decay time. These dependencies were measured with different titration flow of N<sub>2</sub> with mercury vapor. It can be seen that the position of the maximal pink



**Fig. 3.** Mercury titration into the post-discharge: left – zero titration flow; middle – flow of 7.5 Scm; right – flow of 37.5 Scm. End point of titration capillary is visible at the right side.



**Fig. 4.** Dependence of the mercury line (254 nm) intensity on decay time at different titration flows.

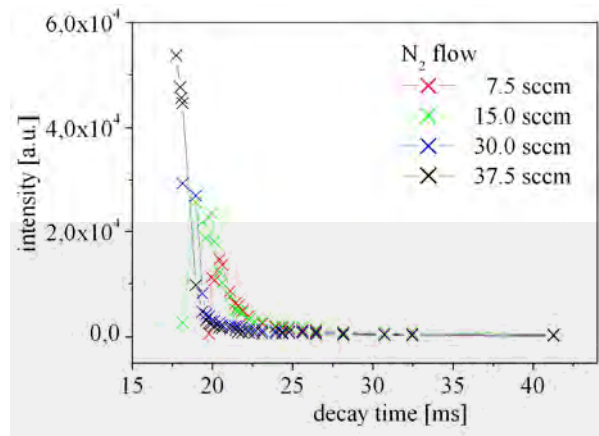


**Fig. 5.** Dependence of the nitrogen 1<sup>st</sup> negative system 0-0 band head intensity on decay time at different titration flows.

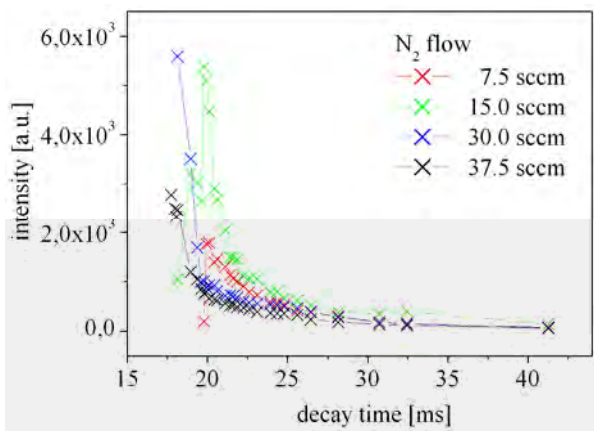


**Fig 6.** Dependence of the nitrogen 2<sup>nd</sup> positive system 0-2 band head intensity on decay time at different titration flows.

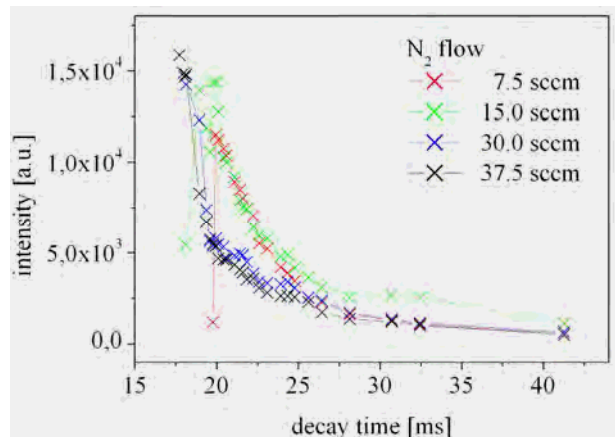
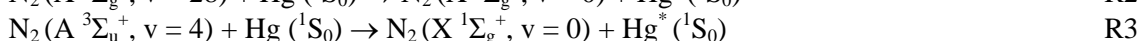
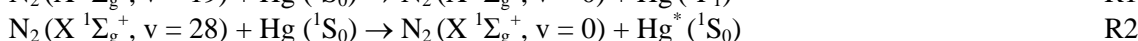
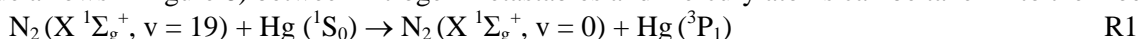


**Fig. 7.** Dependence of the nitrogen 1<sup>st</sup> positive system 2-0 band head intensity on decay time at different titration flows.

afterglow emission intensity depends on titration flow. The maximal intensity lay at decay time of 17-22 ms. The maximal mercury spectral line intensity shifts to the earlier decay times with the increasing titration flow. At later decay time no emission was observed. The detailed observation of the vibrational distributions changes induced by mercury vapor is contemporary under preparation.

### Kinetic model

The simplified kinetic model based on numeric model described in [3, 4] was proposed in [12] and thus the main information is given here. The mercury atomic energy levels lay mainly at higher energies in which nitrogen molecular states are not metastable, see figure 8. Therefore populations of these states are very low and thus no mercury lines from visible and near UV part of the spectrum (marked by blue arrows in figure 8) were observed. Thus only the following reactions (marked by dark blue arrows in figure 8) between nitrogen metastables and mercury atoms can be taken into the model.



Reaction R1 leads to the formation of the excited  $\text{Hg}(^3\text{P}_1)$  mercury state that is the origin of the resonance line at the wavelength of 254 nm that we determined in the spectra. Reactions R2, and R3 produce the excited mercury  $^1\text{S}_0$  state that is the origin of the resonance line at 185 nm but this line was not recorded. Reactions R1 and R2 partially stop the v-v processes in the nitrogen ground state, R3 reaction leads to the depopulation of  $\text{N}_2(\text{A } ^3\Sigma_u^+)$  state. Thus the pooling reactions or step-wise ionization processes could not efficiently create highly excited electronic states as it was observed. The production of the lowest  $\text{N}_2(\text{B } ^3\Pi_g)$  vibrational levels is possible by the reactions of lower excited ground state metastables. Because these states are not influenced by mercury presence, the lower dependence of the nitrogen 1<sup>st</sup> positive 2-0 band intensity was observed. The other channels originating from adjacent metastable nitrogen vibrational levels could play some role but they are not creating any radiative states. These reactions are marked by magenta arrows in figure 8.

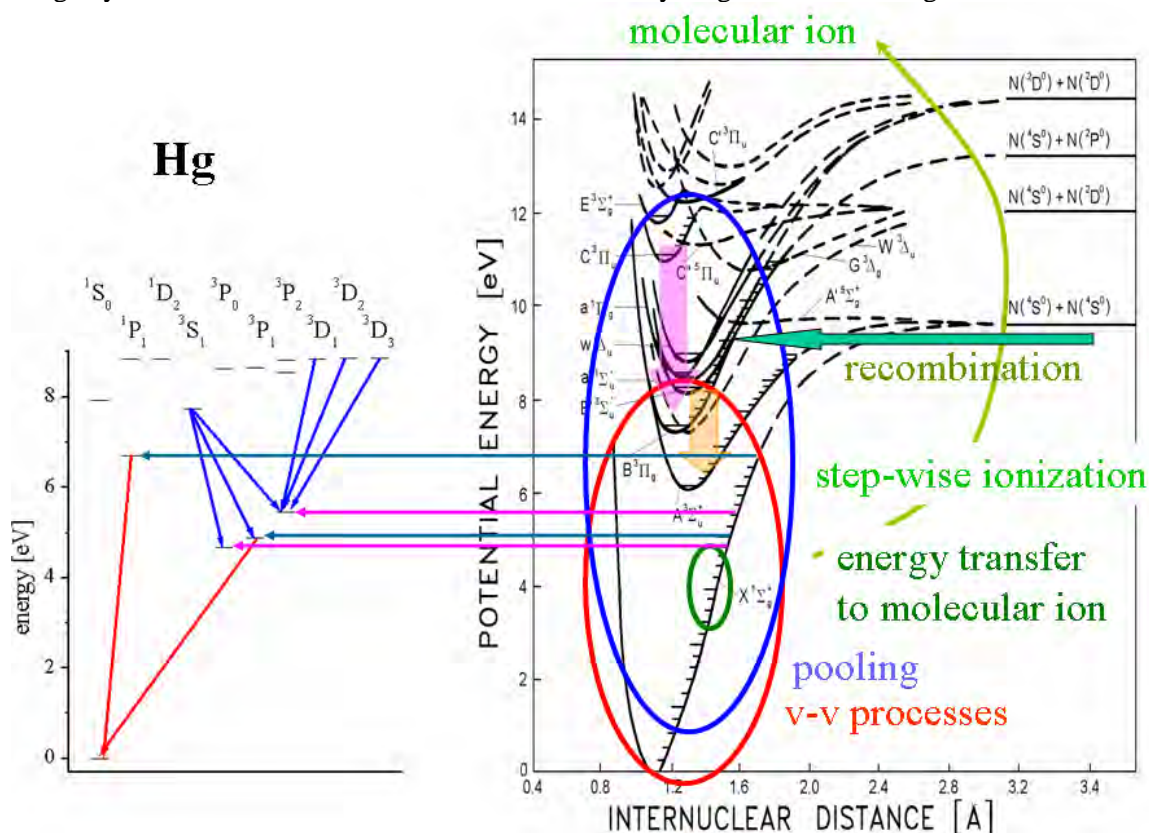


**Fig. 8.** Scheme of kinetic processes among selected mercury and nitrogen states [12] (based on energies given by [14, 15]).

## Conclusions

The influence of mercury traces on the pure nitrogen post-discharge kinetics was experimentally studied in the DC flowing afterglow in Quartz reactor at ambient wall temperatures. Three nitrogen spectral systems (first and second positive and first negative) and the mercury line at 254 nm in the second order spectrum at 508 nm were recorded under these conditions. The upper state of this transition is created by the resonance excitation energy transfer from vibrationally excited nitrogen ground state  $N_2$  ( $X \ ^{14}\Sigma_g^+$ ,  $\nu = 19$ ). The concentration of these nitrogen metastables should be determined based on this reaction. No other mercury spectral lines were observed.

## Acknowledgements

This work was supported by Czech Science Foundation project No. 202/08/1106.

## References

- [1] S. Bockel, T. Belmonte, H. Michel, D. Ablitzer, *Surf. Coat. Technol.*, 97 (1997) 618.
- [2] S. Meikle, H. Nomura, Y. Nakanishi, Y. Hatanaka, *J. Appl. Phys.*, 67 (1990) 483.
- [3] C. D. Pintassilgo, J. Loureiro, V. Guerra, *J. Phys. D: Appl. Phys.*, 38 (2005) 417.
- [4] V. Guerra, P. A. Sa, J. Loureiro, *Eur. Phys. J. – Appl. Phys.*, 28 (2004) 125.
- [5] G. D. Stancu, M. Janda, F. Kaddouri, D. A. Lacoste, C. O. Laux, *J. Phys. Chem. A*, 114 (2010) 201.
- [6] P. F. Ambrico, M. Šimek, G. Dilecce, S. DeBenedictis, *Plasma Chem. and Plasma Proc.*, 28 (2008) 299.
- [7] F. Krčma, V. Mazánková, I. Soral, *Publ. of the Astronom. Observatory of Belgrade*, 82 (2007) 133.
- [8] V. Mazánková, F. Krčma, *Chemické listy*, 102 (2008) 1388.
- [9] J. Hubeňák, F. Krčma, *Journal of Physics D, Applied Physics*, 33 (2000) 3121.
- [10] F. Krčma, A. Hrdlička, V. Kanický, V. Otruba, P. Krásenský, *Europhysics Conference Abstracts 32A, Proceedings of ESCAMPIG XIX*, Granada 2008 pages on CD (P-1-14).
- [11] Z. Stará, F. Krčma, V. Mazánková, V. Kanický, A. Hrdlička, P. Krásenský, *Proceedings of the Seventeenth International Conference on Gas Discharges and their Applications*, Cardiff 2008 421.
- [12] V. Kanický, V. Otruba, A. Hrdlička, P. Krásenský, F. Krčma, *J. Atom. Anal. Spectrometry*, 22 (2007) 754.
- [13] F. Krčma, I. Bocková, V. Mazánková, I. Soral, A. Hrdlička, V. Kanický *Journal of Physics: Conference Series*, (2010) 10 pages.
- [14] A. Lofthus, P. H. Krupenie, *J. Phys. Chem. Ref. Data*, 6 (1977) 113..
- [15] Yu. Ralchenko, A.E. Kramida, J. Reader, and NIST ASD Team (2010). NIST Atomic Spectra Database (ver. 4.0.1), [Online]. Available: <http://physics.nist.gov/asd> [2010, November 29]. National Institute of Standards and Technology, Gaithersburg, MD.

# Discharge fluctuations presentation by entropy maps

O. M. Chumak, M. Hrabovský

Thermal Plasma Department, Institute of Plasma Physics AS CR, v.v.i., Za Slovankou, Prague 18200, Czech Republic

e-mail: chumak@ipp.cas.cz

## Abstract

General statistical procedure for visualization of discharge fluctuations is presented in the paper. It implies mapping of chosen statistical parameter characterizing local brightness variation. It is shown that Shannon entropy that is adopted from the information theory is the most relevant parameter to describe uncertainty degree. Special processing was applied to suppress effect of optical path sensitivity. Resulting maps shows fluctuation space distribution. Their application in investigation of discharge structure is demonstrated on an example of thermal plasma jet.

**Keywords:** discharge stability, plasma fluctuations, statistical processing, entropy maps.

## Introduction

Photographic imaging is often used as primary characterization of discharges and plasmas [1, 2]. Distribution of brightness values gives an idea where more intensive processes are taking place. An analysis of temporal changes of the brightness can be used to identify stable and fluctuating regions in a stationary discharge. For this reason a parameter characterizing brightness variation should be chosen. In order to provide valuable information it should be supported by mathematical and physical background. It would be beneficial if it was secured from noise and experimental set-up imperfections influences.

General statistical procedure for visualization of discharge fluctuation is presented in the paper. It allows using of different statistical parameters. The Shannon entropy that is adopted from the information theory is shown to be the most relevant parameter to use. By an additional procedure it was achieved that resulting maps of brightness fluctuation was not directly dependent on the optical system sensitivity. It gave universal character to the method, which allows simple comparison of structures and regimes of different discharges.

## Experimental set-up

As a visual example was beneficial for all explanations a plasma source and an experimental set-up used for generation of example photographs is described first. A thermal plasma jet was used as the test object. The jet was generated by a plasma torch with water-argon stabilization of arc WSP<sup>®</sup>H 2000 [3]. Its schematic is shown in Fig.1. Plasma is generated from argon added near the cathode and from water surrounding the arc. Resulting argon-hydrogen-oxygen plasma escapes the torch through the nozzle. The anode is situated under the plasma jet outside the arc chamber. A part of the arc leaves the main plasma flow and attaches to the anode surface. The torch is known to generate very stable plasma flow near the nozzle, which, however, rapidly transfers to a mode of intensive turbulent mixing with ambient air. Besides hydrodynamic instabilities the arc-anode attachment is known to be a strong source of plasma disturbances [4].

CCD camera SensiCam Fast Shutter (by PCO AG) was used for plasma jet photographing. It was equipped with common lens Exacta 70-210 mm. A combination of aperture value and a gray filter were used to avoid over-brightness. Exposure time of 3  $\mu$ s was used to get momentary images of the plasma jet. Sequence of at least 200 photographs was used for subsequent digital processing. Matlab program was used to apply digital processing procedures.

## Specification of requirements to processing method

A photographic image of discharges and plasmas can characterize different modes of devices operation. However, comparison of two momentary states of discharge can characterize only the most prominent features. It is obvious that in order to generally characterize any fluctuating object a representative ensemble of its values/images should be treated. It is the task for statistical processing and a digital camera with a computer made possible statistical approach to an image processing.

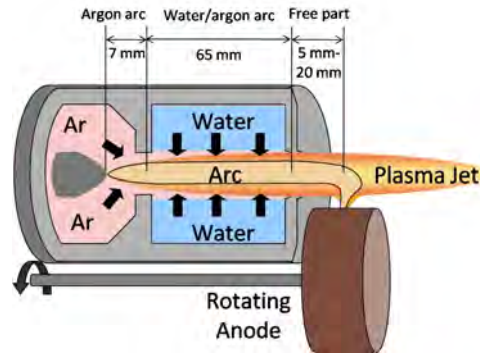


Fig.1. Schematics of thermal plasma torch with argon-water stabilization of arc.

What requirement should be met with a method for brightness fluctuation representation? It is obvious that big number of photographs should be processed to create valid statistical result. Time of taking photographic sequence should be longer than the time of slowest fluctuation expected. In the same time a fluctuations effect can be distinguished only if the exposure time is shorter than the fastest expected fluctuations.

Sensor sensitivity and the optical path power are the most important parameters of the optical system. Resulting photograph brightness depends on these parameters (Fig.2). Setting of absolutely equal parameters is often difficult and it means that brightness fluctuation amplitude will depends not only on discharge fluctuation intensity but on an experimental set-up as well. To be valuable the result should be decoupled from the total brightness value or related to reference value of brightness.

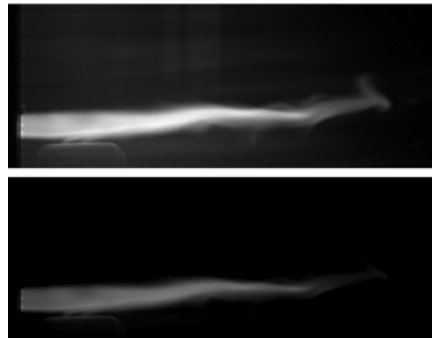


Fig. 2. Photographs of jet with simulation of different sensitivities of optical system.

The brightness of the light could vary in wide range over the discharge area. As example Fig.3 shows the plasma jet with supersonic outflow which features bright region near the nozzle and fast radiation intensity decay. The same fluctuation intensity in different regions will produce different brightness fluctuation amplitudes. Thus different regions should not interfere during the analysis and statistical processing should have local character.

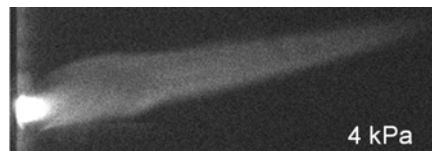


Fig.3. Plasma jet at reduced pressure conditions.

It can be summarized that attention should be paid to have representative set of photographs in number, record duration and exposure time; the processing should have local character and should provide relative value to suppress influence of total brightness in the processed area.

### General principle of statistical processing for brightness fluctuation visualization

Fig.4. demonstrates the basic principle of the statistical processing of the image sequence. Photographs 1-4 represent the first 4 frames of the image sequence. The processing of every point is done independently. For example one point is marked by the red star. An evolution of its brightness over the sequence of the photographs is presented as the green line on the following graph. It can be also represented by a histogram of brightness values frequency. This distribution can be characterized by any statistical parameters as mean, median, standard deviation, skewness, kurtosis etc. In Fig.4. an example of map of mean values and standard deviation values are shown. The mean image shows basic geometrical characteristics of the plasma jet while the standard deviation map showing brightness deviation represents discharge fluctuations region. Standard deviation based parameter was successfully used by in earlier paper [5]. However, the later analysis showed its inaccuracy.

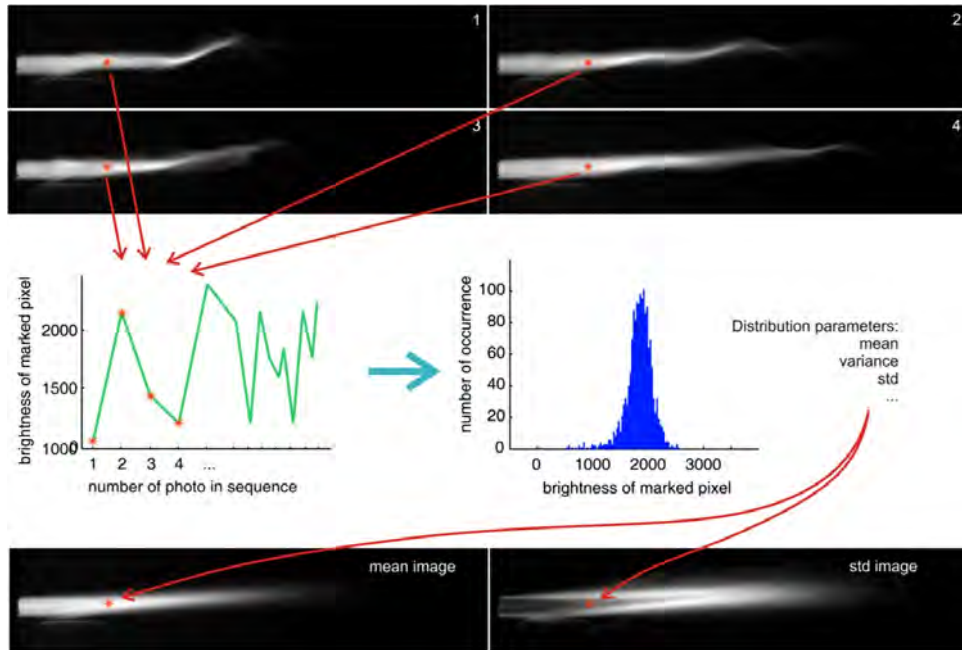


Fig.4. Presentation of principle of statistical processing.

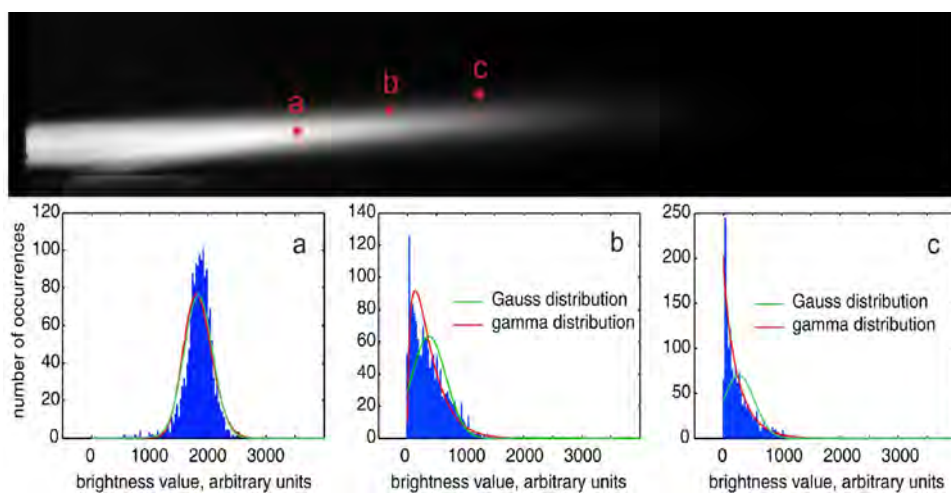


Fig.5. Brightness distribution shapes in different locations of plasma jet.

It is important that the statistical parameter that is in use has clear physical interpretation. Standard deviation can mean width of distribution of brightness values and in such cases would be valid representation of fluctuations. However, direct correlation of standard deviation and distribution width is valid only for the Gauss distribution. Fig.5. demonstrates brightness values distributions in various regions of plasma jet. It can be seen that the Gauss distribution is not often the case. Asymmetrical shapes can be well fitted with the gamma distribution while the Gaussian shape became inapplicable. Other parameters based on central moments of distribution as skewness and kurtosis has less clear and disputable meaning. That was the reason to search more general parameter.

### Using of Shannon entropy as general statistical parameter

In information theory, entropy is a measure of the uncertainty associated with a random variable [6, 7]. In this context, the term usually refers to the Shannon entropy, which quantifies the expected value of the information contained in a message. Entropy of brightness values for particular position in the photograph can be calculated based on the histogram demonstrated in Fig.4 according to the following equation:

$$H(X) = - \sum_{i=1}^n p(x_i) \ln p(x_i), \quad (1)$$

where  $H(X)$  is the entropy of a discrete random variable  $X$  with possible values  $\{x_1, \dots, x_n\}$  and characterized by probabilities  $p(x_i)$ . The number received is the value of information content in nat units. Higher number means higher information content and equal to higher degree of uncertainty.

In our case this value relates to brightness and need to turn into relative units. Comparison to reference distribution could be used. The theoretically maximum uncertainty has uniform distribution. Equal probability for all events complicates the guess and increase uncertainty. Uniform distribution of the same brightness values can be used as the reference. Its entropy can be evaluated as follows:

$$H_u(X) = - \sum_{i=1}^n p_u(x_i) \ln p_u(x_i) = -n p_u \ln p_u = -\ln 1/n = \ln n, \quad (2)$$

where the index  $u$  stands for uniform distribution when probability of all events is equal to  $p_u$ .

In logarithmic scales the ratio operation turns into subtraction. Difference of uniform distribution entropy and actual distribution entropy means difference between the highest possible uncertainty and actual uncertainty:

$$\Delta H(X) = - \sum_{i=1}^n p(x_i) \ln p(x_i) - \ln n, \quad (3)$$

This value will be called here as relative entropy as it is not dependent on the brightness values. A change of brightness that affects entropy value will affect entropy of uniform distribution in the same way and the difference will remain unchanged.

Summarizing the whole processing procedure will have the following line. The sequence of images is loaded to computer memory and then gradual processing of brightness distribution for every point is performed. For particular point the range of brightness values is defined. The whole range is divided to several regions  $n$ . Brightness values are sorted and probability density  $p(x_i)$  of brightness values falling into every region is calculated. The relative entropy is calculated according to equation 3. The map of relative entropy values is created by processing of all points.

### Example of investigation of plasma jet fluctuation in dependence on plasma composition

Plasma jet generated with arc current of 400 A and total power of 120 kW was analyzed using the method. Flow rate of argon, secondary plasma forming gas, had the values of 12.5 slm, 17.5 slm, 22.5 slm. A sequence of 200 phonographs with the exposure time of 3  $\mu$ s was taken for every condition. The brightness values diapason in every point was divided to 30 regions and the described evaluation were preformed. Fig.6 shows maps of relative entropy values. The relative entropy values are shown as gray level in the pictures. Darker regions stand for higher fluctuation intensity and lighter colors means stable regions.

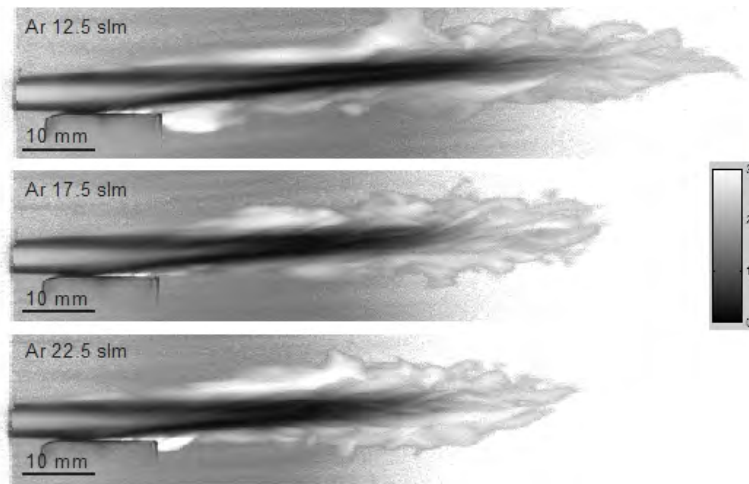


Fig. 6. Maps of relative entropy values in range between 0 (dark) and 3(white)

A common structure of all three jets can be noticed. More intensive fluctuations occur in the jet boundaries and spreading downstream they finally join ending stable jet core. Distinguishable fluctuation region is an area where the arc attaches the anode surface. The jet slightly deflects at this point. Increase of argon flow rate leads to shortening of the plasma jet. It also causes less stable plasma core near the torch nozzle and thicker boundary fluctuation region. Boundary fluctuation regions are joined more rapidly for higher argon flow rate. The pictures demonstrate that argon flow rate significantly changes plasma jet structure and stability, which in this case can be motivation for further research.

### Conclusions

The method of fluctuation intensity visualization is presented as powerful tool in discharge stability analysis. The map of a statistical parameter describing local brightness variation is suggested to be used for visualization of discharge structure. The Shannon entropy concept as brightness distribution characterization brings to the method strong mathematical background and clear result interpretation. Additional processing helps to generate relative values free from absolute brightness influence. It makes the method less dependent on experimental setup parameters and simplifies its interpretation. The maps of relative brightness fluctuation intensity based on entropy concept are showed to be good visual representation of plasma flow structure.

### Acknowledgments

The work was supported by the Grant Agency of the Czech Republic under the project No. P 205/11/2070.

### References

- [1] M.I. Boulos, Visualization and Diagnostics of Thermal Plasma Flows. *Journal of Visualization* 4 (2001) pp.19-28.
- [2] Z. Duan, and J. Heberlein, Arc instabilities in a plasma spray torch, *Journal of Thermal Spray Technology*, 11(1) (2002) pp. 44-51.
- [3] M. Hrabovsky, V Kopecky, V. Sember, T. Kavka, O. Chumak, M. Konrad, Properties of hybrid water/gas DC arc plasma torch, *IEEE Transactions on Plasma Science*, 34(4) (2006) pp. 1566-1575
- [4] O. Chumak, M. Hrabovský, and V. Kopecký, Interaction between anode attachment and plasma jet in DC arc plasma spraying torch, In *International Conference on Physics of Low Temperature Plasma 03, 2003*, p. 6-11.
- [5] O. Chumak, and M. Hrabovský, Diagnostics of plasma jet instabilities using fast shutter imaging, *Czechoslovak Journal of Physics*, 56 (2006) pp. B767-B773
- [6] [http://en.wikipedia.org/wiki/Entropy\\_\(information\\_theory\)](http://en.wikipedia.org/wiki/Entropy_(information_theory))
- [7] R.W.Hamming, *Coding and Information Theory*. Prentice-Hall, New Jersey, 1980, p.259

# Applications of the nanometer-scaled carbon based thin films deposited by TVA technology

R. Vladoiu<sup>1</sup>, V. Ciupina<sup>1</sup>, V. Dinca<sup>1</sup>, M. Contulov<sup>1</sup>, A. Mandes<sup>1</sup>, C.P. Lungu<sup>2</sup>

<sup>1</sup>Department of Plasma Physics, Faculty of Physics, Chemistry, Electronics and Oil Technology, Ovidius University, Mamaia 124, Constanta, 900527, Romania

<sup>2</sup>National Institute of Lasers, Plasma and Radiation Physics, Atomisitorilor 111, P.O. Box MG-36, Magurele-Bucharest, Romania

e-mail: rvladoiu@univ-ovidius.ro

## Abstract

Thin film deposition process by thermionic vacuum arc (TVA), a new discharge type in pure vapor plasma, might become one of the most suitable technologies to significantly improve the tribological properties of the surfaces covered with different materials. TVA can be ignited only in high vacuum (HV) conditions between a heated cathode surrounded by an electron focusing Whemelt cylinder and an anode (crucible) containing the material to be deposited. The electron beam can evaporate the anode materials as much as to create a dense gaseous metal atmosphere between the cathode and anode in which the electrons can build up dense pure plasma which expands out in the surrounding vacuum space toward the substrates. The energy of ions of the TVA plasma can be directly controlled and established at the required value even during arc running by changing the cathode heating current and anode potential.

Due to the deposition in high vacuum conditions and without buffer gas the films have a high purity, increased adhesion, low friction, low roughness, and a compact nanostructure. TVA discharges of various materials such as metals, alloys, ceramics, DLC (Diamond Like Carbon) [1] and refractory metals such as W, Mo, Ta, Nb, Re and B can be generated [2- 4].

In this study, we report the applications of the carbon based materials deposited on different substrates and conditions with the TVA method. C-Me films are suitable for surface coatings applications requiring low roughness, good smoothness and low friction coefficient. CW films are considered in fusion programs to be used to cover the wall of the divertor's also tungsten films are used as thermal barrier coating on the Nb based superalloys for gas turbine blades. Also Beryllium is the candidate material for the First Wall in ITER, oxidation resistant coatings. [5]

**Keywords:** Thermionic Vacuum Arc, carbon based materials

## References

- [1] G. Musa, I. Mustata, V. Ciupina , R. Vladoiu , G. Prodan , E. Vasile, H. Ehrich, Diamond and Related Materials, 2004, p.1398
- [2] H. Ehrich, J. Schuhmann, G. Musa, A. Popescu, I. Mustata, Thin Solid Films, 1998, 95, p. 333
- [3] C. P. Lungu, I. Mustata, G. Musa, A. M. Lungu, V. Zaroschi, K. Iwasaki, R. Tanaka, Y. Matsumura, I. Iwanaga, H. Tanaka, T. Oi and K. Fujita, Surf and Coat. Techn, 200, 2005, p. 399
- [4] H. Ehrich, G. Musa, A. Popescu, I. Mustata, A. Salabas, C. Cretu, G.F, Leu, Thin Solid Films, 1999, 343, p. 63
- [5] A. Anghel, I. Mustata, C. Porosnicu, C. P. Lungu, Journal of Nuclear Materials, 2009, p. 242

# Electron attachment to Radicals relevant to Fluorocarbon Plasmas

S.A. Haughey<sup>1</sup>, T.A. Field<sup>1</sup>, K. Graupner<sup>1,2</sup>, C.A. Mayhew<sup>3</sup>, J. Langer<sup>4</sup>, E. Illenberger<sup>5</sup>

<sup>1</sup>Centre for Plasma Physics, School of Mathematics and Physics, Queen's University Belfast, BT7 1NN, Belfast. N. Ireland, U.K.

<sup>2</sup> Present address: Wolfson School of Mechanical and Manufacturing Engineering, Loughborough University, Loughborough LE11 3TU, UK

<sup>3</sup> School of Physics and Astronomy, University of Birmingham, Birmingham B15 2TT, UK

<sup>4</sup> Institut für Optik und Atomare Physik, Technische Universität Berlin, Hardenbergstrasse 36, 10623 Berlin, Germany

<sup>5</sup> Institut für Chemie und Biochemie-Physikalische und Theoretische Chemie Freie, Universität Berlin, Takustrasse 3, D-14195 Berlin, Germany

e-mail: t.field@qub.ac.uk

## Abstract

Experiments have been undertaken to investigate electron attachment to reactive the fluorocarbon molecules CF<sub>2</sub>, CF<sub>3</sub> and C<sub>2</sub>F<sub>5</sub>. No electron attachment was observed to CF<sub>2</sub> and problems were experienced generating a sample of CF<sub>3</sub> to investigate. Preliminary data for C<sub>2</sub>F<sub>5</sub> will be discussed.

**Keywords:** Dissociative Electron Attachment, Radical, Fluorocarbon Plasma

## Introduction

Fluorocarbon plasmas are used widely in industry, for example, in etching SiO<sub>2</sub> and deposition of hydrophobic layers on fabrics and medical devices. Fluorocarbon plasmas are electronegative plasmas where negatively charged atomic and molecular ions are an important component of the plasma and must be taken into account in modeling the plasma [1].

One of the key mechanisms for negative ion formation is dissociative electron attachment, which can be represented for a general molecule AB by



where AB<sup>\*-</sup> is a super-excited state of the negatively charge molecular ion, or anion, of the molecule AB. The super-excited state may decay back to a neutral molecule and free electron or dissociate to give neutral and negatively charged fragments, A + B<sup>-</sup>. Dissociation is only possible if the lifetime of the super-excited state AB<sup>\*-</sup> is long enough to allow the nuclei to move; in practice this requires electrons to become attached to the molecule in a Shape Resonance or Feshbach Resonance. Dissociation also requires that the energy of the electron plus the electron affinity of B, the negatively charged molecular fragment, is greater than the A-B bond energy. In some cases the super-excited state can have an exceedingly long lifetime, or it can be stabilized by a collision to give the parent negatively charged molecular ion AB<sup>-</sup>.

This presentation will consider electron attachment to reactive molecules such as radicals. Reactive molecules, like CF<sub>2</sub>, CF<sub>3</sub> and C<sub>2</sub>F<sub>5</sub> are difficult to investigate experimentally because of the difficulty in preparing a sample of molecules to investigate. These reactive molecules are, however, vital to the chemistry of fluorocarbon plasmas and interesting to study. One of the principle aims of this research is to observe dissociative attachment to reactive molecules and measure cross sections so that electron attachment to reactive molecules can be included in plasma models.

## Experiment, Results, Discussion, Conclusions

An experiment, ERIC, has been developed to investigate electron attachment to unstable molecules [2]. ERIC includes a microwave plasma discharge in the inlet system as a means of generating reactive molecules *in situ*. Dissociative electron attachment to CF<sub>2</sub> has not been observed although an electron attachment resonance has theoretically predicted at around 1 eV; it appears that the problem is the C-F bond energy is so strong that the minimum electron energy required to cause dissociative electron attachment is 1.8 eV [3]. Attempts have been made to form the radical CF<sub>3</sub>, but without success. For example, small quantities of CF<sub>3</sub> have been made in the reaction CF<sub>3</sub>I + H → CF<sub>3</sub> + HI, but a useable CF<sub>3</sub> sample could not be obtained because it reacts with another H with a faster rate constant by CF<sub>3</sub> +

$\text{H} \rightarrow \text{CF}_2 + \text{HF}$ . Preliminary results for  $\text{C}_2\text{F}_5$  will be delivered in the presentation.

### References

- [1] M.A. Lieberman and A.J. Lichtenberg, *Principles of plasma discharges and materials processing 2<sup>nd</sup> Ed.*, Wiley & Sons, Hoboken, New Jersey, 2005, pp. 340-2
- [2] T.A. Field, A.E. Slattery, D.J. Adams, D.D. Morrison, *J. Phys., B*, 38 (2005) 255
- [3] K. Graupner, T. A. Field and C. A. Mayhew, *New J. Phys.* 12 (2010) 083035

# Low Energy Electron Driven Processes in Halosubstituted Organic Acids: The Case of Trichloroacetic Acid

J. Kopyra<sup>1</sup>, C. König-Lehmann<sup>2</sup>, and E. Illenberger<sup>2</sup>

<sup>1</sup>Chemistry Department, University in Siedlce, 3 Maja 54, 08-110 Siedlce, Poland

<sup>2</sup>Institut für Chemie und Biochemie - Physikalische und Theoretische Chemie, Freie Universität Berlin, Takustrasse 3, D-14195 Berlin, Germany

e-mail: kopyra@uph.edu.pl

## Abstract

Here we present results of low energy electron attachment to halo-containing organic acid namely trichloroacetic acid in the energy range 0-12 eV. DEA to CCl<sub>3</sub>COOH generates as much as seven different anionic fragments, that are formed via a low energy shape resonance which decomposes into the anionic fragments CCl<sub>3</sub>COO<sup>-</sup>, Cl<sup>-</sup>, (M-Cl)<sup>-</sup>, ClHCl<sup>-</sup>, CHCl<sub>2</sub><sup>-</sup>, CCl<sup>-</sup> and C<sub>2</sub>Cl<sub>2</sub><sup>-</sup>. The formation of three of these features (M-H)<sup>-</sup>, Cl<sup>-</sup>, (M-Cl)<sup>-</sup> requires simple bond cleavage while further anionic products arise from a rather complex reactions generating new molecules (CO<sub>2</sub>, HCl).

**Keywords:** halo-substituted organic acid, dissociative electron attachment, mass spectrometry.

## Introduction

In the past electron attachment studies in the gas phase were mainly focused on halogenated compounds such as halocarbons [1,2,3]. The high interest of these investigations is due to many technological applications since they are widely used as gaseous dielectrics or in plasma etching industry [4]. Within the last decade, increasing interest in the study of biologically relevant molecules could be observed. Among them the organic acids are of particular importance. They are considered as the simplest building blocks of biomolecules and can serve as model systems for the properties of larger and more complex systems, e.g., proteins upon exposure to high energy radiation. It is also believed that molecules with carboxylic group could be of great importance in functionalization of semi-conductor material due to its ability to enhance a stickiness of the compounds on the substrate surface.

Here we present results on electron attachment to the halo-substituted organic acid, namely trichloroacetic acid, derived by means of a crossed electron-molecular beam apparatus. We find that this molecule is very ready to attach low energy electrons which results in the formation of low energy resonances. These resonances arise either from simple bond cleavage or from more complicated reaction pathways that go along with multiple bond cleavage and rearrangement in the precursor ion resulting in the formation of new molecules. The most intensive reaction channel is the formation of two complementary ions Cl<sup>-</sup> and (M-Cl)<sup>-</sup> due to the cleavage of the C-Cl bond with the excess charge localized on either of the fragment. Similar situation we have observed in our earlier studies of CClF<sub>2</sub>COOH [5]. In the present contribution we will discuss the influence of the different halogen substituents on electron attachment processes by comparing the results obtained for CCl<sub>3</sub>COOH with the previous results for CClF<sub>2</sub>COOH.

## Experimental

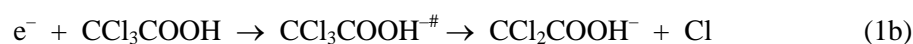
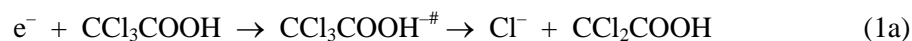
The experiments were performed in a crossed beams apparatus that consists of an oven, a trochoidal electron monochromator and a quadrupole mass spectrometer. In brief an incident electron beam of well-defined energy (energy resolution  $\approx 0.2$  eV, electron current  $\approx 10$  nA) generated from a trochoidal electron monochromator orthogonally intersects with an effusive molecular beam of molecules under investigations. The molecular beam emanates from a capillary that is connected to the collision chamber. Although the trichloroacetic acid is a solid under normal conditions, when introducing into the UHV chamber the pressure of the molecule in the gas phase at an ambient temperature was in the range of  $10^{-6}$  mbar, as measured by an ionisation gauge at one of the flanges. Therefore no heating was required.

Negative ions formed in electron-molecule collisions are extracted from the reaction volume towards a quadrupole mass analyser, and are detected by single pulse counting techniques. The intensity of a certain anion is then recorded as a function of the incident electron energy. The electron energy scale is calibrated by measuring the formation of  $\text{SF}_6^-$  ions, which exhibits a sharp peak located near 0 eV.

## Results and discussion

Dissociative electron attachment DEA to trichloroacetic acid ( $\text{CCl}_3\text{COOH}$ ) in the energy range  $\approx 0$ -12 eV results in the formation of the following anionic fragments:  $\text{CCl}_3\text{COO}^-$ ,  $\text{Cl}^-$ ,  $(\text{M}-\text{Cl})^-$ ,  $\text{ClHCl}^-$ ,  $\text{CHCl}_2^-$ ,  $\text{CCl}^-$  and  $\text{C}_2\text{Cl}_2^-$ . In Fig. 1 the two dominant products  $\text{Cl}^-$  and  $\text{CCl}_3\text{COOH}^-$  ( $(\text{M}-\text{Cl})^-$ ) together with the  $(\text{M}-\text{H})^-$  anion are plotted. All of these anions arise from a single bond cleavages. Apart from that we have observed four further anionic fragments that are formed from much more complicated reactions which require cleavage of several bonds and rearrangement within the transient negative ion TNI (Fig. 2).

The most intensive fragments  $\text{Cl}^-$  and  $(\text{M}-\text{Cl})^-$  (Fig.1, left) are generated by the cleavage of the single C-Cl bond, *viz.*:



with the excess charge localized on either of the fragments. Both of these features are visible via very intensive resonance near zero eV. In general, dissociative electron attachment to chloro-containing molecules results in the formation of the  $\text{Cl}^-$  due to the fact that the C-Cl binding energy is equal or lower than the electron affinity of Cl. Since the intensity of the  $(\text{M}-\text{Cl})^-$  fragment is lower than the  $\text{Cl}^-$  it is likely that the EA of the heavy fragment is lower than that of Cl (3.61 eV).

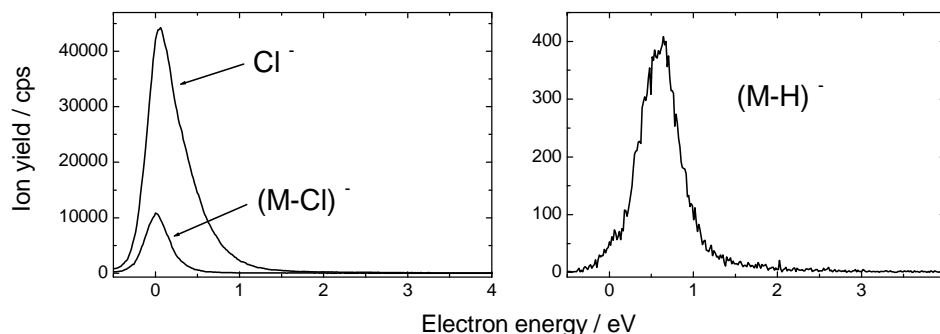
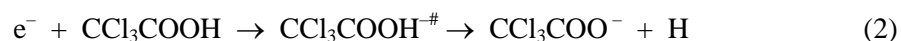


Fig. 1. Yields for the complementary ions  $\text{Cl}^-$  and  $\text{CCl}_2\text{COOH}^-$  ( $(\text{M}-\text{Cl})^-$ ) and for  $(\text{M}-\text{H})^-$  ion from trichloroacetic acid.

While for the simple organic acids (formic, acetic and propanoic acids [6,7]) the common feature is the formation of the dehydrogenated molecular anions as the most intensive resonances and in the energy range 1.25-1.5 eV; for halocontaining organic acids the position of the  $(\text{M}-\text{H})^-$  resonances is appreciable shifted to the lower energy (0.5 eV for  $\text{CF}_3\text{COOH}$  [8] and 0.75 eV for  $\text{CClF}_2\text{COOH}$  [5]). The same is observed for the title molecule and the peak maximum for the  $(\text{M}-\text{H})^-$  structure (Fig. 1, right) appears at 0.6 eV and is assign as a fragment anion formed from the parent molecule by the loss of a neutral H atom from the carboxylic group:



This closed shell anion is the only product generated from  $\text{CCl}_3\text{COOH}$  that appears exclusively above 0 eV. The  $\text{CCl}_3\text{COO}^-$  fragment can be regarded as a shape resonance in which an excess electron is localised in the virtual molecular orbital (MO) without affecting the other electrons. The assignment of

the type of the involved MO, whether this is  $\pi^*(\text{COOH})$  or  $\sigma^*(\text{OH})$  MO, is not straightforward. Upon digging in the literature one can find the different approaches to the assignments of the lowest unfilled orbital that is involved in the formation of the (M-H)<sup>-</sup> ion from the simple organic acids, more specifically from formic acid HCOOH. Aflatooni et al. [9] as well as Rescigno et al. [10] have theoretically predicted that the lowest empty orbital in the HCOOH is of  $\pi^*(\text{COOH})$  character. On the other hand, more recent study on vibrational excitation of the OH stretching mode in HCOOH [11] demonstrate that the low energy resonance is of  $\sigma^*(\text{OH})$  character. This was, in fact, confirmed with the recent application of the R-matrix theory on formic acid and glycine [12]. To the authors knowledge there is so far no theoretical calculations for the halogen derivatives of the acetic acid and an explicit assignments of the character of the involved orbital is not possible.

Apart from these simple processes that require the single bond cleavages we have observed much more complicated reactions that go along with a multiple bond breaks. A very nice example that a slow electrons can trigger a remarkably complex reaction is the formation of bihalide anions. For the case of CCl<sub>3</sub>COOH we observe the formation of symmetric anion ClHCl<sup>-</sup> with a peak maximum already at 0 eV (Fig. 2):



While from the previous molecule CClF<sub>2</sub>COOH the asymmetric complex anion FHCl<sup>-</sup> was generated within a broad resonance peaking at 1 eV. Taking into account the available thermochemical data for CCl<sub>3</sub>COOH [13] this reaction is energetically possible at the energy threshold around 0.2 eV, which is somewhat above the experimentally observed threshold energy.

Although the bihalide anions are known as a very stable species their formation require cleavage of the three bonds which should occur more or less simultaneously. Such reactions have generally high activation energy. However, the presence of an excess charge already at low energy obviously changes the situation. In addition, the energy of the dissociation channel can be lowered due to an extremely high electron affinity of the ClHCl fragment (4.896 eV [13]), which exceed the EA of both halogen and pseudohalogen atoms.

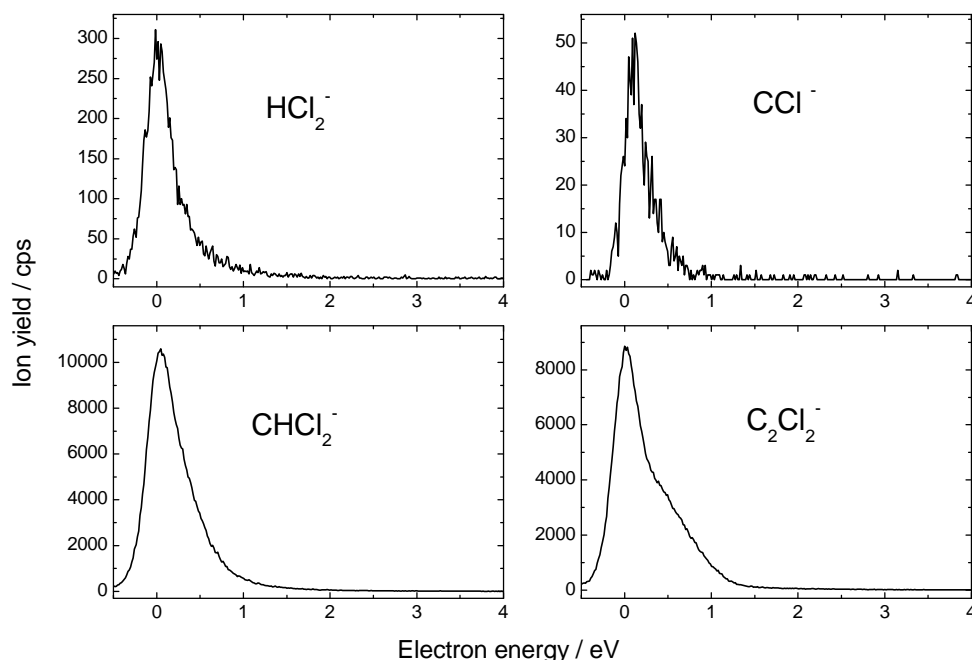


Fig. 2. Ion yields of HCl<sub>2</sub><sup>-</sup>, CHCl<sub>2</sub><sup>-</sup>, CCl<sup>-</sup> and C<sub>2</sub>Cl<sub>2</sub><sup>-</sup> from trichloroacetic acid.

The other anionic product that appears at energy around 0 eV results from the cleavage of the C-C and C-Cl bonds and the hydrogen transfer



Besides the complementary anions ( $\text{Cl}^-$  and  $(\text{M-Cl})^-$ ) this is one of the most abundant anionic fragment. At the same energy but with slightly lower intensity  $\text{C}_2\text{Cl}_2^-$  anion is generated. A closer inspection of the  $\text{C}_2\text{Cl}_2^-$  yield exhibits broader and low intensive but distinct structure at high energy tale. From stoichiometry, the anion could represent an ethylene type radical anion  $\text{Cl}_2\text{C}=\text{C}^-$ . Finally, we have observed the formation of  $\text{CCl}^-$  anion at around 0 eV. This reaction is, however, energetically less favourable since the intensity of the resonance is very small. The neutral counterparts might be  $\text{Cl}_2$  molecule and  $\text{HCOO}$  radical.

## Conclusions

We conclude that trichloroacetic acid is a strong electron scavenger that form several very intensive features at energy range below 1 eV. The subsequent decomposition products arise from simple bond cleavage, but there are also more complicated reaction pathways that go along with multiple bond cleavage and rearrangement in the precursor ion resulting in the formation of new molecules. The most intensive anionic fragments  $\text{Cl}^-$  and  $(\text{M-Cl})^-$  arise from a single bond cleavage and are formed due to the localisation of the excess charge at the  $\sigma^*(\text{C-Cl})$  orbital. We have found that the presence of the halogen substituents cause the substantial shift of the position of the  $(\text{M-H})^-$  towards lower energy in comparison to the non-substituted organic acids.

## Acknowledgment

Work supported by the Polish Ministry of Science and Higher Education, the Deutsche Forschungsgemeinschaft (DFG), the Fonds der Chemischen Industrie and the Freie Universität Berlin. JK gratefully acknowledges support for a visit to Berlin from the European Union via the COST action CM0601 (Electron Controlled Chemical Lithography, ECCL).

## References

- 
- [1] E. Illenberger and J. Momigny, *Gaseous Molecular Ions. An Introduction to Elementary Processes Induced by Ionization*, Steinkopff, Darmstadt, Springer, New York, 1992.
  - [2] J. Kopyra, J. Wnorowska, M. Foryś, I. Szamrej, *Int. J. Mass Spectrom.*, 268 (2007) 60.
  - [3] D. Smith, P. Spanel, *Advances in Atomic, Molecular and Optical Physics*, 32 (1994) 307.
  - [4] L.G. Christophorou, *Electron Molecule Interactions and Their Applications*, ed. L.G. Christophorou, Academic Press, New York, 1984, v.2.
  - [5] J. Kopyra, C. Koenig-Lehmann, I. Szamrej, E. Illenberger, *Int. J. Mass Spectrom.*, 285 (2009) 131.
  - [6] A. Pelc, W. Sailer, P. Scheier, N.J. Mason, E. Illenberger, T.D. Maerk, *Vacuum*, 70 (2003) 429.
  - [7] A. Pelc, W. Sailer, P. Scheier, T.D. Maerk, E. Illenberger, *Chem. Phys. Lett.*, 392 (2004) 465.
  - [8] J. Langer, M. Stano, S. Gohlke, V. Foltin, S. Matejcik E. Illenberger, *Chem. Phys. Lett.*, 419 (2006) 228.
  - [9] K. Aflatooni, B. Hitt, G.A. Gallup, P.D. Burrow, *J. Chem. Phys.*, 115 (2001) 6489.
  - [10] T. Rescigno, C.S. Trevisan, A.E. Orel, *Phys. Rev. Lett.*, 96 (2006) 213201.
  - [11] M. Allan, *J. Phys. B*, 39 (2006) 2939.
  - [12] G.A. Gallup, P.D. Burrow, I.I. Fabricant, *Phys. Rev. A*, 79 (2009) 042701.
  - [13] The NIST Chemistry WebBook: <http://webbook.nist.gov>.

# Higher yield ozone generation using nano-seconds pulsed discharge

T. Namihira<sup>1</sup>, D. Wang<sup>2</sup>, T. Matsumoto<sup>3</sup>, H. Akiyama<sup>3</sup>

<sup>1</sup>Bioelectrics Research Center, Kumamoto University, 2-39-1 Kurokami, Kumamoto 860-8555, JAPAN.

<sup>2</sup>Priority Organization for Innovation and Excellence, Kumamoto University.

<sup>3</sup>Grasuate School of Science and Technology, Kumamoto University.

e-mail: namhira@cs.kumamoto-u.ac.jp

## Abstract

Energy efficient generation of ozone is very important because ozone is being used increasingly in a wide range of industrial applications. In this study, ultra-short duration pulsed streamer discharges with a duration of 5 ns have been used to produce ozone in a wire-to-cylinder electrode reactor. The triaxial Blumlein configuration is used for the nano-seconds pulsed generator. Ozone concentration and ozone production yield were measured at various applied voltages (50 to 70 kV), and pulse repetitions (10 to 60 pps) at atmospheric pressure in oxygen and air. The experimental results showed that the ozone concentration ( $\text{g/m}^3$ ) increased with increasing applied pulse voltage and pulse repetition rate. Higher ozone concentrations were obtained in the oxygen-fed ozonizer than in the air-fed ozonizer. The ozone production yield ( $\text{g/kWh}$ ) was high at low ozone concentration, and higher ozone yield was obtained with lower applied voltages. Characterization maps of ozonizers based on different discharge methods (nano-seconds pulsed discharge, DBD, DBD with narrow-gap, surface discharge, pulsed corona discharge, DC corona, superimposed discharge methods and a commercial ozonizer) were presented with oxygen-fed and air-fed cases. A nano-seconds pulsed discharge showed the highest ozone yield in the characterization maps for both the oxygen-fed and air-fed cases, where the highest ozone yield were 544 and 239  $\text{g/kWh}$  in the oxygen-fed and air-fed cases, respectively.

**Keywords:** nano-seconds, pulsed discharge, pulsed plasma, ozone, yield.

## Introduction

Ozone is known as a powerful oxidizing agent, far better than fluorine, which exists in nature. It is also a gas that does not generate byproducts since ozone decays to ordinary diatomic oxygen. Wide interests are focused on ozone generation studies for practical applications such as treatment of drinking and waste water, air purification, decoloration, bactericide and sterilization of food products etc [1, 2]. Recently, the medical usage of ozone has been widely studied in Europe, mainly in the fields of internal medicine, pediatrics, obstetrics and gynecology, and otorhinology [3]. Therefore, much attention has been paid for developing an energy-efficient ozonizer. However, ozone is an unstable agent which decays into oxygen at high concentrations, so that on-site production of ozone is desired. Several methods are available for ozone production: UV, electrolysis, and discharge method [4]. The leading method is the dielectric barrier discharge (DBD) which has been studied extensively using both ac and dc applied voltages [2, 5]. Several studies of ozone production using corona discharges incorporating dielectric barriers have been reported [6-8]. However, the relatively long time duration of the applied voltage of a DBD leads to energy loss since not only electrons but also ions are accelerated, which generate heating losses during ozone production. Moreover, cooling systems are required for the dielectric materials resulting in further energy loss. Therefore, pulsed discharges, as distinguished without dielectric materials and only accelerated electrons, have been studied for ozone production in recent years [9-11]. A short pulsed streamer discharge has been shown to be effective in producing intense streamer discharges without inducing arc breakdown between the electrodes [12, 13]. In pulsed discharges, it is known that the discharge propagation consists of a streamer discharge phase followed by a glow-like discharge phase [14]. The plasma impedance shows a significant difference between these two discharge phases, typically by a factor of ten. This dramatic change of the plasma impedance makes it difficult to impedance match between the power generator and electrode reactor. Moreover, a temperature rise of the gas occurs during the glow-like discharge phase which causes further energy loss [15]. These losses limit the energy efficiency of ozone generation. Consequently, an ideal configuration of a pulsed discharge is desired for developing an energy efficient ozonizer.

For ozone generation, the streamer discharge energized by a fast rising pulse voltage can produce an intense non-thermal plasma. This creates atomic oxygen by electron dissociation [16]



and



Ozone is formed via



where M is a third collision particle which could be O<sub>2</sub>, O<sub>3</sub> and N<sub>2</sub> in the feeding gas [16]: oxygen or air as used in the present study.

In this paper, a nano-seconds pulsed generator (NS-PG) with a pulse duration of 5 ns was employed for ozone generation. The concentration and production yield of ozone using NS-PG in either the oxygen-fed or dry air-fed cases are discussed.

## Experimental apparatus and methods

### 2.1 Configuration of the Nano-Seconds Pulsed Power Generator

Fig. 1 shows a schematic diagram (a) and photograph (b) of the Nano-Seconds Pulsed Power Generator (NS-PG). The NS-PG consists of a coaxial high-pressure spark gap switch (SGS) as a low inductance self-closing switch, a triaxial Blumlein as a pulse-forming line, and a voltage transmission line which transmits energy from the triaxial Blumlein to load. The SGS was filled with SF<sub>6</sub> gas, and the output voltage from the generator is regulated by varying the pressure of the SF<sub>6</sub>. The gap distance of the SGS was fixed at 1 mm. The triaxial Blumlein consisted of an inner rod conductor, a middle cylinder conductor, and an outer cylinder conductor. The inner, middle, and outer conductors of the triaxial Blumlein were placed coaxially. The triaxial Blumlein and the transmission line were filled with silicon oil (Shin-Etsu Chemical Co., Ltd., Japan) as the insulation and dielectric medium. For operation of the NS-PG, the middle conductor of the triaxial Blumlein line was charged through a charging port that is connected to the pulsed charging circuit shown in Fig. 2. The pulsed charging circuit consisted of a dc source, a charging resistor of 0.67 MΩ, a capacitor of 20 nF, a thyatron switch (Deuterium Thyatron CX1722/2, e2V technologies, UK), and a pulse transformer (PT). The PT had a primary to secondary windings ratio of 1:10. The outer conductor of the triaxial Blumlein was grounded. A capacitive voltage divider (1:17500) and a current transformer (Bergoz current transformer, Model CT-F1.0, Bergoz instrumentation, France) were employed in the charging circuit to measure the charging voltage and current to the NS-PG. A capacitive voltage divider (1:2248) was mounted on the transmission line between the triaxial Blumlein and load to measure the output voltage of the NS-PG. The discharge current through the load was measured using a current transformer (Bergoz current transformer, Model CT-F2.5, Bergoz instrumentation, France) which was located after the transmission line (Fig. 2). The calculated unit inductance and capacitance of the triaxial Blumlein were 140 nH/m and 216 pF/m, respectively, with a characteristic impedance of 50 Ω. The length of the triaxial Blumlein and the transmission line were 500 mm and 200 mm, respectively. The calculated pulse duration (FWHM) of the triaxial Blumlein was approximately 5 ns. It should be mentioned that the capacitive voltage divider was handmade and calibrated using a matched register and a current transformer (Bergoz current transformer, Model CT-F2.5, Bergoz instrumentation, France). The calibration results showed good magnitude and frequency responses.

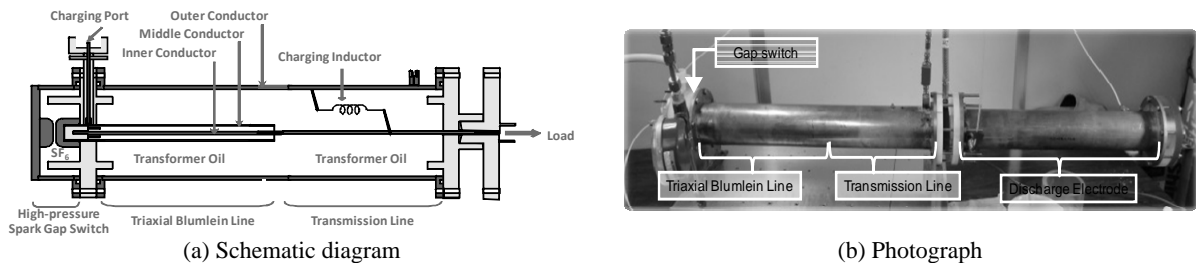


Fig. 1. Schematic diagram and photograph of the nano-seconds pulsed generator.

### 2.2 Ozone Generation

Fig. 2 shows the experimental set-up for ozone generation. A concentric coaxial cylindrical reactor

was employed as the discharge vessel. The central rod was made of stainless steel, 0.5 mm in diameter placed coaxially in a copper cylinder having a 76 mm internal diameter and a length of 500 mm. A gas cylinder of either dry air (79% N<sub>2</sub> + 21% O<sub>2</sub>) or oxygen was used as the feeding gas to the reactor. The purity of oxygen was 99.50%. The gas flow rate was controlled by a mass flow controller (SEC-E440J, STEC Inc., Japan) at 1.0 L/min at standard atmospheric pressure and temperature of 273° K. Positive voltage polarity was chosen for the discharge in the reactor. The output voltage of the NS-PG was controlled at 50, 60 or 70 kV by adjusting the gas pressure of the SF<sub>6</sub> in SGS. A pulse repetition rate of 1-60 pps (pulses per second) was used. A digital oscilloscope (Tektronix DPO7254-R3, Tektronix Japan, Ltd.) with a maximum bandwidth of 6 GHz and a maximum sample rate of 20 G samples/sec recorded the signals from the voltage dividers and the current transformers. The concentration of generated ozone was measured using an UV-Vis spectrophotometer (V560, JASCO Corporation, Japan) after reaching steady state at each pulse repetition rate. The measured absorbance at 253 nm using the UV-Vis spectrophotometer was calculated for the ozone concentration by the Beer-Lambert law. The UV-Vis spectrophotometer was calibrated by the manufacturer.

The energy input to discharge per pulse, in J/pulse, was determined from the recorded signals of the applied voltage (V in V), discharge current (I in A), and time (t in s). The production yield of ozone,  $\eta$  in g/kWh, was determined from

$$\eta = \frac{c \cdot r \cdot 60}{f \cdot E} \quad (4)$$

where  $c$  is the concentration of ozone (in g/Nm<sup>3</sup>),  $r$  is the gas flow rate in the discharge reactor (in L/min),  $f$  is the pulse repetition rate (in pps, pulses/second) and  $E$  is the input energy to the reactor per pulse (J/pulse). It should be noted that 0.048 kg of ozone is equivalent to 1 mol and 22.4 L at 1.01×10<sup>5</sup> Pa and 273° K. Equation (4) can also give the yield in mol/kWh by dividing  $\eta$ (g/kWh) by 48. The concentration of ozone can be given in ppm by multiplying  $c$  (g/Nm<sup>3</sup>) by 467.

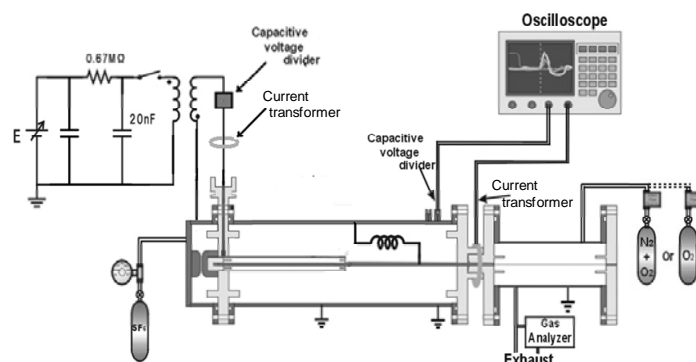


Fig. 2. Schematic diagram of the experimental setup.

## Results and discussion

### 3.1 Ozone Generation by Nano-Seconds Pulsed Discharge

Fig. 3 and Fig. 4 show typical waveforms of the applied voltage (a) and discharge current (b) to the reactor for oxygen-fed and air-fed ozone generation, respectively. From Fig. 3(a) and Fig. 4(a), the peak of the applied voltages are successfully controlled at 50, 60 or 70 kV by adjusting the SF<sub>6</sub> gas pressure in SGS of the generator. The pulse duration, which is determined by the full width at half maximum (FWHM), is approximately 5 ns. It is in good agreement with theoretical calculations. The negative voltage swing following the positive peak was due to oscillations between the inductance of the NS-PG and the capacitance of the reactor. From Fig. 3(b) and Fig. 4(b), the discharge current is increased with increasing applied voltages, typically 258 A and 384 A in the case of 50 kV and 70 kV of the peak applied voltage, respectively, in air-fed ozone generation. The discharge currents in oxygen-fed (Fig. 3(b)) and air-fed (Fig. 4(b)) conditions are almost the same. The current waveforms of Figs. 3(b) and 4(b) include both the displacement current to and conduction current through the reactor. From previous studies, the displacement current is small enough to be neglected [17]. The input energy to the discharge per pulse showed very little difference between feeding gases, and it is typically 150 mJ/pulse for oxygen-fed and 153 mJ/pulse for air-fed gas at 70 kV of the peak applied

voltage.

Fig. 5 shows the dependence of the ozone concentration on pulse repetition rate for different applied pulse voltages for both the oxygen-fed and air-fed cases. For both cases, the ozone concentration increased in proportion to the increase in pulse repetition rate at a fixed applied voltage, and increase in applied voltage at a fixed pulse repetition rate. This is because the input energy increases with increasing pulse repetition rate and applied voltage. The higher concentration of ozone was obtained in the oxygen-fed case due to the higher production of atomic oxygen, which plays an important role in the production of ozone [18, 19]. Typically, the highest ozone concentrations for the oxygen-fed and the air-fed cases were 36.6 and 15.8 g/m<sup>3</sup> at 70 kV for the peak applied voltage and 60 pps for the pulse repetition rate, respectively. In the case of air-fed, the increase in the ozone concentration with increasing pulse repetition rate is less than linear compared to the oxygen-fed case, and seems to saturate at the higher pulse repetition rate (>60 pps). It should be noted that the ozone generation experiments stopped at 60 pps due to the mechanical limitation of the NS-PG. Experiments at over 60 pps of pulse repetition rate are expected in future work.

Fig. 6 shows the dependence of the ozone yield on pulse repetition rate for different applied pulse voltages. It is observed from Fig. 6 that the production yield of ozone gradually decreased with increasing pulse repetition rate for all applied voltages. This means that the ozone production at higher pulse repetition rates, which means the higher ozone concentration, leads to a reduction of ozone production yield. This is possibly due to the dissociative attachment of electrons in ozone increased with increasing concentration of ozone [20-22]. At a fixed pulse repetition rate, a lower applied voltage gave a higher ozone yield. This is because the lower applied voltage leads to a lower input energy in equation (4). Fig. 7 shows the dependence of the ozone yield on ozone concentration for different applied pulse voltages. It is observed from Fig. 7 that the production yield of ozone decreased at higher ozone concentrations for all applied voltages. This is because the increase in the concentration with increasing pulse repetition rate becomes less than linear at higher pulse repetition rates, (Fig. 5). Therefore, the input energy also increases at higher repetition rates than the concentration of ozone, leading to a reduced yield at higher pulse repetition rates and, therefore, at higher concentrations (Fig. 7). From Fig. 6 and Fig. 7, the highest ozone yield for the oxygen-fed case was 544 g/kWh at 20 pps, 50 kV and 10.9 g/m<sup>3</sup>. The highest ozone yield for the air-fed case was 239 g/kWh at 30 pps, 50 kV and 7.3 g/m<sup>3</sup> for the presented study.

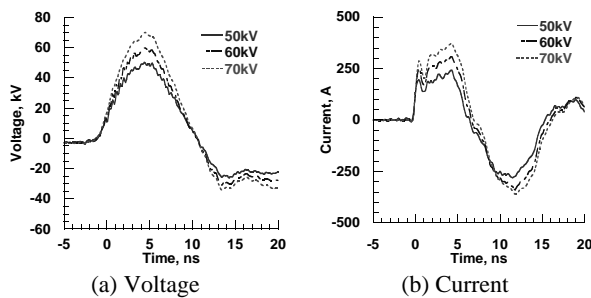


Fig. 3. Typical waveforms of the applied voltage (a) and discharge current (b) to the reactor for oxygen-fed ozone generation.

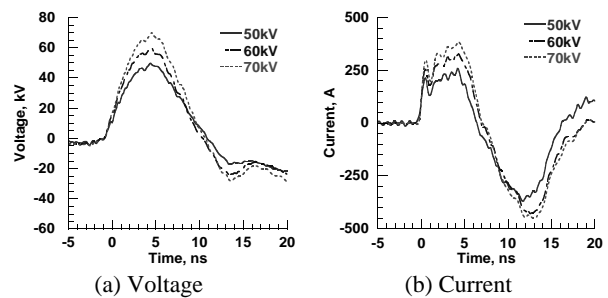


Fig. 4. Typical waveforms of the applied voltage (a) and discharge current (b) to the reactor for air-fed ozone generation.

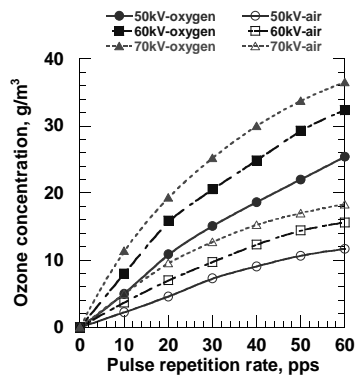


Fig. 5. Dependence of the ozone concentration on the pulse repetition rate for different applied pulse voltages.

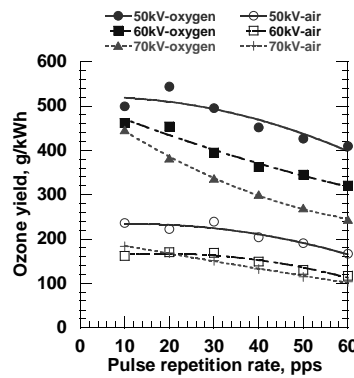


Fig. 6. Dependence of the ozone yield on the pulse repetition rate for different applied pulse voltages.

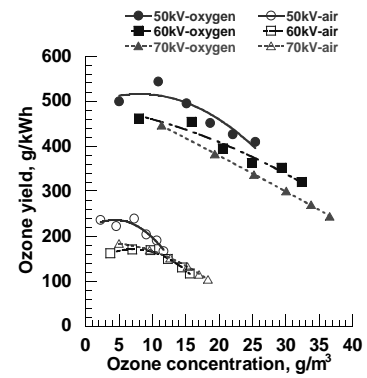


Fig. 7. Dependence of the ozone yield on the ozone concentration for different applied pulse voltages.

## Conclusions

Short duration, 5ns, high power pulses have been used for ozone generation either in an oxygen-fed or air-fed gas. The following conclusions have been deduced:

- 1) Using a wire-to-cylinder reactor, the ozone concentration at 70 kV peak applied voltage and 60 pps pulse repetition ratio was  $36.6 \text{ g/m}^3$  for the oxygen-fed case, and  $15.8 \text{ g/m}^3$  for the air-fed case, respectively.
- 2) For both the oxygen-fed and air-fed cases, the production yield of ozone was higher at low concentration of ozone generation. Higher ozone yield was obtained at lower applied voltages.
- 3) The highest ozone yield in the oxygen-fed case was  $544 \text{ g/kWh}$  at 20 pps, 50 kV and  $10.9 \text{ g/m}^3$ . The highest ozone yield in the air-fed case was  $239 \text{ g/kWh}$  at 30 pps, 50 kV and  $7.3 \text{ g/m}^3$ .

## References

- [1] U. Kogelschatz, B. Eliasson and M. Hirth, "Ozone generation from oxygen and air: Discharge physics and reaction mechanisms", *Ozone: Science & Engineering*, vol. 9, pp. 367-377, 1987.
- [2] B. Eliasson, M. Hirth and U. Kogelschatz, "Ozone synthesis from oxygen in dielectric barrier discharges", *J. Phys. D, Appl. Phys.*, vol. 20, pp. 1421-1437, 1987.
- [3] Renate Viebahn-Haensler, *The Use of Ozone in Medicine, Medicina Biologica*, 4th edition, 2002.
- [4] H. Sugimoto, *Basis and applications of ozone, Korin, in Japanese*, 1996.
- [5] D. Braun, U. Kuchker and G. Pietsch, "Aspects of ozone generation from air", *Ozone: Science & Engineering*, vol. 12, pp.255-268, 1990.
- [6] S. Yagi and M. Tanaka, "Mechanism of ozone generation in air-fed ozonizers", *J. Phys. D, Appl. Phys.*, vol. 12, pp. 1509-1520, 1979.
- [7] S. Masuda, K. Akutsu, M. Kuroda, Y. Awatsu and Y. Shibuya, "A ceramic-based ozonizer using high-frequency discharge", *IEEE Transactions on Industrial Applications*, vol. 24, pp. 223-231, 1988.
- [8] T. Watanabe, Y. Aso and C. Nakayama, "Ozone generation of bipolar-type ceramic ozonizer module with semiconductor ceramic discharge electrode", *Japan J. Appl. Phys.*, vol. 32, pp. 1229-1235, 1993.
- [9] F. Hegeler and H. Akiyama, "Ozone generated by positive and negative wire-to-plate streamer discharges", *Japan J. Appl. Phys.*, vol. 36, pp. 5335-5339, 1997.
- [10] F. Hegeler and H. Akiyama, "Spatial and Temporal distributions of ozone after a wire-to-plate streamer discharge", *IEEE Trans. On Plasma Sci.*, vol. 25, pp. 1085-1090, 1997.
- [11] T. Go, Y. Tanaka, N. Yamazaki, S. Mukaigawa, K. Takaki, T. Fujiwara, "Dependence of initial oxygen concentration on ozone yield using inductive energy storage system pulsed power generator", *IEEJ Transactions on Fundamentals and Materials*, vol. 129, no. 7, pp. 477-482, 2009.
- [12] B. M. penetrante and S. E. Schultheis, "Non-thermal plasma techniques for pollution control", *NATO ASI Series, Ecological Science*, vol. 34, Part A and B, 1993.
- [13] A. Mizuno and Y. Kamase, "Emission of current in pulsed streamer corona discharge", *Conf. Record of IEEE Indust. Appl. Soc. Annual Meeting (Cat. No. 87 CH2499-2)*, vol. 02, pp. 1534-1538, 1987.
- [14] D. Wang, M. Jikuya, S. Yoshida, T. Namihira, S. Katsuki and H. Akiyama, "Positive- and negative-pulsed streamer discharges generated by a 100-ns pulsed power in atmospheric air", *IEEE Transactions on Plasma Science*, vol. 35, no. 4, pp. 1098-1103, 2007.
- [15] D. Wang, T. Namihira and H. Akiyama, "Pulsed discharge plasma generated by nano-seconds pulsed power

- in atmospheric air”, Proceedings of 17th IEEE International Pulsed Power Conference, Washington, DC, USA, in print, 2009.
- [16] U. Kogelschatz, Advanced ozone generation, in process technologies for water treatment, S. Stucki, Ed. New York & London: Plenum, pp.87-120, 1988.
  - [17] D. Wang, T. Namihira, S. Katsuki and H. Akiyama, “Dependence of NOX removal by pulsed streamer discharge on the input energy density to nitric oxide ratio”, Journal of Advanced Oxidation Technologies, vol. 8, no. 2, pp. 248-254, 2005.
  - [18] U. Kogelschatz, “Silent discharges and their applications”, Proc. 10th Int. Conf. on Gas Discharge & their applications, Swansea, pp. 972-980, 1992.
  - [19] W. J. M. Samaranayake, Y. Miyahara, T. Namihira, S. Katsuki, R. Hackam and H. Akiyama, “Pulsed power production of ozone in O<sub>2</sub>/N<sub>2</sub> in a coaxial reactor without dielectric layer”, IEEE Transactions on Dielectrics and Electrical Insulation, vol. 8, no. 5, pp. 826-831, 2001.
  - [20] P. Tegeder, P.A. Kendall, M. Penno, N.J. Mason and E. Illenberger, “Electron stimulated desorption of O- and O<sub>2</sub>- from condensed ozone: Possible implications for the heterogeneous photochemistry of stratospheric O<sub>3</sub>”, Physical Chemistry chemical Physics, vol. 3, pp. 2625-2629, 2001.
  - [21] I.C. Walker, J.M. Gingell, N.J. Mason and G.. Marston, “Dissociative electron attachment (DEA) in ozone 0-10eV”, Journal of Physics B: Atomic, Molecular and Optical Physics, vol. 29, pp. 4749-4759, 1996.

# Plasma Treatment of Drinking Water

Mirosław Dors

Centre for Plasma and Laser Engineering, The Szewalski Institute of Fluid-Flow Machinery,  
Polish Academy of Sciences, Fiszerza 14, 80-952 Gdańsk, Poland

e-mail: mdors@imp.gda.pl

## Abstract

This work was aimed at the investigation of inactivation of all kinds of microorganisms, total *coli* and *E. coli* in river water using corona and spark discharges in water, corona discharge in gas, ozonation and Fenton reaction. Our experiments demonstrated that ozonation and Fenton reaction are the most efficient method of water disinfection comparing to pulsed spark and pulsed corona discharges. The pulsed spark discharge in water is capable of killing all microorganism similarly to ozonation, however, with much lower energetic efficiency. The pulsed corona discharge turned out to be the less effective method of water disinfection.

**Keywords:** electrohydraulic discharges, water disinfection, ozonation

## Introduction

The most frequent reason of epidemic formation is the pollution of the surface and drinking water by wastewater bacteria. The largest part of this pathogenic microorganisms are fecal bacteria, for example *Escherichia coli* (*E. coli*). The wastewater treatment plants reduce the amount of the fecal bacteria by 1-3 orders of magnitude, depending on the initial number of bacteria, which can be  $10^4$ - $10^6$  cfu/ml [1]. To enhance efficiency of bacteria inactivation in the wastewater various methods are tested, like electrochemical [2] and photocatalytic [3] disinfections, chlorination, ozonation [4], Fenton reaction [5-7], UV irradiation [8,9] and electrohydraulic discharges, i.e. electrical discharges in water, such as pulsed arc between needle electrodes [10]-[12], pulsed corona between wire and plate [13], pulsed corona with addition of gas as bubbles [14] and without added gas [15], [16].

In recent years, there is an increasing interest in the study of pulsed electrical discharges in water, recently called electrohydraulic discharges, oriented on the application for disinfection and purification in the drinking water treatment industry. A large number of papers and conference contributions were published during the last few years. Electrohydraulic discharges in water have been shown to be able to induce various reactions including the degradation of organic compounds [17, 18-26] and the destruction of bacteria and viruses [12-16, 33, 34]. The reactions are usually thought to be initiated by various reactive radicals, UV radiation, shockwaves, high electric field, or/and intense heat produced by pulsed electrohydraulic discharge. The concentration of the reactive species and the intensity of the physical effects largely depend on the discharge type and solution properties. Organic compounds are oxidized, first to other organic intermediates and finally, at the energy high enough, to gaseous products, such as carbon dioxide and water. As for the disinfection effect, it is generally assumed that a mechanism of microorganism killing by the electrohydraulic discharges involves an electric field, shock wave, UV radiation and radical reactions. The destruction of microorganism depends on the microorganism cell structure. It is different for each bacteria species and depends also on the mode of electrohydraulic discharge [17], [27]. In the case of the corona discharge, *E. coli* bacteria cells are destroyed mainly due to reactions with oxidizing radicals OH and H<sub>2</sub>O<sub>2</sub> with compounds forming the bacteria cell wall [13], [15], whereas in the spark and arc discharges they are mainly damaged by shock waves and UV radiation [11], [12]. Unfortunately, detailed mechanisms of microorganisms inactivation is still not clarified. In the case of bacteria, including *E. coli*, strong oxidants cause destruction of bacterial membrane through alteration of glycoproteins or glycolipids [28] and certain amino acids such as tryptophan [29]. There is also disruption of enzymatic activity of bacteria by acting on the sulfhydryl groups of certain enzymes [31] as well as affection of both purines and pyrimidines in nucleic acids resulting in inhibited replication of the DNA [28]. The last kind of changes in the DNA is also caused by UV in the range 240-280 nm emitted by electrohydraulic discharges. However, it must be noted that under certain conditions, some organisms are capable of repairing damaged DNA and reverting back to an active state in which reproduction is again possible [30]. Typically, photoreactivation occurs as a consequence of the catalyzing effects of sunlight at

visible wavelengths outside of the effective disinfecting range. The extent of reactivation varies among organisms. *Coli* bacteria and some bacterial pathogens such as *Shigella* have exhibited the photoreactivation mechanism; however, viruses (except when they have infected a host cell that is itself photoreactive) and other types of bacteria cannot photoreactivate [32]. In the case of viruses, strong oxidants cause modification in the viral capsid sites that the virion uses to fix on the cell surfaces. High concentrations of ozone dissociate the capsid completely [30].

There are also several review papers describing physics, chemistry and applications of electrical discharges used for water treatment. Most comprehensive review on the application of strong electric fields in water and organic liquids with 410 references was published in 2006 by Locke et al. [11]. They explained in detail the types of discharges used for water treatment, physics of the discharge, and chemical reactions involved in the discharge in water.

More recently, Bruggeman and Leys [35] published another review paper on non-thermal plasma in contact with water. They discussed three different types of plasmas: direct liquid discharges, discharges in gas phase with a liquid electrode, and discharges in bubbles in liquids. A different excitation method for each type was discussed individually. In addition, plasma characteristics of the different types of plasma in liquids were discussed. Currently several research groups around the world actively study plasma discharges for water treatment, which will be briefly discussed next.

The last review paper was published in 2010 by Y. Yang, A. Fridman and Y.I. Cho [36], and presents electrohydraulic discharges with their dynamics, analysis of microsecond streamer propagation in water and applications for CaCO<sub>3</sub> precipitation and water sterilization.

In most investigations concerning the physics, chemistry and application of the electrohydraulic discharges for water purification, the de-ionized water with additives regulating conductivity was used. There is little amount studies on the influence of electrohydraulic discharges on the chemical pollutants and microorganism present in drinking water as well as in surface water, i.e. rivers and lakes [31-33]. There are a few pilot systems using pulsed arc discharge in water for drinking and waste water cleaning, however, results obtained are not published yet.

In this work we present the influence of selected electrohydraulic discharges, i.e. corona and spark discharges in water, as well as conventional ozonation of water on inactivation of all kinds of microorganisms, total *coli* and *E. coli*. Water samples were taken from two regional rivers: Reda and Strzyża, close to their estuaries. At that places they are both of type IV sanitary class, so they have a total coli number of over 3000 colony forming units (cfu) in 100 ml. Due to this fact, they cannot be used to supplying region inhabitants with drinking water. This would be possible only after complete removal of *coli* bacteria, e.g. by plasma processing.

## Experimental set-up

The processing of the river water samples was conducted in a glass tube reactor (inner diameter of 22.5 mm) equipped with water pumping and cooling systems (Fig. 1). Every sample had a volume of 400 ml.

Water samples were being pumped once through the reactor tube at different flow rates and discharge voltages. A pulsed positive discharge was generated between a high voltage stainless steel hollow needle electrode and a grounded brass rod electrode (10 mm in diameter), both immersed in the water. The inner and outer diameter of the hollow needle were 1.4 mm and 1.6 mm, respectively. The discharge was generated at the edge of the hollow needle, whereas the rest of the needle was covered with an insulator. Corona discharge was generated when the needle-rod spacing was 45 mm, whereas the spark discharge was formed in the spacing of 9 mm.

Part of the river water samples underwent ozonation process in a washing bottle. The O<sub>3</sub> concentration in the inlet gas was 20 g/m<sup>3</sup>. The ozone was created in DBD reactor from pure oxygen, at a flow rate of 1 l/min. The ozonator was operating at 15 W.

The processed water was taken from the Strzyża river in February 2010. The water initial characteristics was as follows: temperature 18°C, pH=7.4, conductivity 376 μS, total number of *coli* bacteria 11750 cfu/ml, number of *E. coli* 280 cfu/ml, total number of microorganisms at 36°C and 22°C were 30500 and 74500 cfu/ml, respectively.

Positive high voltage pulses were applied to the hollow needle electrode from a discharge capacitor C<sub>1</sub> (2 nF) – Fig. 1. The capacitor was charged from a DC power supply through a resistor R (10 kΩ) and a capacitor C<sub>2</sub> (22 nF). The pulse repetition rate of 50 Hz was fixed by the rotation velocity of a

rotating spark gap switch. The amplitudes of the voltage and current corona pulses were measured using a TEKTRONIX P6015A high voltage probe and a PEARSON 2878 current monitor (Rogowski coil), respectively. The waveforms were observed and recorded on a TEKTRONIX TDS 3052B oscilloscope after being averaged over up to 256 acquisitions to eliminate a random noise.

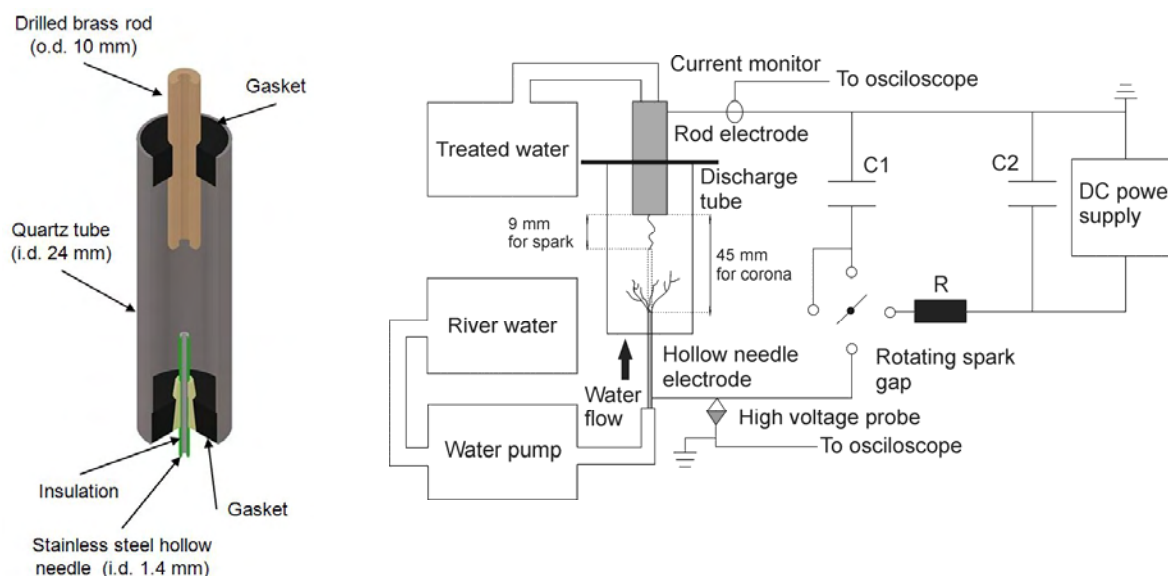


Fig. 1. The corona and spark discharge reactor with water pumping/cooling system and pulsed power system ( $C1 = 2 \text{ nF}$ ,  $C2 = 22 \text{ nF}$ ,  $R = 10 \text{ k}\Omega$ ).

The first set of polluted water samples were processed by corona discharge at 3 different flow rates: 36, 69 and 175 ml/min. Second set of samples was treated by a spark discharge at a flow rate of 38 and 71 ml/min. Third set of samples was treated by ozonation for 45 s, 91 s, 152 s, and 212 s. Every treated sample had a 400 ml volume for comparison purposes, and was tested for microbiological markers such as: number of microorganisms after 24 h of growing in 36°C, number of microorganisms after 72 h of growing in 22°C, total number of *coli* bacteria and number of *E. coli* bacteria.

In all samples the concentration of the total organic carbon was determined using Sievers InovOx TOC analyzer.

## Results and discussion

Photographic images of the electrohydraulic corona and spark discharge are presented in Fig. 2. The first one is named 'corona' or 'corona-like' due to the similar shape as in streamer corona in gaseous phase [17]. For the same reason electrohydraulic discharge generated just after bridging electrodes is named 'spark'. However, one should remember that development mechanisms of such electrohydraulic discharges are quite different than corona and spark discharges in gases and still not well understood.

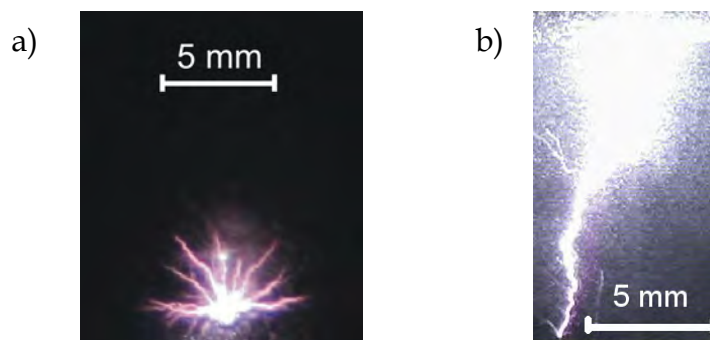


Fig. 2. Photographic images of a) corona and b) spark electrohydraulic discharges.

The amplitudes of the voltage and current corona pulses were up to 40kV and 35 A, respectively, with a full width at half maximum (FWHM) of 3.8  $\mu$ s. The amplitudes of the voltage and current spark pulses were up to 27 kV and 30 A, respectively, with FWHM of 1.4  $\mu$ s. These current and voltage pulses are presented in Figs. 3 and 4. In Fig. 4, a zoom of current waveform in the range of 0-3  $\mu$ s is presented. In contrast to the current waveform recorded by Ceccato et al. [34], we did not observe streamer propagation phase separated from the initiation one. This is probably caused by the geometry of active electrode, which is a hollow needle in our experiment, whereas Ceccato et al. [34] used a simple needle with conical tip. The hollow needle electrode has a ring edge acting as a multipoint electrode. Thus, the probability of simultaneous propagation of several streamers is much higher than for simple needle, which is more like a single point electrode. As can be seen in Fig. 4, initiation phase of the streamer is overlapped by the stray capacitive current and its ripples at the beginning of the current waveform. This 'stray' current superimposed with the initiation current is LC ringing obtained when applying voltage, with L from the power supply and the reactor circuit and C from the interelectrode capacitance [34]. Thus, even these current ripples are taken into account when calculating the pulse energy of the discharge ( $E_p$ ) by integration of the pulse voltage times the current over the pulse duration:

$$E_p = \int_{pulse} U(t)I(t)d(t) \quad (1)$$

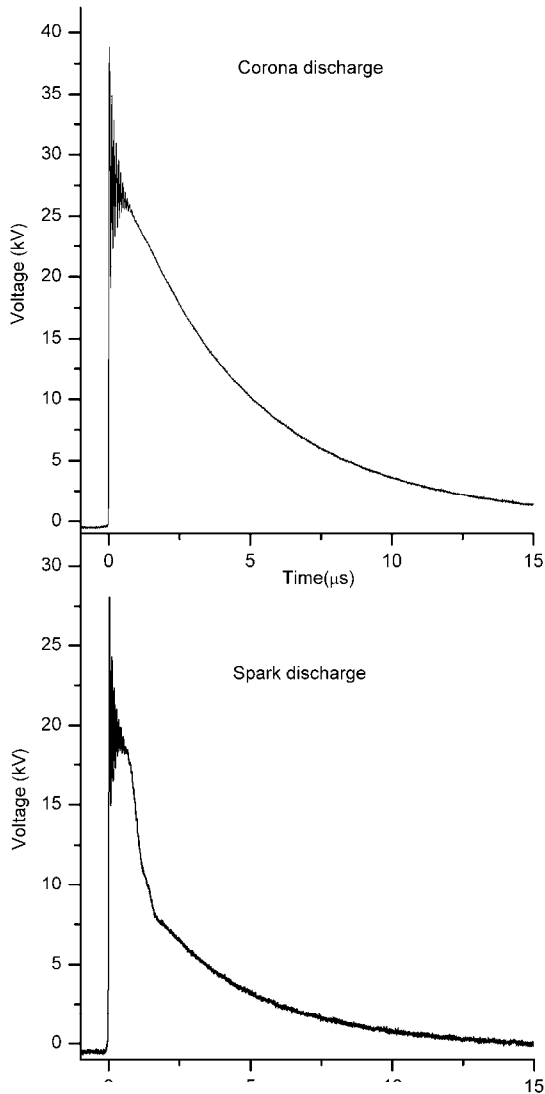


Fig. 3. Typical voltage pulses of corona and spark discharges.

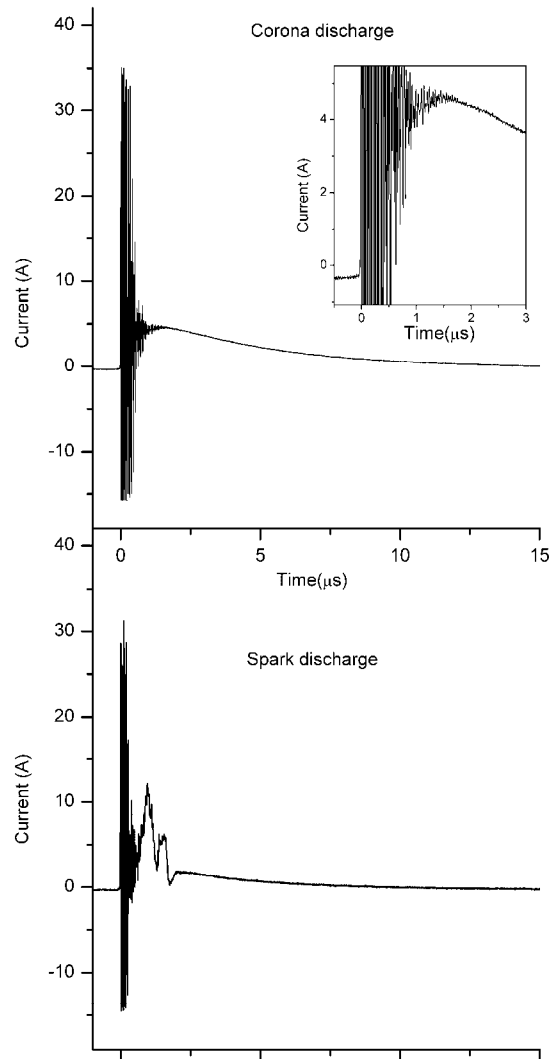


Fig. 4. Typical current pulses of corona and spark discharges.

Since the current pulse is shorter than the voltage one, the  $E_p$  calculation ends with the current pulse. The integration was carried out for 5 oscillograms and then averaged. For the corona and spark discharges the resulted pulse energy was  $0.42 \pm 0.02$  J and  $0.17 \pm 0.01$  J, respectively.

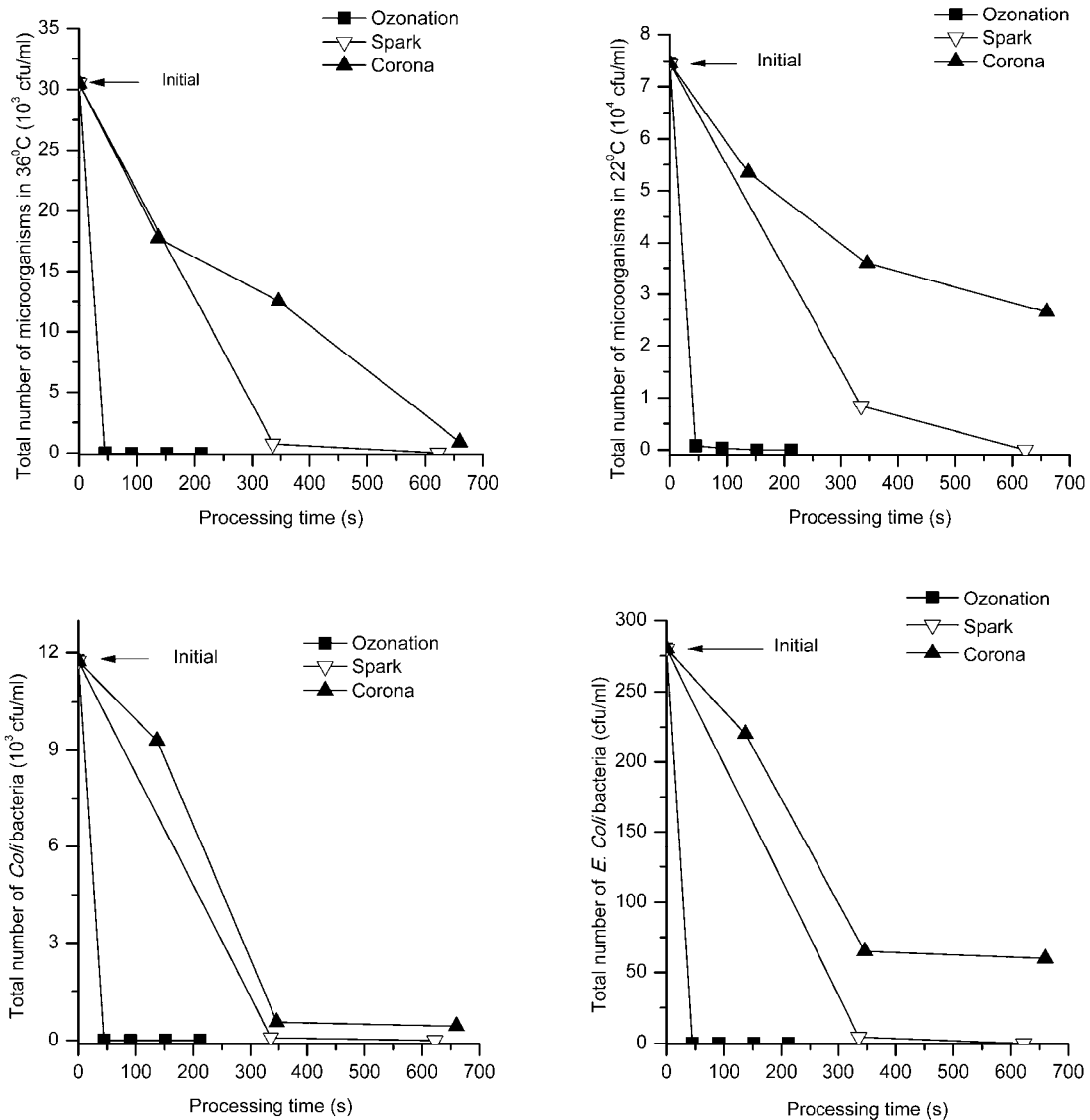


Fig. 5. Concentration of a) microorganisms grown in 36°C, b) microorganisms grown in 22°C, c) total number of *coli* bacteria, and d) *E. coli* bacteria in river water samples as a function of processing time using ozonation, spark discharge and corona discharge.

A comparison of bacteriological results of the total number of microorganisms and *coli* bacteria concentrations in river water samples treated by corona discharge, spark discharge and ozonation are presented in Fig. 5. The energy efficiencies of various treatments are presented in Fig. 6. The energy efficiency  $\eta$  was calculated using the following formulas:

- for the ozonation:

$$\eta = \frac{P_o \cdot t_p}{(C - C_0) \cdot V_s}, \quad (2)$$

where  $P_o$  is a discharge power used in the ozonator (15W),  $t_p$  is a processing time (s),  $C$  and  $C_0$  are initial and final number of microorganisms (cfu/ml), respectively, and  $V_s$  is a sample volume (400 ml),

- for the corona and spark discharges:

$$\eta = \frac{E_p \cdot f \cdot t_p}{(C - C_0) \cdot V_s} \quad (3)$$

where  $E_p$  is the pulse energy calculated from formula (1), and  $f$  is a pulse repetition rate (60 Hz). Other symbols have the same meaning as in formula (2). Processing time  $t_p$  is calculated from formula:

$$t_p = \frac{V_s}{Q} \quad (4)$$

where  $Q$  is a water flow rate (ml/s).

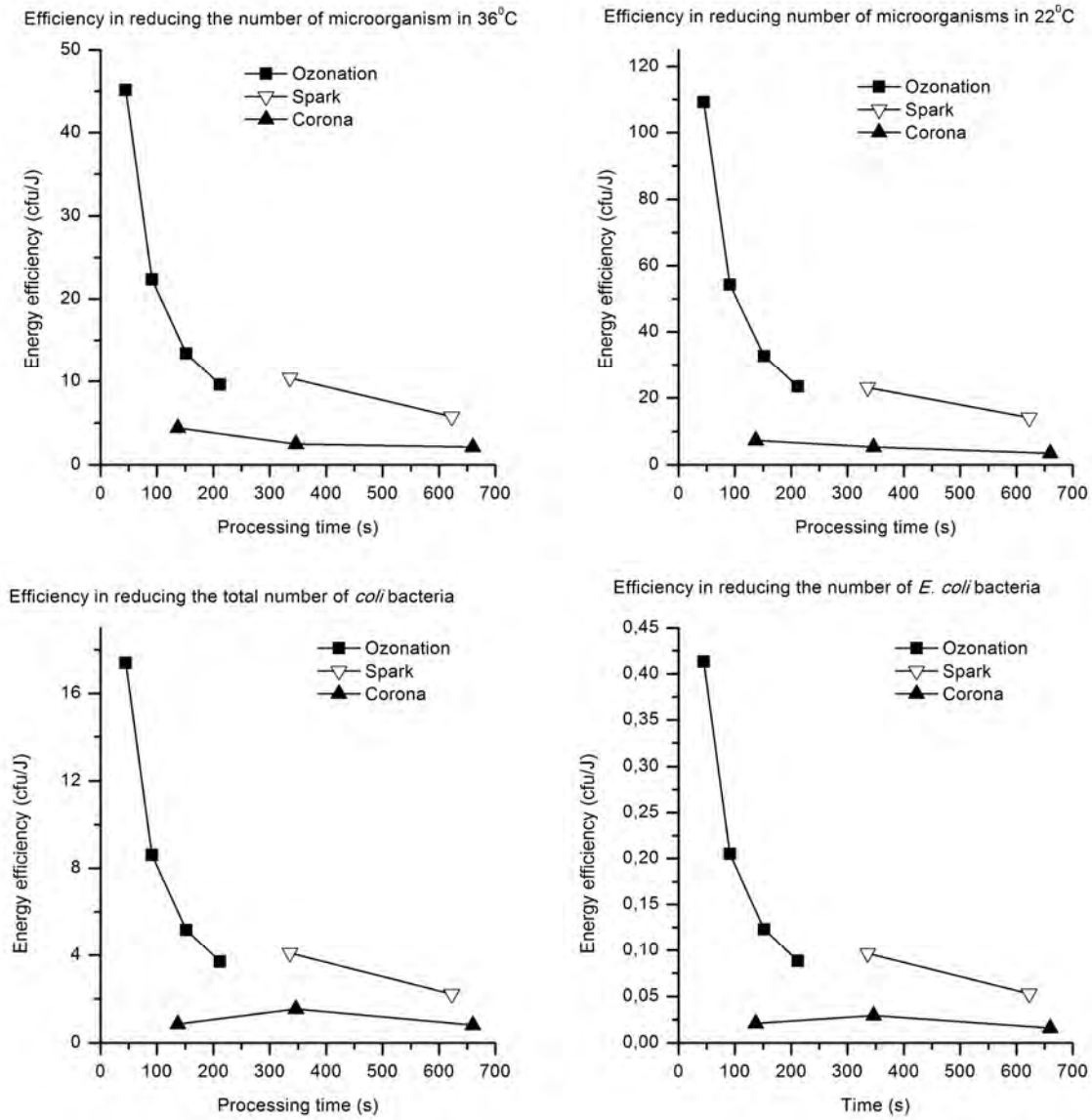


Fig. 6. Energy efficiency of inactivation microorganisms grown in 36°C, microorganisms grown in 22°C, total number of *coli* bacteria and *E. coli* bacteria in river water samples as a function of processing time using ozonation, spark discharge and corona discharge.

It is seen that processing by corona discharge caused significant reduction in the concentrations of microorganisms and bacteria but did not kill them completely. The lower the flow rate, the more energy efficient it was. Comparing to the EU regulations for drinking water, i.e. 0 cfu/100ml for *coli* and *E. coli* bacteria, and 100 and 20 cfu/ml for the number of microorganisms grown in 22°C and 36°C, respectively [37], microbial quality of water processed by corona discharge is far from satisfactory.

The spark discharge was much more effective than the corona, causing a 100% decrease in the number of microorganisms and bacteria after 622 s of processing, except for the total number of microorganisms in 36°C, which survived in the number of 36 cfu/ml. This number is only slightly higher than the regulation and we believe that can be improved. As seen in Fig. 6, the energy efficiency of spark discharge was three times higher than the corona, but still much below that of ozonation.

The ozonation process caused a fast decrease of the total bacteria concentrations with increasing treatment time. After 45 s of processing, the total *coli* number dropped from initial 11750 cfu/ml to 10 cfu/ml and *E. coli* number from 280 cfu/ml to 1 cfu/ml. Processing time of 152 s resulted in killing all of the *coli* bacteria and microorganisms. The energy efficiency was a magnitude higher than that of the electrohydraulic discharges. The reason of higher efficiency of ozonation against corona and spark discharges is the saturation of all water volume with ozone and sustaining this saturation to the end of the ozonation process by ozone excess. In the case of corona and spark electrohydraulic discharges water flowing through the reactor cannot be saturated with oxidizing radicals due to their short lifetime. Thus, their action, is limited to the plasma vicinity. UV generated by discharges is strongly absorbed by the water, so it is harmful for microorganism also in the region close to plasma, whereas pressure waves are relatively strong only in the case of spark discharge, however not intense enough to inactivate all microorganisms.

The total organic carbon concentrations (TOC) measured in every water sample are similar, i.e.  $5 \pm 0.4$  ppm. It is seen that TOC concentrations were not affected by the treatment in this experiment. It shows that neither electrohydraulic discharges, nor ozonation oxidized organic compounds to CO<sub>2</sub>. Thus, their action was limited to inactivation of microorganisms, possibly with destruction of their structure, and to the oxidation of one organic compound into another. Due to the fact that real river water contains different kind of microorganisms, i.e. bacteria, viruses, fungi and protozoa, mechanisms of disinfection in our experiment probably involves all known processes induced by oxidizing agents, pressure wave and UV irradiation [30]. It is known that ozone and OH radicals cause destruction of bacterial membrane through alteration of glycoproteins or glycolipids [38], conversion of certain amino acids such as tryptophan in bacterial cells [39], disruption of enzymatic activity of bacteria by acting on the sulfhydryl groups of certain enzymes [40], affection of both purines and pyrimidines in nucleic acids [38], modification of the viral capsid sites that the virion uses to fix on the cell surfaces (high concentrations of ozone dissociate the capsid completely) [30]. Pressure waves can mechanically damage microorganisms structure, whereas UV irradiation, in particular in the range of 240-280 nm, is able to alter nucleic acids [30].

Destruction of microorganisms cells means that their contents, *inter alia* nucleic acids, contaminated water. This process may be an explanation for the observed increase in conductivity from initial 376  $\mu$ S to 657-680  $\mu$ S in all samples. Presence of organic acids, both nucleic and other formed through the oxidation of organic compounds [17, 19] should result in increased pH. However, measurements of pH showed that there were no changes of this parameter. This may be caused by possible presence of phosphorous fertilizers, which very often contaminate, and which act as chemical buffers keeping pH at the same level.

## Conclusions

Our experiment demonstrated that ozonation is the most efficient method of water disinfection comparing to pulsed spark and pulsed corona discharges. The pulsed spark discharge in water is capable to kill all microorganism similarly to ozonation, however, with much lower energetic efficiency. The pulsed corona discharge turned to be the less effective method of water disinfection.

However, further studies using other electrode configurations and materials, e.g. using porous ceramics increasing the number of discharge channels [39], as well as reactor geometry, e.g. asymmetric shape prohibiting subtraction of pressure waves reflected from the reactor opposite walls, may improve energy efficiency of spark or/and corona discharge and make them competitive to ozonation.

## References

- [1] United Nations, Waste-water treatment technologies: A general review, New York, 2003, Available: <http://www.escwa.un.org/information/publications/edit/upload/sdpd-03-6.pdf>
- [2] M.I. Kerwick, S.M. Reddy, A.H.L. Chamberlain, D.M. Holt, Electrochemical disinfection, an environmentally acceptable method of drinking water disinfection,” *Electrochimica Acta*, vol. 50, pp. 5270-5277, 2005
- [3] P.S.M. Dunlop, J.A. Byrne, N. Manga, B.R. Eggins, “The photocatalytic removal of bacterial pollutants from drinking water,” *J. of Photochemistry and Photobiology A: Chem.*, vol. 8, pp. 355-363, 2002
- [4] T. A. Ternes, J. Stüber, N. Herrmann, D McDowell, A Ried, M. Kampmann, B. Teiser, “Ozonation: a tool for removal of pharmaceuticals, contrast media and musk fragrances from wastewater?,” *Water Research*, vol. 37, pp. 1976–1982, 2003
- [5] H.F. Diao, X.Y. Li, J.D. Gu, H.C. Shi, Z.M. Xie, “Electron microscopic investigation of the bactericidal action of electrochemical disinfection in comparison with chlorination, ozonation and Fenton reaction,” *Process Biochemistry*, vol. 39, pp. 1421-1426, 2004
- [6] J.C. Joret, V. Mennecart, C. Robert, B. Compagnon, P.Cervantes, “Inactivation of indigenous bacteria in water by ozone and chlorine,” *Wat. Sci. Tech.*, vol. 35, no. 11-12, pp. 81-86, 1997
- [7] M. Sato, T. Soutome, S. Mii, T. Ohshima, Y. Yamada, “Decomposition of Phenol in Water using Water Surface Plasma in Wetted-Wall Reactor,” *Int. J. Plasma Env. Sci. Techn.*, vol. 1, no. 1, pp. 71-75, 2007
- [8] J. Koivunen, H. Heinonen-Tanski, “Inactivation of enteric microorganisms with chemical disinfectants, UV irradiation and combined chemical/UV treatments,” *Water Research*, vol. 39, pp. 1519-1526, 2005
- [9] V. Lazarova, P. Savoye, M.L. Janex, E.R. Blatchley, M. Pommepuy, “Advanced wastewater disinfection technologies: state of the art and perspectives,” *Wat. Sci. Tech.*, vol 40, no. 4-5, pp. 203-213, 1999.
- [10] R. d’Agostino, P. Favia, Y. Kawai, H. Ikegami, N. Sato, F. Arefi-Khonsari, “Advanced plasma technology,” ch. 24, pp. 421-432, WILEY-VCH Verlag GmbH & Co. KGaA, Weinheim, 2008
- [11] M.B. Emelko, A.J. Arnold, C.A. Santillan, S.E. Dickson, J.S. Chang, “Treatment of drinking water with pulsed arc electrohydraulic discharge: promising outcomes and future challenges,” *Asia-Pacific Int. Symp. on Air and Water Treatments by Green Oxidation/Reduction Technologies - Catalyst, Plasma and Hybrid Systems*, Dalian, China People Rep., 2006
- [12] W.-K. Ching, A.J. Colussi, H.J. Sun, K.H. Nealson, M.R. Hoffman, “Escherichia coli disinfection by electrohydraulic discharges,” *Environ. Sci. Technol.*, vol. 35, pp. 4139-4144, 2001
- [13] A. Abou-Ghazala, S. Katsuki, K.H. Schoenbach, F.C. Dobbs, K.R. Moreira, “Bacterial Decontamination of Water by Means of Pulsed-Corona Discharges,” *IEEE Trans. Plasma Sci.*, vol. 30, 4, pp. 1449-1453, 2002
- [14] K. Yasuoka, K. Sato, “Development of Repetitive Pulsed Plasmas in Gas Bubbles for Water Treatment,” *Int. J. Plasma Env. Sci. Techn.*, vol. 3, no. 1, pp. 22-27, 2009
- [15] M. Sato, T. Ohgiyama, J.S. Clements, “Formation of Chemical Species and Their Effects on Microorganisms Using a Pulsed High-Voltage Discharge in Water” *IEEE Trans. Ind. Appl.*, vol. 32, no.1, pp. 106-112, 1996
- [16] M. Dors, E. Metel, J. Mizeraczyk, E. Marotta, “Coli bacteria inactivation by pulsed corona discharge in water,” *Int. J. Plasma Env. Sci. Techn.*, vol. 2, no. 1, pp. 34-37, 2008
- [17] B.R. Locke, M. Sato, P. Sunka, M.R. Hoffmann, J.-S. Chang, “Electrohydraulic Discharge and Nonthermal Plasma for Water Treatment,” *Ind. Eng. Chem. Res.*, vol. 45, pp. 882-905, 2006
- [18] B. Sun, M. Sato, J.S. Clements, “Use of a pulsed high-voltage discharge for removal of organic compounds in aqueous solution,” *J. Phys. D: Appl. Phys.*, vol. 32, pp. 1908-1915, 1999
- [19] D.R. Grymonpré, W.C. Finney, R.J. Clark, B.C. Locke, “Hybrid Gas-Liquid Electrical Discharge Reactors for Organic Compound Degradation,” *Ind. Eng. Chem. Res.*, vol. 43, pp. 1975-1989, 2004
- [20] C.M. Miller, R.L. Valentine, M.E. Roehl, P.J.J. Alvarez, “Chemical and microbiological assessment of pendimethalin-contaminated soil after treatment with fenton's reagent,” *Water Research*, vol. 30, pp. 2579-2586, 1996
- [21] K.H. Chan, W. Chu, “The dose and ratio effects of Fe(II) and H<sub>2</sub>O<sub>2</sub> in Fenton's process on the removal of atrazine,” *Environmental Technology*, vol. 24, 6, pp. 703-710, 2003
- [22] A.L. Barros, T.M. Pizzolato, E. Carissimi, I.A.H. Schneider, “Decolorizing dye wastewater from the agate industry with Fenton oxidation process,” *Minerals Engineering*, vol. 19, pp. 87–90, 2006
- [23] N. Kang, D.S. Lee, J. Yoon, “Kinetic modeling of Fenton oxidation of phenol and monochlorophenols,” *Chemosphere*, vol. 47, pp. 915–924, 2002
- [24] M. Pera-Titusa, V. Garcia-Molina, M.A. Baños, J. Giménez, S. Esplugas, “Degradation of chlorophenols by means of advanced oxidation processes: a general review,” *Applied Catalysis B: Environmental*, vol. 47, pp. 219–256, 2004
- [25] J. S. Chang, “Thermal Plasma Solid Waste and Water Treatments: A Critical Review,” *Int. J. Plasma Env. Sci. Techn.*, vol. 3, no. 2, pp. 67-84, 2009

- [26] M. Sato, "Degradation of organic contaminants in water by plasma," *Int. J. Plasma Env. Sci. Techn.*, vol. 3, no. 1, pp. 8-14, 2009
- [27] A. Mizuno, "Recent Progress and Applications of Non-Thermal Plasma", *Int. J. Plasma Env. Sci. Techn.*, vol. 3, no. 1, pp. 1-7, 2009
- [28] D.B.M. Scott, E.C. Leshner, "Effect of Ozone on Survival and Permeability of Escherichia coli.", *J. Bacteriol.*, vol. 85, pp. 567-576, 1963
- [29] B.D. Goldstein, E.M. McDonagh, "Effect of Ozone on Cell Membrane Protein Fluorescence I. *in vitro* Studies Utilizing the Red Cell Membrane.", *Environ. Res.*, vol. 9, no. 1, pp. 179-186, 1975
- [30] "Alternative Disinfectants and Oxidants Guidance Manual", United States Environmental Protection Agency, EPA 815-R-99-014, April 1999
- [31] A.C. Giese, E. Christensen, "Effects of Ozone on Organisms", *Physiol. Zool.*, vol. 27, no. 2. pp. 101-115, 1954
- [32] Hazen and Sawyer, *Disinfection Alternatives for Safe Drinking Water*, Van Nostrand Reinhold, New York, NY, 1992
- [33] T. Vykouk, M. Clupek, P. Lukes, "Inactivation of Escherichia coli by pulsed corona discharge in water," *Proceedings of the 10<sup>th</sup> Int. Symp. on High Pressure Low Temperature Plasma Chemistry*, Saga, Japan, pp. 229-233, 2006
- [34] P. H. Ceccato, O. Guaitella, M. Rabec Le Gloahec, A. Rousseau, "Time-resolved nanosecond imaging of the propagation of a corona-like plasma discharge in water at positive applied voltage polarity," *J. Phys. D: Appl. Phys.*, vol. 43, 2010, doi:10.1088/0022-3727/43/17/175202
- [35] P. Bruggeman and C. Leys, "Non-thermal plasmas in and in contact with liquids", *J. Phys. D: Appl. Phys.* 42, pp. 53001–53027, 2009
- [36] U. Yang, A. Fridman, Y.I. Cho, "Plasma Discharge in Water", *Advances in Heat Transfer*, vol 42, pp. 179-292, 2010
- [37] Council Directive 98/83/EC, "On the quality of water intended for human consumption," *Official J. of the European Communities*, 1998
- [38] D.B.M. Scott, E.C. Leshner, "Effect of Ozone on Survival and Permeability of Escherichia coli", *J. Bacteriol.*, vol. 85, pp.567-576, 1963
- [39] B.D. Goldstein, E.M. McDonagh, "Effect of Ozone on Cell Membrane Protein Fluorescence I. *in vitro* Studies Utilizing the Red Cell Membrane", *Environ. Res.*, vol. 9, pp. 179-186, 1975
- [40] A.C. Giese, E. Christensen, "Effects of Ozone on Organisms", *Physiol. Zool.*, vol. 27, pp. 101-106, 1954
- [41] P. Lukes, M. Clupek, V. Babicky, P. Sunka, "Pulsed Electrical Discharge in Water Generated Using Porous-Ceramic-Coated Electrodes", *IEEE Trans. Plasma Sci.*, vol. 36, no. 4, pp. 1146-1147, 2008

# Gasification of Pyrolytic Oil from Waste Tires in Thermal Plasma Reactor

M. Konrád, M. Hrabovský, M. Hlína, V. Kopecký, T. Kavka, A. Maslani, O. Chumak  
Institute of Plasma Physics AS CR, v.v.i., Za Slovankou 3, 182 00 Praha 8, Czech Republic

e-mail:konrad@ipp.cas.cz

## Abstract

Pyrolytic oil from waste tire pyrolysis was gasified in thermal plasma reactor by means of dc hybrid torch with water stabilization of the arc. The produced syngas had high content of CO and H<sub>2</sub> and its heating value (16 to 19 MJ/kg) was higher than the heating value of natural gas.

**Keywords:** Waste tire pyrolysis, plasma gasification, pyrolytic oil, synthesis gas

## Introduction

Sustainable development in transport includes proper handling of used tires. The amount of waste tires in EU, USA and Japan is around 6 million tones per year and will increase in the future [1]. In EU countries landfill directive imposes a ban on the landfilling of tires from the year 2006. Retreading is environmentally positive solution but not widely used as the costs of new tires are the same as of retreaded tires. Recycling by mechanical shredding and subsequent grinding produces rubber granules. The process consumes lot of energy and has very limited market for application. Recovery of energy by incineration is another possibility (tire derived fuel), but the process brings problems with hazardous emissions and subsequent flue gas cleaning at high capital costs. Also some methods for rubber reclaiming were developed, but the products are of poor quality and the costs are similar to the costs of new rubber.

The mentioned drawbacks of these technologies lead to research on another possibilities of recycling. One of the methods is pyrolysis of rubber from waste tires [2-11]. The products of pyrolysis are solid char, liquid pyrolytic oil and synthetic gas. The pyrolytic products are of poor quality and therefore investigations on upgrading of these products are carried out. In this study we have investigated the possibilities of pyrolytic oil upgrading by gasification in thermal plasma reactor. The pyrolytic oil as low grade fuel should be converted to synthesis gas comprising mainly hydrogen and carbon monoxide with high heating value.

## Tire properties

The composition of tires varies with their intended application. The tires are composed of rubber and cords made from steel or textile. The rubber is mixture of natural and synthetic rubber with additives like carbon black, sulphur, zinc oxide, and fillers. Table 1 presents the typical composition of new passenger and truck tires [12].

Tab. 1. Composition of new passenger and truck tires in wt.%.

| Type of tire    | Natural rubber<br>[wt.%] | Synthetic rubber<br>[wt.%] | Carbon black<br>[wt.%] | Steel<br>[wt.%] | Sulphur<br>[wt.%] | Fabric, Fillers<br>[wt.%] |
|-----------------|--------------------------|----------------------------|------------------------|-----------------|-------------------|---------------------------|
| Passenger tires | 14                       | 27                         | 28                     | 14              | 1.3               | 15.7                      |
| Truck tires     | 24.5                     | 14                         | 28                     | 15              | 2.5               | 16                        |

Each type of tire has about 60 – 70 % of recoverable rubber and about 70 – 80 % of carbonaceous material that can potentially be converted by some thermochemical process into usable products. The primary inorganic material is steel, which can be processed separately.

The ultimate elemental analysis of waste tires is in Table 2. The review article [1] presents data from 15 papers, the Tab. 2. gives the mean values and their range. For comparison data from manufacturers source are given [13].

Tab. 2. Elemental analysis of waste tyres

| Author                   | C [wt.%]  | H [wt.%] | N [wt.%] | S [wt.%] | O [wt.%]  | Ashes [wt.%] |
|--------------------------|-----------|----------|----------|----------|-----------|--------------|
| Mean values from [1]     | 81.8      | 7.1      | 0.38     | 1.53     | 3.25      | 7.1          |
| Range of values from [1] | 73.8-88.5 | 5.3-8.1  | 0.21-0.5 | 0.8-1.99 | 0.11-8.92 | 1.4-17.8     |
| Mean from [13]           | 89.57     | 7.56     | 0.26     | 1.99     | ≤ 0.01    | 4.7          |

The high volatile carbon content of waste tires and the heating value, which is in the range 30 – 35 MJ/kg [1], are important factors for energy recovery.

### Waste tire pyrolysis

The pyrolysis was investigated in a number of papers by different methods: autoclave [2-4], fixed-bed reactor [5,6], fluidized-bed reactor [7], vacuum pyrolysis [8,9] and plasma pyrolysis [10,11]. In this paper we will consider pyrolysis of waste tires in an oven or fixed bed reactor at typical temperature about 500 - 700 °C. The scheme of pyrolysis process is presented in Fig. 1. Pyrolysis of rubber from tires produces char (solid carbon residue, about 30-40 wt.%), liquid pyrolytic oil (about 40-60 wt.%), and synthesis gas ( about 5-20 wt.%) [1]. The exact composition depends on type of tires and on pyrolysis conditions. During rubber pyrolysis more than one degradation temperature regions occur. The maximum conversion of tires takes place at temperature of 600 °C [2], at temperatures over 500 °C the char, oil, and gas yields does not depend on temperature. At lower temperature, the increasing temperature of pyrolysis increases the yield of liquid and gas phases.

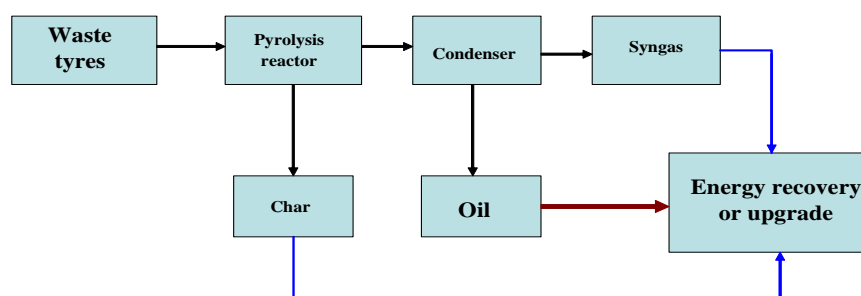


Fig. 1. Scheme of the pyrolysis processes.

As mentioned earlier, the products of pyrolysis are of poor quality. The char can be upgraded for use as activated carbon, but the technique is not economically viable as the classical technology gives activated carbon of better quality for the same costs. The syngas after cleaning can be used as heat source for the pyrolysis, but the flue gases has to be cleaned. Pyrolytic oil can be used as low grade fuel, or added to petroleum refinery feedstocks, but the applications are very limited. One way of upgrading oil properties for use as a high grade fuel are plasma based gasification techniques. For this purpose we have used the plasma-chemical reactor installed at IPP Prague and carried out the preliminary tests. The aim was to produce synthesis gas and find its properties.

### Properties of pyrolytic oil

The elemental composition of the studied pyrolytic oil is presented in Tab. 3. (oil was supplied by the company KFŠ-Delta, Slovakia).

Tab. 3. Elemental composition of pyrolysis oil for the study of gasification

| Laboratory     | C [wt.%] | H [wt.%] | S [wt.%] | N [wt.%] | Cl [wt.%]               |
|----------------|----------|----------|----------|----------|-------------------------|
| Slovnaft VURUP | 85.8     | 10.2     | 0.72     | 0.62     | $8.2 \times 10^{-4}$    |
| Deza           | 88.18    | 9.39     | 1.18     | 0.85     | $\leq 5 \times 10^{-3}$ |

The oil contained more than 21 wt.% of water, the density was 0.9 kg/l, and the heating value based on Dulong equation was 42.1 MJ/kg for oil without water and 39.5 MJ/kg for oil with water. The distillation characteristics of the oil are in Tab. 4.

Tab. 4. Distillation characteristics of pyrolysis oil (from Deza analysis).

| Temperature [°C] | 36    | 82 | 84 | 114 | 115 | 141 | 149 | 177 | 259 | 269 | 358 | 422 | 507 |
|------------------|-------|----|----|-----|-----|-----|-----|-----|-----|-----|-----|-----|-----|
| Fraction [wt%]   | start | 5  | 10 | 20  | 30  | 40  | 50  | 60  | 70  | 80  | 90  | 95  | end |

From the elemental composition of the oil follows its molecular formula  $C_5H_8O$ . For the gasification oxidizing medium was fed into the reactor in stoichiometric ratio to oxidize the surplus of carbon to carbon monoxide. Oxygen or carbon dioxide were used, separately, or in a mixture, along the equations:



### Thermal plasma reactor

The thermal plasma reactor (Fig.2) was designed for operation up to 1700 °C wall temperature. The ceramic lining is from  $Al_2O_3$ , the inner volume is 0.206 m<sup>3</sup> and the outer steel walls of the reactor are water cooled with possibility of calorimetric measurements on cooling circuits [14].

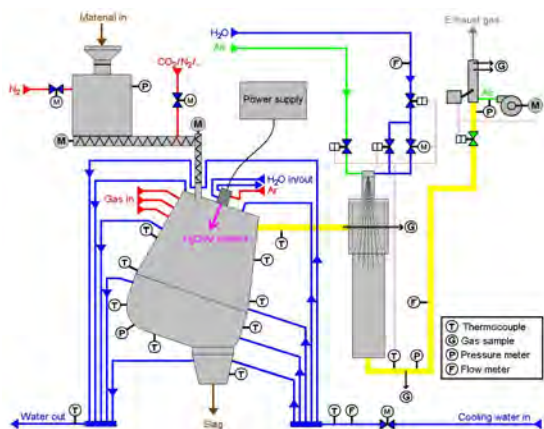


Fig. 2. Scheme of thermal plasma reactor

For the pyrolytic oil gasification the material feeder was removed and the throat for material feeding was closed with a water cooled flange with the feeding nozzle 1.0 mm in diameter. The oil from a pump with the manual control of oil flowrate was fed through a hose into feeding nozzle. Prior to the experiment the calibration of the pump feeding flowrate was carried out.

The ceramic lining of the reactor was preheated by Joule heating of steel rods inserted into the reactor and powered by dc electric current of 400 A for 24 hours to reactor wall temperature 1100 °C. After preheating a hybrid plasma torch [15] was attached to the reactor cover. The hybrid torch generates hydrogen-oxygen plasma by evaporating water from the cylindrical wall formed by a water vortex.

The radial heat flux for evaporation and ionization of steam is generated by an dc electric arc, which is burning at the axis of the water channel. The hybrid design of the torch employs tungsten cathode, which is protected from oxidation by by sheath of argon. During experiment the argon flowrate to cathode chamber was 12 slm, arc current was set to 400 A, the arc voltage was 278 V and the input power 111 kW. The flowrates of oxidizing gases were controlled by thermal mass flow controllers (Brooks Instrument, Aalborg).

The stream of pyrolytic oil crossed the plasma jet about 30 cm downstream of the torch nozzle. The produced synthetic gas (syngas) was quenched in a chamber with water spray. The flow rate of the syngas was measured by two methods, averaging Pitot tube, and by the measurement of the argon concentration in the syngas, in case, when defined amount of argon was fed to the reactor. The

measurement with Pitot tube was rather difficult as char particles choked the tiny openings in the tube, the measured flowrates are therefore given from argon concentrations. The composition of the syngas was measured online by mass spectrometer Omnistar (Pfeiffer Vacuum) with mass range 0-100 amu. The selected gases for monitoring were hydrogen, carbon monoxide, carbon dioxide, methane, oxygen, and argon.

### Results and discussion

The torch heated the inner walls of the reactor to temperature 1150 °C before the pyrolytic oil was fed into the reactor. The temperatures at two points on vertical cylindrical wall T1, T6, at the bottom of the reactor T8 and temperature of the produced syngas T5 at exhaust pipe are given in the Tab. 5.

Tab. 5. Temperatures at 2 points on the cylindrical vertical wall of the reactor (T1, T6), temperature at the bottom of the reactor T8 and temperature of the syngas T5 at exhaust pipe at different runs - see Tab. 6.

| Run | T1 [°C] | T6 [°C] | T8 [°C] | T5 [°C] |
|-----|---------|---------|---------|---------|
| 1   | 1050    | 1100    | 975     | 895     |
| 2   | 1040    | 1130    | 890     | 975     |
| 3   | 1035    | 1100    | 870     | 1000    |
| 4   | 1060    | 1105    | 910     | 1025    |
| 5   | 1160    | 1095    | 895     | 1075    |
| 6   | 1080    | 1080    | 805     | 1090    |
| 7   | 1070    | 1050    | 785     | 1050    |
| 8   | 1050    | 1050    | 750     | 1105    |
| 9   | 1160    | 1050    | 730     | 1015    |
| 10  | 1300    | 1125    | 835     | 1100    |
| 11  | 1310    | 1200    | 980     | 1150    |

The temperatures at runs, when O<sub>2</sub> was fed in the reactor, are higher compared to CO<sub>2</sub> feeding, as oxidation of C to CO brings additional energy to the reactor. The flowrates of materials inputs to the reactor (pyrolytic oil, oxidizing medium), the composition of the produced syngas, its flowrate and its heating values are presented in the Tab. 6.

Tab. 6. The input flowrates of oxidizing medium and pyrolytic oil, the composition of produced syngas, its flowrate and its heating value.

| Run | GAS AND OIL INPUT FLOWRATES |             |                        |               |        | GAS COMPOSITION [vol.%] |      |      |     |     |      | Flowrate<br>from Ar<br>[slm] | Heating<br>value<br>[MJ/kg] |
|-----|-----------------------------|-------------|------------------------|---------------|--------|-------------------------|------|------|-----|-----|------|------------------------------|-----------------------------|
|     | CO2<br>[slm]                | O2<br>[slm] | Ar<br>(added)<br>[slm] | Pyrolysis Oil |        | CO                      | CO2  | H2   | CH4 | O2  | Ar   |                              |                             |
|     |                             |             |                        | [ml/min]      | [kg/h] |                         |      |      |     |     |      |                              |                             |
| 1   | 178.9                       | 0           | 0                      | 205           | 11,3   | 45,4                    | 18,8 | 30,4 | 2,8 | 2,1 | 0,3  | 1327                         | 17.4                        |
| 2   | 178.9                       | 0           | 83,6                   | 205           | 11,3   | 45,2                    | 16,3 | 22,3 | 2,6 | 3,4 | 10,0 | 874                          | 15.9                        |
| 3   | 178.9                       | 0           | 0                      | 205           | 11,3   | 49,2                    | 16,7 | 26,6 | 2,8 | 3,8 | 0,7  | 543                          | 16.3                        |
| 4   | 178.9                       | 0           | 0                      | 205           | 11,3   | 47,7                    | 18,5 | 27,0 | 2,4 | 3,8 | 0,6  | 707                          | 16.3                        |
| 5   | 0                           | 89.3        | 0                      | 205           | 11,3   | 43,1                    | 14,2 | 36,7 | 2,1 | 3,1 | 0,6  | 702                          | 18.7                        |
| 6   | 201.4                       | 0           | 0                      | 227           | 12,5   | 47,1                    | 12,1 | 36,2 | 2,6 | 1,5 | 0,3  | 1363                         | 18.1                        |
| 7   | 201.4                       | 0           | 83,7                   | 227           | 12,5   | 44,9                    | 11,4 | 29,9 | 2,9 | 1,9 | 8,8  | 1001                         | 17.5                        |
| 8   | 201.4                       | 0           | 0                      | 227           | 12,5   | 48,3                    | 11,7 | 33,9 | 2,0 | 3,4 | 0,5  | 780                          | 17.3                        |
| 9   | 200                         | 85.6        | 83,7                   | 408           | 22,5   | 43,7                    | 13,9 | 29,1 | 3,5 | 3,1 | 6,5  | 1343                         | 17.8                        |
| 10  | 0                           | 85.6        | 83,7                   | 205           | 11,3   | 46,1                    | 2,5  | 36,3 | 1,7 | 4,0 | 9,3  | 947                          | 17.9                        |
| 11  | 0                           | 86.8        | 0                      | 205           | 11,3   | 47,3                    | 2,1  | 45,1 | 1,0 | 3,6 | 0,7  | 534                          | 19.0                        |

The produced syngas contains high fraction of CO and H<sub>2</sub> and minor fraction of CO<sub>2</sub>. CO<sub>2</sub> content is higher for the case when CO<sub>2</sub> was used as oxidizing medium, probably part of the CO<sub>2</sub> was not used for partial oxidation of the oil. When oxygen was used as oxidizing medium, the content of the CO<sub>2</sub> was low (mainly at runs 10 and 11). The heating value of the syngas is quite high, about 16 to 19 MJ/kg, higher than the heating value of the natural gas, which is around 12 MJ/kg.

## Conclusions

Management of waste tires represents important environmental issue. The both usual methods of tire treatment, grinding or combustion have many drawbacks. The pyrolysis is promising technology for treatment of waste tyres, but techniques for the upgrade of products of pyrolysis have to be developed. The gasification of pyrolytic oil is one of the possibilities as it produces syngas with heating value of 16 to 19 MJ/kg, higher value comparing than natural gas.

## Acknowledgement

The work was supported by the Grant Agency of the Czech Republic under the project No. P 205/11/2070.

## References

- [1] M. Juma et al., *Petroleum & Coal* 48 (2006), pp. 15-26
- [2] I.M. Rodriguez et al., *Fuel Processing Technology*, 72(2001), pp. 9-22
- [3] M.F. Laresgoiti et al., *J. Anal. Appl. Pyrolysis* 71(2004), pp. 917-934
- [4] F. Murena, *J. Anal. Appl. Pyrolysis* 56 (2000), pp. 195-205
- [5] C. Berrueco et al., *J. Anal. Appl. Pyrolysis* 73 (2005), pp. 65-73
- [6] A.M. Cunliffe, P.T. Williams, *J. Anal. Appl. Pyrolysis* 44 (1998), pp. 131-152
- [7] W. Kaminski, C. Mennerich, *J. Anal. Appl. Pyrolysis* 58-59 (2001), pp. 803-811
- [8] C. Roy et al., *Fuel Processing Technology*, 50 (1997), pp. 87-103
- [9] C. Roy, A. Chaala, *Resources Cons. Recycling*, 32 (2001), pp. 1-27
- [10] L. Tang, H. Huang, *J. Anal. Appl. Pyrolysis* 72 (2004), pp. 35-40
- [11] L. Tang, H. Huang, *Chem. Eng. Comm.*, 197 (2010), pp. 1541-1552
- [12] Scrap tire Characteristics, Rubber Manufacturer's Association, Washington, [www.rma.org](http://www.rma.org)
- [13] M. Karell, Regulation Impacts on Scrap Tire Combustion, Malcolm Pirnie, Inc., [www.pirnie.com](http://www.pirnie.com)
- [14] M. Hrabovsky et al., *Czechoslovak J. of Physics*, Vol. 56 (2006), Suppl. B, B1199-1206
- [15] M. Hrabovsky et al., *IEEE Trans. Plasma Science*, 34 (2006), pp. 1566-1575

# Optical Emission Spectroscopy of Plasma Deposition Processes Using Dimethylphenylsilane Precursor

M. Procházka<sup>1</sup>, F. Krčma<sup>1</sup>, R. Příkryl<sup>2</sup>

<sup>1</sup>Institute of Physical and Applied Chemistry, Brno University of Technology, Purkyňova 118, Brno 612 00, Czech Republic

<sup>2</sup>Institute of Materials Chemistry, Brno University of Technology, Purkyňova 118, Brno 612 00, Czech Republic

e-mail: xcprochazkam@fch.vutbr.cz

## Abstract

The inductively coupled low pressure plasma operating in continuous as well as in pulsed mode was used for the experiments. The aim of the presented experiment was to study the dimethylphenylsilane (DMPS) fragmentation, and the influence of set-up parameters on the deposition process. Fragments of DMPS were identified by optical emission spectroscopy. Dependences of fragment populations on supplied power as well as on DMPS pressure were determined, and consequently, the electron and rotational temperatures were calculated. Some optimal values of set-up parameters as DMPS pressure and duty cycle were found.

**Keywords:** Optical emission spectroscopy, organosilicons, thin film deposition, plasma diagnostics.

## Introduction

Plasma polymerization is a modern technique used for deposition of thin film layers for various purposes. Although this is a kind of polymerization, it differs from conventional polymerizations essentially. In conventional polymerization, the first reactive particle is created that reacts with a molecule of monomer and starts a chain reaction. In plasma polymerization, energy in the form of plasma causes fragmentation of monomer, and then these fragments react with each other to form three-dimensional cross-linked net. Plasma serves here as a source of energy that is needed for fragmentation [1].

Different types of organosilicon precursors have been used in plasma polymerization recently. Some of them showed good properties to be used in plasma polymerization technologies, e.g. HMDSO (hexamethyldisiloxane) [2], TEOS (tetraethylsilane), TMOS (tetramethoxysilane) [3], TVS (tetravinylsilane) [4]. As their properties are pretty well described, the attention of both scientists and investors was turned to new options to improve the production process, such as searching for new precursors with similar structure and/or properties.

DMPS (dimethylphenylsilane) is an isomer of TVS. Its properties make it very suitable to serve as a precursor in plasma polymerization. This compound is in the liquid state at laboratory temperature, it has low boiling point (157 °C at 99.192 kPa) [5], but the most important of all is its structure. Silicon enables to bind to glass surface. Organic groups assure chemical resistance and thanks to spatial arrangement they have a low density (0.899 g.cm<sup>-3</sup>) [5]. Additionally, the aromatic group influences the distribution of the charge in the molecule, and partially allows also the further classical polymerization.

The optical emission spectroscopy (OES) was chosen for plasma diagnostics. It allows determination of various radiating species as well as consequent calculation of some plasma parameters as rotational, vibrational, and electron temperatures [6]. The presented results extend our recent knowledge of deposition plasmas using various precursors [7–9].

## Experimental

Plasma reactor was designed for thin film deposition with inductively coupled plasma using a RF generator (Cesar, 13.56 MHz). Its schematic drawing is presented in Fig. 1. The Quartz tube (i.d. of 40 mm, length of 60 cm) was used as the reactor body. The copper coil was supplied through automatic matching network by an RF source with frequency of 13.56 MHz up to power of 500 W. Flow of argon (used for the experimental device cleaning and surface activation before deposition) was controlled by Bronkhorst mass flow controller. DMPS was stored in thermostatic box fixing its pressure, and it was introduced into the reactor using Pfeiffer dosing valve. The whole device was

continuously pumped by the diffusion pump connected to the rotary oil pump. DMPS pressure and the total pressure in the reactor were monitored by Penning and Pirani manometers. The optical emission spectrometer Jobin Yvon Triax 550 with a 1200 gr/mm grid and a CCD detector was used for the diagnostics. Optical probe was installed at the reactor axis. A metallic mesh was installed between plasma and quartz OES window to protect window against coating during the experiments.

The whole apparatus was pumped down to the ultimate pressure of  $10^{-3}$  Pa, and after that, the argon discharge at pressure of a few Pa was applied for 5 minutes at the argon flow rate of 10 Sccm . The same procedure was applied before the deposition. Thus, the deposition process was carried out in pure DMPS atmosphere at pressure of a few Pa.

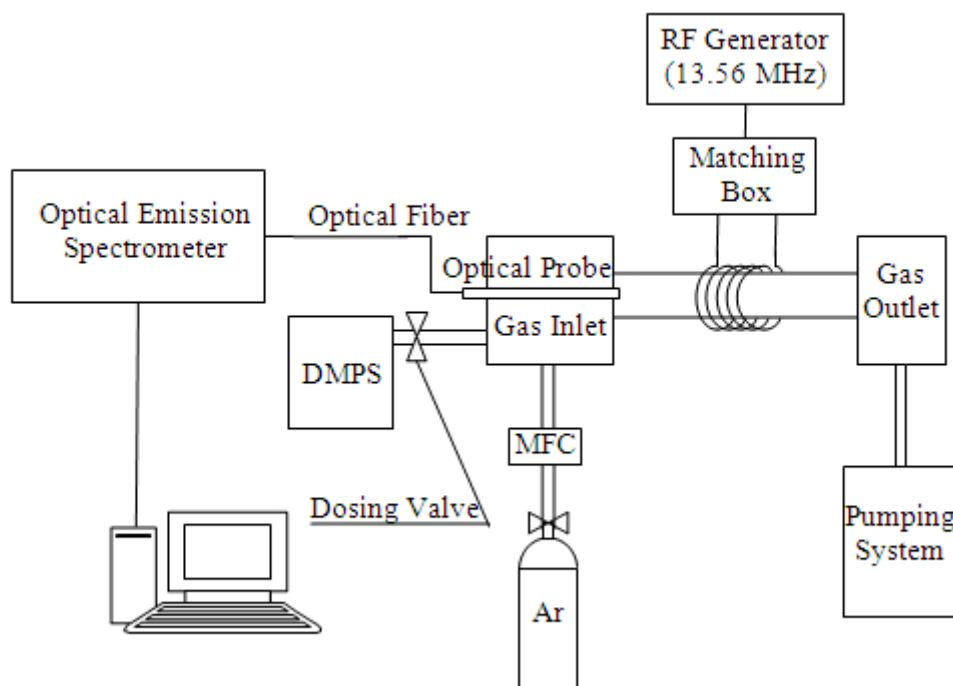


Fig. 1. Scheme of apparatus for ICP plasma polymerization

## Results and discussion

The aim of the presented experiment was to make a series of measurements with different setup, and determine the best conditions for the deposition of desired thin film layer. Our attention was concentrated at two main parameters: amount of energy supplied by the RF generator expressed by the power, and the monomer pressure.

First, we decided to change the applied power. The amount of energy affects the fragmentation of the precursor. In other words, it determines what species are created during the fragmentation, and how much of them are created. It destines the content of the deposited thin film layer. We must also consider the economical point of view. The use of energetically demanding processes should give nice results but they are too expensive for wide application in technology.

Although the range of supplied power might be vast, there are some limitations we have to keep in mind. Every discharge needs a certain minimum amount of energy to be lit, and this energy is expressed by the minimum of supplied power. On the other side, we are limited by the apparatus. It can be supplied by the power of about 500 W, but it has its own electrical resistance which reflects a part of supplied energy back. This decrease is called “reflected power”, and it appears mainly due to the construction of the apparatus.

The study of supplied power influence was held at two different DMPS pressures of 1 Pa and 2 Pa. After the discharge was ignited, the pressure decreased in both cases to the half of its starting value and then, increased linearly with increasing power. However, it didn't reach its starting value until the discharge was switched off. Due to the internal apparatus resistance, a part of the supplied power was reflected back. We kept the increasing supplied power up to 200 W when the reflected power value reached 25 % of the supplied power value.

The optical emission spectra were recorded in the spectral interval of 320–780 nm. Species identified in spectra were atomic hydrogen (Balmer series), molecular hydrogen, CH radical, atomic carbon (in the spectrum of second order), and atomic silicon. No C<sub>2</sub> bands were found in the spectra, neither the SiH peak that are usually observed during similar deposition processes. The fragmentation degree was probably very high at the given conditions and thus dominantly small fragments were created. Fig. 2 a) and b) show intensities of selected species. It can be seen that intensities of nearly all fragments increased more or less linearly with increasing effective power. Atomic hydrogen seemed to grow exponentially, only. We can observe small decrease of all intensities at 100 W at the pressure of 1 Pa. The discharge turned its mode from the type localised inside the coil to the type outside the coil at these conditions. After this breaking point, intensities of all signals started to rise again.

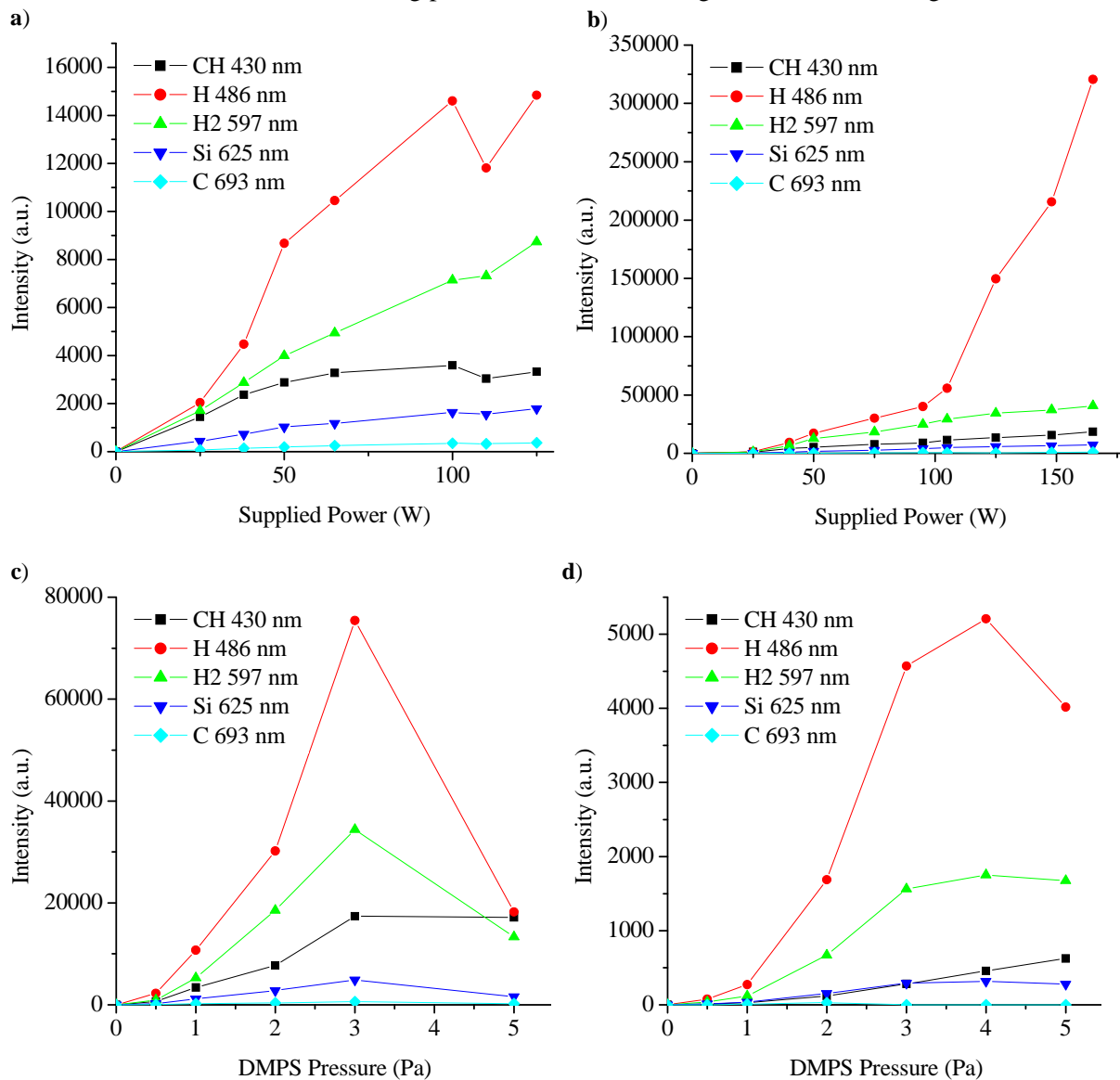


Fig. 2: Intensities of selected fragments:  
a) at 1 Pa of DMPS, b) at 2 Pa of DMPS, c) at 100 W, d) at 200 W

The second parameter which influences the deposition process significantly is the pressure of monomer. By the amount of monomer, expressed by the partial pressure of the monomer, we can control both the content of plasma, and the content of the deposited thin film. Also the degree of fragmentation is dependent on the amount of monomer. The higher the pressure is, the greater fragments are created, and the lower their populations are. If we determine pressure optima for particular fragments, we might be able to establish the right conditions of the deposition process in

order to achieve the desired product – a thin film of required composition. However, plasma processes are dependent on many factors, e.g. fragmentation depends on supplied power, too. So we must look for pressure optima in combination with optima of other parameters, in this case with optimal supplied power.

The second part of experiments was carried out at two fixed applied powers (100, and 200 W), and the DMPS pressure was varied in the range of 0.5–5 Pa. Unfortunately, the apparatus construction did not allow achieving lower or greater pressure of DMPS.

Figs. 2 c) and d) show the dependences of selected fragments intensities on the DMPS pressure. When supplied power of 100 W was used, the most of fragments reached their maximal intensities at pressure of 3 Pa. The best reply of CH radical was estimated at 4 Pa. Similar dependencies were obtained also at the higher applied power, only the maximal intensities (except the intensity of CH radical) were obtained at 4 Pa. Intensity of CH radical increased in the whole studied pressure range, but based on results obtained at lower pressure, we can expect that the maximal CH intensity should be at about 5-6 Pa, i.e. out of the measurable pressure range.

The measured spectra allowed determination of rotational and electron temperatures. The rotational temperature was calculated from CH  $^2\Delta \rightarrow ^2\Sigma$  0-0 band at 431.5 nm using classical pyrometric procedure. Rotational lines assignment as well as rotational constant of the upper state was taken from LifBase software [10]. Electron temperature was calculated from line intensities of hydrogen Balmer series using constants given by NIST [11]. The spectrometer response function was obtained using Oriel standard lamp. Figs. 3 and 4 show the dependences of both temperatures on the experimental conditions. Considering the 15–20% deviation, we can assume that rotational temperature was independent on supplied power or DMPS pressure. Electron temperature was slightly decreasing with increasing supplied power. When pressure of monomer was increasing, electron temperature was decreasing significantly. Vibrational temperature couldn't be determined because any convenient particle for calculation wasn't found in the spectra [12].

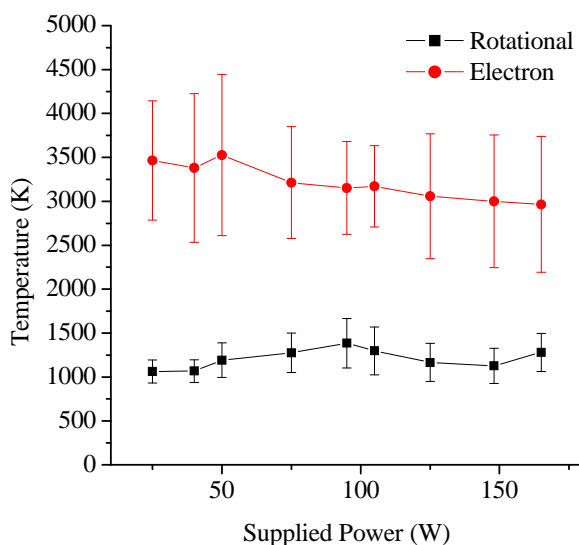


Fig. 3. Temperatures at 2 Pa of DMPS

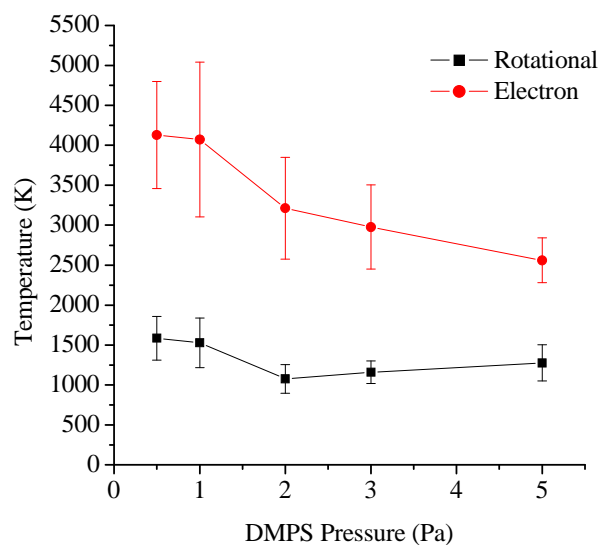


Fig. 4. Temperatures at 200 W

## Conclusions

Evaluation of different parameters was investigated during RF inductively coupled plasma polymerization of dimethylphenylsilane monomer using optical emission spectroscopy. Results show high degree of fragmentation leading to the creation of many small fragments. Dependence of fragments concentration on supplied power was proven to be linear in the most cases. When changing pressure of monomer at constant supplied power, some optima for particular fragments were determined. To get more precise optimal values of DMPS pressure, it is necessary to make more detailed measurements also at higher pressures of DMPS. Rotational and electron temperatures were determined, too. Rotational temperature was nearly independent on the supplied power as well as on

the DMPS pressure. Electron temperature decreased in both cases with the increasing adjusted parameter. However, it decreased significantly with increasing DMPS pressure.

The presented results showed possibility to change the DMPS fragmentation level by varying the plasma parameters. The more detail study of the other setup parameters as well as the detailed exploration of current ones is necessary to complete in the future. Other diagnostics might be performed including in-situ mass spectroscopy or infrared spectroscopy to achieve more precise report about plasma content. These results may be compared to thin film analysis results of the deposited layers. By this way, we would be able to optimize plasma polymerization process in order to predict the composition of thin film layer, and set up the process to produce it.

### Acknowledgement

This work has been supported by the Research plan of Czech Ministry of Education No. MSM0021630501.

### References

- [1] N. Inagaki: *Plasma Surface Modification and Plasma Polymerization*. Technomic Publishing Company, Lancaster, 1996, ISBN 1-56676-337-1, p. 101.
- [2] M. Goujon, T. Belmonte, G. Henrion, *Surf. Coat. Technol.* 188–189 (2004) 756.
- [3] S.B. Bang, T.H. Chang, Y. Kim, *Thin Solid Films* 444 (2003) 125.
- [4] K. Flamíková: *Diagnostics of Thin Film Layer Deposition Using Tetravinylsilane Monomer*, Master Thesis, Brno University of Technology, Brno, 2010, 59 p.
- [5] Sigma-Aldrich: Dimethylphenylsilane [online]. 2010 [cit. 14. 11. 2010] <[http://www.sigmaaldrich.com/catalog/ProductDetail.do?lang=cs&N4=41418|FLUKA&N5=SEARCH\\_CONCAT\\_PNO|BRAND\\_KEY&F=SPEC](http://www.sigmaaldrich.com/catalog/ProductDetail.do?lang=cs&N4=41418|FLUKA&N5=SEARCH_CONCAT_PNO|BRAND_KEY&F=SPEC)>
- [6] P. Worsfold, A. Townshend, E. Poole: *Encyclopedia of Analytical Science*, 2<sup>nd</sup> ed. Volumes 1–10, Elsevier, Amsterdam 2004, ISBN 0-12-764100-9
- [7] Z. Rašková, H. Hajduchová, I. Havelková, F. Krčma, J. Vaněk, R. Příkryl, V. Čech, *Acta Phys. Slovaca* 53 (2003) 401.
- [8] Z. Rašková, K. Brandejs, J. Vaněk, F. Krčma, *Czech. J. Phys.* 54 (2004) C1036.
- [9] V. Brites, G. Chambaud, M. Hochlaf, J. Kočíšek, J.L. Cayao Diaz, Š. Matejčík, F. Krčma, *J. Phys. Chem. A* 113 (2009) 6531.
- [10] J. Luque and D.R. Crosley, "LIFBASE: Database and spectral simulation (version 1.5)", SRI International Report MP 99-009 (1999).
- [11] Yu. Ralchenko, A.E. Kramida, J. Reader, and NIST ASD Team (2010). NIST Atomic Spectra Database (ver. 4.0.1), [Online]. Available: <http://physics.nist.gov/asd> [2010, November 29]. National Institute of Standards and Technology, Gaithersburg, MD.
- [12] M. Procházka: *Plasma Diagnostics of Thin Film Layer Deposition Using Dimethylphenylsilane Monomer*, Master Thesis, Brno University of Technology, Brno, 2010, 72 p.

# Combination of an Electron Spectrometer with an Ion Trap: first results for $\text{H}^- + \text{h}\nu$ and $\text{H}^- + \text{H}$

P. Jusko<sup>1</sup>, Š. Roučka<sup>1</sup>, I. Zymak<sup>1</sup>, R. Plašil<sup>1</sup>, D. Gerlich<sup>1,2</sup>, J. Glosík<sup>1</sup>

<sup>1</sup> Charles University, Faculty of Mathematics and Physics, V Holešovičkách 2, 180 00, Prague, Czech Republic

<sup>2</sup> Institut für Physik, Technische Universität, 09107 Chemnitz, Germany

e-mail: paval.jusko@gmail.com

## Abstract

A new instrument is under development which is able to guide and store anions and to detect simultaneously electrons using the superposition of suitable RF and magnetic fields. It is based on a modular design combining (i) an rf storage ion source with mass spectrometer, (ii) an octopole ion guide or alternatively a temperature variable 22PT (iii) an electron spectrometer based on magnetic adiabatic collimation, and (iv) a channeltron electron multiplier (CEM) detector. All modules are transparent in axial direction and, therefore, the ions can be exposed to a beam of photons or of neutrals, e.g. also an H-atom beam. This allows us to study photo detachment of electrons from trapped anions and the interaction of anions with neutrals. A first successful test has been the observation of the decay time of an  $\text{H}^-$  ensemble exposed to a 532 nm laser. At laser powers of a few mW, storage times are a few s in accordance with the known detachment cross section. Similar loss rates have been measured by exposing the  $\text{H}^-$  ions to a beam of H-atoms, i.e., via the formation of  $\text{H}_2 + \text{e}^-$  products. This contribution discusses the instrument and the ongoing activities, the measurement of absolute rate coefficients for  $\text{H}^- + \text{H}$  as a function of temperature. Long term objectives include to detect the emitted electrons with a CEM detector, utilizing the guiding features of the magnetic bottle principle. The ultimate goal is the determination of the energy distribution of the electrons produced via photons or via associative detachment. Theoretical estimates, accounting for both the rf and the magnetic field, indicate a transmission probability of nearly 100 % and an energy resolution of better than 100 meV.

**Keywords:** ion traps, rf and magnetic fields, detecting electrons, anions, interstellar chemistry

## Introduction

It is generally accepted, that ions and electrons play an important role in the chemistry of interstellar matter, and many related studies have been performed, mainly with cations. The recent detection of molecular anions in the interstellar medium [5] has clearly indicated that there is more demand for laboratory studies of negative ion chemistry [12],[18]. Moreover, hydrogen atoms are the most abundant atomic species in the universe and collisions with H have a significant influence on the chemistry of interstellar clouds. Of special importance is the associative detachment (AD) reaction

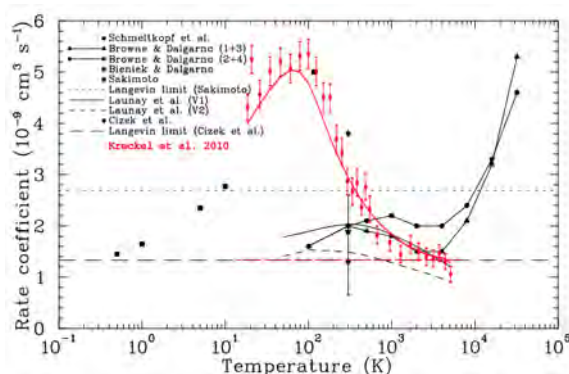


Fig. 1 Overview of theoretical and experimental rate coefficients for associative detachment in collisions of  $\text{H}^-$  and H. The plot is based on [8] and [9].

The role of this fundamental process in cooling of the primordial gas has been discussed recently [8]. It also has motivated the construction of a merged beam apparatus which has been used for

determining the energy dependence of the cross-section for reaction (1) [9]. The present status of our knowledge is shown in Fig. 1.

Our aim is not only to verify these measurements with a complementary method and to extend the measurements towards lower temperatures, but also to measure the kinetic energy distribution of the detached electrons. The theory [6] predicts that the major fraction of the exothermicity of reaction (1) produces  $H_2(v,j)$  molecules with significant vibrational and rotational excitation. Energy conservation results in an electron energy distribution ranging from 0 to 1.5 eV. The planned experimental determination of this distribution will give us a better understanding of the AD process and will be a critical proof of the theory of AD [6].

### Experimental techniques

Our apparatus is based on the well established guided-ion-beam and ion-trapping technique [7]. We extend this technique by adding an electron spectrometer employing a magnetic adiabatic collimator [1]. Fig. 2 shows a schematic drawing of our apparatus. The H atom beam is produced in a microwave discharge source with variable beam temperature  $T = 10 - 300$  K [2], [3]. H ions are produced in an electron impact storage ion source with  $H_2$  as a precursor gas. After mass selection in an RF quadrupole (QMS), ions are captured in the RF octopole utilizing pulsed axial potential barriers. The H atom beam is passing through the octopole and interacts with H by AD reaction.

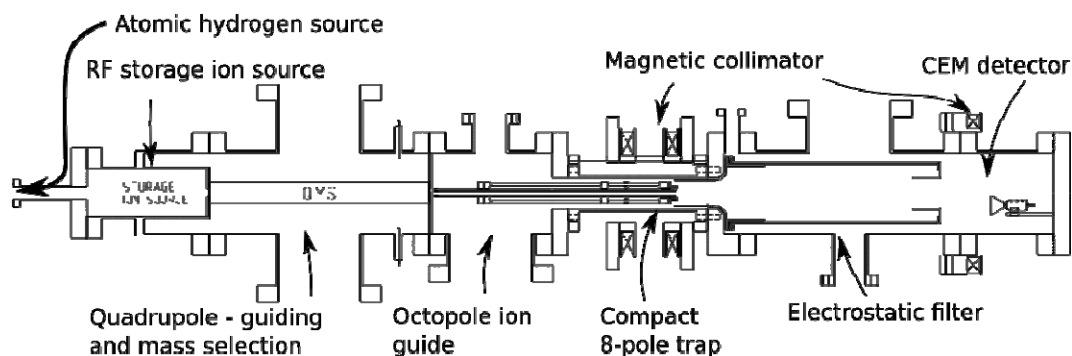


Fig. 2. Combination of a Guided Ion Beam instrument with a MAC Electron Spectrometer. The  $H^+$  ions are produced in the storage ion source. A quadrupole transfers the ions into an octopole ion guide where they can be trapped between the indicated electrostatic barriers. Superimposed to this trapping region is a magnetic field shown in Fig. 3.

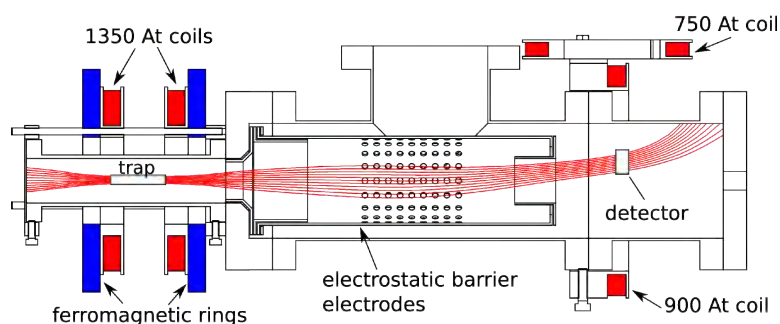


Fig. 3. The design of magnetic adiabatic collimator. Solenoid coils are displayed in red, ferromagnetic rings in blue. Magnetic field lines going through the trap were calculated using FEniCS [11].

Electrons produced in the AD with random velocity direction are guided out of the octopole using an axial magnetic field. Their energy is analyzed with a so-called MAC-E-Filter (Magnetic Adiabatic Collimation combined with an Electrostatic Filter). This type of spectrometer was first proposed in [1] and has been described in [10] and [15]. It is based on adiabatic invariance of magnetic momentum ( $E_{\perp}/B$ ) in slowly varying magnetic field. Our actual construction is shown in Fig. 3. Two solenoids are producing a magnetic guiding field in the trap. Two ferromagnetic rings surrounding these solenoids

enhance the intensity and homogeneity of the field inside the trap and shield the magnetic field outside. This arrangement converts 97 % of the energy associated with radial motion ( $E_{\perp}$ ) into axial motion, creating a collimated beam of electrons. This beam is filtered by a variable electrostatic retarding potential barrier, i.e., only electrons with energy above a selected barrier are detected by the off-axis channeltron electron multiplier.

## Results and discussion

The design of the apparatus was verified by numerical simulations. The configuration of coils and ferromagnetic rings producing the desired shape of magnetic field was designed using femm [13] and FEniCS [11] software. The theoretical estimates for the resolution of the MAC-E filter were verified by simulating trajectories of electrons in the calculated electromagnetic field [16]. We checked the calculations of magnetic field by measuring the axial magnetic field using a Hall probe. The results which are presented in [17], demonstrate a good agreement of the measured field with numerical calculations.

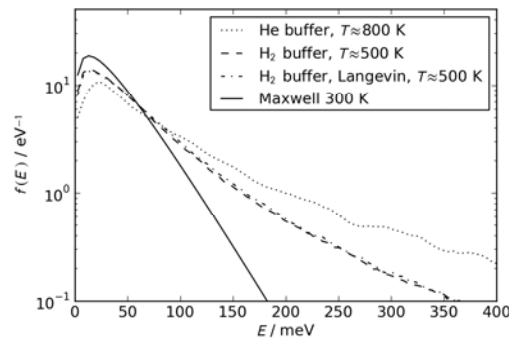


Fig. 4. Calculated energy distributions of  $H^+$  ions the 8-pole for He and  $H_2$  buffer gas at 300 K. The dash-dotted line show a calculation including small angle Langevin scattering.

Confining  $H^+$  ions in an octopole trap has also some issues due to their low mass. We intend to cool the ions by buffer gas cooling. For efficient cooling, the masses of ions and buffer gas should be similar. In order to prevent heating by collisions in the rf field, the buffer gas particles should ideally have slightly lower mass than ions. Therefore we intend to use molecular hydrogen for cooling – the lightest gas that does not react with  $H$ . Energy distributions of ions in an octopole with  $H_2$  and He buffer gasses calculated by particle simulation are shown in Fig. 4. It can be seen that the heavier helium buffer gas causes more RF heating and is less efficient in cooling. The influence of small angle Langevin scattering [14] was also calculated. The graph in Fig. 4 shows the result for small angle collision with a rather high cutoff parameter of 9 as defined by [14]. No significant influence of small angle collisions was observed. The mean energy of ions cooled by  $H_2$  at 300 K is 0.07 eV, which corresponds to temperature  $T \sim 500$  K. The mean energy in collisions with 50 K atomic hydrogen beam is then below 0.08 eV. This energy is small compared to the total energy released during the collision and we expect, that the basic structure of electron spectrum calculated by [6] for collisions at 0.01 eV will be retained. Moreover, the cold effusive beam can be used to increase the collision rate of ions in the field free region, which will decrease this rf heating effect.

Currently we perform test measurements using the CEB-22PT apparatus [2], which combines a cold effusive beam of atomic hydrogen with a 22-pole ion trap. This instrument will be used for measurement of the rate coefficient as a function of temperature. Fig. 5 shows the loss of  $H^+$  caused by photodetachment. A diode pumped solid state green laser (532 nm, 3-5 mW) has been used to detach the electrons. The results are in qualitative agreement with the theoretical cross section. A quantitative analysis requires determination of the effective overlap between the ion cloud and the laser beam. The electrons produced by the laser have a well defined kinetic energy. Therefore, they are ideal for testing and calibrating the electron spectrometer.

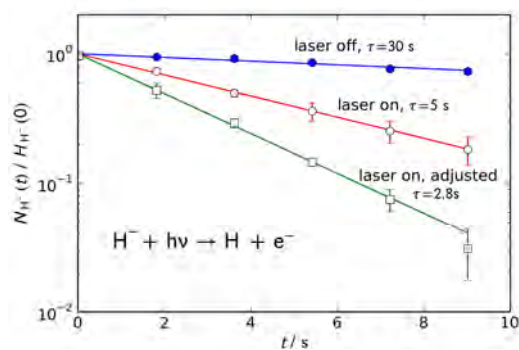


Fig. 5 Loss of  $\text{H}^-$  ions via photodetachment and reactions. The loss with a storage time of 30 s has been due to minor impurities in the trap; improvement of the vacuum leads to much longer times. A diode pumped solid state green laser (532 nm, 3-5 mW) has been used to detach the electrons. .

First measurements with the hydrogen atom beam were also performed. Fig. 6 shows the kinetics with the discharge switched OFF (no H atoms) and two measurements with the discharge switched ON. The results show that, without H atoms, the ions are trapped for long times – no loss is visible in the 10 s time frame. The measurements with the discharge ON were performed 20 minutes apart in order to verify stability of the H atom beam. The results agree with each other within the statistical error for the measurements. The stability of the H atom beam is crucial for measurement of AD rate coefficient as a function of temperature.

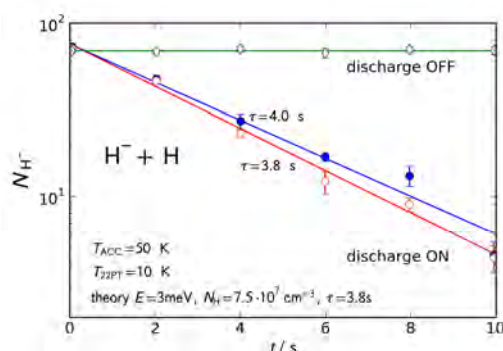


Fig. 6. Reaction of  $\text{H}^-$  with H atoms. Test of the reproducibility and the stability of the H atom beam. The collision temperature 30 K corresponds to a mean collision energy of  $3/2 kT = 4$  meV

## Conclusions

We presented the design of a versatile instrument that will be primarily operated as an octopole ion trap with an electron spectrometer. Alternatively, the arrangement can be used as an guided ion beam instrument. For detecting product ions, the electron spectrometer can be replaced by a quadrupole mass spectrometer. The first results for  $\text{H}^-$  photodetachment and associative detachment measured in a CEB-22PT apparatus illustrate the potential of the technique.

## Acknowledgements

This work is a part of the research plan MSM 0021620834 and grant OC10046 financed by the Ministry of Education of the Czech Republic and was partly supported by GACR (202/07/0495, 202/08/H057, 205/09/1183, 202/09/0642), by GAUK 25709, GAUK 92410, GAUK 86908, GAUK 54010 and by COST Action CM0805 (The Chemical Cosmos).

## References

- [1] G. Beamson, H.Q. Porter, D.W. Turner, *The collimating and magnifying properties of a*

- superconducting field photoelectron spectrometer. J. Phys. Sci. Instrum.* **13** (1980) 64.
- [2] G. Borodi, *On the combination of a low energy hydrogen atom beam with a cold multipole ion trap. PhD Thesis TU Chemnitz* (2008).
- [3] G. Borodi, A. Luca, D. Gerlich, *Reactions of  $\text{CO}_2^+$  with H,  $\text{H}_2$  and deuterated analogues. Int. J. Mass Spectrom.* **280** (2009) 218.
- [4] H. Bruhns, H. Kreckel, M. Lestinsky, W. Mitthumsiri, M. Schnell, B. Seredyuk, D.W. Savin, M.E. Bannister, C.C. Havener, A. Dorn, O. Heber, M.L. Rappaport, A.M. Covington, *A novel merged-beams apparatus for studying anion-neutral reactions. Bull. Am. Phys. Soc.* **53** (2008) 149.
- [5] M.C. McCarthy, C.A. Gottlieb, H. Gupta, P. Thaddeus, *Laboratory and Astronomical Identification of the Negative Molecular Ion  $\text{C}_6\text{H}^-$ . Astrophys. J.* **652** (2006) L141.
- [6] M. Cizek, J. Horacek, W Domcke, *Nuclear dynamics of the  $\text{H}_2^-$ - collision complex beyond the local approximation: associative detachment and dissociative attachment to rotationally and vibrationally excited molecules.. J. Phys. B* **31** (1998) 2571.
- [7] D. Gerlich, *Inhomogeneous Electrical Radio Frequency Fields: A Versatile Tool for the Study of Processes with Slow Ions. Adv. Chem. Phys.* **LXXXII** (1992) 1.
- [8] S. Glover, D. W. Savin, A.-K. Jappsen, *Cosmological implications of the uncertainty in  $\text{H}^-$  destruction rate coefficients. Astrophys. J.* **640** (2006) 553.
- [9] H. Kreckel, H. Bruhns, M. Čížek, S.C.O. Glover, K.A. Miller, X. Urbain, D.W. Savin, *Experimental results for  $\text{H}_2$  formation from  $\text{H}^-$  and  $\text{H}$  and implications for first star formation. Science* **329** (2010) 69.
- [10] V.M. Lobashev, P.E. Spivak, *A method for measuring the electron antineutrino mass. Nucl. Instrum. Methods Phys. Res., Sect. A* **240** (1985) 305.
- [11] A. Logg, G. N. Wells, *DOLFIN: Automated finite element computing, ACM Trans. Math. Softw.,* **37**(2) (2010) Article 20,
- [12] O. Martinez Jr, Z. Yang, N.J. Demarais, T.P. Snow, V.M. Bierbaum, *Gas-phase reactions of hydride anion,  $\text{H}^-$ . Astrophys. J.* **720** (2010) 173.
- [13] D. C. Meeker, *Finite Element Method Magnetics, Version 4.2* (11 Oct 2010 Build), <http://www.femm.info>
- [14] K. Nanbu, Y Kitatani, *An ion-neutral species collision model for particle simulation of glow discharge. J. Phys. D: Appl. Phys.* **28** (1995) 324.
- [15] A. Picard, H. Backe, H. Barth, J. Bonn, B. Degen, Th. Edling, R. Haid, A. Hermann, P. Leiderer, Th. Loeken, A. Molz, R.B. Moore 4, A. Osipowicz, E.W. Otten, M. Przyrembel, M. Schrader, M. Steininger and Ch. Weinheimer, *A solenoid retarding spectrometer with high resolution and transmission for keV electrons. Nucl. Instrum. Methods Phys. Res., Sect. B* **63** (1992) 345.
- [16] Š. Roučka, A. Podolník, P. Jusko, T. Kotrčík, R. Plašil, and J. Glosík, *Combination of a 22-pole Trap with an Electron Energy Filter – Study of Associative Detachment  $\text{H}^- + \text{H} \rightarrow \text{H}_2 + e^-$ , WDS'09 Proceedings of Contributed Papers: Part II Physics* (2009) 121.
- [17] Š. Roučka, P. Jusko, D. Gerlich, R. Plašil, and J. Glosík, *Study of Capture and Cooling of  $\text{H}^-$  Ions in rf Octopole with Superimposed Magnetic Field, WDS'10 Proceedings of Contributed Papers: Part II Physics* (2010) 105
- [18] Z. Yang, B. Eichelberger, M.Y. Carpenter, O. Martinez, T.P. Snow, V.M. Bierbaum, *Experimental and theoretical studies of reactions between H atoms and carbanions of interstellar relevance. Astrophys. J.* **723** (2010) 1325.

# Organic Abundances in Atmospheric Pressure N<sub>2</sub>-CH<sub>4</sub> Discharges

G. Horváth<sup>1,3</sup>, N. J. Mason<sup>3</sup>, F. Krčma<sup>2</sup>, K. Klohnová<sup>2</sup>, L. Poláchová<sup>2,3</sup>, M. Zahoran<sup>1</sup> and Š. Matejčík<sup>1</sup>

<sup>1</sup>Faculty of Mathematics, Physics and Informatics, Comenius University, Mlynská dolina F2, 842 48 Bratislava, Slovakia

<sup>2</sup>Faculty of Chemistry, Brno University of Technology, Purkyňova 464/118, 612 00 Brno, Czech Republic

<sup>3</sup>Department of Physics and Astronomy, The Open University, Walton Hall, MK7 6AA, Milton Keynes, United Kingdom

e-mail: horeszka@gmail.com

## Abstract

A qualitative FTIR analysis of products formed in an abnormal glow discharge was studied at atmospheric pressure and ambient temperature. The used nitrogen-methane mixtures (0.5 – 2 % of methane) was corresponded to the composition of Titan's atmosphere. Fourier Transform Infrared (FTIR) spectra were taken in dependence of discharge current and gas mixture composition. Simple hydrocarbons and nitriles such C<sub>2</sub>H<sub>2</sub>, C<sub>2</sub>H<sub>6</sub>, C<sub>2</sub>H<sub>4</sub>, C<sub>3</sub>H<sub>8</sub>, HCN, NH<sub>3</sub>, HC<sub>3</sub>N and CH<sub>3</sub>CN were identified as the main discharge products. CN and CH<sub>x</sub> radicals have been found to be the main initializers of organic chemistry in our discharge. Such a plasmachemistry may provide some insight into the chemical processes prevalent in the atmosphere of Titan.

**Keywords:** FTIR spectroscopy, atmospheric pressure discharge, Titan like atmosphere, nitrogen-methane gas mixture.

## Introduction

The Cassini space mission to Saturn and the release of its Huygens probe onto its largest moon, Titan, has led to a wealth of data on the atmospheric and surface composition of Titan, presenting us with a set of unexpected results including the observation of hydrocarbon lakes – the first liquid ‘seas’ on a solar system body outside the Earth; and the observation of anions in the upper atmosphere (ionosphere) [1]. In order to understand the physical and chemical processes leading to such observed phenomena, additional laboratory simulations are required.

The dense atmosphere of Titan is mostly composed of N<sub>2</sub> with a few percent of CH<sub>4</sub>. The presence of clouds and strong convective motions are a particular feature of Titan's lower atmosphere. Moreover, charged particles, originating from the Saturnian magnetosphere, can accumulate on droplets within the clouds of the troposphere. Due to these processes the accumulation of charge is observed in Titan troposphere and it can induce strong electric field sufficiently high for the discharge generation (corona, lightning) that can evoke a spread number of chemical reactions in the Titan troposphere [2] leading to the production of higher hydrocarbons, nitriles or even aminoacids [3].

Low pressure experiments have been performed predominantly in glow, RF or microwave discharges [4-9] and the detailed kinetics of chemical reactions in such nitrogen-methane afterglows have been derived [10, 11]. High pressure laboratory studies have been conducted at atmospheric pressure [12-21] using corona, dielectric barrier and spark discharges. The pioneering study by Ponnampereuma *et al* [12] used a dielectric barrier discharge, although it was described by the authors as ‘a semi-corona discharge’ but it had the design of a classical coaxial DBD discharge, where a thin Pyrex tube was placed between two metal cylinders. They reported the production of C<sub>6</sub> to C<sub>9</sub> hydrocarbons from methane in the discharge.

To understand the molecular kinetics during the discharge, the energy distribution as well as knowledge of plasma composition is necessary.

In this paper we provide our results of a qualitative FTIR study of atmospheric glow discharges fed by a N<sub>2</sub>-CH<sub>4</sub> gas mixture.

## Experimental set up

The experimental set up is consisted from a vertically oriented cylindrical stainless steel reactor (i.d. 70 mm, length of 25 cm). The electrode systems were mounted at the reactor central position. In case of the glow discharge study (see Fig. 1), the discharge electrode system had the standard configuration of a classical gliding arc, a pair of stainless steel holders positioned in parallel to the iron electrodes but in this case the plasma was not gliding due to the low flow rate and therefore stable abnormal glow plasma occurred between the electrodes at their shortest distance of 2 mm, thus forming plasma channel with diameter of 1mm. The discharge reactor was connected to the multipass infra-red gas cell (optical length = 3m) equipped with KCl windows and placed in a Nicolet Nexus FTIR spectrometer. The spectra were recorded at a resolution  $2\text{ cm}^{-1}$ , which provided the necessary conditions for both quantitative and qualitative analysis of the products. During the measurement a constant power was set up with electrical parameters  $I = 40\text{ mA}$  and  $U = 400\text{ V}$ . Electrical parameters have been measured by Tektronix oscilloscope using high voltage probe (1:1000) and non inductance resistor. The discharge was powered by a home-made DC HV source.

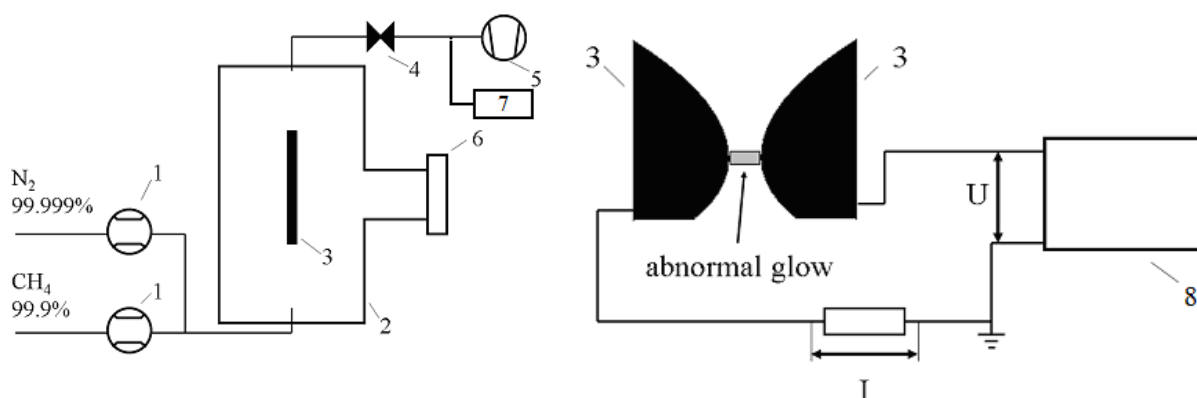


Fig. 1. Simplified scheme of the experimental device for glow discharge study: 1 – mass flow controller; 2 – discharge reactor; 3 – stainless steel electrode; 4 – vacuum valve; 5 – rotary oil pump; 6 – fused silica window; 7 – FTIR spectrometer with external GC-MS analyzer; 8 – HV power supply.

The measurements were carried out in flowing regime for a total flow rate of 200 Sccm. The flow rates for both  $\text{CH}_4$  and  $\text{N}_2$  channels were regulated using MKS mass flow controllers. The present experiment was performed for a constant  $\text{N}_2:\text{CH}_4$  ratio (2%  $\text{CH}_4$  in  $\text{N}_2$ ) at atmospheric pressure. The experiments were carried out at ambient temperatures. The discharge was typically operated for between 60 and 120 minutes during which time the nascent reactor temperature (as measured by thermocouples on the reactor walls) did not rise above 320 K. Whole device was prevacuated before measurement by rotary oil pump to keep the system as oxygen free. It should be just noted that gaseous samples were collected at the reactor exhaust by using a syringe for a further GC-MS analysis. However, this study is a subject of other article.

## Results and discussion

A typical FTIR spectrum obtained *ex-situ* by passing IR beam through the discharge volume is shown in Figure 2. In this discussion five spectral regions are considered in the quantitative analysis: R1 ( $3500\text{--}3000\text{ cm}^{-1}$ ); R2 ( $3000\text{--}2700\text{ cm}^{-1}$ ); R3 ( $2280\text{--}2000\text{ cm}^{-1}$ ); R4 ( $1800\text{--}1200\text{ cm}^{-1}$ ) and R5 ( $1200\text{--}600\text{ cm}^{-1}$ ). Characteristic bending and stretching vibrational frequencies were taken from spectral databases [22, 23].

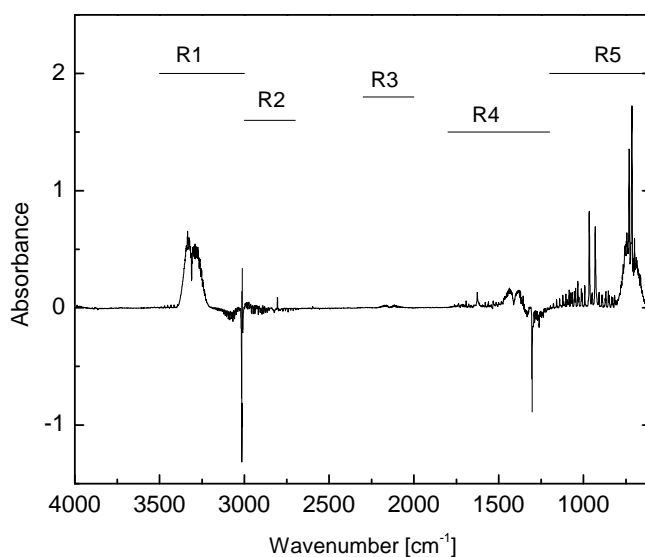


Fig. 2. Typical FTIR spectra of organic products formed in atmospheric glow discharge.

The broad bands in *R1* are consistent with the presence of  $-\text{CH}$  functional group. Features ranging between  $3200$  and  $3400\text{ cm}^{-1}$  are generally assigned to the stretching modes of alkynes and nitriles having a  $-\text{CH}$  groups, furthermore weaker band of aromatic rings between  $3000$ - $3100\text{ cm}^{-1}$ . However, sharp bands of stretching vibrations of  $\text{NH}$  functional groups are built in this region at  $3334$  and  $3342\text{ cm}^{-1}$ .

*Spectral region R2* shows a set of bands which can be assigned to  $-\text{CH}_2-$  and  $-\text{CH}_3$  functions (symmetric and antisymmetric stretching modes at around  $2800$ - $3100\text{ cm}^{-1}$ ). Although, the formation of amines is less possible in such experimental conditions (low concentration of primary H atoms), we can not neglect the weak spectral feature around  $3220\text{ cm}^{-1}$  which could be consistent with either the stretching mode of  $-\text{NH}_2$  or  $-\text{NH}$  functional group. Nevertheless, secondary and tertiary amines connected to  $\text{CH}_2$  or  $\text{CH}_3$  groups can be excluded, because of the lack of features between  $2820$ - $2750\text{ cm}^{-1}$ . The characteristic in-plane aromatic-H stretching modes at  $3050\text{ cm}^{-1}$  are *not* observed, suggesting the lack of or a very low abundance of any protonated aromatic or heteroaromatic rings, containing H bound to C.

*Region R3* reveals a weak band around  $2200\text{ cm}^{-1}$  that usually exhibits  $-\text{CN}$ ,  $-\text{NC}$  and  $-\text{N}=\text{C}=\text{N}-$  units in range  $2215$ - $2260$ . Furthermore, weak  $\text{C}\equiv\text{C}$  stretching is occurred in range  $2100$ - $2140\text{ cm}^{-1}$ .

*Spectral region R4* exhibits a very complex pattern which results from wide variety of functional groups. This spectral range exhibits main peaks at  $1736$ ,  $1626$ ,  $1613$ ,  $1595$ ,  $1579$ ,  $1560$ ,  $1543$ ,  $1532$ ,  $1484$ ,  $1444$ ,  $1435$ ,  $1371$ ,  $1356$  and  $1349\text{ cm}^{-1}$ . These peaks are consistent with  $\text{C}=\text{C}$ ,  $\text{C}=\text{N}$  and  $-\text{NH}_2$  functional groups. The bending modes of these functional groups  $-\text{CH}_2-$  and  $-\text{CH}_3$  are placed in range  $1405$ - $1465\text{ cm}^{-1}$ , resp.  $1430$ - $1470\text{ cm}^{-1}$ . The peak near  $1486\text{ cm}^{-1}$  is a ring stretching of an aromatic compound.

Finally, *R5* is the so-called fingerprint region that was the main identifier of major and minor products formed in the discharge gap. Strong sharp spectral features with peaks centered at wavenumbers  $966$ ,  $930$ ,  $729$ ,  $713$  are assigned to the Q branches of  $\text{NH}_3$ ,  $\text{C}_2\text{H}_2$  and  $\text{HCN}$  that can be well quantified. Weaker absorptions observed at  $1158$ ,  $1054$ ,  $944$ ,  $922$ ,  $872$ ,  $747$  are characteristic bending vibrations of  $\text{C}_3\text{H}_8$ . Band placed at  $673\text{ cm}^{-1}$  together with aromatic ring stretching at around  $1484\text{ cm}^{-1}$  is assigned to benzene. The detection of  $\text{C}_3\text{H}_8$  and  $\text{C}_6\text{H}_6$  is quite difficult because the  $\text{CH}_2$  rocking at  $747\text{ cm}^{-1}$  and  $\text{CH}$  bending at  $673\text{ cm}^{-1}$  are overlapped with the strong P/R-branches of  $\text{C}_2\text{H}_2$  and  $\text{HCN}$ . Small but detectable amount of 1,3-butadiene ( $\text{C}_4\text{H}_6$ ) band were found at  $1112$ ,  $988$  and  $908\text{ cm}^{-1}$ .

Using HITRAN and NIST spectral databases [22, 23] the both stretching and bending regions could be qualitatively assigned to simple organics. A weak  $\text{CH}_3$  bending deformation can be seen in

range from 1350-1470  $\text{cm}^{-1}$ , which together with the C-H  $\text{sp}^3$  stretching at 2973  $\text{cm}^{-1}$  is assigned to  $\text{C}_2\text{H}_6$ . Besides the remaining  $\text{CH}_4$  (negative absorbance data at 3200–2704  $\text{cm}^{-1}$  and 1408–1169  $\text{cm}^{-1}$ ) obvious infrared spectra absorption bands were observed at the wave numbers 3386–3217  $\text{cm}^{-1}$  which is the typical C-H  $\text{sp}^1$  stretching band of hydrogen cyanide HCN and acetylene  $\text{C}_2\text{H}_2$ . However, we found detectable features corresponding to  $\text{C}_2\text{H}_4$  (which has a characteristic band between 800-1100  $\text{cm}^{-1}$ , maximum at 949  $\text{cm}^{-1}$  and a band between 3000-3200  $\text{cm}^{-1}$ , maximum at 3138  $\text{cm}^{-1}$ ). The peak found at 663  $\text{cm}^{-1}$ , is a strong  $\nu_5$  band of cyanoacetylene  $\text{HC}_3\text{N}$ . We have also looked for acrylonitrile's  $\nu_{10}$  band at 954, allyl cyanide's  $\nu_{20}$  band at 942 and methacrylonitrile's  $\nu_{20}$  band at 928  $\text{cm}^{-1}$  but no obvious absorption peaks were observed by such candidate products. Relatively strong bands of propionitrile can be seen at 1075  $\text{cm}^{-1}$ . Acetonitrile,  $\text{CH}_3\text{CN}$  was also expected from the measurements since it has been detected by Cassini-Huygens and its weak characteristic spectral features can be found at around 1042, 1447  $\text{cm}^{-1}$ . From the measured absorbance the concentrations of major compounds were calculated using the Beer-Lambert formula with molecular IR absorption cross-section data being taken from the above mentioned database [22, 23]. Therefore, concentrations of  $\text{C}_2\text{H}_2$ , HCN,  $\text{C}_2\text{H}_6$ ,  $\text{NH}_3$  and  $\text{CH}_3\text{CN}$  were estimated at values 250, 400, 100, 200 and 150 ppm, in the given experimental conditions. All other measured compounds have concentrations below the detection limit 50 ppm. Unfortunately, some minor compounds detected by GC-MS analysis could also not be found by FTIR technique due to their low concentrations and small absorption cross-sections ( $\text{C}_4\text{H}_2$ ,  $\text{C}_3\text{H}_4$ ). As a matter of fact, it can be briefly pointed out that CH,  $\text{CH}_3$  and CN radicals determine the whole organic plasmachemistry.

## Conclusions

In this paper we present the results of FTIR study of the gaseous products formed in glow discharge filled with an atmospheric pressure mixture of  $\text{N}_2:\text{CH}_4 = 98:2$  operated in a flowing regime at constant electrical parameters and ambient temperature. FTIR analysis of the gaseous products showed that HCN,  $\text{C}_2\text{H}_2$ ,  $\text{NH}_3$ ,  $\text{CH}_3\text{CN}$  and  $\text{C}_2\text{H}_6$  are the main products of our  $\text{CH}_4/\text{N}_2$  glow plasma. The yields of these compounds are such that  $\text{HCN} > \text{C}_2\text{H}_2 > \text{NH}_3 > \text{CH}_3\text{CN} > \text{C}_2\text{H}_6$ . Furthermore,  $\text{HC}_3\text{N}$ ,  $\text{C}_3\text{H}_8$ ,  $\text{C}_2\text{H}_5\text{CN}$  and benzene  $\text{C}_6\text{H}_6$  have also been found in traces but due to our spectral limitations they could not be well quantified. Such experiments can provide information that aids our understanding of processes in Titan's atmosphere. Within the discharge we observed the formation of the same compounds as observed in Titan's atmosphere the Huygens Surface Package and by Cassini Observer.

However, we note that different discharges have different sources of ions/excited molecules and thus when using discharges as a planetary atmosphere mimic it is necessary to carefully define the plasma conditions and their relevance to specific regions of the planetary's atmosphere. For lower pressures the glow discharge is specific while the higher pressure regions are related to gliding arc, atmospheric glow, corona and DBD discharges.

Based on the presented data and by comparison of the *ex-situ* diagnostics (FTIR, GC-MS) the kinetic model will be developed in near future.

## Acknowledgements

This work has been supported by the following projects: Research plan of Czech Ministry of Education No. MSM0021630501, APVV 0365-07, Grant UK/140/2010, Slovak Grant Agency project SK-CN-0029-07, Slovak Research and Development Agency VEGA 1/0051/08, ESF COST Actions CM0601, CM0805, EUROPLANET TNA2 and EIPAM.

## References

- [1] V. Vuitton, P. Lavvas, R.V. Yelle, M. Galand, A. Wellbrock, G.R. Lewis, A.J. Coates, J.-E. Wahlund, *Planet. Space Sci.* **57** (2009) 1558.
- [2] V. Vuitton, R. V. Yelle, P. Lavvas, *Philosoph. Trans. Royal Soc. A*, (2009) doi:10.1098/rsta.2008.0233.
- [3] S. Vinatier *et al.*, *Icarus* **188** (2007) 120.
- [4] Bernard J M, Quirico E, Brissaud O, Montagnac G, Reynard B, McMillan P, Coll P, Nguyen M J, Raulin F and Schmitt B 2006 *Icarus* **185** 301.
- [5] Pintassilgo C D, Loureiro J, Cernogora G and Touzeau M 1999 *Plasma Sources Sci. Technol.* **8** 463.
- [6] Szopa C, Cernogora G, Boufendi L, Correia J and Coll P 2006 *Planetary and Space Science* **54** 394.
- [7] Imanaka H, Khare B N, Elsilva J E, Bakes E L O, McKay C P, Cruikshank D P, Sugita S, Matsui T and

- Zare R N 2004 *Icarus* **168** 344.
- [8] Sekine Y, Imanaka H, Matsui T, Khare B N, Bakes E L O, McKay C P and Sugita S 2008 *Icarus* **194** 186.
- [9] Coll P, Coscia D, Gazeau M C, de Vanssay E, Guillemin J C and Raulin F 1995 *Adv. Space Res.* **16** 93.
- [10] Pintassilgo C D, Jaoul C, Loureiro J, Belmonte T and Czerwiec T 2007 *J. Phys. D: Appl. Phys.* **40** 3620.
- [11] Legrand J C, Damiy A M, Hrach R and Hrachova V 1998 *Vacuum* **50** 491.
- [12] Ponnampertuma C and Woeller F 1964 *Nature* **203** 272.
- [13] Gonzalez R N and Ramirez S I 1997 *Adv. Space Res.* **19** 1121.
- [14] Gonzalez R N, Ramirez S I, de la Rosa J G, Coll P and Raulin F 2001, *Adv. Space Res* **27** 271.
- [15] Ramirez S I, Gonzalez R N, Coll P, and Raulin F 2005 *Advances in Space Research* **36** 274.
- [16] G. Horvath, J. D. Skalny, N. J. Mason and M. Zahoran M., 2009 *Plasma Sources Sci. Technol.* **18** 034016.
- [17] Plankensteiner K, Reiner H, Rode B M, Mikoviny T, Wisthaler A, Hansel A, Mark T D, Fischer G, Lammer H and Rucker H O 2007 *Icarus* **187** 616.
- [18] Mfopara A, Kirkpatrick M J and Odic E, 2009 *Plasma Chem Plasma Process* **29**, 91–102.
- [19] G Dilecce, P F Ambrico and S De Benedictis, 2010 *J. Phys. D: Appl. Phys.* **43** 124004.
- [20] G Dilecce, P F Ambrico, G Scarduelli, P Tosi and S De Benedictis, 2009 *Plasma Sources Sci. Technol.* **18** 015010.
- [21] G Scarduelli, G Guella, I Mancini, G Dilecce, Sa De Benedictis, P Tosi 2009 *Plasma Processes and Polymers* **6**, 27 - 33.
- [22] Rothman L.S., Gordon I.E., Barbe A., Benner D.C., Bernath P.F., Birk M., Boudon V., Brown L.R., Campargue A., Champion J.-P., Chance K., Coudert L.H., Dana V., Devi V.M., Fally S., Flaud J.-M., Gamache R.R., Goldman A., Jacquemart D., Kleiner I., Lacombe N., Lafferty W., Mandin J.-Y., Massie S.T., Mikhailenko S.N., Miller C.E., Moazzen-Ahmadi N., Naumenko O.V., Nikitin A.V., Orphal J., Perevalov V.I., Perrin A., Predoi-Cross A., Rinsland C.P., Rotger M., Simeckova M., Smith M.A.H., Sung K., Tashkun S.A., Tennyson J., Toth R.A., Vandaele A.C., Vander Auwera J., "The HITRAN 2008 molecular spectroscopic database," *Journal of Quantitative Spectroscopy & Radiative Transfer* **110**, 533-572 (2009)
- [23] <http://webbook.nist.gov>, "Molecular Vibrational Frequencies" by T. Shimanouchi.

# Interaction of low-temperature plasma with fabric: study by computer simulations

P. Bartoš<sup>1,2</sup>, P. Špatenka<sup>1,2</sup>

<sup>1</sup>University of South Bohemia, Pedagogical Faculty, Department of Physics  
Jeronýmova 10, 371 15 České Budějovice, Czech Republic

<sup>2</sup>Technical University of Liberec, Hálkova 6, 461 17 Liberec, Czech Republic

e-mail: bartos-petr@seznam.cz

## Abstract

The article deals with computer simulations of the interaction of textile materials with reactive particles created in a low-temperature plasma. By the help of the continuous model, a total flux of reactive particles to the surface of the fibre is determined. It is shown that the flux is not uniform at all points of the material and that the working of the material happens even in places which are not oriented directly to the plasma discharge.

By the help of the particle model, a capacity of reactive particles to penetrate to the fibrous structure of the surface is consequently investigated, whereas results for a pressure dependence of this process are presented.

**Keywords:** Plasma surface modification, surface treatment, penetration, textile

## Introduction

A modification of some properties of textile materials by the help of the plasma discharge has recently become, because of its economically undemanding character and environmental friendliness, a popular technology and the one frequently used in practice, and is affected in a range of applications. This can be illustrated by, for instance, plasma modifications resulting in a reduction of textile wettability, surface modifications influencing the elevation of colorant adhesive power or leading to an improvement of fabric abrasion resistance. Materials with specific properties, such as photo-catalytically active surfaces, are also created.

One of the main parameters is the quality of the layer being applied – its thickness, adhesion to the surface or the depth in which the surface of the material has been influenced by reactive particles. One of the ways leading to better understanding of the process of interaction of plasma with the fibre surface is the utilization of procedures of computer simulation. Several studies solving partial tasks have been published in this field recently. The mathematical description of the fibres in a layer is discussed, for instance, in [1-3], the techniques of computer simulation of the interaction of plasma with geometrically complicated surfaces is presented in [4].

Many experimental measurements have also been realized. For instance, N. Geyter states [5], that, during a plasma modification of several layers of the textile material, it is the upper layer which is worked best and which is manifested in experiments also by its best hydrophilicity. The second and every other layer of textile consequently manifest worse results in the test of hydrophilicity, while the orientation of the layer during the process of deposition also plays a vital role – it is markedly lower at the side reverse from the affecting plasma. Similar results have also been reached by other authors [6].

In this short contribution, a macroscopic model enabling to estimate the total flux of reactive particles impacting on the given part of the fabric surface will be described. In the second case, consequently, a particle model is described by the help of which the capability of particles to penetrate to the structure of the textile material is determined. By proper interpretation of the results achieved by solving these models, for instance, optimum durations of the deposition process can be determined.

## Model description

### A) Continuous model

The algorithm described in [7] served as a base for the continuous model being created. The model makes it possible to estimate fluxes of the particles impacting on various parts of the textile material. A mathematical description of the arrangement of the warp and the weft in a fabric is based on the Peirce approximation [8]. The fabric originates as a file of perpendicularly intertwined fibre bundles whose shape conserves a round shape at the section. This mathematical model is slightly modified for the needs of computer simulations and the section of the fibre is considered as elliptical. This corresponds better to the reality when force proportions between individual fibres violate the round shape of bundles.

The description of plasma behaviour subsequently considers only a diffusion of reactive particles in the working area according to the Fick's law. Although this model makes use of many simplifications, it enables, with regard to the geometrical demand factor of the problem, to create a clearer idea of the flux of chemically active particles to the textile surface. The calculation of the model reveals, for instance, that the bottom layer of the fabric which is not exposed to direct action of plasma is impacted by 40 % of particles in comparison to the layer oriented in the direction of the discharge [7]. In places where the warp and the weft intersect, the total flux of particles is consequently minimal, probably due to the influence of a mutual shielding effect. The acquired results correspond well with experimental observations.

### B) Particle model

The computer model used for a research of the penetration of chemically active particles between individual fibres of the textile material is based on the particle simulation technique. In the first phase, the location of individual fibres in the warp (resp. weft) is generated by the help of the Monte Carlo method. In doing so, the fibres are supposed to be placed in a parallel way and they can be considered to be endless long cylinders of circular section. This requirement can be considered, due to the mean free path and the distance between threads in the fabric, to be justifiable.

In the second phase of calculation, the movement of active particles is being observed. Due to the fact that the actions of force on the particle can be ignored, it is supposed that a change of direction of a moving particle occurs only due to collisions between gas particles. A random collision is realized in the model by using the known relationship for putting a random free path to play

$$\zeta = -\lambda \ln \gamma, \quad (1)$$

and this relationship can be deduced for monoenergetic particles from the Poisson division.

In the relationship,  $\zeta$  stands for the random free path,  $\lambda$  stands for the mean free path and  $\gamma$  denotes a random number with uniform division of the interval (0,1).

The value for the mean free path of oxygen radicals was taken from [9], the recalculation for various pressures was performed according to the relationship [10]

$$\lambda_{1330} = \lambda_{133} \cdot \sqrt{\frac{133}{p}}. \quad (2)$$

The influence of various values of the so-called sticking coefficient is further considered in the model. If the particle impacts upon the surface of the particle, a random number of the interval  $\langle 0, 1 \rangle$  is put to play and if its value is lower than the value of the sticking coefficient, the particle is considered to be absorbed at the surface of the fibre. If it be to the contrary, a new location and velocity components of the particle are calculated by the help of methods of analytical geometry as if it really bounced back from the fibre to a space.

## Results and discussion

For the production of textiles, fibres of various diameters are used. For the needs of testing the model, we have chosen a value of 50 micrometers as a diameter of the fibre. The distance between individual fibres in a bunch generally varies between 1-10 micrometers [11].

By the help of the continuous model, a total flux of particles to individual bunches of threads in the fabric has been determined (i.e., to the warp and to the weft). Figure 1 shows that darker colours, corresponding to lower values of the flux, are found in areas of the intersection of fibres. Lower values can be observed also at the side of the textile which is diverted from plasma – in comparison with the flux of particles at the near side, it is lower by about 60 percent.

The results of calculations of the particle model show that the depth of penetration of active particles between individual fibres diminishes in connection with an increasing pressure (see Figure 2). According to some experimental measurements performed for discharges under atmospheric pressure, for example [11-12], the process of penetration is even minimal despite considerably long deposition times. Although in our model a particle disappears only in case of impacting upon the surface of the fibre, in reality the reactive oxygen radical disappears also in other situations, for instance after a collision with another particle. Therefore, the lifetime of the particle is finite and, above all under higher pressure, the particle disappears much sooner than it manages to penetrate into deeper levels of the material. In this regard it can be expected that the real depth of deposition will be smaller than the values acquired by the computer model. To perform a high-quality depth deposition in the whole volume of the fibre, the usage of the discharge under low or average pressures is consequently more favourable. The best results will be reached in cases when the size of a pore between fibres is comparable to the mean free path of active particles.

The capability of particles to penetrate between fibres is also connected with the adhesion of particles at the surface of the fibre. This one is described by the value of the so-called sticking coefficient which determines which number of impacted particles will adhere to the surface. The results of the model show that, together with a decreasing value of the coefficient, the depth of penetration rises. This dependence is considerably significant and it manifests an exponential character. Results presented in Figure 2 were obtained for sticking coefficient equal to 100 percent, i.e. all particles impacting on the surface of the fabric are captured. This is a little unreal assumption, because the value is usually much lower and, therefore the penetration depth is significantly higher.

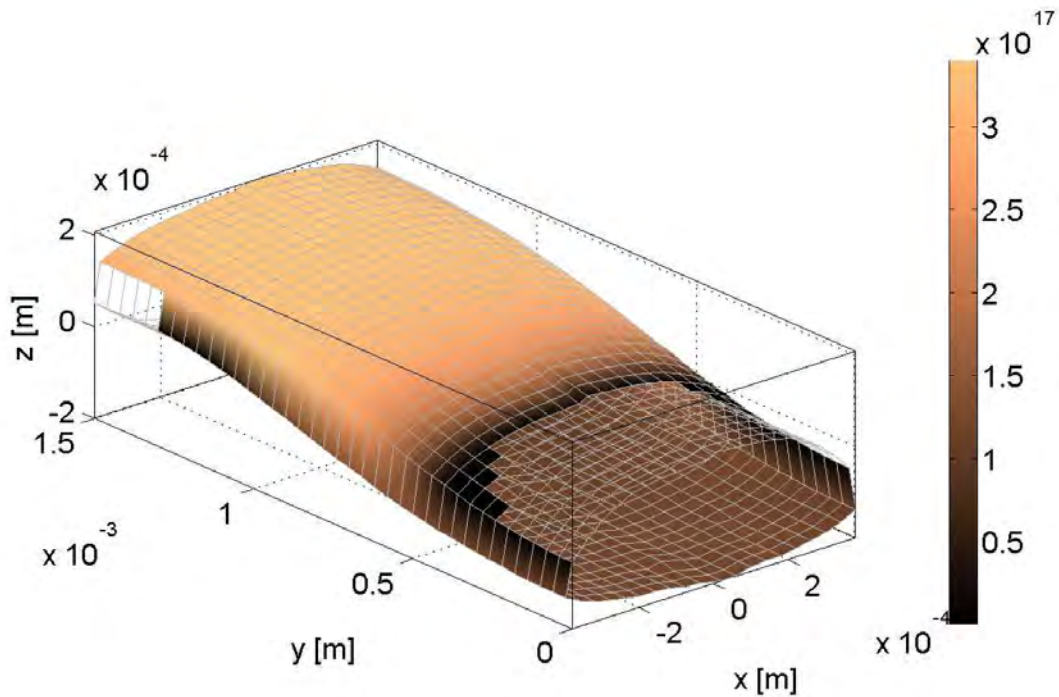


Fig. 1. The flux of reactive particles to a part of a bunch of threads in the warp acquired by solving the continuous model.

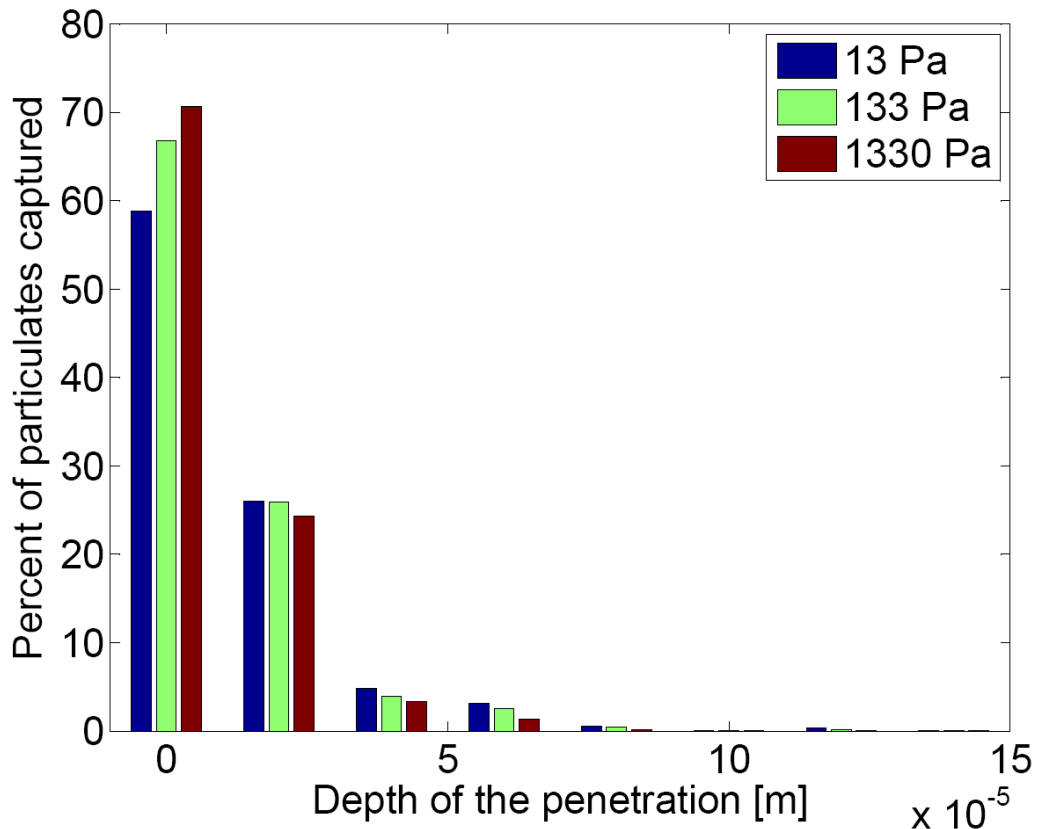


Fig. 2. The dependence of a number of particles caught at the surface by a thread depending on the depth of the thread in a bunch and on the pressure of gas.

### Acknowledgements

The work is supported by the grant projects NANOPIN MSMT 1M0577 and KAN101120701.

### References

- [1] J. Hofstee, F. van Keulen, *Composite Structures*, 54, 2001, pp. 179-195.
- [2] B. Sirkova, *Mathematical description of the fibres interlacing in the fabrics by the fourier series*, Ph. D. Thesis, Liberec, Czech Republic, 2002.
- [3] I. Ivanov, A. Tabiei, *Composite Structures*, 54, (2001), pp. 489-496.
- [4] P. Bartoš, P., *Contrib. Plasma Phys.* 48, (2008), 406 – 411.
- [5] N. De. Geyter, R. Morent, C. Leys, *Plasma Sources Sci. Technol.* 15, (2006), pp. 78-84.
- [6] C.X. Wang et al., *Surface and Coatings Technology* 202, (2007), pp. 77–83.
- [7] P. Bartoš, P. Špatenka, L. Volfová, *Plasma Process. Polym.* 6, (2009), pp. S897–S901.
- [8] F. T. Peirce, *J. Text.*, 28, (1937), pp. T45–96.
- [9] P. Černý, *Vacuum*, 84, Issue 1, (2009), pp. 97-100.
- [10] P. Bartoš, P. Špatenka, *Plasma processes and Polymers*, submitted.
- [11] H. U. Poll, U. Schladitz, S. Schreiter, *Surf. Coat. Technol.* 142–144, 2001, 489–93.
- [12] T. Vatuna, J. Píchal, P. Špatenka, J. Koller, L. Aubrecht, A. Kolouch, *Proc. 2nd Int. Workshop on Cold Atmospheric Pressure Plasmas: Sources and Applications (CAPPSA2005)* (Bruges) pp. 275–80, 2005.

# Plasma Treatment of Corrosion Layers from Brass

V. Sázková<sup>1</sup>, L. Řádková<sup>1</sup>, F. Krčma<sup>1</sup>, M. Zmrzlý<sup>2</sup>, R. Prikryl<sup>2</sup>, M. Zahoran<sup>3</sup>

<sup>1</sup> Institute of Physical and Applied Chemistry and <sup>2</sup> Institute of Materials Chemistry, Faculty of Chemistry, Brno University of Technology, Purkyňova 118, 612 00 Brno, Czech Republic

<sup>3</sup> Department of Experimental Physics, Faculty of Mathematics Physics and Informatics, Comenius University in Bratislava, Mlynská dolina, 842 48 Bratislava, Slovakia

e-mail: xcsazavska@fch.vutbr.cz

## Abstract

New efficacious way of restoration and preservation of metal archaeological artifacts is described. This method is based on generation of reactive atomic hydrogen in low pressure RF hydrogen plasma discharge. Atomic hydrogen reacts with oxygen from corrosion layers of sample and forms OH radical. The value of integral intensity of OH radicals represents quantitative ablation of oxygen from corrosion layer. Another monitored magnitude was temperature of samples. Sample temperature is very significant indicator for protection sample against metallographic changes of metal bulk material and therefore damage of samples. We proved that the corroded sample became much less warm in pulsed than in continuous regime. Thus there is no risk of metallographic changes or damage of sample in pulsed regime.

**Keywords:** corroded brass, radio-frequency plasma, corrosion, electron microscopy, OES.

## Introduction

The plasma treatment of archaeological objects is based on a partial reduction of the incrustation and corrosion layers by RF low pressure hydrogen plasma [1, 2]. The corrosion removal process is very complex. It is not fully known up to now if reducing effect with atomic hydrogen or corrosion sputtering induced by heavy particles plays the main role.

The method is based on using RF low-pressure hydrogen plasma. It was evolved as a by-product of plasmachemical deposition research. This method is a relatively new technique developed by Veprek mainly for iron objects during the 1980s [3, 4]. Compared to conventional techniques, this method provides several significant advantages, as such the possibility of appearance of tiny details of the object shape and of its original surface [5]. The reduced corrosion layer of objects becomes brittle. It can be removed easily by conservators and thus mechanical stress applied to the objects decreases [6].

The technology is used mainly for iron or silver based materials, but even for them, the optimal conditions for the corrosion removal are not fully known yet. Knowledge of other metallic materials is more or less completely missing.

The optical emission spectroscopy of OH radical was used for the process monitoring [7]. Obtained spectrum was also used for the rotational temperature calculation. Sample temperature was measured during plasma treatment by thermocouple. The application of pulsed discharge regime can also conserve the corrosion removal process at lower mean power and thus the treated samples are affected by lower heating stress [7].

## Experimental

Brass is an alloy of copper and zinc, but EDS analysis shows that the used brass has three components. The real atomic composition of brass is 38,1% Zn; 5,2% Pb and 56,8% Cu. Detailed structure from electron microscopy is shown in Figure 1. Structure formed by solid solution of zinc in copper (location A), intermetallic compound CuZn (location B), and lead patterns (location C).

Each archaeological object is an original, and it has its "corrosion history". Due to this fact, any universal way of corroded object treatment is difficult or even impossible to propose. This problem was solved by means of model samples (identical material and corrosion) which were compared to results in the dependence on treatment conditions. Brass samples were prepared using ammonium solution, the samples were stored in this atmosphere for two weeks. Picture of the sample is shown in Figure 2 and composition of corrosion is 24,52% C; 46,69% O; 24,13% Cu and 4,65% Zn (Figure 8).

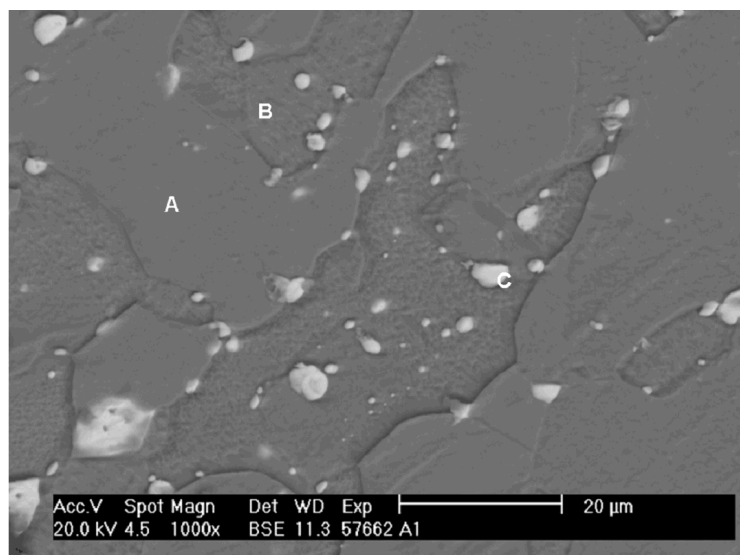


Fig. 1. Metallographic cut of brass. Location A is solid solution of zinc in copper, location B is intermetallic compound CuZn, and white areas in locations C represent lead.



Fig. 2. Corroded sample of brass.

The plasma treatment was carried out in the Quartz cylindrical reactor (i.d. 95 mm, length of 90 cm) with outer copper electrodes (Figure 3). The capacitive coupled RF power supply (frequency of 13.56 MHz) gave the total power up to 600 W in continuous or pulsed regime. We used pulses with duty cycle of 75 %, 50 %, 25 % and frequency was 100 Hz (25 % pulse means 2,5 ms on and 7,5 ms off). Flowing plasma was created in pure hydrogen (gas flow of 50 sccm) at pressure of 150 Pa. The mean applied discharge power was 100–400 W depending on the duty cycle. The real temperature of samples was measured continuously by means of thermocouple installed inside the sample.

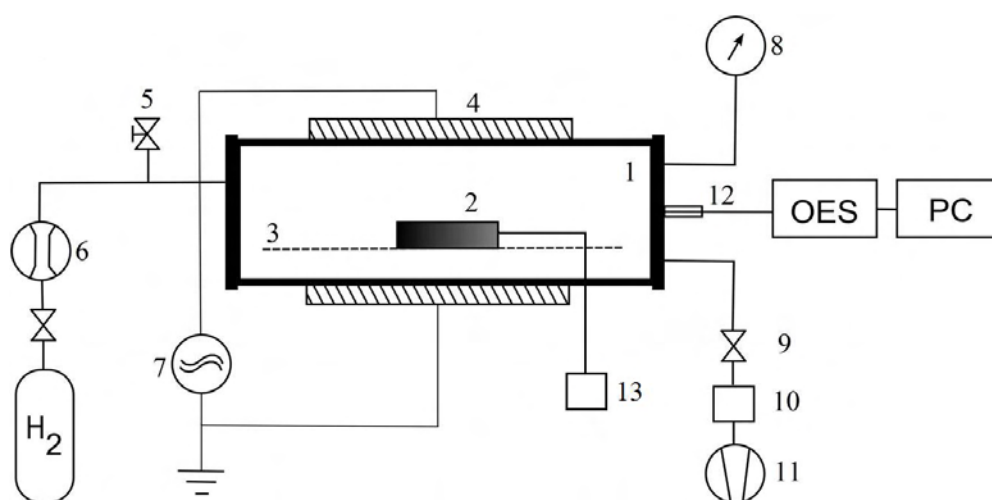


Fig. 3. Experimental set-up: 1 – quartz discharge reactor (90 cm long, i.d. 95 mm); 2 – corroded sample; 3 – glass sample holder; 4 – outer copper electrodes; 5 – air-inlet valve; 6 – mass flow controller; 7 – RF power supply and matching network; 8 – pressure gauge; 9, 10 – valves; 11 – rotary oil pump; 12 – optical fibre; 13 – thermocouple

The optical emission spectroscopy of OH radical was used for the process monitoring using Ocean Optics HR 4000 spectrometer with 2400 gr/mm grating. Atomic hydrogen reacts with oxygen from corrosion layers and forms OH radical (in excited state) [8]. OH radical emits in the spectral region of 305–325 nm, and its integral intensity area this region was used for the quantitative analysis of oxygen removal from the corrosion layer [6]. Plasma treatment was stopped when value of relative intensity of OH radicals reached one tenth of maximum OH radical intensity [7]. The plasma treatment duration was 60–120 minutes depending on the duty cycle. Simultaneously, the rotational temperature from lower rotation levels of OH radical spectrum was calculated.

### Results and discussion

Reduction process is characterized by generated OH radicals in plasma discharge. We calculated rotation temperature from spectrum obtained by means of optical emission spectroscopy. Rotation temperature has predicative value only in the active continuous plasma discharge. In pulsed regime, plasma discharge occurs periodically therefore rotational temperature cannot be equal to temperature of sample. Sample temperature must reach always lower values with respect to rotational temperature. On the contrary, sample temperature can reach up to the rotational temperature in continuous regime. In Figure 4, rotational temperature is shown in both regimes around  $(600 \pm 100)$  K. Sample temperature reach its maximum at 425 K for power of 300 W in 50% pulse, and 500 K for power of 300 W in continuous regime.

It is obvious that the sample temperature shifts according to the used power regime. Measured temperatures of samples are presented in Figures 5, 6, 7 for three applied power. Sample temperature is not such high in the pulsed regime as in the continual regime because the sample was exposed to lower plasma influence in the pulsed regime than in the continual regime.

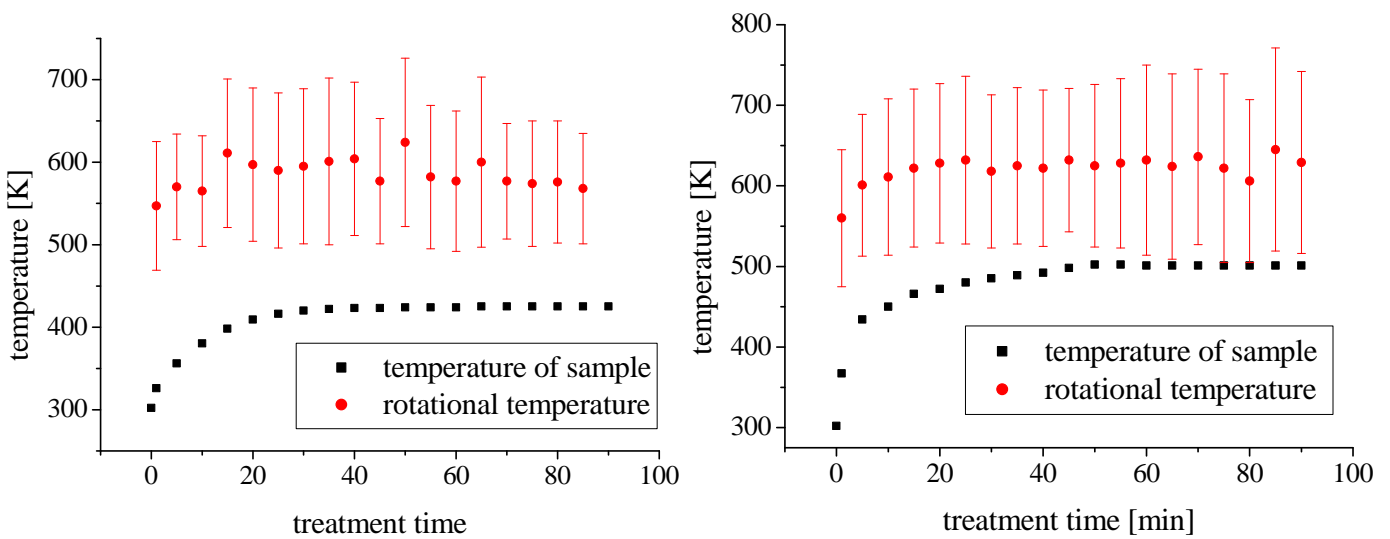


Fig. 4. Comparison of rotation temperature and sample temperature during plasma treatment at 300 W, 50% pulse (left), and 300 W in continual regime (right).

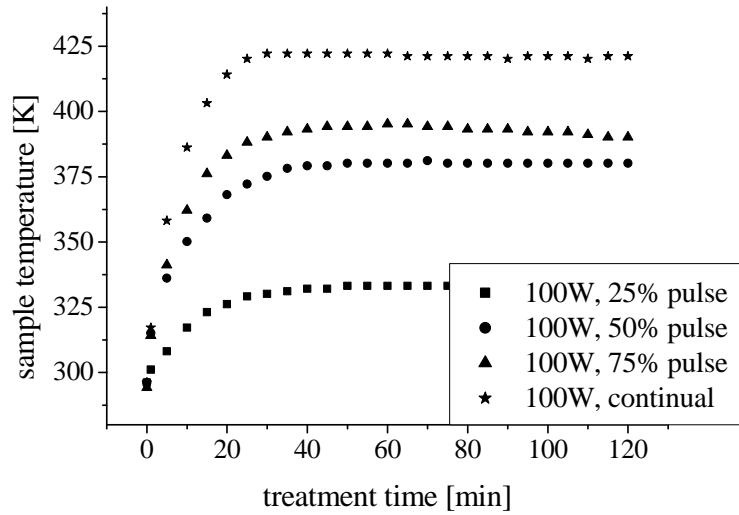


Fig. 5. Temporal evaluation on the sample temperature during the plasma treatment at 100 W.

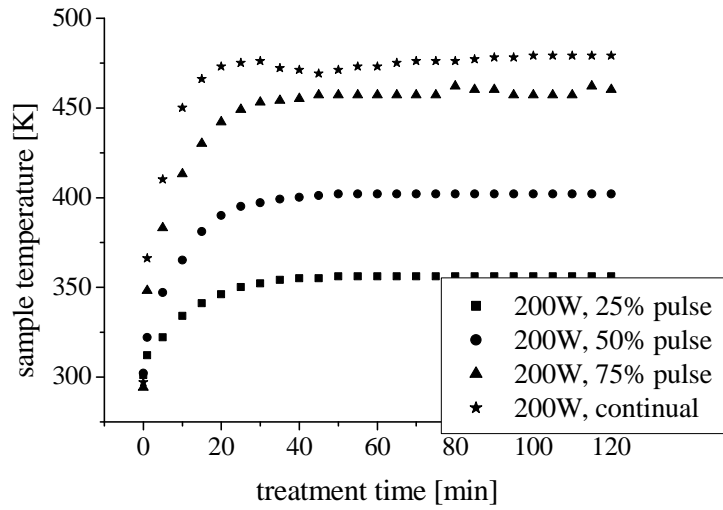


Fig. 6. Temporal evaluation on the sample temperature during the plasma treatment at 200 W.

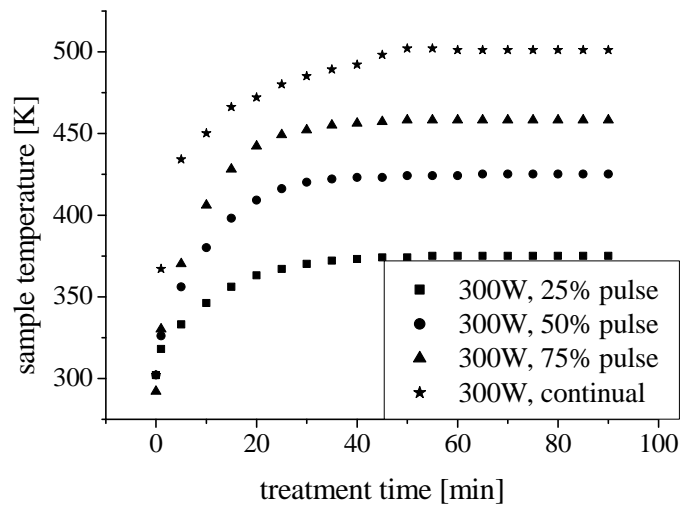


Fig. 7. Temporal evaluation of the sample temperature during the plasma treatment at 300 W.

Very good corrosion removal was observed if samples were treated in continuous plasma regime, but significant heating of samples was observed, too. Treatment in pulsed regimes required higher powers applied during the pulse, but the average energy was lower and thus the sample temperature was not such elevated. EDS analysis (Figure 8) showed the decrease of atomic oxygen abundance, and the increase of copper and zinc abundance after plasma treatment. Accordingly, the corrosion layer was treated only in part. Nevertheless, relatively high atomic oxygen abundance after plasma treatment indicated that reoxidation occurred prior to treated sample analysis. In future, we are going to solve this problem. Treated sample will be put in a box with a protective argon atmosphere promptly after plasma treatment.

Figure 8 shows that power regime significantly influence final treatment of corroded samples. Corrosion removal is nearly directly proportional to the applied power. Unfortunately, the higher power induces sample temperature elevation. The high temperature of sample can induce metallographic changes of metal bulk material and therefore damage of samples [9]. Thus an optimal applied power inducing good corrosion removal without temperature enhancement over critical value is needed.

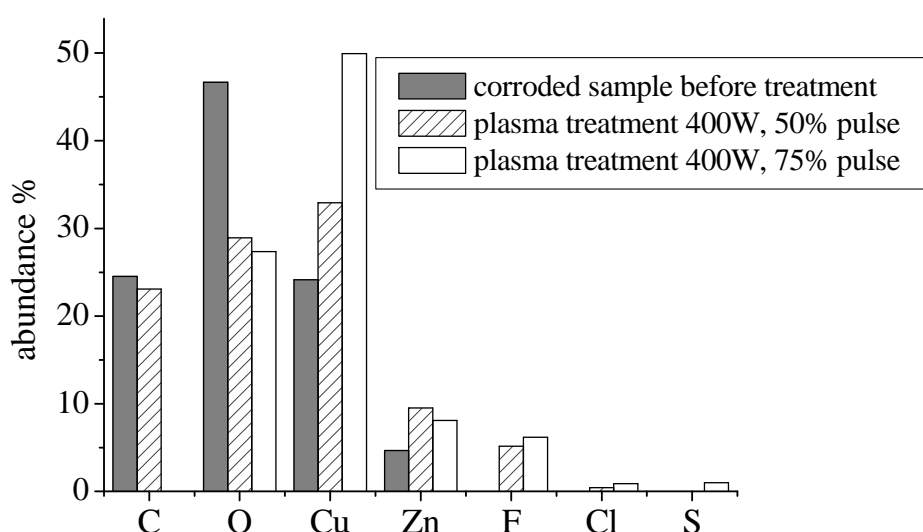


Fig. 8. EDS analysis before (grey column) and after plasma treatment (striped and white column).

## Conclusion

The presented results showed that the corrosion removal process can be effective in the pulsed discharge regime. The main advantage of the pulsed regime is lower heating of sample. The pulse regime disadvantage is that treatment time is longer than in continual regime. We can assume that temperature plays an important role in the kinetics of reduction process. When we used low power of 100 W at 25% pulse, the corroded sample was untreated. On the other side, high power can evocate considerable sample heating that can result in the damage of the sample. The detailed analysis of the sample composition after treatment is the main goal of our contemporary research.

## Acknowledgements

This work has been supported by the Czech Science Foundation, project No. 104/09/H080.

## References

- [1] I. Kotzamanidi et al. (2002). *Anti-Corr. Methods and Materials*, 49, 256.
- [2] M. Klima, L. Zajickova, J. Janca, *Zeitsc. für Schweizerische Archäologie und Kunst-geschichte* 54 (1997) 29
- [3] S. Veprek, Ch. Eckmann, J. Elmer *Plasma Chem. Plasma Process.* 8 (1988)
- [4] S. Veprek, J. Patscheider, J. Elmer, *Plasma Chem. Plasma Process.* 5 (1985) 201.
- [5] S. Veprek, J. Elmer, Ch. Eckmann, M. Jurcik-Rajman, *J. Electrochem. Soc.* 134 (1987)
- [6] Z. Raskova, F. Krcma, M. Klima, J. Kousal, *Czech. J. Phys.* 52 (2002) D927.
- [7] V. Sazavska et al., *J. Phys.: Conf. Ser.* 207, (2010)
- [8] M. Perlík, *Konzervátorský a restaurátorský seminář, České Budějovice*, 89 (2001), in Czech
- [9] M. Cihlár, Dipl. thesis, *Diagnostics of plasma during reduction of corrosion layers from copper*, Brno, (2005)

# Surface activation of the polycarbonate in atmospheric pressure plasma generated in air and Helium by Surface Dielectric Barrier Discharge (SDBD)

R. Vladoiu<sup>1</sup>, V. Dinca<sup>1</sup>, A. Mandes<sup>1</sup>, M. Cernak<sup>2,3</sup>

<sup>1</sup>Department of Physics, Ovidius University, Constanta, 900527, Romania

<sup>2</sup>Department of Experimental Physics, Faculty of Mathematics, Physics and Informatics, Comenius University, Bratislava, Slovakia

<sup>3</sup>Department of Physical Electronics, Faculty of Science, Masaryk University, Brno, Czech Republic

e-mail: rvladoiu@univ-ovidius.ro

## Abstract

In this paper a Surface Dielectric Barrier Discharges (SDBD) plasma treatment has been performed to produce uniform atmospheric plasmas **in He** and **in open air** in order to functionalize the polycarbonate surface. SDBD is used for different application, processing especially of low-cost polymeric materials, combining the advantages of non-equilibrium plasma properties with the ease of atmospheric-pressure operation. Contact angle measurements were used to record the short- and long - term variations in wettability of treated and untreated polycarbonate sheets. The modification process was determined with hydrophilicity measurements evaluated by means of the SEE system drop test. Hydrophilicity of individual sheets of polycarbonate has distinctly decreased after plasma treatment.

Plasma treatments were carried out in the SDBD reactor where the electrode system was supplied by a sinusoidal high voltage with a frequency of 6 kHz and peak-to-peak voltage of 8 kV. This produced a stable surface discharge starting from both edges of each strip electrode and covering uniformly the ceramic surface. This unique discharge system has many important applications such as ozone production, pollution control by oxidation of volatile organic compound and surface treatment. Many advantages, such as having no needed for expensive vacuum equipment, being low cost and simple systems, and easy to operate make this reactor became rapidly very popular. The SDBD reactor used in our experiments is described in detail elsewhere. The material we used was polycarbonate (75 mm x10 mm). The samples were cleaned by immersing in carbon tetrachloride for 10 seconds and dried with cold air for 10 min.

The contact angles and free surface energy were determined by means of Surface Energy Evaluation System – See System. It is based on the usage of a CCD camera, which captures a liquid drop on the studied surface. Recorded pictures are analyzed manually by the user, which is substantial for the full control of the contact angle determination. Selection of several points of solid–liquid and liquid–vapor interface makes possible to fit the drop profile and to calculate the tangent angle of the drop with the solid surface.

The samples became hydrophilic after the shortest time of 30 s and, consequently, wettable immediately after the plasma activation. It was found that the plasma-activated PC exhibit hydrophilicity that decreases slowly with time after exposure, which can be critically important in the practical use of the plasma-activated PC for modern nanotechnological surface treatments.

**Keywords:** Surface Dielectric Barrier Discharges, contact angles, free surface energy, polycarbonate.

## Effect of helium addition in the double M-effect (monochromatization effect)

R. Vladoiu, M. Contulov, A. Mandes

Department of Plasma Physics, Faculty of Physics, Chemistry, Electronics and Oil Technology, Ovidius University,  
Mamaia 124, Constanta, 900527, Romania

e-mail: rvladoiu@univ-ovidius.ro

### Abstract

In some gas mixtures, the spectrum of the gas discharge is reduced to one emission line. This effect was not discovered in earlier researches because no luminescent discharge was obtained at high gas pressure (hundreds of Torr). The thread – like discharges have been avoided by covering the electrodes with a dielectric film, which allows for an uniform discharge on electrode. The discharge is achieved in alternate currents of high frequency and high voltage. Due to the fact that the spectra obtained had practically one line, this phenomenon was called by Musa et al. (1985) the “monochromatization effect”. The explanation is based on the elementary process of three body collision together with the resonant radiation (with negligible energy defect) of plasma or of plasma due to trapped resonance radiation. [1] Additional processes including two particle interactions like resonant radiation trapping or metastable state are parts of M – effect. Studies of this discharge with two elements Ne, Ar and with He and H<sub>2</sub> have revealed the existence of the double M-effect signal, all lines except of those characteristics for individual M-effect of the Ne and Ar.

The objective of this paper is to study the influence of He percentages in the mixture of Ne – Ar – He – H<sub>2</sub> proving the general character of the monochromatization effect (M-effect). As it was already reported [2], in the double M-effect, hydrogen percentages play a leading role, but also the influence of He could not be neglected. The emitted radiation from the plasma region was analyzed by mean of an Optical Multichannel Analyzer (OMA), Spectral Products SM 242 having a wavelength ranging between 130-1050 nm. The signal about the plasma radiation is collected through the quartz tube and transmitted to the spectrometer by an optical fiber. Each corresponded spectrum was recorded and compared (with and without hydrogen), focused on the investigation of the relative intensities of studied lines.

It has been found that for 70 Torr’s total pressure of the mixture - the case when the M-effect has the maximum signal without He - the existence of He in the mixture at a higher percentage - with 50% H<sub>2</sub> as partial pressure - induces a greater increase of the M-effect signal.

**Keywords:** Monochromatization – effect (M-effect), three body collision, and gas mixture discharges physics

### References

- [1] M.A. Popescu, “Dictionary of effects in science”, INOE, Bucharest (2006)
- [2] R. Vladoiu, M. Contulov, A. Mandes, G. Musa, Eur. Phys. J. D 54, 2009, pp. 287-291

# Investigation of the electric field around a carbon nanotube tip in pulsed plasma sheath

H. Goudarzi , H. Ghomi , A. Niknam

Laser and Plasma Research Institute, Shahid Beheshti University, Evin, Tehran, Iran

E-mail: behnood.gdrz@yahoo.com

## Abstract

In this paper the evolutions of the electric field in plasma sheath in the presence of a carbon nano-tube tip have been numerically investigated. Considering appropriate conditions, CNTs in plasma sheath have been simulated. At the beginning of the pulses, a large enhancement of the electric field is observed in the vicinity of CNTs. As the time goes on, diagrams indicate the decline of the electric field at the sharp upper corner of tip. On the other hand, the increase of electric field at the points which are far from nano-tip in the plasma sheath is remarkable. By the advent of these results, the influence of the electric field after a while in plasma sheath is explored.

**Keywords:** carbon nanotubes (CNTs), electric field.

## Introduction

Carbon nanotubes (CNTs) have attracted much research effort since their discovery in 1991 [1]. Their unique structural, chemical, electrical and mechanical properties promise to make nanotubes an appropriate material for a variety of applications, such as field emission sources, nanoelectronics devices and mechanical reinforcement in composite materials [2,3].

Depending on experimental conditions CNTs could grow in one direction (alignment) or in a curly fashion. Only a few attempts have been done to explain the mechanism of the oriented growth, but it is obvious that in a DC plasma sheath the electric field is responsible for the alignment (Yu et al [4]). We use a two-dimensional fluid model to study the electric field around the nanotip in the pulsed plasma sheath of a target with a tip of rectangular cross section.

## Description of the simulation

In order to model potential and electric field in this process, we have extended the model of Widner et al. [5] into two dimensions. The singly charged ions of mass  $M$  are modeled by a cold, collision-less ion fluid. The surface of target and its coordinates are illustrated in Fig. 1. As it is shown, the Y-axis direction is along the sheath depth, the X-axis is in the direction perpendicular to the Y-axis and simulation region extends in the X and Y dimensions.

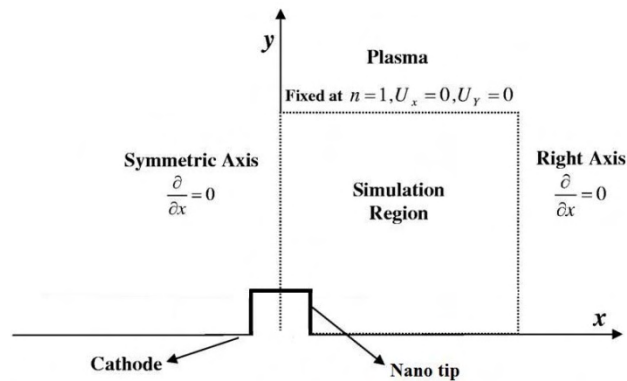


Fig.1. Schematic diagram of nanotip geometry

two-dimensional nano-tip above the cathode is immersed in a charge-neutral plasma in which the ion ( $n_i$ ) and electron ( $n_e$ ) densities are both equal to the plasma density  $n_0$ , i.e.,  $n_i=n_e=n_0$ . At the beginning, the potential ( $\phi$ ) of the target and everywhere is zero ( $\phi=0$ ). Its potential is switched from  $\phi=0$  to a

negative bias  $\phi_t$  ( pulse is considered to have zero rise time)[5] to induce the formation of a sheath. The electrons are repelled from the target. Ions are initially at rest, since the ion mass is much larger than the electron mass. The potential, ion density, and ion velocity then evolve. These evolutions are simulated by using cold, collisionless two fluid theories of plasma and Poisson's equation.[5] The potential distribution is identified by Poisson's equation,

$$\nabla^2 \phi = -\frac{e}{\xi_0} (n_i - n_e) \quad (1)$$

The two-dimensional equations of ion continuity and motion are

$$n_e = n_0 \exp(e\phi / T_e) \quad (2)$$

The electron density  $n_e$  is determined by the Boltzmann relation,

$$\frac{\partial n_i}{\partial t} + \nabla \cdot (n_i v_i) = 0 \quad (3)$$

$$\frac{\partial v_i}{\partial t} + (v_i \cdot \nabla) v_i = -\frac{e}{m} \nabla \phi \quad (4)$$

Therefore the two-dimensional Cartesian relations become

$$\frac{\partial n_i}{\partial t} + \frac{\partial}{\partial x} (n_i v_{ix}) + \frac{\partial}{\partial y} (n_i v_{iy}) = 0 \quad (5)$$

$$\frac{\partial v_{ix}}{\partial t} + v_{ix} \frac{\partial v_{ix}}{\partial x} + v_{iy} \frac{\partial v_{ix}}{\partial y} = -\frac{e}{m} \frac{\partial \phi}{\partial x} \quad (6)$$

$$\frac{\partial v_{iy}}{\partial t} + v_{ix} \frac{\partial v_{iy}}{\partial x} + v_{iy} \frac{\partial v_{iy}}{\partial y} = -\frac{e}{m} \frac{\partial \phi}{\partial y} \quad (7)$$

$$\frac{\partial^2 \phi}{\partial x^2} + \frac{\partial^2 \phi}{\partial y^2} = -\frac{e}{\xi_0} [n_i - n_0 \exp(\frac{e\phi}{T_e})] \quad (8)$$

where  $n_i$  is the ion density,  $\phi$  is the potential,  $e$  is the electron charge,  $T_e$  is the electron temperature,  $\xi_0$  is the free space permittivity,  $m$  is the mass of ion, and  $v_{ix}$  and  $v_{iy}$  are the ion velocity in  $x$  and  $y$  directions, respectively. These equations can be made dimensionless by using the following variables:

$$\tau = t\omega_{pi}, X = \frac{x}{\lambda_D}, Y = \frac{y}{\lambda_D}, \varphi = \frac{e\phi}{T_e}$$

$$n = \frac{n_i}{n_0}, U_x = \frac{v_{ix}}{v_{is}}, U_y = \frac{v_{iy}}{v_{is}} \quad (9)$$

where  $\omega_{pi} = (n_0 e^2 / m \xi_0)$  is the ion plasma frequency,  $\lambda_D = (\xi_0 T / n_0 e^2)^{1/2}$  is the Debye length, and  $v_{is} = (T_e / m)^{1/2}$  is the ion-acoustic velocity. Consequently, the dimensionless equations become

$$\frac{\partial n}{\partial \tau} + \frac{\partial (n U_x)}{\partial X} + \frac{\partial (n U_y)}{\partial Y} = 0 \quad (10)$$

$$\frac{\partial U_x}{\partial \tau} + U_x \frac{\partial U_x}{\partial X} + U_y \frac{\partial U_x}{\partial Y} = -\frac{\partial \varphi}{\partial X} \quad (11)$$

$$\frac{\partial U_y}{\partial \tau} + U_x \frac{\partial U_y}{\partial X} + U_y \frac{\partial U_y}{\partial Y} = -\frac{\partial \varphi}{\partial Y} \quad (12)$$

$$\frac{\partial^2 \phi}{\partial X^2} + \frac{\partial^2 \phi}{\partial Y^2} = -[n - \exp(\phi)] \quad (13)$$

First and foremost, the nonlinear Poisson equation has to be replaced with a linear Poisson equation about this guess by introducing[6]

$$\begin{aligned} \exp(\phi) &= \exp(\phi - \psi) \approx (1 + \phi - \psi) \exp(\psi) \\ &= \exp(\psi) - \psi \exp(\psi) + \phi \exp(\psi) \end{aligned}$$

After neglecting high-order terms, Eq. [13] become

$$\frac{\partial^2 \phi}{\partial X^2} + \frac{\partial^2 \phi}{\partial Y^2} - \phi \exp(\psi) = -[N - \exp(\psi) + \psi \exp(\psi)]$$

Now, this is a linear Poisson equation in the unknown

$\phi$ . We take  $\psi$  from the  $\phi$  of the previous time step, solve Eq.(14) to obtain a new  $\phi$ , set  $\psi$  equal to this new  $\phi$ , and iterate until the process converges. We solve Eq.(14) by the finite difference relaxation method. Boundary conditions are  $\phi = \phi_t$  on the target,  $\phi = 0$  in the plasma, and  $\partial/\partial X = 0$  on the symmetric axis and right axis that is far from the tip. Furthermore  $n=1$ ,  $U_x=0$ , and  $U_y=0$  at the simulation region-plasma surface. Initial condition are  $n=1$ ,  $U_x=0$ , and  $U_y=0$  everywhere. These equations, initial conditions, and boundary conditions precisely specify the time evolution of the two dimensional sheath. The sheath dynamics is simulated near and around a target with a tip of rectangular cross sections whose dimension is  $20 \times 80$  nm.

First we simulate the potential in plasma sheath in the presence of a nano tip then according to the results, the electric field was investigated. The simulation was run to a final time of  $\tau = 10$  microseconds which is much longer than the duration of the ion-matrix pulse of the simulation.

## Results and discussions

Firstly, the profile of normalized potential have been shown in Fig.2. The contour plot indicates a large gap above the nanotip which shows the extension of sheath after 10 microseconds. On the other hand, an important point which has been explored is the length of gap is bigger than the height of nanotip.

Lines in this figure shows the tendency of sheath to extend along the Y-axis than along the X-axis.

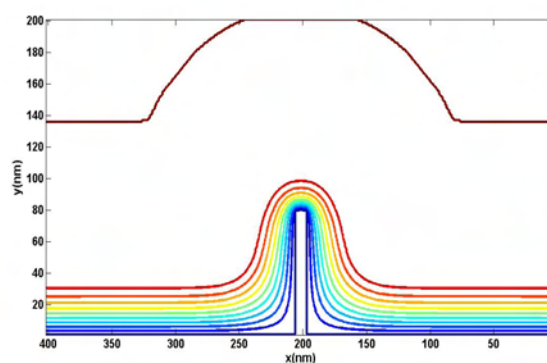


Fig. 2. Profile of normalized potential in  $\tau=10$  microseconds

Secondly, the profile of the electric field around the nanotip has been investigated based on the results of the potential in  $\tau=10$  microseconds. In figure.3 the three dimensional profile of the electric field has been shown. Alteration of the electric field around the nanotip is conspicuous. The first point which draws attentions is enhancement of the electric field at upper sharp corner of nanotip and on the other hand, decline of the electric field at lower corner of nanotip is conspicuously distinct.

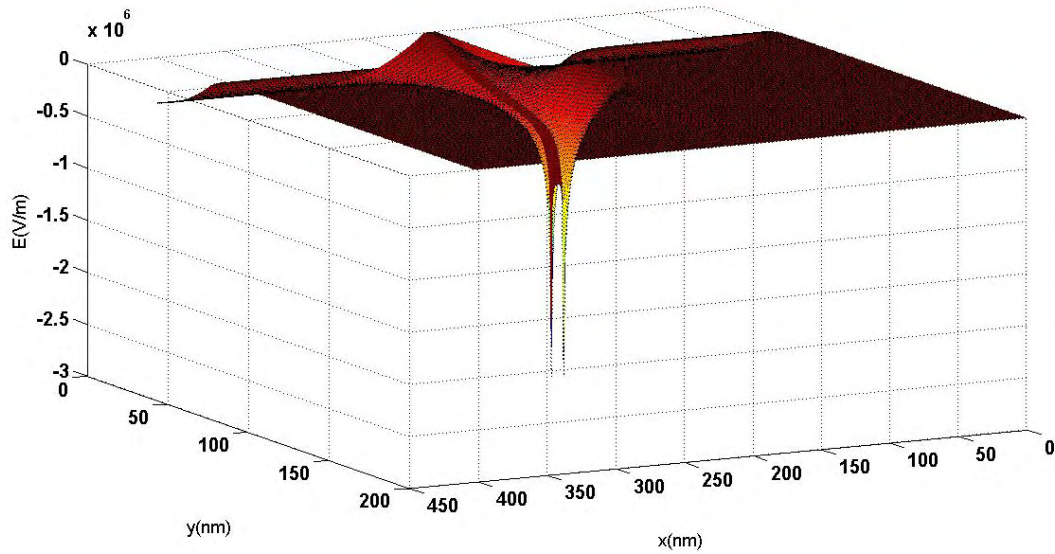


Fig. 3. Three dimensional profile of the electric field in  $\tau=10$

In order to more investigations, the temporal evolutions of the electric field at upper sharp corner of nanotip has been carried out in Fig.4 through the run time. This figure shows the gradual decline of the electric field after a large increase at the beginning. Since ,as the time goes on, the difference of the potential around the CNTs is increased, a gradual decline in magnitude of the electric field at sharp upper corner is observed.

Figure.5(a) shows the comparisons of the electric field above the nanotip along the X-axis. As shown in this figure, magnitude of the electric field after 10 microseconds at sharp upper corner of nanotip is reduced unlike the enhancement of the electric field at points which locate beside the sharp corner of CNTs.

Similar comparison have been carried out beside the side wall along the Y-axis in Fig.5(b). This figure indicates the decline of the electric field in upper sharp coner and side wall of the nano tip after 10 microseconds unlike the increase of the electric field above the nano tip along the Y-axes.

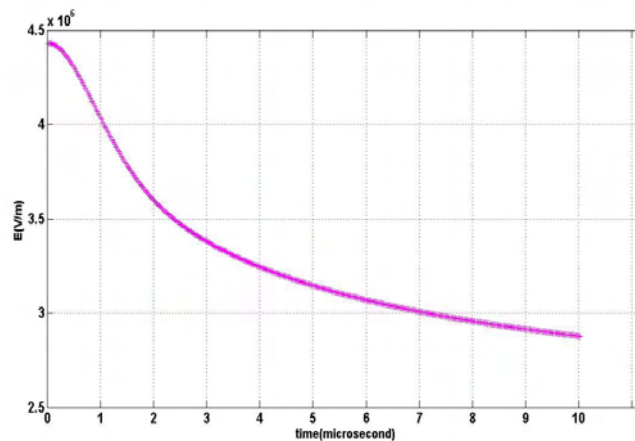


Fig.4. Temporal evolution of the electric field at upper sharp corner of nanotip

The reason of the enhancement of the electric field in both figures is extension of sheath along the X and Y axis into plasma.

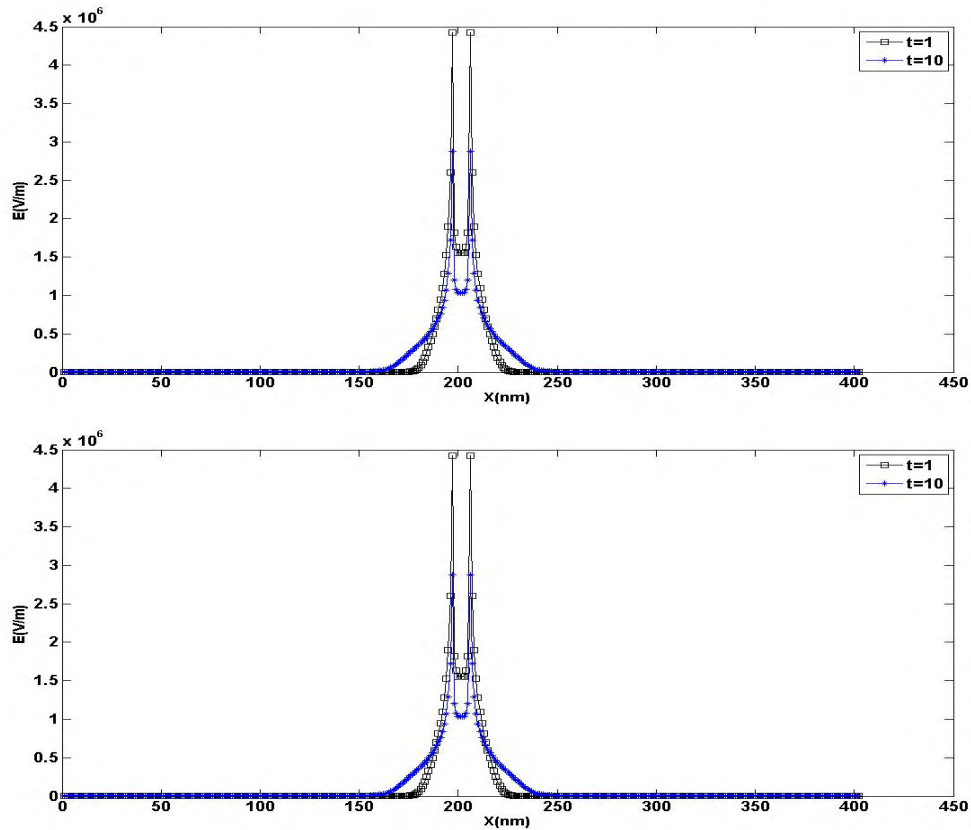


Fig.5. Comparison of the electric field in  $\tau=1$  and  $\tau=10$ . a) along the X-axis at top of the tip. b) along the Y- axis beside the side wall, in plasma sheath.

### Conclusions

Simulation of the electric field evolution in the vicinity of CNTs has been carried out. All of the diagrams related to the electric field indicate the enhancement of the electric forces acting on CNTs due to increase of the electric field around the CNTs. The comparing of the electric field's diagrams indicates the gradual influence of nano tip electric field into plasma. The consequence of this phenomena is enhancement of the electric field in points which locate in the vicinity of CNTs.

### References

- [1] S. Iijima, Nature (Lond.) 354 (1991) 56.
- [2] T.W. Ebbesen, Carbon Nanotubes: Preparation and Properties, FL, 1997.
- [3] S. Subramoney, Adv. Mater. 10 (1998) 1157.
- [4] J. Yu et al: Chem phys. Letters 232 (2000) 529
- [5] T.e. Sheridan, Appl. Phys. Lett 64, 1783\_1994
- [6] G. Emmert and M. A. Henry, J. Appl. Phys. 71, 1 (1992)

# Interaction of deuterated hydrocarbon ions and Ar<sup>+</sup> with CFC surfaces at room temperature

S. Zöttl<sup>1</sup>, A. Keim<sup>1</sup>, B. Rasul<sup>2</sup>, P. Scheier<sup>1</sup>, T. D. Märk<sup>1</sup>, Zdenek Herman<sup>3</sup>

<sup>1</sup>Institut für Ionenphysik und Angewandte Physik, Leopold-Franzens Universität Innsbruck, Technikerstr. 25, 6020 Innsbruck, Austria

<sup>2</sup>Department of Physics, University of Sargodha, 40100 Sargodha, Pakistan

<sup>3</sup>V. Čermák Laboratory, J. Heyrovský Institute of Physical Chemistry, Academy of Sciences of the Czech Republic, Dolejškova 3, 18223 Prague 8, Czech Republic

e-mail: Samuel.Zoetl@uibk.ac.at

## Abstract

Different projectile ions (CD<sub>3</sub><sup>+</sup>, C<sub>2</sub>D<sub>2</sub><sup>+</sup>, C<sub>2</sub>D<sub>4</sub><sup>+</sup>, C<sub>2</sub>D<sub>5</sub><sup>+</sup>, C<sub>2</sub>D<sub>6</sub><sup>+</sup> and Ar<sup>+</sup>) were used to investigate interactions with hydrocarbon-covered carbon-fibre-composite (CFC) surfaces at room temperature. The incident energies were from a few eV up to 100 eV. Mass spectra of the product ions and their dependence on the incident energy of the projectiles were measured. The results showed that the fragmentation of the molecular projectile ions and their surfaced-induced chemical reactions at the CFC surface resemble the interactions of the identical projectile ions with room temperature Highly Oriented Pyrolytic Graphite (HOPG) surfaces. Thus it can be assumed that a layer of surface hydrocarbons determines the energy transfer at the surface and its chemical reactivity. The most significant difference observed is that sputtered alkali ions K<sup>+</sup> and Na<sup>+</sup>, most probably contaminants of the CFC material, were present in the mass spectra of product ions. Measurements with the projectile ion Ar<sup>+</sup> showed the usual ions characterizing sputtering of surface hydrocarbons and the same alkali ions as above.

**Keywords:** Ion-surface interactions, Carbon-fibre-composite surface, Hydrocarbon surface coverage

## Introduction

In order to ensure an efficient operation of fusion devices, the use of suitable materials for the plasma facing walls is obligatory. Hence information on ion surface interactions and their products constitutes an essential part for the simulation and modeling of ITER (International Thermonuclear Experimental Reactor).

Carbon-fibre-composite (CFC) is one possible material for use as surface material in fusion experiments. Therefore, in this work we studied the interaction of selected C1 (CD<sub>3</sub><sup>+</sup>), C2 (C<sub>2</sub>D<sub>2</sub><sup>+</sup>, C<sub>2</sub>D<sub>4</sub><sup>+</sup>, C<sub>2</sub>D<sub>5</sub><sup>+</sup>, C<sub>2</sub>D<sub>6</sub><sup>+</sup>) and Ar<sup>+</sup> ions with the CFC surface kept at room temperature [1]. The aim was to compare the ion-surface interactions of CFC with other (carbon) surfaces.

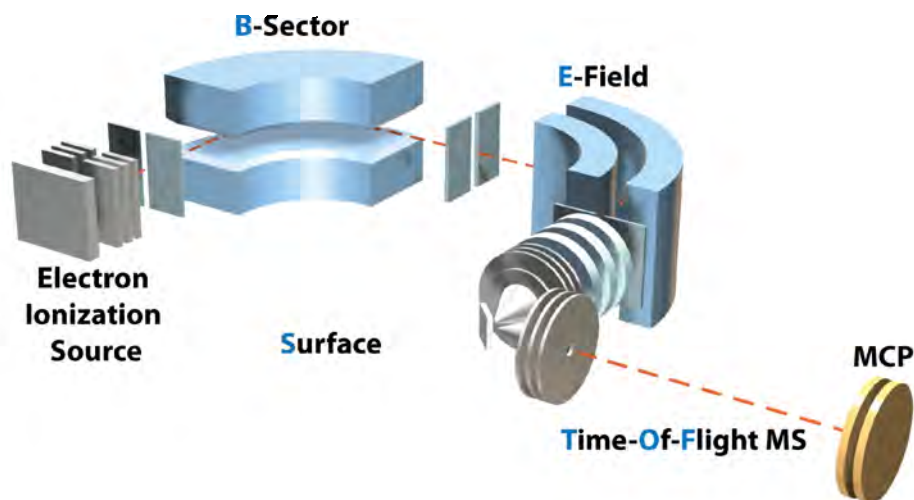


Fig. 1. Schematics of the tandem mass spectrometer BESTOF.

## Experimental

The experimental setup consisted of a double focusing two-sector-field mass spectrometer in reversed geometry (Varian MAT CH5-DF) combined with a linear time-of-flight mass spectrometer (see Figure 1). The instrument was described in detail previously [2]. The sector-field instrument was used to mass select the projectile ions, produced in a Nier-type ion source. The projectile ions then interacted with the CFC surface at a well defined incident energy ranging from a few eV up to 100 eV. The impact angle of the projectiles was  $45^\circ$ , the total scattering angle was fixed at  $91^\circ$ . Product ions formed at the surface were extracted through a 1 mm diameter orifice and mass analyzed with a linear time-of-flight mass spectrometer. The surface interaction, the mass analysis and the detection were performed under ultra-high vacuum conditions ( $10^{-9}$  Torr). The pressure in the ion source was  $2-6 \times 10^{-6}$  Torr.

Mass spectra of the product ions were recorded at different incident energies and their relative abundances were plotted as a function of the projectile ion energy (energy-resolved-mass-spectra, ERMS curves).

The carbon-fibre-composite used was of the type NB-31 and obtained from the Max-Planck Institute of Plasma Physics in Garching.

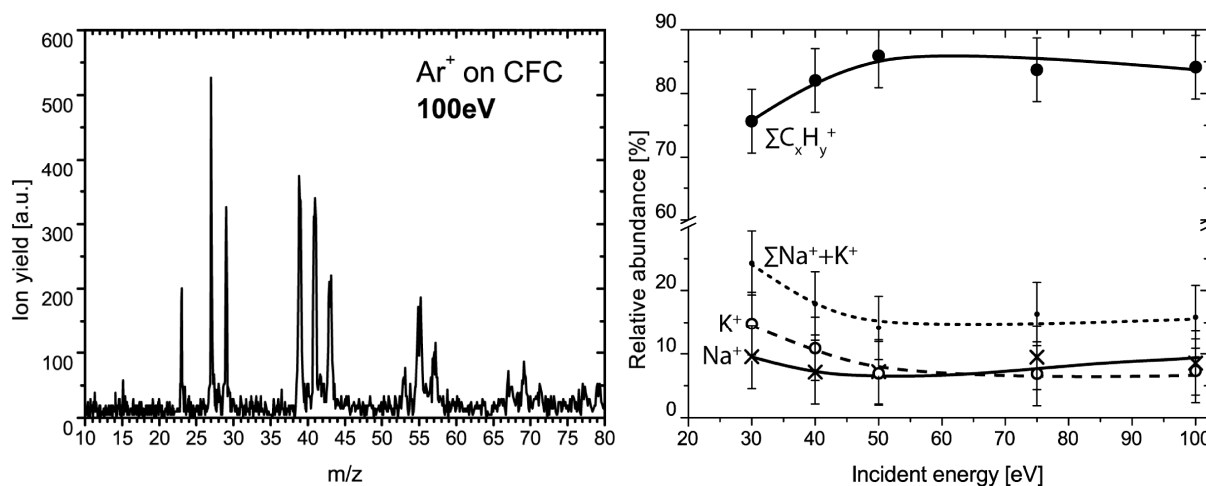


Fig. 2. Product ions from collisions with a CFC surface at room temperature. Left: mass spectrum at the incident energy of 100 eV. Right: relative abundance of the sum of all sputtered hydrocarbon ions, the sum of the abundance of both alkali ions and the  $K^+$  and  $Na^+$  abundance as a function of the incident energy of  $Ar^+$ .

## Results and discussion

$Ar^+$ ,  $CD_3^+$ ,  $C_2D_2^+$ ,  $C_2D_4^+$ ,  $C_2D_5^+$ ,  $C_2D_6^+$  were used as projectile ions and their interaction with the CFC surface at room temperature was investigated.

Fig. 2 shows one of the mass spectra obtained after the interaction with  $Ar^+$ . The mass spectra reflect features typical for hydrocarbon covered surfaces and hence contain the usual sputtered hydrocarbon ions [3]. An unexpected discovery was the presence of alkali ions ( $Na^+$ ,  $K^+$ ) in the mass spectra. It is assumed that these alkali ions are due to contaminations of the CFC surface, since a variety of attempts to clean the surface showed no effect on the intensities of the alkali ions in the mass spectra.

Mass spectra of the projectile ion  $CD_3^+$  show a significant amount of the projectile itself, even at high incident energies. Further contributions to the spectra could originate from various mechanisms. Collision-induced dissociation of the projectile ions results in the formation of fragment ions  $CD_2^+$ . A chemical reaction of H-atom transfer with surface hydrocarbons can also occur. The sputtering of the surface material leads to the formation of alkali ions and sputtered hydrocarbons and a small contribution is due to chemical carbon chain build-up reactions between projectile ion and terminal groups of the surface hydrocarbons.

Measurements with the projectile ions  $C_2D_2^+$ ,  $C_2D_4^+$ ,  $C_2D_5^+$  and  $C_2D_6^+$  at room temperature agree well with results obtained with hydrocarbon-covered surfaces of HOPG [4], tungsten [5] and stainless steel [6]. In general, the mass spectra of ion products from interactions of radical cations ( $C_2D_2^+$ ,

$C_2D_4^+$ ,  $C_2D_6^+$ ) show both fragmentation of the projectile ion and products of chemical reactions with the surface material, while interactions of closed shell cations ( $C_2D_5^+$ ) show only fragmentation of the projectile. In both cases sputtering of the surface material was observed. In Fig. 3 two of the obtained ERMS curves are illustrated, showing the relative abundance of product ions assigned to various surface-induced processes as a function of the incident energy.

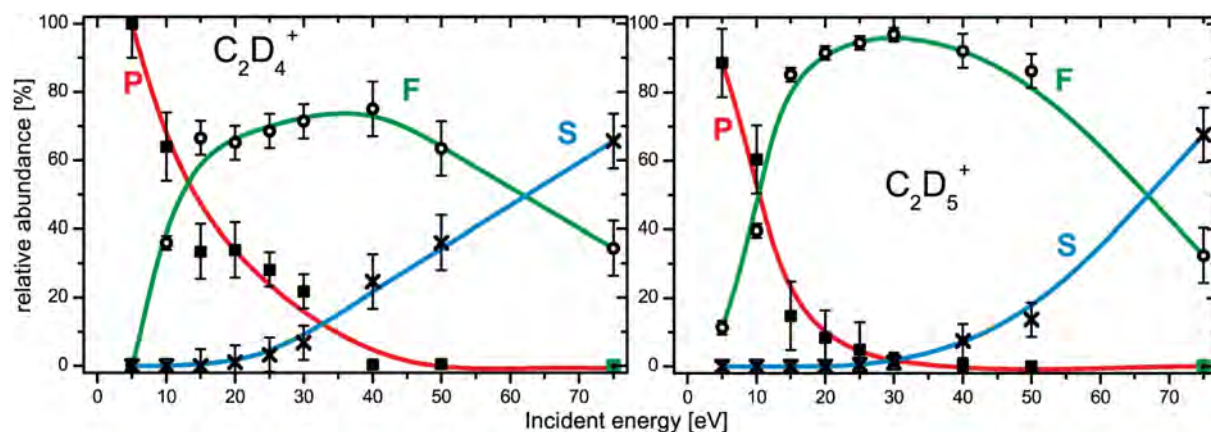


Fig. 3. ERMS curves of product ions from collisions of  $C_2D_4^+$  and  $C_2D_5^+$  with a room temperature CFC surface. P - inelastically scattered undissociated projectile ions, F - sum of all fragment ions, S - sum of all sputtered ions.

## Conclusions

The mass spectra of product ions from collisions of  $Ar^+$ ,  $CD_3^+$ ,  $C_2D_2^+$ ,  $C_2D_4^+$ ,  $C_2D_5^+$ ,  $C_2D_6^+$  ions with the carbon-fibre-composite surface at room temperature show a similar fragmentation as former measurements performed with hydrocarbon-covered surfaces (HOPG, tungsten, stainless steel, and diamond). This indicates that the energy transfer and chemical reactivity of these surfaces is mainly defined by the covering hydrocarbon layer.

The only substantial difference is the presence of alkali contaminants ( $Na^+$  and  $K^+$ ) which may originate in the production process of the CFC surface.

## Acknowledgements

This work was supported by the FWF, Wien and the European Communities under the Contracts of Association between EURATOM ÖAW and EURATOM IPP.CR and carried out within the framework of the European Fusion Development Agreement (EFDA). The views and opinions expressed herein do not necessarily reflect those of the European Commission.

## References

- [1] A. Keim, B. Rasul, N. Endstrasser, P. Scheier, T. D. Märk, Z. Herman, *Int. J. Mass Spectrom.*, in press (2010)
- [2] C. Mair, T. Fiegele, F. Biasioli, Z. Herman, T. D. Märk, *J. Chem. Phys.* 111, 2770 (1999)
- [3] J. Roithová, J. Žabka, Z. Dolejšek, Z. Herman, *J. Phys. Chem. B* 106, 8293 (2002)
- [4] J. Jašík, J. Žabka, L. Feketeová, I. Ipolyi, T. D. Märk, Z. Herman, *J. Phys. Chem. A* 109, 10208 (2005)
- [5] A. Pysanenko, J. Žabka, T. D. Märk, Z. Herman, *Int. J. Mass Spectrom.* 277, 229 (2008)
- [6] L. Feketeová, J. Žabka, F. Zappa, V. Grill, P. Scheier, T. D. Märk, Z. Herman, *J. Am. Soc. Mass Spectrom.* 20, 927 (2009)

# High-speed ambient air plasma cleaning of flat glass surfaces

T. Homola<sup>1</sup>, A. Buček<sup>1</sup>, D. Kováčik<sup>1</sup>, A. Zahoranová<sup>1</sup>, P. Sťahel<sup>2</sup>, P. Slavíček<sup>2</sup>, M. Černák<sup>1,2</sup>

<sup>1</sup>Department of Experimental Physics, Comenius University, Mlynská dolina, Bratislava 842 45, Slovakia

<sup>2</sup>Regional R&D Centre for low-cost plasma and nanotechnology surface treatments, IPE, Faculty of Science, Masaryk University, Kotlářská 2, Veveří, Brno 611 37, Czech Republic

e-mail: cernak@fmph.uniba.sk

## Abstract

Flat glass surfaces were cleaned and activated by diffuse ambient air plasma generated using the so-called Diffuse Coplanar Surface Barrier Discharge. It has been found that a short 3-sec. plasma exposure leads to hydrophilization of the glass surface and a significant increase in its adhesion to glues and coating materials. The observed effects are illustrated also by the results of in-line plasma treatment at a standard industrial line for safety glass manufacturing.

**Keywords:** dielectric barrier discharge, glass cleaning, atmospheric pressure plasma.

## Introduction

Electrical plasmas generated at low gas pressures are widely used for glass surface cleaning and activation, for example in flat panel display manufacturing. However, as the glass substrate size is increased, it is difficult to generate low-pressure plasmas over the large substrate size and the fabrication of the equipment is very costly. This is of particular importance for the coatings deposited onto large-size architectural glass plates. The use of atmospheric pressure plasma cleaning instead of the widely used low pressure plasma cleaning can increase the handling capacity of large-area glass substrates, can increase the throughput by in-line processing under the atmospheric environment, and can decrease the equipment cost.

Several papers have been published on the glass cleaning using standard volume dielectric barrier discharge treaters, however, as such, these devices, called also the “corona“ treaters, are not convenient for the glass surface cleaning, because of their low plasma power densities (less than  $5 \text{ W/cm}^3$ ) resulting in long exposure times, typically of 1 min. Moreover, such devices are not applicable for cleaning of glass substrates thicker than some 2 mm.

More promising atmospheric-pressure plasma sources for the glass cleaning and activation are plasma jets, where the glass substrate is situated some 1 cm from the plasma source and is cleaned by a plasma flow, i.e., a plasma jet generated by the plasma source. A disadvantage is, that working gas flow rates must be sufficiently high to carry the reactive species from the plasma source to the substrate at an acceptable rate (i.e., before they decay or recombine). As a consequence, a substantial part of the discharge power is uselessly dissipated in the plasma volume by, for example, recombination processes and gas heating.]

As exemplified by the results presented, the proprietary atmospheric-pressure plasma cleaning technique based on the use of the so-called Diffuse Coplanar Surface Barrier Discharges offers significant advantages over the above mentioned methods for atmospheric-pressure plasma cleaning of flat glass.

## Results and discussion

The simple scheme of experimental laboratory apparatus is shown in the Figure 1. Surface modification was carried out using DCSBD generated in air at atmospheric pressure.

The DCSBD electrode geometry consists of 38 parallel stripline silver electrodes embedded 0.5 mm below the surface of 96 %  $\text{Al}_2\text{O}_3$  ceramics. The discharge was powered by 14 kHz sinusoidal voltage, supplied by HV generator LIFETECH VF 700. The active plasma area has the dimensions  $200 \times 80$  mm. The thickness of the plasma layer generated on the surface of the  $\text{Al}_2\text{O}_3$  ceramics is approximately 0.5 mm. The power supplied to the reactor was approximately 332 W. The flat glass samples were cleaned by isopropyl alcohol prior to the plasma cleaning.

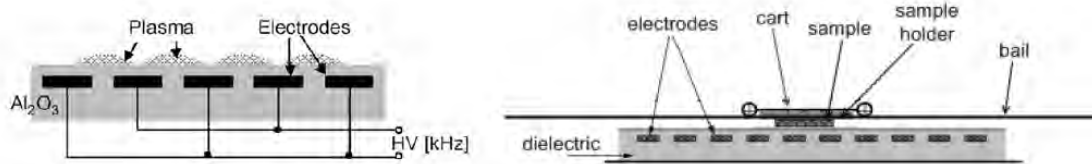


Fig. 1. Schematics of the DCSBD electrode cross section and the laboratory reactor.

For the treatment the samples were attached to a plastic cart. The cart was moving through the discharge area at a constant speed carrying the sample. The distance between the sample surface and the surface of the  $\text{Al}_2\text{O}_3$  ceramics was 0.3 mm. By changing the cart speed it is possible to change the treatment time.

In general, a good wettability of glass surface is considered to be a good indicator of the virtually absent organic surface contamination. As a consequence, the surface energy measurement was used as an indication of the plasma surface cleaning efficiency. As illustrated by Figure 2, the glass surface becomes hydrophilic after some 1 - 3 sec. treatment, which enables an in-line continuous cleaning.

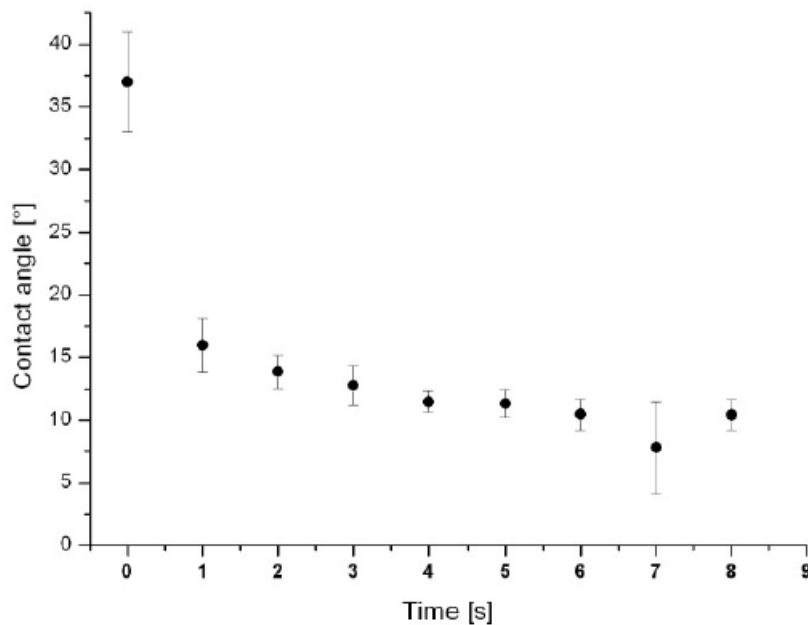


Fig. 2. Effect of the plasma exposure time on water contact angle.  $200\text{ cm}^2$  surface area glass sample was cleaned in ambient air at  $2.5\text{ W/cm}^2$  discharge power.

Such a glass cleaning resulted in a significant increase in the adhesion of glass surface to industrial glues. This is illustrated by Figure 3 that compares the adhesive strength of two 2-cm thick glass plates bonded by an industrial UV curing adhesive with and without the plasma cleaning.

To demonstrate the industrial applicability of the method a system of three electrodes was incorporated into a standard industrial line for safety glass manufacturing at IZOLAS company, Brno. A technically important approximately 30% increase in the adhesion between the glass and the glass safety polymer film was observed.

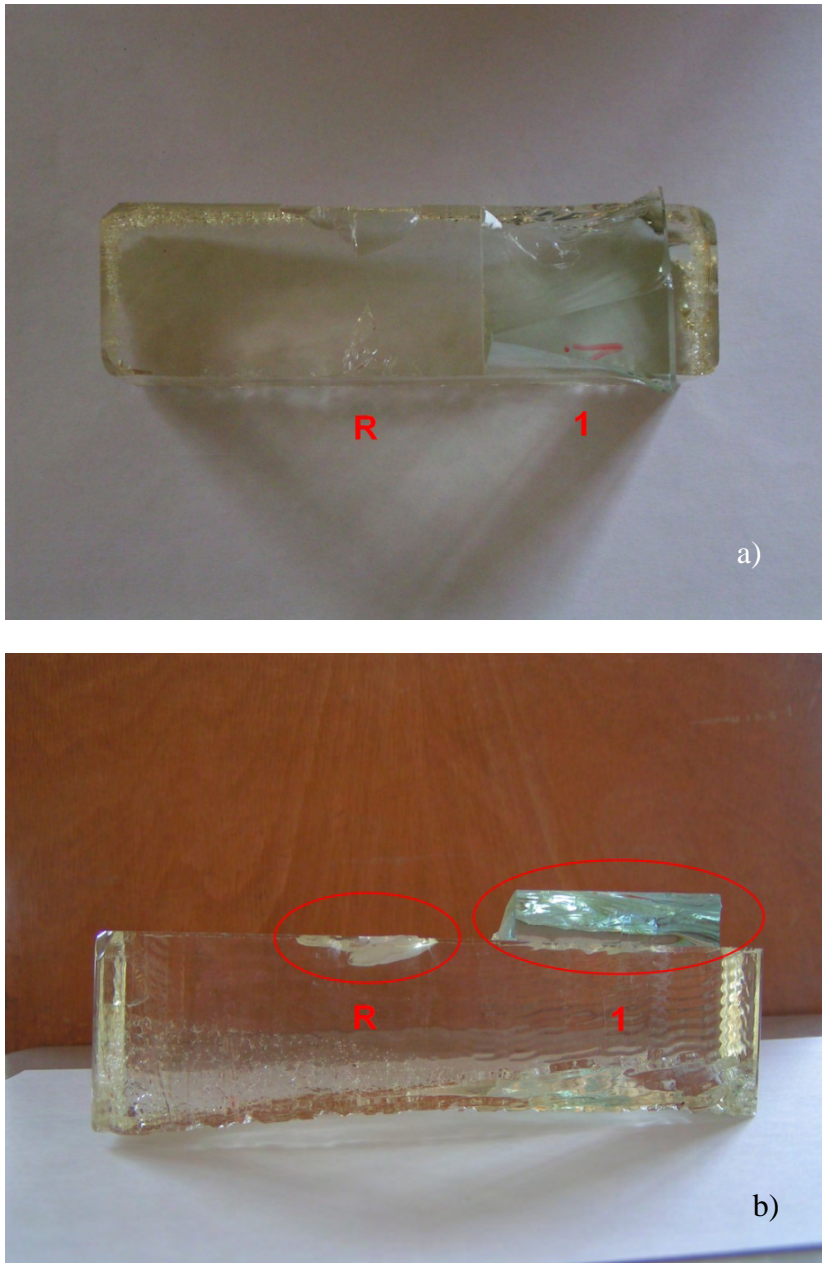


Fig. 3. Two desks of 12 mm thick float glass were bonded to the third polished optical glass base desk. The surfaces to be bonded have been cleaned with ethanol, with a subsequent plasma treatment in the case of sample (1). The bonding was conducted by the means of a standard UV curing adhesive. After being hit by a hammer, the reference sample (R) was separated from the base desk, while the plasma treated sample was broken in the volume (see the rest of the sample (1) still bonded to the base desk). a) top view, b) front view.

### Conclusions

The detailed study of applicability of DCSBD ambient air plasma for glass surface cleaning exemplified by the above presented results indicates that the patent-protected DCSBD technique outperforms the commercially used plasma-jet based techniques in:

- extremely short plasma cleaning time
- extremely low energy consumption
- uniformity of the cleaning and activation
- no roughening of the plasma cleaned glass surface

- the system is very suitable for scale-up and versatile with respect to the working gas
- the robustness, safety, and practically unlimited electrode lifetime

**Acknowledgement**

We acknowledge the kind support of the projects No. APVV-0491-07 and No. CZ.1.05/2.1.00/03.0086.

# BESTOF – a versatile apparatus for fusion relevant experiments

A. Keim<sup>1</sup>, S. Zöttl<sup>1</sup>, F. Zappa<sup>2</sup>, M.M. Sant’Anna<sup>3</sup>, P. Scheier<sup>1</sup>, T.D. Märk<sup>1</sup>, Z. Herman<sup>1,4</sup>

<sup>1</sup> Institute for Ion Physics and Applied Physics, University of Innsbruck, Technikerstraße 25b, 6020 Innsbruck, Austria

<sup>2</sup> Departamento de Física, Instituto de Ciências Exatas, Campus Universitário Juiz de Fora, 36036-330 Juiz de Fora, Brazil

<sup>3</sup> Instituto Instituto de Física, Universidade Federal do Rio de Janeiro, 68528 Rio de Janeiro, Brazil

<sup>4</sup> J. Heyrovský Institute of Physical Chemistry, Academy of Sciences of the Czech Republic, Dolejškova3, 18223 Prague 8, Czech Republic

e-mail: alan.keim@uibk.ac.at

## Abstract

The BESTOF apparatus in Innsbruck contributes to two hot topics in fusion research within the framework of EURATOM. The experiment enables measurements of ion-surface interactions of small hydrocarbon and seeding gas ions with ITER-relevant surfaces heated up to temperatures up to 600°C. In addition it allows for determination of electron ionization cross sections of atoms and molecules in gas phase and measurement of initial kinetic energies of all produced ions. In this work we present recent measurements of both kinds.

**Keywords:** plasma-wall interaction, ion-surface interaction, ionization cross sections, ion kinetic energy

## Introduction

Research and development of feasible fusion reactors require reliable fundamental data quantifying plasma-wall interactions.

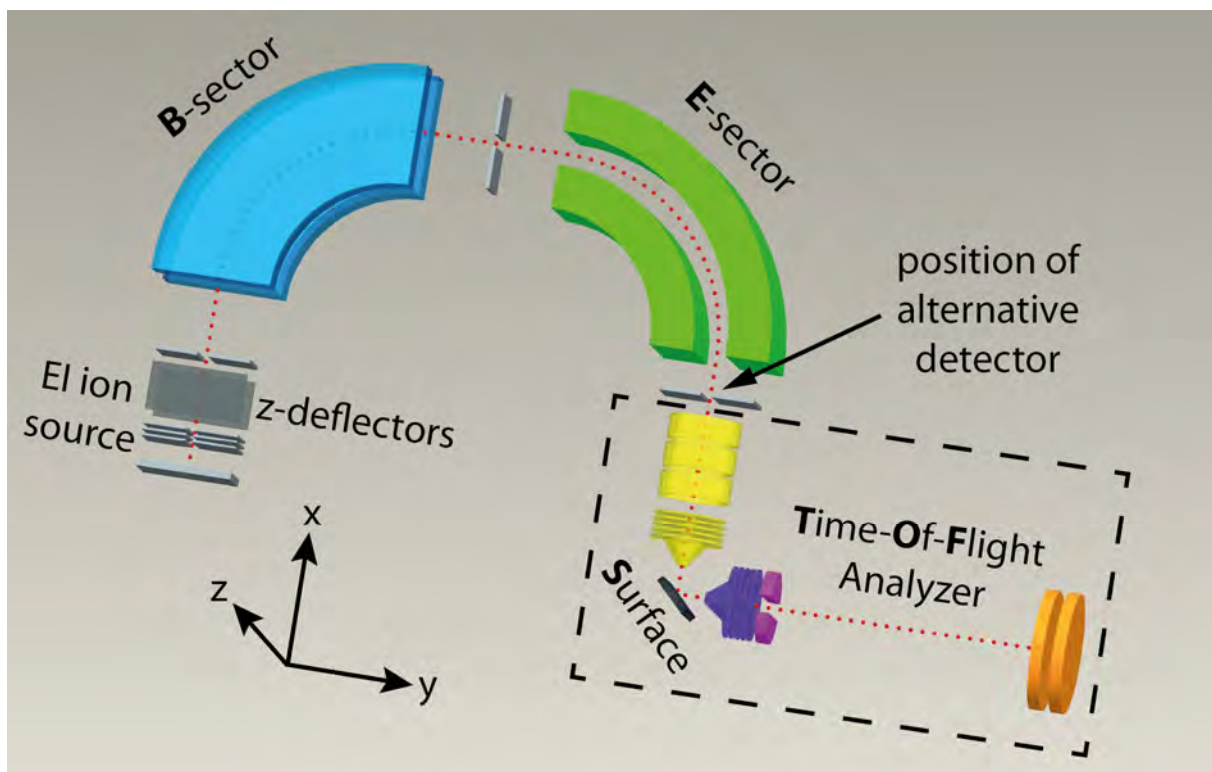


Fig. 1. Experimental setup BESTOF, showing both possible measurement configurations: ion-surface interactions (incl. instruments in dashed box) and ionization cross sections (without dashed box).

Modelling and computational science for the pioneering project ITER depend on the determination of erosion and deposition coefficients of the involved plasma particles, i.e. fuel, impurity and seeding

gas ions, on the materials of choice: beryllium, tungsten and carbon, in the form of carbon-fibre-composite (CFC). Therefore ion-surface interaction measurements have grown to be an important means to determine the interaction processes between plasma particles and wall material.

In addition, knowledge on the influence of hydrocarbon impurities on the plasma burning in fusion experiments is very crucial. Safe operation of a fusion reactor requires profound understanding of the ongoing ionization processes, including information on the energy and momentum of reactants and reaction products. Small hydrocarbon species are formed by interaction of plasma particles with CFC tiles of the inner wall in fusion reactors. Electron ionization cross sections and data on kinetic energies of product ions provide knowledge on inelastic collision processes between electrons and small hydrocarbon species. Those data are used in Kinetic Monte Carlo simulations, modelling the transport of impurities within the vacuum vessel.

## Experimental

The experimental setup BESTOF in Innsbruck is described in large detail in previous publications [1]. It consists of two mass spectrometers arranged in tandem geometry (Fig. 1).

Ions are produced in a Nier-type electron ionization ion source and extracted into the first mass analyzer, a reverse-geometry two-sector-field mass spectrometer. Depending on the type of measurement, at the end of this sector-field instrument the beam of mass selected ions is either directed on a channel electron multiplier detector (ionization cross section measurements) or focused on a surface sample (ion-surface interaction measurements).

In the second case ions then interact with a target surface at  $45^\circ$  incident angle and at well defined incident energies ranging from a few eV up to 100eV. Ions produced in this interaction are extracted into a linear time-of-flight mass analyzer and recorded with a multi-channel-plate detector. Recently, a heating system has been installed to allow for heating of the surface sample up to  $600^\circ\text{C}$ .

## Results and discussion

In previous publications interactions of small hydrocarbons with ITER-relevant surfaces at room temperature have been investigated to determine the extent of plasma-wall interaction [2, 3]. Recently the attention of material studies in fusion science has shifted towards another issue. The divertor region in fusion reactors is planned to be cooled by impurity seeding with gases such as argon or nitrogen. Therefore profound knowledge on interactions between these possible projectiles and the tiles of the inner wall is essential. Following the task proposed by the European Fusion Development Agreement (EFDA) on surface interactions of seeding gas ions, the interaction of ions  $\text{N}_2^+$  with CFC surfaces have been investigated in Innsbruck.

In the experiment a preliminary heating method allowed for measurements at elevated surface temperatures of  $150^\circ\text{C}$ . At this temperature, sputtering of hydrocarbon species is still very dominant for incident energies higher than 20eV (Fig. 2), similarly as with room temperature surfaces.

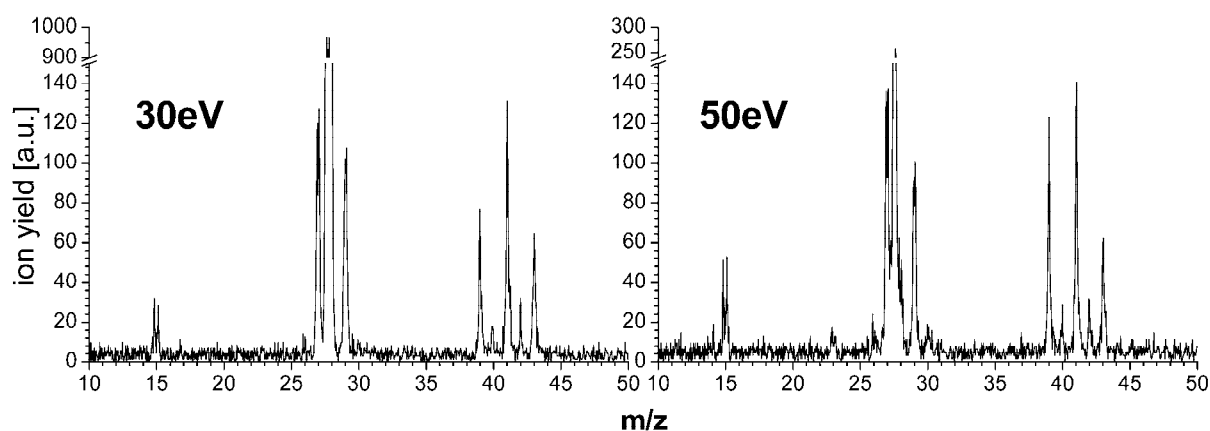


Fig. 2. Ion surface interaction of  $\text{N}_2^+$  with CFC at  $150^\circ\text{C}$ .

In fact J. Roithova et al. have shown that to ensure a surface free of hydrocarbon coverage it is inevitable to heat the surface to at least  $600^\circ\text{C}$  [4]. In BESTOF however, experimental details

complicate the implementation of a simple heating device. A design is currently being explored and intended to be built and installed in the near future.

For the ionization cross section and product ion kinetic energy measurements the instrument was recently improved in several parts in respect to past publications. The lower mass range of the used magnetic sector now allows mass selection of low  $m/z$  fragment ions such as  $H^+$  and  $H_2^+$ . In addition deflection plates were added to the ion source to allow steering of the ion beam in the direction perpendicular to the mass spectrometer plane ( $z$ -axis). Since the direction focusing of two sector-field-mass spectrometers only affects the  $y$ -direction, ions with large initial kinetic energy in  $z$ -direction only reach the detector if they are deflected by applying a  $z$ -voltage. By scanning this voltage from 0V to approximately 60V one gets a  $z$ -profile, which reflects the initial kinetic energy distribution of the investigated ions (Fig. 3, left). To obtain this distribution we fit simulated  $z$ -profiles of different initial kinetic energies (Fig. 3, middle) to our measured profile [5]. The weighting factors of these fits are then plotted and represent the initial kinetic energy distribution (Fig. 3, right). Fig. 3 shows these three steps on the example of  $CH_3^+$  produced from propane  $C_3H_8$  by electron ionization at 70eV.

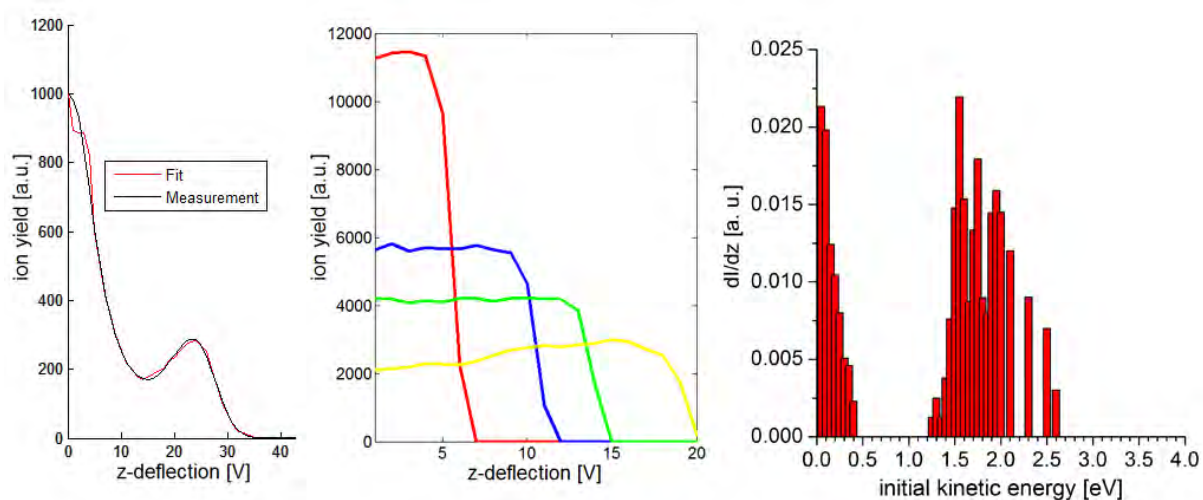


Fig. 3. measured  $z$ -profile of  $CH_3^+$  produced by electron ionization of propane at 70eV (left), simulated  $z$ -profiles for four different initial kinetic energies (middle), initial kinetic energy distribution represented by weighting factors of applied fit functions (right)

These preliminary data compare well with [6]. Both the quasi-thermal contribution at low initial kinetic energy and the higher energetic group at around 2eV are reproduced by our method. It has to be noted that the uncertainty on the right shoulder is considerable, since a larger step width for the fit functions was used for larger initial kinetic energies and therefore values in between were interpolated.

## Conclusions

We highlighted the potential of BESTOF as versatile instrument in contributing to two important topics in fusion research. Preliminary results of ion-surface interactions of  $N_2^+$  with CFC at elevated temperatures confirm the necessity of heating.

Benchmark measurements of initial kinetic energies of fragments produced by propane proof our technique as reliable. Future measurements will cover low mass and low intensity fragment ions.

## Acknowledgement

This work was supported by the FWF, Wien and the European Communities under the Contracts of Association between EURATOM ÖAW and EURATOM IPP.CR and carried out within the framework of the European Fusion Development Agreement (EFDA). The views and opinions expressed herein do not necessarily reflect those of the European Commission.

## References

- [1] C. Mair, T. Fiegele, F. Biasioli, Z. Herman, T. D. Märk, *J. Chem. Phys.* 111, 2770 (1999)
- [2] A. Keim, B. Rasul, N. Endstrasser, P. Scheier, T. D. Märk, Z. Herman, *Int. J. Mass Spectrom.*, in press (2010)
- [3] L. Feketeova, J. Žabka, F. Zappa, V. Grill, P. Scheier, T. D. Märk, Z. Herman, *J. Am. Soc. Mass Spectrom.* 20, 927 (2009)
- [4] J. Roithova, J. Žabka, Z. Dolejšek, Z. Herman, *J. Phys. Chem. B* 106, 8293 (2002)
- [5] S. Feil, K. Gluch, A. Bacher, S. Matt-Leubner, D. K. Böhme, P. Scheier, T. D. Märk, *J. Chem. Phys.* 124, 214307 (2006)
- [6] H. U. Poll, V. Grill, S. Matt, N. Abramzon, K. Becker, P. Scheier, T. D. Märk, *Int. J. Mass Spectrom.* 177, 143 (1998)

# Device for application of PEF

T. Kadlec<sup>1,2</sup>, V. Babický<sup>1</sup> and M. Člupek<sup>1</sup>

<sup>1</sup>Institute of Plasma Physics AS CR, v.v.i., Za Slovankou 1782/3, 182 00 Prague 8, Czech Republic

<sup>2</sup>Faculty of biomedical Engineering CTU in Prague, sq. Sítňá 3105, 272 01 Kladno, Czech Republic

e-mail: tomas.kadlec@fbmi.cvut.cz

## Abstract

The discharges in water were intensively studied [e.g. 1, 2] recently due to their potential application in water and food industry [3, 4]. Several processes are induced in the solution by the discharges. These processes include generation of UV radiation, free radicals, shockwave; pulse electric field (PEF) takes place too. Some of these effects were studied separately [e.g. 5] to better understanding the complex operation of discharges.

This work is focused on the effects of PEF in aqueous solutions only. PEF treatment is non-thermal, chemical-free process affecting microbes. The water solutions or liquid food are treated by high voltage pulses in flow cell that enables to exceed certain threshold value of electric field.

New experimental device for PEF treatment is described in this work. It provides PEF pulses of rectangular shape of the amplitude up to 70 kV/cm, 2 $\mu$ s FWHM and pulse repetition rate of 50 Hz. PEF treatment of water solution containing microbial culture is presented.

**Keywords:** PEF, Water treatment, Food treatment, Device

## Introduction

PEF treatment can be used to sterilize water solutions such as drinking water, fruit and vegetables juices and milk. The advantage of PEF treatment is that it doesn't use any chemicals to sterilize the solution. The PEF treatment can be designed to minimize thermal effects; that means the PEF treatment shouldn't causes thermal degradation of solution treated. Non-thermal application of PEF treatment is achieved by setting proper amplitude of high voltage, pulse shape and time duration and repetition rate of pulses.

The pulse electric field acts on cells of microorganisms. Main effect of PEF treatment is electroporation [3]. Electroporation causes significant increase in the permeability of the cell membrane and finally electroporation will affect the viability of the cells. That means it causes irreversible disruption of cell membrane. The disruption of cell is a threshold effect. Electric field strength must be higher then certain critical value to inflict microorganisms. The critical value of field depends on type of microorganism (e.g. Gram-positive or Gram-negative bacteria) parameters of PEF pulses and outer conditions. It is better to use the pulse of rectangular shape than that of exponential decay or sawtooth shape. In the case of exponential decay shape of pulse, only a narrow part of pulse exceeds critical value ( $E_c$ ) and residual tail of pulse causes heating of solution only (*see Fig. 1*).

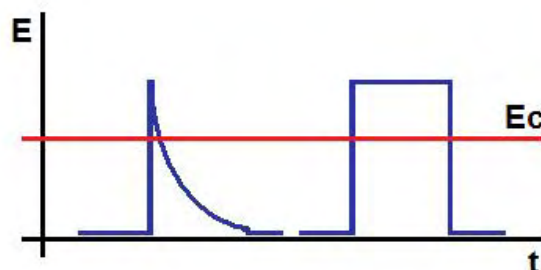


Fig. 1. Comparison between the exponential decay shape of the pulse and the rectangular shape of the pulse.

The experimental equipment for PEF treatment should meet some requirements. The intensity of PEF should be high enough to exceed critical value in the active region of application chamber and the electric field should be homogeneous too. On the contrary, the intensity of PEF should not exceed breakdown limit in the whole device to prevent discharge ignition. The device must be adaptable to wide range of conductivity of treated solutions.

## Results

The high voltage source has been designed and constructed. The pulse forming network was used to achieve quasi-rectangular shape of pulse. The pulse forming network was composed from capacitors and coils. The pulse transformer was used to achieve final value of amplitude of pulse voltage. The high voltage source was designed to work to matched load of approximately  $2\text{ k}\Omega$ , (Fig. 2).

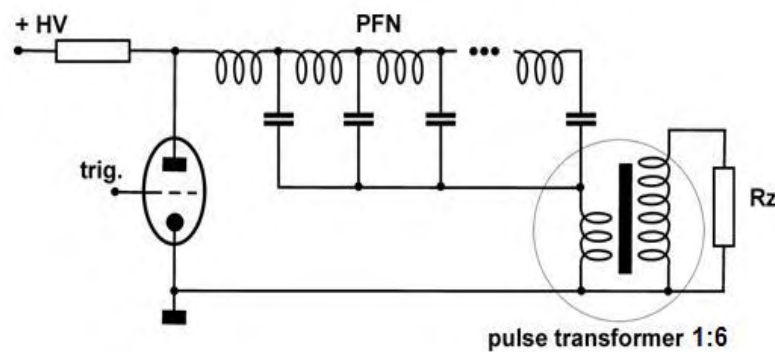


Fig. 2. High voltage sources with pulse forming network and pulse transformer.

The application chamber has been constructed (Fig. 3). It consists of titanium electrodes and PTFE insulators. Design of electrodes and insulators was supported by calculation of electric field configuration using QuickField (Tera Analysis) finite elements analysis system.

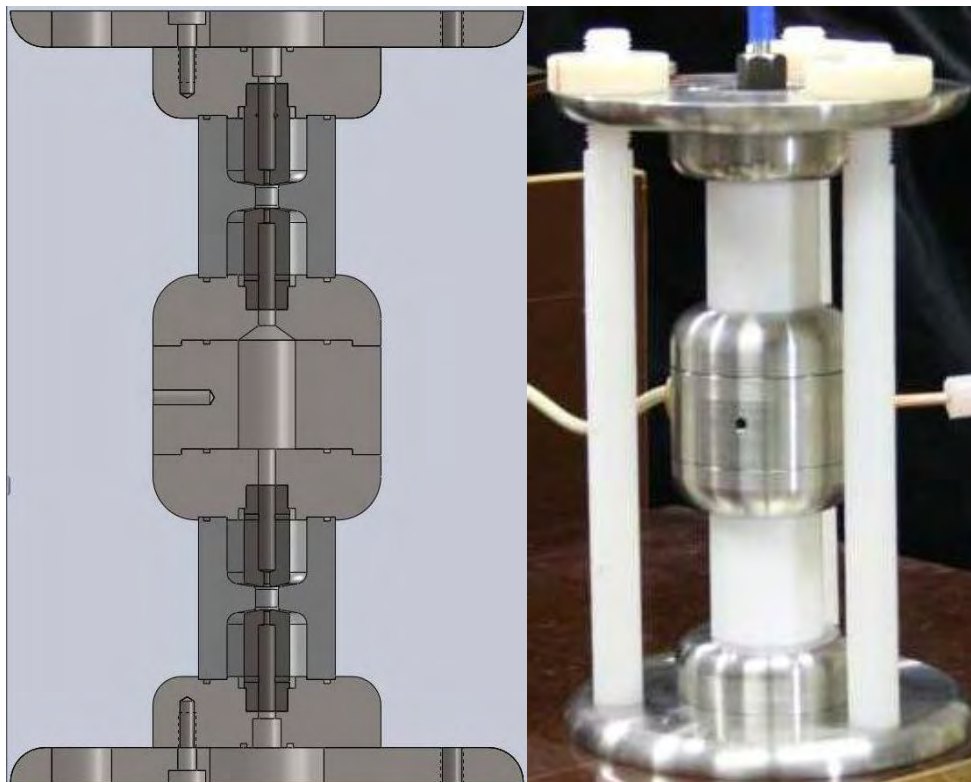


Fig. 3. Design and realization of application chamber.

Water solution flows through the chamber. To avoid discharge ignition the chamber is structured to prevent bubble formation and staying in active area. Homogeneous PEF is generated between electrodes, (Fig. 4). The PEF intensity reached value up to 70 kV/cm. Set of replaceable insulators was designed to meet value of matched load using solutions of wide range of conductivity (250  $\mu$ S/cm to 1 mS/cm).

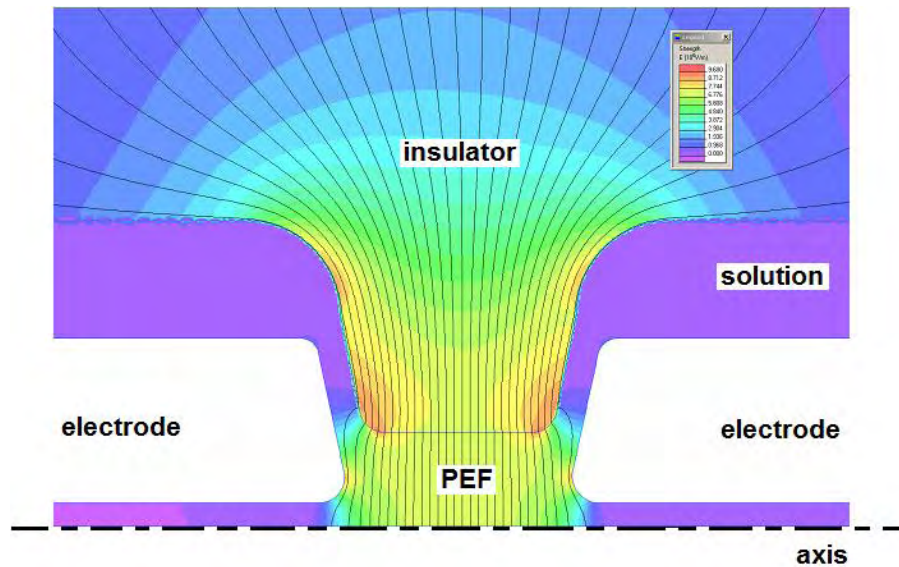


Fig. 4. Intensity of the electric field in the application chamber.

The water solutions containing bacterial suspension of *Bacillus subtilis* CCM 2216 or *Escherichia coli* CCM 3954 were treated using the experimental device. The number of CFU of *Bacillus subtilis* decreases by four orders of magnitude during PEF treatment, (Fig. 5). Similar results (decline of three orders of magnitude) were obtained using *Escherichia coli* strain, (Fig. 6).

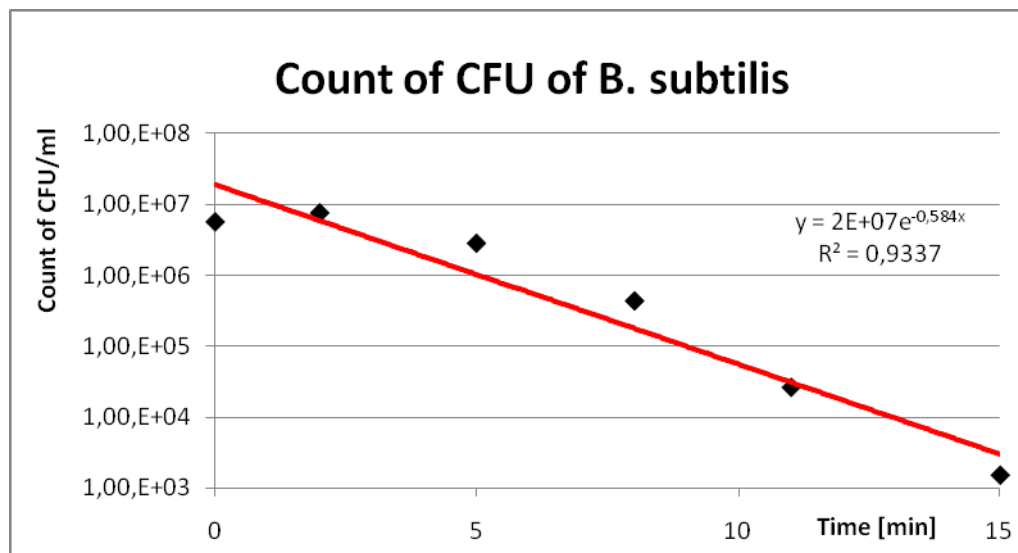


Fig. 5. Dependence of CFU count of bacteria *B. subtilis* on the PEF treatment time, 70 kV/cm.

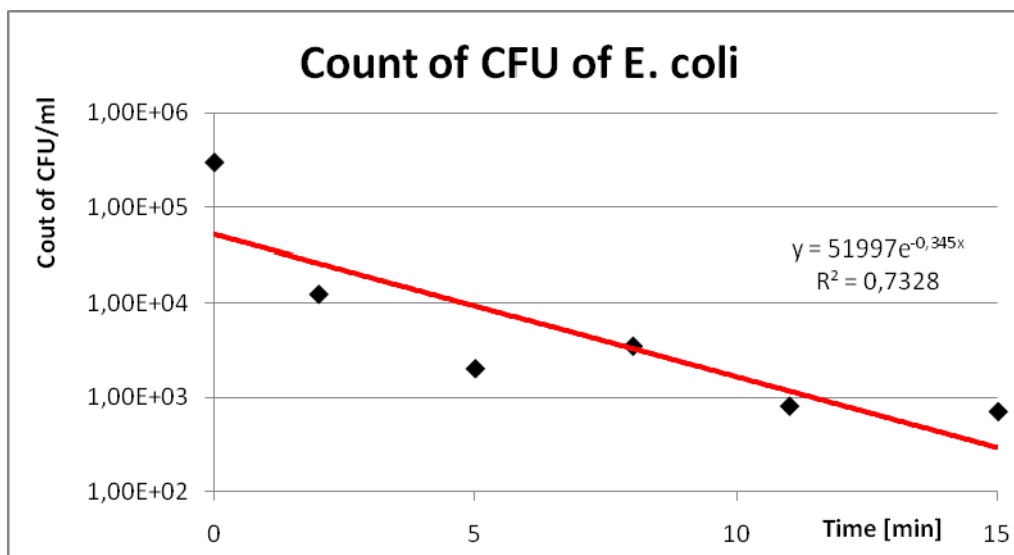


Fig. 6. Dependence of CFU count of bacteria E. coli on the PEF treatment time, 70 kV/cm

### Conclusion

The experimental device for PEF application was constructed. It provides pulsed electric field up to 70 kV/cm, quasi-rectangular shape of pulse 2  $\mu$ s FWHM and 50 Hz repetition rate. The homogeneous field was generated between electrodes of application chamber. Water solution of conductivity of 250  $\mu$ S/cm to 1 mS/cm can be treated. The effective impact on bacteria strains of different types in solution was confirmed.

### Acknowledgments

The work was supported by the Grant Agency of Academy of Sciences CR (IAAX00430802) and by Czech Science Foundation (104/09/H080).

### References

- [1] Sunka P, Babicky V, Clupek M, et al. Potential applications of pulse electrical discharges in water. In ACTA PHYSICA SLOVACA Volume: 54 Issue: 2 Pages: 135-145 Published: APR 2004. Conference Information: 14th Symposium on Application of Plasma Processes, JAN, 2003 LIPTOVSKY MIKULAS, SLOVAKIA.
- [2] Locke, B.R.; Sato, M.; Sunka, P.; Hoffmann, M.R.; Chang, J.-S. Electrohydraulic discharge and nonthermal plasma for water treatment, Ind. Eng. Chem. Res. 2006, 45 (882).
- [3] <http://www.cfsan.fda.gov/> Kinetics of Microbial Inactivation for Alternative Food Processing Technologies - Pulsed Electric Fields
- [4] Spetlikova E, Interaction of corona discharges and electrical fields into biological activation in water, master thesis, Institute of Chemical Technology, Praha 2007, in Czech.
- [5] Lukes P, Clupek M, Babicky V, et al. Ultraviolet radiation from the pulsed corona discharge in water. In PLASMA SOURCES SCIENCE & TECHNOLOGY Volume: 17 Issue: 2 Article Number: 024012 Published: MAY 2008. Conference Information: 28th International Conference on Phenomena in Ionized Gases, JUL 15-20, 2007 Prague, CZECH REPUBLIC.

# Surface properties of antibacterially pre-treated polyvinylchloride

I. Novák<sup>1</sup>, M. Lehocký<sup>2</sup>, I. Chodák<sup>1</sup>, M. Števiar<sup>1</sup>, A. Popelka<sup>1</sup>, A. Vesel<sup>3</sup>, I. Junkar<sup>3</sup>

<sup>1</sup>Polymer Institute, Slovak Academy of Sciences, 842 36 Bratislava, Slovakia

<sup>2</sup>Tomas Bata University in Zlín, T.G.M. Sq. 5555, 760 01 Zlín, Czech Republic

<sup>3</sup>Department of Surface Engineering, Plasma Laboratory, Jožef Stefan Institute, Jamova cesta 39, SI-1000 Ljubljana, Slovenia

e-mail: upolnovi@savba.sk

## Abstract

Medical-grade polyvinyl chloride was coated by polysaccharides through a novel physicochemical approach. An initial surface activation was performed foremost via diffuse coplanar surface barrier discharge plasma in air at ambient temperature and pressure. Then, radical graft copolymerization of acrylic acid through grafting-from pathway was directed to render a well-defined brush of high density, and finally chitosan monolayer and chitosan/pectin alternating multilayer were bound onto the functionalized surfaces. Surface characteristics were systematically investigated using several probe techniques.

**Keywords:** Bacterial adhesion, plasma polymerization, polyvinylchloride, surface modification.

## Introduction

A multistep physicochemical approach making use of plasma technology combined with wet chemistry has fueled considerable interest in delivery of surface-active anti-adherence materials [1 - 4]. In the first step of the approach, concerning an inherent lack of befitting functional groups on pristine substrate, plasma treatment at low temperature and atmospheric pressure has been substantiated to be productive in yielding reactive entities on the surface [1,4]. In the second phase of the approach, an end-functionalized polymer brush is synthesized on the surface via surface-initiated polymerization (SIP). SIP encourages the formation of surface-confined thick brush layers of high grafting density on the surface using generation of appropriate initiators anchored to substrate in which monomers are able to easily make their way through already-grafted layer and contribute to the chain growth. In the final step, biomolecular species are immobilized onto this platform to bear sought after biological activity. Immobilization of the biomolecules onto the surface is feasible in light of the bioconjugation chemistry.

## Experimental

### General

PVC pellets, extrusion medical-grade RB1/T3M of 1.25 g·cm<sup>-3</sup> density, were obtained from ModenPlast (Italy) and used as received. Pectin from apple, (BioChemika, with esterification of 70-75%), acrylic acid (99.0%, anhydrous), and *N*-(3-dimethyl aminopropyl)-*N'*-ethyl carbodiimide hydrochloride (EDAC, 98.0%) were supplied by Fluka (USA). Chitosan from crab shells with medium molecular weight and deacetylation degree of 75-85%.

### Plasma activation, PAA grafting and polysaccharides immobilization

Plasma treatment was implemented in static conditions by DCSBD technology with air as the gaseous medium at atmospheric pressure and room temperature. All samples were treated on both sides with plasma power of 200 W for 15 sec. PVC substrates, upon treatment with plasma, were immersed into spacer solutions containing 10 vol.% AA aq. solution. The reaction was allowed to proceed for 24 h at 30 °C. The samples were taken out, washed with 0.05 vol.% Triton X-100 aq. solution, and also deionized water for 5 min at 30 °C in an ultrasonic bath to remove any unbound PAA species on the surface. Drying was done in an air-circulating oven under 30 °C for 24 h. PAA grafted PVC samples were dipped into 1 w/v % glutaraldehyde aq. solution at 4 °C overnight which acted as an amine-reactive homobifunctional fixative to immobilize chitosan species onto the surface via crosslinking.

## Results and discussion

A highly surface sensitive technique is contact angle analysis which enables a convenient assessment of the surface wettability. PVC exhibits a hydrophobic characteristic ( $\theta_w = 85.9^\circ$ ), which after being treated by plasma, an evident change in  $\theta_w = 64.9^\circ$  arises, and hydrophilicity ascends as anticipated. This trend continues in the case when polyacrylic acid (PAA) chains are grafted where more hydrophilic propensity is shown inferred from  $\theta_w$  value  $46.5^\circ$ ). The elevated hydrophilicity upon multistep modifications is assumed to come from the inclusion of superficial hydrophilic entities. The hydrophilicity then decreases as polysaccharides are coated onto the investigated polymer ( $\theta_w = 50.5^\circ$ ).

## Conclusions

DSBD plasma is capable of raising surface energy of PVC, and introducing oxygen-containing functionalities anchored onto the polymeric surface. A structured PAA brush of high graft density is synthesized using surface-initiated approach to further improve hydrophilicity and develops a stable brush-like assembly to yield a platform for biomolecular binding. Surface-sensitive analyses evidence the presence of chitosan and chitosan/pectin multilayer.

## Acknowledgements

The research was supported by the Slovak Scientific Agency (project VEGA, No. 2/7103/27), by the Slovak Research and Development Agency (VMSP-P-0023-09), and by the Ministry of Education, Youth, and Sports of the Czech Republic (Grant VZ MSM 7088352101) as well as (Grant MPO 2A-1TP1/126).

## References

- [1] T. Desmet, R. Morent, N. D. Geyter, C. Leys, E. Schacht, P. Dubruel, *Biomacromolecules*, 10 (2009) 2351.
- [2] G. Speranza, G. Gottardi, C. Pederzoli, L. Lunelli, R. Canteri, L. Pasquardini, E. Carli, A. Lui, D. Maniglio, M. Brugnara, M. Anderle, *Biomaterials*, 25 (2004) 2029.
- [3] K. Triandafillu, D. J. Balazs, B. O. Aronsson, P. Descouts, P. T. Quo, C. van Delden, H. J. Mathieu, H. Harms, *Biomaterials*, 24 (2003) 1507.
- [4] E. R. Kenawy, S. D. Worley, R. Broughton, *Biomacromolecules*, 8 (2007) 1359.

# High-Density Polyethylene Membranes Pre-Treated by Diffuse Barrier Discharge Plasma

I. Novák<sup>1</sup>, I. Chodák<sup>1</sup>, M. Števiar<sup>1</sup>, M. Špírková<sup>3</sup>, G. Elyashevich<sup>2</sup>,  
A. Olifirenko<sup>2</sup>, A. Popelka<sup>1</sup>, A. Kleinová<sup>1</sup>

<sup>1</sup> Polymer Institute, Slovak Academy of Sciences, 842 36 Bratislava, Slovakia

<sup>2</sup> Institute of Macromolecular Compounds, Russian Academy of Sciences, Saint Petersburg,  
Russian Federation

<sup>3</sup> Institute of Macromolecular Chemistry, Academy of Sciences of the Czech Republic, v. v. i., Praha, Czech Republic

e-mail: upolnovi@savba.sk

## Abstract

The contribution deals with surface modification of high density polyethylene (HDPE) porous film by surface barrier discharge plasma in nitrogen and oxygen. It was observed that the surface energy of HDPE porous film modified by diffuse surface barrier discharge plasma increased even for short time of modification.

**Keywords:** AFM, high-density polyethylene, barrier plasma, modification, surface energy, peel, porous film.

## Introduction

The hydrophobicity of polyethylene represents a permanent problem which cannot be solved without modification of polymer. The securing of good adhesion of more polar liquids to HDPE porous film surface necessitates increasing its surface energy by convenient modification methods. The most advanced method of modification of HDPE porous film surface, due to its practical usability, suitability to continuous modification processes, and efficiency the modification, is based on modification by electric discharge plasma [1 – 4]. The aim of the paper is presentation of research results relating to the change in surface and adhesive properties of HDPE porous film modified by diffuse surface barrier discharge plasma in the medium of N<sub>2</sub> or O<sub>2</sub> at atmospheric pressure.

## Experimental

The experiments were carried out with HDPE porous film (Stavrolen, Russia) prepared by melt extrusion process with subsequent annealing and uniaxial extension. The thickness of HDPE porous film was 14 μm and it contained through channels 100-300 nm in size.

The modification of HDPE porous film was performed in static conditions by diffuse surface barrier discharge (DSBD) plasma. The modification of polymer was realized at atmospheric pressure in N<sub>2</sub> or O<sub>2</sub> of a technical purity.

Measurement of the surface energy of polymer was carried out by direct measurements of contact angles of testing liquids set (re-distilled water, ethylene glycol, formamide, methylene iodide, and α-bromo naphthalene) using Surface Energy Evaluation System (Advex, Czech Republic). The surface energy and its polar component were evaluated by Owens-Wendt–Rable–Kaelble (OWRK) modified by method of least squares [3].

## Results and discussion

The surface properties of HDPE porous film modified by DSBD plasma in O<sub>2</sub> and N<sub>2</sub> are shown in Fig. 1. The surface energy of HDPE porous film treated by DSBD increased markedly after a short treatment time (5 s) in comparison with unmodified polymer. The total surface energy of SBD plasma modified HDPE porous film increased from 33.2 mJ.m<sup>-2</sup> (unmodified sample) up to 51.8 mJ.m<sup>-2</sup> (DSBD, O<sub>2</sub>, 10 s) and 53.9 mJ.m<sup>-2</sup> (DSBD, O<sub>2</sub>, 20 s), or 48.9 mJ.m<sup>-2</sup> (DSBD, N<sub>2</sub>, 10 s) and 51.3 mJ.m<sup>-2</sup> (DSBD, N<sub>2</sub>, 20 s), respectively. The degree of modification of HDPE porous film by DSBD discharge plasma was more pronounced with longer time of modification.

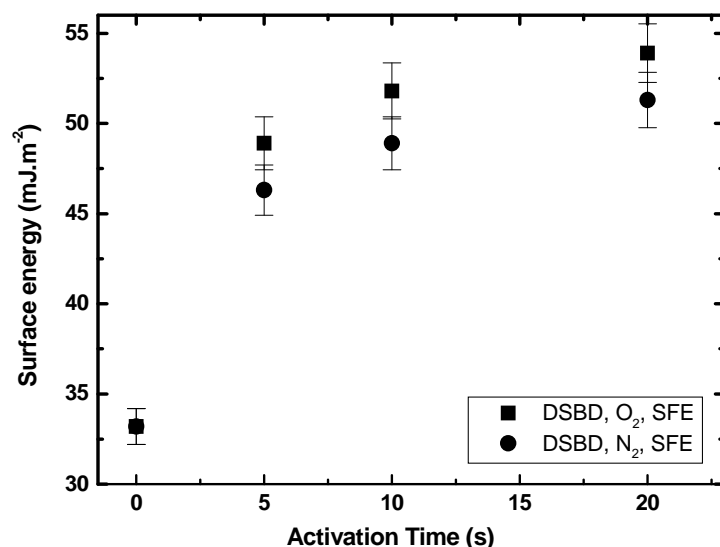


Fig.1. Surface energy of HDPE porous film modified by DSBD (50 W) plasma in O<sub>2</sub> and N<sub>2</sub> vs. time of activation.

### Conclusions

The significant increase of the surface energy and its polar component of HDPE porous film modified by DSBD plasma in O<sub>2</sub> and N<sub>2</sub> at atmospheric pressure was observed. This increase was important even for short times of polymeric porous film modification by DSBD plasma, and for longer times of modification was more pronounced.

### Acknowledgements

The research was supported by the Slovak Scientific Agency (project VEGA, No.2/7103/27), by the Slovak Research and Development Agency (VMSP-P-0023-09) by the Grant Agency of the Academy of Sciences of the Czech Republic (grant A 400500505) and the Russian Foundation for Basic Research (Grant No. 07-03-00177).

### References

- [1] M. Mikula, Z. Jakubíková, A. Záhoranová, J. Adhes. Sci. Technol., 17 (2003) 2097.
- [2] J. Ráhel, M. Šimor, M. Černák, M. Štefečka, Y. Imahori, M. Kando, Surf. Coat. Technol., 169-170 (2003) 604.
- [3] I. Novák, M. Števiar, I. Chodák, I. Krupa, T. Nedelčev, M. Špírková, M. M. Chehimi, J. Mosnáček, A. Kleinová, Polym. Adv. Technol., 18 (2007) 97.
- [4] I. Novák, V. Pollák, I. Chodák, Plasma Process. Polymers, 3 (2006) 355.

# Coating of cyclodextrins on the plasma activated polypropylene non-woven

M. Wolfova, L. Cernakova, K. Reichova

Institute of Polymer Material, Slovak University of Technology, Radlinského 9, Bratislava 812 37, Slovakia

e-mail: magdalena.wolfova@stuba.sk

## Introduction

The plasma technology provides several varieties for surface treatment. Some of the most widely used applications are: cleaning (contaminated devices), plasma activation, etching and coating of layers. That is reason, why this plasma technology is used for various applications, where materials have to be combined or where surface of materials need special modification.

The possible aims by using plasma technology are: improved wettability, adhesions of coating, printability, induced hydro/ or oleophobic properties, changing physical and/ or electrical properties, cleaning or disinfection of fibre surfaces etc.

The modified fabrics are important for medical, hygienic, and home usage applications and have received a great importance because of the recent appearance of fatal diseases. As a result, there is an increased demand of the biocidal textiles, especially those used in hospitals to prevent or minimize infection or transmission of diseases and protecting health care workers.

One of such groups of specific compound is cyclodextrins. Cyclodextrins (CDs) – the essential ingredients for the production of new material are used in the textile field. CDs are mainly used for keeping moisture, reducing odors in fibres added with plant extract, and retaining the anti- bacterial activity in fibres containing and added antibacterial agent [1]. Examples of products utilizing such functions include underwear suitable for dry skin, underwear beneficial for people, with allergies and socks treated to reduce unpleasant smell.

Cyclodextrins, with lipophilic inner cavities and hydrophilic outer surfaces, are capable of interacting with a large variety of guest molecules to form noncovalent inclusion

complexes (Fig.1). Chemically they are cyclic oligosaccharides containing at least 6 D-(+) glucopyranose units attached by  $\alpha$ -(1, 4) glucosidic bonds [2].

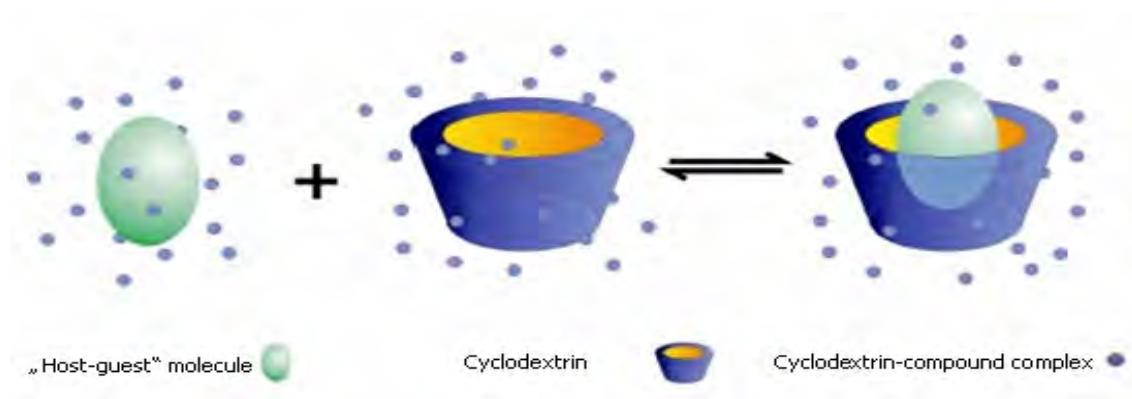


Fig. 1. The formation of Cyclodextrin complex

## Results and discussion

This work is focused on the study of possibility coating of  $\beta$ - cyclodextrins on the textile material, because they have wide application such as “host- guest” molecules. The surface of polypropylene non-woven was activated by an atmospheric-pressure plasma treatment using surface dielectric barrier discharge in  $N_2$  or ambient air.

At first, on the activated surface of PP textile we coated only water solution of  $\beta$ - cyclodextrins and after drying (for 24 hours) modified samples were washed in distilled water. It was found by gravimetric analysis, that 98 % from all coated amount of  $\beta$ - cyclodextrins was removed. Because of that fact, it was choose the possibility of coating  $\beta$ - cyclodextrins with  $\gamma$ - aminopropyltriethoxysilane (APTES). The second series of samples with modified layers of  $\beta$ - cyclodextrine/  $\gamma$ -

aminopropyltriethoxysilane was followed and continued from previous studies, where the base is their good compatibility. The layer of cyclodextrins in combination with APTES was coated on the surface of the polypropylene non-woven after plasma treated. Based on our previous results on the air and nitrogen plasma activation of PPNW the samples were activated for 5 seconds on both sides [3].

In our case, the modified layer cyclodextrin/  $\gamma$ - aminopropyltriethoxysilane was prepared by ultrasound, where solution of  $\gamma$ - aminopropyltriethoxysilane was in the rate of 1 ml APTES: 90 ml EtOH: 9ml H<sub>2</sub>O. We prepared solution of  $\gamma$ - aminopropyltriethoxysilane and powder of  $\beta$ - cyclodextrins together in ultrasound. Activated samples of polypropylene non-woven were immersed in this solution with concentration 6, 12, 18g  $\beta$ - CDs/l of  $\gamma$ - aminopropyltriethoxysilane and dried by air or at a temperature 120°C.

It was found out that the content of linked amount of  $\beta$ - cyclodextrins solution of  $\gamma$ - aminopropyltriethoxysilane depend on fixation method of samples (thermal, air) and it adequately increases to the concentration of  $\beta$ - cyclodextrin in solution (Fig.2)

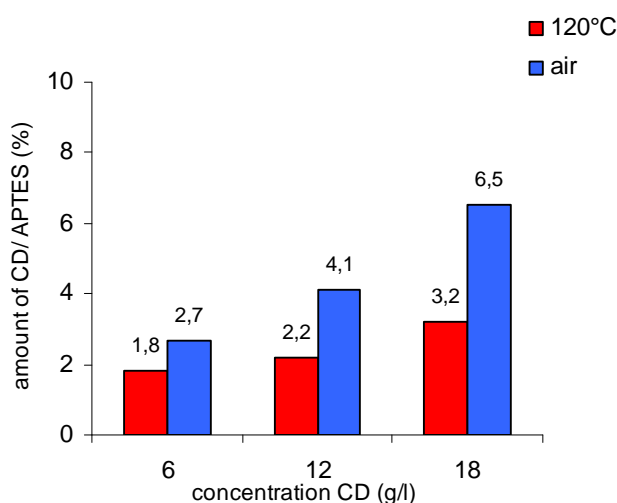


Fig. 2. The dependence amount of  $\beta$ - CD/  $\gamma$ - aminopropyltriethoxysilane coated of polypropylene non-woven from concentration of CD

The presence of modifying layer  $\beta$ - CD/  $\gamma$ - aminopropyltriethoxysilane on the polypropylene non-woven before and after washing was studied by infrared spectroscopy and scanning electron microscopy. Figure 3 shows ATR - FTIR spectra of the samples coated by  $\beta$ - cyclodextrins in combination of  $\gamma$ - aminopropyltriethoxysilane. It can be seen that for  $\beta$ - cyclodextrins are characteristic peaks in field 3000 and 1100  $\text{cm}^{-1}$ , for  $\gamma$ - aminopropyltriethoxysilane are characteristic peaks in field 1100  $\text{cm}^{-1}$ .

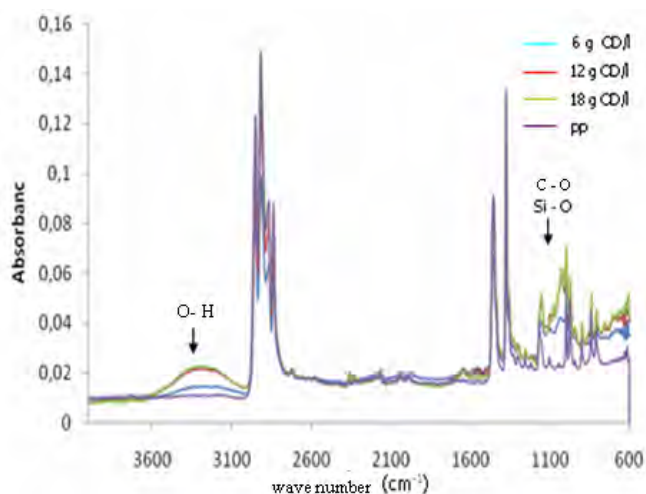


Fig. 3. Spectrum of polypropylene non-woven coated with layer of solution  $\gamma$ - aminopropyltriethoxysilane and  $\beta$ - cyclodextrins

It was found, that more modifying layer remained on the air-dried than thermal fixed samples (Fig. 2). The presence of modifying layer  $\beta$ - cyclodextrin/  $\gamma$ - aminopropyltriethoxysilane was shown by SEM microscopy.

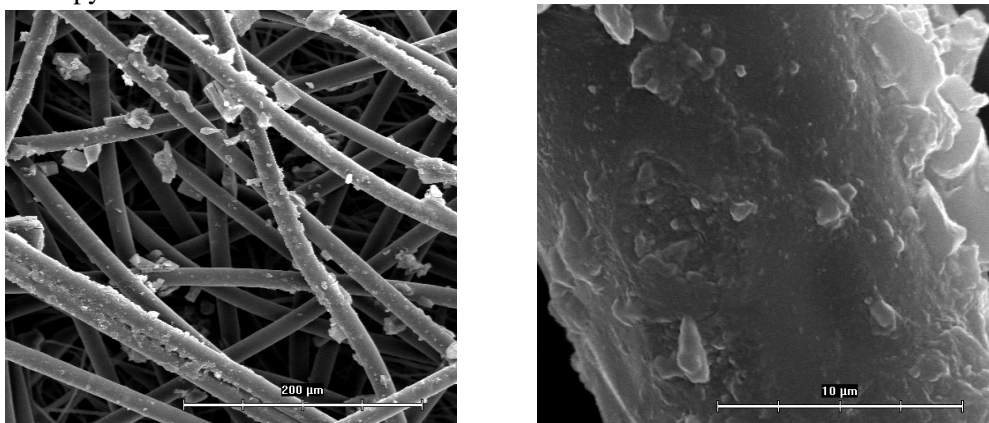


Fig. 4. SEM images of the plasma-activated samples coated by modifying layer cyclodextrin/  $\gamma$ -aminopropyltriethoxysilane

SEM images (Fig. 4) of the samples coated by  $\beta$ - CD/APTES, that fibres are coated with modifying layer inhomogeneously.

### Conclusions

In this work we have presented some experiments of the immobilization of  $\beta$ - cyclodextrins in combination with  $\gamma$ - aminopropyltriethoxysilane onto plasma activated PPNW. It was found out, that plasma activation allows surface modification of PP fibres by  $\beta$ - cyclodextrins.

### Acknowledgements

The authors wish to thanks to the Grant Agency of Slovak Republic Vega 1/0815/08

### References

- [1] Helena Dodziuk: Cyclodextrins and their complexes, Wiley-VCH Verlag GmbH&Co. KGaA, Weinham, 2006, p. 456
- [2] Challa R, Ahuja A, Ali J, Khar R. Cyclodextrins in Drug Delivery: An Updated Review. AAPS PharmSciTech. 2005
- [3] Ľ.Černáková, R. Szabová, M. Wolfová, A. Buček, M.Černák: Surface Modification of Polypropylene Non-woven after plasma Activation at Atmospheric pressure

# The Influence of Atmospheric Pressure Plasma on Polypropylene Films

A. Oravcova, I. Hudec

Institute of Polymer Materials, Faculty of Chemical and Food Technology, Slovak University of Technology, Radlinskeho 9, Bratislava 812 37, Slovakia

e-mail: xoravcovaa@stuba.sk

## Abstract

This paper reports the influence of the atmospheric pressure plasma treatment on the surface properties of polypropylene (PP) films. The films were modified by atmospheric pressure plasma treatment by the diffuse coplanar surface barrier discharge (DCSBD) using ambient air as working gas. The contact angle measurement, the dyne test, atomic force microscopy (AFM) and attenuated total reflection technique Fourier transformed infrared spectroscopy (ATR-FTIR) were applied to analyze the changes of the surface of the polymer film. In all experiments, the contact angle of the treated polypropylene samples decreased and the surface energy of the samples increased in comparison with the plasma untreated samples. The proper surface energy for printing using solvent-based inks was detected by all the samples. There were not observed any significant changes in mechanical properties of the films after plasma treatment by measuring their tear parameters.

**Key words:** Atmospheric pressure plasma, Polypropylene film, Surface energy, Wetting

## Introduction

Recently atmospheric pressure plasma is very attractive for many industrial applications due to its low-cost, high speed and the ability to operate without vacuum.

The advantage of the plasma treatment is the ability to change the surface properties of the most external layers of the material without modifying its bulk characteristics (Inagaki, 1996).

Using appropriate plasma treatment, the surface of the non-polar polymer material may be activated to contain the variety of functional groups including oxygen-based functionalities (carbonyl, carboxyl, ether, peroxide etc.) or nitrogen- based groups resulting in modification of the surface properties. . A low-functionality polymer surface becomes more reactive.

The purpose of this work was to improve surface energy and wettability of the polypropylene films before printing.

The result of plasma modification of the polymer film is the increase of the surface energy of the polymer and the improvement of surface wetting by liquid. The minimum value of the surface free energy of the material being printed using the solvent-based inks is  $38 \text{ mJ m}^{-2}$ .

## Materials and Methods

The transparent PP film (monoaxially oriented polypropylene, 30  $\mu\text{m}$  thickness, CHEMOSVIT FOLIE, a.s. Svit) determined for packaging various food products was studied. The film samples were activated by atmospheric pressure plasma treatment by diffuse coplanar surface barrier discharge DCSBD (350W input) using ambient air as working gas. The treatment time varied from 1s to 5s.

Wetting was characterized by the contact angle measurement of sessile drop (4 $\mu\text{l}$ , testing liquids; water, glycerol,  $\alpha$ -bromonaphthalene, formamide, ethylene glycol) using CCD camera (SEE software 6.1, MU Brno, Czech.Rep.). The calculation of surface energy was performed by using Owens - Wendt regression method.

The test pen Quick Test 38 was also used to confirm changes in wetting of the films.

The functional groups of the polypropylene surface after plasma treatment were monitored by the attenuated total reflection (ATR) technique of FTIR spectroscopy (Excalibur, FTS 3000MX, Digilab, USA).

Atomic force microscopy (AFM, IC-mod, Veeco Di CP-II) was applied to analyze the changes in morphology of the samples.

Mechanical properties were measured and calculated by Zwick Tensile tester (by STN ISO 527).

## Results and Discussion

The surface properties of the plasma-treated PP films were monitored by using contact angle measurements in testing liquids with different polarity and surface free energy calculation.

As it can be seen in the Fig.1a, polar liquids, such water, do not wet the surface of the untreated hydrophobic PP film in comparison with the treated film sample (Fig.1b).

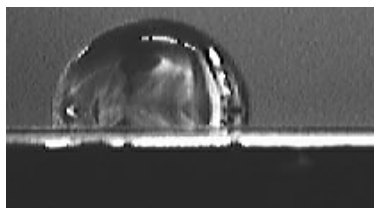


Fig.1a. A drop of water on the PP film **before** plasma treatment

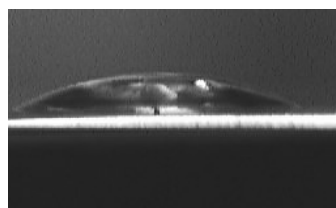
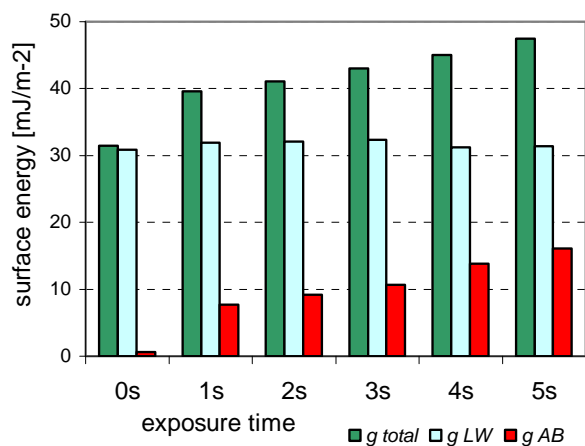


Fig.1b. A drop of water on the PP film **after** plasma treatment (5s)

The angles of water and other testing liquids on PP film are largely decreased with increasing treatment time. The values of total surface energy, calculated by Owens-Wendt regression method, are increased, as shown in Fig.2.



There is a significant increase in the polar (AB) component of surface energy.

The required surface energy for printing using solvent-based inks ( $38 \text{ mJ/m}^2$ ) was detected by all the investigated samples.

Fig.2 Influence of the time of plasma treatment on the surface energy

Printing ink-wettability was also confirmed by the dyne test (Quick Test 38).

AFM technique was used to study changes in morphology of PP films as it can be seen in Fig.3a and Fig.3b. There are changes in roughness, the value of middle roughness (RSM) increased (RSM=3.1nm for untreated film sample) after plasma treatment (RSM=24nm for 5s plasma treated film sample). It can be caused by thermal effects of plasma or chemical reactions and sputtering.

Fig.3a AFM image of untreated PP  
RSM= 3.1nm

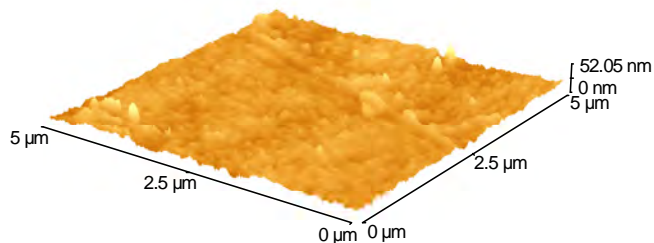
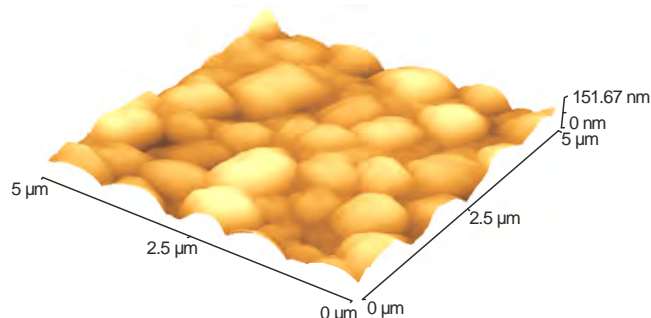


Fig.3b AFM image of 5s plasma treated PP  
RSM= 24nm



The surface functionalities were also detected by ATR-FTIR spectroscopy. Fig.4 shows the influence of plasma discharge on chemical composition of surface of polypropylene films.

There are some small surface changes of PP films, before and after plasma treatment, in the region of carbonyl and carboxyl groups ( $1520\text{-}1750 \text{ cm}^{-1}$ ). It confirms creation of small amount of polar functional groups on the film.

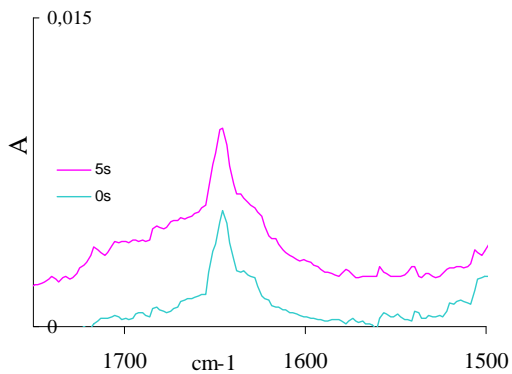


Fig.4 ATR-FTIR spectrum of untreated (0s) and plasma treated (5s) PP films

As it was expected, plasma treatment has no significant influence on mechanical properties (“bulk properties”). The values of tensile strength at break varied from 22.9 (5s) to 23 MPa (1s), the value for untreated sample was 23 MPa.

### Conclusion

Based on obtained results it is possible to note that the plasma treatment at atmospheric pressure by diffuse coplanar surface barrier discharge seems to be a successful technique for improving wettability of hydrophobic polymer film materials.

As performed experiments showed, the contact angle of the treated the PP films decreased and the surface energy of the samples increased in comparison with the plasma untreated samples. The improved wettability of the samples was also obtained by using the dyne test pen. The proper surface energy for printing using solvent-based inks ( $38 \text{ mJm}^{-2}$ ) was detected by all the investigated samples after plasma treatment in ambient air. It was confirmed that plasma treatment has no significant influence on mechanical properties of polypropylene films, too.

### References

- Inagaki N., Plasma Surface Modification and Plasma Polymerization, CRC Press, London, (1996)  
 Panák J. et al., Polygrafické minimum, TYPOSET, Bratislava (2008) 169.

# Surface modification of low-density polyethylene by poly(2-ethyl-2-oxazoline) using high-pressure plasma

A. Popelka, J. Kronek, I. Novák, I. Chodák, A. Kleinová  
Polymer Institute, Slovak Academy of Sciences, 845 41 Bratislava 45, Slovakia

e-mail: juraj.kronek@savba.sk, anton.popelka@savba.sk

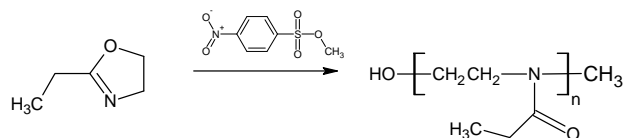
## Abstract

Low-density polyethylene (LDPE) belongs to the most produced polymers in the world. However, it is polymer with rather hydrophobic character what is limiting to the further processing, such as in dyeing, printing and bonding. This problem can be solved by surface modification LDPE by high-pressure plasma and by introduced chemical substances containing functional polar groups such as polyoxazoline. Furthermore, 2-oxazoline based polymers belong to biocompatible and non-toxic materials what is advantageous in biomedical applications. This work was dedicated to the binding of poly(2-ethyl-2-oxazoline) (PETOX) to LDPE using low temperature plasma generated by diffuse coplanar surface barrier discharge (DCSBD).

**Keywords:** Poly(2-ethyl-2-oxazoline), low-density polyethylene, modification, surface energy, FT-IR-ATR.

## Introduction

LDPE excels bulk properties suitable for many applications. However its surface energy reaches low values, which are reflected in low hydrophilic character of LDPE. This feature is related to hydrophobic and chemically inert surface of LDPE, which occur difficulties in further processing, i.e. dyeing, printing and bonding (low adhesion). These difficulties can be eliminated by surface modification of LDPE [1]. Plasma modification techniques belong to the important methods of surface modification of polymers. This change occurs on very thin layer of polymer surfaces without affecting bulk properties. These can be considered as green, clean and dry processes, which do not use chemicals and they are suitable for industrial applications. The surface modification of polymer surfaces using low temperature plasma is widely used in various industries such as electronics, aerospace, automotive, biomedical, textile, optical and paper industry [2]. PETOX was chosen to be bounded to LDPE using low-temperature plasma generated by DCSBD [3], which generates macroscopically homogeneous plasma without direct contact with the electrodes. PETOX represents a polymer containing polar amide groups and belongs to a group of biocompatible materials [4]. This polymer can be prepared by a living cationic polymerization initiated by the various electrophilic species, for example alkyl halides, sulfonic esters, strong acids and others (Scheme 1) [5].



Scheme 1. Cationic polymerization of 2-ethyl-2-oxazoline.

## Experimental

The experiments were carried out with foil of BRALEN FB 2-17 (Slovnaft MOL, Slovakia). The thickness of LDPE film was 20 μm. The surface modification of LDPE foil was performed in dynamic conditions by DCSBD plasma in O<sub>2</sub> atmosphere, for 20 sec, and input supply was 200 W.

The surface properties of unmodified and modified LDPE were carried out by the measurements of contact angles of testing liquids set, such as water, ethylene glycol, glycerol, formamide, and methylene iodide. Surface Energy Evaluation System (See system, Advex Instruments, Czech Republic) was used for contact angle measurements. The surface energy and its polar component were calculated by Owens-Wendt-Rabel-Kaelble model (OWRK). Structure changes of the modified surface were monitored by Fourier Transform Infrared Spectroscopy with Attenuated Total

Reflectance (FT-IR-ATR) using a Nicolet 8700 equipment.

The adhesive properties, namely peel force and peel strength (force per unit width) of adhesive joint of modified LDPE by PETOX using DCSBD to poly(ethylacrylate) deposited onto polypropylene foil (with 15 mm width), were carried out by measurements of peel test (90 deg) using Instron 4301.

## Results and discussion

The water contact angle changes of LDPE treated by DCSBD plasma in O<sub>2</sub>, and subsequently grafted by PETOX are shown in Fig. 1. The water contact angle of treated LDPE foil evidently decreased in comparison with unmodified polymer. Analogously, the surface energy and its polar component significantly increased with increasing PETOX content from 1 wt. % up to 10 wt. % such as shown in Fig. 2. This decrease of water contact angle and the increase of hydrophilicity are caused by the presence of polar functional groups in PETOX.

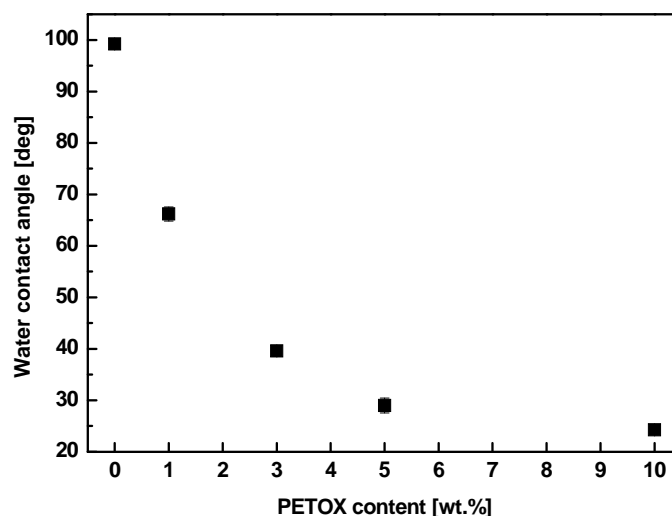


Fig. 1. Water contact angle of LDPE foil modified by PETOX using DCSBD plasma vs. PETOX content.

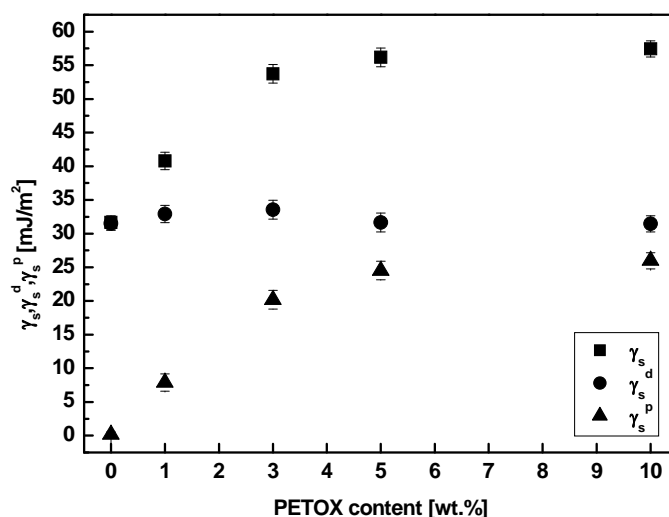


Fig. 2. Surface energy ( $\gamma_s$ ), its dispersive ( $\gamma_s^d$ ) and polar ( $\gamma_s^p$ ) component of LDPE treated by PETOX using DCSBD plasma vs. PETOX content.

The samples of LDPE modified with PETOX were washed in H<sub>2</sub>O to remove non-bounded and

weakly bounded PETOX from LDPE surface. The changes of water contact angle before and after washing in H<sub>2</sub>O are shown in Fig. 3. There is apparent the increase water contact angle after washing in H<sub>2</sub>O what is causing by removal non-covalently bonding chemical substances from LDPE surface.

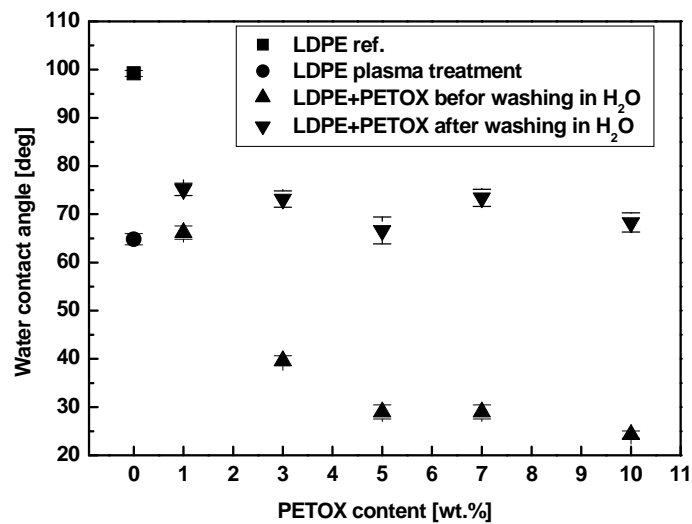


Fig. 3. Water contact angle of LDPE foil modified by PETOX using DCSBD before and after washing in H<sub>2</sub>O vs. PETOX content.

The modification of LDPE by PETOX using DCSBD resulted in the increasing peel force and peel strength which is shown in Fig. 4. It is also obvious that peel force and peel strength negligible decreased after samples washing in H<sub>2</sub>O.

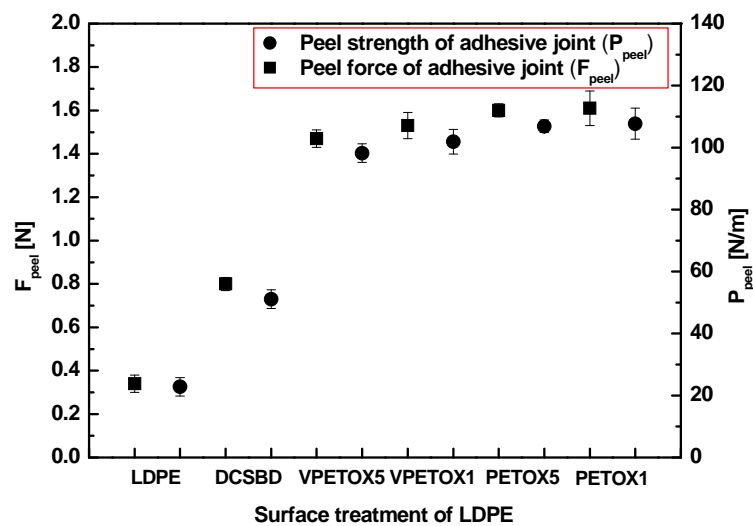


Fig. 4. Peel force and peel strength of adhesive joint modified LDPE by PETOX using DCSBD plasma (VPETOX – after washing in H<sub>2</sub>O, number behind PETOX represents its concentration in g/ml).

The presence of PETOX functional groups (such as –NCO, and –OH group) introduced onto surface of LDPE was confirmed by FT-IR-ATR measurements for LDPE modified in the different concentration of PETOX (Fig. 5).

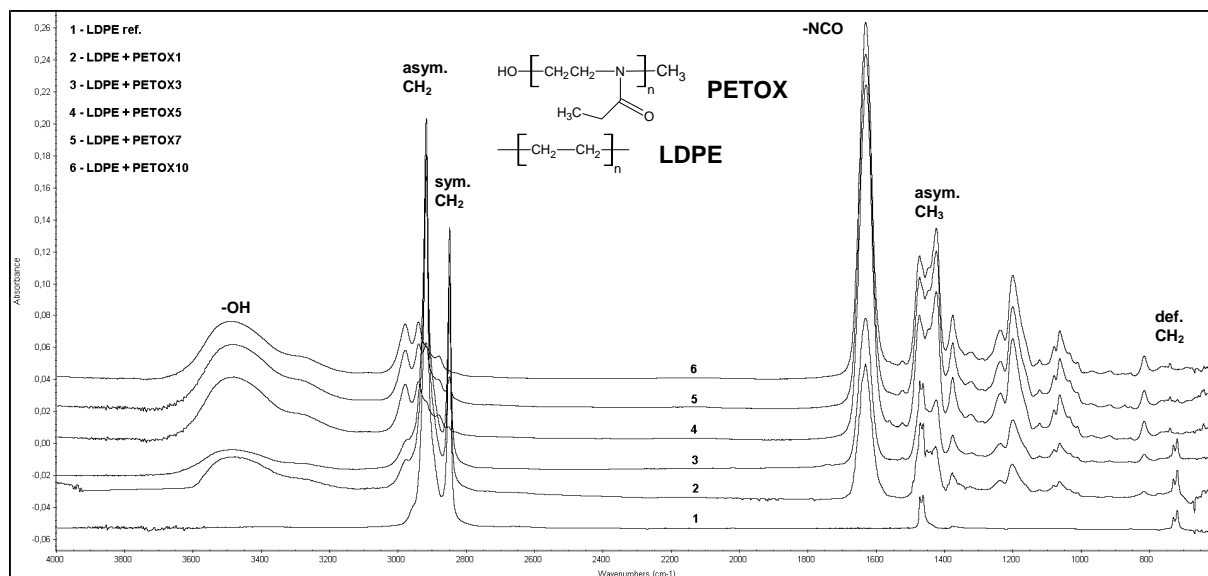


Fig. 5. FT-IR-ATR spectra of LDPE modified by PETOX using DCSBD plasma.

### Conclusions

The marked decrease of the water contact angle and an increase of surface energy of LDPE foil grafted by PETOX using DCSBD plasma in O<sub>2</sub> at atmospheric pressure were observed. The hydrophilicity of LDPE after surface treatment significantly increased. The PETOX remaining onto LDPE surface after washing was covalently-bonded. The presence of amide group in PETOX introduced onto surface of LDPE using DCSBD plasma was confirmed by FT-IR-ATR measurements. The presence of polar functional groups of PETOX grafted onto LDPE surface have been confirmed, because peel force of modified LDPE due to the introduction of polar functional groups of PETOX onto polymer surface significantly increased.

### Acknowledgements

The research was supported by Slovak Grant Agency VEGA (grant No. 2/7103/27 and No. 2/0157/09), and Slovak Research and Development Agency - APVV (grants No. 0044-07, and No. 0023-09).

### References

- [1] I. Novák, M. Števiar, I. Chodák, I. Krupa, T. Nedelčev, M. Špírková, M. M. Chehimi, J. Mosnáček, A. Kleinová, *Polym. Adv. Technol.*, 18 (2007) 97.
- [2] Q. F. Wei, *Mater. Charact.*, 52 (2004) 231.
- [3] M. Šimor, J. Ráhel', P. Vojtek, M. Černák, A. Brablec, *Appl. Phys. Lett.*, 81 (2002) 2716.
- [4] N. Adams, U. S. Schubert, *Adv. Drug Delivery Rev.*, 59 (2007) 1504.
- [5] S. Kobayashi, *Prog. Polym. Sci.*, 15 (1990) 751.

# Morphological and Electrical Properties of Tin/Plasma Polymer Nanocomposites

J. Matoušek<sup>1</sup>, J. Pavlík<sup>1</sup>, S. Novák<sup>1</sup>, R. Hrach<sup>1,2</sup>, M. Švec<sup>1</sup>, L. Kovačik<sup>3</sup>

<sup>1</sup>Department of Physics, Faculty of Science, J. E. Purkinje University, České mládeže 8, Ústí nad Labem 400 96, Czech Republic

<sup>2</sup>Department of Surface and Plasma Science, Faculty of Mathematics and Physics, Charles University, V Holešovičkách 2, Prague 180 00, Czech Republic

<sup>3</sup>Institute of Cellular Biology and Pathology, First Faculty of Medicine, Charles University, Albertov 4, Prague 128 01, Czech Republic

e-mail: jindrich.matousek@ujep.cz

## Abstract

Composite thin films – tin/n-hexane plasma polymer were prepared by means of RF magnetron sputtering of tin target in Ar:n-hexane mixture. The films were characterized by various analytical techniques. The X-ray photoelectron spectroscopy (XPS) was used to examine the chemical composition of the surface, current-voltage characteristics were measured and the structure of the deposited films was investigated by conventional transmission electron microscope (TEM) and electron tomography. The three-dimensional reconstructions were analysed by a self-made computer analytical tool. The analysis was used to estimate the mean form factor and the average effective radius of the reconstructed metal inclusions.

**Keywords:** tin; plasma polymers; magnetron sputtering; nanocomposites

## Introduction

Metal/dielectric nanocomposite films have been studied since the second half of the 20th century [1] and still remain in the focus of research attention thanks to their interesting mechanical, optical and electrical properties. The potential of these materials has not been exhausted yet (sensors, switching and optical devices, data storage, ...) and therefore the nanocomposites are still studied intensively [2-5].

Various deposition techniques (e.g. evaporation and metal sputtering with plasma polymerization) were used to prepare the nanocomposite films [6], the RF magnetron sputtering of metal in the working gas mixture consisting of argon and monomer vapors is one of them. Properties of layers prepared by this method are very sensitive to deposition conditions. We focused our attention on the investigation of the relation between deposition conditions, morphology and electrical properties of the deposited layers.

## Experimental

The nanocomposite thin films were prepared by a tin magnetron sputtering with simultaneous plasma polymerization in a stainless steel deposition chamber, which was pumped by a diffusion pump with a rotary backing pump (the chamber was pumped down to  $10^{-3}$  Pa before each experiment). The working gas mixture of n-hexane vapors (Sigma–Aldrich purity 95 %) and argon (Linde, purity 99.9999 %) was introduced through two needle valves, the n-hexane (liquid) was in a glass container connected to one of the needle valves. The n-hexane fraction  $r_{\text{nhex}}$  (ratio of partial pressures:  $r_{\text{nhex}} = p_{\text{nhex}}/(p_{\text{nhex}} + p_{\text{Ar}})$ ) in the working gas mixture varied from 1 % to 3 %. The total working gas pressure for all experiments was 6 Pa. A balanced magnetron with Sn target was powered by an RF generator (Dressler Cesar 133) with a matching network. The power varied from 65 W to 90 W, the sample to target distance was 40 mm. We used a silicon wafer for XPS analysis, carbon-covered Cu grid for TEM and electron tomography, and  $\text{Al}_2\text{O}_3$  wafer with screenprinted gold electrode system for current-voltage measurements, which were carried out using PC driven voltage source Keithley 230 and electrometer Keithley 617 used as ammeter. TEM images and electron tomography of the thin films were taken on a Tecnai G2 Sphera TEM at the operating voltage of 200 kV. Several single-axis tilted series of TEM images were acquired with  $1^\circ$  angular step in the tilting range  $|\pm 68|^\circ$  at  $\sim -600$  nm nominal defocus. The tilted series were aligned by the Imod reconstruction package [7], this alignment

was further refined by typically two rounds of re-projection matching [8]. Three-dimensional reconstructions were then computed by the Imod package and visualized by the Amira software (Mercury Computer Systems, San Diego). The XPS measurements were performed with the hemispherical analyzer operated in FAT mode (Phoibos 100 from company Specs). The photoelectron spectra were referenced to the aliphatic C1s peak at 285 eV, the elemental composition was calculated from survey spectra. The high resolution photoelectron spectra were acquired to understand the chemical bonds on the surface of the samples.

## Results and discussion

### XPS results

The chemical composition of the thin layers during 45 days after deposition was observed (see Tab.1). It showed up that it is relatively stable within this period. For whole range of used powers (from 65 W to 90 W) the changes were minimal. In general the carbon content slightly (several percent) increased while the tin amount decreased. This is probably related to the surface contamination from ambient environment. The oxidation of tin in Sn3d high resolution peak after 45 days of storage was clearly observed, two components of the Sn3d<sub>5/2</sub> peak were detected and are located at 485.0 eV and 486.9 eV. The component at 485.0 eV can be attributed to the tin in metallic state while the other is probably the mixture of oxides according to [10,11]. From these observations we concluded that the chemical composition of the surface does not change significantly or the main changes take place only several hours after deposition. Although the overall chemical composition seems to be stable, the oxidation during ageing is evident (e.g. in case of the 85 W the Sn3d<sub>5/2</sub> component located at 486.9 eV increased its fraction from 74 to 80 % related to sum of both components).

Tab.1. Chemical composition of the thin films surface after 1 day and 45 days from deposition. Values give amount in % atomic. The peaks used for quantification are given in column headings.

| 1 day | C1s | O1s | Sn3d | 45 days | C1s | O1s | Sn3d |
|-------|-----|-----|------|---------|-----|-----|------|
| 90 W  | 27  | 41  | 32   | 90 W    | 33  | 38  | 28   |
| 85 W  | 28  | 38  | 34   | 85 W    | 32  | 41  | 27   |
| 80 W  | 30  | 39  | 31   | 80 W    | 33  | 38  | 28   |
| 75 W  | 32  | 39  | 29   | 75 W    | 35  | 40  | 25   |
| 70 W  | 28  | 39  | 32   | 70 W    | 33  | 38  | 29   |
| 65 W  | 29  | 44  | 27   | 65 W    | 36  | 39  | 25   |

### Morphological analysis

The 3D reconstructions were computed from the series of TEM images as mentioned above. The output was given in the sets of parallel planar sections in grey scale. In order to enable visualisation and morphological analysis of the metal inclusions, the grey scale images had to be thresholded to distinguish the metal inclusions from the plasma polymer (see Fig.1 for 3D visualisation). The thresholding level had to be set manually due to large variation of intensity within the reconstructed inclusions. The sections close to the middle part of the film, where the inclusions had similar intensity and contrast, were analyzed using the self-made analytical tool. Detailed description of this analytical tool can be found e.g. in [12,13]. The average effective radius and mean form factor of the objects (in the planar section) were estimated. The form factor provides us with information on the shape of the tin inclusions embedded in the plasma polymer matrix – when it is close to 1, the object is close to a circle, when the form factor value is close to 0 then the shape is close to a line segment. As it can be seen from the XPS measurements (Tab.1) the chemical composition does not change much with the power delivered to the magnetron. The TEM pictures (not shown here) also showed the same tendency. For this reason the samples with different n-hexane content in the working gas mixture were selected for computer analysis – our previous observations showed that the chemical composition (and also the nanocomposite structure) is largely dependent on the working gas mixture composition. In case of analyzed samples, the average effective radius changed from  $12.3 \pm 4.8$  nm at 1 % of n-hexane to  $8.1 \pm 2.1$  nm at 3 % of n-hexane in the working gas mixture. The form factor was close to 0.9 in all

cases. The 3D reconstruction made from the thresholded sections can be seen in Fig.1.

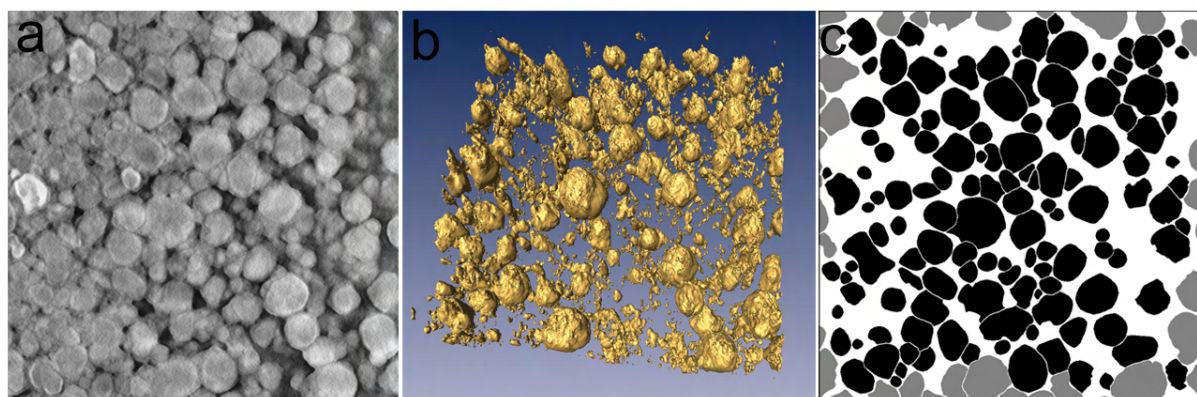


Fig.1. (1 % of n-hexane, 70W) a - Electron tomography reconstruction in grey scale (one of the planes). b - 3D visualisation of thresholded data. c - electron tomography reconstruction - thresholded data (one of the planes, the grey objects were not considered for morphological analysis).

### Electrical properties

We used earlier [9] a sandwich like arrangement of electrodes for electrical properties measurement. However, this arrangement is not very suitable when the films are intended to be used as a gas sensing device. Therefore we decided to use different type of substrate – two golden electrodes on alumina ( $\text{Al}_2\text{O}_3$ ) creating a meander-like structure. The electrode separation is  $150\ \mu\text{m}$  and the length of the system 19 cm (this length is wrapped to a piece of alumina that is  $1 \times 1\ \text{cm}$ ). The contacts were masked during deposition to allow connection to the measuring device. As the n-hexane content in the working gas mixture increased, the film character changed from a material with relatively low sheet resistance ( $1.2 \times 10^6\ \Omega/\text{sq}$ ) at 1 % of n-hexane to insulating material at 3 % of n-hexane in working gas mixture. The sheet resistance reached  $5.7 \times 10^{12}\ \Omega/\text{sq}$  in the case of the 3 % of n-hexane while the substrate with empty electrode system (i.e. without any thin film on it) showed sheet resistance  $5.8 \times 10^{12}\ \Omega/\text{sq}$ , which is in the order of the accuracy of the measurement. The measurement error is larger than 10 % in this case, which is due to very low currents (units of nA) and capabilities of the measuring device (Keithley 617). The sheet resistance values were obtained from the ohmical part of the current-voltage characteristics. In case of 2 % of n-hexane, there was no ohmical part – the slope in logarithmical plot was higher, which implies a higher power of the  $I=f(U^x)$  dependence (there  $x > 1$ ) and therefore there may also occur other charge transport mechanisms than ohmical transport only.

### Conclusions

The nanocomposite thin films Sn/plasma polymer n-hexane were prepared by RF magnetron sputtering with simultaneous plasma polymerization for various powers and working gas compositions. The XPS results show that the surface is relatively chemically stable when exposed to the ambient air for 45 days. We did not observe any ohmical part in the current-voltage characteristics of the sample deposited at 2 % of n-hexane, which can be the consequence of a non-ohmic charge transport mechanism. This will be the object of further study and the computer experiment should help us to better understand the transport mechanisms. The morphology was studied by the electron tomography and these measurements were used as input data for computer analysis. The average effective radius of the tin conclusions was estimated to decrease from 12 to 8 nm when the amount of n-hexane in the working gas mixture increased from 1 % to 3 %.

### Acknowledgement

This work was supported by The Ministry of Education, Youth and Sports of Czech Republic (Projects LC 06041, LC535, MSM0021620834 and MSM0021620834), by AS CR (Project KAN101120701) and by the Grant Agency of Czech Republic, project GACR P205/10/0979. Author J. Matoušek acknowledges the support of the Internal Grant Agency of Faculty of Science, UJEP.

## References

- [1] Abeles B., *Appl. Solid State Sci* 1976;6:1.
- [2] A. Convertino, A. Capobianchi, A. Valentini, E.N.M. Cirillo, *Adv. Mater.*, 15 (2003) 1103.
- [3] J. Ouyang, C.-W. Chu, R. Szmanda, L. Ma, Y. Yang, *Nat. Mater.*, 3 (2004) 918.
- [4] J. Musil, J. Vlcek, *Surface and Coatings Technology*, Vol. 142-144, (2001) 557-566.
- [5] J. Wang, Y. Sun, L. Wang, et al., *Colloids and Surfaces B*, Vol. 81, Issue 2, (2010) 600-606.
- [6] H. Boldryeva, P. Hlidek, H. Biederman, D. Slavinska, A. Choukourov, *Thin Solid Films*, 442 (2003) 86.
- [7] J.R. Kremer, D.N. Mastronarde, J.R. McIntosh, *J. Struct. Biol.*, 116 (1996) 71.
- [8] L. Kovacik, J.M. Plitzko, M. Grote, R. Reichelt, *J. Struct. Biol.*, 166 (2009) 263.
- [9] J. Matousek et al., *Vacuum*, 84 (2010) 86–89.
- [10] F. Morazzoni et al., *Materials Science and Engineering C*, Vol 15, (2001), p.167-169
- [11] B.V. Crist, *Handbook of Monochromatic XPS Spectra*, (Vol.1 The Elements and Native Oxides), XPS International LLC, Mountain View, 2004.
- [12] M. Švec, R. Hrach, S. Novák, J. Škvor, *Vacuum*, 82 (2008) 138-141.
- [13] S. Novák, R. Hrach, M. Švec, V. Hrachová, *Thin Solid Films*, 518 (2010) 4537-4541.

# Sheath Structure in a Multiply Ionized Electronegative Plasma

M. Khoramabadi<sup>1</sup>, H. Ghomi<sup>2</sup>

<sup>1</sup>Department of Physics, Boroujerd Branch, Islamic Azad University, Boroujerd, Iran.

<sup>2</sup>Laser and Plasma Research Institute, Shahid Beheshti University, Evin 1983963113, Tehran, Iran.

e-mail: m.khoramabadi@srbiau.ac.ir

## Abstract

The effects of the electric charge of the negative and positive ions are examined on the sheath structure of an electronegative plasma. For doing this work an electrodynamic model of the plasma is used and the sheath equations inclusive the electric charge of the ions are numerically solved. For example it is found that the electric charge of the both positive and negative ions increase the positive net current to the wall.

**Keywords:** electronegative plasma, multiply ionized plasmas.

## Introduction

A sheath lies between the plasma and the wall of the plasma vessel. A sheath forms a potential barrier so that the more mobile species, *i.e.* electrons, are confined electrostatically. Electronegative plasmas have extensive applications in plasma technology and are formed of electric discharge in electronegative gases such as oxygen, hydrogen, iodine, chlorine, fluorocarbons and SF<sub>6</sub>. In surface processing of materials by plasma, the recognition of the sheath structure has a great significance. Indeed you need to know the particle energy and flux on the surface and their dependence on plasma parameters such as plasma pressure and temperature.

The structure of electronegative plasma sheath has been extensively investigated by several authors. Fernandez Palop et al [1] have analyzed the effects of the positive and negative ion temperature and negative ion density on the sheath structure which formed around a plane probe. Chung [2] has calculated the spatial distribution of electric potential, positive ion velocity and density as well as its current in the sheath of a cylindrical probe immersed in electronegative plasmas. In these works the plasma ions are singly ionized, while it has been shown that there are multiply ionized particles in the warm plasmas [3].

An electrodynamic model is used to explain the sheath structure in thermal electronegative plasmas. The model developed here is the same as the model of Ghomi *et al.* [4]. The plasma is compound of electrons, and multiply charged positive and negative ions. Both the electron and negative ion densities is assumed to obey the Boltzmann relation, so we have

$$n_e = n_{e0} \exp\left(\frac{-q_e V}{k_B T_e}\right), \quad (1)$$

and

$$n_n = n_{n0} \exp\left(\frac{-q_n V}{k_B T_n}\right), \quad (2)$$

where  $n_e$  and  $n_n$  are the electron and negative ion number densities, respectively, and  $n_{e0}$  and  $n_{n0}$  are their number densities at the sheath edge,  $T_e$  and  $T_n$  are their temperatures in the plasma bulk,  $q_e$  and  $q_n$  are their electric charge,  $k_B$  is the Boltzmann constant, and  $V$  is the local electric potential.

In the normal to the wall direction, the continuity and the force balance equations for the positive ion fluid in the generation less sheath in the steady state ( $\partial/\partial t = 0$ ), are respectively,

$$n_p v = n_{p0} v_0, \quad (3)$$

and

$$m_p v \frac{dv}{dx} = -e \frac{dV}{dx} - \gamma k_B T_p \left( \frac{n_p}{n_{p0}} \right)^{\gamma-1} \frac{1}{n_p} \frac{dn_p}{dx} - m_p (N_n \sigma v) v, \quad (4)$$

where  $v$  and  $v_0$  are the velocity and initial velocity of the positive ion flow in the  $x$  direction (normal to the wall) respectively,  $e$  is the electric charge of the positive ion,  $E_x$  is the  $x$  component of the sheath electric field,  $m_p$  is the positive ion mass, and  $n_p$  is the positive ion number density in the sheath and  $n_{p0}$  is the positive ion number density at the sheath edge respectively,  $N_n$  is the neutral gas density,  $\sigma = \sigma_s (v/c_s)^\beta$  is the momentum-transferring cross section for collision between the positive ions and the neutrals [ $c_s$  is the ion acoustic velocity,  $\sigma_s$  is the cross section measured at the ion acoustic velocity and  $\beta$  is a dimensionless parameter ranging from 0 in the constant mean free path ( $\lambda = 1/N_n \sigma_s$ ) case to 1 in the constant collision frequency case]. The pressure force  $-dp_p/dx$  has been replaced with

$$\frac{dp_p}{dx} = \gamma k_B T_p \left( \frac{n_p}{n_{p0}} \right)^{\gamma-1} \frac{dn_p}{dx}, \quad (5)$$

where  $\gamma = 1 + (n_p/T_p) dT_p/dn_p$  is the positive ion polytropic coefficient.  $\gamma$  is a function of the sheath potential, however with the exception of its sharp peak at the sheath edge, it is approximated by some constant values. The constant values are  $\gamma = 5/3$  corresponding to three-dimensional adiabatic law and  $\gamma = 1$  corresponding to one-dimensional adiabatic law. For convenience, one uses the assumption  $\gamma = 1$ , corresponding to the isothermal law [5,6].  $T_p$  is the positive ion temperature in the plasma bulk.

For a self-consistent plasma sheath boundary, these equations should be combined with the Poisson's equation

$$\frac{d^2 V}{dx^2} = -\frac{1}{\epsilon_0} (q_p n_p + q_e n_e + q_n n_n). \quad (6)$$

Introducing the dimensionless variables  $\eta = -eV/k_B T_e$ ,  $P = n_p/n_{e0}$ ,  $N = n_n/n_{e0}$ ,  $E = n_e/n_{e0}$ ,  $\Delta = n_{n0}/n_{e0}$ ,  $\xi = x/\lambda_{De}$ ,  $u = v/c_s$ ,  $\alpha = \lambda_{De} N_n \sigma_s$ ,  $\tau = T_p/T_e$ ,  $\theta = T_n/T_e$ ,

where  $\lambda_{De} = \sqrt{\epsilon_0 k_B T_e / n_{e0} e^2}$  is the electron Debye length and  $\alpha$  is a dimensionless collisional parameter, we can rewrite the above equations as,

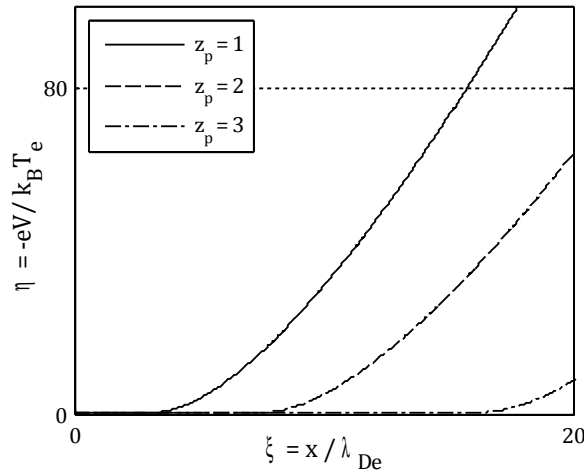


Fig. 1 The normalized electric potential as a function of penetration depth in the sheath region for different values of  $\gamma_p$ . The boundary conditions and plasma parameters are  $\eta_0 = 0$ ,  $\eta'_0 = 0.01$ ,  $u_0 = Ma$ ,  $\gamma = 3$ ,  $\beta = 0$ ,  $\eta_0 = 0$ ,  $\alpha = 0.005$ ,  $\tau = \theta = 0.3$ , and

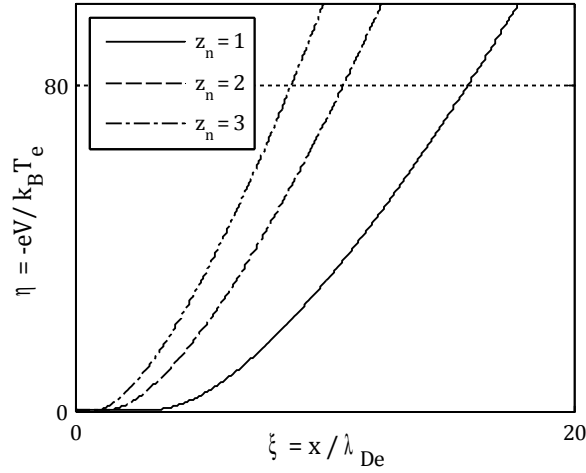


Fig. 2 The normalized electric potential as a function of penetration depth in the sheath region for different values of  $z_n$ . The boundary conditions and plasma parameters are  $\eta_0 = 0$ ,  $\eta'_0 = 0.01$ ,  $u_0 = Ma$ ,  $\gamma = 3$ ,  $\beta = 0$ ,  $\eta_0 = 0$ ,  $\alpha = 0.005$ ,  $\tau = \theta = 0.3$ , and

$$\frac{du}{d\xi} = \left( z_p \frac{d\eta}{d\xi} - \alpha u^{2+\beta} \right) \frac{u^\gamma}{u^{\gamma+1} - \gamma \tau u_0^{\gamma-1}} \quad (7)$$

$$\frac{d^2\eta}{d\xi^2} = z_p P - E - z_n N. \quad (8)$$

$$P = \frac{1 + z_n \Delta}{z_p} \frac{u_0}{u}, \quad (9)$$

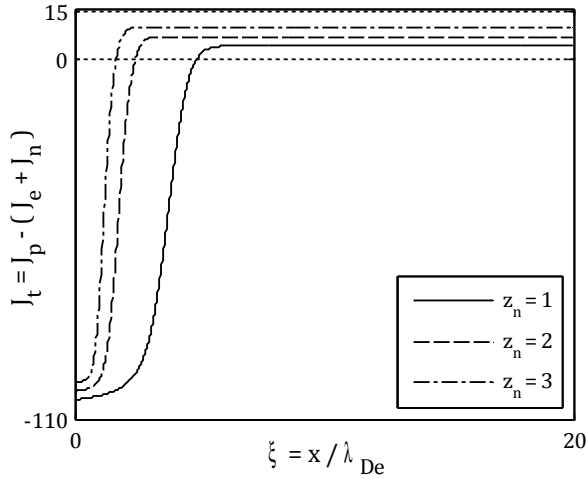


Fig. 3 The normalized net electric current to the wall as a function of penetration depth in the sheath region for different values of  $z_n$ . The boundary conditions and plasma parameters are the same as Fig.1.

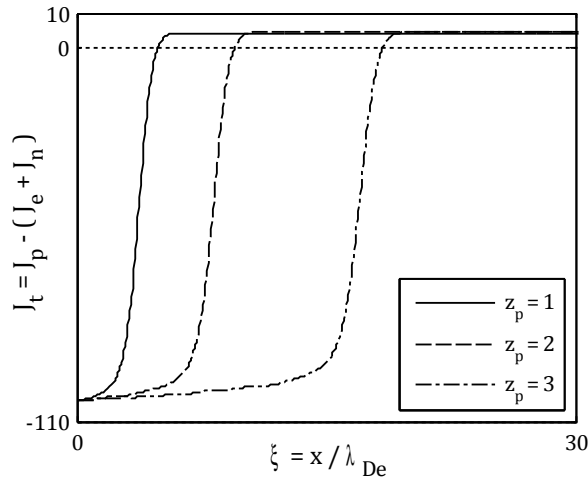


Fig. 4 The normalized net electric current to the wall as a function of penetration depth in the sheath region for different values of  $z_p$ . The boundary conditions and plasma parameters are the same as Fig.2.

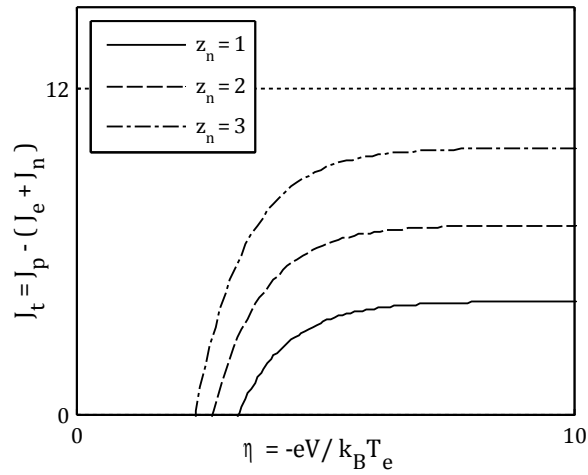


Fig. 5 The normalized net electric current to the wall as a function of the normalized electric potential in the sheath region for different values of  $z_n$ . The boundary conditions and plasma parameters are the same as Fig. 1.

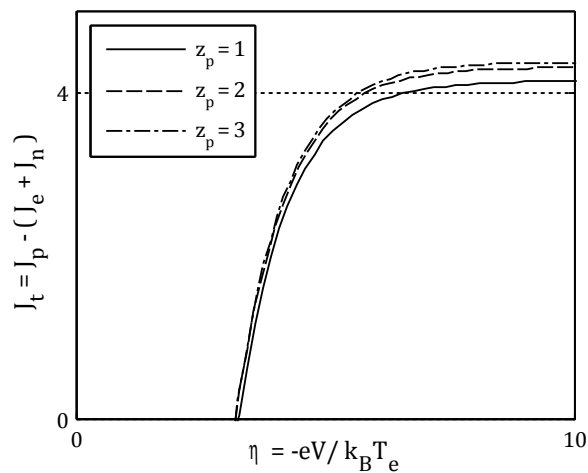


Fig. 6 The normalized net electric current to the wall as a function of the normalized electric potential in the sheath region for different values of  $z_p$ . The boundary conditions and plasma parameters are the same as Fig. 2.

$$N = \Delta \exp\left(-\frac{z_n \eta}{\theta}\right). \quad (10)$$

$$E = \exp(-\eta). \quad (11)$$

where  $u_0$  is the normalized velocity of the positive ion at the sheath edge and also we have used the quasi-neutrality relation at the sheath boundary,  $z_p n_{p0} / n_p = 1 + z_n \Delta$ .

### Results and discussion

Solving equations (7-11) with the boundary conditions at the sheath edge,  $\eta_0 = 0, \eta'_0 = 0.1$   $u_0 = Ma$ , with

$$Ma = \left[ \frac{1 + z_n \Delta + \gamma \tau (1 + z_n^2 \Delta / \theta)}{(1 + z_n \Delta) \alpha / z_p \eta'_0 + 1 + z_n^2 \Delta / \theta} \right] \quad (12)$$

and for different values of plasma parameters, we can find the sheath structure. For example for  $\gamma = 3$  (one-dimensional adiabatic law),  $\beta = 0$  (collision with the constant mean free path),  $\alpha = 0.005$ ,  $\tau = \theta = 0.3$ , numerical solution of these equations has been shown in Figs. (1-6).

Figure (1) and (2) show the normalized electric potential in the sheath region for different values of  $z_n$  and  $z_p$  the electric charge of the negative and positive ions, respectively. One can see from these figures that the negative ion electric charge increases the electric potential so decreases the sheath width, while the positive ion electric charge descends the electric potential in the sheath region and raises the sheath width.

In Figs. (3) and (4) we have displayed the net electric current in the sheath region as a function of the penetration depth in the sheath and Figs. (5) and (6) show the characteristics curve (I-V) of the sheath region for different values of ions electric charges. Figs. (3) and (4) illustrate an increasing net current to the wall that saturate to a constant value. As it can be seen from these figure, both the positive and negative ions electric charge increase the constant value.

### Conclusions

The effect of the ion electric charge on the plasma-sheath structure has been examined and the sheath characteristics such as electric potential and net current distribution in the sheath region are analyzed. The positive and negative ions electric charge have inverse effects on the electric potential distribution while they have the same effects on the positive saturation current toward the wall.

### References

- [1] J. I. Fernandez Palop, J. Balesteros, M. A. Hernandez, R. Morales Crespo, and S. Borrego del Pino, J. Appl. Phys. 95, (2004) 4585.
- [2] T. H. Chung, J. Appl. Phys. 103, (2008) 123302.
- [3] R. M. S. Almeida, M. S. Benilov, and G. V. Naidis, J. Phys. D: Appl. Phys. 33 (2000) pp. 960– 967.
- [4] H. Ghomi, M. Khoramabadi, P. K. Shukla, and M. Ghorannevis, (2010) J. Appl. Phys. 108, 063302.
- [5] F. F. Chen, Introduction to Plasma Physics (Plenum, New York, 1974).
- [6] N. Jelic, K. U. Riemann, T. Gyergyek, S. Kuhn, M. Stanojevic and J. Duhovnik, (2007) Phys. Plasma 14, 103506.

# Electron impact induced fluorescence of second positive system of N<sub>2</sub> molecule

M. Danko, J. Országh, A. Ribar, Š. Matejčík

Department of Experimental Physics, Comenius University, Mlynská dolina, Bratislava 842 45, Slovakia

e-mail: mdanko@centrum.sk

## Abstract

The aim of this study was to study the electron impact excitation of the second positive system of N<sub>2</sub> and gain the emission spectrum and emission cross sections for certain transitions from the fluorescence radiation. New crossed electron - molecular beams apparatus with narrow electron energy distribution was used. The excited states C<sup>3</sup>Π<sub>u</sub>(v') (v'=0..4) were measured. The fluorescence emission spectrum in UV/VIS range (280 – 440 nm), the excitation thresholds of particular vibrational states C<sup>3</sup>Π<sub>u</sub>(v'), the emission cross sections of the second positive system, and the excitation cross sections of the C<sup>3</sup>Π<sub>u</sub>(v') states were measured with high resolution and sensitivity.

**Keywords:** electron induced fluorescence, second positive system, cross section, nitrogen, emission spectrum

## Introduction

Electron induced fluorescence (EIF) is a process, during which an electron collides with a molecule, and causes the molecule to change its energy state. Consequently the molecule drops to the lowest optically allowed energy state by emitting a photon, which energy corresponds to the energy difference of the two states. By measuring the optical radiation from fluorescence induced by electrons of narrow energy distribution, we gain the emission spectrum of the concrete molecule that is being studied. Thus we can study its structure of energy states. Moreover we can study efficiency of excitation and emission processes between two concrete energy states in dependence on energy of colliding electrons. The gained parameter is called emission cross section from which we can get excitation cross section.

Our work deals with the molecule of N<sub>2</sub>, more precisely the second positive system C<sup>3</sup>Π<sub>u</sub>(v') → B<sup>3</sup>Π<sub>g</sub>(v''), which is very important in laser physics and in the atmospheric physics, both of Earth and of extraterrestrial atmospheres. The second positive system is excited by low-energetic electrons present in atmosphere during daylight and in the auroras. [1], [2], [3], [4]

The other important fact about nitrogen molecule for our experiment is that the molecule has been studied for a long time and its cross sections are quite well known. The goal of our work is to further improve our new apparatus so that we will be able to get high-resolution data and process very weak photon flux signals. By using N<sub>2</sub> we have enough data to calibrate the apparatus by normalizing data to previously measured accurate results, and to compare our results with.

## Experiment

The experimental apparatus, shown in the Fig.1, consists of an ultra-vacuum chamber, inside which there is a trochoidal electron monochromator. The monochromator produces electron beam with energy distribution of about 150 meV wide with typical electron current of over 100 nA. The electron beam is crossed with molecular beam in the reaction region of the monochromator. The molecular beam is formed by pushing studied gas through a capillary. The photons emitted from the reaction region are collected by a plane-convex MgF<sub>2</sub> lens and transmitted via quartz vacuum window out of the vacuum chamber. They are refocused by second MgF<sub>2</sub> plane-convex lens onto the entrance slit of a 0.25 m optical monochromator with resolution of 0.15 nm. Detection of the photons is done by the Hamamatsu H8259 photomultiplier, which is thermoelectrically cooled to -20°C, which helps to decrease electronic noise significantly. The magnetic field of about 5x10<sup>-3</sup> T is produced by three pairs of coils (x, y, z coordinates) which allow accurate alignment of the direction of the field with respect to the electron monochromator symmetry axis. The measurements were carried out for pressure range of 1.10<sup>-4</sup> mbar in the collision region which gave linear dependence between detected photons intensity and target pressure. It was also ensured that the detected photon intensity increased linearly with the electron beam current.

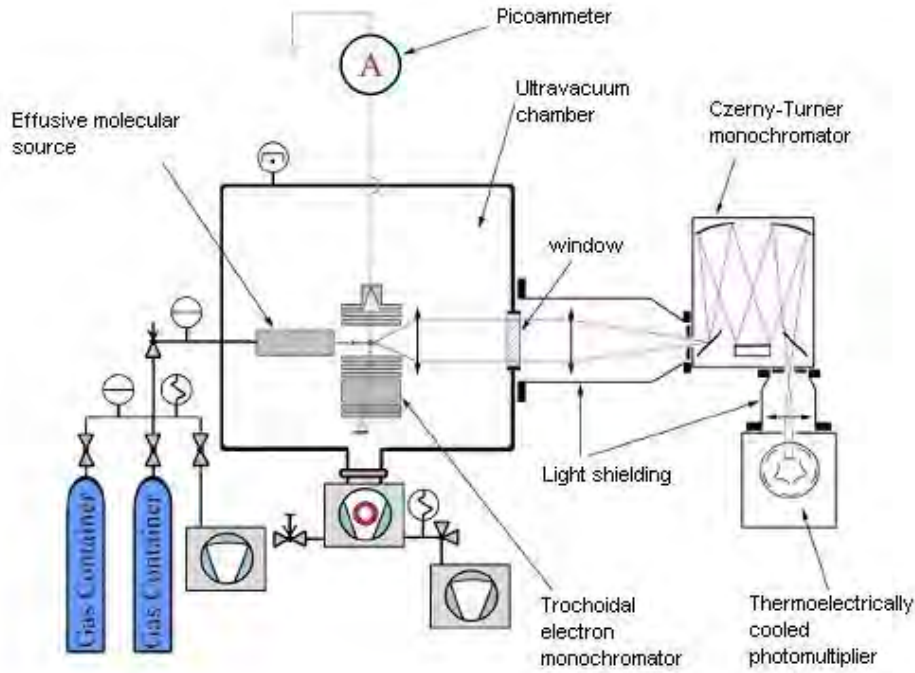


Fig.1. Scheme of the experimental apparatus

In order to gain excitation cross sections from the measured emission cross sections, or otherwise called emission functions, we used the normalization method. We normalized our measurements to values of Zubek [5]. The measured intensity of a concrete transition between different vibrational states  $v' \rightarrow v''$ , if the excitation occurs at basic electronic and vibrational state is

$$I_{v'v''}(E) = I_e N_g l \sigma_{v'}(E) A_{v'v''} \tau_{v'} \eta(\lambda) \quad (1)$$

$I_e$  is the electron current,  $N_g$  is the density of studied gas,  $l$  is the interaction length observed by the collecting lens,  $\sigma_{v'}(E)$  is absolute cross section for excitation to  $v'$  state,  $A_{v'v''}$  is corresponding Einstein coefficient,  $\tau_{v'}$  is mean lifetime of  $v'$  state,  $\eta(\lambda)$  is quantum efficiency of the optical detection system for the wavelength  $\lambda$ . The emission cross section for transition of  $v' \rightarrow v''$  is given by

$$\sigma_{v'v''}^{em}(E) = \sigma_{v'}(E) A_{v'v''} \tau_{v'} \quad (2)$$

The normalization method uses one already known emission cross section for one transition of the new measurement that we chose as a reference transition. By using the reference transition we can calculate excitation cross sections relative to that one for every other transition using the equation (1), usually for the electron energy corresponding to the maximum of the emission function. We use ratios of the measured intensities in the calculations. Using equation (2) and the normalized emission cross section for the reference transition we can calculate values of absolute excitation cross section  $\sigma_{v'}(E)$  for that transition. For the absolute excitation cross sections of other transitions we use their relative cross sections gained from previous calculations.

## Results and discussion

We measured emission spectrum of the second positive system of  $N_2$   $C^3\Pi_u(v') \rightarrow B^3\Pi_g(v'')$  in region of 280-440 nm. The gas of pressure  $1.4 \times 10^{-4}$  mbar was excited by electron beam with energy 14 eV. We identified the vibrational transitions. The result is shown in the Fig.2. Comparison can be made with the spectrum in Fig.3, which clearly demonstrates the high resolution of our apparatus.

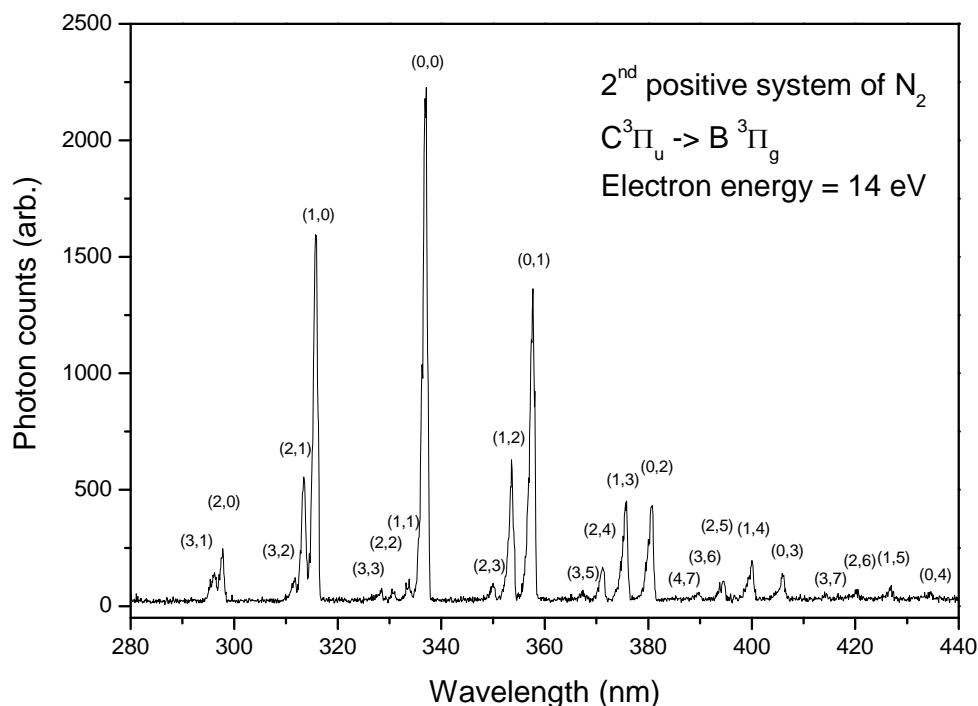


Fig.2. Emission spectrum of the second positive system of  $N_2$  induced by electron impact excitation. Electron energy was 14 eV. Vibrational transitions are marked on the picture.

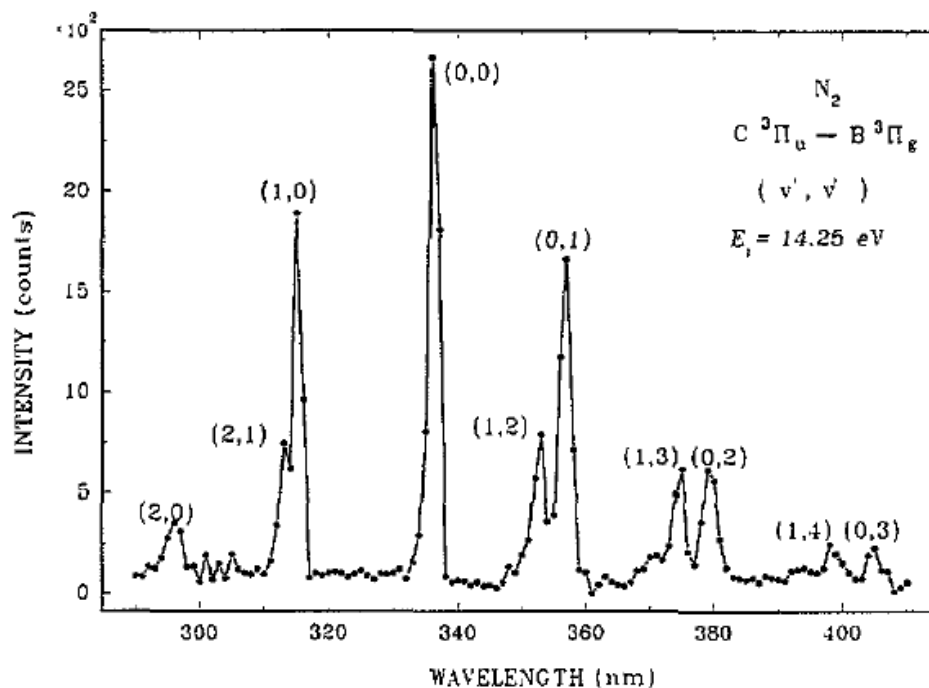


Fig.3. Emission spectrum of the second positive system of  $N_2$  induced by electron impact excitation. Electron energy was 14,25 eV. Data from Mariusz Zubek [5].

Electron energies corresponding to the maxima of the measured emission cross sections were found by fitting the cross sections by polynomial and thus gaining the maxima of the fits. Results can be

found in Table 1. The usual tendency of the maxima is to move to higher electron energies in the transitions with rising  $v''$  while  $v'$  does not change, or vice versa –  $v'$  is rising and  $v''$  does not change. Examples of fitted emission cross sections can be found in Fig.4.

Tab. 1. Electron energies at maximum  $N_2$  fluorescence radiation (excitation efficiency) for different vibrational transitions of  $C^3\Pi_u(v') \rightarrow B^3\Pi_g(v'')$  gained from the measured emission cross sections.

| Transition ( $v', v''$ ) | Energy for maximum efficiency of excitation (eV) | Transition ( $v', v''$ ) | Energy for maximum efficiency of excitation (eV) |
|--------------------------|--|--------------------------|--|
| (0,0)                    | $11.84 \pm 0.02$                                 | (2,1)                    | $12.14 \pm 0.05$                                 |
| (0,1)                    | $11.77 \pm 0.05$                                 | (2,2)                    | $12.53 \pm 0.05$                                 |
| (0,2)                    | $11.99 \pm 0.05$                                 | (2,4)                    | $12.38 \pm 0.05$                                 |
| (0,3)                    | $12.04 \pm 0.05$                                 | (2,5)                    | $12.30 \pm 0.05$                                 |
| (1,1)                    | $12.29 \pm 0.05$                                 | (3,1)                    | $12.63 \pm 0.05$                                 |
| (1,2)                    | $12.22 \pm 0.05$                                 | (3,2)                    | $12.60 \pm 0.05$                                 |
| (1,3)                    | $12.14 \pm 0.05$                                 | (3,3)                    | $12.55 \pm 0.05$                                 |
| (1,4)                    | $12.19 \pm 0.05$                                 | (3,5)                    | $12.88 \pm 0.05$                                 |
| (2,0)                    | $12.54 \pm 0.05$                                 | (3,6)                    | $12.57 \pm 0.05$                                 |

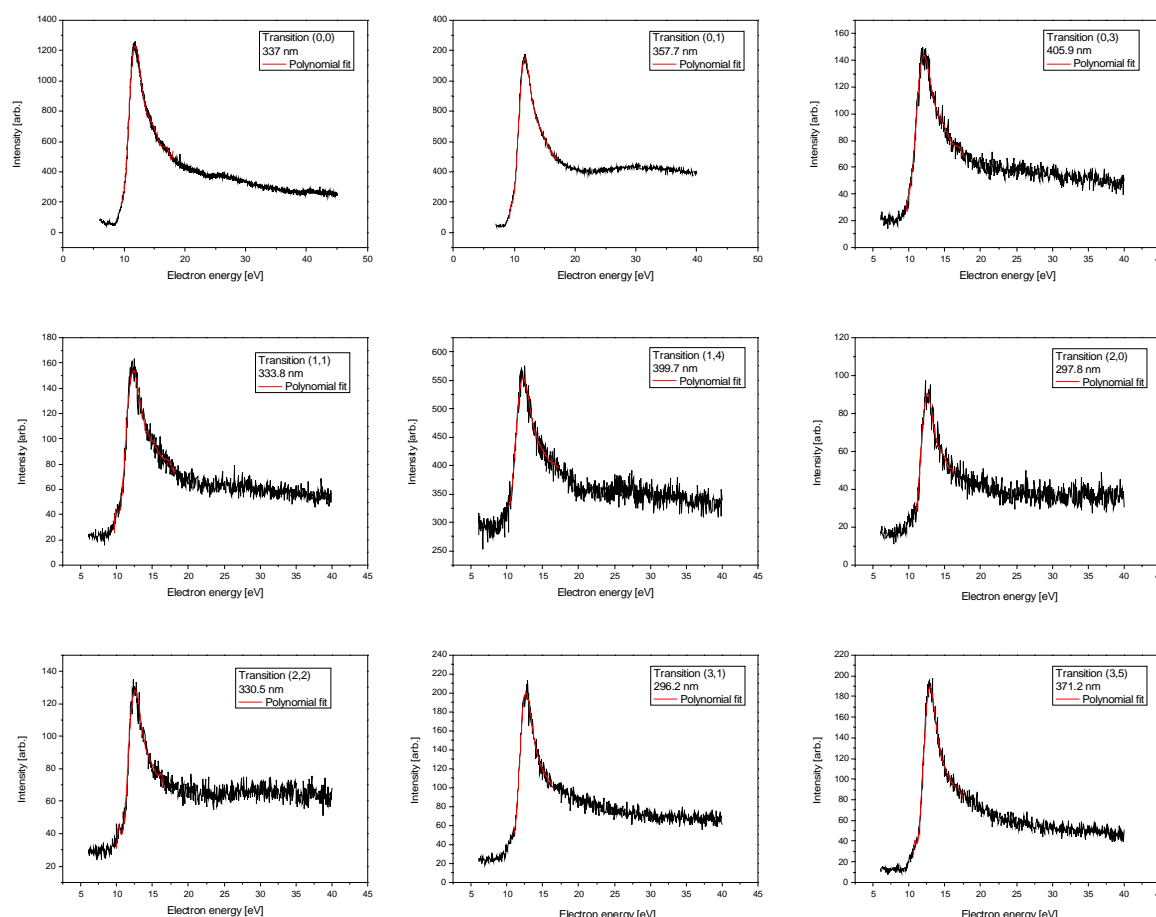


Fig.4. Some of the measured emission cross sections (emission functions) with polynomial fits we used to get electron energy at the fluorescence efficiency maxima.

Finally we gained the excitation cross sections for the emission bands of the second positive system  $C^3\Pi_u(v'=0,1,2,3,4)$  to  $B^3\Pi_g(v''=0)$ . They can be found in the Fig.5. The excitation cross sections were normalised to the absolute emission cross section at its maximum at 14.1 eV. The electron energy

range and the absolute value of the cross section for transition (0,0) was calibrated to cross section measured by Mariusz Zubek [5]. The results are in good agreement also with the work of Malone et al [6].

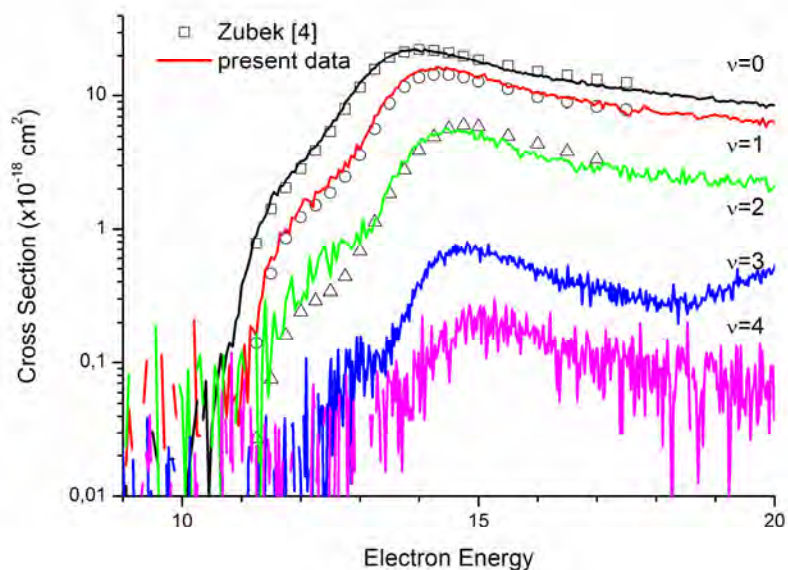


Fig.5. Excitation cross section of the  $C^3\Pi_u(v'=0,1,2,3,4)$   $N_2$ . Comparison with results of Mariusz Zubek [5] for  $v' = 0,1,2$ .

## Conclusions

We studied the second positive system of  $N_2$  ( $C^3\Pi_u(v') \rightarrow B^3\Pi_g(v'')$ ) by electron induced fluorescence. The new apparatus we used has high resolution and good sensitivity, as can be seen by the results we gained in comparison to other published results. We measured high resolution emission fluorescence spectrum, emission cross sections and determined excitation cross sections for the excited states  $C^3\Pi_u$  ( $v'=0,1,2,3,4$ ). Finally, we found the electron energies corresponding to the maximum reaction efficiency for different vibrational transitions from the measured emission cross sections.

## Acknowledgements

This project has been supported by projects VEGA-1/0558/09, VEGA-1/0379/11 and APVV-0365-07.

## References

- [1] John T.Fons, R.Scott Schappe, Chun C.Lin: *Physical Review A* 53 (1996) 2239
- [2] D.J. Burns, F.R. Simpson, J.W. McConkey: *J. Phys. B (Atom. Molec. Phys.)* ser. 2, vol. 2 (1969) 52
- [3] D.E. Shemansky, J.M. Ajello, I. Kanik: *The Astrophysical Journal* 452 (1995) 472
- [4] A. Chutjian, D.C. Cartwright, S. Trajmar: *Physical Review A* 16 (1977) 1052
- [5] Mariusz Zubek: *J. Phys. B: At. Mol. Opt. Phys.* 27 (1994) 573
- [6] Malone, C.P., et. al.: *J. Phys. B: At. Mol. Opt. Phys.* 42 (2009) 225202

# On Progress using Mid-Infrared Absorption Techniques for Plasma Diagnostics – from Basic Research to Industrial Applications

J. Röpcke<sup>1</sup>, P.B. Davies<sup>2</sup>, S. Glitsch<sup>1</sup>, F. Hempel<sup>1</sup>, M. Hübner<sup>1</sup>, N. Lang<sup>1</sup>, A. Rousseau<sup>3</sup>, S. Welzel<sup>1,4</sup>

<sup>1</sup>INP Greifswald, D-17489 Greifswald, Germany

<sup>2</sup>University of Cambridge, Lensfield Road, Cambridge CB2 1EW, United Kingdom

<sup>3</sup>LPP, Ecole Polytechnique, CNRS, 91128 Palaiseau Cedex, France

<sup>4</sup>Eindhoven University of Technology, P.O. Box 513, 5600 MB, Eindhoven, The Netherlands

e-mail: roepcke@INP-Greifswald.de

## Abstract

Mid infrared absorption spectroscopy between 3 and 20  $\mu\text{m}$ , known as Infrared Laser Absorption Spectroscopy (IRLAS) and based on tunable semiconductor lasers, namely lead salt diode lasers (often called tunable diode lasers (TDL)), and quantum cascade lasers (QCL) has progressed considerably as a powerful diagnostic technique for *in situ* studies of the fundamental physics and chemistry of molecular plasmas. The increasing interest in processing plasmas containing hydrocarbons, fluorocarbons, organo-silicon and boron compounds has lead to further applications of IRLAS because most of these compounds and their decomposition products are infrared active. IRLAS provides a means of determining the absolute concentrations of the ground states of stable and transient molecular species, which is of particular importance for the investigation of reaction kinetics. Since plasmas with molecular feed gases are used in many applications such as thin film deposition, semiconductor processing, surface activation and cleaning, and materials and waste treatment, this has stimulated the adaptation of infrared spectroscopic techniques to industrial requirements. The recent development of QCLs offers an attractive new option for the monitoring and control of industrial plasma processes and for trace gas analysis as well as for highly time-resolved studies on the kinetics of plasma processes. The aim of the present contribution is to review recent achievements using TDLs and QCLs for plasma diagnostics and trace gas monitoring in research and industry.

**Keywords:** Mid infrared absorption spectroscopy, plasma chemistry, quantum cascade laser, trace gas measurements

## 1. Introduction

Low-pressure, non-equilibrium molecular plasmas are of increasing interest not only in fundamental research but also in plasma and vapor processing technology. Molecular plasmas and vapors are used in a variety of applications such as thin film deposition, semiconductor processing, surface activation and cleaning, and in materials and waste treatment. The investigation of plasma physics and chemistry *in situ* requires detailed knowledge of plasma parameters, which can be obtained by appropriate diagnostic techniques. The need for a better scientific understanding of plasma physics and chemistry has stimulated the improvement of established diagnostic techniques and the introduction of new ones. The methods of absorption spectroscopy are of great importance in plasma diagnostics because they provide a means of determining the population densities of species in both ground and excited states. The spectral line positions provide species identification while line profiles are often connected with gas temperature and relative intensities provide information about population densities and thus give information on the excitation dynamics. An important advantage of absorption spectroscopy (AS) over Optical Emission Spectroscopy (OES) methods is that only relative intensities need to be measured to determine absolute concentrations, avoiding the problems of complete instrument calibration inherent in the OES methods. Absorption spectroscopy has been applied across the spectrum from the vacuum ultra violet (VUV) to the far infrared (FIR). A wide variety of light sources, dispersive elements, detectors and data acquisition methods can be used. The classic absorption spectroscopy experiment uses a continuous light source in combination with a narrow bandwidth frequency filter, in particular a spectrograph, and a detector suitable for the spectral range of interest. Besides continuous emission lamps (e.g. the Xe-lamp for the VIS and NIR, and the D<sub>2</sub>-lamp for the UV) tunable narrow-band light sources (e.g. tunable dye lasers, diode lasers) can be used as external light sources as well. Two principle cases need to be distinguished: (I) the measurement of

the absorption of light emitted by the plasma itself (*self absorption* or *reabsorption*), or (II) absorption of an external light source. In the case of self absorption measurements the light from the plasma is measured with and without a retro-reflector or compared with the direct light emitted from an identical plasma. This ensures identical line profiles for the emitted and the absorbed light. This method is particularly important for checking the optical thickness of the plasma. The probing light intensity of an external light source in case (II) has to be low to avoid saturation effects of the excited states of the species under investigation. The change in light intensity  $dI_\nu$  when a beam passes through a transparent homogeneous plasma zone of thickness  $dl$  is given by the net balance of the intensity due to absorption and emission within the layer  $dl$ :

$$dI_\nu = (\varepsilon(\nu) - \kappa(\nu)I_\nu)dl \quad (1)$$

where  $\varepsilon(\nu)$  is the emission coefficient and  $\kappa(\nu)$  is the absorption coefficient per unit length. The absorption coefficient  $\kappa(\nu)$ , describing the light absorption in an infinitesimally thin layer of a plasma, is given by

$$\kappa(\nu) = \sum_i N_i \sigma_i(\nu) \quad (2)$$

where the sum is over all absorbing species and states  $i$ .  $N_i$  are the species population densities and  $\sigma_i(\nu)$  their absorption cross sections at frequency  $\nu$ . The line profile  $P_\nu$  is normalised by :

$$\int_{line} P_\nu d\nu = 1 \quad (3)$$

Assuming the upper level  $k$  of a transition  $i \rightarrow k$  is not populated, the absorption coefficient,  $\kappa(\nu)$ , can be expressed as:

$$\int_{line} \kappa(\nu) d\nu = \frac{h\nu}{c_0} N_i B_{ik} . \quad (4)$$

Here  $h$  denotes the Planck constant and  $c_0$  the velocity of light. Hence, the line absorption coefficient is,

$$\kappa(\nu) = \frac{h\nu}{c_0} N_i (\alpha, \beta, \gamma, \dots) B_{ik} P_\nu , \quad (5)$$

where  $N_i (\alpha, \beta, \gamma, \dots)$  is the population density of level  $i$ , which depends on different plasma parameters  $(\alpha, \beta, \gamma, \dots)$ , and  $B_{ik}$  is the Einstein coefficient for the transition between the levels  $i$  and  $k$ .

In the case where (a) the external light source has much higher intensity than that of the plasma itself and (b) the absorption is continuous over the entire distance  $l$  ( $\kappa(\nu) = \text{constant}$ ), the absorption of radiation can be described by the Beer-Lambert law:

$$I_\nu(l) = I_\nu(0) \exp(-\kappa(\nu)l). \quad (6)$$

$I_\nu(0)$  and  $I_\nu(l)$  are the fluxes of the radiation entering and leaving the plasma,  $l$  is the length of the absorbing (homogeneous) plasma zone. Figure 1 illustrates this situation [1].

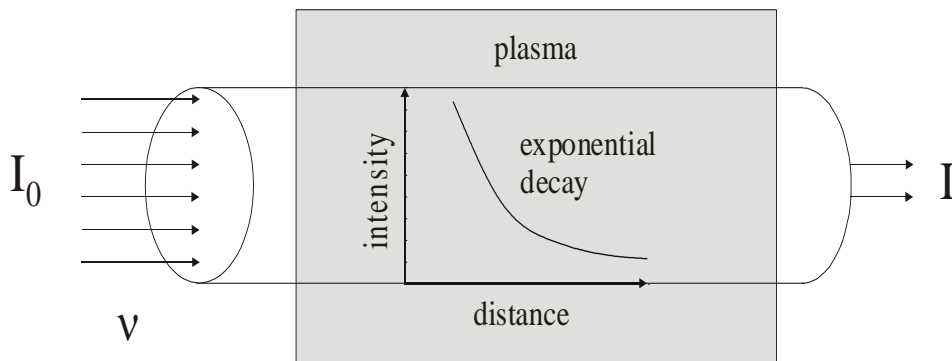


Fig. 1. Absorption of external radiation in a plasma according to the Beer-Lambert law [1].

It should be noted that the definition of the effective absorption length of the plasma zone and the assumption of a constant absorption coefficient over the complete distance  $l$  are two non-trivial questions in plasma spectroscopy. Inhomogeneities, anisotropies and temperature gradients caused by

local changes in the plasma may lead to significant errors.

With the development of tunable, narrow band light sources such as tunable dye lasers and infrared diode lasers, these have been substituted for continuous light sources in absorption spectroscopy experiments. These narrow band laser sources have the advantage of high spectral intensity, narrow bandwidth, and continuous tunability over the absorption profile. The increasing interest in processing plasmas containing hydrocarbons, fluorocarbons or organo-silicon compounds has led to further applications of specifically infrared absorption spectroscopy techniques because most of these compounds and their decomposition products are infrared active. Fourier Transform Infrared (FTIR) spectroscopy has been used for *in situ* studies of molecular plasmas for a number of years, but it is generally insufficiently sensitive for detecting free radicals or ions in processing plasmas. Tunable diode laser absorption spectroscopy (TDLAS) is increasingly being used in the spectral region between 3 and 20  $\mu\text{m}$  for measuring the concentrations of free radicals, transient molecules and stable products in their electronic ground states. TDLAS can also be used to measure neutral gas temperatures [2] and to investigate dissociation processes in molecular low temperature plasmas [3-6]. The main applications of TDLAS until now have been for investigating molecules and radicals in fluorocarbon etching plasmas [2,5,7], in plasmas containing hydrocarbons [6,8-14,19,22] and nitrogen, hydrogen and oxygen [17,18,20,21]. A wide variety of low molecular weight free radicals and molecular ions has been detected by TDLAS in purely spectroscopic studies e.g.  $\text{Si}_2^-$  [15] and  $\text{SiH}_3^+$  [16] in silane plasmas. Most of these spectroscopic results have yet to be applied in plasma diagnostic studies.

Molecular plasmas are increasingly being used not only for basic research but also, due to their favorable properties, for materials processing technology. These fields of application have stimulated the development of infrared spectroscopic techniques for industrial requirements. In order to exploit the capabilities of infrared TDLAS for effective and reliable on-line plasma diagnostics and process control in research and industry, compact and transportable tunable infrared multi-component acquisition systems (IRMA, TOBI) have been developed [17,18]. These systems are mainly focused on (i) high speed detection of stable and transient molecular species in plasmas under non-stationary excitation conditions and (ii) on sensitive (sub-ppb) trace gas detection with the aid of multi-pass absorption cells.

The main disadvantage of TDLAS systems, based on lead salt diode lasers, is the necessary cryogenic cooling of the lasers (and also of the detectors), because they operate at temperatures below 100 K. Systems based upon lead salt diode lasers are typically large in size and require closed cycle refrigerators and/or cryogenics like liquid nitrogen. The recent development and commercial availability of quantum cascade lasers (QCL) offers an attractive new option for infrared absorption spectroscopy.

The present contribution is intended to give an overview of recent achievements which have led to an improved understanding of phenomena in non-equilibrium molecular plasmas based on the application of IRLAS techniques including the current status of advanced spectroscopic instrumentation.

## 2. TDLAS studies of Ar/H<sub>2</sub>/N<sub>2</sub>/O<sub>2</sub> microwave plasmas

Low temperature plasmas, in particular microwave and radio frequency (RF) plasmas, have high potential for applications in plasma technology. In molecular low temperature plasmas, the species and surface conversion is frequently governed by high degrees of dissociation of the precursor molecules and by the high amounts of chemically active transient and stable molecules present [23-25]. In order to gain further insight into plasma chemistry and kinetics the study of (mainly) electron induced plasma reactions is an important objective. These processes lead to entire series of different secondary chemical reactions involving all the source gas molecules. In all cases, the monitoring of transient or stable plasma reaction products, in particular the measurement of their ground state concentrations, is the key to improved understanding of fundamental phenomena in molecular non-equilibrium plasmas which can in turn be applied to many other aspects of plasma processing. Radicals containing carbon and oxygen are of special interest for fundamental studies and for applications in plasma technology.

In recent years several types of microwave discharge with different precursor gases have been at the centre of interest. The most recent applications of TDLAS for plasma diagnostic purposes include studies in which many different species have been monitored under identical plasma conditions [24,26]. This experimental data has frequently been used to model plasma chemical phenomena.

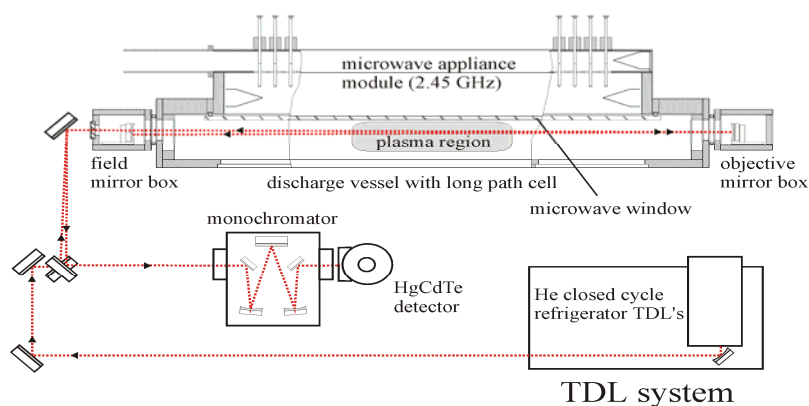


Fig. 2. Experimental arrangement of a planar microwave plasma reactor (side view) used in plasma diagnostics with a White type multiple pass optical arrangement, and tunable diode laser (TDL) infrared source. The path of the diode laser beam is indicated by dotted lines [24].

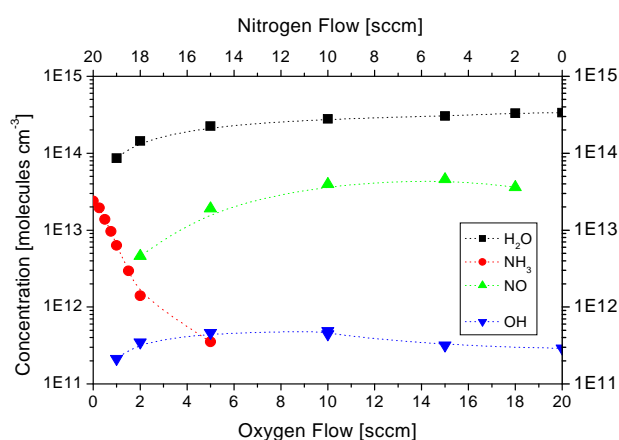


Fig. 3. Concentrations of the most abundant species and of OH in an Ar/H<sub>2</sub>/N<sub>2</sub>/O<sub>2</sub> microwave plasma (420 sccm Ar, 10 sccm H<sub>2</sub>, (0 ... 20 sccm) N<sub>2</sub> + O<sub>2</sub>; 1.5 mbar). [NH<sub>3</sub>] was below the detection threshold for oxygen flows higher than 6 sccm, p= 1.5 mbar, P= 1.5 kW [27].

Although hydrogen and hydrocarbon containing plasmas with admixtures of oxygen and nitrogen have been extensively studied [1,19,24] there is a lack of experimental data concerning the absolute densities of radicals in these discharges. Furthermore the discrimination between formation processes of molecules in the gas phase and due to plasma-surface interactions are still subject of present studies. The hydroxyl radical is known to be one of the main oxidising radicals. So far only a few studies have been reported on absolute OH concentrations in plasmas. Mostly, they have been monitored and measured in the UV spectral region [28-30]. The example of quantitative measurements of OH in a plasma by means of TDLAS at 530 cm<sup>-1</sup> has therefore been chosen here since it also highlights aspects of the complex chemistry in molecular plasmas. The measurements were performed in a planar microwave reactor in Ar/H<sub>2</sub>/N<sub>2</sub>/O<sub>2</sub>- discharges. The reactor was equipped with multiple pass cell (White cell) in order to increase the absorption length (figure 2). An effective absorption length of 60 m was achieved employing a mirror spacing of 1.5 m and an alignment to 40 passes. The pressure was kept constant at 1.5 mbar during the experiments. With a typical input power of 1.5 kW and 420 sccm Ar the following gas mixture was used: (0 ... 20) sccm H<sub>2</sub>, 10 sccm N<sub>2</sub>, (0 ... 20) sccm O<sub>2</sub>.

For an Ar/H<sub>2</sub> plasma H<sub>2</sub>O and - depending on the oxygen flow - NH<sub>3</sub> or NO turned out to be the most abundant species (figure 3). The mixing ratio of water was typically in the order of 1 %. Further details on the experimental setup, data acquisition and data processing can be found elsewhere [6,31-33].

It can be seen in figure 3 that the ammonia concentration is quite sensitive to even small amounts of oxygen in the plasma, and as its concentration decreases the NO and OH concentrations increase.

This behaviour was additionally studied for different H<sub>2</sub> admixtures (5 ... 20 sccm) and is shown in figure 4 in conjunction with the development of the OH density. It is evident from figure 4 that even

higher H<sub>2</sub> flows cannot compensate the strong NH<sub>3</sub> decrease with O<sub>2</sub>.

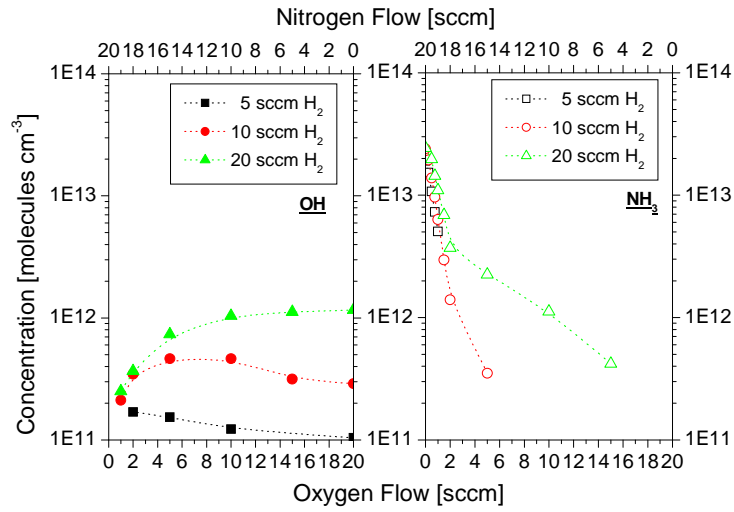


Fig. 4. Concentrations of OH (left panel) and NH<sub>3</sub> (right panel) for Ar/H<sub>2</sub>/N<sub>2</sub>/O<sub>2</sub> microwave plasmas (420 sccm Ar, (0 ... 20) sccm H<sub>2</sub>, (0 ... 20) sccm N<sub>2</sub> + O<sub>2</sub>; 1.5 mbar) plasmas [27].

The significant decrease of NH<sub>3</sub> with increasing O<sub>2</sub> flow (figure 3) can be qualitatively understood by taking into account the strong influence of surface processes. The surface dominated production of ammonia by subsequent pick-up reactions of H radicals from the gas phase by surface adsorbed NH<sub>i</sub> (i = 0 ... 2) followed by NH<sub>3</sub> desorption is well-known and has been discussed and validated several times [34 and ref. therein, 35]. In equations (1) to (4) several gas phase reactions with a considerably high rate constant are summarised. Specifically equations (1) and (2) might explain the observed oxygen dependence of NH<sub>3</sub>, i.e. ammonia and its precursors (NH<sub>i</sub>) are affected by O and OH radicals in the gas phase. The system is thus characterized by a deficiency of precursor fragments for the ammonia production. On the other hand, all suggested gas phase reactions may not explain why an increase of the H<sub>2</sub> flow has almost no influence on the NH<sub>3</sub> mixing ratio.

It is therefore reasonable to assume that surface reactions not only govern the formation of NH<sub>3</sub> in H<sub>2</sub> - N<sub>2</sub> and of NO in N<sub>2</sub> - O<sub>2</sub> mixtures, but also efficiently suppress the NH<sub>3</sub> formation in H<sub>2</sub> - N<sub>2</sub> - O<sub>2</sub> systems as soon as oxygen is added. The flux of O radicals lead to a change of the surface coverage which enhances the formation of N<sub>2</sub>O and NO at the expense of the ammonia production. This in turn also reduces the subsequent dissociation of NH<sub>3</sub> and was found to be essential to provide precursors for the NH<sub>i</sub> pick-up reactions at the surface [36]. Both effects are thus synergetic and lead to the observed strong decrease.



In contrast to ammonia the OH abundance increases with a higher H<sub>2</sub> content and the OH maximum appears to be stoichiometric (figure 4) suggesting that equation (3) is dominant. (4) should be valid for both gas phase and the surface. For higher H<sub>2</sub> and O<sub>2</sub> flows H<sub>2</sub>O also serves as a precursor for OH via secondary reactions (H<sub>2</sub>O → H<sub>2</sub>O<sub>2</sub> → OH).

### 3. Quantum Cascade Laser Absorption Spectroscopy for Plasmas Diagnostics and Control

#### 3.1 General considerations

The recent development of pulsed and continuous wave QCLs and their commercial availability offer promising new possibilities for infrared absorption spectroscopy [37-39]. QCLs are unipolar semiconductor injection lasers based on intersubband transitions in a multiple quantum-well heterostructure. QCLs are designed using band-structure engineering and are grown by molecular beam epitaxy or metalorganic chemical vapour deposition. These lasers are able to emit mid infrared

radiation at near room temperature. Compared to lead salt laser systems, QCL systems employ very compact mid infrared sources characterized by narrow line width combining single-frequency operation and considerably higher powers, i.e. tens of mW.



**Fig. 5.** Q-MACS Basic with laser head, supply unit, connection cable and optical collimation module [45].

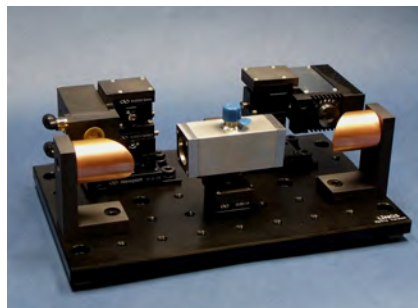


**Fig. 6.** New generation of compact QCLAS equipment with laser head in TO-8 configuration (left-hand side), reference gas cell (middle) and detector (right-hand side). The laser beam is guided by two off-axis parabolic mirrors [45].

The output power is sufficient to combine them with thermoelectrically cooled infrared detectors, which permits a decrease of the apparatus size and provides an opportunity to design compact cryogen-free mid infrared spectrometer systems. The positive features of quantum cascade laser absorption spectroscopy (QCLAS) opens up new fields of application in research and industry. Recently a compact quantum cascade laser measurement and control system (Q-MACS) has been developed (figures 5 and 6) for time-resolved plasma diagnostics, process control and trace gas monitoring which can be used as platforms for various applications of QCLAS [1,40].

QCLAS is now used to detect atmospheric trace constituents or trace gases in exhaled breath. Furthermore it has already been successfully applied to the study of plasma processes, e.g. of microwave and RF discharges [41,42]. Of special interest for all hydrocarbon-based processes is the possibility to detect transient molecules like the  $\text{CH}_3$  radical, as the supposed key growth species, by means of QCLAS [45].

Using pulsed QCL the scan through an infrared spectrum is commonly achieved by two different methods. In the *inter* pulse mode a bias DC ramp is applied to a series of short laser pulses of a few ten nanoseconds [43]. Another option is the *intra* pulse mode, i.e. the scanning in single, longer pulses acquiring an entire spectrum [44]. Since this scan is performed in tens up to a few hundred nanoseconds a time resolution below 100 ns has become feasible for quantitative *in situ* measurements of molecular concentrations in plasmas for the first time. Therefore it fits very well to measurements of rapidly changing chemical processes [52].

### 3.2 Oxidation of NO into NO<sub>2</sub> by surface adsorbed O atoms

Plasma-surface interactions are increasingly recognised as a key factor in explaining molecule production and conversion processes. In order to scrutinise such effects well-defined surface and gas phase conditions are required. Hence, the inner surface of a Pyrex tube was treated by a capacitively coupled RF plasma at low pressure.

The experiments were carried out in a cylindrical plasma reactor made of Pyrex, length  $l = 60$  cm, inner diameter  $d = 2$  cm (figure 7). The inner surface of the tube is pre-treated by a capacitively coupled RF plasma,  $f = 13.56$  MHz, for 1 h at flowing conditions at a pressure of 0.53 mbar. Outside the tube two metallic rings serve as electrodes in order to avoid any contact between plasma and metal which could induce additional chemical reactions.

The pre-treatment plasma was fed with different precursor gases, namely  $\text{O}_2$ ,  $\text{N}_2$ , Ar, and synthetic air (80 %  $\text{N}_2$ , 20 %  $\text{O}_2$ ). The injected power was 30 W. After the wall conditioning, the tube was filled with a gas mixture of 1% NO in  $\text{N}_2$  or in Ar at a pressure of 5.3 mbar. Next, NO and  $\text{NO}_2$  densities are simultaneously measured without plasma during a period of 2 h while the tube was

closed. Using a two-beam Q-MACS arrangement [48], NO and NO<sub>2</sub> concentrations are monitored by means of absorption lines at 1897 cm<sup>-1</sup> and 1612 cm<sup>-1</sup>, respectively (figure 8).

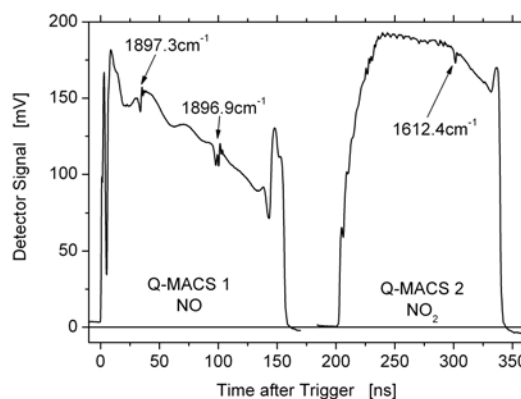
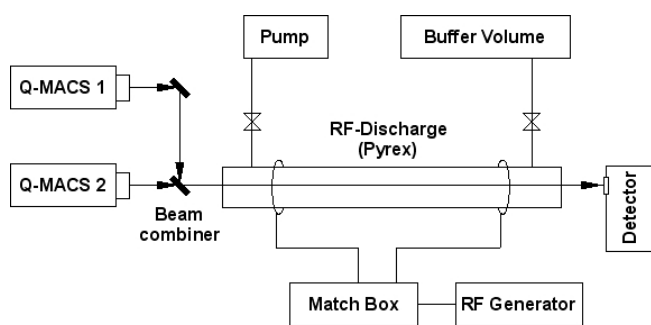


Fig. 7. Experimental set up: RF discharge tube, length  $l = 60$  cm, inner diameter  $d = 2$  cm, combined with a QCLAS system for *in situ* concentration measurements of NO and NO<sub>2</sub> [47].

Fig. 8. Two typical QCLAS spectra demonstrating the detection of NO and NO<sub>2</sub>.

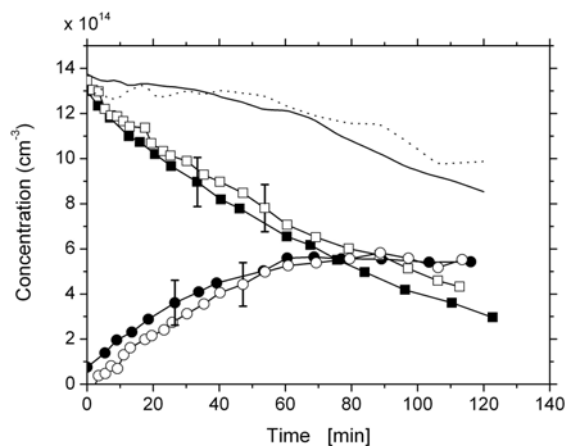


Fig. 9. Time dependence of the NO and NO<sub>2</sub> concentrations after a 1 h oxygen plasma pre-treatment of the Pyrex tube. Probe gas: (i) N<sub>2</sub>+1% NO (NO, ■, NO<sub>2</sub>, ●), (ii) Ar+1% NO (NO, □, NO<sub>2</sub>, ○),  $p=5.3$  mbar. Upper curves show the sum of the NO and NO<sub>2</sub> concentrations [47].

Figure 9 shows the results for two types of probing gas (i) 1% of NO in N<sub>2</sub> and (ii) 1% of NO in Ar. In both cases the concentration of NO decreases while NO<sub>2</sub> simultaneously increases. For both experiments a first order exponential fit gives a rate coefficient of  $2.3 \times 10^{11}$  molecules s<sup>-1</sup> for NO losses. The NO<sub>2</sub> production rate coefficient is nearly the same ( $2.1 \times 10^{11}$  molecules s<sup>-1</sup> for the experiment in N<sub>2</sub> and  $1.9 \times 10^{11}$  molecules s<sup>-1</sup> for the experiment in Ar). Therefore it can be concluded, that NO is oxidized into NO<sub>2</sub> by O containing species (O<sub>2</sub>, O<sub>2</sub><sup>-</sup>, or O atoms) adsorbed on the Pyrex surface during the pre-treatment phase. In the case of an Ar or N<sub>2</sub> plasma treatment of the Pyrex surface a significant NO<sub>2</sub> production could not be measured suggesting that this kind of pre-treatment does not lead to a considerable number of adsorption sites for NO [47]. Under the present conditions NO is probably oxidized to NO<sub>2</sub> via an Eley-Rideal mechanism. A recently developed surface model accords well with the experimental results [49].

### 3.3 *In situ* monitoring of plasma etch processes with a QCL arrangement in semiconductor industrial environment

During the last 40 years plasma etching has become a fundamental feature for processing integrated circuits. The optimization of the plasma chemistry in etch processes includes the identification of the mechanisms responsible for plasma induced surface reactions combined with the achievement of

uniformity in the distribution of molecules and radicals for homogeneous wafer treatment.

In etch plasmas used for semiconductor processing concentrations of the precursor gas  $\text{NF}_3$  and of the etch product  $\text{SiF}_4$  were measured on-line and *in situ* using a new experimental arrangement, designated the Q-MACS Etch system, which is based on QCLAS. In addition, the etch rates of  $\text{SiO}_2$  layers and of the silicon wafer were monitored including plasma etching endpoint detection. For this purpose the Q-MACS Etch system was operated in an interferometric mode. The experiments were performed in an industrial dual frequency capacitively coupled magnetically enhanced reactive ion etcher (MERIE), which is a plasma reactor developed for dynamic random access memory (DRAM) technologies (figure 10). The QCL system (Q-MACS Etch) consists of a pulsed QCL source with the laser emission tunable in the range  $1027 - 1032 \text{ cm}^{-1}$ , optical components, detectors and data acquisition cards controlled by a PC (figure 11). The infrared beam is split into two channels using two ZnSe beam splitters. The main part of the beam is coupled into an infrared fibre using an off axis parabolic mirror, collimated, and directed into the plasma reactor. The second channel provides a reference spectrum of  $\text{C}_2\text{H}_4$  used for line locking. Industrial requirements, such as (i) no open optical path and (ii) the availability of just one optical access port makes coupling the infrared beam into the reactor a challenging task. The solution realized in the Q-MACS Etch is based on the use of (a) mid infrared fibers and (b) internal reflections in the reactor chamber. The capability of Q-MACS Etch for  $\text{SiF}_4$  concentration monitoring via reactor side access and for monitoring the etch rates via reactor top access is shown in figure 10.

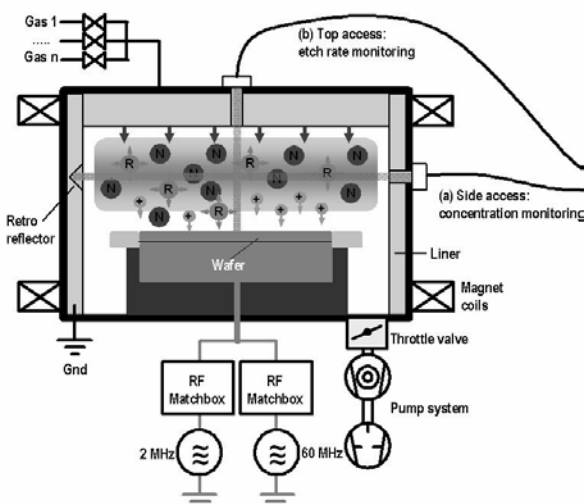


Fig. 10. Experimental arrangement of the MERIE plasma etching reactor: a) side access and b) top access monitoring of the Q-MACS Etch system [42].



Fig. 11. Picture of the Q-MACS Etch with the optical module and the separate control unit in a rack [46].

Figure 12 compares results obtained by QCLAS using a pulsed laser source during batch processing (figure 12a), i.e., deep-trench etching, of 25 wafers with inline data of the deduced trench depth of these wafers (figure 12b) [50]. For about half of the processed wafers a common  $\text{SiF}_4$  number density range is detected (figure 12a). However, the highlighted run (No. 21) was clearly not enclosed by both envelope traces which could be correlated to an incomplete previous cleaning step. The behavior of the  $\text{SiF}_4$  signal also agrees well with deviations found in the trench depth for this wafer (figure 12b). The trench depth values are homogeneously distributed around  $6.9 \mu\text{m}$  except for the wafers 6, 21, and 22. The deviations (marked in red) correlate with those found in (a) [50]. Etch product monitoring in industrial environments may therefore be considered as powerful tool to detect and tackle process errors in real-time.

This first application of a quantum cascade laser arrangement for monitoring of industrial etch processes has opened up a challenging new option for control of demanding semiconductor production applications. Focused on sensitive and fast concentration measurements of key molecular components, while ensuring compactness, robustness and long term stability, this new class of process control

equipment has the potential to become implemented into other fields of technology [42,46,51].

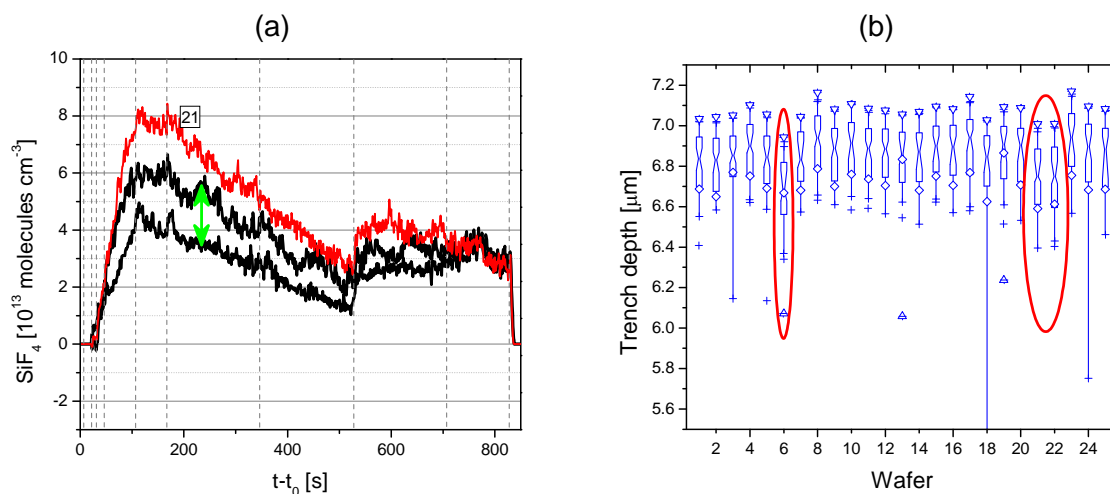


Fig. 12. (a)  $\text{SiF}_4$  number densities as a function of time ( $t - t_0$ ) during the etch process of 25 wafers (results are shown for the last 11 runs). The arrow denotes the range of scatter (heavy solid black lines) during 11 runs. A run (21, thin solid trace) exceeding the typical scatter is plotted separately. Single-process steps are shown by vertical dashed lines.

(b) Box plot of deep-trench etch depth of the processed wafer: the symbols represent the mean value (diamond), the first percentile (triangle up), and the 99<sup>th</sup> percentile (triangle down) of the distributions. The 25<sup>th</sup> - 75<sup>th</sup> percentile range is shown by notched boxes, and their whiskers symbolize the 10<sup>th</sup> - 90<sup>th</sup> percentile range. Outliers are marked by crosses.

#### 4. Summary

During the past few years a variety of phenomena in molecular plasmas in which many short-lived and stable species are produced have been successfully studied based on laser absorption techniques in the mid infrared spectral range. It has been possible to determine absolute concentrations of ground states using spectroscopy thereby providing a link with chemical modeling of the plasma. The need for a better scientific understanding of plasma physics and chemistry has stimulated the application of IRLAS, which has been proven to be one of the most versatile techniques for studying molecular plasmas. Based on the recent development of quantum cascade lasers the further spread of this method of high resolution mid infrared spectroscopy to industrial applications has become a reality.

#### Acknowledgements

The authors convey their sincere thanks to all present and former members of the laboratories involved in Greifswald and Palaiseau for permanent support and a stimulating scientific climate. This work was partly supported by (a) the German Research Foundation (DFG) within the framework of the Collaborative Research Centre Transregio 24 "Fundamentals of Complex Plasmas" and the Transfer Unit 36 "Infrared Lasers for Plasma Process Controlling", (b) the Federal Ministry of Education and Research (BMBF), FKZ 13N7451/8 and by the Federal Ministry of Economics and Technology (BMW), FKZ KF 0086503FK6, (c) by the EFRE fund of the European Community and by funding of the State Saxony of the Federal Republic of Germany, (d) the German Academic Exchange Service (DAAD) and EGIDE as part of the French–German PROCOPE Collaboration Program.

#### References

- [1] Röpcke J, Lombardi G, Rousseau A and Davies P B, *Plasma Sources Sci. Technol.* **2006**, *15*, S148.
- [2] Haverlag M, Stoffels E, Stoffels W W, Kroesen G M W and de Hoog F J 1996 *J. Vac. Sci. Technol. A* **14** 380
- [3] Davies P B and Martineau P M 1992 *Adv Mater.* **4** 729
- [4] Naito S, Ito N, Hattori T and Goto T 1995 *Jpn. J. Appl. Phys.* **34** 302
- [5] Haverlag M, Stoffels E, Stoffels W W, Kroesen G M W, de Hoog F J 1994 *J. Vac. Sci. Technol. A* **12** 3102
- [6] Röpcke J, Mechold L, Käning M, Fan W Y and Davies P B 1999 *Plasma Chem. Plasma Process.* **19** 395
- [7] Haverlag M, Stoffels E, Stoffels W W, Kroesen G M W., de Hoog F J 1996 *J. Vac. Sci. Technol. A* **14** 384

- [8] Yamada C and Hirota E 1983 *J. Chem. Phys.* **78** 669
- [9] Naito S, Ikeda M, Ito N, Hattori T and Goto T 1993 *E Jpn. J. Appl. Phys.* **32** 5721
- [10] Naito S, Ito N, Hattori T and Goto T 1994 *Jpn. J. Appl. Phys.* **33** 5967
- [11] Ikeda M, Ito N, Hiramatsu M, Hori M and Goto T 1997 *J. Appl. Phys.* **82** 4055
- [12] Kroesen G M W, den Boer J H W G, Boufendi L, Vivet F, Khouli K, Bouchoule A and de Hoog FV 1996 *J. Vac. Sci. Technol. A* **14** 546
- [13] Busch C, Möller I and Soltwisch H 2001 *Plasma Sources Sci. Technol.* **10** 250
- [14] Serdioutchenko A, Möller I and Soltwisch H 2004 *Spectrochim. Acta* **60A** 3311
- [15] Liu Z and Davies P B 1996 *J. Chem. Phys.* **105** 3443
- [16] Davies P B and Smith D M 1994 *J. Chem. Phys.* **100** 6166
- [17] Rousseau A, Dantier A, Gatilova L V, Ionikh Y, Röpcke J and Tolmachev Y A 2005 *Plasma Sources Sci. Technol.* **14** 70
- [18] Ionikh Y, Meshchanov A V, Röpcke J and Rousseau A 2006 *Chem. Phys.* **322** 411
- [19] Zijlmans R A B, Gabriel O, Welzel S, Hempel F, Röpcke J, Engeln R, Schram D C 2006 *Plasma Sources Sci. Technol.* **15** 564
- [20] Gatilova L V, Allegraud K, Guillon J, Ionikh Y Z, Cartry G, Röpcke J and Rousseau A 2007 *Plasma Sources Sci. Technol.* **16** S107
- [21] Van Helden, J H, Wagemans W, Yagci G, Zijlmans R A, Schram D C, Engeln R, Lombardi G, Stancu G D and Röpcke J 2007 *J. Appl. Phys.* **101** 043305
- [22] Rousseau A, Guaitella O, Gatilova L, Hannemann M. and Röpcke J 2007 *J. Phys. D.* **40** 2018
- [23] J. Röpcke, P.B. Davies, F. Hempel, B.P. Lavrov, in *Low Temperature Plasmas – Fundamentals, Technol. and Techniques*, R. Hippler, H. Kersten, M. Schmidt, K.H. Schönbach Eds., Wiley-VCH, Berlin, 2008, **1**, 215
- [24] F. Hempel, P.B. Davies, D. Loffhagen, L. Mechold, J. Röpcke, *Plasma Sources Sci. Technol.* **12**, S98 (2003)
- [25] A. Cheesman et al., *J. Phys. Chem. A* **110**, 2821 (2006)
- [26] G. Lombardi, G.D. Stancu, F. Hempel, A. Gicquel, J. Röpcke, *Plasma Sources Sci. Technol.* **13**, 27 (2004)
- [27] S. Welzel, A. Rousseau, P.B. Davies, J. Röpcke, *J. Phys.: Conf. Series* **86**, 012012 (2007)
- [28] A. Ershov, J. Borysow, *J. Phys. D: Appl. Phys.* **28**, 68 (1995)
- [29] R. Sankaranarayanan, B. Pashaie, S.K. Dhali, *Appl. Phys. Lett.* **77** 2970 (2000)
- [30] Z. Falkenstein, *J. Appl. Phys.* **81** 7158 (1997)
- [31] J. Röpcke, L. Mechold, M. Käning, J. Anders, F.G. Wienhold, D. Nelson, M. Zahniser, *Rev. Sci. Instrum.* **71**, 3706 (2000)
- [32] J.B. McManus, D. Nelson, M. Zahniser, L. Mechold, M. Osiac, J. Röpcke, A. Rousseau, *Rev. Sci. Instr.* **74**, 2709 (2003)
- [33] A. Ohl, *J. Phys. IV* **8**, 83 (1998)
- [34] van Helden J H, Wagemans W, Yagci G, Zijlmans R A B, Schram D C, Engeln R, Lombardi G, Stancu G D, Röpcke J, *J. Appl. Phys.* **101**, 043305 (2007)
- [35] Gordiets B, Ferreira C M, Pinheiro M J, Ricard A, *Plasma Sources Sci. Technol.* **7**, 379 (1998)
- [36] van Helden J H, van den Oever P J, Kessels W M M, van de Sanden M C M, Schram D C, Engeln R, *J. Phys. Chem. A* **111**, 11460 (2007)
- [37] Faist J, Capasso F, Sivco D L, Sirtori C, Hutchinson A L and Cho A 1994 *Science* **264** 553
- [38] Gmachl C, Sivco D L, Colombelli R, Capasso F and Cho A Y 2002 *Nature* **415** 883
- [39] Beck M, Hofstetter, D., Aellen, T., Faist, J, Oesterle, U., Ilegems, M., Gini, E. and Melchior, H., 2002 *Science* **295** 301
- [40] Hempel F, Glitsch S, Röpcke J, Saß S and Zimmermann H 2005 in: *Plasma Polymers and Related Materials* (M. Mutlu ed.), Hacettepe University Press 142
- [41] Cheesman A et al., 2006 *J. Phys. Chem. A* **110** 2821
- [42] Stancu G D, Lang N, Röpcke J, Reinicke M, Steinbach A and Wege S, *Chem. Vap. Dep.* **13** (2007) 351.
- [43] Namjou K et al., 1998 *Opt. Lett.* **23** 219
- [44] Beyer T et al., 2003 *J. Appl. Phys.* **93** 3158
- [45] Welzel, S., Rousseau, A., Davies, P. B. and Röpcke, J., *J. Phys.: Conf. Series* **86** (2007) 012012 .
- [46] Lang, N., Röpcke, J., Steinbach, A., Wege, S., 6. OPTAM, Düsseldorf 2008, VDI-Ber. 2047, 11-21 (2008).
- [47] Guaitella O, Hübner M, Welzel S, Marinov D, Röpcke J and Rousseau A , 2010, *Plasma Sources Sci. Technol.* **19** 045026
- [48] Lang N, Röpcke J, Wege S, Steinbach A, 2010 *Eur Phys J-Appl Phys* **49** 13110
- [49] Guaitella, O, Hübner, M., Marinov, D., Guerra, V., Pintassilgo, C.D., Welzel, S., Röpcke, J. and Rousseau, A., *Contrib. Plasma Phys.* (2011) in print.
- [50] Lang, N.; Röpcke, J.; Steinbach, A.; Wege, S. *IEEE T Plasma Sci.* 2009, **37**, 2335.
- [51] Welzel, S., Hempel, F., Hübner, M., Lang, N., Davies, P.B. and Röpcke, J., *Sensors* **10** (2010) 6861
- [52] J. Röpcke, R. Engeln, D. Schram, A. Rousseau and P. B. Davies, in "Introduction to Complex Plasmas", Springer, Eds. Michael Bonitz et. Al. Springer Series on Atomic, Optical, and Plasma Physics, **59**, 2010, p. 315

# A single target RF magnetron co-sputtered iron doped tin oxide films with nano pillars

M. Kormunda, J. Pavlik

Faculty of Science, J.E. Purkinje University, Ceske mladeze 8, Usti nad Labem, Czech Republic

e-mail: martin.kormunda@ujep.cz

## Abstract

The tin oxide is a material with a wide range of applications. The doped tin oxide can be used for gas sensors, in catalytic applications, protective applications and certain potential is also in spintronics. Each application requires a specific surface morphology from a very flat surface up to porous or nanostructured surfaces.

The iron doped SnO<sub>2</sub> coatings were deposited by RF single target magnetron co-sputtering in three different positions of the substrates at various conditions. The target composed of the SnO<sub>2</sub> and small Fe inset. The depositions were carried out in pure argon and argon/oxygen gas mixtures. Substrate positions were off axis when smooth coatings with R<sub>max</sub> about 1nm were deposited. Pillars could grow on the top of smooth doped tin oxide films at room temperature deposition temperature when proper conditions used. A typical diameter of the single pillar was around 400 nm. The stoichiometry of coatings was not influenced significantly by the pillars. The typical O/Sn ratio was inside 7 % error range around average value 1.7. The iron concentration was controlled in wide range from 0 at.% up to 6 at.%. The XPS measurements confirmed the dominant presence of SnO<sub>2</sub> phase without any influence of the surface morphology.

**Keywords:** Magnetron co-sputtering; off-axis deposition; amorphous stannic oxide; nanostructures

## Introduction

The considerable effort has been devoted to the synthesis of nanostructured SnO<sub>2</sub> materials, including nanorods, nanowires and nanobelts [1]. One of used techniques is a thermal evaporation when from mixtures of SnO<sub>2</sub> and carbon powders under the assistance of a stainless steel grid at 950 °C synthesized a fish bone like structures. Nanowires in those structures had a typical diameter of 200 nm and range from 3 to 10 μm in length [2]. Dendritic SnO<sub>2</sub> nanostructures were synthesized from mixture ZnS and Sn powders in 500 °C temperature zone of furnace [3]. Nanoneedles were grown on n-type (100) Si substrates with a 20 nm thick gold coating at 900 °C [4,5,6]. Wet chemistry produced SnC<sub>2</sub>O<sub>4</sub> was mixed with NaCl and the mixture was annealed at 800 °C for 2 h. Such a way prepared material was rich in 10 – 60 nm diameter nanorods of crystalline SnO<sub>2</sub> [7].

The iron doped SnO<sub>2</sub> nanostructures were already prepared by wet chemistry. The iron sulfate (FeSO<sub>4</sub>) and tin chloride (SnCl<sub>4</sub>) with Fe<sub>3</sub>O<sub>4</sub> nanosheets precursor were used and then the SnO<sub>2</sub>/α-Fe<sub>2</sub>O<sub>3</sub> hierarchical nanostructures were formed [8]. The iron doped tin oxide coatings were also prepared by pulsed laser discharges from powders when the magnetic properties were investigate and the R<sub>rms</sub> was below 5 nm. The high temperature intrinsic ferromagnetism was detected [9].

Above reported techniques for preparation of nanostructures require powders or liquid precursors and a high temperature. In contrary here proposed technique uses bulk SnO<sub>2</sub> material and whole process is carry out at room temperature. The magnetron sputtering at proper conditions can deposits nanostructures.

The experimental setup described elsewhere [10] was used with modifications described here. The process pressure was measured by capacitive diaphragm gauge MKS Baratron. The MKS gas flow controllers were used for argon (99.9999 %, Linde) and oxygen (99.9999 %, Linde) gases. Two equipments were used to evacuate the chamber; first, a turbo molecular pump 60 l/s with a membrane fore vacuum and second, a turbo molecular pump 190 l/s with a rotary fore vacuum pump. Background pressures before the deposition were always better than 7 x 10<sup>-3</sup> Pa.

The RF 13.56 MHz power supply Advance Energy Dressler Cesar 133 with external matching box was used for sputtering in set A and set B, when Advance Energy Dressler Interigo 133 was used for sputtering from set C and set D. The RF power was up to 100 W with reflected power below 1 W.

The 50 mm diameter magnetron cathode was used with 3 mm thick SnO<sub>2</sub> (99.9 %) target. The iron

doping was achieved by placing the iron strips on the magnetron target [10]. The target with iron strip dopant was always before deposition cleaned by argon ion bombardment.

The polished n-Si(100) substrates (ON Semiconductor) in size about 12 x 10 mm were mechanically clamped on the 83 mm diameter grounded copper table.

The thin films were deposited in three different off-axis arrangements; set A - the angle between the planes of the substrate and the target was 30° from the parallel plane where the upside of the substrate was turned toward to the target and the distance between centre of samples and centre of target's face was about 80 mm, see simplified schematic sketch in Figure 1(left). The iron doping was achieved by placing the iron strips over the erosion area of the magnetron target and the process gas was pure argon at 2 Pa and 5 Pa. Set B - the substrate was perpendicular to the target when the centre of the substrate was at distance of 70 mm from the face of target and 40 mm from the target's axis, both faces were vertical, see in Figure 1(left). The iron doping was achieved by placing the iron strip in the centre of the magnetron target with small overlap of erosion zone and the process gas was pure argon at typical pressure 0.8 Pa. Set C - the substrate was tilted to 85° from 90° in previous set B when the iron strip was again in the centre of the magnetron. The argon/oxygen gas mixture had 25% of oxygen at pressure 0.3 Pa. Set D – the position of substrate was identical to set B but when the iron strip was also in the centre of the magnetron but the argon/oxygen gas mixture had 25% of oxygen at pressure 0.3 Pa.

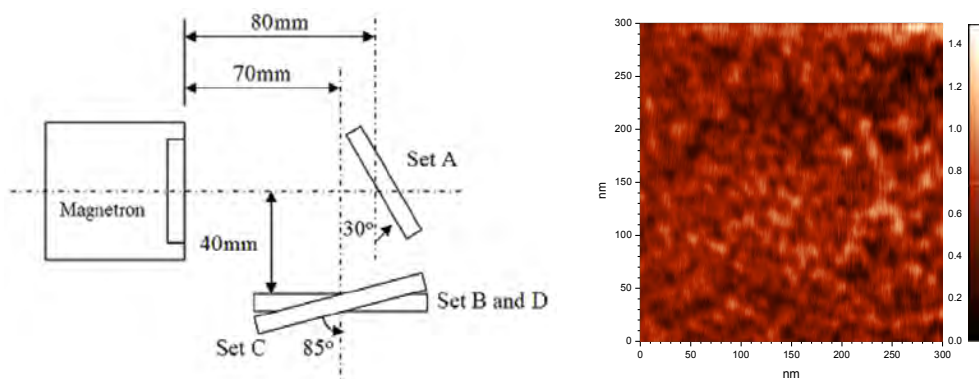


Fig. 1. (left) Simplified sketch of the substrate position in combined top view and side view, (right) The AFM measured topology of coating deposited in set B at room temperature and post-annealed under vacuum at 600 °C

We also investigated the surface chemical composition by X-ray photoelectron spectroscopy (XPS) method. The binding energies were corrected on C 1s peak maximum at 285 eV. In measurements, an X-ray source, Al K $\alpha$  (1486 eV), was used and the details are elsewhere [10].

The surface morphology was investigated by Atomic Force Microscope (AFM) Integra Probe NanoLaboratory (NT-MDT) in a semi contact mode. The surface topology was also studied by Tescan Vega LSU electron microscope.

## Results and discussion

The coatings deposited in set A were very flat with  $R_{\text{rms}}$  about 1 nm when the thicknesses were for all coatings estimated about 15 nm. The process pressures 2 Pa and 5 Pa and RF power from 5 W to 20 W were investigated and no significant influence on the surface morphology was observed. The iron concentration was independent on the process pressure and the concentration was increased from initial 0.8 at. % at 5 W to 5.3 at. % at 10 W when the O/Sn ratio was constant about 1.8. The change in substrate position from set A to set B had no influence on the surface morphology. The coatings had practically identical flat surface as illustrated in Figure 1(right). It is known that the deposition rate in such off axis arrangement is also a function of the pressure. Therefore the experiments were carried out at lower pressure 0.8 Pa when a sufficient deposition rate was reached. The move of iron inset from the erosion zone of the magnetron target in set A to centre of the magnetron target in other sets allowed an increase in RF power when the iron concentration remained below 6 at. % because less iron was sputtered. The iron concentration was reduced by this inset position by 50 % to 5.5 at. % at 20 W and 3 at. % at 10 W. The deposition rate reached about 2.8 nm/min at 20 W. Because the gas sensors

are usually used at elevated temperatures up to 600 °C the influence of post deposition annealing on the surface morphology and the composition were also investigated. The iron content, the O/Sn ratio and surface morphology were not influenced by the annealing up to 600 °C at varied atmosphere [10].

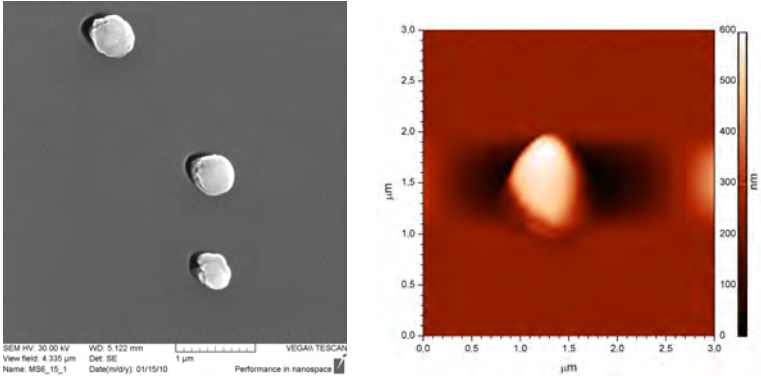


Fig. 2. (left) The typical SEM image in secondary electrons of pillars with flat surroundings after 32 min deposition deposited in set C, image scale size 1 mm, (right) The AFM image of a typical single pillar

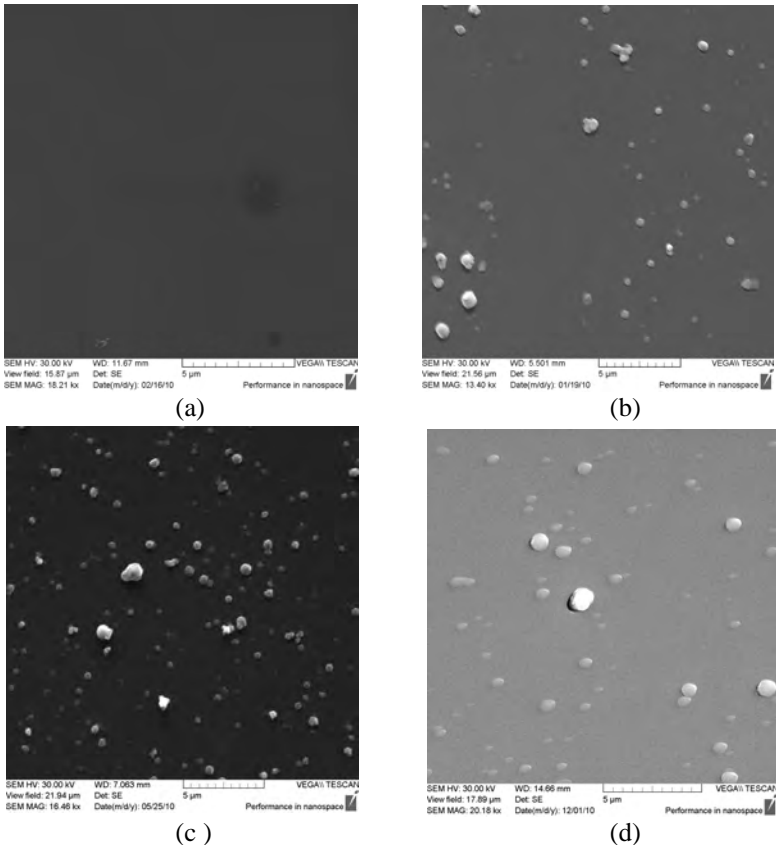


Fig. 3. The SEM picture in secondary electrons typical for the coating deposited by 75W in (a) set C for 8 min, the gas flow 2.5 sccm, (b) set D for 32 min, the gas flow 2.5 sccm, (c) set D for 15 min, the gas flow 7 sccm (d) set D for 32 min by RF power 120W, image scale size 5 μm

It is expected that gas sensors and catalytic surfaces would benefit from a large active area. Therefore the substrate was arranged to another position in set C and oxygen was introduced to the gas mixture at lower total pressure 0.3 Pa. Because due to presence of oxygen the iron content in the coatings decreased therefore an increase in the RF power was allowed. The RF power was fixed to 75 W for those experiments and the deposition rate reached 9 nm/min. The coatings deposited in the thicknesses below approximately 100 nm had similar flat surface as reported before, see Figure 3(a).

But when the deposition continued certain nanostructures appeared. The details on such nanostructures are visualized by SEM in Figure 2(left). The nanostructures look like pillars.

When the number of pillars was high, the thickness measured from the substrate up to top of the continuous coating without pillars was significantly reduced because a high amount of the deposited material was already used for the pillars. Those pillars were from 400 to 500 nm in diameter when their height was above 500 nm as visible from AFM measurement in Figure 2(right). Those pillars are about double times in diameter compare to nanowires prepared by thermal evaporation at 950° C [2] and about 20 times compare to thin nanoneedles [4,5,6].

The growth of pillars started from spherical caps on the flat surface. It is visible on many places in Figures 3(d). The high pillars in Figure 2 had started to grow from the spherical cap and then their growth was much faster than surrounding coatings therefore they are more than 500nm above the continuous coating. The shadowing effect is visible on the left side of the surrounding coating close to the pillar. But the observed shadowing effect cause only small deformations of the continuous film when the missing material in the continuous coating by shadowing effect has to be equal to material in pillar.

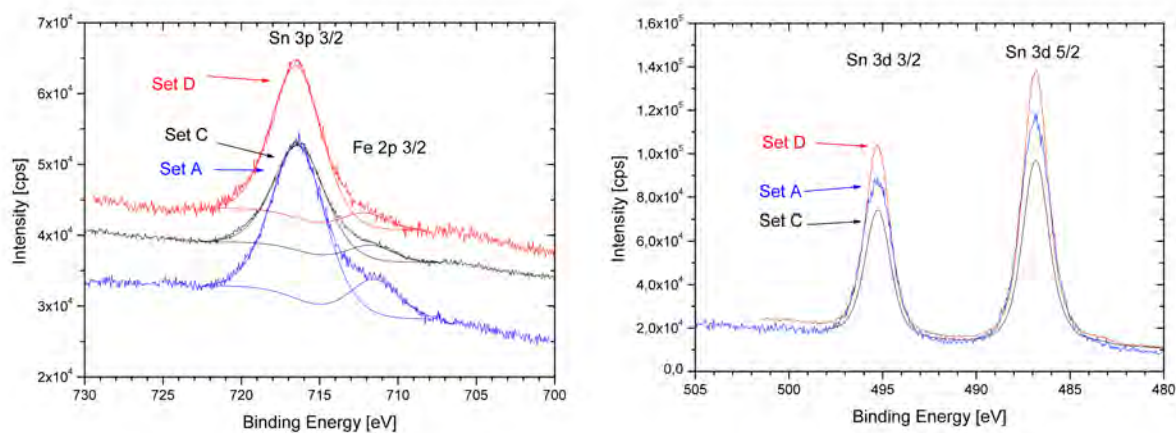


Fig. 5. XPS spectra of (left) Fe2p and Sn 3p and (right) Sn 3d measured on coatings deposited at conditions Set A - 20W, 2 Pa, 5 min, Set C – 75W, 0.8 Pa, 30 min, Set D – 75W, 0.8 Pa, 30 min

The density of pillars on surface was controlled simply by the deposition time. The pillars had probably an identical composition as the surrounding surface because the presence of pillars had no influence on the iron content (about 1.5 at. %) and the O/Sn ratio (about 1.8). Because for substrates in set C appeared certain obstacles those experimental conditions were repeated by set D where the substrate was in identical position as before in set B. The nanostructures were also created in this deposition arrangement but their shape was more modified by the shadowing effect, see Figure 3(b). Otherwise the densities of pillars on surface in both arrangements (set C and set D) were similar. Because the density on pillars on the substrates were relatively low as illustrated in Figure 3(b) an increase was required. Based on the computer model [11] the improvement was expected for increased gas flow. Therefore the gas flow was increased from initial total flow 2.5 sccm to 7 sccm at the constant total pressure 0.3 Pa by employing more powerful vacuum pump. The deposition rate was increased imperceptibly to 10 nm/min. But the density of pillars on the surface was increased significantly. Therefore similar densities of nanopillars were reached already for half deposition time when only the gas flow was increased, compare in Figure 4(b) after 32 min (2.5 sccm) to similar Figure 4(c) for half deposition time 15 min (7 sccm).

Because the number of pillars depends on the gas flow at the constant RF power it can be concluded that the dust particles initialize the process of pillars formation. To destroy this presumption coatings were deposited by higher 120 W RF power at condition of set D with gas flow 7 sccm. The set of coatings was investigated and all the coatings had significantly reduced number of pillars comparable to coatings deposited by 75 W at identical gas flow about 7 sccm, compare in Figure 3(c) after 15 min (7 sccm) to Figure 3(d) for 32 min (7 sccm). There is no evidence of dust particles influence because the identical deposition time does not lead to similar number of pillars. The number of pillars depends also on the RF power and the RF power around 75 W creates higher

number of pillars. The increase in RF power to 120 W or decrease to 20 W leads to low number of pillars at the certain gas flow.

The iron atomic concentration was for all samples deposited by 75 W constant about 1.7 at. % with typical precision about 0.5 at. %. But the Sn 3p and Fe 2p peaks overlap details of deconvolution process are elsewhere [10]. The literature reports binding energy Fe 2p<sub>3/2</sub> at 711.6 eV for  $\alpha$ -Fe<sub>2</sub>O<sub>3</sub>, 709.8 eV for FeO and 707 eV for metallic Fe [12] and the binding energy of deconvoluted peak Fe2p<sub>3/2</sub> was about 712eV that this binding energy indicates  $\alpha$ -Fe<sub>2</sub>O<sub>3</sub> bonding structure, see in Figure 5(left). The wet chemistry prepared SnO<sub>2</sub>/ $\alpha$ -Fe<sub>2</sub>O<sub>3</sub> hierarchical nanostructures reported in literature incorporated the same oxide state about 712 eV [3].

The binding energies in XPS spectra were about 495.3eV for Sn 3d<sub>3/2</sub> and 487eV for Sn 3d<sub>5/2</sub> and those binding energies, see in Figure 5(right), correspond to literature reported 496.7eV and 487.9eV binding energies for pure SnO<sub>2</sub> [12]. The shape of the peak was not significantly differences between the films deposited at different conditions. High resolution O 1s peak had a single peak character with maximum about 530.6 eV instead a literature reported 531.2eV for SnO<sub>2</sub> structure [12]. The O 1s peak shows only O to Sn bond with certain asymmetry, not illustrated. There is again no significant difference in O 1s peak between the films deposited at different conditions. There is also no significant evidence of O to Fe bonding at binding energy 530.4 eV ( $\alpha$ -Fe<sub>2</sub>O<sub>3</sub> structure). But iron concentration was typically a few at. % therefore no significant evidence of O-Fe bond was expected.

Because the presence of pillars has no effect on O/Sn ratio and shape of XPS peaks it can be concluded that the nano pillars have the chemical composition similar to coating's base material.

## Conclusions

The iron doped tin oxide coatings were prepared with controlled dopand concentration. The coatings were very flat and at certain conditions the pillars started to grow up with typical diameter from 400 nm to 500 nm when deposited at room temperature. The density of pillars was controllable by deposition time and the gas flow. The stoichiometry of coatings was not influenced significantly by the changes in surface morphology; the typical O/Sn ratio was in 7% error range around 1.7 for catings deposited by RF power 75 W. The iron concentration was controlled up to 6 at. % by the inset position, the RF power and the gas composition. The XPS measurements confirmed a dominant presence of SnO<sub>2</sub> phase without any influence of the surface morphology.

## Acknowledgments

This work was supported by The Ministry of Education of Czech Republic (Project LC06041) and by AS CR (Project KAN400720701).

## References

- [1] Y. Zhang, K. Yua, G. Li, D. Peng, Q. Zhang, H. Hu, F. Xu, W. Bai, S. Ouyang, Z. Zhu, *Applied Surface Science* 253 (2006) 792.
- [2] Q. Wang, K. Yu, F. Xu, *Solid State Communications* 143 (2007) 260.
- [3] X. Wu, J. Sui, W. Cai, F. Qu, *Materials Chemistry and Physics* 112 (2008) 325.
- [4] L.A. Ma, T.L. Guo, *Materials Letters* 63 (2009) 295.
- [5] B. Wang, Y.H. Yang, C.X. Wang, G.W. Yang, *Chemical Physics Letters* 407 (2005) 347.
- [6] Z. Ying, Q. Wan, Z.T. Song, S.L. Feng, *Materials Letters* 59 (2005) 1670.
- [7] C. Xu, G. Xu, Y. Liu, X. Zhao, G. Wang, *Scripta Materialia* 46 (2002) 789.
- [8] W.-W. Wang, *Materials Research Bulletin* 43 (2008) 2055.
- [9] C. B. Fitzgerald, M. Venkatesan, L. S. Dorneles, R. Gunning, P. Stamenov, J. M. D. Coey, P. A. Stampe, R. J. Kennedy, E. C. Moreira, *Physical Review B* 74 (2006) 115307
- [10] M. Kormunda, J. Pavlik, A. Mackova, P. Malinsky, *Surface & Coatings Technology* 205 (2010) S120–S124
- [11] T. Kubart, S. Zhao, G. Wingqvist, T. Nyberg, E. Wäckelgård, S. Berg, *Journal of Physics: Conference Series* 100 (2008) 082024.
- [12] B. Crist, *Handbooks of Monochromatic XPS Spectra*, XPS International LLC, Leona Lane, 2004.

# Deposition of SiO<sub>x</sub> films by means of atmospheric pressure microplasma jets

J. Benedikt, R. Reuter, D. Ellerweg, K. Rügner, A. von Keudell  
Research Department Plasmas with Complex Interactions, Ruhr-University Bochum,  
Universitaetsstr. 150, Bochum 44780, Germany

e-mail: jan.benedikt@rub.de

## Abstract

Atmospheric pressure plasma jet sources are currently in the focus of many researchers for their promising applications in medical industry (e.g. treatment of living tissues), surface modification or material etching or synthesis. Here we report on the study of fundamental principles of deposition of SiO<sub>x</sub> films from microplasma jets with admixture of hexamethyldisiloxane [(CH<sub>3</sub>)<sub>3</sub>SiOSi(CH<sub>3</sub>)<sub>3</sub>, HMDSO] molecules and oxygen. The properties of the deposited films, the composition of the plasma as measured by molecular beam mass spectrometry and the effect of additional treatment of grown film by oxygen or hydrogen atoms will be presented.

**Keywords:** atmospheric pressure plasma, microplasma, HMDSO, plasma chemistry, silicon dioxide.

## Introduction

Atmospheric pressure microplasma discharges have attracted a great deal of attention due to their interesting properties such as high electron density inaccessible for typical low pressure plasmas ( $n_e$  up to  $10^{21} \text{ m}^{-3}$  and very low gas temperature ( $T_g$  as small as 300 K). Moreover, the operation at atmospheric pressure and low power consumption ( $\sim 1 \text{ W}$ ) make them attractive for on chip implementation and mass production. Up to now, a number of different configurations have been described in the literature for microplasmas operated at atmospheric pressure. Examples are microhollow cathode discharges, capillary plasma electrode discharges, cylindrical dielectric barrier discharges, miniature inductively and capacitively coupled plasmas, jets or devices fabricated in semiconductor structures [1-3]. Microplasma sources can be DC, RF or MW driven and they can be used for example as photonic devices [4,5], as analytical tools [6], for bacterial inactivation [7], for etching of silicon wafers [8] or for localized deposition [9,10].

Here we present the study of the SiO<sub>x</sub> thin film deposition by means of atmospheric pressure microplasma jets. We use two different sources: i) a source with coaxial electrode structure with a 250  $\mu\text{m}$  gap and with dielectric barrier at outer electrode and ii) a parallel metal-electrode jet with electrode gap of 1 mm. Both are used for the study of atmospheric pressure deposition of SiO<sub>x</sub> thin films. The former one can be operated for a very long times and produces good quality SiO<sub>2</sub> films [11,12], whereas the latter source is effective in dissociation of HMDSO, but his operation time is reduced due to deposition on its electrodes.

## Experimental Setup

Fig. 1 shows a scheme of the microplasma jet. The detailed description of the setup has been published previously [13-15]. A stainless steel capillary tube is inserted into a ceramic tube leaving an annular gap of 250  $\mu\text{m}$  between the tubes. The capillary ends 2 mm prior to the end of the ceramic tube. Around the ceramic tube and 1 mm apart from its end, an aluminum tube serves as counter electrode. A 13.56 MHz radio frequency power supply is attached through a matching network to the capillary or to the outer electrode. Outer electrode is powered in this case. Plasma forming gas (He or Ar in this case) is introduced into the annular space between the ceramic tube and the capillary with a flow rate of 3000 sccm. Additional flow of 160 sccm is guided through the capillary in order to maintain similar gas velocities in the annular space between electrodes and in the capillary. This is especially important when some reactive gas is added to the capillary flow [15]. The reactive gases are in this case HMDSO and oxygen. The HMDSO flow, since it is liquid under standard conditions, is obtained by guiding Ar or He gas through a bubbler containing HMDSO. The plasma can be ignite easily in He by applying root mean square (RMS) voltage of about 100 V. The ignition in Ar is not possible without an external high voltage pulse and therefore an Ar-plasma operation is realized through ignition in He and switching gas flows to Ar. Previous studies assessed the effect of

environmental air around the jet on the plasma [13,14]. Nitrogen and oxygen of the surrounding atmosphere do not interfere with the plasma jet, since the main flow through the ceramic tube acts as a barrier.

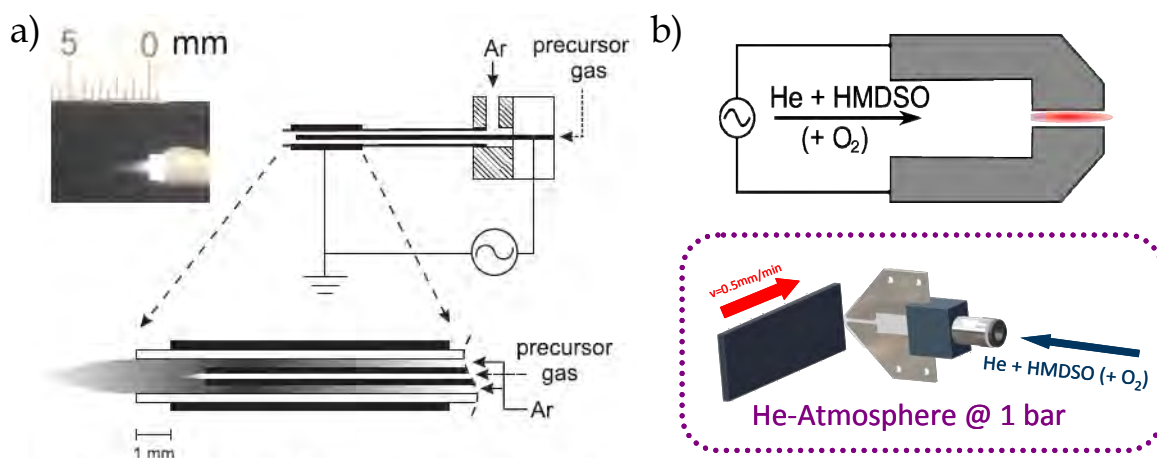


Fig. 1. The schemes of the microplasma jets used in this work: a) coaxial microplasma jet, b) planar microscale atmospheric pressure plasma jet ( $\mu$ -APPJ)

The second source, microscale atmospheric pressure plasma jet ( $\mu$ -APPJ), is a capacitively coupled microplasma jet consisting of two stainless steel electrodes (length 10 mm, width 1 mm) with a 1 mm gap in between (cf. Fig. 2). The plasma is ignited in this gap filling a volume of  $1 \times 1 \times 10 \text{ mm}^3$ . The plasma volume is confined on two sides by glass plates. One electrode is connected to a power supply (13.56 MHz,  $<30 \text{ W}$ ) through a matching network and the other one is grounded. The gas flow through the  $\mu$ -APPJ is 5 slm helium with a small admixture of molecular oxygen and HMDSO. The deposition takes place on an moving substrate ( $v = 0.5 \text{ mm/min}$ ) to deposit film on a larger area and it takes place in an reactor with helium atmosphere to avoid admixture of surrounding air into the plasma. It has been shown that this microplasma jet is a typical  $\alpha$  mode discharge [16].

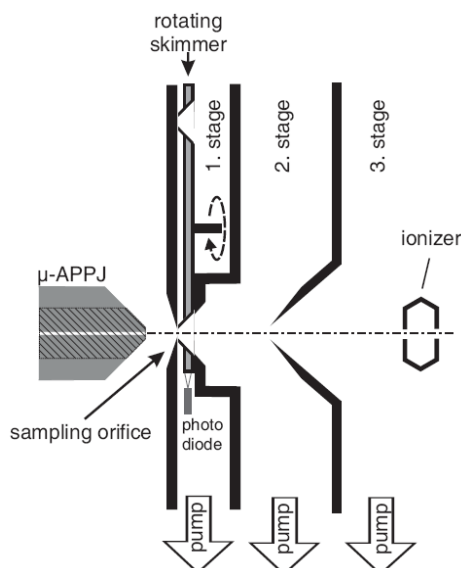


Fig. 2. The scheme of the sampling system used for the molecular beam mass spectrometry.

The effluent of this  $\mu$ -APPJ is analyzed by the molecular beam mass spectrometry (MBMS) system also shown in Fig 2. This MBMS system uses a novel chopper of the molecular beam, which reduces significantly the background pressure in the mass spectrometer and which allows measurements of

species concentrations at ppm level. The detailed description can be found elsewhere [17,18].

## Results and discussion (Times 11, bold)

### Deposition of $\text{SiO}_x$ films

First films deposited from "pure" HMDSO by means of coaxial jet are discussed. By using oxygen containing precursor such as HMDSO, the  $\text{SiO}_x$  films could be theoretically deposited even without addition of oxygen. We have observed this for deposition with the coaxial jet as shown in Fig. 3a), where FTIR spectra of films deposited at varying HMDSO flow rates and without addition of oxygen are shown.

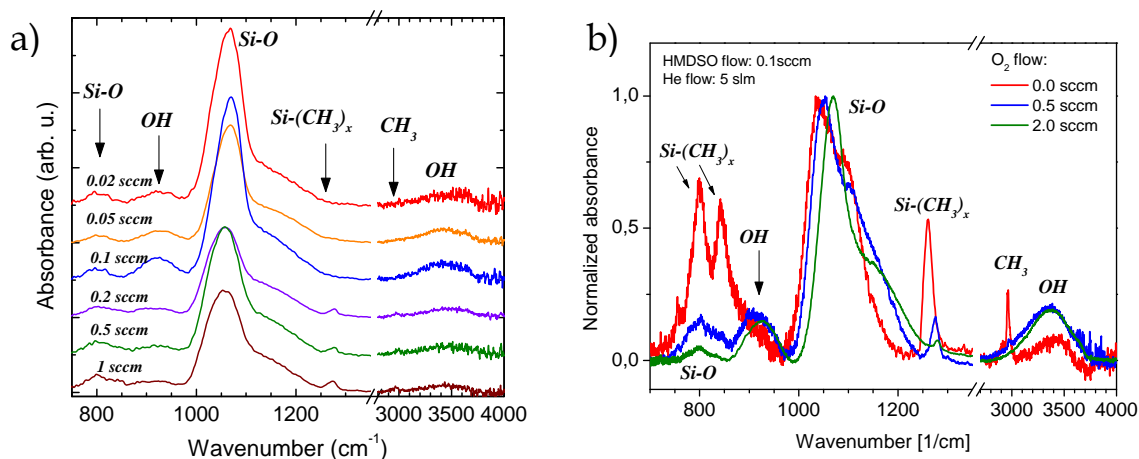


Fig. 3. FTIR spectra of deposited films. a) Coaxial jet used with different HMDSO flows and without addition of  $\text{O}_2$ , adopted from [12], b)  $\mu$ -APPJ used.

At high HMDSO flow rates, the absorption peaks corresponding to the  $\text{Si}-(\text{CH}_3)_x$  bending mode at  $\sim 1275 \text{ cm}^{-1}$  and the  $\text{CH}_3$  stretching mode at around  $2960 \text{ cm}^{-1}$  are visible. By decreasing the HMDSO flow rates, the intensities of these carbon related absorption peaks decrease. For very low HMDSO flow rates (below 0.1 sccm), absorption peaks originating from carbon completely disappear: the film changes abruptly from an organic to an inorganic silicon oxide composition. This is surprising, since carbon is usually observed in films deposited from pure HMDSO either at low [19,20] or at atmospheric pressure [21,22]. When  $\text{O}_2$  flow in the range from 1 to 50 sccm is added to the gas, inorganic  $\text{SiO}_2$  films without carbon are deposited, which was also corroborated by XPS measurements [12]. These films are still porous with high content of OH groups. The porosity is significantly reduced by heating the substrate to  $200 \text{ }^\circ\text{C}$ .

When  $\mu$ -APPJ is used and no  $\text{O}_2$  is added into the gas mixture, a carbon rich film is deposited as shown in Fig. 3b). The  $\text{SiO}_x$  film with low carbon content is only observed when 2 sccm or more of  $\text{O}_2$  are added into the plasma. Both plasmas behave quite differently indicating, that Ar plasma chemistry and He plasma chemistry are different.

### Mass spectrometry analysis

The deposition mechanism of these films, especially under conditions where no oxygen is actively added to the gas flows, is still not well understood. We have proposed that ion-induced polymerization of HMDSO can be responsible for the observed behavior [12], however direct measurement of the depositing species is still not available. To resolve this issue, we have decided to apply MBMS and analyze the composition of the gas mixture emanating from the jets. The  $\mu$ -APPJ with He as a carrier gas is studied only, because the presence of He significantly enhances the MS signal and improves the detection limit. It is a critical issue in this case because better quality  $\text{SiO}_x$  films are deposited when HMDSO flow is small, below 100 ppm. The concentrations of stable products of plasma chemistry are similar or lower than this value. Radical densities are most probably below the detection limit of our MBMS system ( $\sim 1 \text{ ppm}$ ).

The presence of organosilicone compounds detected in atmospheric pressure HMDSO plasmas [23] has been checked by measuring their parent masses under different conditions. An electron

energy of 20 eV in the ionizer of the MS is chosen for these measurements to minimize the fragmentation of large molecules. The signal intensities at masses of 28 amu (representative for CO and N<sub>2</sub>), 73 amu (tetramethylsilan), 75 amu (trimethylsilanol), 131 amu [(CH<sub>3</sub>)<sub>3</sub>SiOSi(CH<sub>3</sub>)(CH<sub>2</sub>)], 133 amu (pentamethyldisiloxan) and 147 amu (HMDSO) under plasma off, plasma on without addition of O<sub>2</sub> and plasma on with addition of O<sub>2</sub> conditions are shown in Fig. 4.

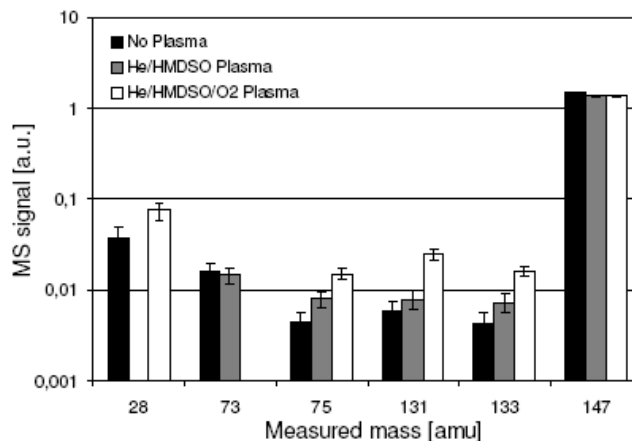


Fig. 4. The change of the MS signal at selected masses as measured without plasma, with He/HMDSO plasma and He/HMDSO/O<sub>2</sub> plasma

First it can be seen at mass 147, which represents the precursor gas, that the consumption of HMDSO is very low, only 7 % of it are consumed in the plasma, even if O<sub>2</sub> is added into the gas mixture. This is typical for atmospheric pressure plasmas and it would corroborate the hypothesis of the ion driven polymerization reaction scheme, which needs large amount of HMDSO molecules for polymerization. The one of the main products of this polymerization scheme is the tetramethylsilan (TMS) detected at mass 73. No change observed at this mass when the plasma is ignited (only the conditions without O<sub>2</sub> has been measured) is however in contradiction with this proposed scheme. The main products detected under our conditions are at masses 131 and 133 amu. These are most probably molecules, which are formed directly from HMDSO molecule by a loss of one methyl group. Surprisingly, these molecules are more abundant, when O<sub>2</sub> is added to the plasma, even if the HMDSO consumption stays the same. Small increase is also observed at mass 75 amu [trimethylsilanol (CH<sub>3</sub>)<sub>3</sub>SiOH] The larger molecules with molecular mass beyond that of HMDSO (detected usually for example at masses 207 and 221 amu) have densities below our detection limit of ~1 ppm, when no O<sub>2</sub> is added, but become measurable when O<sub>2</sub> is present in the gas mixture. Slight increase is also observed at mass 28 amu, which is probably CO and indicates that combustion occurs in presence of oxygen.

#### *Exposure of the surface to atomic oxygen*

The microplasma jet geometry and localization of the deposition/treatment at a spot of few square millimetres allow us to study the role of oxygen in the  $\mu$ -APPJ deposition process. This is done by alternating the application of He/HMDSO plasma (deposition of the carbon-rich film) and He/O<sub>2</sub> plasma (surface oxidation) to the same deposition area, here achieved by a treatment of a rotating substrate by two jets with only He/HMDSO on one hand and He/O<sub>2</sub> on the other hand, cf the scheme of the experiment in Fig. 5. Interestingly, the SiO<sub>x</sub> film similar to films deposited with HMDSO and O<sub>2</sub> in one jet, can be deposited in this way, cf. FTIR spectra in Fig. 5. Moreover, the carbon content is under the detection limit of the FTIR. Apparently, the oxidation of carbon from the surface of the growing film, most probably by atomic oxygen produced in the second jet, is the main carbon elimination step during the deposition of carbon free SiO<sub>x</sub> films in this case. It should be noted that application of just O<sub>2</sub> flow without plasma in the second jet was not enough to induce this effect and just carbon rich films with very similar FTIR spectra as those deposited without rotating disk and without addition of O<sub>2</sub> has been deposited.

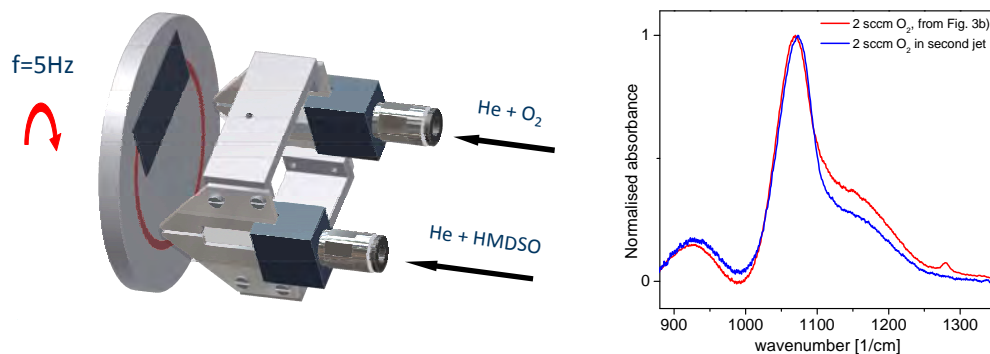


Fig. 5. The scheme of the experiment with the rotating substrate and the corresponding FTIR spectrum of the deposited film.

The study of HMDSO plasma chemistry in atmospheric pressure non-equilibrium plasmas is an ongoing process and further analysis are still needed for its better understanding and understanding of the  $\text{SiO}_x$  film growth, especially regarding the difference between plasmas with He or Ar as a plasma forming gas.

### Acknowledgement

This work has been done within the project C1 of the research group FOR1123 approved by the German Research Foundation (DFG). This support is gratefully acknowledged.

### References

- [1] K.H. Becker, K.H. Schoenbach, and J.G. Eden. *J. Phys. D* 39 (2006) R55
- [2] R. Foest, M. Schmidt, and K. Becker. *Int. J. Mass Spectrometry*, 248 (2006) 87
- [3] F. Iza, G.J. Kim, S.M. Lee, J.K. Lee, J.L. Walsh, Y.T. Zhang, and M.G. Kong. *Plasma Process. Polym.* 5 (2008) 322
- [4] A. El-Habachi, W. Shi, M. Moselhy, Robert H. Stark, and K. H. Schoenbach. *J. Appl. Phys.* 88 (2000) 3220
- [5] J. G. Eden, S.-J. Park, N. P. Ostrom, and K.-F. Chen. *J. Phys. D* 38 (2005) 1644
- [6] J. Franzke, K. Kunze, M. Miclea, and K. Niemax. *J. Anal. At. Spectrom.* 16 (2003) 802
- [7] R. Rahul, O. Stan, A. Rahman, E. Littlefield, K. Hoshimiya, A. P. Yalin, A. Sharma, A. Pruden, C. A. Moore, Z. Yu, and G. J. Collins. *J. Phys. D*, 38 (2005) 1750
- [8] T. Ichiki, R. Tauro, and Y. Horiike. *J. Appl. Phys.* 95 (2004) 35
- [9] R. M. Sankaran and K. P. Giapis. *J. Phys. D* 36 (2003) 2914
- [10] Y. Shimizu, T. Sasaki, T. Ito, K. Terashima, and N. Koshizaki. *J. Phys. D* 36 (2003) 2940
- [11] V. Raballand, J. Benedikt, and A. von Keudell. *Appl. Phys. Lett.* 92 (2008) 091502
- [12] V. Raballand, J. Benedikt, S. Hoffmann, M. Zimmermann, and A. von Keudell. *J. Appl. Phys.* 105 (2009) 083304
- [13] A. Yanguas-Gil, K. Focke, J. Benedikt, and A. von Keudell. *J. Appl. Phys.* 101 (2007) 103307
- [14] J. Benedikt, K. Focke, A. Yanguas-Gil, and A. von Keudell. *Appl. Phys. Lett.* 89 (2006) 251504
- [15] J. Benedikt, V. Raballand, A. Yanguas-Gil, K. Focke, and A. von Keudell. *Plasma Phys. Control. Fusion* 49 (2007) B419
- [16] V. Schulz-von der Gathen, V. Buck, T. Gans, N. Knake, K. Niemi, S. Reuter, L. Schaper, and J. Winter. *Contr. Plasma Phys.* 47 (2007) 510
- [17] J. Benedikt, D. Ellerweg, and A. von Keudell. *Rev. Sci. Instrum.* 80 (2009) 055107
- [18] D. Ellerweg, J. Benedikt, A. von Keudell, N. Knacke, and V. Schulz von der Gathen. *New J. Phys.* 12 (2010) 013021
- [19] G. Borvon, A. Goulet, A. granier, and G. Turban. *Plasmas Polymers* 7 (2002) 341
- [20] M.F.A.M. van Hest, B. Mitu, D.C. Schram, and M.C.M. van de Sanden. *Thin Solid Films* 449 (2004) 52
- [21] F. Massines, N. Gheradi, and A. Fornelliand S. Martin. *Surf. Coat. Technol.* 200 (2005) 1855
- [22] S. Starostine, E. Aldea, H. de Vries, M. Creatore, and M.C.M. van de Sanden. *Plasma Process. Polym.* 4 (2007) S440
- [23] F. Fanelli, S. Lovascio, R. d'Agostino, F. Arefi-Khonsari, and F. Fracassi. *Plasma Process. Polym.*, 7 (2010) 535

## **Address List**

**Dr. Hassan Abdoul-Carime**

Institut de Physique Nucléaire - Lyon  
4 rue Enrico Fermi  
69622 Villeurbanne, France  
hcarime@ipnl.in2p3.fr

**Dr. Daniela Ascenzi**

University of Trento  
Faculty of Science  
Department of Physics  
Via Sommarive 14  
38123 Povo, Trento, Italy  
ascenzi@science.unitn.it

**Dr. Nail Asfandiarov**

Institute of Molecular & Crystal Physics  
Atomic Collision Physics Lab  
October prospect 151  
450075 Ufa, Russia  
nail\_asf@mail.ru

**Dr. Wiesława Barszczewska**

Siedlce University  
Konarskiego 2  
08-110 Siedlce, Poland  
wbar@uph.edu.pl

**Dr. Petr Bartos**

University of South Bohemia  
Faculty of Education  
Jeronymova 10  
371 15 České Budějovice, Czech Rep.  
bartos-petr@seznam.cz

**Prof. Kurt Becker**

NYU-Poly  
Physics  
6 MetroTech Center  
11201 Brooklyn, NY, USA  
kbecker@poly.edu

**Prof. Jan Benedikt**

Ruhr University Bochum  
Faculty of Physics and Astronomy  
Universitaetsstrasse 150  
44780 Bochum, Germany  
jan.benedikt@rub.de

**Prof. Ralf Peter Brinkmann**

Ruhr University Bochum  
Universitaetsstrasse 150  
44801 Bochum, Germany  
Ralf-Peter.Brinkmann@tet.ruhr-uni-bochum.de

**Dr. Andrej Bucek**

Comenius University  
Faculty of Mathematics, Physics and Informatics  
Mlynska dolina F2  
842 48 Bratislava, Slovakia  
bucek@gimmel.ip.fmph.uniba.sk

**Dr. Nathalie Carrasco**

Université de Versailles St Quentin  
LATMOS  
11 bld d'Alembert  
78280 Guyancourt, France  
nathalie.carrasco@latmos.ipsl.fr

**Prof. Mirko Černák**

Masaryk University  
Faculty of Science  
Kotlarska 2  
61137 Brno, Czech Rep.  
cernak@gimmel.ip.fmph.uniba.sk

**Prof. Valeriy Chernyak**

Kyiv National Taras Shevchenko University  
Radio Physical  
Volodymyrska 64  
01033 Kyiv, Ukraine  
chernyak\_v@ukr.net

**Prof. Ivan Chodak**

Slovak Academy of Sciences  
Polymer Institute  
Dúbravská 9  
84501 Bratislava, Slovakia  
upolchiv@savba.sk

**Dr. Oleksiy Chumak**

Institute of Plasma Physics AS CR, v.v.i.  
Thermal Plasma Department  
Za Slovankou 3  
18200 Prague, Czech Rep.  
chumak@ipp.cas.cz

**Dr. Martin Člupek**

Institute of Plasma Physics AS CR, v.v.i.  
Pulse Plasma Systems Dept  
Za Slovankou 3  
182 00 Praha, Czech Rep.  
clupek@ipp.cas.cz

**Mr. Marián Danko**

Comenius University  
Faculty of Mathematics, Physics and Informatics  
Mlynská dolina F2  
84248 Bratislava, Slovakia  
mdanko@centrum.sk

**Mr. Matthias Daxner**

University of Innsbruck  
Institute for Ionphysics and Applied Physics  
Techinkerstrasse 25b  
6020 Innsbruck, Austria  
matthias.daxner@uibk.ac.at

**Prof. Pierre Defrance**

Catholic University of Louvain  
Institute of Condensed Matter and Nanosciences  
Chemin du Cyclotron, 2  
1348 Louvain-la-Neuve, Belgium  
pierre.defrance@uclouvain.be

**Ms. Aranka Derzsi**

Research Institute for Solid State Physics and Optics  
Konkoly-Thege 29-33  
1121 Budapest, Hungary  
derzsi@mail.kfki.hu

**Mr. Petr Dohnal**

Charles University in Prague  
Faculty of Mathematics and Physics  
Ke Karlovu 3  
12116 Praha 2, Czech Rep.  
pr.dohnal@seznam.cz

**Mr. Kim Dong Hong**

Jeju National University  
Chemical and Biological Engineering  
Ara 1-dong, 102 Jejud  
690-756 Jeju, South Korea  
smokie1@jejunu.ac.kr

**Dr. Zoltan Donko**

Research Institute for Solid State Physics and Optics  
Konkoly Thege Miklos 29-33  
1121 Budapest, Hungary  
donko@mail.kfki.hu

**Mr. Jang Doo-II**

Jeju National University  
Energy Chemical Engineering  
Ara 1-dong, 102 Jejud  
690-756 Jeju, South Korea  
parachute@jejunu.ac.kr

**Prof. Miroslaw Dors**

Polish Academy of Sciences  
Institute of Fluid Flow Machinery  
Fiszera 14  
80952 Gdansk, Poland  
mdors@imp.gda.pl

**Dr. Juraj Fedor**

J. Heyrovsky Institute of Physical Chemistry  
Dolejskova 3  
18223 Prague, Czech Rep.  
juraj.fedor@jh-inst.cas.cz

**Dr. Tom Field**

Queen's University Belfast  
Centre for Plasma Physics  
School of Mathematics and Physics  
University Road  
BT7 1NN Belfast, United Kingdom  
t.field@qub.ac.uk

**Dr. Hamid Ghomi**

Shahid Behesti University  
Laser and Plasma Research Institute  
Velenjak  
1983963113 Tehran, Iran  
h-gmdashty@cc.sbu.ac.ir

**Prof. Juraj Glosik**

Charles University in Prague  
Faculty of Mathematics and Physics  
V Holesovickach 2  
180 00 Prague, Czech Rep.  
juraj.glosik@mff.cuni.cz

**Prof. Bill Graham**

Queens University Belfast  
Centre for Plasma Physics  
University Road  
BT71NN Belfast, United Kingdom  
b.graham@qub.ac.uk

**Mr. Sean Haughey**

Queen's University Belfast  
Centre for Plasma Physics  
School of Mathematics and Physics  
University Road  
BT7 1NN Belfast, United Kingdom  
shaughey08@qub.ac.uk

**Dr. Vladimír Havránek**

Nuclear Physics Institute AS CR, v.v.i.  
Řež  
250 68 Řež near Prague, Czech Rep.  
havranek@ujf.cas.cz

**Mr. Michal Hlína**

Institute of Plasma Physics AS CR, v.v.i.  
Za Slovankou 1782/3  
182 00 Prague, Czech Rep.  
hlina@ipp.cas.cz

**Mr. Gabriel Horváth**

Comenius University  
Faculty of Mathematics, Physics and Informatics  
Mlynská dolina F2  
84248 Bratislava, Slovakia  
horeszka@gmail.com

**Prof. Eugen Illenberger**

Freie Universität Berlin  
Department of Chemistry  
Takustrasse 3  
14195 Berlin, Germany  
iln@chemie.fu-berlin.de

**Prof. Antoni Jówko**

Siedlce University  
3-go Maja 54  
08-110 Siedlce, Poland  
ajowko@uph.edu.pl

**Mr. Pavol Jusko**

Charles University  
Ke Karlovu 3  
12116 Prague, Czech Rep.  
pavol.jusko@gmail.com

**Mr. Tomas Kadlec**

Institute of Plasma Physics AS CR, v.v.i.  
Pulse Plasma Systems Dept.  
Za Slovankou 3  
18200 Praha, Czech Rep.  
tomas.kadlec@fbmi.cvut.cz

**Mr. Alan Keim**

University of Innsbruck  
Institute for Ionphysics and Applied Physics  
Technikerstrasse 25b  
6020 Innsbruck, Austria  
alan.keim@uibk.ac.at

**Dr. Mansour Khoramabadi**

Boroujerd Azad University  
Department of Physics  
Navab St. - Navab Sq.  
1983963113 Boroujerd, Iran  
makhoram1351@yahoo.com

**Mr. Matej Klas**

Comenius University  
Faculty of Mathematics, Physics and Informatics  
Mlynská dolina F2  
84248 Bratislava, Slovakia  
matej.klas@gmail.com

**Dr. Miloš Konrád**

Institute of Plasma Physics, v.v.i.  
Za Slovankou 3  
182 00 Praha 8, Czech Rep.  
konrad@ipp.cas.cz

**Dr. Janina Kopyra**

Siedlce University  
3 Maja 54  
08-110 Siedlce, Poland  
kopyra@ap.siedlce.pl

**Dr. Martin Kormunda**

Purkinje University  
Horeni 13  
40096 Usti nad Labem, Czech Rep.  
martin.kormunda@ujep.cz

**Dr. Ihor Korolov**

Hungarian Academy of Sciences  
Research Institute for Solid State Physics and  
Optics  
Konkoly-Thege Miklos ut 29-33  
1121 Budapest, Hungary  
ihor.korolov@gmail.com

**Mr. Tomáš Kotřík**

Charles University in Prague  
Faculty of Mathematics and Physics  
Ke Karlovu 3  
12116 Praha 2, Czech Rep.  
kotrik.tomas@gmail.com

**Prof. Frantisek Krcma**

Brno University of Technology  
Faculty of Chemistry  
Purkynova 118  
612 00 Brno, Czech Rep.  
krcma@fch.vutbr.cz

**Dr. Juraj Kronek**

Slovak Academy of Sciences  
Polymer Institute  
Dubravska cesta 9  
84541 Bratislava, Slovakia  
upolkron@savba.sk

**Mr. Marek Kučera**

Comenius University  
Faculty of Mathematics, Physics and Informatics  
Mlynská dolina F2  
84248 Bratislava, Slovakia  
kucera@fmph.uniba.sk

**Prof. Tilmann D. Märk**

University of Innsbruck  
Institute of Ion Physics and Applied Physics  
Faculty of Mathematics, Computer Science and  
Physics  
Technikerstraße 25  
6020 Innsbruck, Austria  
tilmann.maerk@uibk.ac.at

**Prof. Nigel Mason**

The Open UNiversity  
Department of Physics and Astronomy  
Walton Hall  
MK7 6AA Milton Keynes, United Kingdom  
n.j.mason@open.ac.uk

**Prof. Štefan Matejčík**

Comenius University  
Faculty of Mathematics, Physics and Informatics  
Mlynská dolina F2  
84248 Bratislava, Slovakia  
matejcik@fmph.uniba.sk

**Dr. Michal Matejka**

Comenius University in Bratislava  
Faculty of Mathematics, Physics and Informatics  
Mlynská dolina F2  
842 48 Bratislava, Slovakia  
miso.matejka@gmail.com

**Mr. Jindrich Matousek**

University of J.E.Purkinje  
Faculty of Science  
Ceske mladeze 8  
400 96 Usti nad Labem, Czech Rep.  
jindrich.matousek@ujep.cz

**Mr. Ján Matúška**

Comenius university  
Faculty of Mathematics, Physics and Informatics  
Mlynská dolina F2  
84248 Bratislava, Slovakia  
matuska@neon.dpp.fmph.uniba.sk

**Dr. Vera Mazankova**

Brno University of Technology  
Faculty of Chemistry  
Purkyňova 118  
612 00 Brno, Czech Rep.  
mazankova@fch.vutbr.cz

**Ms. Romana Mikšová**

Nuclear Physics Institute AS CR, v.v.i.  
Řež  
250 68 Řež near Prague, Czech Rep.  
miksova@ujf.cas.cz

**Dr. Takao Namihira**

Kumamoto University  
Bioelectrics Research Center  
2-39-1 Kurokami  
860-8555 Kumamoto, Japan  
namihira@cs.kumamoto-u.ac.jp

**Ms. Lucie Němcová**

Brno University of Technology  
Faculty of chemistry  
Purkyňova 464/118  
612 00 Brno, Czech Rep.  
xcnemcova@fch.vutbr.cz

**Prof. Stanislav Novak**

J. E. Purkinje University  
Faculty of Science  
Ceske mladeze 8  
400 96 Usti nad Labem, Czech Rep.  
Stanislav.Novak@ujep.cz

**Ms. Andrea Oravcova**

Slovak University of Technology, Bratislava  
FCHPT  
Radlinskeho 9  
81237 Bratislava, Slovakia  
xoravcovaa@stuba.sk

**Dr. Juraj Országh**

Comenius University  
Faculty of Mathematics, Physics and Informatics  
Mlynská dolina F2  
842 48 Bratislava, Slovakia  
orszagh@fmph.uniba.sk

**Dr. Radomir Panek**

Institute of Plasma Physics AS CR, v.v.i.  
Za Slovankou 3  
18200 Prague, Czech Rep.  
panek@ipp.cas.cz

**Dr. Peter Papp**

Comenius University  
Faculty of Mathematics, Physics and Informatics  
Mlynská dolina F2  
842 48 Bratislava, Slovakia  
papp@fmph.uniba.sk

**Prof. Jaroslav Pavlik**

J. E. Purkinje University  
Faculty of Science  
Česke mládeže 8  
40096 Ústí nad Labem, Czech Rep.  
jaroslav.pavlik@ujep.cz

**Dr. Vratislav Peřina**

Nuclear Physics Institute AS CR, v.v.i.  
Řež  
250 68 Řež near Prague, Czech Rep.  
perina@ujf.cas.cz

**Ms. Lucie Polachova**

Brno University of Technology  
Faculty of Chemistry  
Purkynova 118  
61200 Brno, Czech Rep.  
xcpolachova@fch.vutbr.cz

**Dr. Radek Přikryl**

Brno University of Technology  
Faculty of Chemistry  
Purkynova 464/118  
612 00 Brno, Czech Rep.  
prikryl@fch.vutbr.cz

**Mr. Michal Procházka**

Brno University of Technology  
Faculty of Chemistry  
Purkyňova 118  
61200 Brno, Czech Rep.  
xcprochazkam@fch.vutbr.cz

**Prof. Marija Radmilovic-Radjenovic**

Institute of Physics  
Pregrevica 118  
11080 Zemun, Serbia  
marija@ipb.ac.rs

**Prof. Juergen Roepcke**

INP Greifswald  
Dept. of Plasma Diagnostics  
Felix-Hausdorff-Str. 2  
17489 Greifswald, Germany  
roepcke@inp-greifswald.de

**Mr. Stepan Roucka**

Charles University  
Faculty of Mathematics and Physics  
V Holesovickách 2  
180 00 Prague, Czech Rep.  
stepan.roucka@mff.cuni.cz

**Dr. Martin Sabo**

Comenius University  
Faculty of Mathematics, Physics and Informatics  
Mlynská dolina F2  
84248 Bratislava, Slovakia  
martin.sabo@gmail.com

**Ms. Věra Sázavská**

Brno University of Technology  
Faculty of Chemistry  
Purkyňova 118  
612 00 Brno, Czech Rep.  
xcsazavska@fch.vutbr.cz

**Dr. Julian Schulze**

Hungarian Academy of Sciences  
Institute for Solid State Physics and Optics  
Liliom utca 20  
2040 Budaörs, Hungary  
fjschulze@hotmail.com

**Dr. Galina Shpatakovskaya**

Keldysh Institute of Applied Mathematics RAS  
Miusskaya sq. 4  
125047 Moscow, Russia  
shpagalya@yandex.ru

**Mr. Ivo Soural**

Brno University of Technology  
Faculty of Chemistry  
Purkynova 118  
61200 Brno, Czech Rep.  
xcsoural@fch.vutbr.cz

**Dr. Michal Stano**

Comenius University  
Faculty of Mathematics, Physics and Informatics  
Mlynská dolina F2  
84248 Bratislava, Slovakia  
stano@fmph.uniba.sk

**Dr. Seyed Hassan Tavassoli**

Shahid Beheshti University  
Laser and Plasma Research Institute  
Evin  
1983963113 Tehran, Iran  
h-tavassoli@sbu.ac.ir

**Dr. András Tóth**

Hungarian Academy of Sciences  
Institute of Materials and Environmental  
Chemistry  
Chemical Research Center  
Pusztaszeri út 59-67  
1025 Budapest, Hungary  
totha@chemres.hu

**Dr. Rodica Vladoiu**

Ovidius University  
Physics  
Mamia 124  
900527 Constanta, Romania  
rvladoiu@univ-ovidius.ro

**Mrs. Jana Vyhnalíková**

Brno University of Technology  
Faculty of Chemistry  
Purkyňova 464/118  
61200 Brno, Czech Rep.  
xcvyhnalikova@fch.vutbr.cz

**Dr. Karol Wnorowski**

Siedlce University  
3-go Maja 54  
08-110 Siedlce, Poland  
karolw@uph.edu.pl

**Ms. Magdalena Wolfova**

Slovak University of Technology  
FCHPT  
Radlinskeho 9  
812 37 Bratislava, Slovakia  
magdalena.wolfova@stuba.sk

**Mr. Chang-Heon Yi**

LG Electronics  
Product Engineering Research Institute  
19-1 Cheongho-ri  
451-713 Pyeongtaek-si, South Korea  
changheon.yi@lge.com

**Mr. Samuel Zoettl**

University of Innsbruck  
Institute for Ionphysics and Applied Physics  
Technikerstrasse 25b  
6020 Innsbruck, Austria  
Samuel.Zoettl@uibk.ac.at